



UNIVERSITAT DE BARCELONA

On the experimental and theoretical studies of ZnO precursors: towards Green Chemistry

Alberto Gómez Núñez

ADVERTIMENT. La consulta d'aquesta tesi queda condicionada a l'acceptació de les següents condicions d'ús: La difusió d'aquesta tesi per mitjà del servei TDX (www.tdx.cat) i a través del Dipòsit Digital de la UB (diposit.ub.edu) ha estat autoritzada pels titulars dels drets de propietat intel·lectual únicament per a usos privats emmarcats en activitats d'investigació i docència. No s'autoritza la seva reproducció amb finalitats de lucre ni la seva difusió i posada a disposició des d'un lloc aliè al servei TDX ni al Dipòsit Digital de la UB. No s'autoritza la presentació del seu contingut en una finestra o marc aliè a TDX o al Dipòsit Digital de la UB (framing). Aquesta reserva de drets afecta tant al resum de presentació de la tesi com als seus continguts. En la utilització o cita de parts de la tesi és obligat indicar el nom de la persona autora.

ADVERTENCIA. La consulta de esta tesis queda condicionada a la aceptación de las siguientes condiciones de uso: La difusión de esta tesis por medio del servicio TDR (www.tdx.cat) y a través del Repositorio Digital de la UB (diposit.ub.edu) ha sido autorizada por los titulares de los derechos de propiedad intelectual únicamente para usos privados enmarcados en actividades de investigación y docencia. No se autoriza su reproducción con finalidades de lucro ni su difusión y puesta a disposición desde un sitio ajeno al servicio TDR o al Repositorio Digital de la UB. No se autoriza la presentación de su contenido en una ventana o marco ajeno a TDR o al Repositorio Digital de la UB (framing). Esta reserva de derechos afecta tanto al resumen de presentación de la tesis como a sus contenidos. En la utilización o cita de partes de la tesis es obligado indicar el nombre de la persona autora.

WARNING. On having consulted this thesis you're accepting the following use conditions: Spreading this thesis by the TDX (www.tdx.cat) service and by the UB Digital Repository (diposit.ub.edu) has been authorized by the titular of the intellectual property rights only for private uses placed in investigation and teaching activities. Reproduction with lucrative aims is not authorized nor its spreading and availability from a site foreign to the TDX service or to the UB Digital Repository. Introducing its content in a window or frame foreign to the TDX service or to the UB Digital Repository is not authorized (framing). Those rights affect to the presentation summary of the thesis as well as to its contents. In the using or citation of parts of the thesis it's obliged to indicate the name of the author.

On the experimental and theoretical studies of ZnO precursors: towards Green Chemistry

By

ALBERTO GÓMEZ NÚÑEZ



UNIVERSITAT DE
BARCELONA

Institute of Nanoscience and Nanotechnology (IN²UB)
Department of Electronics and Biomedical Engineering
UNIVERSITY OF BARCELONA

A dissertation submitted to the University of Barcelona in accordance with the requirements of the degree of DOCTOR OF PHILOSOPHY in Nanoscience. Faculty of Physics.

OCTOBER 2017

Tutor and Director: Dr. Anna M^a Vilà i Arbonès

RESUMEN

El primer objetivo del presente trabajo ha sido el del estudio profundo del precursor más frecuentemente utilizado para generar óxido de cinc mediante descomposición térmica de la tinta que lo contiene. La causa de este primer estudio fue la necesidad de entender y poner un poco más de orden en los procesos que intervienen no sólo en la estabilidad de este precursor en condiciones normales sino en la descomposición que genera ese ZnO. Ambas necesidades de conocimiento son fundamentales cuando se requiere la utilización de una tinta (que no contiene ya el ZnO deseado en forma de nano-partículas) para producir ZnO con aplicaciones en electrónica impresa. Aunque un extenso número investigadores, durante el auge de esta tecnología de impresión de materiales, han hecho descubrimientos muy interesantes en lo relativo a las propiedades del ZnO final dependiendo de las condiciones iniciales de esta tinta, así como su degradación y su descomposición, no se han llegado a descifrar los motivos por los cuales el ZnO tiene esa propiedad y no otra con esas condiciones iniciales, por lo que, finalmente, se ha ido obteniendo con los años una especie de *receta de cocina* para la síntesis de ZnO mediante esa tinta específica, en forma de catálogo o de lista de variables a tener en cuenta durante el proceso. Esto, sin embargo, aunque muy útil desde el punto de vista ingenieril, es limitado en lo que al método científico se refiere.

Con esto en mente el primer esfuerzo considerable que se llevó a cabo fue el de la resolución de la estructura que genera la sal de Zn (Acetato de cinc dihidratado) con el estabilizador (Ethanolamina) que comúnmente se emplea para evitar aglomeraciones de Zn en la tinta que previene no sólo su correcta impresión, sino la homogeneidad de producto en la impresión y la posibilidad de almacenaje largos periodos de tiempo antes de su uso. Es imprescindible conocer primero el material con el que se va a trabajar. Experimentos de Resonancia magnética, de Espectroscopia infrarroja y de Espectrometría de masas de este precursor dieron luz sobre, como mínimo los enlaces específicos que se estaban produciendo y de las unidades de masa molecular que se estaban obteniendo o, lo que es lo mismo, las distintas nucleaciones posibles que se estaban dando. No contentos con esto, se intentó resolver la estructura mediante difracción de monocristal. Puesto que parecía que los posibles cristales que aparecían no eran de calidad para aplicar la técnica, no hubo éxito en esta hazaña. Lo único que quedaba entonces era el camino largo y tedioso: La resolución de estructura mediante difracción en polvo. La mezcla altamente viscosa de sal y estabilizador fue almacenada con gel de sílice durante meses hasta que esa forma viscosa se hubo secado, momento en el cual se procedió a realizar experimentos de difracción en polvo con

éxito (Figura 1). Viendo que, fuera del ambiente con gel de sílice, de nuevo la muestra almacenada volvía a adquirir esa forma viscosa, se recogió el espectro de difracción pasados 5 días, momento en el que sólo era posible observar una de las reflexiones. Estos experimentos de difracción en polvo fueron útiles para conocer el tipo de simetría, volumen y tipo de cristal que compone la estructura así como, teniendo en cuenta las unidades de masa que surgieron con Espectrometría de masas, conocer la cantidad de estas unidades que componen la celda de la estructura.

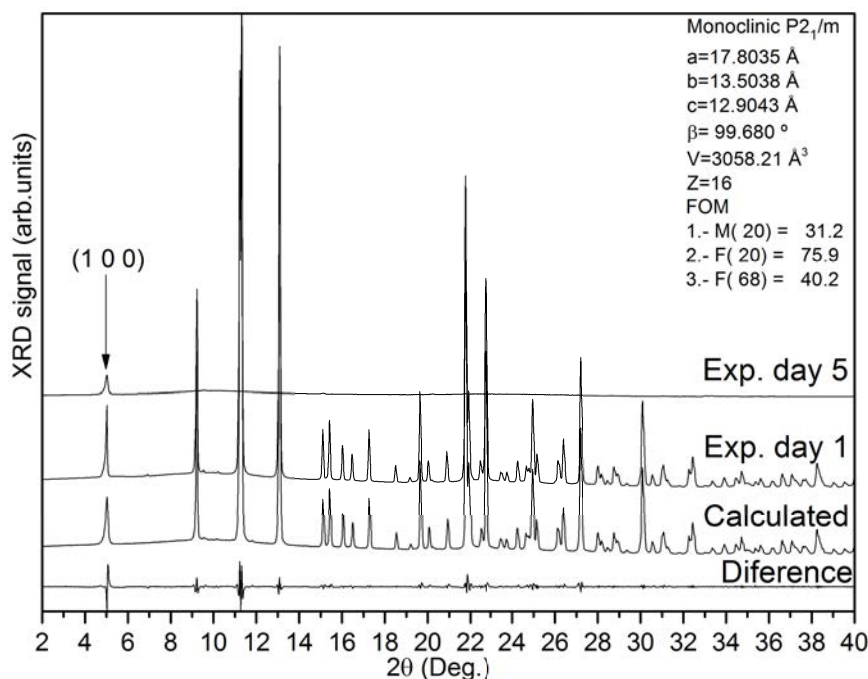


Figura 1: Experimentos de difracción polvo del precursor seco (Ethanolamina + Acetato de zinc dihidratado - Exp. day 1), difractograma calculado para un sistema monoclinico $P2_1/m$ con los parámetros mostrados en la esquina superior derecha y la diferencia entre ambos. Después de 5 días de almacenaje en condiciones normales, (Exp. day 5) sólo permanece la reflexión (100).

El siguiente paso fue el de diseñar el modelo molecular a partir de todos los experimentos anteriores. Para esto se hizo uso de simulaciones con el programa Gaussian03. Con este, se optimizaron las estructuras moleculares del monómero, dímero y tetrámero (Figura 2), siendo este el punto de partida de todas las simulaciones que se llevarían a cabo más adelante. La optimización del tetrámero fue muy útil para poder realizar un refinamiento Rietveld y acercarnos más a la estructura final (que finalmente no ha podido ser publicada). Gaussian03 fue también útil en el estudio de degradación que veíamos se estaba produciendo al dejar la tinta unas semanas en contacto con luz y aire. Se demostró que tanto la luz como el dióxido de carbono (un hecho probado por otros autores sólo en aminoalcoholes) potenciaban la excitación electrónica a orbitales responsables de la desestabilización de enlaces clave en la degradación del precursor y la posterior modificación de la apariencia de la tinta (color anaranjado del disolvente y un precipitado blanco producido por enlaces Zn-OH). Se propuso una teoría para explicar este cambio

de apariencia (los compuestos que se estaban generando y modificando el color del disolvente) y que después sería validada con los experimentos térmicos.

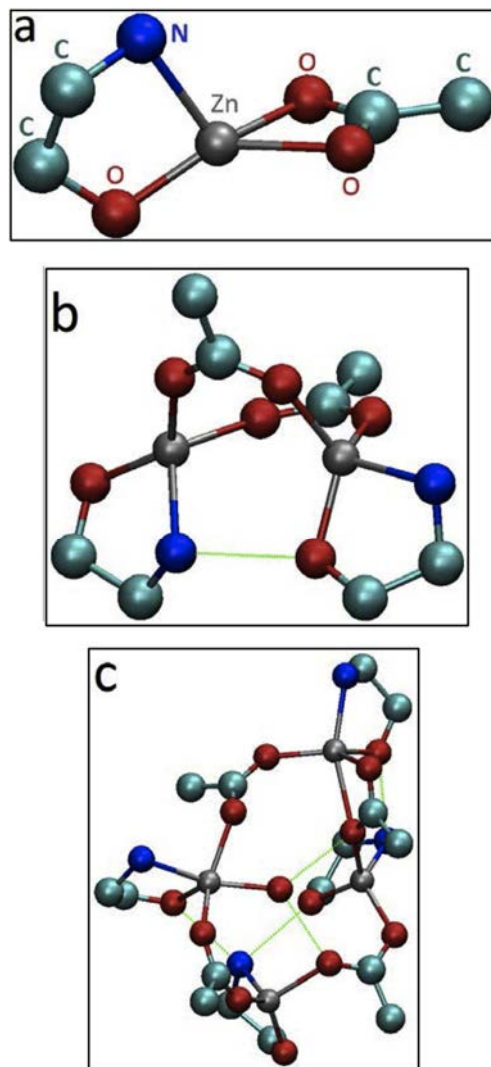


Figura 2: Geometrías optimizadas del monómero (a), dímero (b) and tetrámero (c) usando el funcional UB3LYP y la base LANLD2DZ. Los átomos de hidrógeno se han omitido por claridad.

Por lo que respecta a la formación de ZnO a partir de la descomposición térmica del precursor, análisis térmicos y de dinámica molecular (con el programa CPMD) fueron de la mano en este estudio. Se pudo demostrar el motivo por el cual el ZnO final estaba teniendo trazas de nitrógeno incluso a altas temperaturas. Para ello, presentó una teoría que tenía en cuenta los análisis de gases salientes durante la descomposición (Figuras 3 y 4). En ella, el compuesto con masa $m/z=44$ se podía explicar, mediante cálculos, con la aparición de compuestos cíclicos nitrogenados. Además se validó la teoría sobre los compuestos que surgen cuando una tinta se degrada, relacionando este hecho con una familia de masas (generadas a partir de la masa $m/z=76$) en el análisis de gases salientes. Aunque también se pudo estudiar con detalle el momento de la aparición

del ZnO cristalino, la evolución térmica del tamaño de cristal y de la pureza del material que se iba obteniendo, la presencia incontrolada de nitrógeno a altas temperaturas (que muchas publicaciones anteriores no estaban teniendo en cuenta) era un hecho grave.

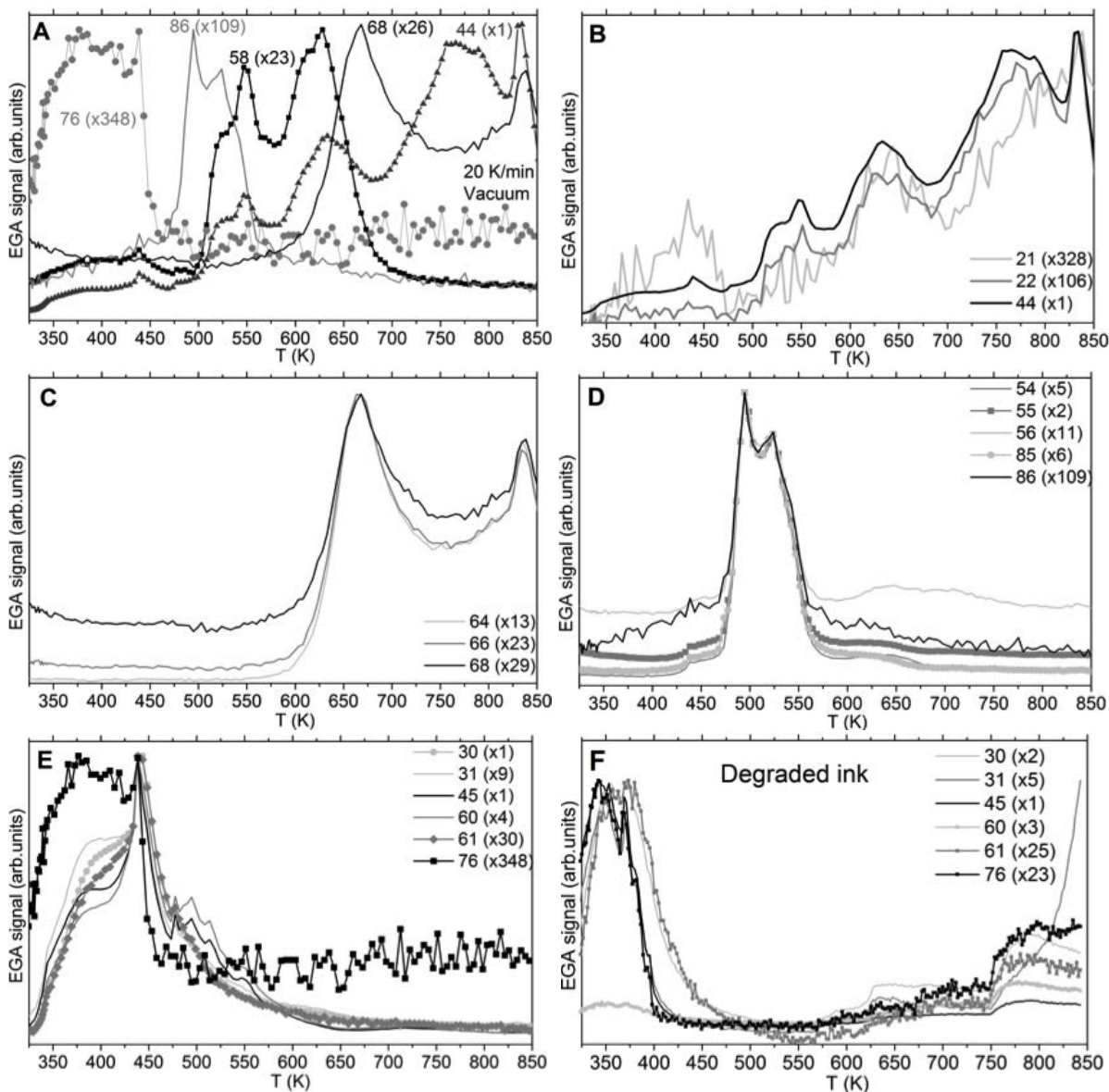


Figura 3: Señales EGA normalizadas con sus respectivos factores de normalización en paréntesis. Las masas m/z detectadas de 12 a 86 fueron separadas por sus comportamientos térmicos, donde cada grupo es representado por una masa principal (A), y clasificadas en esos grupos (B-E). Dejando de lado la masa $m/z = 44$ en el rango 500 - 680 K, la $m/z = 58$ tiene un comportamiento térmico único. Las otras masas m/z detectadas pueden deconvolucionarse siguiendo algunos de estos grupos. En (F), se muestran también las señales EGA de los compuestos relacionados con la masa $m/z = 76$ (como en el caso de E) para la muestra de EA+ME degradada.

Puesto que se había llegado a un nivel profundo de detalle con este precursor, se quiso investigar la dependencia del tipo de estabilizador en esta problemática. Para ello, siete aminoalcoholes

con el mismo esqueleto que la ethanolamina (Figura 5) fueron utilizados en este segundo gran estudio con el objetivo de conocer qué relevancia tiene la elasticidad o rigidez del aminoalcohol en los efectos vistos anteriormente y, por tanto, en la estabilidad y la descomposición del precursor. Para esto, los siete aminoalcoholes con el mismo esqueleto que la ethanolamina (EA) disponían de diferentes radicales situados en dos zonas concretas a la par que interesantes del cuerpo del aminoalcohol.

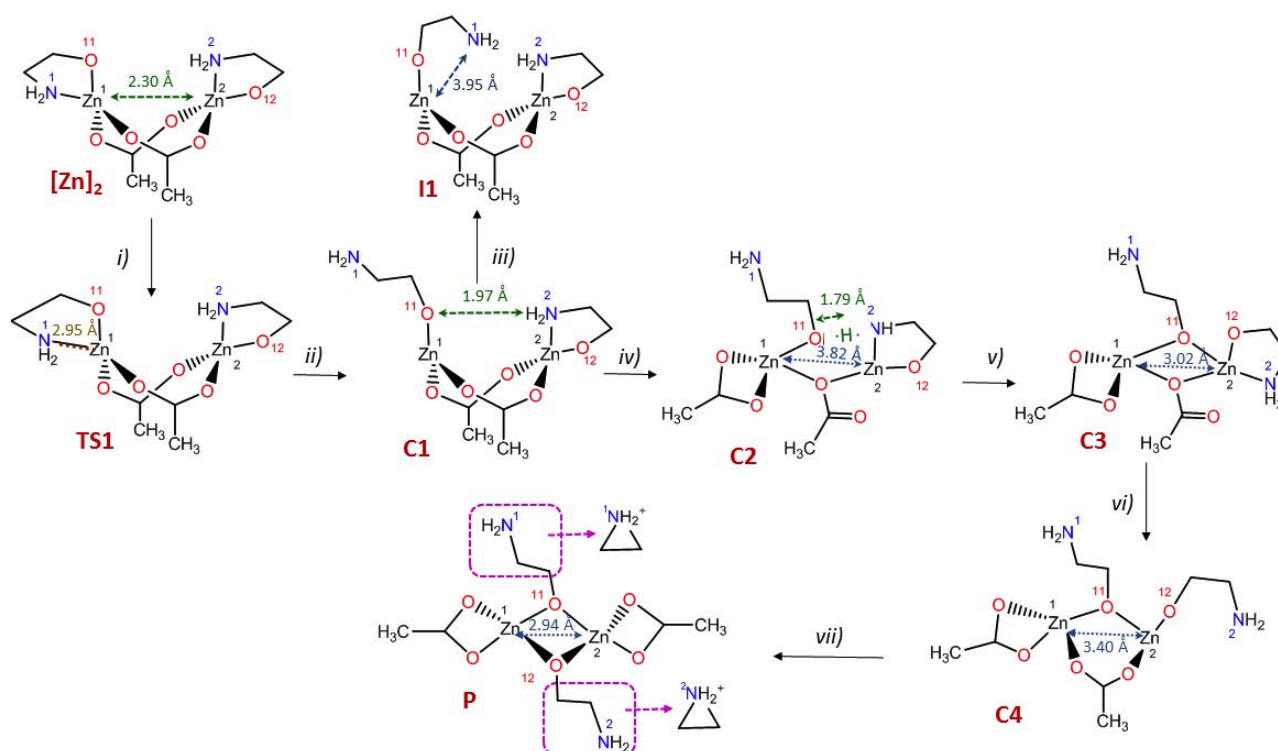


Figura 4: Esquema propuesto sobre la modificación del dímoro para generar la molécula triangular, según resultados de la metadinámica.

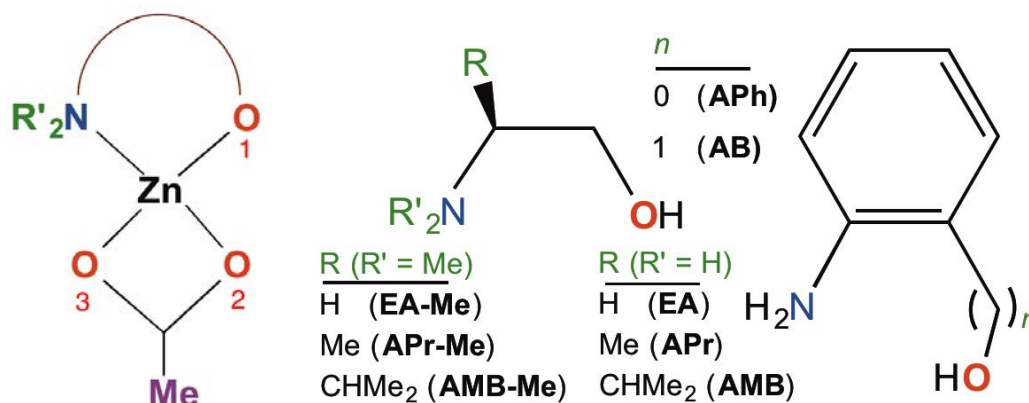


Figura 5: Fórmula química del precursor (izquierda), donde los 8 aminoalcoholes usados en el presente estudio están representados en la parte central (alifáticos) y la parte derecha (aromáticos).

Por motivos de accesibilidad material a algunos de estos siete aminoalcoholes, se decidió tratar experimentalmente cuatro de los siete, pero seguir tratando los siete desde el punto de vista computacional. Los cuatro aminoalcoholes fueron: (S)-(+)-2-amino-1-propanol (APr), (S)-(+)-2-amino-3-methyl-1-butanol (AMB), 2-amino-phenol (APh) y 2-aminobenzyl alcohol (AB). De estos, dos son, como en el caso de la etanolamina, alifáticos y dos son aromáticos. Así pues, se disponía de aminoalcoholes con volumen y rigidez crecientes. De los tres aminoalcoholes alifáticos a comparar, se decidió simular, además, el caso en el que los protones del nitrógeno fuesen substituidos por metilos (EA-Me, APr-Me y AMB-Me - Figura 5), de manera que se pudiera estudiar la dependencia de los radicales utilizados en la intensidad del enlace del aminoalcohol con el Zn en distintas condiciones.

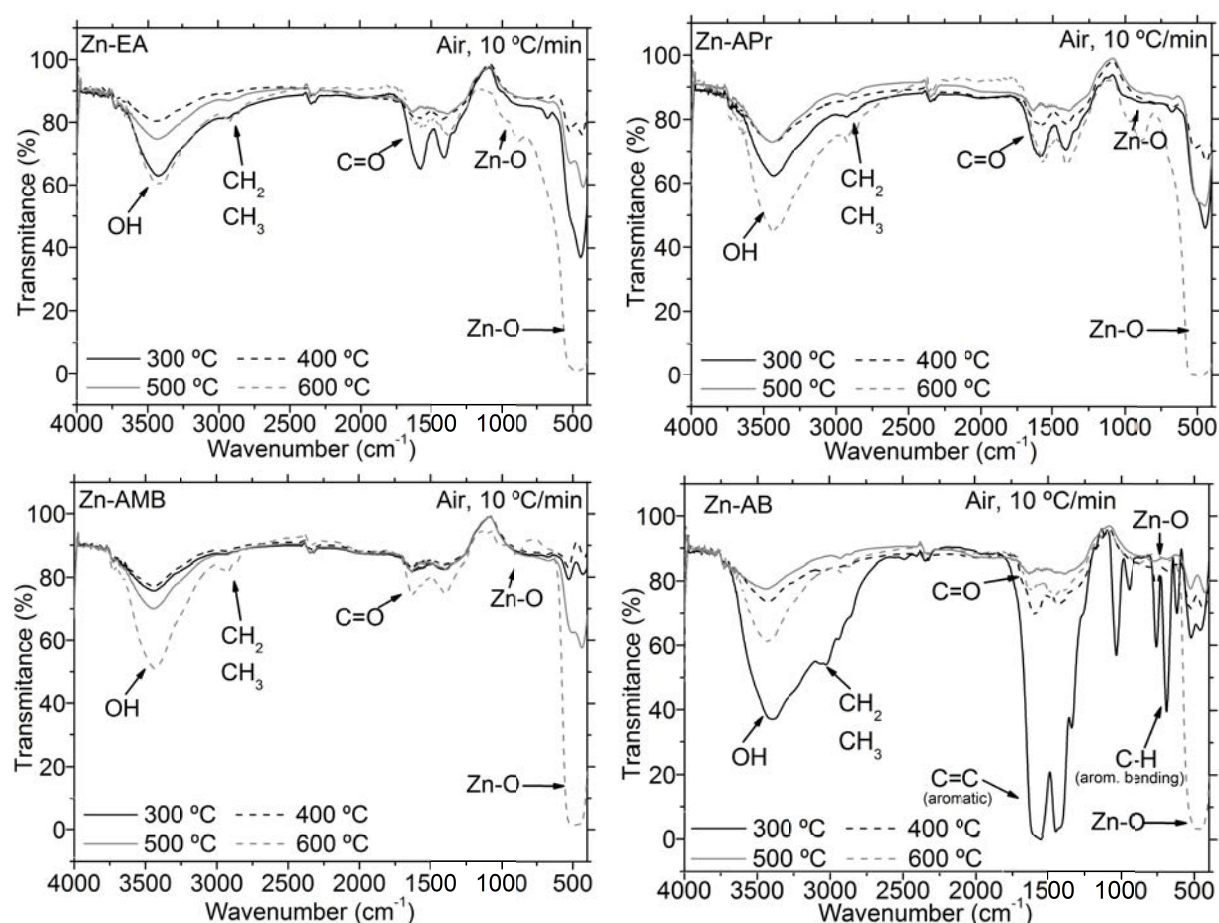


Figura 6: Espectros IR de los precursores nitrogenados (Zn-EA, Zn-APr, Zn-AMB y Zn-AB) a diferentes temperaturas.

Los experimentos demostraron que el uso de cualquiera de los tres aminoalcoholes alifáticos produce una mayor estabilidad de la tinta a temperatura ambiente y en contacto con luz y dióxido de carbono si se comparan con el caso del uso de aminoalcoholes aromáticos, donde la degradación sucede en el plazo de minutos (2-amino-phenol) u horas (2-aminobenzyl alcohol). Además la generación de ZnO a partir de la descomposición de los precursores formados por

cualquiera de esos tres aminoalcoholes alifáticos, no producía un cambio substancial, puesto que seguía produciéndose un paso de descomposición a los 250 °C seguido por un menor paso de descomposición a los 370 °C, en contraste con el caso del uso de aminoalcoholes aromáticos, que padecen una importante descomposición sobre los 400 °C. Además, para el caso de uno de los dos aromáticos, el que produce el precursor más rígido con diferencia, el ZnO final no formaba capa, sino polvo, debido a la gran combustión que genera la descomposición del anillo aromático. Por lo que respecta a los otros 4 casos (3 alifáticos y uno aromático), en cuanto a morfología de la capa, pureza y cristalización del ZnO con la temperatura, se hicieron experimentos de análisis elemental, microscopía electrónica, espectroscopía infrarroja y difracción (Figura 6 y Cuadro 1).

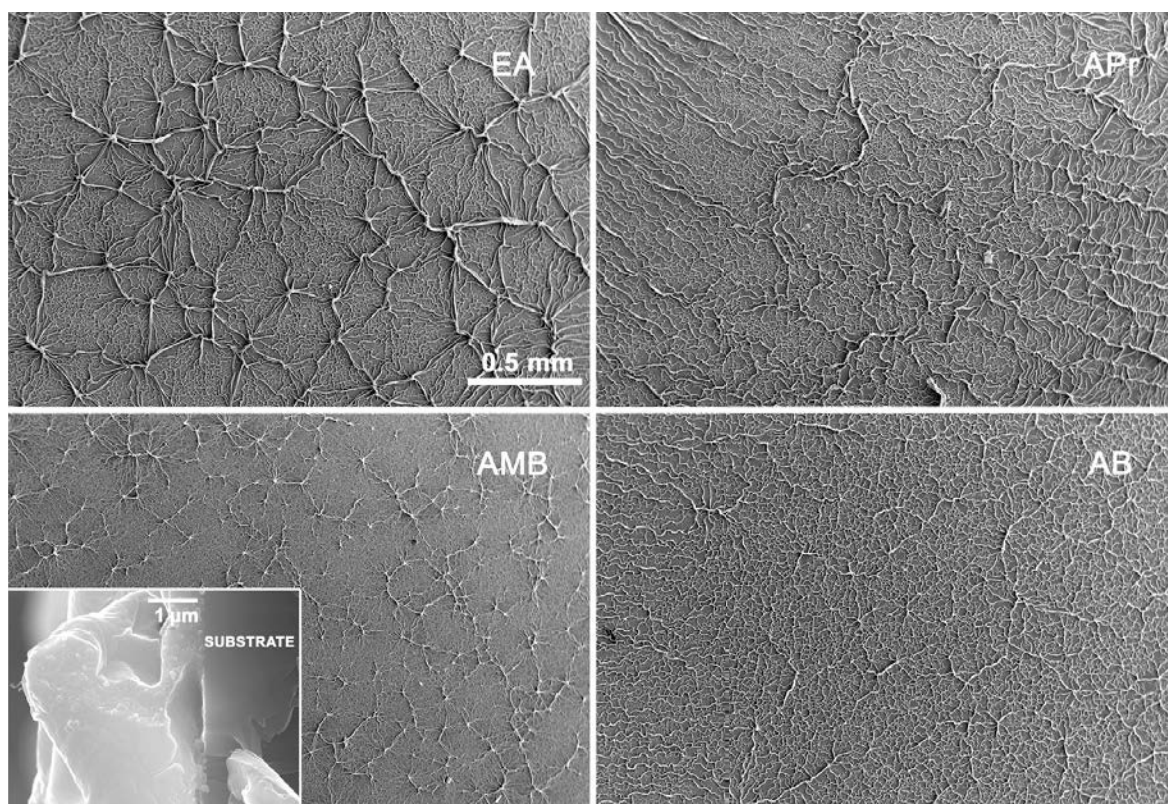


Figura 7: Imágenes SEM de las capas de las tintas de los 4 precursores tratadas a 600 °C. Recuadro: Sección transversal de la capa de **Zn-AMB**.

Comparado con el precursor formado utilizando ethanolamina como estabilizador, en el caso del uso de (S)-(+)-2-amino-1-propanol y 2-aminobenzyl alcohol, la apariencia del ZnO resultante, desde el punto de vista de la difracción, era más monocristalina, en contraste con el caso del uso de (S)-(+)-2-amino-3-methyl-1-butanol, para el cual el ZnO final tenía la misma apariencia cristalina. Sin embargo, en lo que respecta la pureza de ese ZnO, se detecta una mínima cantidad de carbono e hidrógeno (dentro incluso de la capacidad de detección del aparato) en el caso del (S)-(+)-2-amino-1-propanol, mientras que para el caso de 2-aminobenzyl alcohol, la contaminación es 10 veces mayor, debido a los restos del gran anillo aromático que contiene el aminoalcohol. Comparando esté caso de uso de un aminoalcohol aromático con el caso del uso del otro aminoalcohol aromático

(2-amino-phenol), donde el ZnO no formaba capa, se puede apreciar la enorme dependencia de la rigidez del aminoalcohol en las propiedades del ZnO final. En este caso, aunque el volumen del aminoalcohol sea aproximadamente el mismo, la única (y enorme) diferencia entre ellos es un "codo" extra formado por un carbono de más, que provee de una mayor flexibilidad a la molécula ante vibraciones, torsiones y estreses durante la descomposición térmica.

Cuadro 1: Análisis elemental de los precursores alifáticos (tabla superior) y aromáticos (tabla inferior) (Abundancia en % ($\pm 0,2$))

T (°C)	Zn-EA			Zn-APr			Zn-AMB		
	N	C	H	N	C	H	N	C	H
Initial	7.6	26.1	4.9	7.1	30.3	5.6	6.2	37.2	6.6
300	1.2	6.9	0.9	1.3	12.0	1.3	0.7	12.3	1.3
400	1.3	6.9	0.8	1.0	5.8	0.7	0.6	5.8	0.7
500		2.9	0.5		0.8			3.6	
600	≤ 0.2	≤ 0.2	≤ 0.2	≤ 0.2	≤ 0.2	≤ 0.2	≤ 0.2	0.4	≤ 0.2

T (°C)	Zn-AB			Zn-APh		
	N	C	H	N	C	H
Initial	5.7	43.9	4.5	6.0	41.4	3.9
300	2.2	32.2	3.5	5.2	42.2	3.2
400	4.3	29.3	2.0	4.5	33.3	2.4
500	0.6	7.1	0.9	3.0	20.7	1.9
600	0.4	3.5	≤ 0.2	≤ 0.2	0.7	≤ 0.2

En todos los casos en los que estos aminoalcoholes formaban capa, la apariencia de esta capa de ZnO, desde el punto de vista de microscopía electrónica, era la misma (Figura 7). En estas, aunque sin discontinuidades, se formaban el mismo tipo de estructuras (llamados *wrinkles*, o arrugas en forma de neuronas) debidas a tensiones y estreses internos en la capa durante la descomposición. Estas arrugas disminuían en tamaño y grosor a medida que se aumentaba el tamaño del aminoalcohol alifático utilizado. Así pues, se pudo confirmar que, efectivamente, la rigidez del aminoalcohol (no tanto el volumen del mismo) tiene un claro efecto en la calidad del material final. Se confirmó que el caso del uso de aminoalcoholes aromáticos (que o no forman capa o bien contienen demasiadas trazas orgánicas) aunque flexibles, podría contraproducente su uso desde el punto de vista de estabilidad a temperatura ambiente. Por lo que respecta a los alifáticos, estos son una mejor opción, generando un ZnO con una menor presencia orgánica (aunque a demasiado altas temperaturas). Desde el punto de vista computacional el estudio comparativo de los ocho precursores (los cinco anteriores más los tres con metilos sustituyendo los protones del nitrógeno) clarifica, aun más si cabe, la influencia de la incorporación de sustituyentes en el esqueleto de la ethanolamina, en la distribución de cargas, en sus propiedades de estabilidad (Cuadro 2) cuando se une al Zn y en la descomposición térmica del precursor formado. En general, para los seis aminoalcoholes alifáticos, el HOMO está centrado en el grupo amino y la diferencia energética HOMO-LUMO es muy superior al caso del uso de aminoalcoholes aromáticos, demostrando el motivo por el cual se tuvieron los resultados experimentales concernientes a la

estabilidad nombrados anteriormente.

Cuadro 2: Cálculos TD-DFT. Longitudes de onda de excitación (λ), fuerza de oscilación y probabilidad (en %) de transición HOMO-LUMO para el caso de las geometrías optimizadas de los 8 precursores.

	λ (nm)	assignment	oscill. strength	wt. (%)		λ (nm)	assignment	oscill. strength	wt. (%)	
Zn-EA	269.07	HOMO \rightarrow LUMO	-0.298	18	Zn-EA-Me	266.7	HOMO \rightarrow LUMO	-0.405	33	
		HOMO \rightarrow LUMO+1	0.617	76			HOMO \rightarrow LUMO+1	0.561	63	
		HOMO \rightarrow LUMO+2	0.106	2			HOMO \rightarrow LUMO+4	-0.112	3	
		HOMO \rightarrow LUMO+3	-0.116	3			249.6	HOMO \rightarrow LUMO	-0.466	44
252.63	HOMO \rightarrow LUMO	-0.380	29	HOMO \rightarrow LUMO+1	0.521	54				
	246.81	HOMO \rightarrow LUMO+1	0.587	69	244.7	HOMO-1 \rightarrow LUMO	-0.374	28		
HOMO-1 \rightarrow LUMO		-0.326	21	HOMO-1 \rightarrow LUMO+1		0.581	68			
HOMO-1 \rightarrow LUMO+1		0.602	73	HOMO-1 \rightarrow LUMO+4		-0.109	2			
Zn-APr	266.66	HOMO \rightarrow LUMO+1	-0.684	94	Zn-APr-Me	267.5	HOMO \rightarrow LUMO	-0.433	38	
		HOMO \rightarrow LUMO+2	-0.106	2			HOMO \rightarrow LUMO+1	0.541	58	
		HOMO \rightarrow LUMO+4	0.112	3			HOMO \rightarrow LUMO+4	-0.103	2	
		249.87	HOMO \rightarrow LUMO+1	0.692			96	250.5	HOMO \rightarrow LUMO	0.511
244.97	HOMO-1 \rightarrow LUMO+1		-0.683	93	HOMO \rightarrow LUMO+1	-0.477	45			
	Zn-AMB	266.82	HOMO \rightarrow LUMO	0.196	8	245.6	HOMO-1 \rightarrow LUMO	0.404	33	
HOMO \rightarrow LUMO+1			0.653	85	HOMO-1 \rightarrow LUMO+1		-0.562	63		
HOMO \rightarrow LUMO+2			0.112	3	HOMO-1 \rightarrow LUMO+4		0.102	2		
251.14			HOMO \rightarrow LUMO+4	-0.116	3		Zn-AMB-Me	268.1	HOMO \rightarrow LUMO	-0.441
	246.37	HOMO \rightarrow LUMO	0.292	17	HOMO \rightarrow LUMO+1	0.534			57	
Zn-APh		346.42	HOMO \rightarrow LUMO+1	0.633	80	251.4	HOMO \rightarrow LUMO	0.534	57	
	HOMO-1 \rightarrow LUMO		-0.228	10	HOMO \rightarrow LUMO+1		-0.449	40		
	HOMO-1 \rightarrow LUMO+1		-0.645	83	246.7		HOMO-1 \rightarrow LUMO	0.415	34	
	HOMO-1 \rightarrow LUMO+2		-0.102	2			HOMO-1 \rightarrow LUMO+1	-0.554	61	
Zn-AB	336.3	HOMO-1 \rightarrow LUMO+4	0.107	2	336.3	HOMO-3 \rightarrow LUMO	0.243	12		
		346.42	HOMO-1 \rightarrow LUMO+1	-0.269		14	HOMO-3 \rightarrow LUMO+1	-0.315	20	
			HOMO \rightarrow LUMO+1	0.520		54		HOMO-2 \rightarrow LUMO	0.392	31
		330.37	HOMO \rightarrow LUMO+3	-0.375		28	HOMO-2 \rightarrow LUMO+1	0.291	17	
			292.53	HOMO-1 \rightarrow LUMO+1		0.253		13	HOMO-2 \rightarrow LUMO+3	-0.115
		Zn-AB		289.2		HOMO \rightarrow LUMO+1	0.471	44	289.2	HOMO-1 \rightarrow LUMO
HOMO \rightarrow LUMO+3	0.444		39		HOMO \rightarrow LUMO	0.111	2			
274.4	HOMO \rightarrow LUMO		0.606		73	274.4	HOMO \rightarrow LUMO	0.655		86
	HOMO \rightarrow LUMO+2		0.350		24		HOMO \rightarrow LUMO+3	0.175		6

Además, en el caso de los alifáticos con metilos sustituyendo protones en el grupo amino, la llamada metilación, hay un incremento sustancial de la diferencia energética HOMO-LUMO, reduciendo así su foto-excitación con respecto a los alifáticos no *metilados*. Cálculos de dinámica molecular a diferentes temperaturas han proveído de evidencias conclusivas sobre la prevalencia del nitrógeno del grupo amino, enlazado al cinc, incluso a altas temperaturas. Esto podría explicar la contaminación por nitrógeno detectada experimentalmente en la formación del ZnO final. Estos resultados sugieren que la de-protonación de los aminoalcoholes y su enlace con el cinc en el precursor tiene efectos en su descomposición térmica pero, en cualquier caso, el enlace Zn-N es el menos proclive a romperse, en comparación con el enlace Zn-O (del acetato). El nitrógeno hace "demasiado" bien su trabajo, enlazándose fuertemente al Zn para estabilizar el metal, en ausencia de luz y dióxido de carbono, evitando también "demasiado" su marcha del sistema a bajas

temperaturas. Es por eso que estos sistemas, *i.e.* conteniendo aminoalcoholes como estabilizadores del metal en la tinta, no son los mejores candidatos para obtener ZnO puro - o, como mínimo, con un control de su contaminación - como aplicación en electrónica impresa. Un aditivo, como el caso de un estabilizador, no debería afectar en las propiedades finales del material deseado. A esto se le deben añadir, como puede verse con los análisis de gases salientes, la gran cantidad de compuestos tóxicos (NO_x o NH_3) que desprende este precursor al descomponerse.

Estos hechos dan paso al último objetivo del presente trabajo. Puesto que no es posible controlar los efectos que tienen los aminoalcoholes, teóricamente inocuos, sobre el material final deseado, no hay que conformarse con esta solución para estabilizar el metal en la tinta por el simple hecho de que un enlace Zn-N sea más estable que uno Zn-O. Aumentando el número de enlaces Zn-O y eliminando el nitrógeno como variable en el sistema, se puede llegar a obtener precursores estables a temperatura ambiente, más proclives a la descomposición a más bajas temperaturas y, sobre todo, menos generadores de gases tóxicos salientes al descomponerse. El último capítulo de resultados de este trabajo, propone un cambio en las *reglas de juego* y es la síntesis y caracterización de precursores de ZnO basándose en la, tan de moda, Química verde. Entre los principios que en 1998 Paul Anastas y John Warner propusieron como definición de Química verde, destacan la de prevenir residuos, diseñar síntesis cuanto menos tóxicas y más seguras mejor, así como maximizar la incorporación de todos los materiales usados en los procesos de síntesis. Hasta cinco precursores de ZnO se sintetizaron, siguiendo los principios de Química verde, resolviendo sus estructuras cristalinas y estudiando su descomposición térmica para producir ZnO. La sal de cinc utilizada siguió siendo la del acetato y, para maximizar la estabilidad de este metal de transición en el precursor se decidió recurrir a ácidos carboxílicos totalmente naturales. Así pues, para producir estos 5 nuevos precursores se utilizaron los ácidos salicílico, cítrico, láctico y succínico, en el caso del láctico, además, se diseñaron 2 precursores en diferentes. Teníamos, por tanto dos monómeros (basados en salicilato y lactato de cinc) y tres polímeros (basados en succinato, lactato y citrato de cinc).

Análisis térmicos muestran descomposiciones que acaban en temperaturas hasta $150\text{ }^\circ\text{C}$ inferiores a las requeridas cuando los precursores son nitrogenados. Además estas descomposiciones muestran pasos mucho más limpios y los ZnO finales son significativamente más puros (no sólo el ZnO no contiene nitrógeno, sino que además, en diversos casos, el contenido de carbono e hidrógeno entra dentro del límite de detección del 0.2% del aparato de análisis elemental - Figura 8) a una menor temperatura que en el caso de los nitrogenados, donde las medidas de masa final después de la descomposición coinciden con las masas teóricas si todo el precursor acaba transformándose en ZnO. Experimentos de difracción (Figura 8) muestran ZnO con tamaños de cristal de entre 20 y 35 nm. De estos cinco precursores de ZnO se decidió escoger los que menos tiempo tardaran en ser sintetizados y, a su vez, los que mejor se disolvieran en los disolventes más seguros y abundantes en cualquier laboratorio químico. De esta forma, se diseñaron dos tintas (una en agua y la otra en ethanol) y se procedió a realizar los mismos estudios térmicos que con las tintas basadas en precursores nitrogenados.

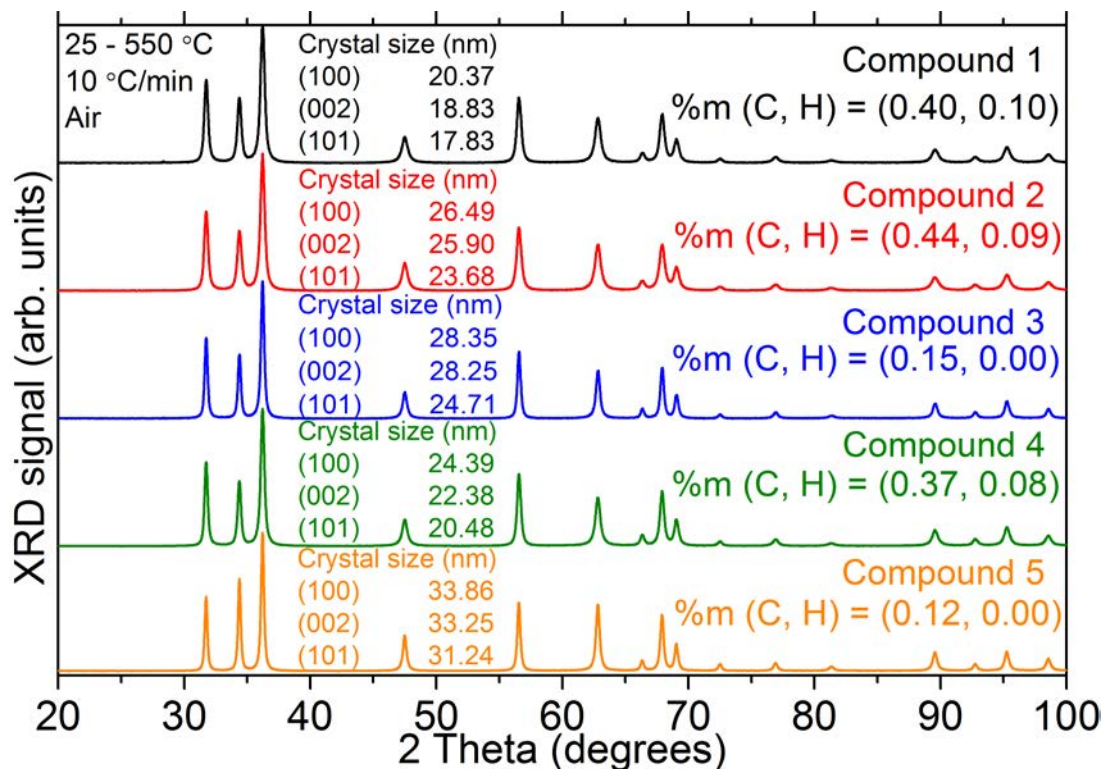


Figura 8: Curvas XRD de los nuevos precursores de ZnO (no nitrogenados) sintetizados. Se muestran también las concentraciones de carbono e hidrógeno.

Este trabajo mostró numerosas mejoras para la tecnología de impresión de ZnO mediante precursores. Con ambas tintas se conseguían capas continuas y mucho más homogéneas de ZnO y con contenidos de carbono e hidrógeno por debajo del límite de detección de la técnica de análisis elemental a una temperatura $>50\text{ }^{\circ}\text{C}$ inferior a la requerida con precursores nitrogenados y, además, con gases salientes mucho menos tóxicos (básicamente CO_2). Además, se intentó rebajar aún más la temperatura máxima para conseguir ZnO igual de puro mediante el control de la velocidad de calentamiento o el tiempo de espera a esa temperatura máxima, llegando a rebajar la temperatura máxima a $450\text{ }^{\circ}\text{C}$, $150\text{ }^{\circ}\text{C}$ por debajo de los $600\text{ }^{\circ}\text{C}$ requeridos con los compuestos nitrogenados del estudio anterior. Llegados a este punto, sólo quedaba una única propuesta a realizar: la adición de nuevas propiedades a las ya existentes en este ZnO. Aunque desde el punto de vista electrónico el ZnO está muy bien valorado, se consideró interesante la idea de poder añadir propiedades magnéticas mediante la inclusión de un segundo metal, el hierro, sin perder de vista los principios de Química verde. A esta adición de propiedades entre dos metales, muy conocida en Química, se le llama hibridación molecular. En la naturaleza pueden encontrarse ejemplos de minerales que contienen en comunidad compuestos de cinc y hierro. El caso de la Franklinita, mineral perteneciente al grupo de la denominada espinela es, quizás, uno de los más interesantes para el caso del presente estudio. La variación de la relación Zn:Fe en su composición, provoca que sea un mineral con un nivel variable de magnetismo. Así pues, el objetivo de este trabajo fue el de sintetizar un precursor heteropolimetálico que, al descomponer

térmicamente, pueda generar el tándem Franklinita/ZnO con un contenido de hierro variable a voluntad mediante el control de la atmósfera en la que se descompone térmicamente este precursor.

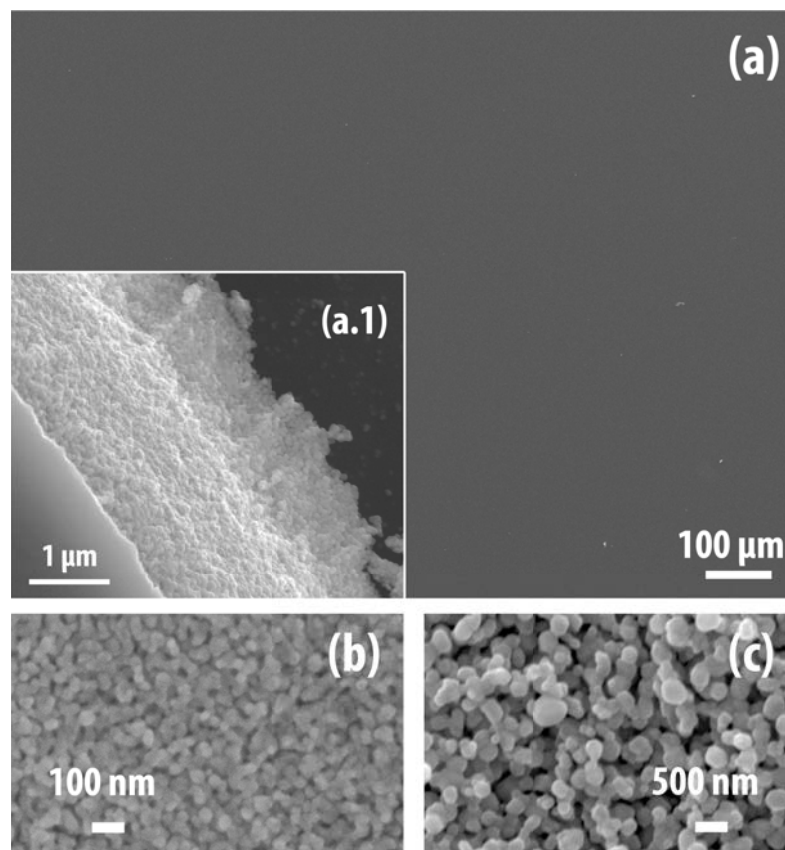


Figura 9: Imágenes SEM de la capa de una de las tintas generadas con uno de los precursores no nitrogenados a una T_{max} de 450 °C (a y b), donde a.1 muestra el límite de la capa, y de 550 °C (c). La rampa de calentamiento fue de 5 °/min y las capas se mantuvieron a esas T_{max} durante 20 min antes de extraerlas del horno.

Para la síntesis, se prosiguió con el mismo procedimiento que en el caso de los otros cinco precursores "verdes". En este caso se debía escoger un ácido carboxílico que contuviera hierro y que fuese extensamente utilizado para fines biológicos, bioquímicos o biomédicos. El ácido escogido fue el Ferroceno carboxílico. Puesto que era probable que este ácido difícilmente pudiera interactuar con el acetato de cinc, entrando de esa manera en contradicción con el principio de Química verde que habla sobre maximizar la incorporación de todos los materiales en la síntesis, previniendo residuos, se diseñó primero la sal sódica del ácido mediante una técnica comúnmente utilizada por uno de los colaboradores en este trabajo y después se procedió a la síntesis de este compuesto heteropolimetálico (HPNOMC - Esquema de la Figura 10). De esta manera se reconducía la síntesis hacia la Química verde otra vez. El resultado fue un éxito y se consiguió resolver la estructura cristalina de este compuesto mixto de hierro y cinc.

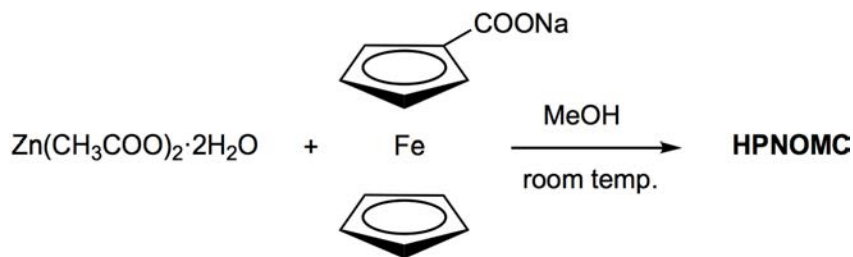


Figura 10: Esquema de la reacción de generación del compuesto heteropolimetálico.

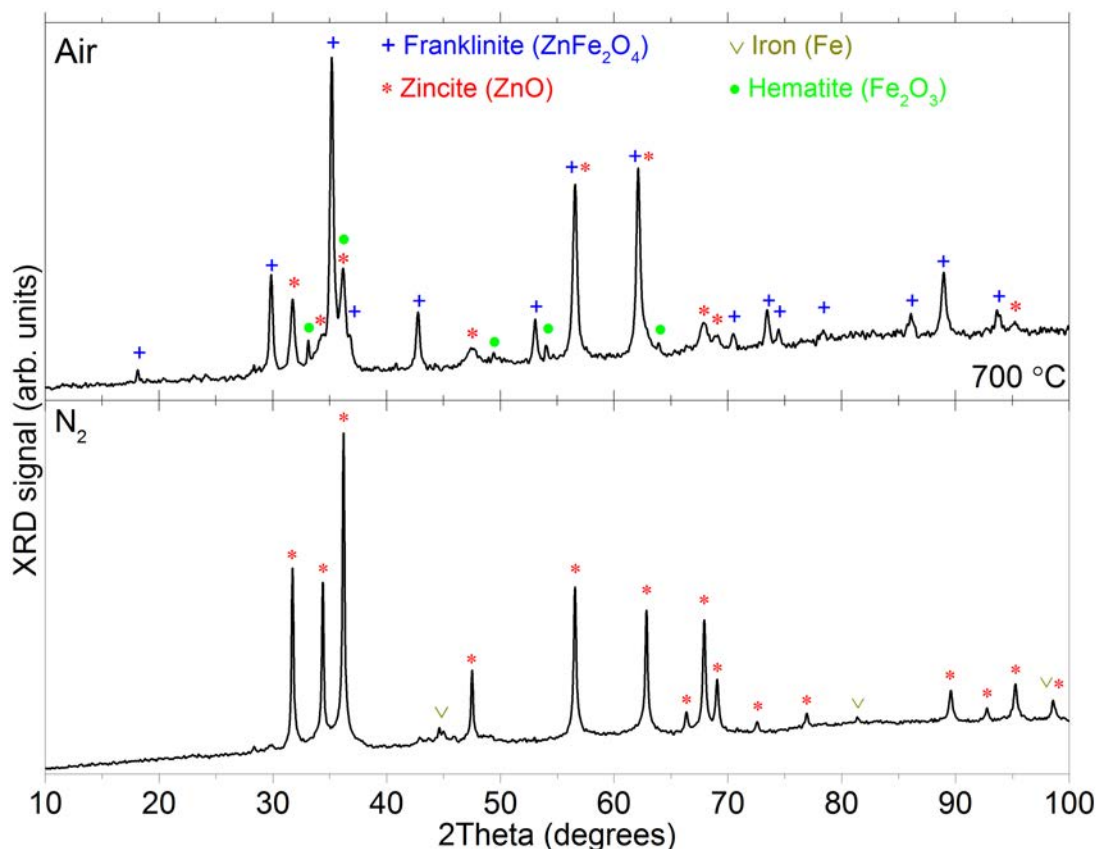


Figura 11: Curvas XRD después de calentar el compuesto **HPNOMC** a 700 °C siguiendo una rampa de calentamiento de 20 °/min en N₂ y aire seco.

El siguiente paso, como siempre, fue el de estudiar su descomposición térmica, esta vez en función de la atmósfera. Los resultados preliminares - puesto que estos fueron los últimos experimentos realizados en el doctorado - mostraron altos contenidos de Franklinita en comparación con el contenido de ZnO cuando la descomposición se producía en una atmósfera oxidante y, por el contrario, un contenido inexistente de Franklinita cuando la descomposición térmica se realizaba en una atmósfera reductora (Figura 11). Trazas de hematita y de hierro metálico se encontraron también en los materiales posteriores a la descomposición en atmósfera oxidante y reductora respectivamente. Esto demuestra que, controlando la atmósfera, se podría controlar el ratio Zn:Fe y, por tanto, las potenciales propiedades magnetoelectrónicas.

DEDICATION AND ACKNOWLEDGEMENTS

First and foremost I want to thank my supervisor Dr. Anna Vilà. It has been an honor to be her Ph.D. student. She has been supportive since the days I began working as an undergraduate, around 2011, and with the Master's degree thesis and a tremendous mentor for me. Ever since, Anna has supported me not only by providing a research assistantship more than six years, but also academically and emotionally through the rough road to finish this thesis. Thanks to her encouragement, I had the opportunity to grow and became the scientist who is writing this lines. She helped me also with the teaching period and guided me with her advises all the way. Not only, but especially during the most difficult times, when writing this thesis, she gave me always the moral support and the freedom I needed to move on.

I would also like to thank Prof. Concepción López. She has taught me, both consciously and unconsciously, how good experimental chemistry is done. I appreciate all her contributions of time and ideas to make my Ph.D. experience productive and stimulating. The joy and enthusiasm she has for her research was contagious and motivational for me, even during tough times, in the Ph.D. pursuit.

I am thankful for the excellent example they both have provided me with as a successful women scientists and professors.

Talking about brilliant minds, I have the duty to mention Prof. Pere Roura. Throughout my work, I have had the benefit of discussions with a number of researchers but, framed within a series of collaborations with his group, he has been one of the best referees one could ever have. His experience and deep knowledge of science and his fruitful comments and constructive criticism were a big pillar of this work. I will always be grateful to him, to Dr. Jordi Farjas and to their group also for the technical support I had with countless thermal experiments.

I gratefully acknowledge the individuals, impossible to forget, that also made my Ph.D. work possible. With that I would like to give special thanks to Dr. Angel Dieguez and his group for letting me use two of their most powerful servers. Without them, and also without one of my best friends, Dr. Santiago Alonso, I could only have dreamed of the enormous amount of theoretical experiments and results that I have been able to performed in my thesis. Half the intensity and power of this work would not have been possible. I also have to be grateful for the huge help and assistance provided from the unforgettable Edurne Máñez, Teo Puig, Marc Roig and Oriol Martinez. I cannot fail to recall Dr. Paolo Pellegrino, Dr. Christophe Serre, Dr. Oriol Monereo, Dr. Giovanni Vescio, Dr. Sonia Estrade, Dr. Oscar Ruiz and Dr. Cèsar Ferrater for their support, help and comments.

Another big part of this milestone could not have been possible without the Scientific and Technological Centers of the University of Barcelona (CCiTUB). I would like to thank the big minds and careful work of Xavier Alcobé, Maria Barba, Dr. Merce Font and Dr. Josep Bassas for their tremendous help with the X-ray diffraction experiments. Special thanks also to Dr. Irene Fernandez and Laura Ortiz (Mass spectrometry), to Dr. Regina Roca (Elemental analysis), Eva Prats and Javier García (Electronic microscopy), to Dr. Lorenzo Calvo (Surface analysis), to Dr. Cristina Puigjaner and Mercedes Aguilar (Thermal experiments), Dr. Tariq Jawhari (Raman spectroscopy), to Dr. Elies Molins and Dr. Ignasi Mata (Mössbauer spectroscopy), and to Dr. Nuria Ferrer and Dr. Josep Socias (Molecular spectroscopy).

I also thank the funding sources that made this work possible: Dr. Albert Cirera for his first-years patronage and to the University of Barcelona for the scholarship that was granted to me during the last part of this trip. My time at the University of Barcelona was made enjoyable in large part due to people that became a part of my life. I am grateful for the time spent with my dear friends (you know who am I talking about), colleagues, office-mates and many other people and memories that I will always carry with me.

A special thanks to my family. Words can not express how grateful I am to my parents for all their love while growing and for their encouragement and support in all my pursuits and the sacrifices they have made on my behalf. Last but never least, a warm thanks to my loving, supportive, encouraging, and patient life partner Izabela, whose faithful and unconditional accompaniment, especially during the final stages of this Ph.D., is so appreciated. THANK YOU.

Alberto Gómez Núñez
University of Barcelona
October 2017

AUTHOR'S DECLARATION

I declare that the work in this dissertation was carried out in accordance with the requirements of the University's Regulations and Code of Practice for Research Degree Programmes and that it has not been submitted for any other academic award. Except where indicated by specific reference in the text, the work is the candidate's own work. Work done in collaboration with, or with the assistance of, others, is indicated as such. Any views expressed in the dissertation are those of the author.

SIGNED: DATE:

TABLE OF CONTENTS

	Page
List of Tables	xxiii
List of Figures	xxv
Glossary	xxx
1 Dissertation summary	1
1.1 Contribution of this work	1
1.2 List of publications and communications	6
1.2.1 Chapter 4	6
1.2.2 Chapter 5	6
1.2.3 Chapter 6	6
1.2.4 Appendix B	7
2 Introduction	9
2.1 Using Zinc Oxide as a semiconductor	9
2.1.1 General considerations	9
2.1.2 Properties and device applications	11
2.1.3 Searching for a p-type ZnO	13
2.1.4 ZnO synthesis and growth	14
2.2 Sol-gel ZnO formation: State of the art	14
2.2.1 Salts	15
2.2.2 Stabilizers	16
2.2.3 Solvents	16
2.2.4 Film formation and treatments	17
2.3 Zn-based Coordination Polymers (Zn-CPs)	18
2.4 Green Chemistry	19
2.5 Motivation of this work	20
3 Methods	25
3.1 Materials science	25

TABLE OF CONTENTS

3.1.1	X-Ray Diffraction (XRD)	25
3.1.1.1	The single-crystal method	28
3.1.1.2	The Powder method	34
3.1.2	X-ray spectroscopy	38
3.1.2.1	X-ray Photoelectron Spectroscopy (XPS)	38
3.1.2.2	Energy Dispersive X-ray Spectroscopy (EDX/EDS)	42
3.1.3	Scanning Electron Microscopy (SEM)	43
3.2	Physical Chemistry studies	46
3.2.1	Infrared (IR) spectroscopy	46
3.2.2	Nuclear Magnetic Resonance (NMR)	47
3.2.3	Thermogravimetric analysis (TGA)	50
3.2.4	Differential Scanning Calorimetry (DSC)	52
3.2.5	Mass Spectrometry (MS) & Evolved Gas Analysis (EGA)	54
3.2.6	Elemental Organic Analysis (EOA)	57
3.3	Computational approach	58
3.3.1	Quantum mechanics: The Schrödinger equation	58
3.3.1.1	Born-Oppenheimer Approximation	59
3.3.1.2	Density Functional Theory (DFT)	60
3.3.1.3	Time-dependent DFT (TD-DFT)	62
3.3.2	Car-Parrinello Molecular Dynamics (CPMD)	63
3.3.3	Metadynamics	65
4	The common sol-gel ZnO precursor	69
4.1	Study of a sol-gel precursor and its evolution towards ZnO	70
4.1.1	Experimental Procedure	70
4.1.2	Results and Discussion	71
4.1.2.1	Characterization of the Precursor	71
4.1.2.2	Computational study of the Precursor	75
4.1.2.3	Comparative studies of the thermal evolution of the Precursor and the Ink	76
4.1.2.4	Evolution of the crystalline structure with the temperature	79
4.1.2.5	Atomic environment	79
4.1.3	Conclusions	80
4.2	Role of ethanolamine on the stability of a sol-gel ZnO ink	80
4.2.1	Materials and procedures	81
4.2.2	Quantum mechanical simulations	81
4.2.3	Results and discussion	82
4.2.3.1	Stability of EA with ME and ZAD under different conditions	82
4.2.3.2	Time-Dependent Density Functional Theory, TD-DFT, calculations	85

4.2.3.3	Dimerization	91
4.2.4	Conclusions	93
4.3	Molecular-dynamics study of ZnO formation from a sol-gel ink containing ethanolamine	93
4.3.1	Experimental and theoretical methods	93
4.3.1.1	Materials and procedures	93
4.3.1.2	Quantum-mechanical calculations	94
4.3.2	Experimental results	96
4.3.3	Theoretical calculations	98
4.3.3.1	Car-Parrinello molecular-dynamics simulations	98
4.3.3.2	Metadynamics simulations	99
4.3.4	Conclusions	103
5	Substituent effects in nitrogen-based ZnO precursors	105
5.1	Comparison of the thermal decomposition processes	106
5.1.1	Experimental procedure	106
5.1.1.1	Samples preparation	106
5.1.1.2	Thermal analysis	106
5.1.1.3	Structural analyses	107
5.1.2	Results and discussion	107
5.1.2.1	TGA/DSC experiments	107
5.1.2.2	XRD, IR and EOA results	110
5.1.2.3	Analysis of the evolved gases	112
5.1.2.4	Film morphology	113
5.1.3	Conclusions	114
5.2	Electronic and dynamic DFT studies	116
5.2.1	Methodology	116
5.2.2	Results and discussion	116
5.2.2.1	Electronic behaviour at 0 K	116
5.2.2.2	Molecular dynamics	120
5.2.3	Conclusions	123
5.3	The 300-600 °C range: New experimental results	123
5.3.1	Elemental Organic Analysis (EOA) and X-ray Diffraction (XRD)	123
5.3.2	Scanning Electron Microscopy (SEM) and Infrared Spectroscopy (IR)	126
5.4	Theoretical results using PBE	129
6	Green Chemistry as a new strategy route to ZnO	133
6.1	Zn(II)-CPs as ZnO precursors	134
6.1.1	Procedure	134
6.1.1.1	Materials and Methods	134

TABLE OF CONTENTS

6.1.1.2	Synthesis of the compounds	134
6.1.1.3	X-ray diffraction studies	135
6.1.2	Results and Discussion	136
6.1.2.1	Characterization of the precursors	136
6.1.2.2	Thermal study of the precursors	143
6.1.2.3	Thermal study of the inks	145
6.1.3	Conclusions	151
6.2	Zn(II)-Fe(II or III) HPNOMC	152
6.2.1	Procedure	152
6.2.1.1	Materials and methods	152
6.2.1.2	Synthesis and crystal resolution	153
6.2.2	Results and discussion	154
6.2.2.1	Characterization of the HPNOMC	154
6.2.2.2	Thermal decomposition of compound 6	159
7	Conclusions and Horizons	163
	Bibliography	169
	Appendix A Supporting Informations	205
	Study of a sol-gel precursor and its evolution towards ZnO	206
	Role of ethanolamine on the stability of a sol-gel ZnO ink	211
	Molecular-dynamics study of ZnO formation from a sol-gel ink containing ethanolamine	218
	Electronic and dynamic DFT studies on the substituent effects of aminoalcohol stabiliz- ers in sol-gel ZnO precursor	231
	Appendix B Related articles prior to this work	241
	Article 7. Influence of In and Ga additives onto SnO ₂ inkjet-printed semiconductor . . .	242
	Article 8. Metal oxides as functional semiconductors. An inkjet approach	247

LIST OF TABLES

TABLE	Page
3.1 XRD methods depending on the ways λ and θ are varied	27
3.2 Algebraic expressions of d_{hkl} for the various crystal systems.	35
3.3 Properties of nuclei most useful for NMR studies.	49
4.1 Evolution of the area percentage for the deconvoluted O_{1s} lines at 530.0 eV (corresponding to Zn-O-Zn bonds) and 531.6 eV (O-H and O-C-O bonds) after XPS measurements on the Ink at different temperatures.	80
4.2 Excitation wavelengths (λ) with their respective assignments, oscillation strengths and probability weights, calculated with TD-DFT for EA and EA+ME.	87
4.3 Excitation wavelengths (λ) with their respective assignments, oscillation strengths and probability weights, calculated with TD-DFT for the monomer in vacuum and with 2-ME, CO_2 and both. In contrast with the presence of 2-ME, the increase of nuclearity and the presence of CO_2 makes increase the wavelength towards the visible range and its probability.	91
4.4 Electronic Kinetic Energies (EKE) obtained for the systems $[Zn]_1$ and $[Zn]_2$ by CPMD at different temperatures.	95
5.1 Average ZnO crystal size at 600 °C obtained from the XRD curves by applying Scherrer's formula to the (100), (002) and (101) diffraction peaks and carbon content measured by elemental analysis at the same temperature.	112
5.2 Fundamental energy (E_T) and free energy (ΔG) calculated from DFT-optimized structures for the eight studied precursors.	117
5.3 Excitation wavelengths (λ), oscillation strengths, and percent probabilities for the most probable HOMO-LUMO transitions for the optimized geometries of the eight precursors, as calculated with TD-DFT.	118
5.4 Values of the adiabaticity obtained after the 2500-step MD test for each simulated molecule at different temperatures.	121
5.5 Expected value for the Zn-N bond length ($\langle Zn-N \rangle$, in Å) at 300, 500, 600, and 700K with its standard deviation in parentheses ($\times 10^{-3} \text{Å}$) for the eight precursors using CPMD calculations.	121

5.6	Elemental Organic Analysis for the aliphatic-based (Top table) and aromatic-based (Bottom table) precursors (Abundance in % ($\pm 0,2$))	124
5.7	Crystallite size of the three ZnO principal reflections of the precursors (Zn-EA, Zn-APr, Zn-AMB, Zn-AB and Zn-APh) at different temperatures.	124
6.1	Crystal data and details of refinement of the crystal structure for compounds 1-3 . The approximate crystal dimensions were (in mm \times mm \times mm) 0.058 \times 0.075 \times 0.504 (1), 0.168 \times 0.212 \times 0.574 (2) and 0.050 \times 0.084 \times 0.405 (3).	136
6.2	Crystal data and details of refinement of the crystal structure for compounds 4 and 5 . The approximate crystal dimensions were (in mm \times mm \times mm) 0.237 \times 0.0662 \times 0.036 (4) and 0.171 \times 0.142 \times 0.129 (5).	137
6.3	Layer images when different HR, DwT and MT are applied to Ink-1 and Ink-2 in a 2 \times 2cm ² glass substrate.	150
6.4	⁵⁷ Fe Mössbauer Hyperfine Parameters: isomer shift, <i>i.s.</i> , quadrupole splitting, ΔE_q , and full-width at half-height, Γ (in mm/s) for compound 6 . For comparison purposes data for ferrocene and some mono-substituted derivatives at 298 K and are also included (standard deviation parameters are given in parenthesis).	156
6.5	Angles (in deg.) between every pair of six-membered chelate rings shown in figure 6.21157	
6.6	Tilt and Twist angles (in deg.) for each Fc unit.	157

LIST OF FIGURES

FIGURE	Page
2.1 ZnO crystal structures	10
3.1 Atomic levels involved in copper and his typical X-ray spectrum	26
3.2 Bragg diffraction	27
3.3 Single-crystal diffractometer	29
3.4 Cyclic process to calculate the electron density maps	33
3.5 The basic principle of XPS	40
3.6 Auger electron emission v X-ray photon emission	41
3.7 Schematic of an XPS spectrometer	41
3.8 Types of interactions between electrons and a sample.	45
3.9 Main components of a typical SEM.	46
3.10 Stretching and bending vibrations in molecules.	47
3.11 TGA chemical reactions.	51
3.12 TGA Gravimetric effects.	51
3.13 Types of DSC: Heat-flux and Power-compensation.	53
3.14 Schematic illustration of compound Taylor cone formation.	56
4.1 Infrared spectra (in the range 1800-400 cm^{-1}) of ZAD and the Precursor	72
4.2 ^1H NMR spectra of ethanolamine and the Precursor	73
4.3 ^1H NMR spectra of ethanolamine and the Precursor	74
4.4 Experimental powder-XRD spectrum of dried Precursor (Exp. days 1 and 5) and the calculated diffractogram for a monoclinic $\text{P2}_1/\text{m}$ system.	74
4.5 Optimized geometries of the monomer, dimer and tetramer using UB3LYP method and LANLD2DZ base.	75
4.6 TGA curves of Ink and Precursor	76
4.7 Derivative of the TGA curve and coupled MS signals for $m/z = 43$ and $m/z = 44$ of the Precursor	77
4.8 XRD spectra measured at various temperatures of <i>in-situ</i> dried Precursor and <i>ex-situ</i> Ink	78
4.9 Ethanolamine, monomer and dimmer models.	81

4.10	The bimolecular system reconstructed by changing the distances d_1 and d_2 around their respective equilibrium values.	82
4.11	Pictures of EA, EA in 2-ME and the Ink , freshly prepared and after 2, 4, 6 or 8 weeks of storage at room temperature and in the presence of light and air.	83
4.12	Degradation mechanism proposed for EA in the presence of CO ₂	84
4.13	Normalized EGA signals of compounds related to $m/z = 76$	85
4.14	Frontier orbitals calculated with Gaussian for EA and EA+ME.	86
4.15	Frontier orbitals HOMO and LUMO of the monomer system in vacuum and in presence of 2-ME, CO ₂ and both.	89
4.16	Frontier orbitals HOMO and LUMO of the dimer system in vacuum and in presence of 2-ME, CO ₂ and both.	90
4.17	Potential energy surface (PES) with the most relevant structures during the dimerization process.	92
4.18	Schematic views of the monomer and dimer Zn(II) complexes used in Car-Parrinello molecular dynamics.	94
4.19	IR spectra of the precursor after heating up to 570, 670, 770 and 870 K and immediate cooling to room temperature.	96
4.20	Normalized EGA signals with their required normalization factor in parenthesis.	97
4.21	Simplified core of the precursor and an example of one more complex N-containing cyclic cation detected by EGA.	98
4.22	Label scheme and free energy surface (FES) of the Zn-N bond, as calculated by metadynamics.	100
4.23	Free and potential energy profiles of the whole decomposition process, and optimized geometries of intermediate and minima states C2 , C3 , C4 and P	101
4.24	Scheme of the dimer modification to generate a triangular molecule, according to metadynamics.	103
5.1	Chemical formula of the precursor and the eight amino-alcohols used in this study.	106
5.2	TG and DSC curves of ink decomposition for the aliphatic and the aromatic stabilizers.	108
5.3	TG curves of the EA ink decomposed inside an alumina pan and on a glass substrate.	109
5.4	XRD spectra measured after heating the films up to 300 °C 600 °C.	110
5.5	IR spectra measured after a heat treating of 300 °C and 600 °C.	111
5.6	EGA curves of intense volatile fragments detected during decomposition of the AMB ink in vacuum and the mass-loss rate curve.	113
5.7	Approximated temperature range in which nitrogenated cyclic fragments are detected by EGA during decomposition of the EA , APr and AB inks.	114
5.8	SEM micrographs of the films treated at 600 °C.	115
5.9	Frontier orbitals calculated with Gaussian03 for the eight precursors, with the excitation energies for the main transitions at 0K.	119

5.10	Expected value for the electronic kinetic energy $\langle \text{EKE} \rangle$ obtained after test simulations for precursors with $R'=H$ and for N-methylated and non-substituted aliphatic-based precursors.	122
5.11	XRD spectra of Zn-EA at different temperatures.	125
5.12	XRD spectra of the proposed precursors at different temperatures.	125
5.13	SEM images of Zn-EA at different temperatures, showing the morphology of the resultant ZnO films.	126
5.14	SEM images of Zn-APr at different temperatures, showing the morphology of the resultant ZnO films.	127
5.15	SEM images of Zn-AMB at different temperatures, showing the morphology of the resultant ZnO films.	127
5.16	SEM images of Zn-AB at different temperatures, showing the morphology of the resultant ZnO films.	128
5.17	IR spectra of Zn-EA at different temperatures.	128
5.18	IR spectra of the proposed precursors at different temperatures.	129
5.19	Expected value and standard deviations for Zn-EA and Zn-EA-Me precursor's mean bond lengths (in Å) using PBE functional.	130
5.20	Expected value and standard deviations for the proposed precursor's mean bond lengths (in Å) using PBE functional.	131
6.1	Infrared spectra of the ZnO precursors (1-5) used on this study.	138
6.2	Synthesis of compounds 1 , 2 , 3 , 4 and 5	139
6.3	Compound 1 : View of the coordination environment of Zn(II) atom and the binding of the lactic acid and assembly of the resulting structural units.	140
6.4	Compound 2 : View of the coordination environment of Zn(II) atom and the binding of the lactic acid and the MeOH and assembly of the resulting structural units.	140
6.5	Compound 3 : View of the coordination environment of Zn(II) atom and the binding of the salicylic acid and assembly of the resulting structural units.	141
6.6	Compound 4 : View of the coordination environment of Zn (II) atom and the binding of the succinic acid and propagation of the resulting structural units.	141
6.7	Compound 5 : Views of the coordination environment of the two different types of Zn (II) atoms (Zn1 and Zn2), the binding of the citrate ligand ($\text{C}_i\bar{3}$) and the propagation of the resulting structural unit.	142
6.8	TGA curves for the compounds 1-5	143
6.9	XRD curves for the ZnO precursors.	144
6.10	Infrared spectra of the Ink-1 (Compound 2 in water) at various MT, HR and DwT.	146
6.11	Infrared spectra of the Ink-2 (Compound 3 in ethanol) at various MT, HR and DwT.	147
6.12	Elemental Organic Analysis of Ink-1 at various MT, HR and DwT.	148
6.13	SEM micrographs for thermal treated Ink-1	148

6.14	Elemental Organic Analysis of Ink-2 at various MT, HR and DwT.	149
6.15	SEM micrographs for thermal treated Ink-2	149
6.16	Scheme of the HPNOMC synthesis (compound 6).	154
6.17	Reaction scheme of the compound 6 (HPNOMC).	154
6.18	The IR spectra of the sodium ferrocenecarboxylate and of compound 6	155
6.19	⁵⁷ Fe Mössbauer spectrum of compound 6 at room temperature.	156
6.20	Crystal structure and core part of compound 6 . Hydrogen atoms have been omitted for clarity.	158
6.21	The six-membered chelate rings of compound 6 . Hydrogen atoms have been omitted for clarity.	159
6.22	TGA and DSC curves of compound 6 with a 20 °/min heating rate up to 700 °C in N ₂ and dry air.	160
6.23	XRD curves after thermally treating the compound 6 with a 20 °/min heating rate up to 700 °C in N ₂ and dry air.	161

GLOSSARY

- 2-ME or ME** 2-Methoxyethanol. 15, 70
- BOMD** Born-Oppenheimer Molecular Dynamics. 65
- CP** Coordination Polymer. xix, 18, 133
- CPMD** Car-Parrinello Molecular Dynamics. xx, 22, 63, 98
- CV** Collective Variables. 66, 95
- DFT** Density Functional Theory. xx, 13, 60, 98
- DSC** Differential Scanning Calorimetry. xx, 52, 54, 69, 153
- EA (Mono-)** Ethanolamine. 15, 20, 69, 70
- EDX/EDS** Energy Dispersive X-ray Spectroscopy. xx, 42, 146, 151
- EGA** Evolved Gas Analysis. xx, 54, 69, 105, 153
- EOA** Elemental Organic Analysis. xx, xxi, 57, 96, 123, 146
- ESI** Electrospray Ionization. 55
- ESP** Electro-Static Potential. 95
- EtOH** Ethanol. 16
- FES** Free-Energy Surface. 66, 67, 94
- FOM** Figure Of Merit. 34, 36
- FWHM** Full Width at Half Maximum. 71
- GGA** Generalised Gradient Approximation. 62
- HKS** Hamiltonian Kohn-Sham. 60

- HPN** Heteropolynuclear. 22, 134, 152
- HPNOMC** Heteropolynuclear Organometallic Compound. xxii, 23, 152, 153, 155, 157, 159, 161
- IR** Infrared (Spectroscopy). xx, xxi, 46, 126
- LDA** Local Density Approximation. 62, 129
- MALDI** Matrix-Assisted Laser Desorption Ionization. 55, 56
- MD** Molecular Dynamics. 64, 105
- MeOH** Methanol. 16
- MS** Mass Spectrometry. xx, 54, 69, 138
- NMR** Nuclear Magnetic Resonance. xx, 47
- OMC** Organometallic Compounds. 134
- PBE** Perdew-Burke-Ernzerhof functional. 21
- PES** Potential Energy Surface. 60, 76
- QMS** Quadrupole Mass Spectrometer. 54, 57
- SEM** Scanning Electron Microscopy. xx, xxi, 43, 126, 149, 153
- TD-DFT** Time-Dependent Density Functional Theory. xx, 62, 69, 105
- TGA** Thermogravimetric Analysis. xx, 50, 54, 69, 153
- TOF** Time-of-Flight. 57
- XPS** X-ray Photoelectron Spectroscopy. xx, 38, 39, 69
- XRD** X-Ray Diffraction. xx, xxi, 25, 69, 123, 153
- ZAD** Zinc Acetate Dihydrate. 16, 20, 69, 70, 133
- ZnO** Zinc Oxide. 9

*"We wish to pursue the truth no matter where it leads,
but to find the truth we need imagination and skepticism both.
We will not be afraid to speculate, but careful to distinguish speculation from fact.
The cosmos is full beyond measure of elegant truths"*
- Carl E. Sagan in *Cosmos: A Personal Voyage* Episode I

C H A P T E R

1

DISSERTATION SUMMARY

1.1 Contribution of this work

The first aim of the present dissertation was to deeply study the bibliography's most used sol-gel precursor to thermally produce ZnO. All this work is collected in the first chapter of results (Chapter 4). The cause of this first study was the need of understanding and putting some order in the processes involved not only in the stability of this precursor but in its thermal decomposition to produce ZnO. Both needs of knowledge are fundamental when the utilization of an ink, not yet containing the ZnO *per se*, is required to produce ZnO with applications in printed electronics. Although an extensive number of investigators, during the arise of this printed materials technology, were devoted to make very interesting discoveries concerning the precursor-based ink properties (stability and thermal decomposition) and their relation with the ZnO nature, the motives for which the ZnO material is formed in a certain way from a certain initial conditions is not yet well understood. The consequence of this fact is thus a *cooking-like* recipe to produce ZnO from this precursor, made by the effort of all these researchers. Nevertheless, although useful from an engineering point of view, is limited concerning the scientific method.

With this purpose in mind, the first effort carried out was to try to solve the crystal structure, never reported before, arising from the mixture between the zinc salt (Zinc acetate dihydrate) and the typical stabilizer used to avoid agglomerations of zinc metals in the ink (Ethanolamine) that prevent this ink to be printed, to be storage for a relatively long time and to have an homogeneous films after calcine it. It should be mandatory to know from the very first moment the material that one will have to work with from now on. After mixing these two compounds, Nuclear magnetic resonance, Infrared spectroscopy and Mass spectrometry were used as a first approach to shed some light on the issue. Specific bonds and ligands as well as the molecular mass units and

nuclearities that had been occurring were studied.

Next, since it was impossible to grow a single-crystal of the mixture, a long way was travelled trying to solve the crystal structure. The viscous mixture of zinc acetate and ethanolamine was kept with silica gel for months until the mixture become a dried powder, at which point it was studied by means of powder X-ray Diffraction. The crystal cell, the asymmetric units, among others, were studied and compared with the molecular models designed and optimized by means of simulations, carried out with the Gaussian03 software, as well as with the experiments explained before. These models were the starting point of all the studies and theories that would be performed and proposed later on. In particular simulations were useful in refining the cell structure using FOX¹ software.

Gaussian software was also useful in the study of the stability of this precursor and explaining the experimental results on its degradation in presence of light and CO₂. It was demonstrated that both light and CO₂ strengthened the electronic excitation to orbitals responsible of destabilizing key bonds in the precursor's degradation and the subsequent appearance modification (the ink turns yellowish-orange with a white precipitate), validated afterwards with evolved gas analysis experiments. Regarding the ZnO formation from the precursor's thermal decomposition, thermogravimetric analysis and molecular dynamics (with the software CPMD) walked hand in hand in this work. It could be demonstrated the reason why the final ZnO was having traces of nitrogen at high temperatures. To do so, a theory was proposed taken into account the evolved gas analysis of the precursor while decomposing. In this theory, the specimen with mass $m/z=44$ could be explained, performing CPMD calculations, with the appearance of nitrogen cyclic specimens. In addition, the theory regarding the specimens arising when the precursor is being degraded was also validated, relating that effect to the group of masses generated from the mass $m/z=76$ also with evolved gas analysis.

Although the moment of ZnO appearance, the thermal evolution of the crystal size and the purity were studied, among others, the presence of nitrogen at high temperatures as well as the toxic species that were evolving from the precursor when decomposing (NO_x and NH₃) were a serious matter to confront. The aim of the dissertation's next part (Chapter 5) was to investigate the substituent effects in this nitrogen-based ZnO precursor. To do so, up to seven aminoalcohols, with the same ethanolamine's skeleton but with different radical substitutions in concrete places of the aminoalcohol, were used in order to study the dependence of rigidity on the stability and the decomposition process of the precursor.

Due to material accessibility, it was decided to experimentally study four of these seven aminoalcohols but to study them all computationally. These four aminoalcohols were (S)-(+)-2-amino-1-propanol, (S)-(+)-2-amino-3-methyl-1-butanol, 2-amino-phenol and 2-aminobenzyl alcohol. The first two were aliphatic and the last two aromatics, in order to have different sizes and rigidities. In addition, three other aliphatic aminoalcohols, replacing the nitrogen

¹FOX, Free Objects for Crystallography (<https://fox.vincefn.net/FoxWiki>)

protons with methyl groups (methylation), were used for computational purposes to characterize what dependence these radicals used have on the intensity of the Zn-N bond for different scenarios (environmental and solvation). Experiments confirmed that the use of any of the aliphatic aminoalcohols in the precursor produce high stability comparing to those using aromatic aminoalcohols, where the degradation occurs within minutes (2-amino-phenol) or hours (2-aminobenzyl alcohol). Moreover, the ZnO generation from the thermal decomposition of these aliphatic-based precursors do not produce any significant change, since a decomposition step was taking place at 250 °C followed by other at 370 °C, in contrast with the case when aromatic aminoalcohols have being used, where an important exothermic decomposition process is showing up at 400 °C. In addition, when the most rigid aminoalcohol (2-amino-phenol) is used, the resultant ZnO does not produce film, but nanoparticles, due to the reach of a tremendous combustion of the ring at this temperature.

Comparing with the ethanolamine-based precursor, the ZnO appearance, from the crystal point of view, was similar to the (S)-(+)-2-amino-3-methyl-1-butanol-based one and the crystal size increased when (S)-(+)-2-amino-1-propanol or 2-aminobenzyl alcohol were used. Nevertheless from the point of view of the purity, carbon and hydrogen traces fell into the detection capacity of the elemental analysis apparatus for the (S)-(+)-2-amino-1-propanol-based precursor, in contrast with the use of 2-aminobenzyl alcohol, where the carbon and hydrogen concentrations were up to 10 times greater, due to the need for the aromatic ring to be removed, although this was the only aromatic-based precursor the ZnO from which formed a continuous film. This fact bolsters the conclusion that the aminoalcohol's rigidity plays an important role, since the only difference between the 2-amino-phenol (no film formation) and 2-aminobenzyl alcohol is an extra elbow generated by a carbon atom between the aromatic ring and the oxygen, absent in the 2-amino-phenol, that provides a greater flexibility when vibrations, twists and stresses are occurring while decomposing. Using electronic microscopy, it was discovered that the ZnO aspect of the layer was identical in all cases. Although no cracks were sighted, wrinkle-like structures appeared, due to internal tensions, twists and stresses during the decomposition processes. These wrinkles decreased in size when increasing the substituent's volume, bolstering the conclusion that, indeed, the aminoalcohol's rigidity has a clear effect on the final material's quality. It was additionally confirmed that the use of flexible aromatic stabilizers (*e.g.* 2-aminobenzyl alcohol), could be counterproductive, regarding the poor stability and the ZnO purity, while the aliphatic-based aminoalcohols provide better performances.

Simulations were useful to comparatively study seven different aminoalcohols with the same skeleton of ethanolamine in terms of stability and molecular dynamics at different temperatures. These were, in addition to the five experimentally studied aminoalcohols, a methylated version (*i.e.* replacing the N protons by methyl groups) of the aliphatic aminoalcohols in order to clarify even more the influence of the substituents on the charge distribution, stability properties when bonded to the Zn atom and on the thermal decomposition of that specific aminoalcohol-based

precursor. In general, for the six aliphatic-aminoalcohol-based precursors the HOMO was centred in the amino group and the HOMO-LUMO energy difference is much higher than for the uses of aromatic-aminoalcohols, thus decreasing the probability of photoexcitation and demonstrating the reason of the several experimental behaviours explained before.

Dynamic simulations at different temperatures provided conclusive evidences on the nitrogen prevalence in the precursor even at high temperatures. This fact explains the reason why the final ZnO contains traces of nitrogen, suggesting that the Zn-N bond has effects on the thermal decomposition since, in all cases, this bond is the one with the least tendency to cleave, comparing with the Zn-O (acetate) bonds. Therefore, nitrogen is fulfilling his purpose - this is, intensively bonded to the metal atom to avoid agglomerations - too well, in absence of light and CO₂. For that reason, additives containing nitrogen are not the best solution to stabilize the metal and to produce pure ZnO (or at least with control on the contamination) at the same time. An additive, as an stabilizer, should not influence the properties of the final material nor cause the release of toxic gases (NO_x and NH₃ in this case).

These conclusions were the *starting shot* for a change in the *game plan*, giving a step to the last part of results of this dissertation (Chapter 6). Since there is no control over the effects these aminoalcohols, *a priori* innocuous, have on the final and desired material, one cannot settle for this nitrogen-based solution as long as one may desire to increase the number of Zn-O (weaker) interactions at the expense of eliminate the Zn-N bonds (stronger). Moreover, since new precursors had to be designed, it was the perfect opportunity to use the so-popular *Green Chemistry*. Within the principles that Paul Anastas and John Warner proposed in 1998 as one definition for Green Chemistry, is worth highlighting the need to prevent waste, to design synthesis the less toxic and the more secure the better as well as to maximize the incorporation of all the materials used in the processes. Up to five ZnO precursors were synthesised following these principles, solving their crystal structure and studying their thermal decomposition. The starting Zn-based salt used was the acetate and, in order to increase the stability of the transition metal in the precursor, it was decided to resort to natural occurring carboxylic acids such as salicylic, citric, succinic and lactic acids. In addition, two different lactic-based precursors were synthesised and thus two monomers (based on salicylate and lactate) and three polymers (based on succinate, lactate and citrate) were assembled.

Thermal analysis found decomposition processes lasting *ca.* 150 °C less than the required temperature for nitrogen-based precursors. Furthermore these decomposition processes consisted of cleaner steps and purer ZnO (not only the final ZnO does not contain nitrogen at all, but also the carbon and hydrogen contents fall within the detection limit of the elemental organic apparatus, 0.2 %) with a lower temperature. In addition, the final mass corresponded to the theoretical ZnO mass, assuming that no Zn was sublimating. X-ray diffraction experiments showed crystal sizes of 20 - 35 nm. Two of the five precursors were chosen, taking into account their delay in synthesising and their solubility in common solvents (water and ethanol), to compare the behaviour of inks

based on these precursors with the ones based on nitrogen compounds from the previous study. This work showed numerous improvements for the ZnO precursor-based printing technologies. Continuous and homogeneous films of highly pure ZnO were obtained at lower temperatures adjusting the dwell time at the maximum temperature as well as the heating rate with either one of the inks generated and, additionally, with less toxic evolving gases (mainly CO₂).

At this point, there was only one proposal to make: the addition of new properties to those already existing in this ZnO. Although from an electronic point of view ZnO is highly valued, it was considered interesting to be able to add magnetic properties by including a second metal, iron, without losing sight of the principles of Green Chemistry. The addition of properties between two metals, well-known in Chemistry, is called molecular hybridization. Examples of minerals containing zinc and iron compounds in community can be found in nature. The case of Franklinite, a mineral belonging to the so-called spinel group, is perhaps one of the most interesting case of the present study. The variation of the Zn:Fe ratio in its composition causes it to be a mineral with a variable level of magnetism. Thus, the objective of this work was to synthesize an heteropolymetallic precursor that, through thermal decomposition, could generate the Franklinite / ZnO tandem with a variable iron content at will by controlling the atmosphere in which this precursor is decomposing.

For the synthesis, the same procedure was followed as in the case of the other five "green" precursors. In this case, a carboxylic acid containing iron should be chosen and it had to be extensively used for biological, biochemical or biomedical purposes. The chosen acid was the Ferrocene carboxylic acid. Since it was likely that this acid could hardly interact with zinc acetate, thus entering into contradiction with the principle of green chemistry concerning to maximize the incorporation of all materials in the synthesis, thus preventing residues, a sodium salt was first designed by a technique commonly used by one of the collaborators in this work. Only then the synthesis of this heteropolymetallic compound synthesis could proceed. Doing so, the synthesis was redirected again towards the Green Chemistry. The result was a success and the crystalline structure of this mixed compound of iron and zinc was solved.

The next step, as always, was to study its thermal decomposition, this time depending on the atmosphere. Preliminary results - since these were the last experiments carried out in the doctorate - showed high Franklinite content in comparison to the ZnO was found when the decomposition took place in an oxidizing atmosphere while, on the contrary, a non-existent content of Franklinite was found when the thermal decomposition was performed in a reducing atmosphere. Traces of hematite and metallic iron were also found in the post-decomposition materials using an oxidizing and a reducing atmosphere, respectively. This fact shows that by controlling the atmosphere, the Zn: Fe ratio and, therefore, the potential magnetoelectronic properties could be controlled.

1.2 List of publications and communications

1.2.1 Chapter 4

1. **Gómez-Núñez, A.**; Alonso-Gil, S.; López, C.; Roura, P.; Vilà, A., "Study of a sol-gel precursor and its evolution towards ZnO", *Materials Chemistry and Physics*, **2015**
DOI: 10.1016/j.matchemphys.2015.06.038
2. **Speaking:** "No more mysteries concerning the role of the ethanolamine in sol-gel ZnO formation", *E-MRS Fall Meeting*, Warsaw, Poland, Symposium G, **2015**.
3. **Speaking:** "Electronic structure modelling of the interactions in the synthesis of inkjet inks for semiconductor printing", *E-MRS Fall Meeting*, Warsaw, Poland, Symposium K, **2014**.
4. **Speaking:** "Understanding oxide formation from precursors in Inks", *E-MRS Fall Meeting*, Warsaw, Poland, Symposium L, **2014**.
5. **Gómez-Núñez, A.**; López, C.; Roura, P.; Alonso-Gil, S.; Vilà, A., "Role of Ethanolamine on the stability of a sol-gel ZnO ink". **Submitted**.
6. **Gómez-Núñez, A.**; Alonso-Gil, S.; López, C.; Roura, P.; Vilà, A., "Molecular dynamics of ZnO formation from a sol-gel ink containing Ethanolamine". **Submitted**.

1.2.2 Chapter 5

1. **Gómez-Núñez, A.**; Roura, P.; López, C.; Vilà, A., "Comparison of the thermal decomposition processes of several aminoalcohol-based ZnO inks with one containing ethanolamine", *Applied Surface Science*, **2016**
DOI: 10.1016/j.apsusc.2016.03.138.
2. **Gómez-Núñez, A.**; Alonso-Gil, S.; López, C.; Vilà, A., **Speaking:** "Substituent effects of aminoalcohol stabilizers in sol-gel ZnO precursor", *Physica Status Solidi*, **2016**
DOI: 10.1002/pssa.201532885
3. **Poster:** "Thermal decomposition of some Nitrogen-based precursors towards ZnO", *E-MRS Fall Meeting*, Warsaw, Poland, Symposium L, **2015**.
4. **Speaking:** "Substituent effects of Nitrogen-based stabilizers in their degradation", *E-MRS Fall Meeting*, Warsaw, Poland, Symposium N, **2015**.

1.2.3 Chapter 6

1. **Speaking:** "Chemical engineering of self-assembly nanoscale Zn(II) coordination polymers", *E-MRS Fall Meeting*, Warsaw, Poland, Symposium C, **2016**.

2. **Speaking:** "A novel heteropolymetallic (Fe_6Zn_4) nano-compound: from synthesis to applications", *E-MRS Fall Meeting*, Warsaw, Poland, Symposium E, **2016**.
3. **Speaking:** "Looking for bioactive compounds based on Zn-Coordination polymers", *Chemistry Conference for Young Scientists*, Blankenberge, Belgium, **2016**.
4. **Speaking:** "Green Chemistry as a new strategy route to a highly pure ZnO synthesis", *12th International symposium on electrochemical / chemical reactivity of new materials*, *E-MRS Fall Meeting*, Warsaw, Poland, Symposium D, **2015**.
5. **Gómez-Núñez, A.**; Máñez, E.; Puig-Walz, T.; López, C.; Font-Bardia, M.; Aguilar, M.; Vilà, A., "Chemical engineering of self-assembly nanoscale Zn(II) coordination polymers". **Article in preparation**.

1.2.4 Appendix B

1. Vilà, A.; **Gómez-Núñez, A.**; Portilla, L.; Morante, Juan R., "Influence of In and Ga additives onto SnO_2 inkjet-printed semiconductor", *Thin Solid Films*, **2014**
DOI: 10.1016/j.tsf.2013.12.044
2. Vilà, A.; **Gómez-Núñez, A.**; Portilla, L.; Cirici, M.; Morante, Juan R., "Metal oxides as functional semiconductors. An inkjet approach", *MRS proceedings*, **2013**
DOI: 10.1557/opl.2013.741

*"Nullius addictus iurare in uerba magistri,
quo me cumque rapit tempestas, deferor hospes"*

- Horace: Epistles, Book I, epistle I, lines 14 and 15 (20 BC)

INTRODUCTION

Inkjet has become a household word through its ubiquitous presence on the consumer desktop as a low cost, reliable, quick and convenient method[1]. In theory, inkjet is simple. In practice, implementation of the technology is complex and requires multidisciplinary skills. Nevertheless, inkjet not only underlies complexity, the characteristics of inkjet technology offer advantages to a wide range of applications and is increasingly viewed as more than just a printing or marking technique. It can also be used to apply coatings, to accurately deposit precise amounts of materials and even to build micro and nano structures. The list of industrial uses for inkjet technology seems endless and includes the reduction of manufacturing costs, provision of higher quality output, conversion of processes from analogue to digital, reduction in inventory, reduction of waste, mass customization, faster prototyping and implementation of just-in-time manufacturing. This is the reason why this technique had been used in the present work as a deposition method of ZnO. This chapter will firstly introduce the reader to the zinc oxide as a material and semiconductor¹ and secondly to the state of the art regarding the zinc oxide formation from precursors in inks, not only for printed electronics but also their chemical and biomedical applications.

2.1 Using Zinc Oxide as a semiconductor

2.1.1 General considerations

ZnO is a very promising material for semiconductor device applications. Most of the II-VI group semiconductors, and specifically the Zinc Oxide (ZnO), have a crystal structure either

¹Reproduced from the immense work of Janotti and Van de Walle[2]

zinc blende² (cubic), rocksalt (cubic) or wurzite (hexagonal), as shown in figure 2.1. Four cations surround every anion forming a tetrahedron, with a sp^3 covalent coordination, but these materials have also an ionic character which tends to increase their bandgap. While under ambient conditions the stable phase is that of wurzite symmetry, the zinc blende can only be stabilized by growth on cubic substrates and the rocksalt at relatively high pressures.

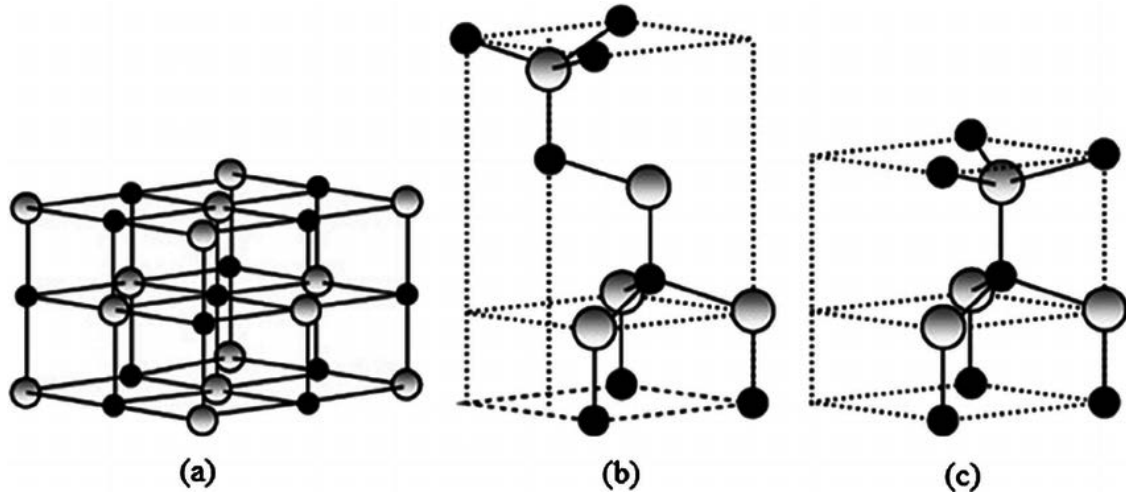


FIGURE 2.1. ZnO crystal structures: (a) cubic rocksalt, (b) cubic zinc blende and (c) hexagonal wurzite. Shaded gray and black spheres denote Zn and O atoms, respectively. Figure reproduced from [3].

Over the past two decades it has been witnessed a significant improvement in the quality of ZnO single-crystal substrates and epitaxial films. This, in turn, has led to a revival of the idea of using ZnO as an optoelectronic or electronic material in its own right. Controlling the conductivity in ZnO has remained a major issue. Even relatively small concentrations of native point defects and impurities (down to 10^{-14} cm⁻³ or 0.01 ppm) can significantly affect the electrical and optical properties of semiconductors. Therefore, understanding the role of native point defects (*i.e.* vacancies, interstitials, and antisites) and the incorporation of impurities is key toward controlling the conductivity in ZnO. For a long time it has been postulated that the unintentional n-type conductivity in ZnO is caused by the presence of oxygen vacancies or zinc interstitials [4, 5]. However, state-of-the-art DFT calculations corroborated by optically detected electron paramagnetic resonance measurements on high quality ZnO crystals have demonstrated that this attribution to native defects cannot be correct[6]. It has been shown that oxygen vacancies are actually deep donors and cannot contribute to n-type conductivity[7].

In addition, it was found that the other point defects (*e.g.* Zn interstitials and Zn antisites) are also unlikely causes of the observed n-type conductivity in as-grown ZnO crystals [8, 9]. Instead, the cause would be related to the unintentional incorporation of impurities that act as shallow

²Although the term has been used ubiquitously for semiconductors with cubic structure, it was originated from compounds such as ZnS *i.e.* not only for cubic phases but also for hexagonal phases.

donors such as hydrogen, present in almost all growth and processing environments[10]. By means of DFT calculations it has been shown that interstitial H forms a strong bond with O (or also substituting O) in ZnO and acts as a shallow donor, contrary to the amphoteric behavior of interstitial H in conventional semiconductors. Subsequently, interstitial H has been identified and characterized in ZnO [11, 12]. However, interstitial H is highly mobile[13] and can easily diffuse out of the samples, making it difficult to explain the stability of the n-type conductivity at relatively high temperatures [14, 15]. Substitutional H is much more stable than interstitial H and can explain the stability of the n-type conductivity and its variation with oxygen partial pressure.

2.1.2 Properties and device applications

The wide range of useful properties displayed by ZnO has been recognized and studied since the early days of semiconductor electronics, but the use of ZnO as a semiconductor in electronic devices has been hindered by the lack of control over its electrical conductivity: ZnO crystals are almost always n-type, the cause of which has been a matter of extensive debate and research[16]. With the recent success of nitrides in optoelectronics, ZnO has been considered as a substrate to GaN, to which it provides a close match. What has captured most of the attention in recent years is the fact that ZnO is a semiconductor with a direct band gap of 3.44 eV, which in principle enables optoelectronic applications in the blue and UV regions of the spectrum. The prospect of such applications has been fueled by impressive progress in bulk-crystal and thin-film growth. A partial list of the properties of ZnO that distinguish it from other semiconductors or oxides or render it useful for applications includes:

1. **Direct and wide band gap.** Since the lattice parameters change with temperature and pressure, the electronic band structure also changes. The bandgap shrinks with increasing temperature following the empirical relationship 2.1 ([17]), where α and β are constants.

$$(2.1) \quad E_g = E_g(T = 0) - \frac{\alpha T^2}{T + \beta}$$

The band gap of ZnO is 3.44 eV at low temperatures ($E_g(T = 0) \approx 3.4\text{eV}$ in 2.1) and 3.37 eV at room temperature. As mentioned elsewhere, this enables applications in optoelectronics in the blue/UV region, including light-emitting diodes, laser diodes and photodetectors. Optically pumped lasing has been reported in ZnO platelets, thin films, clusters consisting of ZnO nanocrystals and ZnO nanowires.

2. **Large exciton binding energy.** The large free-exciton binding energy in ZnO of 60 meV indicates that efficient excitonic emission in ZnO can persist at room temperature and higher. Since the oscillator strength of excitons is typically much larger than that of direct electron-hole transitions in direct gap semiconductors, the large exciton binding energy makes ZnO a promising material for optical devices that are based on excitonic effects.

3. **Large piezoelectric constants.** In piezoelectric materials, an applied voltage generates a deformation in the crystal and vice versa. These materials are generally used as sensors, transducers and actuators. The low symmetry of the wurtzite crystal structure combined with a large electromechanical coupling in ZnO gives rise to strong piezoelectric and pyroelectric properties. Piezoelectric ZnO films with uniform thickness and orientation have been grown on a variety of substrates using different deposition techniques.
4. **Strong luminescence.** Due to a strong luminescence in the green-white region of the spectrum, ZnO is also a suitable material for phosphor applications. The emission spectrum has a peak at 495 nm and a very broad half-width of 0.4 eV. The n-type conductivity of ZnO makes it appropriate for applications in vacuum fluorescent displays and field emission displays. The origin of the luminescence center and the luminescence mechanism are not really understood, being frequently attributed to oxygen vacancies or zinc interstitials, without any clear evidence. These defects cannot emit in the green region, and it has been suggested that zinc vacancies are a more likely cause of the green luminescence. Zn vacancies are acceptors and likely to form in n-type ZnO.
5. **Strong sensitivity of surface conductivity to the presence of adsorbed species.** The conductivity of ZnO thin films is very sensitive to the exposure of the surface to various gases. It can be used as a cheap smell sensor capable of detecting the freshness of foods and drinks, due to the high sensitivity to trimethylamine present in the odor. The mechanisms of the sensor action are poorly understood. Some experiments reveal the existence of a surface electron accumulation layer in vacuum annealed single crystals, which disappears upon exposure to ambient air[18]. This layer may play a role in sensor action. The presence of this conducting surface channel has been suggested to be related to some puzzling type-conversion effects observed when attempting to obtain p-type ZnO.
6. **Strong non-linear resistance of polycrystalline ZnO.** Commercially available ZnO varistors are made of semiconducting polycrystalline films with highly non-ohmic current-voltage characteristics. While this nonlinear resistance has often been attributed to grain boundaries, the microscopic mechanisms are still not fully understood and the effects of additives and microstructures, as well as their relation to degradation mechanisms, are still under debate.
7. **Large non-linear optical coefficients.** ZnO crystals and, in particular, thin films exhibit second- and third-order non-linear optical behavior, suitable for non-linear optical devices. The linear and non-linear optical properties of ZnO depend on the crystallinity of the samples. ZnO films grown by laser deposition, reactive sputtering and spray pyrolysis show strong second-order non-linear response. Third-order non-linear response has been observed in ZnO nanocrystalline films[19]. The non-linear optical response in ZnO thin films is attractive for integrated non-linear optical devices.

8. **High thermal conductivity.** This property makes ZnO useful as an additive (*e.g.* ZnO is added to rubber in order to increase the thermal conductivity of tires). It also increases the appeal of ZnO as a substrate for homoepitaxy or heteroepitaxy[20]. High thermal conductivity translates into high efficiency of heat removal during device operation.
9. **Availability of large single crystals.** One of the most attractive features of ZnO as a semiconductor is that large area single crystals are available, and epi-ready substrates are now commercialized. The epitaxial growth of ZnO on native substrates can potentially lead to high quality thin films with reduced concentrations of extended defects.
10. **Amenability to wet chemical etching.** Semiconductor device fabrication processes greatly benefit from the amenability to low-temperature wet chemical etching. It has been reported that ZnO thin films can be etched with acidic, alkaline as well as mixture solutions. This possibility of low-temperature chemical etching adds great flexibility in the processing, designing and integration of electronic and optoelectronic devices.
11. **Radiation hardness.** Radiation hardness is important for applications at high altitude or in space. It has been observed that ZnO exhibits exceptionally high radiation hardness[21], the cause of which is still unknown.

2.1.3 Searching for a p-type ZnO

The prospect of using ZnO in optoelectronics has driven many research groups worldwide to focus on its semiconductor properties, trying to control the unintentional n-type conductivity and to achieve p-type conductivity. Theoretical studies, in particular first-principles calculations based on density functional theory (DFT), have also contributed to a deeper understanding of the role of native point defects and impurities on the unintentional n-type conductivity in ZnO[22, 23]. Acceptor doping has remained challenging, however, and the key factors that would lead to reproducible and stable p-type doping have not yet been identified and has proved to be a very difficult task. One reason is that ZnO has a tendency toward n-type conductivity, and progress toward understanding its causes is fairly recent. Another reason is that the defects, which it is known that are not responsible for n-type conductivity, do play a role as compensating centers in p-type doping [9, 10]. A third reason is the fact that there are very few candidate shallow acceptors in ZnO[24]. Column-IA elements (Li, Na, K) on the Zn site are either deep acceptors or are also stable as interstitial donors that compensate p-type conductivity. Column-IB elements (Cu, Ag, Au) are deep acceptors and do not contribute to p-type conductivity. And because oxygen is a highly electronegative first-row element, only nitrogen is likely to result in a shallow acceptor level in ZnO.

The other column-V elements (P, As, Sb) substituting on oxygen sites are all deep acceptors. In order to explain the reports on p-type doping using P, As or Sb, it was suggested that these impurities would substitute for Zn and form complexes with two Zn vacancies. One problem

with this explanation is that these complexes have high formation energies and are unlikely to form. In addition, the reports on p-type ZnO using P, As or Sb often include unexpectedly high hole concentrations, and contain scant information about the crystal quality of the samples or the stability of the p-type conductivity. Reports on p-type doping in nitrogen-doped ZnO have provided more detail and display a higher level of consistency.

2.1.4 ZnO synthesis and growth

ZnO nanostructures have been synthesized by a wide range of techniques, such as wet chemical methods ([25, 26, 27]), physical vapor deposition ([28, 29, 30]), metal-organic chemical vapor deposition (MOCVD) ([31, 32, 33]), molecular beam epitaxy (MBE)[34], pulsed laser deposition ([35, 36]), sputtering[37], flux methods[38], eletrospinning ([39, 40, 41]), and even top-down approaches by etching[42]. Among those techniques, physical vapor deposition and flux methods usually require high temperature, and easily incorporate catalysts or impurities into the ZnO nanostructures. Therefore, they are less likely to be able to integrate with flexible organic substrates for future foldable and portable electronics. MOCVD and MBE can give high quality ZnO nanowire arrays, but are usually limited by the poor sample uniformity, low product yield, and choices of substrate. Also, the experimental cost is usually very high, so they have been less widely adopted.

Pulsed laser deposition, sputtering and top down approaches have less controllability and repeatability compared with other techniques. Electrospinning gives polycrystalline fibers. Comparatively speaking, wet chemical methods are attractive for several reasons: they are low cost, less hazardous, and thus capable of easy scaling up ([43, 44]); growth occurs at a relatively low temperature, compatible with flexible organic substrates; there is no need for the use of metal catalysts, and thus it can be integrated with well-developed silicon technologies[45]; in addition, there are a variety of parameters that can tuned to effectively control the morphologies and properties of the final products ([46, 47]). However, wet chemical methods (such as sol-gel processes) are particularly adapted to produce ZnO colloids and films in a simple, low-cost and highly controlled way[48].

2.2 Sol-gel ZnO formation: State of the art

The sol-gel process, called also soft chemistry (*chimie douce*)³, allows elaborating a solid material from a solution by using a sol or a gel as an intermediate step, and at much lower temperatures than is possible by traditional methods of preparation. It enables the powderless processing of glasses and ceramics, and thin films or fibers directly from solution. The synthesis of solid materials via *chimie douce* often involves wet chemistry reactions and sol-gel chemistry based on the transformation of molecular precursors into an oxide network by hydrolysis and condensation reactions. One can summarize the film preparation in three parts:

³Reproduced from the enormous effort of Lamia Znaidi[48]

1. Preparation of the precursor solution.
2. Deposit of the prepared solution on the substrate by the chosen technique.
3. Heat treatment of the film.

The synthesis and thermal treatment of precursors (metal salt with stabilizer) in solvents to obtain a very well crystalline ZnO film is crucial. Search for the sol-gel precursor to minimize problems related with solubility or high temperature decomposition is a key point for this evolving technology⁴.

2.2.1 Salts

Several Zn salts have been used in the literature: nitrate, chloride, perchlorate, acetylacetonate and alkoxides such as ethoxide and propoxide, but the most often used is the acetate. Metal alkoxides, although they offer several chemical advantages, are not suitable because they are very sensitive to moisture, highly reactive and remain still rather expensive. Because of their low cost, facility of use, and commercial availability, metal salts are interesting as salts and could be more appropriate for large-scale applications. Since metal salts include inorganic and organic ones, one can underline the comparisons made between them and reported by some authors. Inorganic salts like nitrates are often used, as salts for sol-gel ZnO-based materials, even though their main drawback is related to the inclusion or difficult removal of anionic species in the final product ([49, 50, 51]). Transparent colloidal suspensions of zinc oxide in water have been also synthesised with 2-propanol, acetonitrile and using different zinc salts[52]. They reported that the anion, in zinc salt, is critical for the preparation of transparent and stable ZnO colloids. They mentioned that the use of zinc perchlorate instead of zinc acetate yields a turbid suspension; *i.e.*, coagulation of the particles takes place, the acetate acts so as stabilizer of the colloidal solution. Also, the experiments with $ZnCl_2$ or $Zn(NO_3)_2$ reveal a faster coagulation than in the case of $Zn(ClO_4)_2$ following the initial formation of a clear colloidal suspension. Matijević[53] reported that the preparation of mono-dispersed solutions of metal (hydrous) oxides from metal salts is very sensitive to such factors as salt concentration, nature of the anion, pH, and temperature. He demonstrated that entirely different products result when the anions are changed in the studied systems.

Other works[54] showed the importance of the counter anion in zinc salts, where hydrated ones (acetate, nitrate, perchlorate) were dissolved in ethanol or 2-Methoxyethanol (2-ME or ME) in the presence of Ethanolamine (EA), which acts at the same time as a base and a complexing agent. Further ageing at 60-100 °C, during variable periods, leads to translucent coloured colloidal solutions or precipitates, according to the counter anion and concentration. For nitrate, no solutions could be reproducibly obtained. In perchlorate solutions, excess EA leads to the

⁴To be consistent with the motivation of this work, only the literature prior to 2013 is used in this section and in the previous one (on the techniques used to synthesise ZnO). Nevertheless, the motivation's section will swing also with recent literature.

formation of solutions, after a slow dissolution of the initially formed precipitates. On the contrary, systems stemming from Zinc Acetate Dihydrate (ZAD) and EA lead to reproducible systems, under a great variety of experimental conditions. For example, ageing at 60 °C for 72 h results in the formation of stable translucent solutions by forced hydrolysis of Zn^{2+} complexes; the necessary water is supplied by the hydrated salt. Thus, acetate must play an important role in solution formation, by complexing Zn^{2+} cations, in competition with the EA.

2.2.2 Stabilizers

Additives such as stabilizers are chemical species presenting at least one functional group, which enables these species to play several roles. They act as basic or acid and/or chelating agent. Alkali metal hydroxides, carboxylic acids, alkanolamines, alkylamines, acetylacetone and polyalcohols are used for this purpose. They may facilitate the zinc salt dissolution in some alcoholic media. For example, ZAD has a limited solubility in alcohols like ethanol and 2-propanol in the absence of other agents or heating. Agents like (mono- to tri-) EA help in complete dissolution and formation of a stable solution[55]. Furthermore, the additives are believed to play the role of chelating and stabilizing ligands, which avoid the rapid precipitation of zinc hydroxide and allow stable dispersions or solutions to be formed. The amino groups and/or the hydroxyl groups of alkanolamines are known to coordinate the metal atoms of alkoxides, improving the solubility and stability against hydrolysis of the alkoxides[56]. This is also the case with ZAD and addition of alkanolamine provides a clear solution. Among inorganic bases, lithium or sodium hydroxide is often used to form stable dispersions of colloids.

Altogether, solvent and additives likely react with zinc cations to give zinc complexes that appear to be the precursor for zinc oxide. Several works have been devoted to the structural characterization of such complexes[54] (ZAD and EA, using ethanol). In this medium, forced hydrolysis and condensation of the Zn^{2+} cation are relatively slow, due to the low quantities of water (resulting from zinc salt). EA acts as a complexing agent, also retarding Zn^{2+} condensation; however, the presence of this amine also increases the pH, which should promote the formation of ZnO. The acetate group plays a very relevant role, by complexing Zn^{2+} in competition with the EA. In fact, three nucleophilic species (EA, HO⁻ and CH₃COO⁻) compete for the Zn^{2+} Lewis acid center: attack of an HO⁻ group leads to the formation of small zinc-oxo-acetate oligomers, which are expected to be formed in the initial stage, from gradual forced hydrolysis of Zn-EA or Zn-OCOCH₃ soluble complexes during ageing. The progressive condensation of the hydrolyzed moieties gives rise to colloids or precipitates.

2.2.3 Solvents

The solvent must present a relatively high dielectric constant in order to dissolve the inorganic salts ([50, 57, 58]). Most alcohols are dipolar, amphiprotic solvents with a dielectric constant that is dependent on the chain length[59]. Alcohols with low carbon number, up to 4, are the most used solvents: methanol (MeOH), ethanol (EtOH), 1-propanol, 2-propanol, 1-butanol and 2-ME.

In addition, a few works use ethylene glycol (HOCH₂CH₂OH) as a solvent that has a dielectric constant of 40.61 (at 25 °C) and a boiling point of 197.4 °C. Among all the mono-alcohols, the most used ones are ethanol and 2-propanol. It should be noted that 2-ME, despite its good physical properties and its extensive use in sol-gel ZnO formation, is toxic to reproduction, labelled with Risk Phrase R60 (category 2: "May impair fertility") by the International Programme on Chemical Safety, among others.

Hosono[57] made a comparative study of chemical reactions from ZAD to ZnO using different types of alcoholic solvents, *i.e.* MeOH, EtOH, and 2-ME. ZAD was more soluble in MeOH than in EtOH or 2-ME according to dielectric constants of these alcohols. The reflux time necessary for the formation of ZnO increases with the solutions in order: MeOH (12h), EtOH (48h), 2-ME (72h). Besides, the same authors demonstrated that diffraction analysis of particles, obtained from the three alcoholic solutions of ZAD revealed, after refluxing, the formation of intermediate product as Zn₅(OH)₈(Ac)₂·2H₂O called layered hydroxide zinc acetate (LHZA). This complex (LHZA) was also observed using EtOH[60] and MeOH ([61, 62]) as a solvent. On the other hand, other studies[63] have shown that ZAD dissolved in EtOH forms zinc oxy-acetate, Zn₄O(Ac)₆. Whichever their nature, these complexes undergo hydrolysis and inorganic polymerization leading to the formation of solutions consisting of zinc oxide nanoparticles, although no concrete mechanism has come to light.

2.2.4 Film formation and treatments

In general, films are prepared by dip- or spin-coating of substrate from solutions or sols freshly prepared or aged at room temperature or around 60 °C. The heat treatment of the deposited films is carried out in two steps⁵. For the first step, a pre-heat treatment (40-500 °C) is applied during a short time for solvent evaporation and organic compounds removal. The second step, a post-heat treatment is employed in order to obtain a well-crystallized films and the final decomposition of organic by-products varying from 250 to 900 °C, according to the substrate nature among others.

In the direct dense film formation, ZAD is dissolved in a 2-ME solution with EA. The ratio ([EA]/[Zn²⁺]) is normally fixed at 1 or 2, and the final concentration of ZAD at 0.75 mol/L. The resultant mixture is allowed to stand at 60 °C for 120 min under stirring leading to a clear and colorless solution, which remain stable for several days. Freshly prepared solution is then deposited on silica glass by spin-coating at 3000 rpm (30 s). These films are pre-heated at 300 °C for 10 min after each coating and this procedure is repeated up to six times. The films are post-heated at 550 °C (1-2 h) in order to obtain crystallized ZnO in wurtzite structure. The heat treatment appears to be one of the most important factors governing the film orientation. The preheat treatment appears to be a crucial step. Indeed, it governs the orientation of the crystallites during solvent evaporation and removal of the organic compounds. The temperature

⁵There is plenty of bibliography on the issue in the period 90s-2010, [64, 65, 66, 67, 68, 69, 70, 71, 72, 73, 55, 74, 75, 76, 77, 78, 79, 80, 81, 82, 83, 84, 85, 86, 87, 88, 89, 90]

of this treatment varies from case to case, but a clear rule can be deduced in its choice. It should be higher than the boiling point of the solvent and the additives and near the crystallization temperature of ZnO. A temperature around 300 °C appears to be the most appropriate ([91, 87]) in the case of 2-ME and EA to produce (002) oriented films, although the motive is unclear. Beside the pre-heat treatment, the post-heat temperature should be carefully chosen. The preferential orientation, for instance (002), increases with increasing temperature. For a great number of systems, a temperature range of 500-600 °C appears to be the most appropriate one, again with no fulfillment of the motive.

Up to this point, the reader may as well ascertain some concrete *cooking-like* recipe for a well-crystalline ZnO via sol-gel. Nevertheless, not only most of the compounds (solvent or additive) used are toxic and very high temperatures are required (up to 900 °C), but it appears to be non-industrialized and not even understandable process, since no tangible explanation is contributed for each one of these multiple steps but, on the contrary, more like a trial-and-error kind of procedure. Removal of the solvent and organic substances produced by precursor decomposition prior to crystallization may be one of the key factors that provide oriented crystal growth, but no one has yet fully studied it.

2.3 Zn-based Coordination Polymers (Zn-CPs)

A Coordination Polymer (CP) is an inorganic or organometallic polymer structure containing metal cation centers linked by organic ligands. More formally, a coordination polymer is a coordination compound with repeating coordination entities extending in 1, 2, or 3 dimensions. It can also be described as a polymer whose repeat units are coordination complexes. The design and development of coordination polymers (CP) is nowadays one of the most appealing and interesting areas of research. The rational selection of the metal center (M^{m+}), organic linkers and solvent provide a huge number of possibilities to achieve materials with different structures, properties and potential industrial and technological applications. Examples of the utility of CPs in photonics, for gas storage, as magnetic materials, in catalysis, as multimodal biomedical imaging, drug delivery and also as precursors in synthesis have been reported ([92, 93, 94, 95], demonstrating that these Zn-CPs are attractive in Nanoscience and Nanotechnology areas.

In this context, Zn(II) ion, with a d^{10} configuration and capable to adopt different coordination numbers and geometries[96], is probably one the most attractive M^{m+} ions to achieve new CPs. The discovery of novel uses of Zn-CPs prepared in the late years has stimulated considerably the interest in this sort of products. Articles showing their utility as sensors, as guests for molecular recognition and storage, as light-harvesting, as responsive sensitive materials and also as effective (homogeneous and also heterogeneous) catalyst have been reported. In the majority of Zn-CPs reported so far, the linkers are polydentate [N or (N,O) donor] ligands [97, 98, 99, 100, 101, 102, 103, 104, 105, 106] (*i.e.* bipyridines, aminoalcohols, etc.) and rigid di- (or to a lesser extent also tri- or tetra-) carboxylates with phenyl, naphthyl, anthracenyl, pyridinyl,

imidazolyl or thienyl moieties (even with additional functional groups). Examples of Zn-CPs without N-donor atoms in the linkers are less common [107, 108, 109]. Moreover, contributions on Zn-CPs have shown their great potential as precursors to achieve nanomaterials, *i.e.* nanopowders of ZnO and related morphology-preserved ZnO phases for technological applications and uses [110, 111, 112, 113, 114, 115]. In addition, recent studies suggest that the use of flexible or semiflexible ligands, which can adopt several conformations, may provide new paths to achieve CPs with novel topologies, properties, activities or applications [116, 117, 118].

2.4 Green Chemistry

In 1998, Paul Anastas and John Warner⁶ gave definition to the term *green chemistry*:

"Green Chemistry is the utilization of a set of principles that reduces or eliminates the use or generation of hazardous substances in the design, manufacture and applications of chemical products."

Green chemistry applies the following principles:

1. **Prevent waste:** Design chemical syntheses to prevent waste, leaving no waste to treat or clean up.
2. **Maximize atom economy:** Design synthetic methods to maximize the incorporation of all materials used in the process into the final product.
3. **Design less hazardous chemical syntheses:** Design syntheses to use and generate substances with little or no toxicity to humans and the environment.
4. **Design safer chemicals and products:** Design chemical products to be fully effective, yet have little or no toxicity.
5. **Use safer solvents and auxiliaries:** Avoid using solvents, separation agents, or other auxiliary chemicals. If these chemicals are necessary, use innocuous chemicals.
6. **Increase energy efficiency:** Run chemical reactions at ambient temperature and pressure whenever possible.
7. **Use renewable feedstocks:** Use raw materials and feedstocks that are renewable rather than depleting. Renewable feedstocks are often made from agricultural products or are the wastes of other processes; depleting feedstocks are made from fossil fuels (petroleum, natural gas, or coal) or are mined.
8. **Avoid chemical derivatives:** Avoid using blocking or protecting groups or any temporary modifications if possible. Derivatives use additional reagents and generate waste.

⁶Extracted from the work of Paul Anastas and John Warner "*Green Chemistry: Theory and Practice*", Oxford University Press: New York, 1998

9. **Use catalysts, not stoichiometric reagents:** Minimize waste by using catalytic reactions. Catalysts are used in small amounts and can carry out a single reaction many times. They are preferable to stoichiometric reagents, which are used in excess and work only once.
10. **Design chemicals and products to degrade after use:** Design chemical products to break down to innocuous substances after use so that they do not accumulate in the environment.
11. **Analyze in real time to prevent pollution:** Include in-process real-time monitoring and control during syntheses to minimize or eliminate the formation of by-products.
12. **Minimize the potential for accidents:** Design chemicals and their forms (solid, liquid, or gas) to minimize the potential for chemical accidents including explosions, fires, and releases to the environment.

2.5 Motivation of this work

ZnO properties are well known ([3, 119, 120, 2]) and sol-gel based processes are among the methodologies with greatest expectation to achieve low cost ZnO[121]. An optimal sol-gel precursor design is a key point for the emerging flexible and printed electronics development. Nowadays, sol-gel-derived ZnO is one of the most attractive oxides, due to its high electrical conductivity[20], good ultraviolet absorption behaviour, strong room-temperature luminescence[122], piezoelectricity, excellent environmental stability, chemical sensing[123], compatibility with large-scale processing, low cost, abundance, biocompatibility and easy fabrication. Various precursors involving ZAD mixed with nitrogen-based organic compounds have been studied ([124, 125]), demonstrating that these mixtures evolve towards periodic oligomer molecules. In these cases, aminoalcohols are expected to bridge zinc-acetate units in a single molecule, thus covering the metal-oxygen core with an organic shell and making it more soluble in non-polar solvents. Other works add a stabilizer to the precursor ([126, 127, 128, 129]). In most reports published so far[48], sol-gel ZnO is obtained by using Zinc Acetate Dihydrate (ZAD) as salt and Ethanolamine (EA) as stabilizer.

Deep studies of the synthesis conditions (crystallization temperature, deposition method, concentration,...) of ZAD is responsible of a well crystalline film and then *e.g.* of nice ZnO nanowires ([130, 131]). Some works demonstrate the huge influence that ambient humidity[132], precursor[133] or solvent[134] have on the pyrolysis of ZAD and the subsequent formation of ZnO ([135, 136, 137]). Other reports highlight the appearance of different intermediate compounds, such as hydroxyl- or anhydrous acetates[138], oxo-acetates[139] or hydrated hydroxyl-acetates[140] when similar ZAD species decompose, giving rise to nanowires[141], nanobelts[142] or other nanostructures ([143, 144, 145]).

It has been demonstrated that the annealing at 200 °C, which is the temperature commonly used to process the deposited ZnO precursor in order to use it in polymer solar cells, is not able to completely remove its organic traces[146]. Detailed investigations on sol-gel-derived ZnO thin films concluded that the suitable temperature range for annealing treatment is 300-700 °C[147], but these temperatures are not enough to remove residues from ZnO independently from the solvent used with ZAD+EA[148]. A sudden increase in carrier mobility in films annealed above 800 °C has been recently reported[149] and attributed to increase in crystallite size, because the large crystallites can lead to a decrease in electron scattering centres. However, this does not explain the large difference between the reported maximum mobility (100 cm^2/Vs) and that of high-quality bulk ZnO (205 cm^2/Vs)[2].

This mobility difference, together with the presence of an interfacial layer and traps at the interface between ZnO and p-type Si[149], assumed to be the cause of bad rectification behaviour, could be related to contamination in the sol-gel ZnO. The complexing agent and, in particular, EA, could be responsible of this fact, because of the residue that is left behind after thermal decomposition[150]. It is known that EA facilitates Zn(II) chelation and it promotes the formation of ZnO due to the amine functional group that increases the solution pH[151]. Consequently, a higher amount of EA leads to higher chelation rates of Zn^{2+} ions along the (002) minimum-surface-energy plane, resulting in higher *c*-axis orientation with less porosity[152]. Recently, processes such as hydrolysis, polymerization and complexation have been identified in sol-gel process using aminoalcohols[153].

Moreover, although the nature of ink additives should not influence the final material by any means, in this context, the presence of EA on the top of ZnO thin films has demonstrated to significantly decrease the optical performance of ZnO devices[151] and, in general, amines, cause dramatic impact on sol transparency, stability, and consequently on structural, optoelectronic, and morphological properties of films[154]. Some works demonstrate that aminoalcohols present high photosensitivity. Radicals based on CH_3-OCH_2 are formed after UV-irradiation of some aminoalcohols[155] and photo-oxidative cyclization of aminoalcohols produce 1,3-oxazines[156]. However the picture of the microscopic processes and technology that transform the sol-gel precursor film to pure ZnO is not definitively controlled yet and the understanding of the photosensitivity observed in the ZAD+EA precursor is far from complete and requires further investigation.

The computer power and the accuracy of theoretical approaches have been highly improved, allowing use of computational tools to understand the behaviour of metal organic species. For instance,

1. Recent studies on wurtzite (the most stable polymorph of ZnO[157]) demonstrate the power of the Perdew-Burke-Ernzerhof (PBE)[158] functional to analyze the electronic structure of bulk ZnO systems.
2. Zn(II) behavior is now better known thanks to the analysis of the electronic structure of zinc

complex molecules[159], the thermic fluctuations of $XZnO$ ($X = Al, Ga$ and In) materials around 3000-5000 K[160] and the speciation in $ZnCl_x$, ZnO and $ZnCO_3$ at different chloride concentrations[161] in all cases using the Car-Parrinello approach[162].

3. It is well known that computational studies at a Density Functional Theory level using Gaussian[163] and Car-Parrinello Molecular Dynamics (CPMD, [162]) software combined with metadynamics algorithms[164] are among the most valuable approaches to explain and rationalize, from condensed-matter physics to chemical processes, the stability, properties, and reactivity of a large variety of coordination compounds, providing a reasonable estimation of the successive paths of a chemical transformation for a variety of transition-metal ions ($Zn(II)$ in particular).

In addition, the substituent effects on the decomposition processes of the ZAD-stabilizer system must have a strong dependence[165]. For elucidating these aspects, EGA results are sometimes complemented with quantum chemical simulations[166], and molecular dynamics are usually a very useful tool to study the thermal decomposition processes of some nitrogen-based materials ([167, 168, 169]), carbonic acid[170], some pyrolysis mechanisms ([171, 172, 173, 174]), or many organic molecules [173, 175, 176], condensed substances like nitrobenzene[168], coal[174] or polymers [177, 178], metalorganic complexes[179] and, even, conformational changes in organic molecules[180] have been described by using this approach.

The increasing interest in the development of sol-gel ZnO inks is reflected by the recent specific studies again on the effect of solvents ([148, 181]), precursor nature and concentration ([182, 183]), sol ageing[184], annealing time ([146, 147]), temperature ([185, 149]), molar ratios EA:ZAD ([186, 152]) and even specific process parameters such as withdrawal speed in deep coating[187] on the properties of the ZnO product and its use as seed for nanostructures ([188, 189]). Nevertheless, the detailed progress from ZAD+EA towards pure crystalline ZnO was still ambiguous before the present work. In view of this and due to: a) the growing interest on Zn -based coordination polymers, b) the lack of studies centered on the use of naturally occurring polycarboxylic acids in the fabrication of Zn -CPs and c) the ongoing interest on synthesizing with green chemistry routes, it has been decided in the last part of this work to explore the use of CP as ZnO precursors.

Finally, it is widely accepted that the incorporation of ferrocenyl moieties into the frameworks of potentially bioactive cores commonly modifies the lipophilicity and solubility of the products and in general widens up the biological activity of CPs, increasing their interest. The anchorage of ferrocenyl units or the use of ferrocene derivatives as ligands might lead to hetero di- tri or, in general, polymetallic compounds or polymers. In this aspect, Heteropolynuclear (HPN) compounds are attracting a growing interest ([190, 191, 192]) to produce new materials for even more utilizations. For this aspect, the novel ferrocene derivatives are one of the most exciting areas of organometallic Chemistry since they also can be used as active centers in a wide variety of applications (catalysis, biomedicine...) ([193, 194, 195, 196, 197, 198]). One can ask oneself

whether is possible to add the individual properties of two metals, Zn and Fe in this case, in a single CP and also whether is there any mutual Zn-Fe cooperation[199]. This approach is called Molecular Hybridization and, in spite of its potential, few Zn-Fe CP are reported ([200, 201]). Thus, the study of the reaction between ZAD and the ferrocenecarboxylic to form an HPN Organometallic Compound (HPNOMC) would be the final goal of this work.

*"We have to confront the students with the frontiers of science
and I think you need a playground there to go in an unknown territory
and not to be guided too much along the paths we already know.
So let the university be a playground for young researchers"*
- Bernard L. Feringa in an interview about his Nobel in Chemistry 2016

METHODS

This chapter will present all the useful and necessary techniques and tools required for this work. These have been separated in three blocks: Materials science, Physical Chemistry studies and Computational approach. The first block is related to all the experiments needed to study the relationship between structure and properties of solid materials. X-ray diffraction should be highlighted as the most used technique in this first block, and a more detailed explanation will be provided. The second block is dedicated to all studies involved in the comprehension of processes occurring in both syntheses and evolution of the present compounds. Last but not least a Computational approach will close the third block of this large chapter. Sometimes experiments are not enough to understand the complexities of a system and thus one should have to roll up the sleeves and take a closer look towards the fundamentals.

3.1 Materials science

3.1.1 X-Ray Diffraction (XRD)

Understanding X-rays and diffraction.¹ X-rays were discovered in 1895 by the German physicist Roentgen and were so named because their nature was unknown at the time. Now we know that x-rays are electromagnetic radiation of exactly the same nature as light but of very much shorter wavelength. X-rays are produced when any electrically charged particle of sufficient kinetic energy is rapidly decelerated. When the voltage on an x-ray tube is raised above a certain value, characteristic of the target metal, sharp intensity maxima appear at certain wavelengths, superimposed on the continuous spectrum. They are called *characteristic lines*, since they are so narrow and since they are characteristic of the target metal used. These lines fall into several

¹Extracted from the work *Elements of X Ray Diffraction*, by Cullity and Stock [202]

sets, referred to as K, L, M, etc., in order of increasing wavelength, all the lines together forming the *characteristic spectrum* of the metal used as a target.

There are several lines in the K set, but only the three strongest are observed in normal diffraction work. These are K_{α_1} , K_{α_2} and K_{β_1} (Figure 3.1). The α_1 and α_2 components have wavelengths so close together that they are not always resolved as separate lines. The characteristic x-ray lines were discovered by W.H.Bragg and systematized by H.G.Moseley. The latter found that the wavelength of any particular line decreased as the atomic number of the emitter increased. In particular, he found a linear relation (Moseley's law) between the square root of the line frequency ν and the atomic number Z (relation 3.1, where C and σ are constants).

$$(3.1) \quad \sqrt{\nu} = C(Z - \sigma)$$

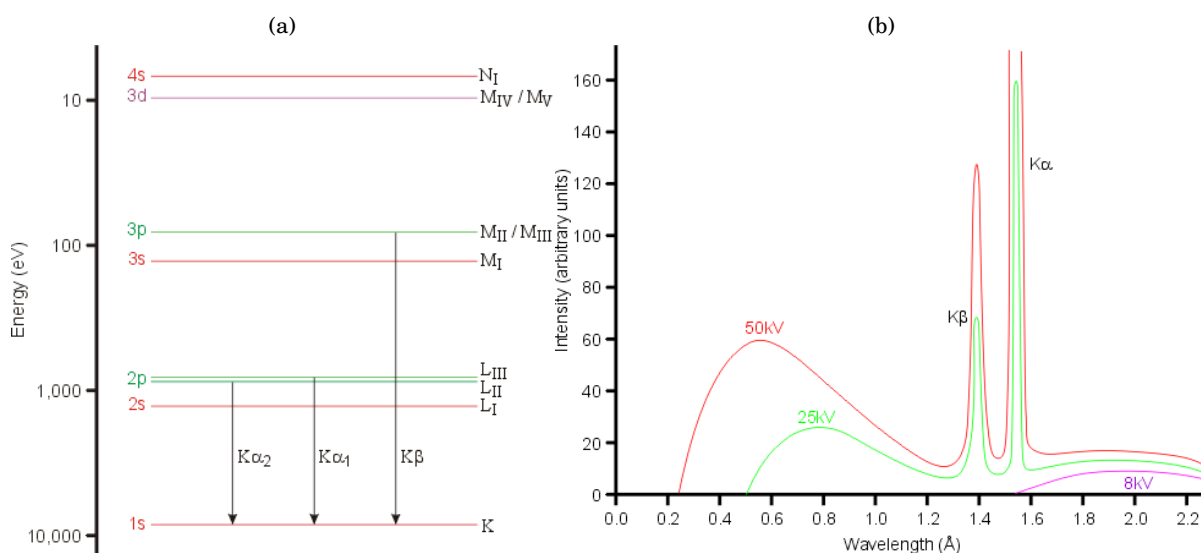


FIGURE 3.1. (a) Atomic levels involved in copper K_{α} and K_{β} emission. (b) A typical X-ray spectrum from a copper target.

Many x-ray diffraction experiments require radiation which is as closely monochromatic as possible. However, the beam from an x-ray tube contains both K_{α} and K_{β} at the continuous spectrum. The intensity of these undesirable components can be decreased relative to the intensity of the K_{α} line by passing the beam through a filter made of a material whose K absorption edge lies between K_{α} and K_{β} . Such a material will have an atomic number 1 or 2 less than that of the target metal. The thicker the filter, the lower the ratio of intensity of K_{β} to K_{α} in the transmitted beam. Filtration, however, is never perfect no matter how thick the filter, and one must compromise between reasonable suppression of K_{β} component and the inevitable weakening of the K_{α} .

Diffraction is, essentially, a scattering phenomenon in which a large number of atoms cooperate. Since the atoms are arranged periodically on a lattice, the rays scattered by them have definite phase relations between them. Diffraction in general occurs only when the wavelength of

the wave motion is of the same order of magnitude as the repeat distance between scattering centers. Indeed, since $\sin\theta$ cannot exceed unity, from the Bragg's law (figure 3.2):

$$(3.2) \quad \frac{n\lambda}{2d} = \sin\theta < 1$$

being n a positive integer (the diffraction order), d the interplanar distance and θ the incident angle, $n\lambda$ must be less than $2d$ and, since the smallest value of n is 1, the condition for diffraction at any observable angle 2θ is $\lambda < 2d$.

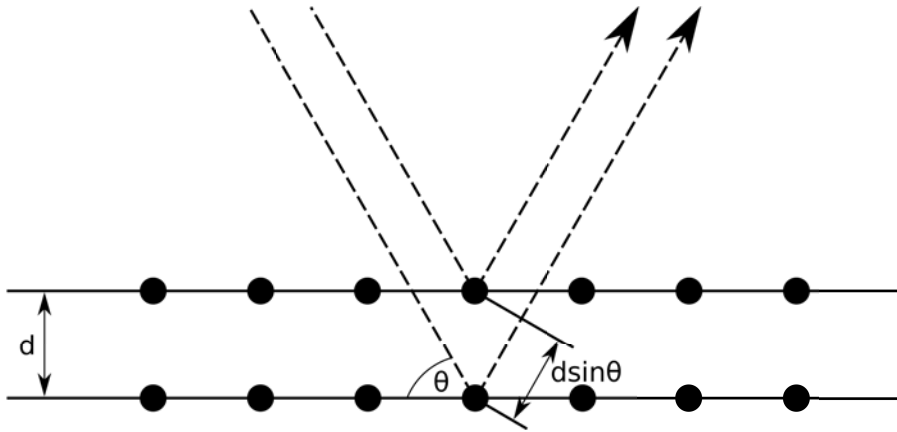


FIGURE 3.2. Bragg diffraction. Two beams with identical wavelength and phase approach a crystalline solid and are scattered off two different atoms within it. The lower beam traverses an extra length of $2d\sin\theta$. Constructive interference occurs when this length is equal to an integer multiple of the wavelength of the radiation.

Experimentally, the Bragg's law can be utilized to determine the spacing d of various planes in a crystal by using x-rays of known wavelength and θ . The orientation of planes in a lattice may also be represented symbolically, according to a system popularized by the English crystallographer Miller. The *Miller indices* are defined as the *reciprocals of the fractional intercepts which the plane makes with the crystallographic axes*. In particular, a family of lattice planes is determined by three integers h , k , and l , the Miller indices. They are written (hkl) , and denote the family of planes orthogonal to $h\mathbf{b}_1 + k\mathbf{b}_2 + l\mathbf{b}_3$, where b_i are the basis of the reciprocal lattice vectors².

Table 3.1: XRD methods depending on the ways λ and θ are varied

	λ	θ
Laue method	Variable	Fixed
Rotating-crystal method	Fixed	\approx Variable
Powder method	Fixed	Variable

Since diffraction can occur whenever the Bragg's law is satisfied, this equation puts conditions on λ and θ . The ways in which these quantities are varied distinguish three main diffraction

²For an infinite three-dimensional lattice, defined by its primitive vectors $(\mathbf{a}_1, \mathbf{a}_2, \mathbf{a}_3)$, its reciprocal lattice $(\mathbf{b}_1, \mathbf{b}_2, \mathbf{b}_3)$ can be determined by using matrix inversion $[\mathbf{b}_1 \mathbf{b}_2 \mathbf{b}_3]^T = (2\pi)[\mathbf{a}_1 \mathbf{a}_2 \mathbf{a}_3]^{-1}$

methods (Table 3.1). Although Laue's method is not used in the present work, it deserves to be mentioned, since it was the first ever used and reproduces von Laue's original experiment.

3.1.1.1 The single-crystal method

Single-crystal XRD is a non-destructive analytical technique which provides detailed information about the internal lattice of crystalline substances, including unit cell dimensions, bond-lengths, bond-angles, and details of site-ordering. Directly related is single-crystal refinement, where the data generated from the X-ray analysis is interpreted and refined to obtain the crystal structure. Single-crystal X-ray diffraction is most commonly used for precise determination of a unit cell, including cell dimensions and positions of atoms within the lattice. Bond-lengths and angles are directly related to the atomic positions.

Instrumentation, sample selection and preparation.³ The crystal structure of a mineral is a characteristic property that is the basis for understanding many of the properties of each mineral. Strengths and Limitations of Single-crystal X-ray Diffraction include:

Strengths

- Non-destructive and no separate standards required.
- Detailed crystal structure, including unit cell dimensions, bond-lengths, bond-angles and site-ordering information.

Limitations

- Must have a single, robust (stable) and optically clear sample, generally between 50 and 250 μm in size, although crystals can be broken off a larger sample and the best fragment selected.
- Twinned samples can be handled with difficulty and data collection generally requires between 24 and 72h.

After a proper crystal is chosen with a microscope it is introduced in an oriented way inside the diffractometer. Samples are mounted on the tip of a thin glass fiber using an epoxy or cement. Care should be taken to use just enough epoxy to secure the sample without embedding it in the mounting compound. The fiber may be ground to a point to minimize absorption by the glass. This fiber is attached to a brass mounting pin, usually by the use of modeling clay, and the pin is then inserted into the goniometer head. The goniometer head and sample are then affixed to the diffractometer. Samples can be centered by viewing the sample under an attached microscope or video camera and adjusting the X,Y and Z directions until the sample is centered under the cross-hairs for all crystal orientations.

Single-crystal diffractometers use either 3- or 4-circle goniometer (figure 3.3). These circles refer to the four angles (2θ , χ , ϕ , and Ω) that define the relationship between the crystal lattice,

³Extracted from the work *Single-crystal X-ray Diffraction*, by Christine M. Clark and Barbara L. Dutrow[203]

the incident ray and detector. Once the crystal is centered, a preliminary rotational image is often collected to screen the sample quality and to select parameters for later steps. X-rays leave the collimator and are directed at the crystal. Rays are either transmitted through the crystal, reflected off the surface, or diffracted by the crystal lattice. A beam stop is located directly opposite the collimator to block transmitted rays and prevent burn-out of the detector. Reflected rays are not picked up by the detector due to the angles involved. Diffracted rays at the correct orientation for the configuration are then collected by the detector. Modern single-crystal diffractometers use CCD (Charge-Coupled Device) technology to transform the X-ray photons into an electrical signal which are then sent to a computer for processing.

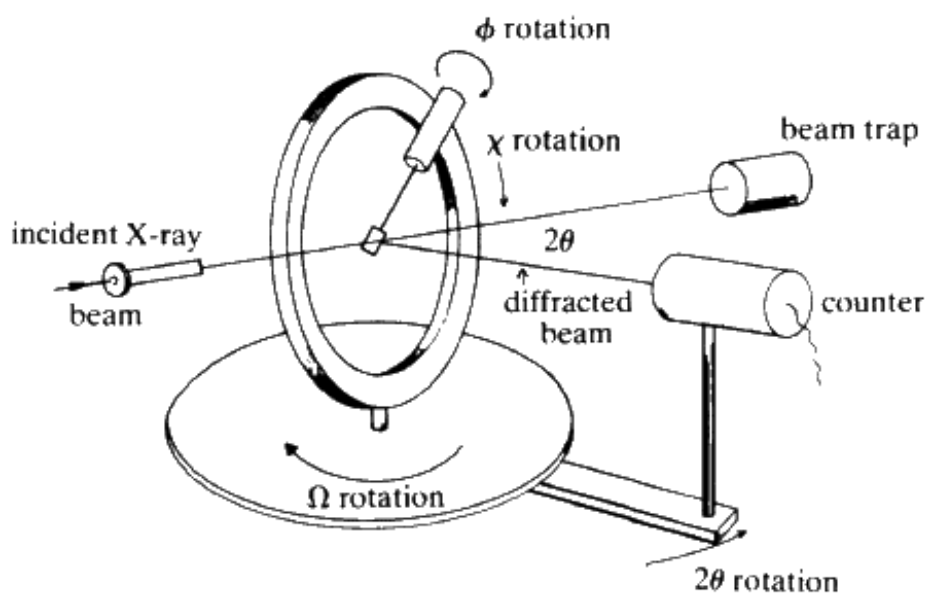


FIGURE 3.3. Schematic of 4-circle diffractometer; the angles between the incident ray, the detector and the sample.

An automatic collection routine can then be used to collect a preliminary set of frames for determination of the unit cell. Reflections from these frames are auto-indexed to select the reduced primitive cell and calculate the orientation matrix (which relates the unit cell to the actual crystal position within the beam). The primitive unit cell is refined using least-squares and then converted to the appropriate crystal system and Bravais lattice. This new cell is also refined using least-squares to determine the final orientation matrix for the sample. After the refined cell and orientation matrix have been determined, intensity data is collected. Generally this is done by collecting a sphere (Ewald's sphere) using an incremental scan method.

After the data have been collected, corrections for instrumental factors, polarization effects, X-ray absorption and (potentially) crystal decomposition must be applied to the entire data set. This integration process also reduces the raw frame data to a smaller set of individual integrated intensities. These correction and processing procedures are typically part of the software package which controls and runs the data collection.

Crystal structure resolution and the Phase problem.⁴ To be able to solve the crystal structure one must determine the electron density for all x, y, z in the unit cell ($\rho(x, y, z)$) solving the equation 3.3, that means taking the Fourier transform of the equation for $F(hkl)$. $F(hkl)$ represents the resultant diffracted beams of all atoms contained in the unit cell for a given direction. These magnitudes (actually waves), one for each diffracted beam, are known as *structure factors*. Their modules are directly related to the diffracted intensities. Also ϕ_{hkl} represents the phases of the structure factors. Actually one have limitations due to the extent for which the diffraction pattern (= the reciprocal space = the number of structure factors) is observed, that is, the number of structure factors is finite. Therefore the synthesis will be approximate only and may show some truncation effects.

$$(3.3) \quad \rho(x, y, z) = \frac{1}{V} \sum_{h, k, l} |F(hkl)| \exp[-2\pi(hx + ky + lz)i + i\phi_{hkl}]$$

Once one record the position (hkl) and intensity (I_{hkl}) of each reflection (the spots on the detector), the measured intensities are proportional to the coefficients ($I_{hkl} \propto |F(hkl)|^2$) of the electron density equation (3.3). However, in order to calculate $\rho(x, y, z)$ one also needs to know the phases of the different diffracted beams (ϕ_{hkl}). Unfortunately, this valuable information is lost during the diffraction experiment (there is no experimental technique available to measure the phases) and thus one must face to the so-called *phase problem*.

The phase problem can be easily understood if one compares the diffraction experiment (as procedure to see the internal structure of crystals) with a conventional optical microscope. In what one might call the *the impossible X-ray microscope* (the process of viewing inside the crystals to locate the atomic positions), the visible light is replaced by X-rays (with wavelengths close to 1 Å) and the sample (the crystal) also scatters this "light" (the X-rays). However one do not have any system of lenses that could play the role of the optical lenses, to recombine the diffracted waves providing one with a direct "picture" of the internal structure of the crystal. The X-ray diffraction experiment just gives one a picture of the reciprocal lattice of the crystal on a photographic plate or detector. The only thing one can do at this stage is to measure the positions and intensities of the spots collected on the detector but, regarding the phases, nothing can be concluded for the moment, preventing one from obtaining a direct solution of the electron density function.

Some alternatives are needed in order to retrieve the phase values. Currently, structures are usually solved either using an *ab initio* approach (direct methods) or the Patterson method, which relies on having several recognizable "heavy" atoms in the structure. The phase problem can still be an issue during structure solution and refinement today, especially with large, non-centrosymmetric structures with no heavy elements.

Solutions to the phase problem: The Patterson function. The very first solution to the phase problem was proposed by Arthur Lindo Patterson. Patterson introduced a new function ($P(uvw)$, equation 3.4), which defines a new space (the Patterson space). This function removes

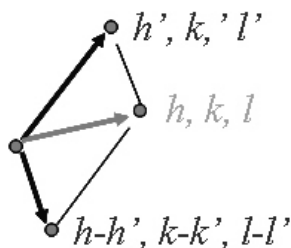
⁴Extracted from the work *Crystallography*, by Martín Martínez-Ripoll [204]

the term containing the phases, and the amplitudes of the structure factors are replaced by their squares. It is thus a function that can be calculated immediately from the available experimental data (intensities, which are related to the amplitudes of the structural factors). Formally, from the mathematical point of view, the Patterson function is equivalent to the convolution of the electron density with its inverse $\rho(x, y, z) * \rho(-x, -y, -z)$.

$$(3.4) \quad P(uvw) = \frac{1}{V} \sum_{hkl} |F(hkl)|^2 \cos(2\pi[hu + kv + lw])$$

The Patterson function provides a map of interatomic vectors (relative atomic positions), the height of its maxima being proportional to the number of electrons of the atoms implied. We will see that this feature means an advantage in detecting the positions of "heavy" atoms (with many electrons) in structures where the remaining atoms have lower atomic numbers. Once the Patterson map is calculated, it has to be correctly interpreted (at least partially) to get the absolute positions (x, y, z) of the heavy atoms within the unit cell. These atomic positions can now be used to obtain the phases ϕ_{hkl} of the diffracted beams by inverting $\rho(x, y, z)$ (equation 3.4) and therefore this will allow the calculation of the electron density function $\rho(x, y, z)$.

Solutions to the phase problem: The Direct methods. The phase problem for crystals formed by small and medium size molecules was solved satisfactorily by several authors throughout the 20th century with special mention to Jerome Karle (1918-2013) and Herbert A. Hauptmann (1917-), who shared the Nobel Prize in Chemistry in 1985 (without forgetting the role of Isabella Karle, 1921-). The methodology introduced by these authors, known as the direct methods, generally exploit constraints or statistical correlations between the phases of different Fourier components. The atomicity of molecules, and the fact that the electron density should be zero or positive, at any point of the unit cell, creates certain limitations in the distribution of phases associated with the structure factors. In this context, the direct methods establish systems of equations that use the intensities of diffracted beams to describe these limitations. The resolution of these systems of equations provides direct information on the distribution of phases. However, since the validity of each of these equations is established in terms of probability, it is necessary to have a large number of equations to overdetermine the phase values of the unknowns (phases ϕ_{hkl}).



$$(3.5) \quad F(h, k, l) = \phi_{hkl} \sum_{h'} \sum_{k'} \sum_{l'} F(h', k', l') \cdot F(h - h', k - k', l - l')$$

The direct methods use equations that relate the phase of a reflection (hkl) with the phases of other neighbor reflections (h', k', l') and $(h - h', k - k', l - l')$, assuming that these relationships are

"probably true" (P)...

$$(3.6) \quad P = \frac{1}{2} + \frac{1}{2} \tanh \left[\frac{1}{\sqrt{N}} |E(h, k, l)E(h', k', l')E(h - h', k - k', l - l')| \right]$$

where $E(h, k, l)$, $E(h', k', l')$ and $E(h - h', k - k', l - l')$ are the so-called *normalized structure factors*. That is, structure factors corrected for thermal motion, brought to an absolute scale and assuming that structures are made of point atoms. In other words, structure factor normalization converts measured $|F|$ values into "point atoms at rest" coefficients known as $|E|$ values. At present, direct methods are the preferred method for phasing structure factors produced by small or medium sized molecules having up to thousand atoms in the asymmetric unit. However, they are generally not feasible by themselves for larger molecules such as proteins.

Completing the structure. From several known atomic positions one can always calculate the structure factors: amplitudes, $|F_{cal}(hkl)|$, and phases, $\phi_{cal;hkl}$ (figure 3.4). Obviously, the calculated amplitudes can be rejected, because they are calculated from a partial structure and the experimental ones represent the whole structure. Therefore, the electron density map is calculated with the experimental (or observed) amplitudes, $|F_{obs}(hkl)|$, and the calculated phases, $\phi_{cal;hkl}$. This function is now evaluated in terms of possible new atomic positions that are added to the previously known ones, and the cycle repeated. Historically this process was known as *successive Fourier syntheses*, because the electron density is calculated in terms of a Fourier sum.

$$(3.7) \quad \Delta\rho(x, y, z) = \frac{1}{V} \sum_{h, k, l} [F_{obs}(hkl) - F_{cal}(hkl)] \exp[-2\pi i(hx + ky + lz)]$$

In any case, from atomic positions or directly from phases, if the information is correct, the function of electron density will be interpretable and will contain additional information (new coordinates) that can be injected into the cyclic procedure shown above until structure completion, which is to say until the calculated function $\rho(x, y, z)$ shows no changes from the last calculation. The lighter atoms of the structure (those with lower atomic number, *i.e.* usually hydrogen atoms) are the most difficult ones to find on an electron density map. Their scattering power is almost obscured by the scattering of the remaining atoms.

For this reason, the location of H atoms is normally done via a somewhat modified electron density function (the difference electron density), whose coefficients are the differences between the observed and calculated structure factors of the model known so far (equation 3.7). In practice, if the structural model obtained is good enough, if the experiment provided precise structure factors, and there are no specific errors such as X-ray absorption, the difference map $\Delta\rho(x, y, z)$ will contain enough signal (maxima) where H atoms can be located. Additionally, to get an enhanced signal from the light atoms scattering, this function is usually calculated with the structure factors appearing at lower diffraction angles only, usually with those at $\sin(\theta)/\lambda < 0.4$, that is, using the region where the scattering factors for hydrogens are still "visible".

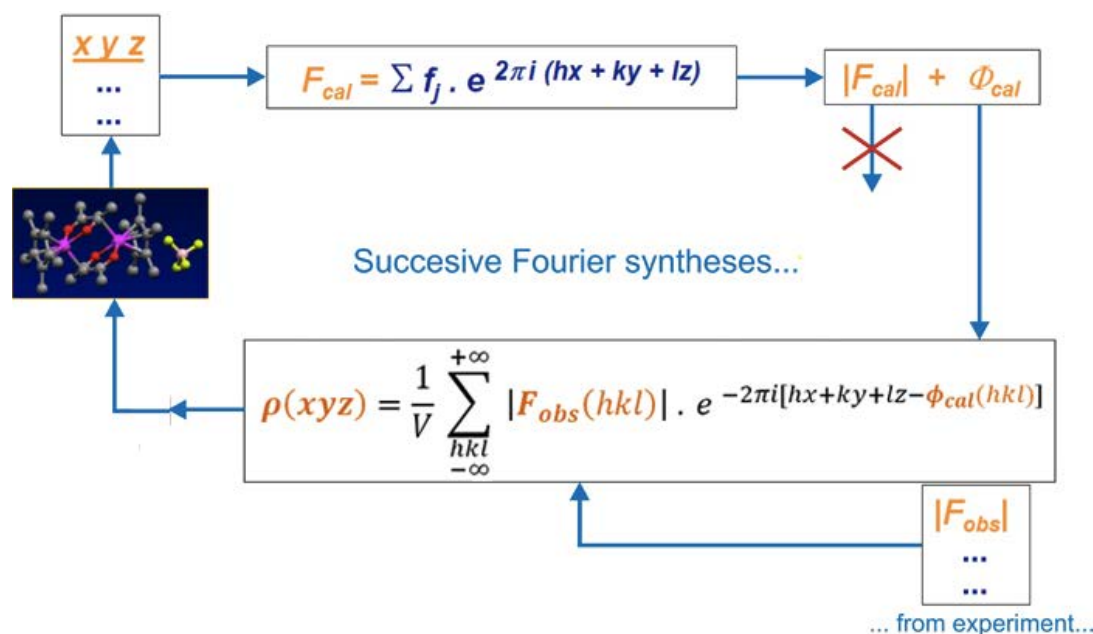


FIGURE 3.4. Scheme showing a cyclic process to calculate electron density maps $\rho(x, y, z)$ which produce further structural information.

Refining the structure. The electron density map generated by solution of the phase problem can be seen as a basic structure map. However, the assignment of atoms to different intensity centers is key to understand the structure, since the step of atom assignment is referred to as solving the crystal structure. The procedure can be mystifying to the beginner, but is reasonably straightforward. There are two basic procedures for structure solutions

- **Known crystal.** If the sample is a known mineral species, a template of a solved structure of that species may be used for initial atom assignment. This speeds solution, as the major sites can be assigned quickly. Once these have been assigned, the solution can be further manipulated to extract a better agreement between observed F_{obs} and calculated (F_{cal}) data. Typical steps include changing the site occupancy, splitting the site occupancy between two elements, allowing the sites to become anisotropic, and locating hydrogen. As hydrogen is the lightest element, it can be difficult to locate in minerals with significant "heavy" element content. Small changes are made at each step and then run through least-squares cycles, which recalculate the structure using Fourier transformations. Refiners tend to follow the same steps each time.
- **Unknown crystal.** More challenging is when the crystal is unknown or a new specimen. Here, a template may not be able to be used and elements must instead be assigned based on the geometry of the intensity centers and the chemistry of the material. This procedure can be much more difficult, as it is often through "trial and error" that the correct assignment is found. Once it has, the structure will be further refined as described above.

3.1.1.2 The Powder method

The powder method is the only method that can be employed when a single crystal specimen is no available⁵. Is also the most common method used worldwide to ascertain the crystal phases one might expect in a sample. It consists in a crystalline sample reduced to a very fine powder placed in a beam of monochromatic x-rays. Depending on the type of sample (whether it forms or can form a layer or not), different geometries can be used. Each particle of the powder is a tiny crystal oriented at random with respect to the incident beam. The result is that every set of lattice planes will be capable of reflection. The mass of powder is equivalent, in fact, to a single crystal rotated, not about one axis, but about all possible axes.

A single-crystal diffraction experiment generates thousands of diffracted beams whose intensities may be measured in correspondence to the reciprocal lattice points. The crystal structure determination from a decent single-crystal is rather straightforward but often provides doubtful results when only powder diffraction data are available. The hkl bragg peak on a 2D detector is no longer a single spot in space but the sum of spots arising from each contributing crystal. All the spots of one hkl form the same 2θ angle between the incident and the diffracted beam. They all lie in the diffracting cone (Debye-Scherrer cone). The intersections of a 2D detector plane with the diffracting cones produce rings and since its pattern is one-dimensional, the reciprocal lattice of the individual crystallites collapse onto the 2θ axis.

Solving a crystal structure: Indexing a powder pattern and determining the space group. As explained before, when it is not possible to get single crystals or when a re-crystallization of a polycrystalline powder material is not recommendable, it is meaningful the approach to a crystal structure solution and refinement from (X-ray) powder diffraction data. In general the (laboratory) x-ray powder diffractometers used to collect good diffraction data to obtain right intensities for crystal structure solution or refinement (or for quantitative phase analysis) are (still) not diffractometer with 2D detectors but with 1D or 0D. In addition most of the laboratory x-ray powder diffractometers are of Bragg-Brentano reflection (para)focusing geometry.

For convenience, it is quote in Table 3.2 the algebraic expressions of d_{hkl} for the various crystal systems. The main goal of the powder-pattern indexing⁶ process is the geometrical rebuilding of the 3D reciprocal space from the 1D distribution of the observed d values. Despite its long history and the great recent advances in experimental devices, mathematical methods and computing speed, powder pattern indexation can still be a challenge.

Whatever the indexing method, many plausible cells are usually suggested. Systematic ambiguities may occur when two or more different lattices, characterized by different reduced forms, may give calculated powder patterns with identical 2θ positions. It is then useful to apply a figure of merit (FOM) for discriminating the most probable ones and for assessing their

⁵Extracted from the book *Powder Diffraction*[205]

⁶Indexing is related to the fact that the unit cell determination step is equivalent to assigning the appropriate triple of Miller indices to each observed inter-planar distance.

reliability. The most adopted FOMs are M_{20} and F_N , proposed by de Wolff[206] and by Smith and Snyder[207], respectively (equations 3.8).

Table 3.2: Algebraic expressions of d_{hkl} for the various crystal systems.

System	$1/d_{hkl}^2$
Cubic	$\frac{h^2 + k^2 + l^2}{a^2}$
Tetragonal	$\frac{h^2 + k^2}{a^2} + \frac{l^2}{c^2}$
Orthorhombic	$\frac{h^2}{a^2} + \frac{k^2}{b^2} + \frac{l^2}{c^2}$
Hexagonal	$\frac{4}{3} \left[\frac{h^2 + hk + k^2}{a^2} \right] + \frac{l^2}{c^2}$
Monoclinic	$\frac{1}{\sin^2 \beta} \left[\frac{h^2}{a^2} + \frac{k^2 \sin^2 \beta}{b^2} + \frac{l^2}{c^2} - \frac{2hl \cos \beta}{ac} \right]$
Rhombohedral	$\frac{(h^2 + k^2 + l^2) \sin^2 \alpha + 2(hk + kl + hl)(\cos^2 \alpha - \cos \alpha)}{a^2(1 - 3 \cos^2 \alpha + 2 \cos^3 \alpha)}$
Triclinic	$\frac{1}{V^2} (S_{11}h^2 + S_{22}k^2 + S_{33}l^2 + 2S_{12}hk + 2S_{23}kl + 2S_{13}hl)$
	$S_{12} = abc^2(\cos \alpha \cos \beta - \cos \gamma) \quad S_{11} = b^2c^2 \sin^2 \alpha$
	$S_{23} = a^2bc(\cos \beta \cos \gamma - \cos \alpha) \quad S_{22} = a^2c^2 \sin^2 \beta$
	$S_{13} = ab^2c(\cos \gamma \cos \alpha - \cos \beta) \quad S_{33} = a^2b^2 \sin^2 \gamma$

$$(3.8) \quad M_{20} = \frac{Q_{20}}{2\langle \epsilon \rangle N_{20}} \quad ; \quad F_N = \frac{1}{\langle |\Delta 2\theta| \rangle N_{poss}} \frac{N}{N_{poss}}$$

where Q_{20} is the Q value in case of the 20th observed peak, $\langle \epsilon \rangle$ is the average discrepancy between the observed and calculated Q values for the 20 indexed peaks⁷, N_{20} is the number of calculated reflections⁸ up to the d value corresponding to Q_{20} , $\langle |\Delta 2\theta| \rangle$ is the average absolute discrepancy between the observed and calculated 2θ values and N_{poss} is the number of possible diffraction lines up to the N th observed line.

⁷ M_{20} depends on the fit between calculated and observed lines via $\langle \epsilon \rangle$.

⁸ M_{20} also depends on the volume of the unit cell via N_{20} .

There is not a threshold value of M_{20} ensuring the correctness of the cell⁹. Smith and Snyder[207] compared F_N and M_{20} performances, analysing a set of compounds and emphasizing the superiority of F_N with respect to M_{20} , due to the fact that the latter is defined for exactly 20 lines and depends strongly on the crystal class and space group.

The Direct space methods for indexing can be divided in two groups: Via Genetic Algorithm (GA) and via Monte Carlo approach - McMaille. The first exploits the idea of Darwinian evolution, where the aim is to find the lattice parameters $(a, b, c, \alpha, \beta, \gamma)$ having the best agreement with the experimental powder diffraction pattern. The agreement corresponds with the global minimum of hypersurface $R_{wp}(a, b, c, \alpha, \beta, \gamma)$ (equation 3.9).

$$(3.9) \quad R_{wp} = \sum_{regions} \sqrt{\frac{\sum_i w_i (y_i - y_{ci})^2}{\sum_i w_i y_i^2}}$$

\sum_i indicates the sum on the 2θ regions in which the pattern has been split by the user, i runs over the points in each region, y_i and y_{ci} are the observed and calculated diffraction patterns at the i th experimental step, with the intensities are estimated via the Le Bail algorithm ([208]). The second group exploits the information of the whole powder profile and used the Monte Carlo methods to randomly generate cell parameters. Then, Miller indices and the peak positions are calculated and the goodness of the cell is assessed by a suitable FOM.

One of the most common and widely used indexing program is DICVOL[209],[210]. It has an indexing approach based on the *dichotomy method*, introduced by Louër. The dichotomy method is based on the variation in direct space, by finite increments, of the lengths of cell edges and of the interaxial angles (an m -dimensional search, where m is the number of unknown unit cell parameters): the variations are reduced when they contain a possible solution. For example, if the a ($=b=c$) parameter is varied from a minimum value a_0 up to a maximum value a_M by using a step of p (in Å), the search space can be exploited via the interval $[a_0 + np, a_0 + (n + 1)p]$, where n is a variable integer. So:

$$(3.10) \quad Q(hkl) = \frac{h^2 + k^2 + l^2}{a_0 + (n + 1)p^2} \quad ; \quad Q_+(hkl) = \frac{h^2 + k^2 + l^2}{a_0 + np^2}$$

If, for the given n value, all the observed Q_i lines satisfy the relation

$$(3.11) \quad Q(hkl) - \Delta Q_i \leq Q_i \leq Q_+(hkl) + \Delta Q_i$$

where ΔQ_i is a suitable tolerance value, then the domain $[a_0 + np, a_0 + (n + 1)p]$ is halved and the procedure is repeated for six times ($n=6$) up to a final step length of $p/2^6$. In addition, DICVOL has been recently revisited[211],[212], and now it has a zero-point refinement of powder data, a tolerance for unindexed lines and the used of a systematic reduced-cell analysis in monoclinic

⁹De Wolff suggested that if the number of unindexed peaks among the first 20 lines is not larger than 2, and if $M_{20} > 10$, the indexing results should be substantially correct.

and triclinic systems to choose among equivalent solutions. Nevertheless, what makes indexing a difficult task are the large asymmetrical units (severe peak overlapping), lines measured with poor accuracy, the presence of impurities, pseudosymmetry, unequal lattice parameters¹⁰ and a large etcetera.

In order to determine the space group, one must note the systematic absences (reflection conditions), due to the presence of translational symmetries. Once the peaks have been indexed and the lack of diffraction peaks have been noticed, one can determine a possible crystal system, its cell volume and the space group by taking a closer look to the reflection conditions for its crystal system ([213]).

Solving a crystal structure: Asymmetric units, Pattern Matching and Rietveld refinement. The next step to solve the crystal structure of a compound when no single-crystal is accessible, is the determination of the asymmetric unit: the possible content of the molecular models. Using the observed (or known) density (ρ), a possible molar mass (M) and the cell volume (V), one should check whether a solution (cell parameters result of an indexation) corresponds to an integer number of chemical formula in the cell (Z , equations 3.12).

$$(3.12) \quad \rho = \frac{MZ}{N_A V_c} \quad ; \quad Z = \frac{V(\text{\AA}^3)\rho(g \cdot cm^{-3})}{1.66M(g \cdot mol^{-1})}$$

Once an integer Z is obtained, the cell parameters and the space group determine the peak positions and then it is time then to make a *Pattern matching*¹¹: the experimental powder pattern must be compared with a theoretical one based on the crystal system, the space group and the cell parameters. On the contrary, although the indexation of the powder pattern provided a clear crystal system, a volume cell and a space group, if Z is found to be a non-integer, one must check the proposed molar mass, and thus the molecular model.

A powder diffraction pattern is a set of peaks, some overlapped, superimposed on a smooth and slowly varying background. Rietveld ([214],[215]) realized that a the whole pattern is a smooth curve that consists of Gaussian peaks (Y_{hkl}) on top of a smooth background (Y_b) and that the best way of extracting the maximum information from it was to write a mathematical expression to represent the observed intensity at every step in this pattern (equation 3.13). Then, the adjustable parameters for this model can be refined by a least-squares minimization of the weighted differences between the observed and calculated intensities.

This approach is so powerful that it led to a renaissance in powder diffraction and it is now known as the *Rietveld refinement*.

$$(3.13) \quad Y_{cal} = Y_b + \sum Y_{hkl}$$

The Rietveld method refines user-selected parameters to minimize the difference between an experimental pattern (observed data) and a model based on the hypothesized crystal structure and instrumental parameters (calculated pattern). It considers a full profile fitting using

¹⁰But e.g. a) equal within experimental error, 2)one much longer than the other two, c)one much shorter than the other two (dominant zone), ...

¹¹The intensities can vary free, they are not constrained by any structural model.

crystallographic constraints, such as the lattice parameters and space group to constrain peak positions and the crystal structure to constrain the peak intensities. If the data is reliable, one should be able to interpolate the curve properly "*connecting de dots*" and if the structure model makes physical and chemical sense one can finally solve the crystal structure.

When the number of observations (powder profile points) exceeds the number of parameters a minimization of equation 3.14 by least-squares will give parameter estimates of minimum variance in any linear combination. The weight w is computed from the variance in the observed powder profile intensity, Y_{obs} , and it is generally assumed that there are nonzero covariances between different Y_{obs} across the powder pattern.

$$(3.14) \quad M = \sum w(Y_{obs} - Y_{cal})^2 \quad ; \quad Y_{cal} = K|F(hkl)|^2 H(\Delta T_{hkl})$$

The calculated powder profile intensity, Y_{cal} , depends on the product of various correction and scaling factors, K , on the reflection intensities, $|F(hkl)|$ (see section 3.1.1.1), and on the value of the profile function for the location of the profile point relative to the reflection position, $H(\Delta T_{hkl})$. Consequently, the models used to describe the powder diffraction profile must accurately represent a close correspondence to the scattering process that gives rise to features in the observed pattern to avoid significant systematic errors. The quality of the least squares refinement is indicated by the residual functions R_{wp} (equation 3.9), R_p and the goodness of fit, χ^2 , (equations 3.15).

$$(3.15) \quad R_p = \frac{\sum |Y_{obs} - Y_{cal}|}{\sum Y_{obs}} \quad ; \quad \chi^2 = \frac{M}{N_{obs} - N_{var}}$$

The free software used in the present work for *ab initio* structure determination from powder diffraction is called *Free Objects for Crystallography* (FOX, [216]). Although a further yet deeper explanation of the Rietveld refinement is not the aim of this work, occasionally other parameters have to be mentioned. These describe preferred orientation or texture, absorption and other effects and may be directly related to other parameters via space group symmetry or by relations that are presumed to hold by the experimenter. These relations can be described in the refinement as "constraints" and as they are related with shifts in the parameters. Finally, once Rietveld method has been successfully applied, the crystal structure resolution can be reported.

3.1.2 X-ray spectroscopy

3.1.2.1 X-ray Photoelectron Spectroscopy (XPS)

What happens at surfaces of a sample is extremely important in a vast range of applications, from environmental corrosion to medical implants. A surface can be thought of as the interface between different phases (solid, liquid or gas) and as the top layer of atoms, although in reality the state of this layer is very much influenced by the 2-10 atomic layers below it. A surface modification treatments are often in the range of 10-100 nm thick and > 100 nm can be considered *the bulk*. In a surface analysis, there are a vast of techniques available for one wanting to study

the properties and reactivity of the surface as a function of the bonding geometry of molecules, the physical topography, the chemical composition, its chemical or atomic structure or its electronic state. No one technique can provide all these pieces of information, however, to solve a specific problem it is seldom necessary to use every available technique.

The basic principle of X-ray photoelectron spectroscopy (XPS) is based on the photoelectronic effect, which was first discovered by Albert Einstein in 1905. The photoemission process from a solid sample takes place when a highly energetic photon ($h\nu$) interacts with matter, causing an electron to be removed from an atomic orbital or from a band (with binding energy E_B), to reach the vacuum level (E_V figure 3.5), sometimes even with a certain kinetic energy (E_{kin}). The excitation energy must be large enough for the electrons to overcome the work function (Φ) of the solid (equation 3.16 relative to the Fermi level E_F).

$$(3.16) \quad h\nu = E_B + \Phi + E_{kin}$$

Once the electron is removed from the orbital, leaving a vacancy, an electron from a higher energy level may fall into the vacancy, resulting in a release of energy. Although most often this energy is released in the form of an emitted photon (figure 3.6), the energy can also be transferred to another electron, which is ejected from the atom. This second ejected electron is called an *Auger electron*.

Quoting Duparc[217] "It has been claimed by R. Sietmann[218] that the attribution of the discovery of the so-called "Auger" effect to Pierre Auger was a false attribution and that Lise Meitner should have got the credit for that discovery. However Sietmann himself recognised that Meitner's description of this effect was "buried in" two larger papers ([219], [220]) whose primary concern was nuclear physics. Sietmann only mentioned Auger's 1925 article and did not mention his 1923, an omission now found in many places. When examined again L. Meitner's and P. Auger's contributions to the description of the "Auger effect", it can be noticed that Meitner's concern was the exact nature of the (nuclear) beta radiations about which she opposed Ch. D. Ellis, and this had been the subject of an intense Berlin-Cambridge controversy where Ellis' description eventually prevailed. Auger's observations[221] were the central theme of his PhD thesis at the J. Perrin's laboratory on the composed photoelectric effect.

While thus L. Meitner should have shared the Nobel Prize with O. Hahn, the Auger effect has rightly been attributed to Auger". An XPS spectrum is a measure of the intensity of photoelectrons as a function of E_B or E_{Kin} , meaning that that one can perform an elemental identification and look at the chemical state of an element, also a relative composition of the constituents in the surface region and the valence band structure. An schematic of an XPS apparatus is shown in figure 3.7. The basic requirements for a photoemission experiment are: a source of fixed-energy radiation (an x-ray source), an electron energy analyser (which can disperse the emitted electrons according to their kinetic energy, and thereby measure the flux of emitted electrons of a particular energy) and a high vacuum environment (to enable the emitted photoelectrons to be analysed without interference from gas phase collisions).

Chemical effects and quantification with XPS. For each and every element, there will be a characteristic energy associated with each core atomic orbital and will give rise to a set of peaks related to the concentration of the element within the sample region. Thus, the technique provides a quantitative analysis of the surface composition and is sometimes known by the alternative acronym ESCA (Electron Spectroscopy for Chemical Analysis). Some XPS quantitative measurements are as accurate as $\approx 10\%$. In addition, the exact binding energy of an electron depends not only upon the level from which photoemission is occurring, but also upon the formal oxidation state of the atom and on the local chemical and physical environment. Changes in these two points produce small shifts in the peak positions in the spectrum, called *chemical shifts*.

Atoms of a higher positive oxidation state exhibit a higher binding energy due to the extra coulombic interaction between the photo-emitted electron and the ion core. This ability to discriminate between different oxidation states and chemical environments is one of the major strengths of the XPS technique. In practice, the ability to resolve between atoms exhibiting slightly different chemical shifts is limited by the peak widths, which are governed by a combination of factors, such as: the intrinsic width of the initial level and the lifetime of the final state, the line-width of the incident radiation (for traditional x-ray sources can only be improved by using x-ray monochromators) and the resolving power of the electron-energy analyser. In most cases, the second incident radiation factor is the major contribution to the overall line width.

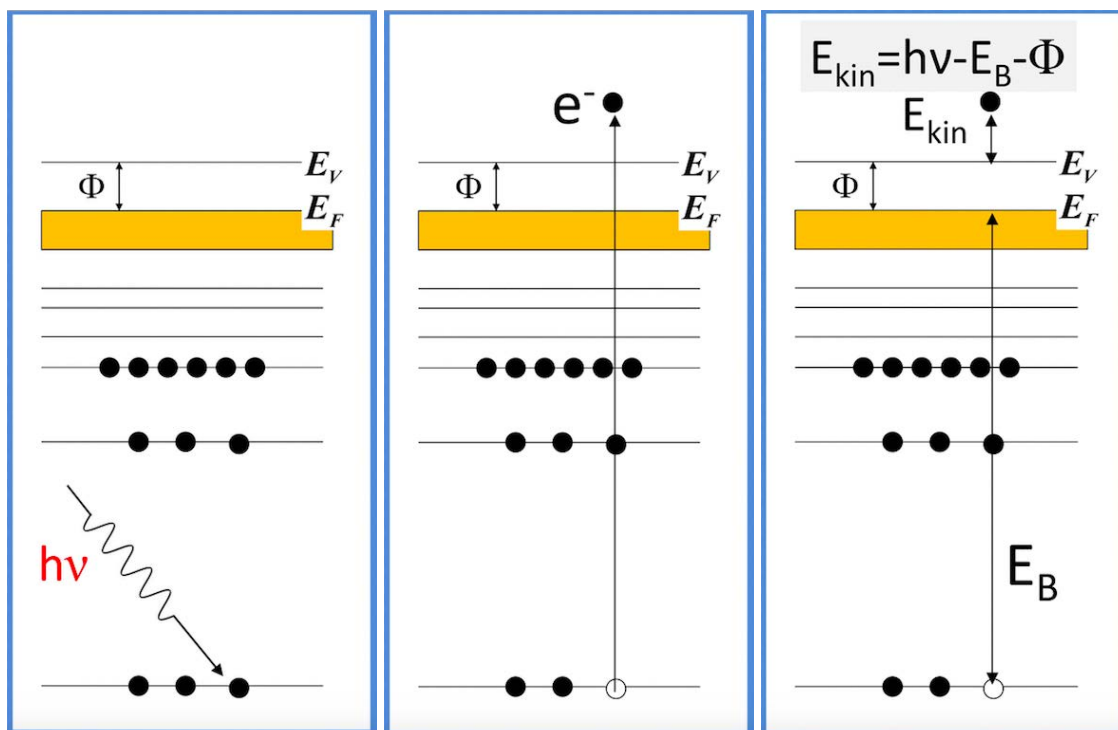


FIGURE 3.5. Schematic of XPS physics, the Photoelectric Effect.

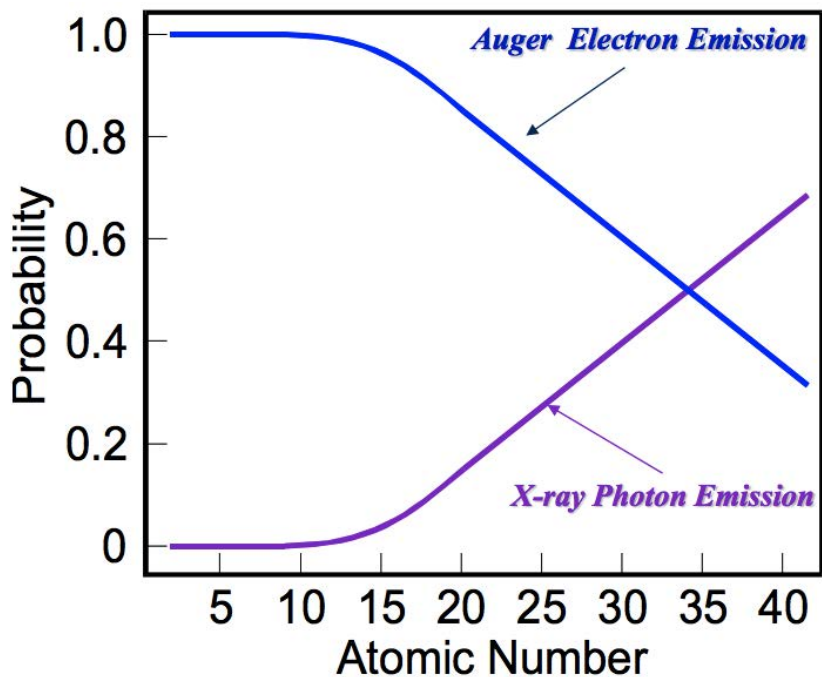


FIGURE 3.6. Auger electron v X-ray photon emission depending on the atomic number.

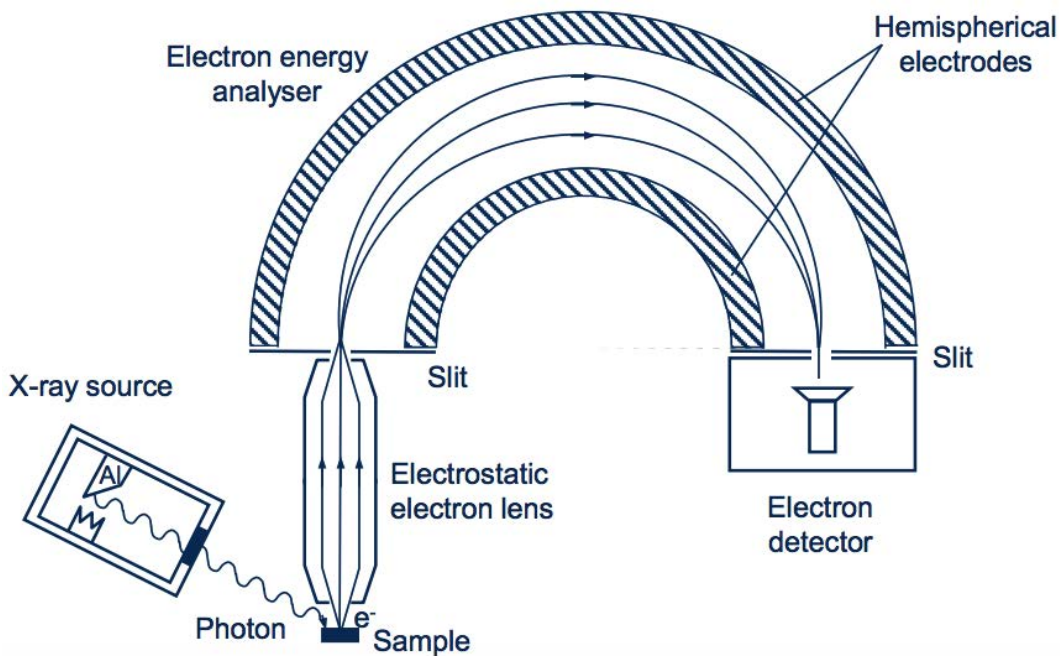


FIGURE 3.7. Schematic of an XPS spectrometer. The number of emitted electrons measured as function of their kinetic energy

3.1.2.2 Energy Dispersive X-ray Spectroscopy (EDX/EDS)

With EDS, the X-ray spectrum emitted by a solid¹² can be used to obtain a localized chemical analysis. In principle, all elements $4 < Z < 92$ can be detected. X-ray intensities are measured by counting photons and the precision obtainable is limited by statistical error. For major elements, it is usually not difficult to obtain a precision better than a relative $\pm 1\%$, but the overall analytical accuracy is commonly nearer the $\pm 2\%$. The detachability of small peaks is limited by the X-ray spectrum produced by the bombarding electrons, owing to the presence of "background". The detection limits are typically about 1000 ppm (by weight), but can be reduced by using long counting times.

Spectrometers: Qualitative analysis. The Energy-dispersive (ED) spectrometers employ pulse height analysis: a detector giving output pulses proportional in height to the X-ray photon energy is used in conjunction with a pulse height analyser. Incident X-ray photon cause ionization in the detector, producing an electrical charge, which is amplified by a sensitive preamplifier located close to the detector. An ED spectrometer is specially useful for both qualitative analysis because a complete spectrum can be obtained very quickly. The fact that the total spectrum of interest, from 0.1 keV to the beam energy (e.g. 20 keV) can be acquired in a short time (10 - 100 s), allows for a rapid evaluation of the specimen.

In performing qualitative analysis, one has to identify the specific energy of the characteristic x-ray peaks for each element. This information is available in the form of tabulations, graphs or as computer database. Since the EDS detector has virtually constant efficiency (near 100 %) in the range 3 to 10 keV, the relative peak heights observed for the families of x-ray lines are close to the values expected for the signal as it is emitted from the sample. On the negative side, the relatively poor energy resolution of the EDS leads to frequent spectral interference problems as well as the inability to separate the members of the x-ray families, which occur at low energy (< 3 keV). Also, the existence of spectral artifacts such as escape peaks or sum peaks increases the complexity of the spectra.

Spectrometers: Quantitative analysis. X-ray intensities are measured by counting pulses generated in the detector by X-ray photons, which are emitted randomly from the sample. If the mean number of counts recorded in a given time is n , then the numbers recorded in a series of discrete measurements form a Gaussian distribution with a standard deviation (σ) of $\frac{\sqrt{n}}{n}$. A suitable measure of the statistical error in a single measurement is $\pm 2\sigma$. It follows that 40 000 counts must be collected to obtain a 2σ precision of $\pm 1\%$ (relative). Such statistical considerations thus dictate the time required to measure intensities for quantitative analysis.

The optimum choice of accelerating voltage is determined by the elements present in the specimen. The accelerating voltage (in kV) should be not less than twice the highest excitation

¹²As explained before the Characteristic X-rays result from electron transitions between inner orbits, which are normally full. An electron must first be removed in order to create a vacancy into which another can "fall" from an orbit further out.

energy (E_C , in keV) of any element present, in order to obtain adequate intensity. For instance, in silicates, the element with the highest atomic number is commonly Fe, which also has the highest excitation energy (7.11 keV), hence the accelerating voltage should be at least 15 kV. Line intensities increase with accelerating voltage, but so does electron penetration, making spatial resolution worse and increasing the absorption suffered by the emerging X-rays. The other important variable selected by the user is beam current. The higher the current the higher the X-ray intensity, but there are practical limitations. Some samples are prone to beam damage, which necessitates the use of a low current. In the case of ED analysis, the limited throughput capability of the system has to be considered and a current as low as a few nA may be appropriate.

With decreasing concentration, statistical errors and uncertainties in background corrections become dominant. For a concentration in the region of 100 ppm the intensity measured on the peak consists mainly of background. The smallest detectable peak may be defined as three times the standard deviation of the background count. An order-of-magnitude detection limit estimate can be obtained as follows. If the count rate for a pure element is 1000 counts/s and the peak-to-background ratio is 500:1, the background count rate is 2 counts/s. In 100 s a total of 200 background counts will be accumulated, giving a relative standard deviation of $\frac{\sqrt{200}}{200}$ (or 0.07). Since the background intensity in this case is equivalent to the peak count rate for a concentration of 1000 ppm, three standard deviations is thus equivalent to a concentration of $0.07 \times 3 \times 1000 = 212$ ppm.

Reducing the detection limit requires more counts, which can be obtained by increasing the counting time and /or the beam current. In ED analysis, detection limits are typically about 0.1 %, although reduction can be achieved by using long counting times or better count rate. Values given here for detection limits refer to samples such as silicates, for which the mean atomic number (which determines continuum intensity) is quite low. Phases containing heavy elements give higher detection limits due to the higher background. Further, detection limits for heavy elements (using L or M lines) tend to be somewhat higher because the peak-to-background ratio is lower than for K lines.

3.1.3 Scanning Electron Microscopy (SEM)

The scanning electron microscope uses a focused beam of high-energy electrons to generate a variety of signals at the surface of solid specimens. Accelerated electrons in an SEM carry significant amounts of kinetic energy, and this energy is dissipated as a variety of signals produced by electron-sample interactions (figure 3.8) when the incident electrons are decelerated in the solid sample. These signals include secondary electrons (that produce SEM images), backscattered electrons, diffracted backscattered electrons (that are used to determine crystal structures and orientations of minerals), photons (characteristic X-rays that are used for elemental analysis and continuum X-rays), visible light (cathodoluminescence), and heat. Secondary electrons and backscattered electrons are commonly used for imaging samples: secondary electrons are most

valuable for showing morphology and topography on samples and backscattered electrons are most valuable for illustrating contrasts in composition in multiphase samples (*i.e.* for rapid phase discrimination).

X-ray generation is produced by inelastic collisions of the incident electrons with electrons in discrete orbitals (shells) of atoms in the sample. As the excited electrons return to lower energy states, they yield X-rays that are of a fixed wavelength (that is related to the difference in energy levels of electrons in different shells for a given element), as explained before. Thus, characteristic X-rays are produced for each element in a mineral that is "excited" by the electron beam. SEM analysis is considered to be "non-destructive"; that is, x-rays generated by electron interactions do not lead to volume loss of the sample, so it is possible to analyze the same materials repeatedly.

The main components of a typical SEM are electron column, scanning system, detector(s), display, vacuum system and electronics controls (figure 3.9). The electron column of the SEM consists of an electron gun and two or more electromagnetic lenses operating in vacuum. The electron gun generates free electrons and accelerates these electrons to energies in the range 1-40 keV in the SEM. The purpose of the electron lenses is to create a small, focused electron probe on the specimen. Most SEMs can generate an electron beam at the specimen surface with spot size less than 10 nm in diameter while still carrying sufficient current to form acceptable image. Typically the electron beam is defined by probe diameter in the range of 1 nm to 1 μm , probe current from pA to μA ; and probe convergence from 10^{-4} to 10^{-2} radians.

In order to produce images the electron beam is focused into a fine probe, which is scanned across the surface of the specimen with the help of scanning coils. Each point on the specimen that is struck by the accelerated electrons emits signal in the form of electromagnetic radiation. Selected portions of this radiation, usually secondary and/or backscattered electrons, are collected by a detector and the resulting signal is amplified and displayed on a TV screen or computer monitor. The resulting image is generally straightforward to interpret, at least for topographic imaging of objects at low magnifications. The electron beam interacts with the specimen to a depth approximately 1 μm . Complex interactions of the beam electrons with the atoms of the specimen produce wide variety of radiation. The need of understanding of the process of image formation for reliable interpretation of images arises in special situations and mostly in the case of high-magnification imaging. In such case knowledge of electron optics, beam-specimen interactions, detection, and visualization processes is necessary for successful utilization of the power of the SEM.

Interaction volume. The concept of interaction volume of the primary beam electrons and the sampling volume of the emitted secondary radiation are important both in interpretation of SEM images and in the proper application of quantitative X-ray microanalysis. The image details and resolution in the SEM are determined not by the size of the electron probe itself but rather by the size and characteristics of the interaction volume. When the accelerated beam electrons strike a specimen, they penetrate inside it to depths of about 1 μm and interact both elastically

and inelastically with the solid, forming a limiting interaction volume from which various types of radiation emerge.

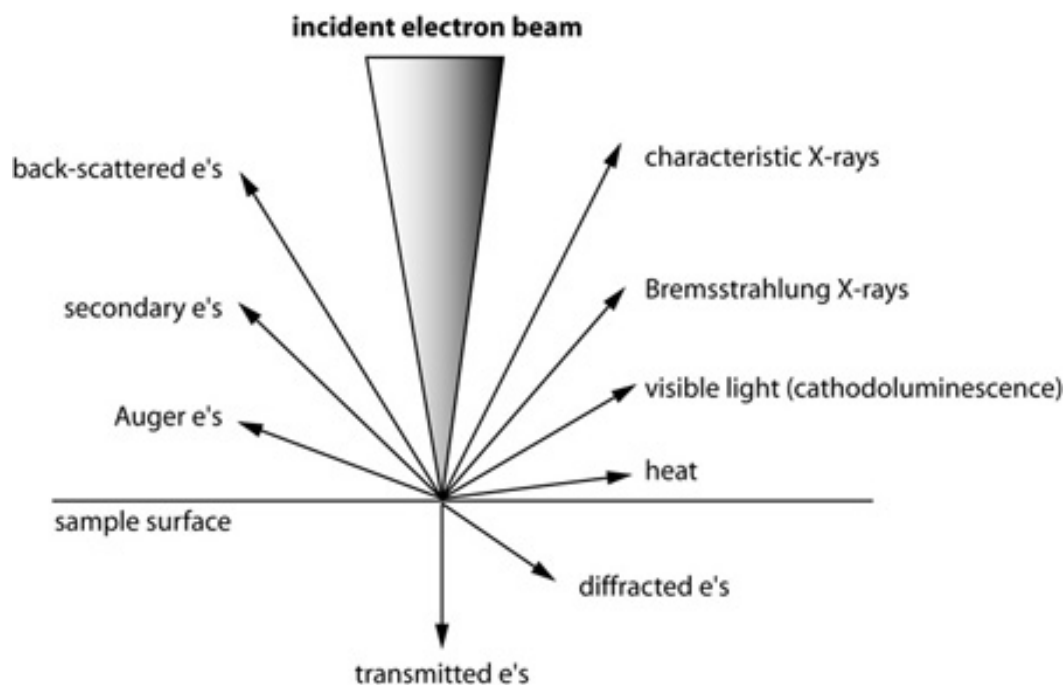


FIGURE 3.8. Types of interactions between electrons and a sample.

The combined effect of elastic and inelastic scattering controls the penetration of the electron beam into the solid. The resulting region over which the incident electrons interact with the sample is known as interaction volume. The interaction volume has several important characteristics, which determine the nature of imaging in the SEM. The energy deposition rate varies rapidly throughout the interaction volume, being greatest near the beam impact point. The interaction volume has a distinct shape. For low-atomic-number target it has distinct pear shape. For intermediate and high-atomic number materials the shape is in the form of hemisphere. The interaction volume increases with increasing incident beam energy and decreases with increasing average atomic number of the specimen. For secondary electrons the sampling depth is from 10 to 100 nm and diameter equals the diameter of the area emitting back-scattered electrons. Ultimately the resolution in the SEM is controlled by the size of the interaction volume.

Image formation. The SEM image is a 2D intensity map in the analog or digital domain. Each image pixel on the display corresponds to a point on the sample, which is proportional to the signal intensity captured by the detector at each specific point. Unlike optical or transmission electron microscopes, no true image exists in the SEM. It is not possible to place a film anywhere in the SEM and record an image. The image is generated and displayed electronically. The images in the SEM are formed by electronic synthesis, no optical transformation takes place, and no real or virtual optical images are produced in the SEM. In an analog scanning system, the beam is moved continuously with a rapid scan along the X-axis (line

scan) supplemented by a step-wise slow scan along the Y-axis at predefined number of lines. The time for scanning a single line multiplied by the number of lines in a frame gives the frame time.

In digital scanning systems, only discrete beam locations are allowed. The beam is positioned in a particular location remains there for a fixed time, called dwell time, and then it is moved to the next point. When the beam is focused on the specimen an analog signal intensity is measured by the detector. The voltage signal produced by the detector's amplifier is digitized and stored as discrete numerical value in the corresponding computer registry. Typically, the intensity is digitized into 8 bits (256 levels), 12 bits (4096) or 16 bits (65536). The digital image is viewed by converting the numerical values stored in the computer memory into an analog signal for display on a monitor.

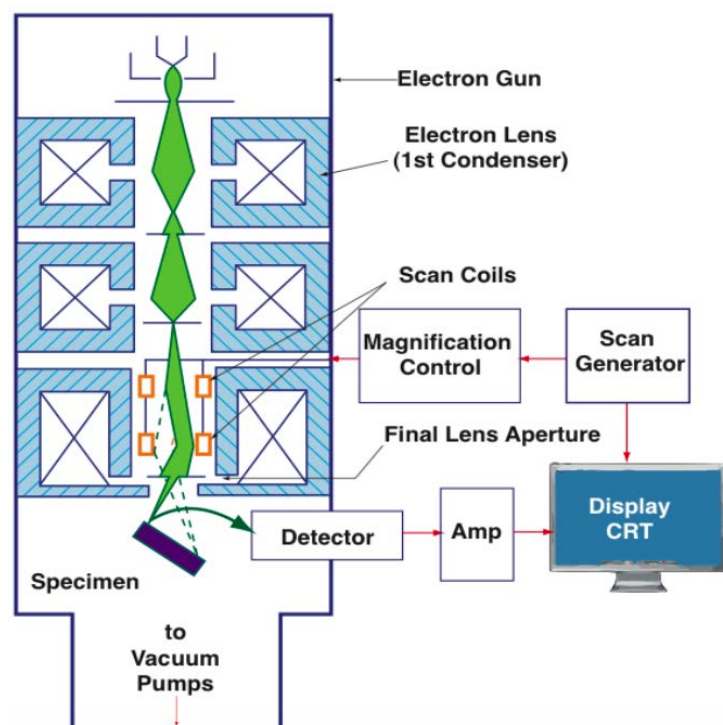


FIGURE 3.9. Main components of a typical SEM.

3.2 Physical Chemistry studies

3.2.1 Infrared (IR) spectroscopy

Radiation is absorbed and emitted in photons. The defining characteristic of a photon is that its energy cannot be split into smaller pieces and each photon's energy is defined by its frequency ν or wavelength λ as $E_{\text{photon}} = h\nu$, where h is the Planck's constant ($h = 6.626 \times 10^{-34}$ J·s). Infrared is absorbed by organic molecules between 600 and 4000 cm^{-1} , and since the IR's photon energy is very small with respect to the covalent bond energy, the absorbing IR should not trigger substantial chemical changes, although IR contains more energy than random thermal motion at room temperature ($\approx 0.6 \text{ kcal/mol}$).

IR spectroscopy is certainly one of the most important analytical techniques available to today's scientists. An infrared spectrum is commonly obtained by passing IR radiation through a sample and determining what fraction of the incident radiation is absorbed at a particular energy. The energy at which any peak in an absorption spectrum appears corresponds to the frequency of a vibration of a part of a sample molecule. One of its great advantages is that virtually any sample in virtually any state may be studied. Is a technique based on the vibrations of the atoms of a molecule. The IR spectrum plots the % Transmittance (%T) with respect to the IR energy (in wavenumbers, cm^{-1}). The %T compares intensity of IR striking the sample with intensity of IR leaving the sample, so a 100 %T (or 0 %) means no light (or all light) has been absorbed by the sample. It follows change in dipole caused by vibrating atoms: Polar bonds (strong bond dipoles) for example O–H, C=O, C≡N or C–O, absorb strongly, and on the contrary nonpolar bonds, for example C≡C or C=C, absorb weakly.

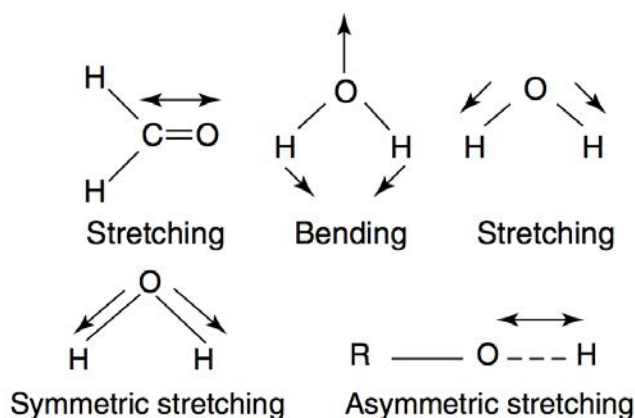


FIGURE 3.10. Stretching and bending vibrations in molecules.

It also follows the number of overlapping bands, since C–H bands tend to overlap. The energy follows the vibration frequency of atoms. Light atoms vibrate more rapidly (CH, NH or OH vibrations $> 2800 \text{ cm}^{-1}$), and multiple bonds also vibrate more rapidly: C≡C ($2100 - 2200 \text{ cm}^{-1}$), C≡N ($2240 - 2280 \text{ cm}^{-1}$), C=O ($1680 - 1750 \text{ cm}^{-1}$), C=C ($2240 - 2280 \text{ cm}^{-1}$), C–C ($1025 - 1200 \text{ cm}^{-1}$). Vibrations can involve either a change in bond length (stretching) or bond angle (bending) (figure 3.10). Some bonds can stretch in-phase (symmetrical stretching) or out-of-phase (asymmetric stretching). If a molecule has different terminal atoms such as HCN, ClCN or ONCl, then the two stretching modes are no longer symmetric and asymmetric vibrations of similar bonds, but will have varying proportions of the stretching motion of each group. In other words, the amount of coupling will vary.

3.2.2 Nuclear Magnetic Resonance (NMR)

Nuclei have positive charges and most of them behave as though they were spinning. Anything that is charged and moves has a magnetic moment and produces a magnetic field.

Therefore, a spinning nucleus acts as a tiny bar magnet oriented along the spin rotation axis. This tiny magnet is often called a nuclear spin. If one puts this small magnet in the field of a much larger magnet, its orientation will no longer be random. There will be one most probable orientation. However, if the tiny magnet is oriented precisely 180° in the opposite direction, that position could also be maintained. In scientific jargon the most favorable orientation would be the low-energy state and the less favorable orientation the high-energy state.

The small nuclear magnet may spontaneously "flip" from one orientation (energy state) to the other as the nucleus sits in the large magnetic field. However, if energy equal to the difference in energies (ΔE) of the two nuclear spin orientations is applied to the nucleus, much more flipping between energy levels is induced. The irradiation energy is in the radiofrequency range and is typically applied as a short pulse (e.g., many microseconds). The absorption of energy by the nuclear spins causes transitions from higher to lower energy as well as from lower to higher energy. This two-way flipping is a hallmark of the resonance process. The energy absorbed by the nuclear spins induces a voltage that can be detected by a suitably tuned coil of wire, amplified, and the signal displayed as a free induction decay. Relaxation processes eventually return the spin system to thermal equilibrium, which occurs in the absence of any further perturbing radiofrequency pulses.

Sensitivity. In practice, the nucleus is not putted in a magnetic field. Rather a huge number (approaching Avogadro's number) of nuclei are in the sample that is placed in a magnetic field. The distribution of nuclei in the different energy states (i.e., orientations of nuclear magnets) under conditions in which the nuclear spin system is unperturbed by application of any radiofrequency energy is given by the Boltzmann equation 3.17, where N_{up} and N_{lo} represent the population of nuclei in upper and lower energy states, respectively, k is the Boltzmann constant and T is the absolute temperature. Thus, a small population difference presents a significant sensitivity problem for NMR because only the difference in populations is detected (the others effectively cancel one another). The low sensitivity of NMR is probably its greatest limitation. The sensitivity can be increased by the use of stronger magnetic fields (which increase the population ratio), as well as the choose of different nuclei (since they have different natural abundances, table 3.3).

$$(3.17) \quad \frac{N_{up}}{N_{lo}} = \exp[-\Delta E/kT]$$

Although a description of nuclear magnetization is based essentially on quantum mechanics, another way of viewing the NMR phenomenon is to use a classical mechanical description. For a spin $1/2$ nucleus in a magnetic field of strength B_0 , the nucleus' magnetic moment will precess about the z -axis defined by the direction of the magnetic field. The angular frequency of precession ω_0 is proportional to B_0 . The nuclei may be oriented either parallel or antiparallel to the direction of the magnetic field. Consequently, some spins precess about the positive z -axis and some about the negative z -axis. From the previous discussion, there will be a slight excess of nuclei oriented

Table 3.3: Properties of nuclei most useful for NMR studies.

Nucleus	Spin (I)	Abundance (%)	Sensitivity (% vs ^1H)
^1H	1/2	99.9844	100
^2H	1	0.0156	0.965
^{13}C	1/2	1.108	1.59
^{15}N	1/2	0.365	0.104
^{19}F	1/2	100	83.3
^{31}P	1/2	100	6.63

with the magnetic field, *i.e.*, in the lower energy state, so the sum will yield a magnetization along the positive z-axis. It will be the total magnetization that determines an NMR signal, not the magnetic moment of an individual nucleus.

Relaxation and chemical shifts. The process by which a nuclear spin system returns to thermal equilibrium after absorption of radiofrequency energy is called *relaxation*. Relaxation processes, which neither emit nor absorb radiation, permit the nuclear spin system to redistribute the population of nuclear spins. Some of these processes lead to the nonequilibrium spin distribution ($N_{lo} - N_{up}$) exponentially approaching the equilibrium distribution (N_{eq} , equation 3.18), with a spin-lattice relaxation time τ for which the perturbed system return 63 % of the way toward thermal equilibrium.

$$(3.18) \quad N_{lo} - N_{up} = N_{eq}(1 - \exp[-t/\tau])$$

Nuclei of different elements, having different gyromagnetic ratios, will yield signals at different frequencies in a particular magnetic field. However, it also turns out that nuclei of the same type can achieve the resonance condition at different frequencies. This can occur if the local magnetic field experienced by a nucleus is slightly different from that of another similar nucleus; for example, the two ^{13}C NMR signals of ethanol occur at different frequencies because the local field that each carbon experiences is different. The reason for the variation in local magnetic fields can be understood if one takes into account that B_0 will induce electron currents in the molecule in the plane perpendicular to the applied magnetic field, and that these induced currents will then produce a small magnetic field opposed to the applied field, acting to partially cancel the applied field, thus shielding the nucleus. In general, the induced opposing field is about a million times smaller than the applied field and the frequency at which a particular nucleus achieves resonance clearly will depend on the shielding reflecting the electronic environment of the nucleus.

Spin-Spin coupling (Splitting) and peak intensity. A nucleus with a magnetic moment may interact with other nuclear spins resulting in mutual splitting of the NMR signal from each nucleus into multiplets. The number of components into which a signal is split is $2nI+1$, where I is the spin quantum number and n is the number of other nuclei interacting with the nucleus. For example, a nucleus (^{13}C or ^1H) interacting with three methyl protons will give rise to a

quartet. To a first approximation, the relative intensities of the multiplets are given by binomial coefficients: 1:1 for a doublet, 1:2:1 for a triplet, and 1:3:3:1 for a quartet. The difference between any two adjacent components of a multiplet is the same and yields the value of the spin-spin coupling constant J (in Hz). One important feature of spin-spin splitting is that it is independent of magnetic field strength, so increasing the magnetic field strength will increase the chemical shift difference between two peaks, but the coupling constant J will not change.

The area of an NMR signal (the peak intensity), but not the height (the peak amplitude), is directly proportional to the number of nuclei contributing to the signal under suitable experimental conditions. Those conditions are that the delay between acquiring free induction decays for signal averaging purposes should be higher than 4τ . Consequently, if the concentration of nuclei is known for a particular peak, it can be used as a standard. This delay is required for complete relaxation of all nuclei.

3.2.3 Thermogravimetric analysis (TGA)

Thermogravimetric Analysis is a technique in which the mass of a substance is monitored as a function of temperature or time as the sample specimen is subjected to a controlled temperature program in a controlled atmosphere. A TGA consists of a sample pan that is supported by a precision balance. That pan resides in a furnace and is heated or cooled during the experiment, while the mass of the sample is monitored. A sample purge gas controls the sample environment. This gas may be inert or a reactive gas that flows over the sample and exits through an exhaust. Measurements are used primarily to determine the composition of materials and to predict their thermal stability. The technique can characterize materials that exhibit weight loss or gain due to absorption/desorption of volatiles, decomposition, oxidation and reduction.

If the identity of the product after heating is known, then the yield can be found from analysis of the ash content. By taking the weight of the known product and dividing it by the initial mass of the starting material, the mass percentage of all inclusions can be found. Knowing the mass of the starting material and the total mass of inclusions, such as ligands, structural defects, or side-products of reaction, which are liberated upon heating, the stoichiometric ratio can be used to calculate the percent mass of the substance in a sample. The results from thermogravimetric analysis may be presented by mass versus temperature (or time) curve, referred to as the thermogravimetric curve, or by rate of mass loss versus temperature curve, referred to as the differential thermogravimetric curve.

Most TGA curves display weight losses. These are typically caused by chemical reactions (decomposition, combustion, reduction...) or physical transitions (vaporization, evaporation, sublimation, desorption, drying...). Occasionally, a gain in weight is observed. This also can result from chemical reactions (reactions with gaseous substances in the purge gas such as O_2 , CO_2 with the formation of non-volatile or hardly volatile compounds) or physical transitions (adsorption of gaseous substances on samples such as active charcoal).

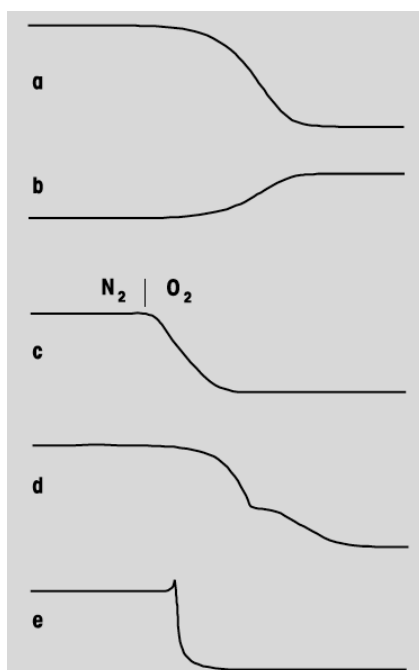


FIGURE 3.11. TGA chemical reactions:

a: Thermal decomposition with the formation of gaseous reaction products.

b: Corrosion, oxidation of metals (formation of non-volatile oxides).

c: Combustion of carbon black on gas switching.

d: Multi-step decomposition.

e: Explosive decomposition with recoil effect.

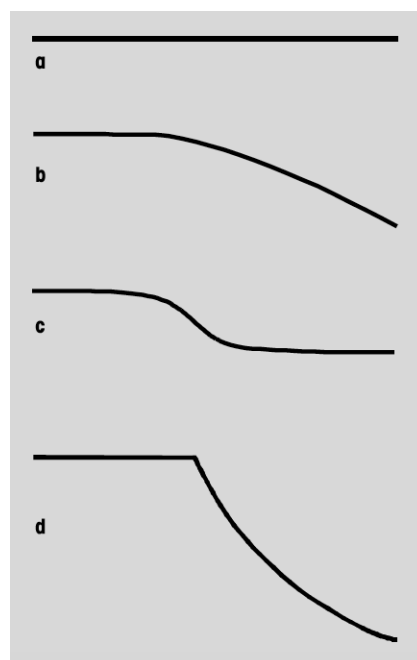
FIGURE 3.12. TGA Gravimetric effects:

a: Sample with low vapor pressure (no TGA effect).

b: Volatile melt (the liquid sample evaporates).

c: Moisture escapes on melting.

d: Sample melts with decomposition.



Interpreting TGA curves: Chemical reactions and gravimetric effects. Thermogravimetry is often used to investigate chemical reaction in which weight changes occur. A typical weight loss step usually develops slowly from the initially horizontal TG curve. The point of inflection is at about 60% conversion. The radius of curvature is appreciably smaller at the end of the reaction than at the beginning (figure 3.11). In theory, one does not expect to observe a gravimetric effect when a substance melts (figure 3.12). Despite the difference in buoyancy due to the slight change

in the density of the sample on melting is usually less than $1 \mu\text{g}$, the melting of a substance often causes a noticeable change on the TGA curve. Many gravimetric effects have nothing to do with chemical reactions or melting processes. The most frequently observed are drying steps. These usually occur at the beginning of the temperature program. Low molecular weight organic compounds often show a tendency to sublime and liquids evaporate in open crucibles over a wide temperature range below their boiling point. If, however, a sealed crucible with a small hole in the lid is used, a so-called self-generated atmosphere is created in the crucible. The molecules of vapor remain in equilibrium with the liquid phase until the boiling point is reached.

3.2.4 Differential Scanning Calorimetry (DSC)

Differential scanning calorimetry is a technique for measuring the energy necessary to establish a nearly zero temperature difference between a substance and an inert reference material, as the two specimens are subjected to identical temperature regimes in an environment heated or cooled at a controlled rate. Whether the temperatures of the sample and reference are controlled independently (using separate, identical furnaces) or are connected by a low-resistance heat-flow path (a metal disc), one can distinguish two types of DSC, power-compensation DSC and heat-flux DSC respectively (figure 3.13). For convenience, only the latter will be deeply explained hereby.

Heat-flux DSC: Characteristics. In this technique, the sample and reference are enclosed in the same furnace. The difference in energy required to maintain them at a nearly identical temperature is provided by the heat changes in the sample. Any excess energy is conducted between the sample and reference through the connecting metallic disc. The thermocouples are not embedded in either of the specimens; the small temperature difference that may develop between the sample and the inert reference (usually an empty sample pan and lid) is proportional to the heat flow between the two. The fact that the temperature difference is small is important to ensure that both containers are exposed to essentially the same temperature programme. The main assembly of the DSC cell is enclosed in a cylindrical, silver heating block, which dissipates heat to the specimens via a constantan disc attached to the silver block.

The sample and reference pans are placed on a two raised platforms on the disc. A chromel disc and a connecting wire are attached to the underside of each platform, and the resulting chromel-constantan thermocouples are used to determine the differential temperatures of interest. Alumel wires attached to the chromel discs provide the chromel-alumel junctions for independently measuring the sample and reference temperature. A separate thermocouple embedded in the silver block serves a temperature controller for the programmed heating cycle. An inert gas is passed through the cell at a constant flow rate of about 40 mL/min. The thermal resistances of the system vary with temperature, but the instruments can be used in the calibrated mode, where the amplification is automatically varied with temperature to give a nearly constant calorimetric sensitivity.

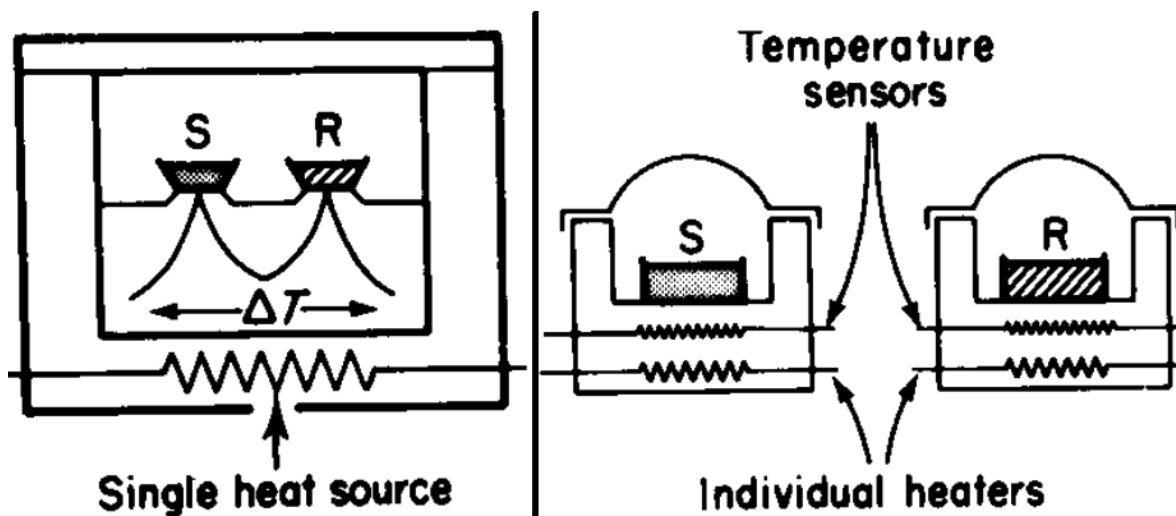


FIGURE 3.13. Types of DSC: Heat-flux (left) and Power-compensation (right). S=Sample, R=Reference.

Heat-flux DSC: Calibration. The Temperature lag ΔT_L of the sample relative to the sample thermocouple is non-zero since the thermocouple is not in direct contact with the sample. When the transition temperature does not vary a plot of the apparent transition temperature versus the heating rate (H) keeping the other quantities fixed, would at zero H extrapolate to the true value of the transition temperature, which is then the true value plus the lag. Alternatively, the sample may be allowed to reach the temperature of the sample-platform by holding at a temperature just beyond the transition temperature, and recording a DSC curve corresponding to the equilibration event. The area of this curve can then be used to deduce the temperature lag; this kind of an analysis requires more sophisticated equipment than is normally available.

The temperature plotted on the abscissa of a DSC record is related to the electromotive force generated at the thermocouple located under the sample. For standard thermocouple conditions, the electromotive force may be reliably converted to temperature units using established calibration charts, but a variety of effects can cause the thermocouple to age and shift calibration. It is advisable to calibrate the abscissa using substances with precisely known melting points; most DSC instruments have facilities which allow calibration over limited temperature ranges. In changing the abscissa scale to a true temperature reading, allowances have to be made for the thermal lag effect (ΔT_L), but this can be avoided by using very low heating rates for the purposes of calibration.

Calibration is also carried out by measuring the changes in specific heat or in enthalpy content of samples for which these quantities are known. The heat balance equation for the heat-flux DSC system can be shown to be as follows:

$$(3.19) \quad \frac{dH'}{dt} = \frac{T_{SP} - T_{RP}}{R_D} + (C_S - C_R) + H + \frac{d(T_{SP} - T_{RP})}{dt} C_S \frac{R_D + R_S}{R_D}$$

where,

dH'/dt = Heat evolution of an exothermic transition.

T_{SP} and T_{RP} = Temperature of the sample and reference platforms, respectively, as measured by the thermocouples. T_{SP} is normally plotted as the abscissa of a DSC curve.

R_D = Thermal resistance between the furnace wall and the sample or reference platforms (units C·min/J).

R_S = Thermal resistances between the sample platform and the sample.

C_S and C_R = Heat capacity of the sample (or reference) and its container.

H = Imposed heating rate.

The first term on the right hand side is the area under the DSC peak, after correcting for the baseline. The second term on the right refers to the actual baseline, and it is this which is used in specific heat determinations. The last term takes account of the fact that some of the evolved heat will be consumed by the specimen to heat itself, and does not affect the area under the DSC peak, but may distort the peak shape. From equation 3.19 it is clear that when dH'/dt can be arranged to be zero, the second term can be used to determine specific heat.

3.2.5 Mass Spectrometry (MS) & Evolved Gas Analysis (EGA)

Evolved gas analysis (EGA) is a method used to study the gas evolved from a heated sample that undergoes decomposition or desorption¹³. Therefore different analytical methods can be employed such as Mass Spectrometry (MS). MS is a powerful analytical technique¹⁴ used to quantify known materials, to identify unknown compounds within a sample, and to elucidate the structure and chemical properties of different molecules. The complete process involves the conversion of the sample into gaseous ions, with or without fragmentation, which are then characterized by their mass to charge ratios (m/z) and relative abundances. This technique basically studies the effect of ionizing energy on molecules. It depends upon chemical reactions in the gas phase in which sample molecules are consumed during the formation of ionic and neutral species.

Basic Principle. A MS generates multiple ions from the sample under investigation, it then separates them according to their specific mass-to-charge ratio (m/z) and then records the relative abundance of each ion type. The first step in the mass spectrometric analysis of compounds is the production of gas phase ions of the compound, basically by electron ionization. This molecular ion undergoes fragmentation. Each primary product ion derived from the molecular ion, in turn, undergoes fragmentation, and so on. The ions are separated in the mass spectrometer according to their mass-to-charge ratio, and are detected in proportion to their abundance. A mass spectrum

¹³By coupling the thermal analysis instrument, *e.g.* TGA or DSC, with a fast Quadrupole Mass Spectrometer (QMS) the detection of gas separation and identification of the separated components are possible in exact time correlation with the other thermal analysis signals.

¹⁴Extracted from the book *Mass Spectrometry: Principles and Applications*[222]

of the molecule is thus produced. It displays the result in the form of a plot of ion abundance versus mass-to-charge ratio. Ions provide information concerning the nature and the structure of their precursor molecule. In the spectrum of a pure compound, the molecular ion, if present, appears at the highest value of m/z (followed by ions containing heavier isotopes) and gives the molecular mass of the compound.

Components: The Ion Source. In the ion sources, the analysed samples are ionized prior to analysis in the mass spectrometer. A variety of ionization techniques are used for mass spectrometry. The most important considerations are the internal energy transferred during the ionization process and the physico-chemical properties of the analyte that can be ionized. Some ionization techniques are very energetic and cause extensive fragmentation. Other techniques are softer and only produce ions of the molecular species. Electron ionization, chemical ionization and field ionization are only suitable for gas-phase ionization and thus their use is limited to compounds sufficiently volatile and thermally stable. However, a large number of compounds are thermally labile or do not have sufficient vapour pressure. Molecules of these compounds must be directly extracted from the condensed to the gas phase.

The present work will only explain Electrospray Ionization (ESI) and Matrix-Assisted Laser Desorption Ionization (MALDI). ESI is produced by applying a strong electric field, under atmospheric pressure, to a liquid passing through a capillary tube with a weak flux. The electric field is obtained by applying a potential difference between this capillary and the counter-electrode. This field induces a charge accumulation at the liquid surface located at the end of the capillary, which will break to form highly charged droplets. A gas injected coaxially at a low flow rate allows the dispersion of the spray to be limited in space. These droplets then pass either through a curtain of heated inert gas, most often nitrogen, or through a heated capillary to remove the last solvent molecules. If one examines with a microscope the nascent drop forming at the tip of the capillary while increasing the voltage, at low voltages the drop appears spherical, then elongates under the pressure of the accumulated charges at the tip in the stronger electric field; when the surface tension is broken, the shape of the drop changes to a "Taylor cone" (figure 3.14) and the spray appears. The breakdown of the droplets can occur before the limit given by the Rayleigh equation is reached because the droplets are mechanically deformed, thus reducing the repulsion necessary to break down the droplets.

The solvent contained in the droplets evaporates, which causes them to shrink and their charge per unit volume to increase. Under the influence of the strong electric field, deformation of the droplet occurs. The droplet elongates under the force resulting from the accumulation of charge, similarly to what occurred at the probe tip, and finally produces a new Taylor cone. From this Taylor cone, about 20 smaller droplets are released. These small, highly charged droplets will continue to lose solvent, and when the electric field on their surface becomes large enough, desorption of ions from the surface occurs. ESI has important characteristics: for instance, it is able to produce multiply charged ions from large molecules. The formation of ions is a result of

the electrochemical process and of the accumulation of charge in the droplets. The ESI current is limited by the electrochemical process that occurs at the probe tip and is sensitive to concentration rather than to total amount of sample.

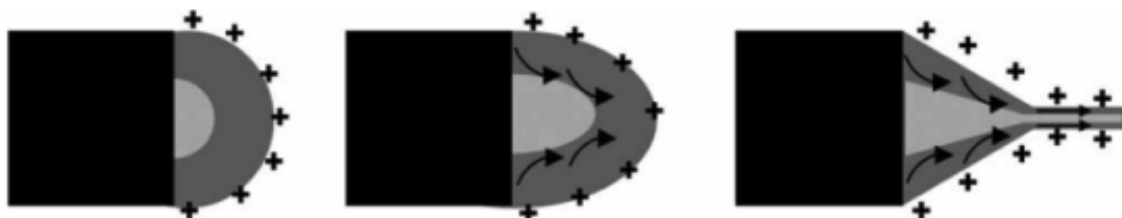


FIGURE 3.14. Schematic illustration of compound Taylor cone formation. From left to right: Surface charges on the sheath solution, viscous drag exerted on the core by the deformed sheath droplet and sheath-core compound Taylor cone formed due to continuous viscous drag.

MALDI is achieved in two steps. In the first step, the compound to be analysed is dissolved in a solvent containing in solution small organic molecules, called the matrix. These molecules must have a strong absorption at the laser wavelength. This mixture is dried before analysis and any liquid solvent used in the preparation of the solution is removed. The result is a "solid solution" deposit of analyte-doped matrix crystals. The analyte molecules are embedded throughout the matrix so that they are completely isolated from one another. The second step occurs under vacuum conditions inside the source of the mass spectrometer. This step involves ablation of bulk portions of this solid solution by intense laser pulses over a short duration.

Ionization reactions can occur under vacuum conditions at any time during this process but the origin of ions produced in MALDI is still not fully understood. Among the chemical and physical ionization pathways suggested for MALDI are gas-phase photoionization, excited state proton transfer, ion-molecule reactions, desorption of preformed ions, and so on. The most widely accepted ion formation mechanism involves proton transfer in the solid phase before desorption or gas-phase proton transfer in the expanding plume from photoionized matrix molecules. The ions in the gas phase are then accelerated by an electrostatic field towards the analyser.

MALDI is more sensitive than other laser ionization techniques. Indeed, the number of matrix molecules exceeds widely those of the analyte, thus separating the analyte molecules and thereby preventing the formation of sample clusters that inhibit the appearance of molecular ions. The matrix also minimizes sample damage from the laser pulse by absorbing most of the incident energy and increases the efficiency of energy transfer from the laser to the analyte. So the sensitivity is also highly increased. MALDI is also more universal than the other laser ionization techniques. Indeed, it is not necessary to adjust the wavelength to match the absorption frequency of each analyte because it is the matrix that absorbs the laser pulse. Furthermore, because the process is independent of the absorption properties and size of the compound to be analysed, MALDI allows the desorption and ionization of analytes with very high molecular mass.

Components: Mass Analyser. Once the gas-phase ions have been produced, they need to be separated according to their masses, which must be determined. The physical property of ions that is measured by a mass analyser is their mass-to-charge ratio (m/z) rather than their mass alone. Therefore, it should be mentioned that for multiply charged ions the apparent m/z values are fractional parts of their actual masses. As there are a great variety of sources, several types of mass analysers have been developed. Indeed, the separation of ions according to their mass-to-charge ratio can be based on different principles. All mass analysers use static or dynamic electric and magnetic fields that can be alone or combined. Most of the basic differences between the various common types of mass analyser lie in the manner in which such fields are used to achieve separation. Here will only be explained Time-of-Flight (TOF) and Quadrupole (Mass Spectrometer, QMS) Analysers.

A positive ion entering the space between the rods of a Quadrupole Analyser will be drawn towards a negative rod. If the potential changes sign before it discharges itself on this rod, the ion will change direction. The quadrupole analyser is thus a device which uses the stability of the trajectories in oscillating electric fields to separate ions according to their m/z ratios. The quadrupole is a real mass-to-charge ratio analyser. It does not depend on the kinetic energy of the ions when they leave the source. The only requirements are, first, that the time for crossing the analyser is short compared with the time necessary to switch from one mass to the other, and, second, that the ions remain long enough between the rods for a few oscillations of the alternative potential to occur. This means that the kinetic energy at the source exit must range from one to a few hundred electronvolts.

The TOF analyser separates ions, after their initial acceleration by an electric field, according to their velocities when they drift in a free-field region that is called a flight tube. Ions are expelled from the source in bundles which are either produced by an intermittent process such as plasma or laser desorption, or expelled by a transient application of the required potentials on the source focusing lenses. These ions are then accelerated towards the flight tube by a difference of potential applied between an electrode and the extraction grid. As all the ions acquire the same kinetic energy, ions characterized by a distribution of their masses present a distribution of their velocities. When leaving the acceleration region, they enter into a field-free region where they are separated according to their velocities, before reaching the detector positioned at the other extremity of the flight tube. Mass-to-charge ratios are determined by measuring the time that ions take to move through a field-free region between the source and the detector.

3.2.6 Elemental Organic Analysis (EOA)

For organic chemists, Elemental Organic Analysis (EOA) refers to CHN analysis and the determination of the mass fractions of carbon, hydrogen and nitrogen of a sample. This information is very important to help determine the structure of an unknown compound, as well as to help ascertain the structure and purity of a synthesized compound. In present day NMR XRD or MS

techniques have replaced EOA as the primary technique for structural determination, although it still gives very useful complementary information. It is also the fastest and most inexpensive method to determine sample purity.

The most common form of elemental analysis, CHN analysis, is accomplished by combustion analysis. In this technique, a sample is burned in an excess of oxygen with a various traps that collect the combustion products: carbon dioxide, water, and nitric oxide. The masses of these combustion products can be used to calculate the composition of the unknown sample. Modern elemental analysers are also capable of simultaneous determination of sulfur along with CHN in the same measurement run. A quantitative determination methods include:

- Gravimetry, where the sample is dissolved, the element of interest is precipitated and its mass is measured. Also the mass loss can be measured when the element of interest is volatilized.
- Optical atomic spectroscopy, such as flame atomic absorption, graphite furnace atomic absorption and inductively coupled plasma atomic emission spectroscopy, which probe the outer electronic structure of atoms.
- Neutron activation analysis, which involves the activation of a sample matrix through the process of neutron capture. The resulting radioactive target nuclei of the sample begin then to decay, emitting gamma rays of specific energies that identify the radioisotopes present in the sample. The concentration of each analyte can be determined by comparison to an irradiated standard with known concentrations of each analyte.

The analysis of results is performed by determining the ratio of elements within the sample, working out a chemical formula that fits with those results. This process is useful determining whether a sample is the desired compound, confirming its purity. The accepted deviation of elemental analysis results from the calculated is 0.2 %.

3.3 Computational approach

From a nanoscale point of view, one can understand and explain physical-chemistry events solving a bunch of equations. However, since one's knowledge is conditioned by the complexity of the models, sometimes one must use computational tools to assist in solving the mathematical expressions that describes them. This section will explain and describe several theoretical methodologies used in the present work, beginning with a bit of quantum mechanics explanation and then going deeper into those useful tools.

3.3.1 Quantum mechanics: The Schrödinger equation

Being a nuclei (N_A), the electrons (n_i), the kinetic (T) and potential (V) terms and the energy needed to define the state of the molecule (ϵ), the relationship between the molecular

wave-function ($\Psi(N_A, n_i)$) and the energy is called the Schrödinger equation (3.20)¹⁵,

$$(3.20) \quad \hat{H}\Psi(N_A, n_i) = \epsilon\Psi(N_A, n_i)$$

where $\hat{H} = \hat{T}_{N_A} + \hat{T}_{n_i} + V_{N_A} + V_{n_i} + V_{N_A-n_i}$ is the Hamiltonian operator[223]. Since the expression of the Schrödinger equation increases in complexity, it is imperative to search for simplicity, although sometimes a non-trivial matter, thus trying to separate the nuclei-electrons interactions.

3.3.1.1 Born-Oppenheimer Approximation

In 1927, Robert Oppenheimer and Max Born propose a central approximation to solve the molecular Schrödinger equation. Since nuclei are much heavier than electrons, they move more slowly. Is the assumption that the motion of atomic nuclei and electrons in a molecule can be separated. In mathematical terms, it allows Ψ to be broken into its electronic and nuclear (vibrational, rotational) components. Being the Hamiltonian for N electrons with the i th electron position vector, \mathbf{r}_i , and M nuclei with the A th nuclei position vector, \mathbf{R}_A :

$$(3.21) \quad \mathcal{H} = -\sum_{i=1}^N \frac{\nabla_i^2}{2} - \sum_{A=1}^M \frac{\nabla_A^2}{2M_A} - \sum_{i=1}^N \sum_{A=1}^M \frac{Z_A}{r_{i,A}} + \sum_{i=1}^N \sum_{j>i}^N \frac{1}{r_{i,j}} + \sum_{A=1}^M \sum_{B>A}^M \frac{Z_A Z_B}{R_{AB}}$$

where M_A is the ratio of the mass of nucleus A to the mass of an electron, and Z_A is the atomic number of nucleus A . The distance between the i th electron and the A th nucleus is $r_{i,A}$ and the distance between the i th and j th electron is $r_{i,j}$. Finally, the distance between the A th nucleus and the B th nucleus is R_{AB} . The first and second terms in equation 3.21 are the operator for the kinetic energy of the electrons and nuclei, respectively. The third term represents the coulomb attraction between electrons and nuclei and the fourth and fifth terms represent the repulsion between electrons and between nuclei, respectively. Hence within this approximation, the second term can be neglected and the last term can be considered to be constant. The remaining terms are called the electronic Hamiltonian. The expression of the electronic Schrödinger equation in atomic units is:

$$(3.22) \quad \left(-\sum_{i=1}^N \frac{\nabla_i^2}{2} + \sum_{i=1}^N \sum_{j>i}^N \frac{1}{r_{i,j}} - \sum_{A=1}^M \sum_{i=1}^N \frac{Z_A}{r_{i,A}} \right) \Psi_{el,A}(i) = E_{el,A} \Psi_{el,A}(i)$$

and when including the constant nuclear repulsion to the total energy for fixed nuclei:

$$(3.23) \quad \mathcal{E}_{tot} = \mathcal{E}_{el} + \sum_{A=1}^M \sum_{B>A}^M \frac{Z_A Z_B}{R_{AB}}$$

one finds the two equations (3.22 and 3.23) that constitute the electronic problem.

After solving the electronic problem, it is subsequently possible to solve for the motion of the nuclei under the same assumptions as used to formulate the electronic problem. As the electrons

¹⁵It was named after Erwin Schrödinger, who derived the equation in 1925 and published it 1926, forming the basis for his work that resulted in Schrödinger being awarded the Nobel Prize in Physics in 1933

move much faster than the nuclei, it is reasonable approximation in equation 3.21 to replace the electronic coordinates by their average values, averaged over the electronic wave function. This then generates a nuclear Hamiltonian (\mathcal{H}_{nuc}) for the motion of the nuclei in the average field of the electrons,

$$(3.24) \quad \mathcal{H}_{nuc} = - \sum_{A=1}^M \frac{\nabla_A^2}{2M_A} + \mathcal{E}_{tot}(\mathbf{R}_A)$$

where $\mathcal{E}_{tot}(\mathbf{R}_A)$ provides a potential for nuclear motion. This function constitutes a Potential Energy Surface (PES). The point now is to properly define the Ψ to describe the electronic behaviour of the chemical systems. In this issue, the mathematical expression of these functions are approximated by a group of methods. Here only the methods based in Density Functional Density (DFT) will be used.

3.3.1.2 Density Functional Theory (DFT)

Basic principles. In 1964, Pierre Hohenberg and Kohn proved two theorems[224]. The first may be stated as follows:

"The electron density determines the external potential (to within an additive constant)"

Being true this statement, it follows that the electron density uniquely determines the Hamiltonian operator. Thus, in principle, given the charge density, the Hamiltonian operator could be uniquely determined and Ψ (of all states) computed. The second theorem establishes a variational principle:

"For any positive definite trial density, ρ_t , such that $\int \rho_t(\mathbf{r})d\mathbf{r} = N$, then $E(\rho_t) \geq E_0$ "

And so the energy of the ground state, E_0 is a lower asymptotic value for the energy of the system from a testing density functional, $E(\rho_t)$. With a Lagrange multiplier of this constraint being the electronic chemical potential, μ , the two theorems lead to the fundamental statement of the density functional theory (equation 3.25).

$$(3.25) \quad \delta \left[E(\rho) - \mu \int \rho(\mathbf{r})d\mathbf{r} \right] = 0$$

The Kohn-Sham (KS) method. A year later, Kohn and Lu Jiu Sham developed a method to approximate the expression of the $E(\rho)$ functional[225]. The KS method is simply a fictitious system of non-interacting electrons, chosen to have the same density as the physical system. The total Hamiltonian (HKS) is then the sum of all monoelectronic hamiltonians, \hat{h}_i^{KS} , applied to every spin-orbital, ψ_i^{KS} , generating the ground state wave-function, Ψ_0 . The result is the expression known as the KS equation:

$$(3.26) \quad \hat{h}_i^{KS} \psi_i^{KS} = \epsilon_i^{KS} \psi_i^{KS}$$

and thus the density function ρ is defined as a combination of the n single electron orbitals, ψ_i ,

$$(3.27) \quad \rho(r) = \sum_{i=1}^{occ} n_i |\psi_i(r)|^2$$

The main objective of the DFT method is then to find the suitable energy that minimizes the expression of E^{KS} . From the form of the Schrödinger equation one can see that the energy functional contains three terms: the kinetic energy (T), the interaction with the external potential (V_{ex}) and the electron-electron interaction (V_{ee}) and so one may write the functional as

$$(3.28) \quad E(\rho) = T(\rho) + V_{ex}(\rho) + V_{ee}(\rho)$$

where the kinetic and electron-electron functionals are unknown. If good approximations to these functionals could be found, direct minimisation of the energy would be possible. With the KS method, the kinetic energy and electron density are known exactly from the orbitals

$$(3.29) \quad T_s(\rho) = -\frac{1}{2} \sum_i^N \langle \psi_i | \nabla^2 | \psi_i \rangle$$

Here the suffix emphasises that this is not the true kinetic energy but is that of a system of non-interacting electrons, which reproduce the true ground state density. If one also notes that a significant component of the electron-electron interaction will be the classical Coulomb interaction or Hartree energy (V_H), the energy functional can be rearranged as

$$(3.30) \quad E(\rho) = T_s(\rho) + V_{ex}(\rho) + V_H(\rho) + E_{xc}(\rho)$$

$$(3.31) \quad V_H(\rho) = \frac{1}{2} \int \frac{\rho(\mathbf{r}_1)\rho(\mathbf{r}_2)}{r_{1,2}} d\mathbf{r}_1 d\mathbf{r}_2$$

being E_{xc} the exchange-correlation functional and $r_{1,2}=|\mathbf{r}_1 - \mathbf{r}_2|$. E_{xc} is simply the sum of the error made in using a non-interacting kinetic energy and the error made in treating the electron-electron interaction classically. Writing the functional (equation 3.30) explicitly in terms of the density built from non-interacting orbitals (equation 3.27) and applying the variational theorem (equation 3.25) one finds that the orbitals, which minimise the energy, satisfy

$$(3.32) \quad \left(-\frac{\nabla^2}{2} + V_{ex}(\mathbf{r}) + \int \frac{\rho(\mathbf{r}')}{|\mathbf{r} - \mathbf{r}'|} d\mathbf{r}' + \frac{\delta E_{xc}(\rho)}{\delta \rho} \right) \psi_i(\mathbf{r}) = \epsilon_i \psi_i(\mathbf{r})$$

This set of non-linear equations (the KS equations) describes the behaviour of non-interacting "electrons" in an effective local potential. For the exact functional, and thus exact local potential, the "orbitals" yield the exact ground state density and exact ground state energy. The KS approach achieves an exact correspondence of the density and ground state energy of a system consisting of non-interacting fermions and the "real" many body system described by the Schrödinger equation.

For calculations in which the energy surface is the quantity of primary interest DFT offers a practical and potential highly accurate alternative to the wave-function methods here discussed. In practice, the utility of the theory rests on the approximation used for E_{xc} .

Approximations on E_{xc} : The Local Density (LDA) and the Generalised Gradient (GGA). Given a neutral charge and uniform density, E_{xc} can be described[226] as

$$(3.33) \quad E_{xc}(\rho) = \int \rho(\mathbf{r})\epsilon_{xc}(\rho)d\mathbf{r}$$

An obvious choice is then to take $\epsilon_{xc}(\rho(\mathbf{r}))$ to be the exchange and correlation energy density of the uniform electron gas of density ρ . This is the Local Density Approximation (LDA, used in the present work). The LDA has proven to be a remarkably fruitful approximation. Properties such as structure, vibrational frequencies, elastic moduli and phase stability (of similar structures) are described reliably for many systems. However, in computing, one of the principal disadvantages of the LDA is in the van der Waals interactions. These problems are insuperable in cases where the π -stacking has an important role. Nevertheless, the remarkable fact is that the LDA works as well as it does given the reduction of the energy functional to a simple local function of the density.

In the generalised gradient approximation (GGA) a functional form is adopted which ensures the normalisation condition and that the exchange hole is negative definite. This leads to an energy functional that depends on both the density and its gradient but retains the analytic properties of the exchange correlation hole inherent in the LDA. The typical form for a GGA functional[227] is

$$(3.34) \quad E_{xc} \approx \int \rho(\mathbf{r})\epsilon_{xc}(\rho, \nabla\rho) d\mathbf{r}$$

The most popular GGA functionals are BLYP (exchange part by Becke and correlation part by Lee, Yang and Parr[228] and PBE (used in the present work) of Perdew, Burke and Ernzerhoff[158]. Furthermore, hybrid functionals are extensively used and contain a variable contribution of the exact correlation energy, being the B3LYP functional (used also in the present work, formed by three parameters: Slater exchange, Hartree-Fock exchange and LYP correlation contributions) the most popular, although the computational cost increases for the kind of simulations carried here.

3.3.1.3 Time-dependent DFT (TD-DFT)

TD-DFT extends the concept of stationary DFT to time-dependent (TD) situations: For any interacting quantum many-particle system subject to a given TD potential all physical observables are uniquely determined by knowledge of the TD density and the state of the system at an arbitrary single instant in time. This is called the Runge-Gross (RG) theorem[229], although additional simplifications are obtained in the linear response regime[230]. The most popular application of TD-DFT is in the calculation of the energies of excited states of isolated systems

and, less commonly, solids. Such calculations are based on the fact that the linear response function (that is, how the electron density changes when the external potential changes) has poles at the exact excitation energies of a system, and require, in addition to the exchange-correlation potential, the exchange-correlation kernel: the functional derivative of the exchange-correlation potential with respect to the density.

RG considers a single-component system in the presence of a TD scalar field for which the Hamiltonian (see equation 3.28) takes the form

$$(3.35) \quad \hat{H}(t) = \hat{T} + \hat{V}_{ex}(t) + \hat{V}_{ee}$$

Nominally, the external potential contains the electrons' interaction with the nuclei of the system. For non-trivial time-dependence, an additional explicitly time-dependent potential is present which can arise, for example, from a time-dependent electric or magnetic field. The many-body wave-function evolves according to the time-dependent Schrödinger equation under a single initial condition,

$$(3.36) \quad \hat{H}(t)|\Psi(t)\rangle = i\hbar \frac{\partial}{\partial t} |\Psi(t)\rangle$$

with $|\Psi(0)\rangle = |\Psi\rangle$. Employing the Schrödinger equation as its starting point, the RG theorem shows that at any time, the density uniquely determines the external potential. The KS approaches chooses a non-interacting system to form the density that is equal to the interacting system. The advantage of doing so lies in the ease in which non-interacting systems can be solved¹⁶ and that the kinetic energy of a non-interacting system can be expressed exactly in terms of those orbitals. Doing so, and assuming that $\psi_i(\mathbf{r}, 0) = \psi_i(\mathbf{r})$ the equation can be expressed as

$$(3.37) \quad \left(-\frac{\nabla^2}{2} + V_s(\mathbf{r}, t) \right) \psi_i(\mathbf{r}, t) = i \frac{\partial}{\partial t} \psi_i(\mathbf{r}, t)$$

with a density equal to the density of the interacting system at all times

$$(3.38) \quad \rho_s(\mathbf{r}, t) = \sum_{i=1}^N |\psi_i(\mathbf{r}, t)|^2 = \rho(\mathbf{r}, t)$$

3.3.2 Car-Parrinello Molecular Dynamics (CPMD)

Now that it has been introduced the quantum mechanics, it is time to see what happens with molecules in movement. Translations, vibrations and rotations due to forces are important events to understand the conformational changes of systems and its applications in Physics, Chemistry and Biology. With this goal in mind, one has to enter in the world of the Molecular Dynamics

¹⁶The wave-function of a non-interacting system can be represented as a Slater determinant of single-particle orbitals, each determined by a single partial differential equation in three variable

(MD). Atoms basically interact with each other through van der Waals forces and electrostatic forces. When they are covalently bonded to others, strong forces hold them together as stable chemical groups. A widely used mathematical model for the potential energy of a molecular system consists of six types of interactions:

1. The Lennard-Jones potential, that has an attractive part, representing the van der Waals energy and a repulsive part, representing the Pauli repulsion.
2. The Electrostatic potential energy, according to Coulomb's Law.
3. The Bond-stretching energy standing for the elastic interaction between a pair of atoms connected by a covalent bond.
4. The Angle-bending energy standing for the interaction among three covalently-bonded atoms that form a stable angle.
5. and 6. The Proper and Improper torsional energies standing for the interactions among four covalently-bonded atoms that form a stable proper and improper dihedral angle.

The last four items are called the bonded interactions, which maintain the bond lengths, the bond angles and the dihedral angles so that chemical groups will remain sterically stable in an MD simulation. The first two terms are called the non-bonded interactions. In MD simulations, they are more important than the bonded interactions. The non-bonded interactions, among the atoms of a macromolecule, affect its secondary structure and, among different molecules, organize them into crystals, complexes and other assemblies.

MD system and initialization: The Verlet method. Since it is not possible to simulate chemical reactions and changes in the electronic configuration of a system, CPMD[162] has become lately a very useful tool, since allows one to carry shorter simulations with a better description of the electronic degrees of freedom. For starting velocities, Maxwell-Boltzmann distribution is used,

$$(3.39) \quad f(v)dv = 4\pi \left(\frac{m}{2\pi kT} \right)^{3/2} v^2 \exp \left(-\frac{mv^2}{2kT} \right)$$

Then, the position and acceleration of each atom are calculated using a numerical methods, such as the Verlet method[231]. The Verlet algorithm uses positions and accelerations at time t and the positions from time $t - dt$ to calculate new positions at time $t + dt$, but uses no explicit velocities:

$$(3.40) \quad r(t + \delta t) = 2r(t) - r(t - \delta t) + \ddot{r}(t)\delta t^2$$

The advantages of the Verlet algorithm are, i) it is straightforward, and ii) the storage requirements are modest. The disadvantage is that the algorithm is of moderate precision. The next step is to solve Newton's equations of motion according to the forces derived from the

gradients of the interaction potentials involving the atom. The numeric integration is carried out step-wisely. The process is repeated at each discrete time step and the trajectory of each individual object can be tracked by connecting its states to form a time series. The time evolution of the entire system can be viewed as a fiber bundle of time series in the phase space.

Fictitious mass and Lagrangian. CPMD uses fictitious dynamics[232] to keep the electrons close to the ground state, preventing the need for a costly self-consistent iterative minimization at each time step. The fictitious dynamics relies on the use of a fictitious electron mass (μ) to the KS orbitals ($\psi_i(\mathbf{r})$) to ensure that there is very little energy transfer from nuclei to electrons, *i.e.* to ensure adiabaticity. The value of the chosen fictitious electronic mass and the time step is thus crucial. Any increase in the fictitious electron mass resulting in energy transfer would cause the system to leave the ground-state surface. Then the electronic and nuclear degrees of freedom evolve according to a modified set of classical equations of motion

(3.41)

$$\mu\ddot{\psi}_i(\mathbf{r}, t) = -\frac{\delta E}{d\psi_i^*} + \sum_j \Lambda_{ij} \psi_j(\mathbf{r}, t) \quad (\text{for electrons}) \quad ; \quad M_N \ddot{\mathbf{R}}_N = -\nabla_N E(\psi_i, \mathbf{R}_N) \quad (\text{for nuclei})$$

where Λ_{ij} is a Lagrangian multiplier matrix to comply with the orthonormality constraint

(3.42)

$$\int d\mathbf{r} \psi_i^*(\mathbf{r}, t) \psi_j(\mathbf{r}, t) = \delta_{ij}$$

So the description of a system's interaction treated with the CP method is described by a Lagrangian function,

(3.43)

$$\mathcal{L} = \frac{1}{2} \left(\sum_N^{nucl} M_N \dot{\mathbf{R}}_N^2 + \mu \sum_i^{orb} \int d\mathbf{r} |\dot{\psi}_i(\mathbf{r}, t)|^2 \right) - E(\psi_i, \mathbf{R}_N)$$

and for the limit $\mu \rightarrow 0$, the equations of motion approach Born-Oppenheimer Molecular Dynamics (BOMD)[233].

3.3.3 Metadynamics

MD is today a precious instrument for understanding the mechanisms underlying complex processes, interpreting the experimental results, and making novel predictions. However, the results of an MD simulation are meaningful only if the run is long enough for the system to visit all the energetically relevant configurations or, in other words, if the system is ergodic in the timescale of the simulation. In practical situations, this is not always the case. One frequent source of difficulty is that the relevant configurations might be separated by high free-energy barriers. In such case, the change from one metastable state to another can take place only if activated by those rare fluctuations that take the system over the free energy. Another possibility is that the system diffuses extremely slowly in configuration space. Under these conditions, obtaining sufficient statistics requires an impractical amount of computer time. From these considerations, it emerges clearly that MD is plagued by a timescale problem.

Collective variables CV: Conditions. Metadynamics is a powerful technique for enhancing sampling in MD simulations and reconstructing the Free-Energy Surface (FES) as a function of few selected degrees of freedom, often referred to as Collective Variables (CVs)[234]. In metadynamics, an external history-dependent bias potential which is a function of the CVs is added to the Hamiltonian of the system. This potential can be written as a sum of Gaussians deposited along the system trajectory in the CVs space to discourage the system from revisiting configurations that have already been sampled. A CV is a function of the microscopic coordinates of the system.

To guarantee an effective application of metadynamics, the CVs must respect the following guidelines:

- They should distinguish between the initial and final state and describe all the relevant intermediates. For the CVs to be dynamically meaningful, *i.e.* to correspond to the reaction coordinate, stricter conditions must be fulfilled
- They should include all the slow modes of the system. One defines as "slow" those variables that cannot be satisfactorily sampled in the timescale of the simulation. One also expects that the other "fast" variables adjust rapidly to the evolution of the slow variables. If any of the latter is not added to the CVs list, the bias potential may not converge to the FES in a reasonable simulation time.
- They should be limited in number. The number of CVs should be kept small because the use of many CVs implies that a high-dimensional space has to be explored. Even using well-tempered metadynamics, this may take a considerable amount of computational time. Furthermore, analysing a high-dimensional surface is far from trivial.

The algorithm and the FES. The working principle of the algorithm can be qualitatively understood by a simple example.

"Imagine a walker who, during the night, falls into an empty swimming pool. The walls of the swimming pool are too steep for the walker to climb and the complete darkness makes it difficult for him to localize the shallowest point (lowest saddle). In these conditions the walker will move more easily downhill, and it is rather unlikely that he will find by chance the lowest saddle. His walk in these conditions resembles that performed by microscopic systems in normal molecular dynamics or Monte Carlo: a random walk with a bias in the direction of lower free energy, with a very small probability to explore transition regions (climb out of the pool). In metadynamics, the walker has access to a large source of sand that he can deposit in his current position. The sand will slowly fill the pool. Thus, even if at the beginning he visits more often the region at the bottom of the pool, little by little he fills the pool with sand (Gaussians), and he almost deterministically starts exploring regions that are higher and higher.

Sooner or later, the walker is destined to fill sufficiently the pool to be able to climb out of it. And most probably he will climb out from the shallowest point of the pool. The novel idea that differentiates metadynamics from pre-existing methods is that if the walker is able to keep memory of all the positions in which he has deposited sand (the Gaussians), he will be able to reconstruct a negative image of the underlying pool (the free energy). More precisely, one assumes that the time dependent potential defined by the sum of Gaussians deposited up to time t provides an unbiased estimate of the free energy in the region explored during the dynamics." [235]

Considering a system described by a set of coordinates x and a potential $V(x)$ evolving under the action of a dynamics, where x may include not only ordinary atomic positions but also electronic coordinates, one can define the properties of the system as a function of a finite number of CVs as $S_\alpha(x)$, being α the number of CVs. Then, the equilibrium behaviour of these variables is completely defined by the probability distribution

$$(3.44) \quad P(s) = \frac{\exp(-(1/T)F(\mathbf{s}))}{\int \exp[-(1/T)F(\mathbf{s})] d\mathbf{s}}$$

where s denotes the value of the CVs as the d dimensional vector. The Free Energy $F(s)$ is given by

$$(3.45) \quad F(s) = -T \ln \left[\int \exp \left(-\frac{1}{T} V(\mathbf{x}) \right) \delta(s - S(\mathbf{x})) d\mathbf{x} \right]$$

When a trajectory $x(t)$ at a temperature T is considered, $P(s)$ could be obtained if the trajectory is computed for a very long time. The FES is then reconstructed using the combined information obtained from simulations restrained or constrained at several values of s recursively, starting from the bottom of the well by a history-dependent random *walk* that explores a larger and larger portion of the configuration space. In the simplest MD implementation of the algorithm, the mathematical equivalent of the *sand* deposited by the *walker*, is a small repulsive Gaussian potential added every τ_G MD steps

$$(3.46) \quad V_G(S(x), t) = w \sum_{t'=n\tau_G}^t \exp \left[-\frac{(S(x) - s(t'))^2}{2\delta s^2} \right]$$

With $n \in \mathbb{N}$ and w and δs the Gaussian's height and width respectively. $s(t) = S(x[t])$ is the value taken by the CV at time t . This manner of biasing the dynamics is usually referred to as "direct metadynamics", and so, after a sufficiently long time

$$(3.47) \quad \lim_{t \rightarrow \infty} V_G(s, t) \sim -F_s$$

Lagrangian metadynamics. With Lagrangian metadynamics[236], the history-dependent potential has to force the system to cross barriers of several tenths of kcal/mol in a short time,

usually a few picoseconds. Since that means that a lot of energy has to be injected and that this might lead to instabilities in the dynamics, Lagrangian metadynamics introduces auxiliary variables \tilde{s} and harmonic restraining potentials with constant k . Then, a fictitious kinetic energy $M\tilde{s}^2/2$ is also assigned. Modifying the potential

$$(3.48) \quad \tilde{V}(x, \tilde{s}) = V(x) + \frac{1}{2}k(\tilde{s} - S(x))^2$$

the free energy is given by

$$(3.49) \quad \tilde{F}(\tilde{s}) = -T \ln \left[\int \exp \left(-\frac{1}{T} \left[V(\mathbf{x}) + \frac{k(\tilde{s} - S(\mathbf{x}))^2}{2} \right] \right) d\mathbf{x} \right]$$

Finally, the implementation of a metadynamic subroutine inside a MD routine loop has to be after the forces are computed and before the positions/velocities are updated. With this in mind, the subroutine performs three tasks:

1. It computes the value of the CVs(= $S(x)$).
2. Every τ_G time steps, it stores the value of s (or \tilde{s}) in an array that contains the centers of all Gaussians.
3. It computes the derivative of $V_G(S(x), t)$ with respect to x ,

$$(3.50) \quad \frac{\partial}{\partial x} V_G(S(x), t) = \frac{\partial V_G(s, t)}{\partial s} \frac{\partial S(x)}{\partial x}$$

and then these derivatives are added to the usual forces on the atoms, biasing the dynamics of the system.

*"Come to the book as you would come to an unexplored land.
Come without a map. Explore it and draw your own map"*
- Stephen King in *Hearts in Atlantis*

THE COMMON SOL-GEL ZNO PRECURSOR

Although most of the papers published so far make use of Zinc Acetate Dihydrate (ZAD) as salt and Ethanolamine (EA) as stabilizer, the interaction of the latter with ZAD in the ink at room conditions and its influence during thermal decomposition are not well understood. This information is crucial and especially valuable to improve the design of the ink for optimization of the thermal decomposition conditions when designing new systems with improved properties in view of their applications (*e.g.* of ZnO) in printed electronics. As the quotation preceding this chapter says, the section of results cannot start otherwise than putting a little order into the matter by drawing a new map of the subject no one has done before.

The first section is devoted to identify the molecular nature of the ZAD+EA precursor complex. TGA, DSC, XRD, MS and XPS experiments have been used together to draw a path to humbly elucidate and understand the thermal evolution from the precursor in the ink to the ZnO. Also presents a simple guide to theoretically know how stabilizer works with the metal ion. Gaussian software has been used not only to do so, but to help solving a first approximation of the new crystal structure with the Powder XRD method (section 3.1.1.2), never reported before, made by the free-solvent stabilized precursor.

The second and third sections are an extension of the first study. They report experiments and calculations that shed light on the evolution of the film precursor to ZnO during its thermal decomposition. In addition, CPMD software has been useful to simulate, via TD-DFT, the ZAD+EA precursor complex in different conditions of isolation/solvation/CO₂ presence. This has allowed identifying unambiguously the cause of its degradation at room conditions. Moreover Molecular Dynamics and Metadynamics simulations also helped explain the volatiles detected by EGA at the various decomposition stages contributing to the understanding of the decomposition dynamics and, especially, when and how nitrogen is leaving the system.

4.1 Study of a sol-gel precursor and its evolution towards ZnO

The processes involved in the assembly of zinc acetate dihydrate (ZAD) and ethanolamine (EA), with or without 2-Methoxyethanol (2-ME or ME) as solvent, have been analysed by infrared spectra, mass spectrometry, nuclear magnetic resonance, powder X-ray diffraction and computational studies. Thermal evolution of the mixtures was characterized by thermoanalytical and structural techniques (thermogravimetry, differential thermal analysis, differential scanning calorimetry, X-ray diffraction and X-Ray photoelectron spectroscopy). Computational studies together with experiments served to thoroughly describe the precursor and its decomposition. The thermal decomposition of the mixture and its transformation into crystalline ZnO take place in a temperature range between 50 and 450 °C through different processes. With solvent, the processes need temperatures 90 °C higher with respect to the mixture without solvent, and ZnO arises at 250 °C.

4.1.1 Experimental Procedure

Zinc acetate dihydrate [$\text{Zn}(\text{CH}_3\text{COO})_2 \cdot 2\text{H}_2\text{O}$, ZAD], ethanolamine ($\text{H}_2\text{NCH}_2\text{CH}_2\text{OH}$, EA) and 2-methoxyethanol [$\text{CH}_3\text{O}(\text{CH}_2)_2\text{OH}$, 2-ME] were purchased from Panreac, Acrös Organics and Aldrich, respectively, and used as received. The two samples used in this study (hereinafter referred to as **Precursor** and **Ink**) were prepared as follows:

- Synthesis of the **Precursor**: ZAD (1.8 g, 7.7×10^{-3} mol) was treated with an equimolar amount (see section 2.2) of EA (0.47 mL). The mixture was kept at 60 °C under continuous stirring for 24 h. After this period the flask containing the homogeneous gel was stored in a silica gel desiccator for several days until a powder was formed.
- Preparation of the **Ink**: This sample, suitable for printed electronics, was prepared as described for the Precursor but adding ME (7 mL) as solvent.

Ink thin films were prepared by the drop coating method on a glass substrate. The as-obtained **Precursor** was characterized by Infrared (IR) spectroscopy, ^1H and ^{13}C (^1H), Nuclear Magnetic Resonance (NMR) and Mass Spectrometry (MS). IR spectra were registered with a Nicolet 400FTIR instrument using KBr pellets. ^1H and ^{13}C (^1H) NMR studies were carried out at 25 °C by a Mercury-400 MHz instrument using CDCl_3 (99.9 %) as solvent and SiMe_4 as reference. ESI⁺-MS was performed with a LC/MSD-TOF (Agilent Technologies) mass spectrometer. The dried **Precursor** powder was characterized by X-ray diffraction (XRD) in a PANalytical X'Pert PRO MPD θ/θ powder diffractometer, with $\text{Cu K}\alpha_1$ radiation ($\lambda = 1.5406 \text{ \AA}$) in a convergent-beam configuration with a transmission geometry. To study the thermal evolution of both **Precursor** and **Ink**, Thermogravimetric Analyses (TGA), Differential Scanning Calorimetry (DSC) and Differential Thermal Analyses (DTA) were carried out in an atmosphere of dry air with 50

mL/min flow rate and heating rate of 10 °C/min up to 600 °C. DSC was performed by a Mettler-Toledo DSC-822e calorimeter, with uncovered aluminium crucibles (of 40 μ L volume). TGA experiments were performed on a Mettler-Toledo TGA-851e thermobalance, also with uncovered aluminium crucibles (of 70 μ L volume). Complementary Evolved Gas Analysis (EGA) of the evolved species (up to $m/z = 70$) was done by coupling a mass spectrometer at the exit of the TGA apparatus. A MKS quadrupole mass spectrometer (Microvision Plus) was used.

The evolution of the crystalline structure with temperature was analysed by *in-situ* and *ex-situ* (for **Precursor** and **Ink**, respectively) XRD experiments. In *ex-situ* measurements, the Ink samples were heated at 10 °C/min up to the desired temperature and then cooled down without any delay. A new sample was used for each temperature. In contrast, *in-situ* experiments were carried out on the dried powders that were held during 8 min at isothermal conditions (to allow for an XRD measurement) every 10 °C, with a high-temperature camera (HTK e 1200N, Antoon Paar). The heating rate between isotherms was 10 °C/min from room temperature to 600 °C.

The deposited **Ink** was analysed by X-Ray photoelectron spectroscopy (XPS) in an ultra-high vacuum (UHV) chamber using a PHI 5500 Multitechnique System (from Physical Electronics) with a monochromatic X-ray source (Al K_{α} line of 1486.6 eV energy and 350 W), placed perpendicular to the analyser axis and calibrated using the 3d5/2 line of Ag with a full width at half maximum (FWHM) of 0.8 eV. The selected resolution for the spectra was 187.85 eV of Pass Energy and 0.8 eV/step for the general spectra and 23.5 eV of Pass Energy and 0.1 eV/step for the spectra of the different elements in the depth profile spectra. A low energy electron gun (less than 10 eV) was used in order to discharge the surface when necessary. The Ink films were heated at a constant rate of 10 °C/min up to several maximum temperatures and cooled down without any delay before the XPS measurements.

Computational studies (optimization of the geometries, calculation of total and free energies and frequencies) were performed with UB3LYP method implemented in the Gaussian 03[163] software, using the LANLD2Z basis set.

4.1.2 Results and Discussion

4.1.2.1 Characterization of the Precursor

As stated above, the **Precursor** was characterized by IR, ^1H and $^{13}\text{C}(^1\text{H})$ -NMR and mass spectrometry. Figure 4.1 shows the IR spectra obtained for the **Precursor** and ZAD. A larger separation between asymmetric and symmetric stretching bands of the carboxylate unit (ν_{as} and ν_s , respectively) is detected for the **Precursor** than for ZAD. According to the bibliography¹, this indicates the existence of bridging acetate ligands in the **Precursor**. In the ^1H NMR spectrum of the **Precursor** (Figure 4.2), the signal due to the $-\text{NH}_2$ protons (*ca.* 3.6 ppm) is broad and shifted

¹K.Nakamoto, *Infrared and Raman Spectra of Inorganic and Coordination Compounds*, 5th ed., Wiley, New York, USA, 1997.

in relation to EA. Moreover, some changes are detected in chemical shifts and multiplicities of the resonances of the $-(\text{CH}_2)_2-$ protons (*ca.* 2.85 ppm), when compared with those of the free ligand. These differences suggest, according to the literature[237], the presence of "[Zn(κ^2 - κ^2 ,N,O-(H₂N-(CH₂)₂O))]" cores that arise from the binding of the amine nitrogen and the deprotonated oxygen to the Zn(II) cation. In addition, the singlet at $\delta \approx 2.1$ ppm is attributed to the acetato-ligand.

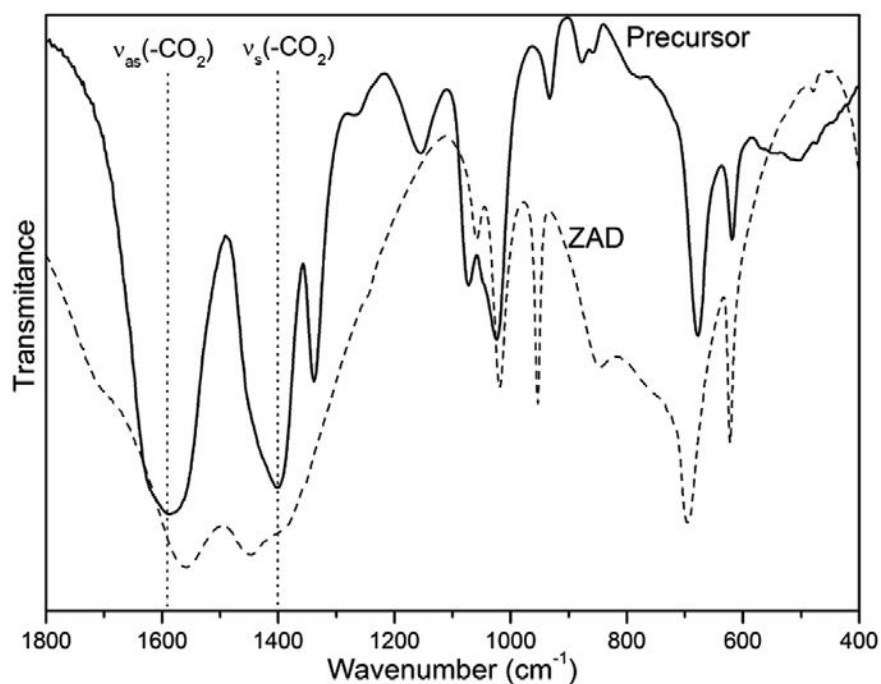


FIGURE 4.1. Infrared spectra (in the range 1800-400 cm^{-1}) of ZAD (dashed line) and the **Precursor** (solid line). The bands due to asymmetric (ν_{as}) and symmetric (ν_s) stretching modes of the carboxylate unit in the **Precursor** are marked.

The $^{13}\text{C}(^1\text{H})$ -NMR spectrum of **Precursor** (Figure 4.3) shows four singlets: two of them at lower and higher fields are due to the acetate ligand; while the remaining two correspond to the $-\text{CH}_2-$ carbons of the coordinated EA. It should be noted that the chemical shifts of these resonances were not coincident with those of the free ZAD or EA. All these findings suggest that ZAD interacts with EA, giving rise to new species in which the environment of the metal centre is " $\text{Zn}(\text{H}_2\text{NCH}_2\text{CH}_2\text{O})(\mu\text{-OAc})$ ". It is well-known that these monomeric arrays may assemble giving polynuclear complexes of higher nuclearity. Some authors have postulated the formation of tetranuclear and hexanuclear Zn(II) complexes containing simultaneously carboxylate and aminoalcoholate ligands. Only a few among these crystal structures have been determined by X-ray diffraction ([125, 238, 239, 240, 124]), and in most of them there is one H₂O molecule "trapped" in tetrametallic units.

Complementary, the ESI⁺-MS spectrum of the **Precursor**² shows peaks with the isotopic

²See Figure S1 of the Supporting Information *Study of a sol-gel precursor and its evolution towards ZnO* in Appendix A

pattern expected for cations with different nuclearities: $[\text{Zn}]_x$ (with $x = 2, 4$ or 6) and $[\text{Zn}]_x + \text{H}_2\text{O}$. Unfortunately, data available do not allow stabilising whether these species arise by fragmentation of cations with higher nuclearity or by assembly of smaller units (*i.e.* monomers or dimers). However, it is clear that only Zn dimers, tetramers and hexamers are compatible with our results, and XRD could help describing the exact composition resulting from the interaction between ZAD and EA.

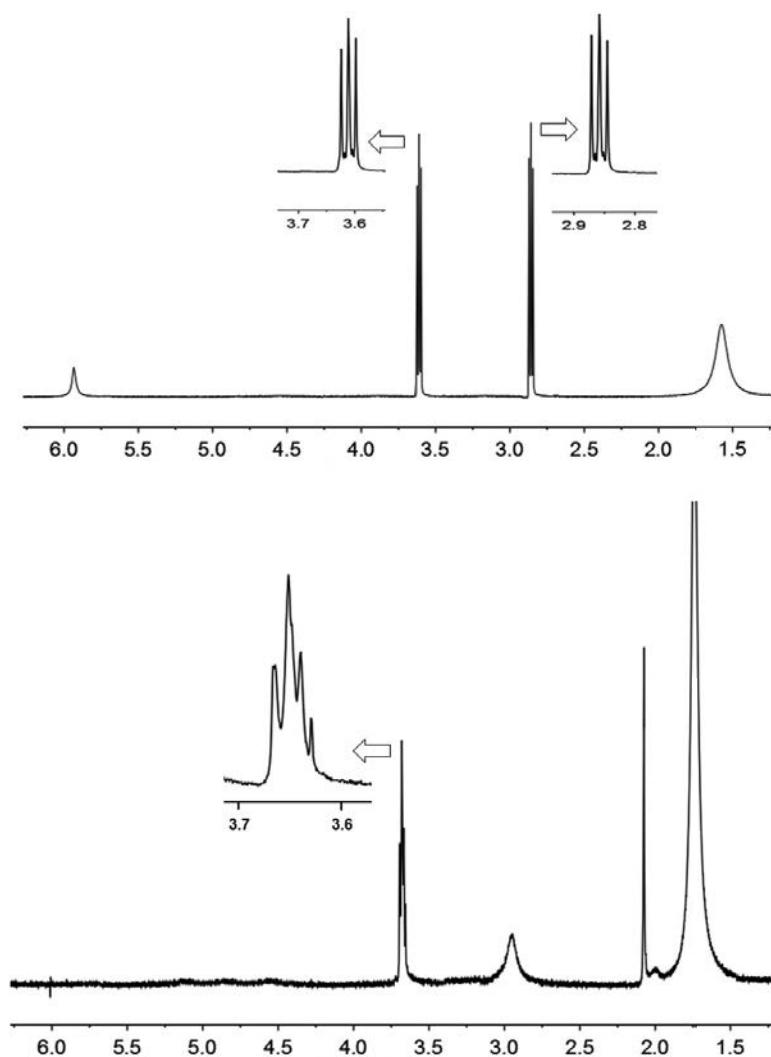


FIGURE 4.2. ^1H NMR spectra (400 MHz) of ethanolamine (EA) (top) and the **Precursor** (bottom). The intense signal that appears in the spectrum of the Precursor in the range $1.5 \text{ ppm} \leq \delta \leq 1.8 \text{ ppm}$ is due to the residual water of the solvent.

Since attempts to obtain single crystals suitable for X-ray diffraction failed, powder XRD studies of the dried precursor were performed (Exp. day 1 in Figure 4.4). Indexation of the peaks observed in the spectrum is consistent with a monoclinic system and $Z = 16$. The lack of $(0k0)$ reflections with $k=\text{odd}$ values indicates that the space group is $P2_1$. As shown in figure 4.4, the experimental XRD spectrum of freshly-prepared dried **Precursor** matches with the calculated

one for the Monoclinic $P2_1/m$ system, although after a few days at room conditions of temperature and humidity, the **Precursor** becomes amorphous (Exp. day 5 in Figure 4.4). However, the $P2_1/m$ system is centrosymmetric and implies 4 asymmetric units, what, since $Z = 16$, indicates that only $[Zn]_X$ with $x = 4$ is possible in fresh dried **Precursor**. As a conclusion, the present structure must be made from four tetramers ($4[Zn]_4$), in good agreement with the literature[240].

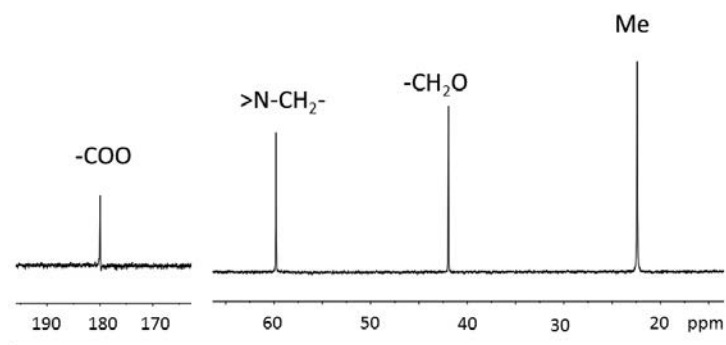


FIGURE 4.3. Partial views of the $^{13}C(^1H)$ -NMR spectrum of the **Precursor** in $CDCl_3$ at 25 °C.

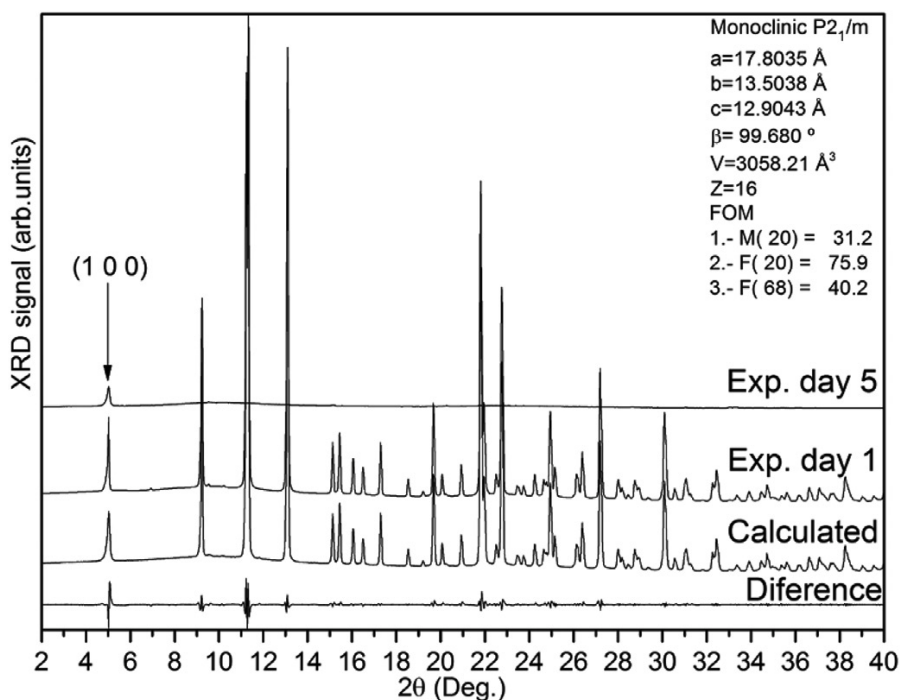


FIGURE 4.4. Experimental powder-XRD spectrum of freshly-obtained dried **Precursor** (Exp. day 1), calculated diffractogram for a monoclinic $P2_1/m$ system with the parameters shown at the upper-right corner, and the difference between both. After five days of storage at room conditions (Exp. day 5) only the (100) reflection remains.

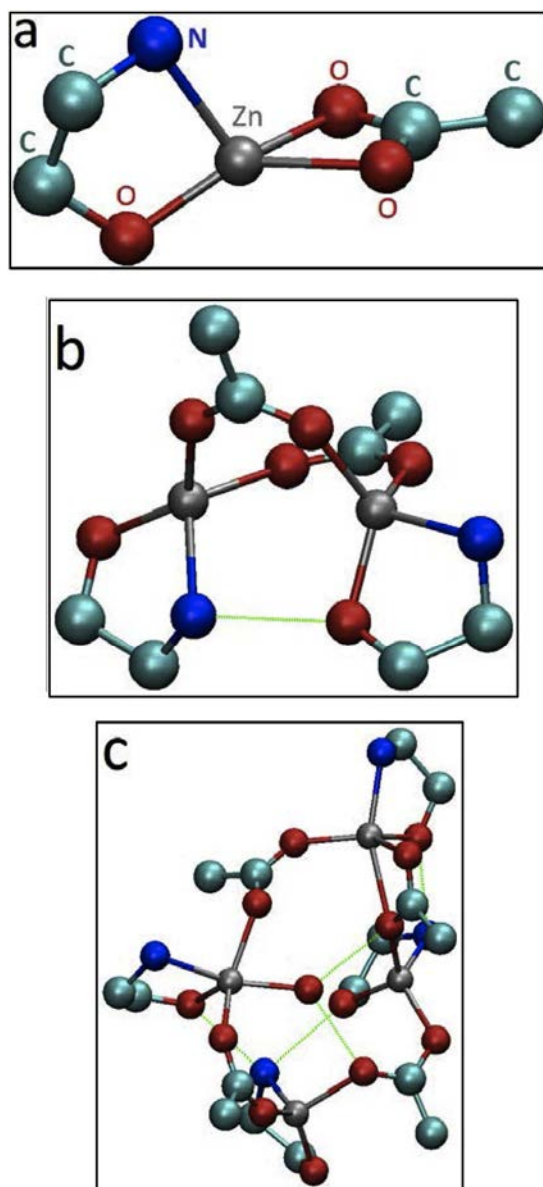


FIGURE 4.5. Optimized geometries of the monomer (a), dimer (b) and tetramer (c) using UB3LYP method and LANLD2DZ base. Hydrogen atoms have been omitted for clarity.

4.1.2.2 Computational study of the Precursor

In order to understand why small mononuclear ($[Zn]_1$) or dinuclear ($[Zn]_2$) blocks assemble to form $[Zn]_4$ oligomers compatible with XRD results, computational studies were undertaken. In a first stage, the geometries of the $[Zn]_x$ entities ($x = 1, 2$ or 4) were optimized (Figure 4.5) by means of Gaussian 03 software. In the three cases bond lengths and angles of the optimized geometries were consistent with those reported for other Zn(II) complexes with identical sets of donor atoms[240]. Vibrational calculations were also carried out, and no peaks at negative

frequencies appeared, indicating that these systems remained at the minimum state of the Potential Energy Surface (PES, see section 3.3).

On the other hand, calculations of free energy (ΔG) suggest that each individual tetramer is much more stable than two isolated dimers or four monomers, indicating that tetramers are the stable form for this type of system. Referring to their formation, binary collision (two monomers into a dimer or two dimers into a tetramer) is kinetically more probable than quaternary collision (four monomers into a tetramer). Furthermore, calculated free energies at 300 K were used to estimate the ΔG for the assembly of: a) 2 dimers or b) 4 monomers to give the tetramer. The results showed that ΔG of process a) is (*ca.* 33 kcal/mol) smaller than that of b), thus indicating that tetramers coming from the union of two dimers with a water molecule are the stable form for this type of system, in good agreement with our experimental results and with crystal structures of similar Zn-carboxilate aminoalcohol compounds.

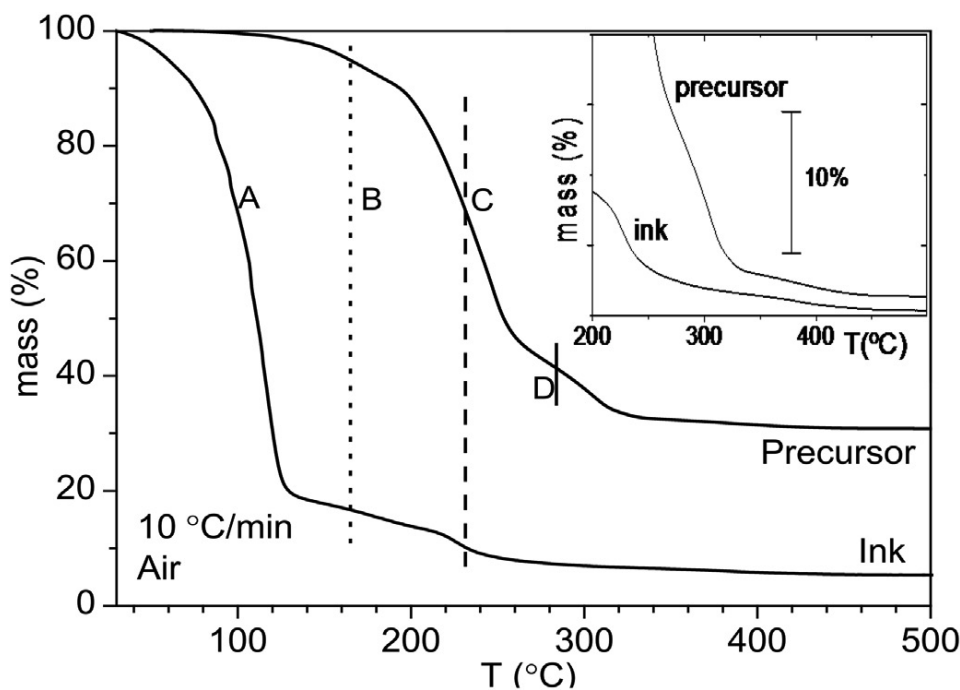


FIGURE 4.6. TGA curves of **Ink** and **Precursor**. Step A is due to ME evaporation whereas steps B, C and D correspond to decomposition. An expansion of the plot in the range 200-500 °C is shown as an inset.

4.1.2.3 Comparative studies of the thermal evolution of the Precursor and the Ink

Once the **Precursor** has been fully characterized, research has been focused on its thermal behaviour and the influence of the solvent (2-ME) on it. To this aim, TGA analyses were performed for both the **Ink** and the **Precursor**. As depicted in Figure 4.6, the **Ink** undergoes a very pronounced mass-loss process (step A), that is not observed for the **Precursor**, near the boiling point of 2-ME (120 °C) that is attributed to solvent evaporation. At higher temperatures, TGA

curves of both **Ink** and **Precursor** also show two additional mass-loss steps (B and C) at around 170 and 230 °C respectively, but with different relative heights. This feature deformations, together with the clear shape difference of the additional higher-temperature step D (290 °C) in the **Ink** curve (see the Inset of Figure 4.6), makes evident that the residual 2-ME solvent has an effect on the oligomers decomposition. The final mass measured after the Precursor decomposition ($m_f = 0.31 m_i$) is very close to the one expected for the transformation of an equimolar mixture of ZAD and EA into ZnO ($m_f = 0.29 m_i$). It can be concluded that, in contrast with studies carried out on pure ZAD[132], no Zn loss occurred during decomposition, as if interaction with EA prevented it.

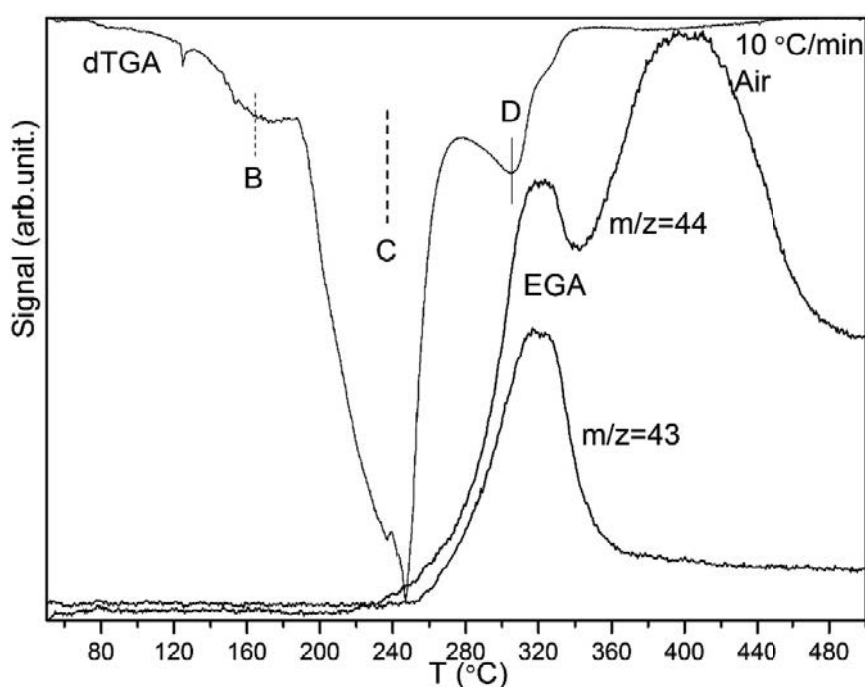


FIGURE 4.7. Derivative of the TGA (dTGA, thin line) curve and coupled MS signals (EGA, thick lines) for $m/z = 43$ and $m/z = 44$ of the **Precursor**.

Simultaneous DTA and EGA signals recorded during the TG experiment ([241, 242]) on the **Precursor** have been used to deduce some general characteristics of the oligomers decomposition process (steps B, C and D). First of all, since DTA signal (not shown) is always endothermic, it is sure that decomposition proceeds without substantial oxidation of the organic ligands. This conclusion is reinforced by the fact that CO_2 ($m/z = 44$) begins to evolve after the two main decomposition steps (Figure 4.7). In fact, steps B and C do not correlate with any EGA peak despite that most of the mass is lost during step C. It can be concluded that these steps involve evolution of large fragments that cannot be detected with the present experimental setup (having $m/z > 70$). Finally, the last step D correlates with peaks of $m/z = 44$ and $m/z = 43$, that might correspond to CO_2 and to the superposition of acetone and other volatile signatures. Most of these volatiles have been also detected in previous studies on the thermal stability of Zn(II) complexes

and have been ascribed to the formation of cyclic nitrogen-species[243].

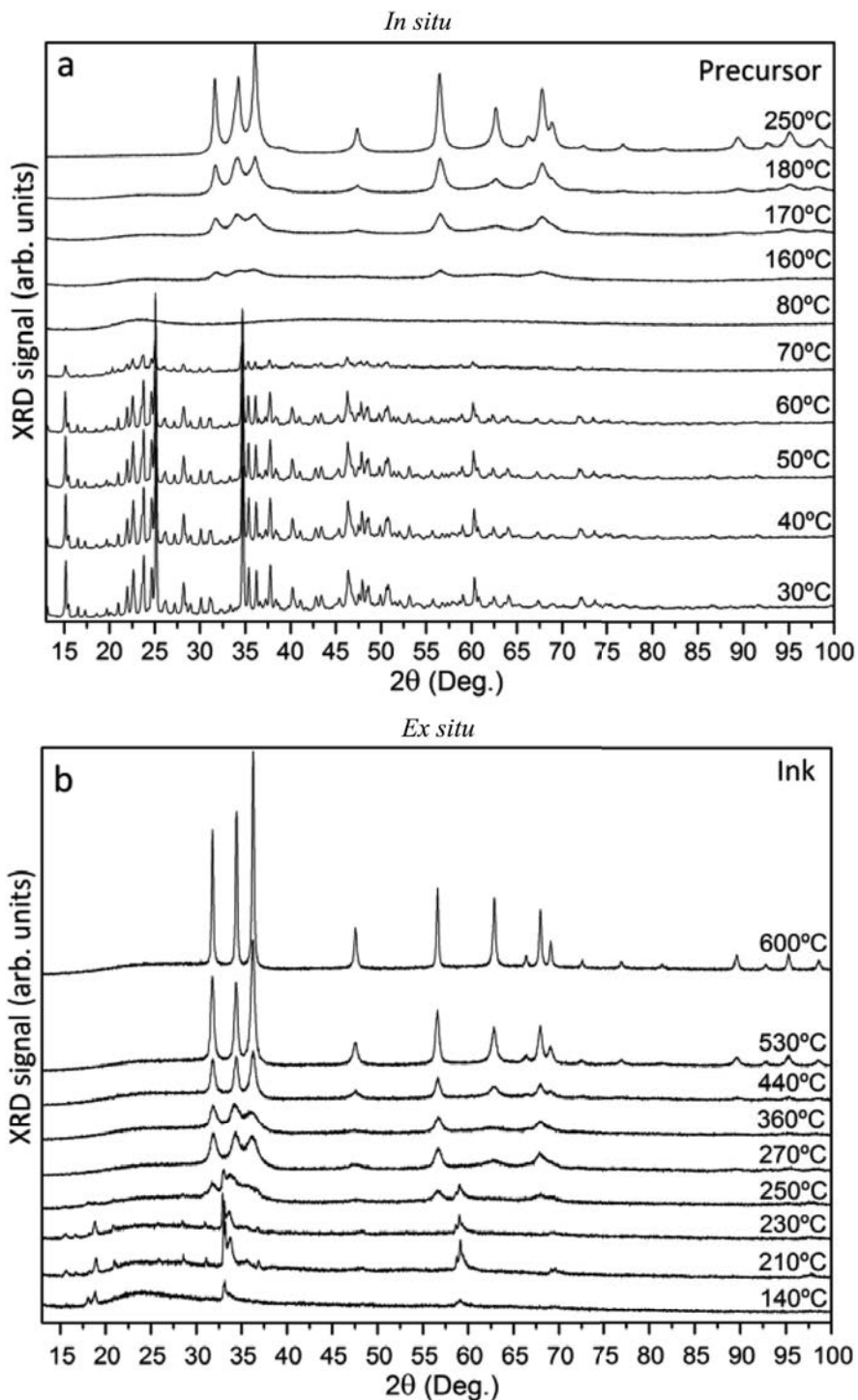


FIGURE 4.8. XRD spectra measured at various temperatures of: (a) *in-situ* dried **Pre-
cursor** and (b) *ex-situ* **Ink**.

4.1.2.4 Evolution of the crystalline structure with the temperature

To study the evolution of the crystalline structure, an additional *in-situ* and *ex-situ* XRD experiments on the dried **Precursor** and **Ink**, respectively, were performed at temperatures up to 600 °C (Figure 4.8). As shown in Figure 4.8a, the dried Precursor is highly crystalline at room temperature, it becomes amorphous for temperatures higher than 80 °C and transforms into crystalline ZnO above 160 °C. This early formation of ZnO during the *in-situ* XRD experiments seems contradictory with the TGA measurements, where the **Precursor** decomposition process occurs in the 190-260 °C range.

This different behaviour is probably due to: a) the more difficult gas exchange, and consequently slower decomposition rate[244], in a bulky sample (necessary for TG experiments) than for the layer needed for powder XRD; and b) the long stabilization time required for each *in-situ* XRD measurement, so the dwell time at each temperature has an important role. In contrast, the *ex-situ* XRD spectra obtained for the **Ink** (Figure 4.8b) show that crystallinity of the initial phase steadily increases up to 210 °C, while in the range 210-270 °C it coexists with crystalline ZnO, that becomes the only phase above 270 °C, that is *ca.* 90 °C higher than the temperature required for the **Precursor**.

4.1.2.5 Atomic environment

The structural evolution of the **Ink** has been further analysed by looking at the atomic environment of the Zn, C, O and N atoms by XPS analyses of the Zn 2p, Zn LMM and O_{1s} Auger lines at different temperatures (up to 600 °C). Modified Auger parameter, calculated from the binding energy of Zn 2p_{3/2} photoelectron peak and the kinetic energy of Zn LM₄₅M₄₅ Auger peak is similar to the one (2010 eV) reported in the NIST database for ZnO³, above 250 °C. In addition, the atomic ratio between Zn and N varies from 1 to 5, from room temperature to 180 °C (after steps A and B in TGA curves), respectively. From 180 °C to 250 °C, the Zn/N ratio increases above 20 (step C in TGA curves) and some few N remains at the **Ink** at T > 250 °C. Indeed, a weak N_{1s} signal still remains up to 600 °C, it is concluded that some N atoms remain after decomposition even at so high temperatures.

The evolution of the area percentage for the deconvoluted O_{1s} lines is summarized in Table 4.1. This deconvolution shows the presence of two different O_{1s} peaks. For ZnO, the 530 eV peak corresponds to O₂ ions surrounded by Zn atoms[64], and 531.6 eV to O₂ ions in the oxygen deficient regions and to OH bonds[245]. From 180 °C to 250 °C, when the ZnO just starts to crystallize according to XRD experiments, the main peak is that of organic surrounded O₂ ions, whereas from 270 to 600 °C many organic species have evaporated and the main peak is associated to O₂ surrounded by Zn. Moreover, the thermal evolution of atomic concentration ratio between Zn and O reveals that, above 250 °C, ZnO becomes more stoichiometric: Zn/O varies from 0.6 to 0.9 up to 600 °C. These results are in good agreement with the fact that starting from 250 °C, crystal reconfiguration and last organic compound evaporations befall.

³NIST X-ray Photoelectron Spectroscopy Database, <http://srdata.nist.gov/xps/>.

Table 4.1: Evolution of the area percentage for the deconvoluted O_{1s} lines at 530.0 eV (corresponding to Zn-O-Zn bonds) and 531.6 eV (O-H and O-C-O bonds) after XPS measurements on the **Ink** at different temperatures.

Bonds	BE O_{1s} (eV)	180 °C	210 °C	230 °C	250 °C
Zn-O-Zn	530.0	19	21	24	39
O-H	531.6	81	79	76	61
O-C-O					

4.1.3 Conclusions

The detailed study of the system ZAD, EA as precursor, in the presence of 2-ME as solvent, summarized in this work provides conclusive evidences for the roles of the stabilizer (EA) and the solvent (2-ME) in the formation of ZnO from ZAD. First, it has been proved that EA reacts with ZAD giving tetramers with "Zn(H₂NCH₂CH₂O) (μ -OAc)" cores. Second, with 2-ME an intermediate crystalline phase, not detected for the precursor (solvent-free system), appears below 270 °C and ZnO is formed at higher temperatures, although many volatiles are detected at higher temperatures (experimental studies revealed that even at 600 °C some N atoms remained in the film) and, thus, a detailed description of how these tetrameric units evolve into crystalline ZnO during thermal decomposition is still an issue. Nevertheless, these studies constitute the first step for further works centred also on the investigation of the effects produced by other skeleton-like aminoalcohols, which may be important to reduce the temperatures required to achieve ZnO or to minimize stability problems. These two aspects are relevant in view of the design of new procedures to achieve materials for technological applications such as printed electronics.

The next two sections present a detailed structural and chemical characterization of the system formed by ZAD and EA (**Precursor**) with 2-ME as solvent (**Ink**), in order to describe how they progress towards ZnO and how N evolves (*i.e.* the nature of the nitrogen volatiles) with the temperature. In addition, the origin of the **Ink** degradation during storage at room conditions, that represents a serious handicap to industrialize its use, will be analyzed. The experimental results will be correlated with Molecular Dynamics (MD) in the last section of this chapter, which is known to be a useful and powerful tool to understand the decomposition of many organic molecules, condensed substances and even metal-organic complexes. For convenience, the temperature values in both sections will be presented in Kelvin.

4.2 Role of ethanolamine on the stability of a sol-gel ZnO ink

This paper presents a detailed analysis of the origin of the ink (ZAD+EA+ME) degradation during storage at room conditions. Experiments are supported by the theoretical calculation of the frontier orbitals of the system ZAD plus EA under interaction with ME and CO₂. Since, as already shown in the previous section of this chapter[246], the reaction of EA with ZAD produces tetramers that, in contrast with dimmers, are not stable in solution, the dimerization

process leading from the simplest configuration (monomer) to the most abundant (dimer) is also theoretically analyzed and used to describe the effect of the nuclearity raise on the mixture stability. These results provide a better understanding of the role played by EA in the formation of ZnO and, consequently, allow optimizing the technological processes to achieve a controlled ZnO.

4.2.1 Materials and procedures

The ZnO precursor was prepared by stabilizing zinc acetate dihydrate ($\text{Zn}(\text{CH}_3\text{COO})_2 \cdot 2\text{H}_2\text{O}$, ZAD, from Panreac) with ethanolamine ($\text{H}_2\text{NCH}_2\text{CH}_2\text{OH}$, EA, from Acrös Organics). Then, 2-methoxyethanol ($\text{CH}_3\text{O}(\text{CH}_2)_2\text{OH}$, ME, from Aldrich) was added as a solvent to prepare the ink, following the method reported in previous work[246]. Some of these mixtures were stored at various room conditions for some weeks, showing evidences of chemical degradation. Sensitivity to light was tested by leaving the samples over the lab desk. ^1H Nuclear Magnetic Resonance (NMR) studies were performed at 298 K in a Mercury-400 MHz instrument, using MeOD (99.9%) as solvent. Complementary Evolved Gas Analysis (EGA) was performed in vacuum with a heating rate of 20 K/min using a MKS quadrupole mass spectrometer (Microvision Plus).

4.2.2 Quantum mechanical simulations

To elucidate the effect of light, CO_2 and ME on the stability of the reagents and the precursor, the energy levels and stability of the different molecules appearing in the ZAD-EA-ME system were deduced from quantum mechanical simulations. Ten molecular models were defined for Time-Dependent Density Functional Theory (TD-DFT) simulations:

- The isolated EA, monomer $[\text{Zn}]_1$ and dimer $[\text{Zn}]_2$ (Figure 4.9).
- The previous three models solvated with implicit ME [$\epsilon = 17.2$].
- The $[\text{Zn}]_1$ and $[\text{Zn}]_2$ with one and two CO_2 molecules, respectively, before and after solvation.

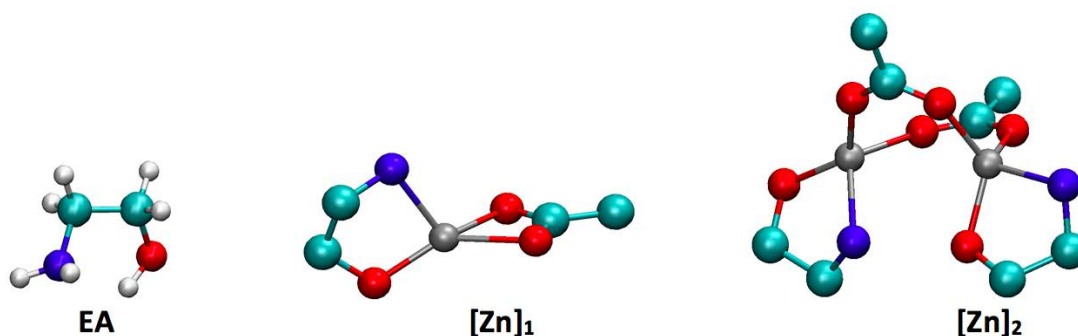


FIGURE 4.9. Ethanolamine, monomer $[\text{Zn}]_1$ and dimer $[\text{Zn}]_2$ models according to the structures optimized in the previous section of this chapter[246]. The H atoms in $[\text{Zn}]_1$ and $[\text{Zn}]_2$ are not represented for clarity.

All these models were optimized by means of the Gaussian 03 software[163] and the UB3LYP hybrid method[247, 248] using the LANLD2Z basis set[249, 250] with a threshold of 10^{-7} a.u. in the potential energy and 10^{-5} a.u. in the maximum nuclear force component⁴. The implicit solvent models were performed using the Polarizable Continuum Model (PCM) via a set of overlapping spheres[251]. Moreover, the models were tested as potential energy minimum and their photo-absorption spectra were simulated using the Time-Dependent DFT approach[252, 253].

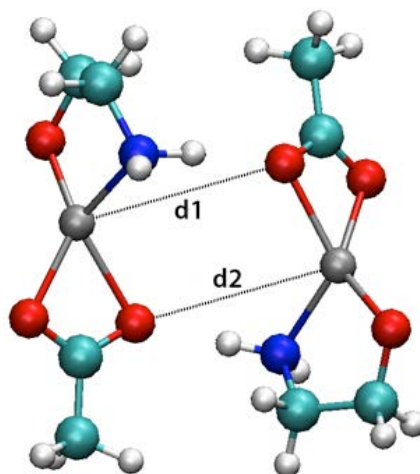


FIGURE 4.10. The bimolecular $2[\text{Zn}]_1$ system reconstructed by changing the distances d_1 and d_2 around their respective equilibrium values.

For the simulations of the dimerization process, a new isolated model of a bimolecular $2[\text{Zn}]_1$ system was reconstructed by forcing the hydrogen-bond interaction between every N-H \cdots O_{AcO} pair (Figure 4.10 by means of Gaussian 03 and using the previously mentioned DFT method and basis set. From this structure, the potential free energy surface (PES) of the dimerization process was generated by using the relaxed scan methodology over two catalytic variables. In total, 121 structures (11×11 changing each variable around the starting values of $d_1 = 4.03$ Å and $d_2 = 3.94$ Å) were optimized to calculate the PES and to predict the Minimum Potential Energy Pathway (MPEP) followed by the system.

4.2.3 Results and discussion

4.2.3.1 Stability of EA with ME and ZAD under different conditions

Several experiments were carried out in order to compare the stability of the freshly prepared ink (EA+ZAD+ME) with those of the free ethanolamine (EA) and EA in 2-methoxyethanol (EA+ME). In a first step, the samples were kept under illumination but avoiding the contact with air. After 4 weeks, no modification was apparent in any of the samples (Figure 4.11a). Next, the samples were exposed to the action of air by uncovering the flasks.

⁴See the optimized atomic coordinates in Tables S1-S10 of the Supporting Information with the same title as this section, Appendix A.

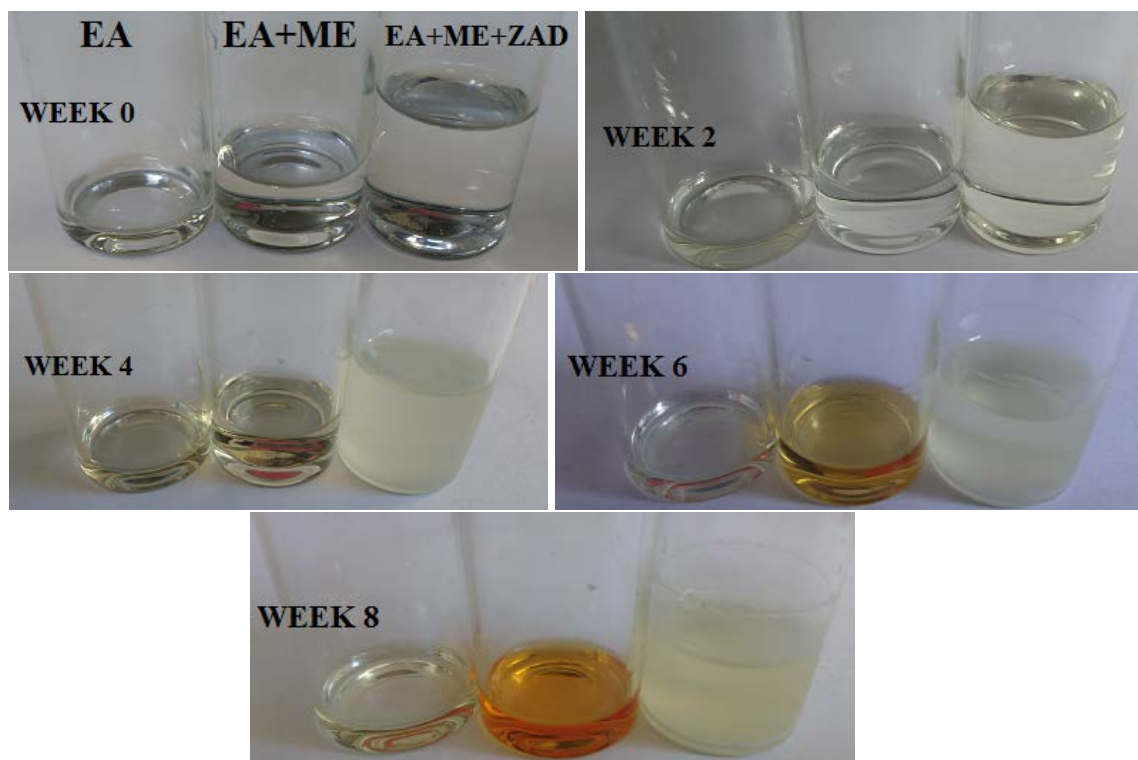


FIGURE 4.11. Pictures of EA (EA, at left), EA in 2-ME (EA+ME, middle) and the **Ink** (EA+ZAD+ME, right), freshly prepared and after 2, 4, 6 or 8 weeks of storage at room temperature and in the presence of light and air.

Figures 4.11b to 4.11e show the evolution of the appearance of the samples after 2, 4, 6 and 8 weeks in contact with air under illumination. A slight change in the aspect of EA and EA+ME+ZAD was detected during the first 3 weeks, while EA+ME remained colourless and transparent (Figure 4.11b). This observation indicates that this ink is clearly more stable than those containing more rigid aminoalcohols (see next chapter[254, 255]). At the fourth week, the ink became cloudy and precipitated, while EA and EA+ME turned yellowish and orange, respectively, suggesting that some chemical transformation was taking place. As shown in Figure 4.11c to Figure 4.11e, the colour change is more apparent in EA+ME, thus indicating that the solvent ME plays a role in this process and perhaps determines the nature of the products. Although some degradation by light may have occurred before the flasks were uncovered, degradation was only visible when the samples were kept in contact with air.

To assess how important was light excitation in these degradation processes, in a third experiment fresh samples were kept uncovered in the dark. After 4 weeks, the appearance of EA and EA+ME was similar to that observed in the previous experiment, while the complete ink showed less precipitate. Consequently, the presence of light mainly affects the sample containing Zn. In summary, these experiments demonstrate that the degradation of all three samples is mainly due to reaction with some species contained in air, with a minor influence of light excitation in the ink degradation. The following experiments are thus focused on identifying the

reacting species through the degradation products.

A $^1\text{H-NMR}$ experiment was performed for the 8-weeks degraded EA+ME sample (at the centre in Figure 4.11e), to find out the degradation products. MeOD was used as solvent for NMR, owing to the low solubility of the mixture. During specimen preparation, the deep orange colour of EA+ME faded giving a pale-yellow solution. This could be ascribed a) to the different polarity of the solvent (MeOD, $\mu_D = 3.09$ D) and ME ($\mu_D = 2.14$ D), or b) to their ability to establish intermolecular hydrogen-bond contacts with the species in solution. The H-NMR spectrum⁵ suggests the coexistence of several species in solution, as several singlets were detected in the range 6.8 - 8.5 ppm. Their positions are compatible with the presence of protons bound to N atoms attached to -CO or -COO arrays, as the carbamic acids, zwitterions and carbamates (see scheme of Figure 4.12) recently proposed[256] when amines and aminoalcohols capture CO_2 .

The nature of the final products and their relative abundance are described to depend on a wide variety factors such as temperature, amine or aminoalcohol concentration, solvent nature (specially its polarity and its tendency to establish hydrogen bonds), and CO_2 partial. In turn, these complexes have been reported to react with -OH groups and form several lactams and lactims with different colouration[257, 258] and the pH (and thus the presence of ME and MeOD) seems to influence the tautomer ratio between them[259, 260].

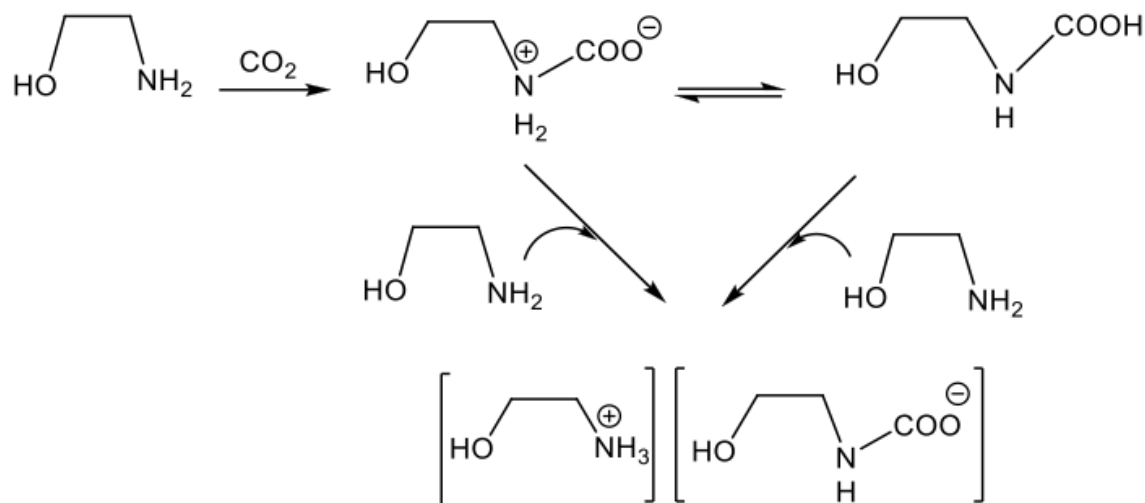


FIGURE 4.12. Degradation mechanism proposed for EA in the presence of CO_2 . Next reaction with -OH would give lactams or lactims.

Hence, these observations suggest that ME promotes EA degradation even at room temperature. However, the precursor formed when ZAD is added to the EA+ME mixture contains deprotonated EA which acts as an (N, O)- bidentate ligand stabilizing EA. The reactions proposed in the scheme of Figure 4.12 can explain the observed colours, as well as the presence (or coexistence) of several compounds with -NHC(O)- functional groups detected by NMR in EA+ME after long storage periods. Consequently, capture of both CO_2 and -OH seems demonstrated.

⁵Figure S1, supporting information with the same title that this section, Appendix A.

As a complementary experiment, Evolved Gas Analysis was used to elucidate the composition of the samples before and after degradation under illumination in air. A variety of mass fragments from $m/z = 12$ to 86 was detected from the inks, and their respective EGA curves were classified according to their dependence on temperature (see also next section and next chapter[254]). In particular, the group related with $m/z = 76$ (Figure 4.13a) can be associated with some non-bonded and degraded EA decomposition fragments[261]. Our previous results support this possibility, since some carbamate groups (with $m/z = 76$) have been detected by NMR at room temperature (scheme of Figure 4.12).

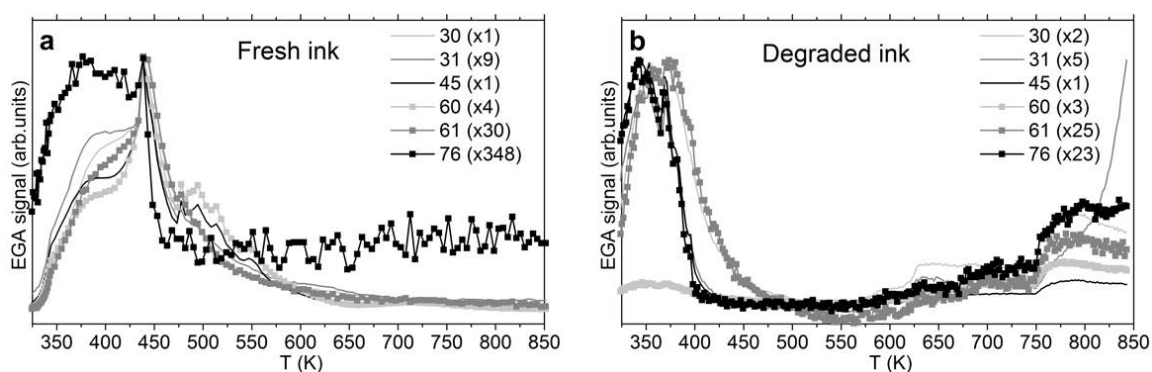


FIGURE 4.13. Normalized EGA signals of compounds related to $m/z = 76$ for freshly-prepared EA+ME+ZAD (a) and EA+ME after 8-weeks degradation in air and light (b), with their respective normalization factors in parenthesis.

To confirm this hypothesis, the degraded samples were also measured by EGA. The peak patterns obtained in this case were similar to the non-degraded ones, but the $m/z = 76$ EGA signal appeared to be much more intense. As shown in Figure 4.13b, the degraded EA+ME presents an $m/z = 76$ peak which is one order of magnitude more intense than the one in Figure 4.13a (as indicated by the multiplication factors in both graphs), suggesting a more relevant presence of carbamates (as no ME was added) as compared to complete EA ($m/z = 60$) and the other fragments. Consequently, a mass spectrometry of EGA can provide not only qualitative but also quantitative clues of the ink degradation at room temperature by means of the $m/z = 76$ vs. $m/z = 60$ ratio.

4.2.3.2 Time-Dependent Density Functional Theory, TD-DFT, calculations

Most of the experimental studies carried out so far focused on EA degradation as well as on its CO_2 absorption process have been undertaken in vacuum or in aqueous media. On the other hand, the theoretical studies on these phenomena reported up to date were carried out in vacuum, in water or more recently also in methanol[262]. Despite ME is the typical solvent used in sol-gel ZnO formation, parallel studies involving ME and CO_2 or both simultaneously have not been reported so far, and those on the precursor formed in the reaction $\text{ZAD} + \text{EA}$ in ME

still remain unknown. In order to fill in this gap, here it was prompted to undertake theoretical studies to understand the different stability and reactivity of these systems.

It is still not clear what prevents EA and EA+ME to degrade more under illumination, while the complete ink does. In order to understand the influence of external factors -such as exposition to light or air- on the mixtures stability and their tendency to react, computational studies based on TD-DFT and Molecular Orbital (MO) calculations were undertaken. For comparison purposes, an initial study of EA both in vacuum and in ME was carried out. The results, summarized in Figure 4.14 and Table 4.2, revealed that:

- The HOMO-LUMO gap energy is high (> 8.5 eV) in both cases.
- The first absorption bands involve mainly the electronic HOMO \rightarrow LUMO transition.
- In ME, these bands shift to higher energies and the weight of the HOMO \rightarrow LUMO transition increases as well as its oscillator strength, indicating a higher tendency of this transition to occur.

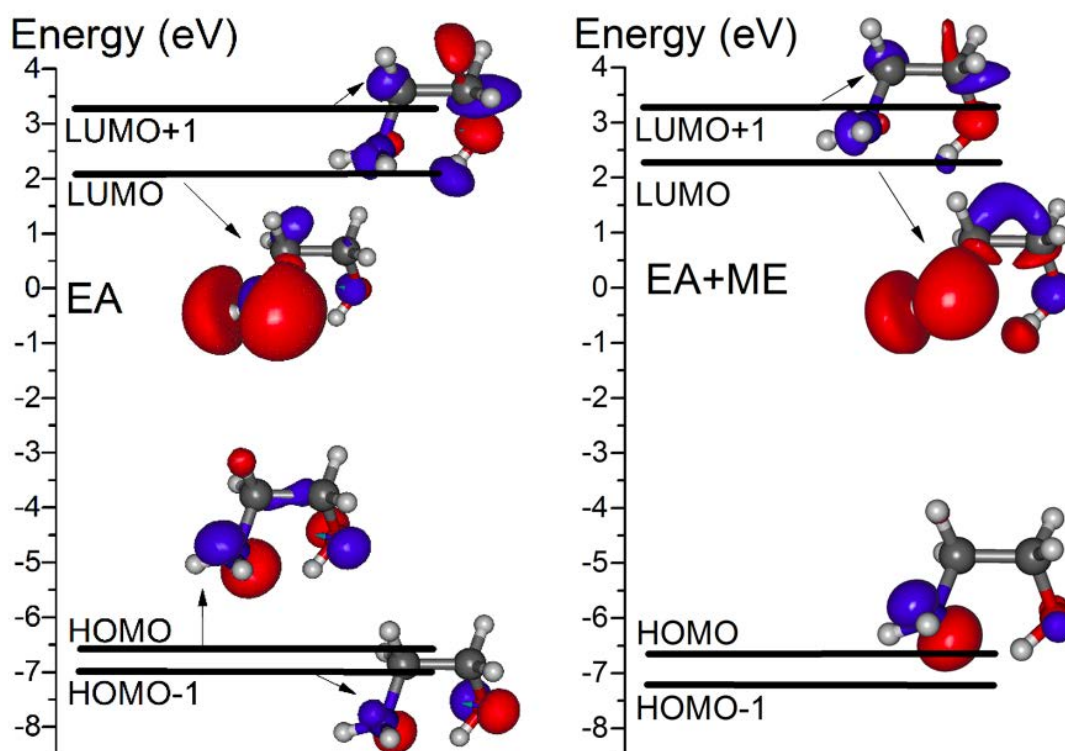


FIGURE 4.14. Frontier orbitals calculated with Gaussian for EA and EA+ME. Hereinafter, different close energy levels with similar orbital scheme (e.g. HOMO and HOMO-1 in EA+ME) are not marked with arrows.

Moreover, the contribution of the nitrogen $2p_z$ orbital in the HOMO of EA+ME is higher than for the isolated aminoalcohol (see Figure 4.14). This indicates that it becomes more nucleophilic, and therefore more prone to react with CO_2 . This is consistent with the faster degradation of EA+ME during storage in air. Keeping these results in mind, the influence of CO_2 , ME and nuclearity on the stability of the system with Zn at room conditions was analyzed. Since $[\text{Zn}]_4$ seems only stable in crystals (see previous section of this chapter[246]), and in solution $[\text{Zn}]_4$ evolves to produce the monomer $[\text{Zn}]_1$ and the dimer $[\text{Zn}]_2$, here it will be skipped the tetramer simulation, comparing the results of $[\text{Zn}]_1$ and $[\text{Zn}]_2$ to infer the influence of the nuclearity on the system stability.

The HOMOs and LUMOs of $[\text{Zn}]_1$ and $[\text{Zn}]_2$ (Figures 4.15 and 4.16) are markedly different from those of EA and EA+ME (Figure 4.14). In these Zn(II) complexes, HOMO is concentrated on the $2p_z$ orbital of the deprotonated oxygen of EA, instead of the nitrogen atom of EA. So is the O and not the N atom that will react with CO_2 . Concerning the effect of degradation under illumination, one has to look at the HOMO-LUMO gap. In $[\text{Zn}]_1$, the LUMO is basically Zn(II) centred, while for $[\text{Zn}]_2$ it is mainly located on the donor atoms of the two bridging ligands (Figures 4.15 and 4.16). Besides that, the energy gaps (5.7 eV for $[\text{Zn}]_1$ and 4.7 eV for $[\text{Zn}]_2$) decrease considerably in relation to EA (> 8.5 eV).

Table 4.2: Excitation wavelengths (λ) with their respective assignments, oscillation strengths and probability weights, calculated with TD-DFT for EA and EA+ME.

EA			
λ (nm)	Assignment	Oscill. Str.	Wt. (%)
184	HOMO-1 \rightarrow LUMO	-0.287	16
	HOMO \rightarrow LUMO	-0.638	81
167.9	HOMO \rightarrow LUMO	0.683	93
246.8	HOMO-1 \rightarrow LUMO	0.524	55
	HOMO \rightarrow LUMO+1	0.281	16
EA + ME			
176.3	HOMO \rightarrow LUMO	0.687	94
162	HOMO \rightarrow LUMO	0.701	98

When considering the contact with ME, the energy required for the first electronic transition is smaller -and closer to the visible region- for $[\text{Zn}]_2$ +ME than for $[\text{Zn}]_1$ +ME (Table 4.3) thus suggesting that the dimer can be more easily photoexcited than $[\text{Zn}]_1$. It is well known that EA can absorb acid components such as CO_2 , CO, H_2S or SO_2 . The study of the reactivity of EA with these reagents including CO_2 under different experimental conditions is still an attractive topic. Some of the previous experiments were carried out in open vessels; consequently, the detected changes could be induced by the absorption of minor components of air (especially CO_2 and CO).

Since it has been published[263] that:

1. The reaction of CO with amines is much slower than that of CO₂ (*i.e.* for EA the rate constant for CO₂ is *ca.* 108 times that of the CO at 323 K);
2. The activation energy is higher for CO (92 kJ/mol) than for CO₂ (55.4 kJ / mol) and
3. In basic medium, the reaction with CO involves a high energy intermediate.

The reaction with CO₂ is kinetically and thermodynamically more favored than that with CO under identical experimental conditions. Therefore, here it is centered the computational studies on the effect produced by CO₂.

As it can be seen, CO₂ affects significantly the frontier orbitals of both [Zn]₁ and [Zn]₂, mainly the LUMO. For [Zn]₂+CO₂, (Figures 4.15 and 4.16 and Table 4.3) the LUMO is mainly a π^* orbital of the bidentate AcO⁻ ligand, while it is basically Zn(II) centred when the calculations are performed in vacuum or in ME. For [Zn]₂+CO₂, the contribution of the atoms of the bridging ligands and EA's N is also modified. Thus, carbon dioxide will react not only with the excited state but it will act as an assistant during photoexcitation, leading to a destabilization of the precursor. In addition, in contrast with the presence of ME, the increase of nuclearity and the presence of CO₂ shift the band towards the visible range and its transition probability.

Finally, the combined presence of both ME and CO₂ does not change significantly the excitation wavelengths and probability weights of the monomer. However, for [Zn]₂, TD-DFT calculations suggest that ME slightly reduces these two parameters independently of the presence of CO₂. Therefore, the dimer is found to be sensitive to ME and CO₂ but, when both are present, ME seems to dominate. In summary, these TD-DFT calculations have proved that a) ME and CO₂ induce significant and relevant changes on the properties and reactivity of both [Zn]₁ and [Zn]₂, and b) the dimer is expected to be more reactive and photosensitive than the monomer. In view of these findings, and in order to get further information on the relative stability of the two species, the study of the formation of [Zn]₂ from two isolated [Zn]₁ units was envisaged.

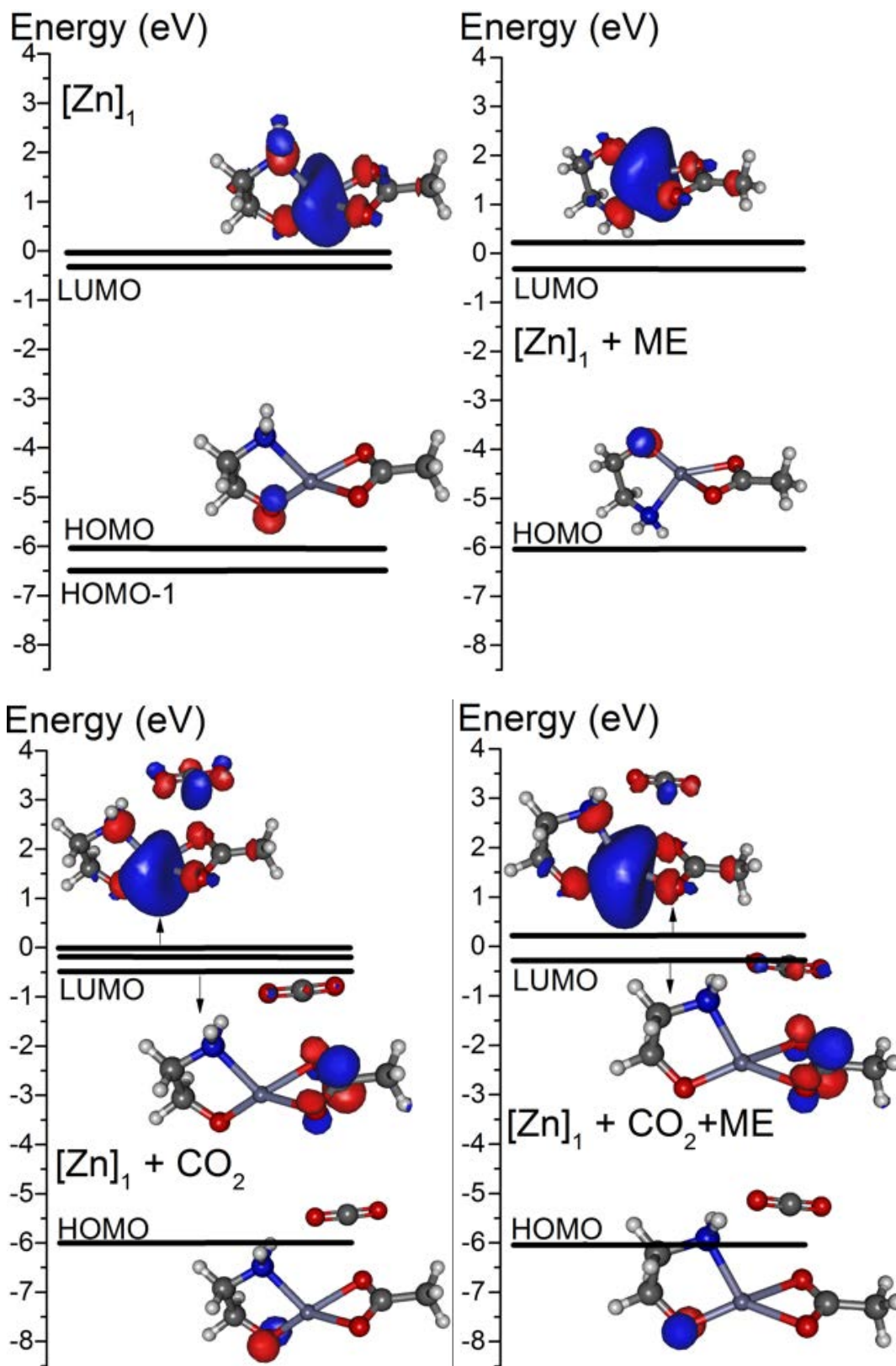


FIGURE 4.15. Frontier orbitals HOMO and LUMO of the monomer system in vacuum and in presence of 2-ME, CO_2 and both.

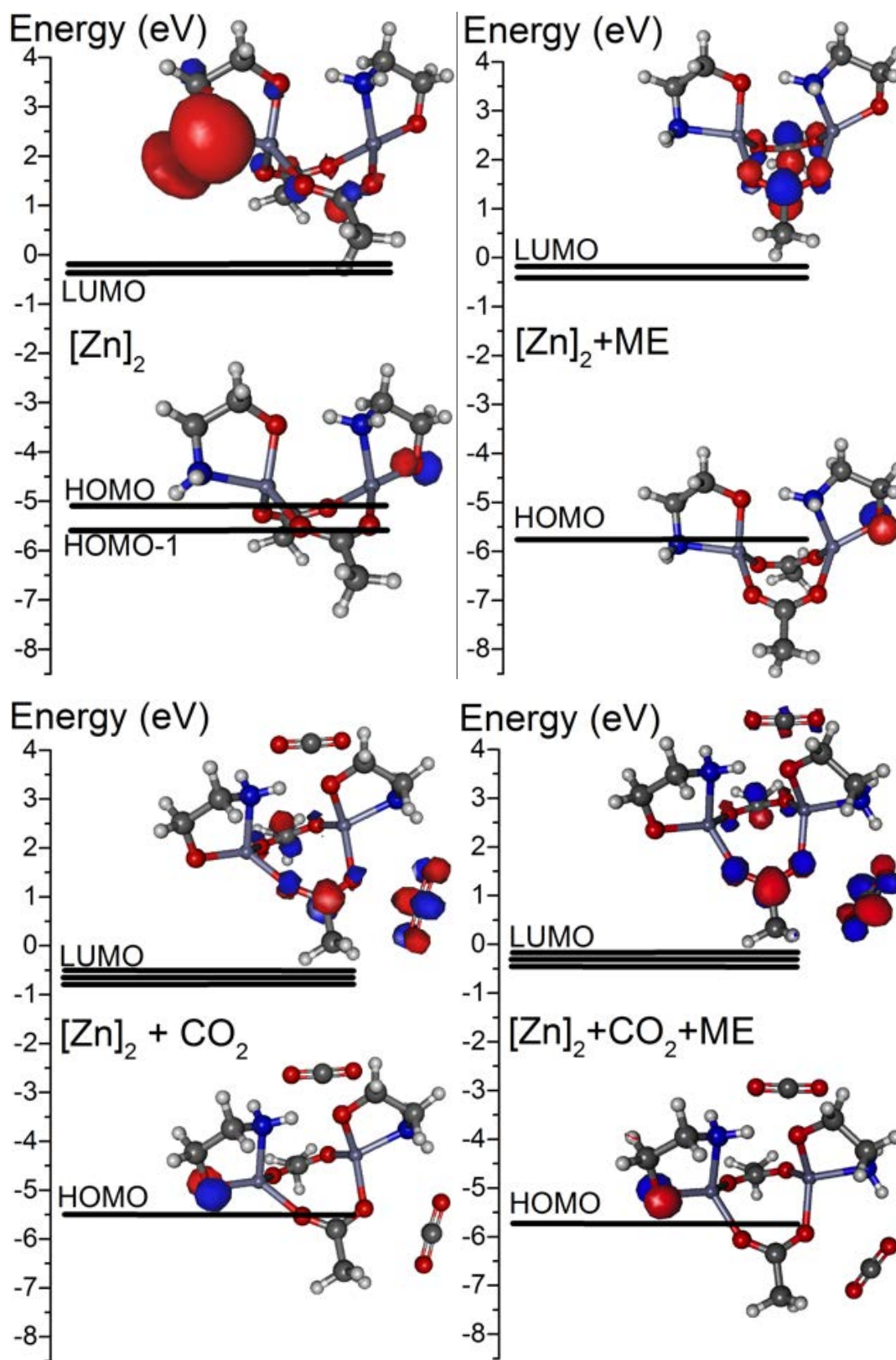


FIGURE 4.16. Frontier orbitals HOMO and LUMO of the dimer system in vacuum and in presence of 2-ME, CO₂ and both.

Table 4.3: Excitation wavelengths (λ) with their respective assignments, oscillation strengths and probability weights, calculated with TD-DFT for the monomer in vacuum and with 2-ME, CO₂ and both. In contrast with the presence of 2-ME, the increase of nuclearity and the presence of CO₂ makes increase the wavelength towards the visible range and its probability.

[Zn]₁			
λ (nm)	Assignment	Oscill.Str.	Wt. (%)
269.1	HOMO \rightarrow LUMO+1	0.617	76
252.6	HOMO \rightarrow LUMO	-0.380	29
	HOMO \rightarrow LUMO+1	0.587	69
246.8	HOMO-1 \rightarrow LUMO	-0.326	21
	HOMO-1 \rightarrow LUMO+1	0.602	73
[Zn]₁+ME			
247.6	HOMO \rightarrow LUMO	-0.416	35
	HOMO \rightarrow LUMO+1	0.544	59
237.8	HOMO \rightarrow LUMO	0.642	82
	HOMO \rightarrow LUMO+1	-0.274	15
236.0	HOMO-4 \rightarrow LUMO	-0.616	76
[Zn]₁+CO₂			
271.5	HOMO \rightarrow LUMO+2	0.275	15
	HOMO \rightarrow LUMO+3	0.585	68
260.6	HOMO-2 \rightarrow LUMO	0.233	11
	HOMO \rightarrow LUMO	0.618	76
258.5	HOMO \rightarrow LUMO	0.665	89
[Zn]₁+ME+CO₂			
257.8	HOMO \rightarrow LUMO	-0.337	23
	HOMO \rightarrow LUMO+3	-0.582	68
253.0	HOMO-3 \rightarrow LUMO	0.645	83
247.3	HOMO-2 \rightarrow LUMO	0.460	42
	HOMO \rightarrow LUMO	-0.393	31
	HOMO \rightarrow LUMO+3	0.274	15

4.2.3.3 Dimerization

Calculations based on Density Functional Theory (DFT) to elucidate the reaction path from two infinitely separated monomers and to confirm the higher stability of [Zn]₂ were carried out at 0 K. According to these simulations, when one monomer approaches each other, the total energy of the system is reduced by 18.7 kcal/mol, due to the formation of hydrogen bonds between their [EA]-[Ac] pairs ([Zn]₁ - [Zn]₁ state in Figure 4.17). As shown in Figure 4.17, the reaction goes through two acetate bridge formations. First, both hydrogen bonds are maintained while the [Ac] right approaches to the Zn left (state A in Figure 4.17). Then, the hydrogen bond between [Ac]_{left} and [EA]_{right} is cleaved and the first acetate bridge is formed (state B). Next, the [EA]_{left}

- $[\text{Ac}]_{\text{right}}$ hydrogen bond is cleaved and a new stable interaction is formed between both $[\text{EA}]$, while $[\text{Ac}]_{\text{left}}$ starts approaching to Zn_{right} (state C).

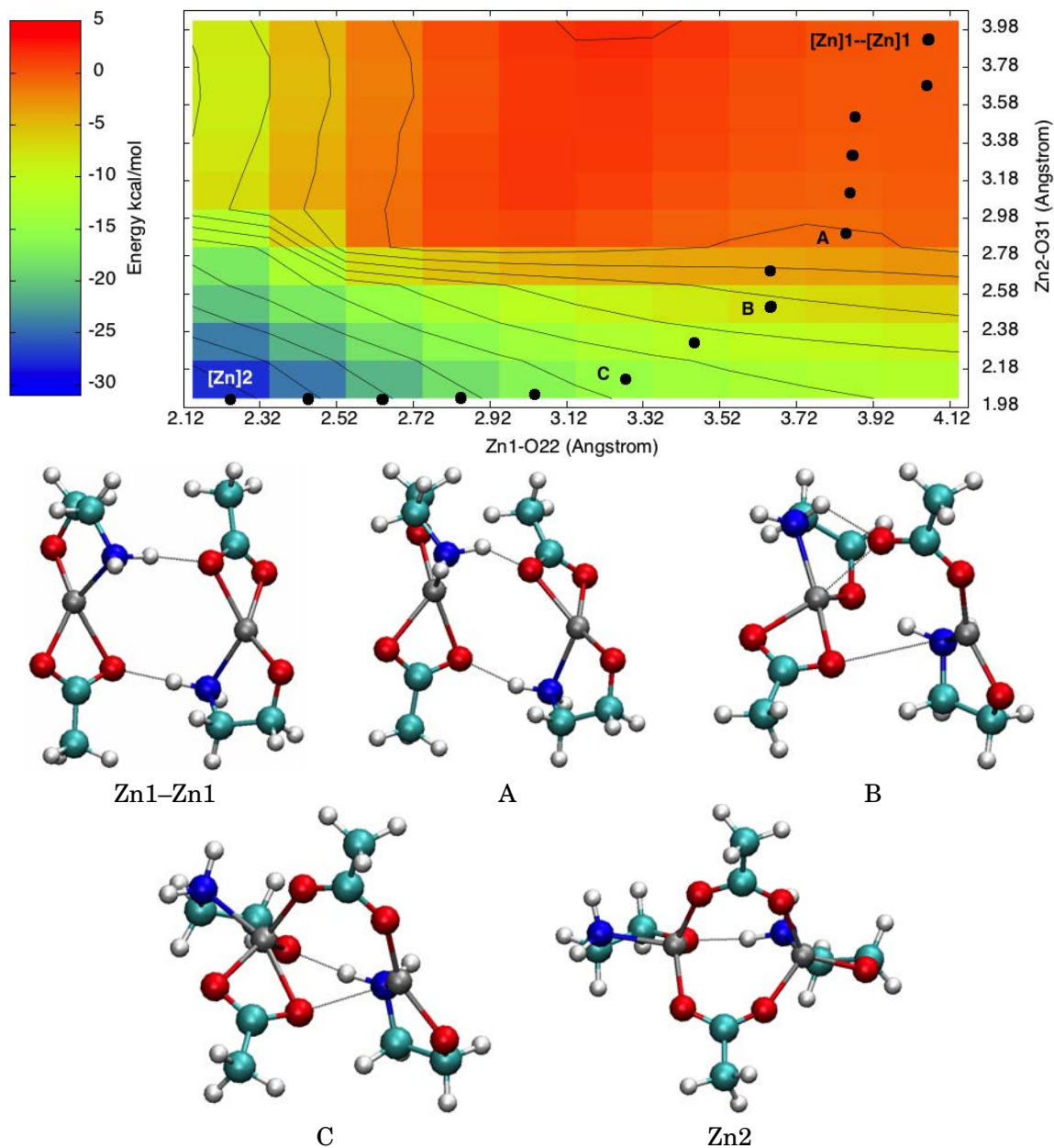


FIGURE 4.17. Potential energy surface (PES) with the most relevant structures during the dimerization process.

Finally, both acetate bridges are formed and the $[\text{EA}]_{\text{left}} - [\text{Ac}]_{\text{right}}$ bond is maintained (state $[\text{Zn}]_2$). From $2[\text{Zn}]_1$ to $[\text{Zn}]_2$ the total energy diminishes around 50 kcal/mol. This simulation indicates that dimmers are highly preferred to monomers. Since, as seen in the previous section, the dimer has a smaller gap energy, it is more sensitive to degradation by light.

4.2.4 Conclusions

The present section has reported on a detailed study, relying on experiments as well as on computational simulations, on the stability of an ink based on ZAD+EA for generating ZnO films. It has been shown that degradation is mainly driven by reaction of EA with atmospheric CO₂, and that EA reactivity increases when it is dissolved in ME and, even further, in the EA+ME+ZAD ink. This has been explained by TD-DFT calculations as because N and O atoms of deprotonated EA become more nucleophilic in EA+ME and in EA+ME+ZAD, respectively. The diminution of EA concentration in the degraded ink has been seen by EGA and NMR experiments, which also delivered information about the degradation products.

Experiments have also shown that reactivity with CO₂ is affected by illumination mainly when the sample contains Zn. In fact, the energy required for the first electronic transition decreases when EA+ZAD is exposed to ME, but CO₂ destabilizes the precursor, acting as assistant during photo-degradation. Finally, calculations make clear that the monomers tend to combine into dimers, which are more photosensitive and reactive than the monomer. This results suggest that the [Zn]₂ plays a key role in the transformation from precursor into ZnO.

4.3 Molecular-dynamics study of ZnO formation from a sol-gel ink containing ethanolamine

In this section is presented Density-Functional-Theory studies on the ZnO formation after decomposition of a sol-gel precursor containing ethanolamine and Zn(II) acetate. The structural modifications suffered during decomposition by the monomeric and dimeric Zn complexes formed, containing bidentate deprotonated ethanolamine and acetate ligands, have been described experimentally and explained via Car-Parrinello Molecular Dynamics. Additional metadynamics simulations provide an overview of the dimer evolution by the cleavage of the Zn-N bond, the structural changes produced and their effects on the Zn(II)-centers environment. The results yield conclusive evidences of the relevance of ethanolamine used as stabilizer in the formation of ZnO.

4.3.1 Experimental and theoretical methods

4.3.1.1 Materials and procedures

The ZnO precursor and the ink were prepared following the method reported in previous sections [246]. The samples obtained after calcination of the ink at 570, 670, 770 and 870 K were characterized by infrared spectroscopy with a Nicolet 400FTIR instrument using KBr pellets. Quantitative determinations of nitrogen, carbon and hydrogen content in the samples were carried out with a Thermo EA Flash 2000 (Thermo Scientific, Milan, Italy) equipment working in standard conditions (helium flow of 140 mL/min; combustion furnace at 1223 K; chromatographic column oven at 338 K). Complementary Evolved Gas Analysis (EGA) of the evolved species was

performed in vacuum at a heating rate of 20 K/min using a MKS quadrupole mass spectrometer (Microvision Plus).

4.3.1.2 Quantum-mechanical calculations

Several approaches were used to describe the EA-ZAD compounds at the molecular level using Car-Parrinello molecular-dynamics (CPMD) simulations[162] with PBE ([158]) functional and pseudopotentials for the core electrons[249]. First, to elucidate the reaction paths towards ZnO formation, the energy and stability of the $[Zn]_1$ and $[Zn]_2$ complexes (shown in Figure 4.18) were obtained. Next, the evolution of chemical bonding with temperature was analysed by full Quantum-Mechanical Molecular-Dynamic calculations. Finally, the molecular decomposition was described thanks to the reconstruction of the free energy surfaces by means of a metadynamics calculation.

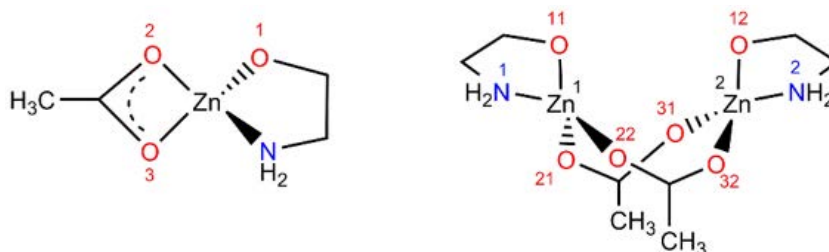


FIGURE 4.18. Schematic views of the monomer and dimer Zn(II) complexes used in Car-Parrinello molecular dynamics, together with the atom labelling scheme used for the computational studies.

The strategy followed to study the effect of temperature on the molecular decomposition was:

1. To test the electronic and nuclear behaviour of the system at the subsequent temperature (0.25 ps MD simulation).
2. To apply a Nosé-Hoover[264] thermostat over the nuclei (with a frequency of 3500 cm^{-1}) and the electrons (expected value of the Electronic Kinetic Energy, EKE, along the test MD with a frequency of 10000 cm^{-1} , Table 4.4) to run a 5000 MD step simulation at a given temperature, and then
3. To repeat the last step by increasing the temperature slowly until the system reaches 870 K. Due to the fact that we have not explained all about the decomposition mechanisms, a proper methodology to accelerate events (reactions, bond cleavage, etc.) will be used in metadynamic simulations.

To reconstruct the free energy surface (FES) of the first decomposition step of the dimer at 300 K (room temperature), a metadynamics calculation was performed using the CPMD software. In this study, the geometry of the last compound obtained from the molecular dynamics simulation was used as input, and then it was subjected to the activation of the Zn-N and the

4.3. MOLECULAR-DYNAMICS STUDY OF ZNO FORMATION FROM A SOL-GEL INK
CONTAINING ETHANOLAMINE

C-O bonds of one of the deprotonated EA ligands in the dimer. After optimization, the $[\text{Zn}]_2$ simulation was restarted from the same temperature; during a 9.4 ps MD simulation (0.12 fs per step), 391 repulsive Gaussians (deposition time of 200 MD steps) have been applied to allow the system to evolve over the FES. The height of the Gaussian was 1 kcal/mol and the width σ was 0.15 a.u. (for the Zn-N bond) and 0.075 a.u. (for the C-O bond).

Table 4.4: Electronic Kinetic Energies (EKE) obtained for the systems $[\text{Zn}]_1$ and $[\text{Zn}]_2$ by CPMD at different temperatures.

T (K)	300	573	673	773	873
$[\text{Zn}]_1$	0.005	0.0089	0.0101	0.0114	0.0128
$[\text{Zn}]_2$	0.01	0.021	0.024	0.027	0.03

Once a representative structure from the products minima was chosen, a second metadynamics simulation was performed at 300 K to activate the cleavage of the C-O11 bond, and also to activate the H-bond interaction between the O11 and the neighbouring EA (O11—H2-N2). This simulation did not show relevant mechanistic results because the C-O11 bond could not be broken after adding 60-70 kcal/mol. However, during the first steps of the simulation, the structure of the complex molecule changed its shape to an intermediate species. The structure of this intermediate was optimized and the Electro-Static Potential (ESP) charges of its atoms were calculated. Afterwards, quantum-mechanical molecular dynamics at 300 K of this intermediate was performed during 1.8 ps leading to a new structural change. This new intermediate species was optimized and its ESP charges were calculated.

In order to reconstruct the FES of the second Zn-N bond cleavage at 300 K, a 1-Collective Variable (CV) metadynamics simulation was performed, through activation of the Zn2-N2 bond. This study was carried out starting from the last optimized geometry of the second intermediate and after a 0.6 ps molecular dynamics at 300 K. During the full metadynamics simulation, 126 repulsive Gaussian potentials (deposition time 200 MD steps) were applied over the mono-dimensional FES along a 3.07 ps MD. The height of the Gaussian was 1 kcal/mol during the first picosecond and it was decreased to 0.5 kcal/mol during the rest of the process and the width σ was 0.20 a.u. Finally, a representative structure of the products was optimized and its ESP charges were calculated. Since the final structure showed one three-coordinated zinc atom, the authors decided to rationalize a restructured more-symmetric geometry, with two tetra-coordinated zinc atoms. This structure was not obtained by molecular dynamics calculations, but it was handily constructed, optimized and its ESP charges were calculated.

Since the final structure showed one three-coordinated zinc atom, the authors decided to rationalize a restructured more-symmetric geometry, with two tetra-coordinated zinc atoms. This structure was not obtained by molecular dynamics calculations, but it was handily constructed, optimized and its ESP charges calculated.

4.3.2 Experimental results

The structural evolution of the precursor has been analyzed by IR spectroscopy and by elemental analysis. After heating at 570 K, the IR spectrum (Figure 4.19) shows the typical bands of the asymmetric and symmetric stretching vibration modes of the bridging acetate ligands at around⁶ 1580 and 1400 cm^{-1} , in addition to the C-N and C-O bands of the amine and ether groups in the 1100-900 cm^{-1} range[265] and to the wagging mode of $-\text{NH}_2$ groups bound to transition metals around 680 cm^{-1} . After heating at 670 K, the bands related to acetate groups diminish whereas those related to EA almost disappear. At this temperature, formation of ZnO is revealed by the intense band appearing below 600 cm^{-1} . At 770 K the intensity of the organic ligands diminishes further, and at 870 K the Zn-O band reaches its maximum intensity. These results suggest that the main decomposition step occurs between 570 K and 670 K, and it involves the deprotonated EA with possible cleavage of the Zn-N bond.

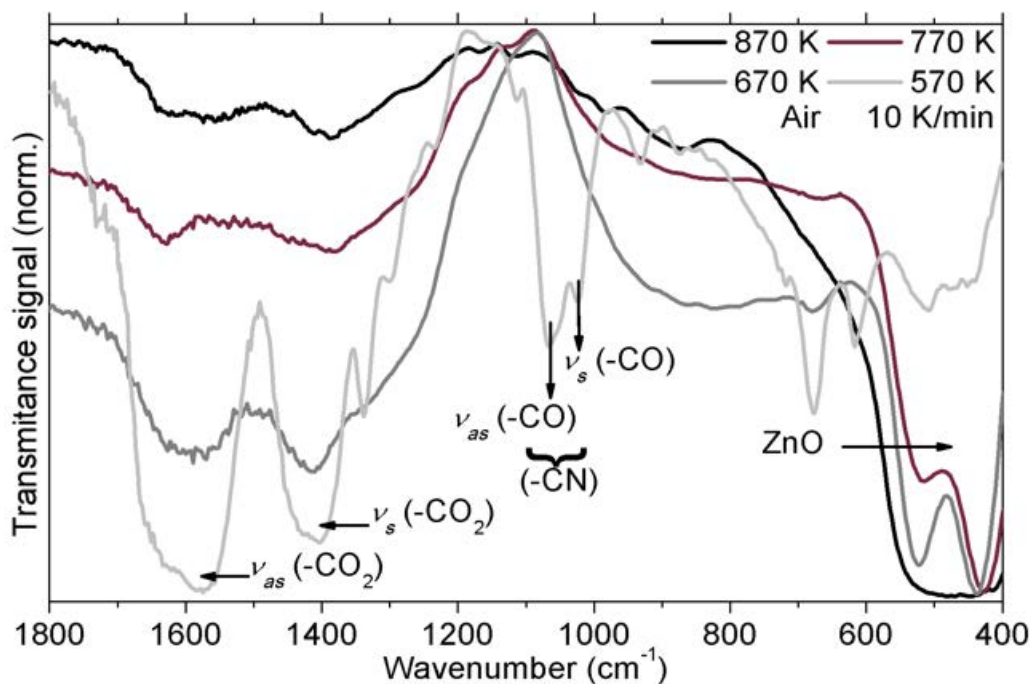


FIGURE 4.19. IR spectra of the precursor after heating up to 570, 670, 770 and 870 K and immediate cooling to room temperature.

Accordingly, elemental organic analysis (EOA) indicates that after heating at 670 K, the nitrogen content (1.3 %wt) is significantly lower than in the fresh precursor (4.0 %wt) whereas the C/N molar ratio increases from 4.0 in the precursor to 6.2. This evolution continues at higher temperatures.

⁶Nakamoto, K.; *Infrared and Raman spectra of inorganic and coordination compounds* (5th Edition), Wiley, New York, USA, (1997).

On the other hand, even at the highest temperature tested (870 K), traces of the organic ligands still remained (0.6 %wt C, <0.1 %wt N and H). Complementary EGA experiments have given information about the nature of the volatile species leaving the precursor film as a function of temperature. A large number of fragments from $m/z = 12$ to 86 a.m.u. (atomic mass units) have been detected. The fragments have been classified accordingly to their intensity dependence on temperature⁷ and one representative fragment of each group has been plotted in Figure 4.20.

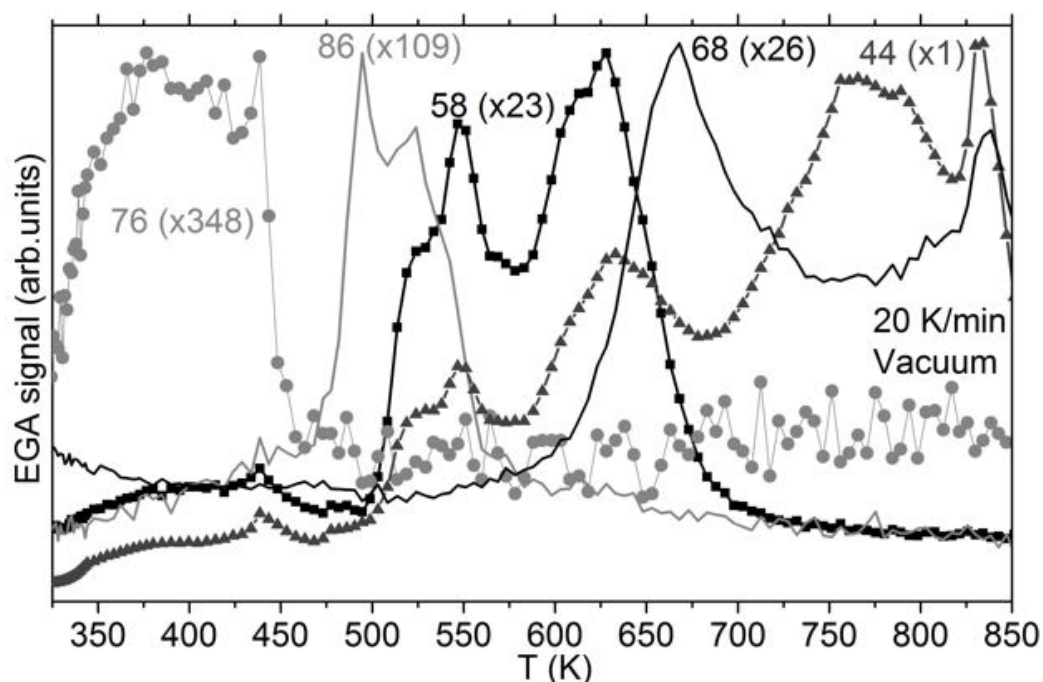


FIGURE 4.20. Normalized EGA signals with their required normalization factor in parenthesis. The m/z detected from 12 to 86 were separated by their thermal behaviors, each one represented by one main m/z and then classified in five groups (see also Figure S1).

Apart from the fragment $m/z = 58$ a.m.u., which may also include acetone formed during acetate decomposition[266, 267], all the other fragments can be associated with a family of nitrogenated cyclic compounds identified by Bouchoux et al.[243] during EA dehydration. As it will be seen in the theoretical section, the most significant cycle is the one with $m/z = 44$ a.m.u., $[C_2H_6N]^+$, that could be produced after cleaving of the N-Zn bond in $[Zn]_i$ (see scheme of Figure 4.12). According to Bouchoux, the initial linear configuration (**A**) would evolve into the triangular cycle, which has a smaller energy (**B**). All the other cyclic compounds (such as **C** in Figure 4.12), whose masses coincide with those of the EGA fragments of Figure 4.20, are the result of subsequent reactions beginning with the triangular cycle.

⁷Details are given in Figure S1 A to E of the Supporting Information, with the same title of this section, in Appendix A

4.3.3 Theoretical calculations

4.3.3.1 Car-Parrinello molecular-dynamics simulations

To analyse the Zn-N and Zn-O bonds evolution with temperature, full Quantum-Mechanical Car-Parrinello molecular dynamics (CPMD[162], based on Density-Functional-Theory (DFT[225]) calculations of $[\text{Zn}]_1$ and $[\text{Zn}]_2$ at different temperatures (300, 570, 670, 770 and 870 K) were undertaken. The distances between Zn and N and O atoms were obtained for the monomer as a function of temperature (Figure S2, Supporting Information with the same title as this section, Appendix A). Surprisingly, no thermal evolution of neither the mean bond length or the oscillation amplitude around it is observed for any bond except for Zn-O3 at 870 K.

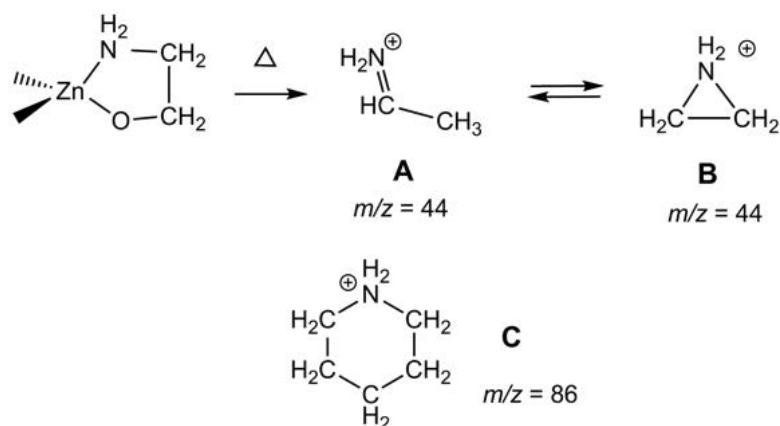


FIGURE 4.21. Simplified core of the precursor, in which the remaining coordination sites are occupied by acetate ligands, cation $[\text{C}_2\text{H}_6\text{N}]^+$ in its linear (**A**) or closed (**B**) forms, and an example of one more complex N-containing cyclic cation (**C**) detected by EGA.

Comparing the two bonds between deprotonated EA and Zn, one realizes that the oscillations of the Zn-O1 bond are much smaller ($\approx 0.1 \text{ \AA}$) than those of the Zn-N bond ($\approx 0.5 \text{ \AA}$), thus suggesting that the Zn-O bond will be easier to cleave, leaving the EA ligand hanging from the Zn-O1 bond. Concerning the acetate group, the Zn-O2 and Zn-O3 bonds oscillate with amplitudes of ≈ 0.3 and $\approx 0.7 \text{ \AA}$, respectively, that are much larger than that of the Zn-O1 bond (with the EA ligand). It seems then reasonable to conclude that the oxygen atom of EA will remain in the final product (ZnO). On the other hand, the very wide oscillations of the Zn-O3 bond could help this particular oxygen atom to play a crucial role in establishing a bridge between two Zn atoms during an intermediate decomposition step. The calculations on the dimer reinforce the provisional conclusions reached with the monomer.

It can be realized (Figure S3, Supporting Information) that none of the Zn-O bonds between the two Zn atoms and their respective EA ligands increases its length with temperature, while their oscillations are always small. On the contrary, both the bond length and oscillation amplitude of the Zn-N bonds do increase with temperature. It seems now clear that the EA ligands will

remain bonded to their own Zn thanks to the Zn-O bond. And, since the oscillations of the oxygen atoms belonging to the acetate ligands are larger, the oxygen of EA will be incorporated in ZnO. Finally, as the temperature increases, one of the acetate oxygens gets farther from its Zn atom (*e.g.* Zn1-O21 increases from 2.1 to 4.2 Å) and gets closer to the other Zn atom (Zn2-O21 diminishes from 3.3 to 2.4 Å). This particular O atom could establish the bridge among the Zn atoms, as already envisaged with the monomer. In summary, these CPMD calculations suggest that, as the temperature increases, the EA oxygen will remain in the final ZnO and the acetate oxygens might establish the bridge among Zn atoms during decomposition.

4.3.3.2 Metadynamics simulations

The previous part has shown that MD is a precious instrument for understanding the mechanisms underlying the ZnO-formation process. Nevertheless, it suffers from a timescale problem, as its results are meaningful only if the run visits all the energetically relevant configurations. In the case that high free-energy barriers separate metastable states, the change from one to another can take place only if activated by those rare fluctuations that can take the system over the barrier. Under these conditions, to obtain sufficient statistics requires an impractical amount of computer time. Metadynamics is then required to scan all the configurations and deepen in the process comprehension. The process leading to Zn-N bond cleavage can be understood thanks to the metadynamics simulations of the dimer shown in Figure 4.22.

As the Zn1-N1 distance is increased, the FES shows that the system passes through a transition state (**TS1**) (Zn1-N1 at 2.95 Å) and an intermediate state **I1** (Zn1-N1 at *ca.* 4 Å) before reaching the cleaved state **C1** (Zn1-N1 at *ca.* 5 Å). Figure 4.22 also shows the approximated structures of these states, as the whole systems are continuously vibrating around their atomic positions. Accordingly, the distance between atoms Zn1 and N1 - as well as the one between O11 and H2(N2) - reaches values larger than 3.5 Å (Figure S5, Supporting information), putting in evidence its cleavage. Moreover, as it can be seen at the left part of Figure 4.23, at 0 K the energy of **C1** and the barrier attributed to **TS1** are rather high (18 and 20 kcal/mol respectively, as shown by the PES curve in Figure 4.23), indicating a negligible probability of evolution from [Zn]₂ to **C1** at 0 K.

On the contrary, at the processing temperatures, the state **C1** that lays just at 4 kcal/mol higher than energy the dimer (see left part of the graph in Figure 4.23). Thus, the energy barrier of 14 kcal/mol is low enough to be easily accessible at the processing temperatures. It corresponds to the energy of the **TS1** state. In addition to the energy, the evolution of the electrical charge was calculated. For that, the [Zn]₂ and **C1** structures (the last one obtained via metadynamics) were optimized using CPMD. Tables S1 and S2 (Supporting Information with the same title as this section, Appendix A) summarize the coordinates and charges for the optimized structures. They suggest significant changes in the charge of relevant atoms between states [Zn]₂ and **C1**. For instance, N becomes more negative due to the cleavage of the Zn-N bond.

Once at the **C1** state, the system could go back to **I1** and again to the dimer thanks to the free rotation of the pendant EA arm. Alternatively, the O atom of the EA arm could approach the amino group of the other EA ligand through an intramolecular H interaction [O11 \cdots H₂(N₂)]. To consider this possibility, this bond was activated in next calculations. The results indicate that the C-O bond may cleave after giving the intermediate species **C2** (Figure 4.23). When relaxed to its ground state, the Zn1 \cdots Zn2 distance in **C2** is 3.8 Å (as indicated in Figure 4.23). To achieve this state, the distance O11-Zn2 must have decreased significantly (from 4.0 in **C1** to 3.8 Å in **C2**). This is possible thanks to an attraction effect of the neighbouring EA onto the O11, which can be quantified via the reduction of the O11 \cdots H₂(N₂) distance (from 2.0 to 1.8 Å).

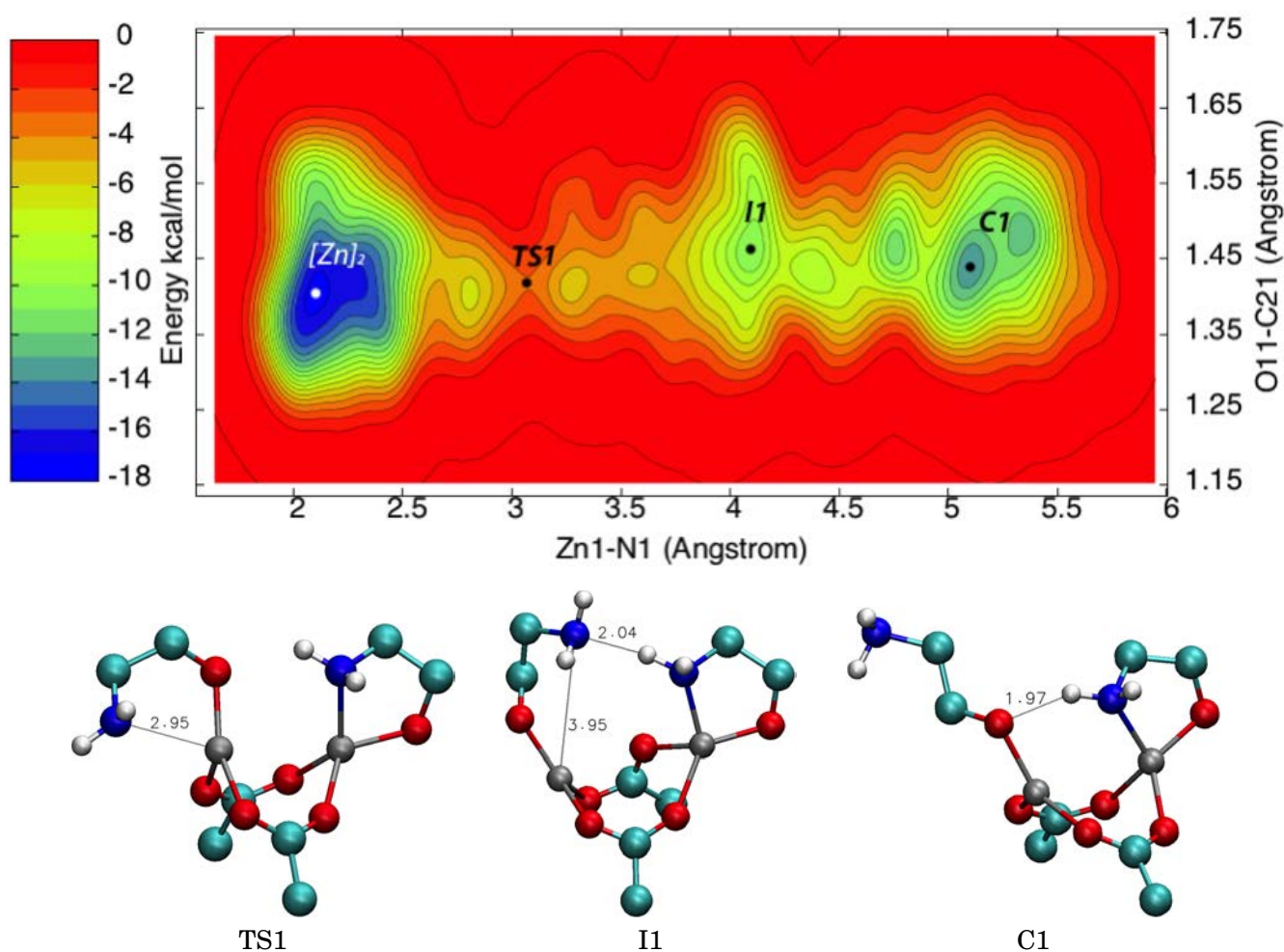


FIGURE 4.22. Label scheme and free energy surface (FES) of the Zn-N bond, as calculated by metadynamics. **I1** and **C1** correspond to energy minima, while **TS1** is a transition state.

4.3. MOLECULAR-DYNAMICS STUDY OF ZNO FORMATION FROM A SOL-GEL INK CONTAINING ETHANOLAMINE

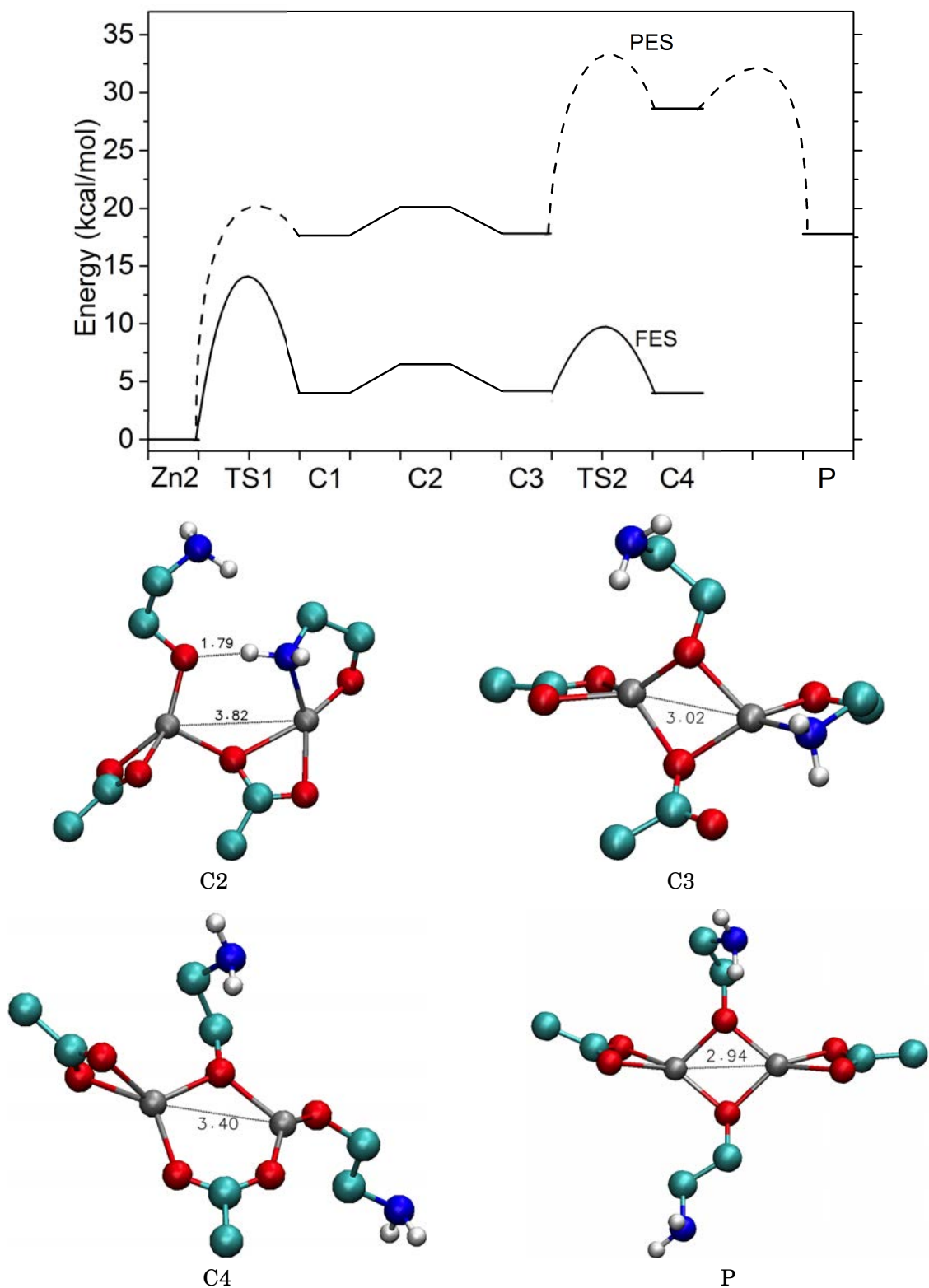


FIGURE 4.23. Free and potential energy profiles of the whole decomposition process, and optimized geometries of intermediate and minima states **C2**, **C3**, **C4** and **P**.

Next, a 1.8 ps MD simulation at 300 K of **C2** structure was performed. This calculation showed that the system evolves to a new intermediate state (**C3**) whose optimized Zn1···Zn2 distance decreases to 3.0 Å (as indicated in Figure 4.23). This situation can be due to the formation of an -OR bridge with the O11 between both zinc atoms and the reorientation of the neighbouring EA ligand. As presented in Figure 4.23, both **C2** and **C3** intermediates show four-coordinated Zn(II) atoms, due to the reorganization of the acetate-oxygen atoms. In this new species **C3**, both EA molecules do not interact with each other, and thus the second Zn-N bond is allowed to cleave. Figure S6 (Supporting Information) presents the resulting FES of the Zn2-N2 cleavage. Two important minima arise from the FES: one around a Zn2-N2 distance of 2.5 Å, corresponding to state **C3**, and the second around 5.4 Å, corresponding to **C4** (represented in Figure 4.23).

In the formation process of **C3**, the Zn1-O32 bond is confirmed, and one acetate group is now bridging both Zn (II) atoms. This situation allows the Zn2-N2 cleavage that brings to **C4** through a second transition state **TS2** (not marked in Figure S6). According to Figure S6 (Supporting information), the free-energy difference between **C3** and **C4** is of around 0.7 kcal/mol, and the small barrier between them (*ca.* 5.4 kcal/mol) demonstrates the Zn2-N2 tendency to cleave. In this process, the Zn1···Zn2 distance fluctuates between 2.8 and 3.6 Å.

Finally, stabilization of **C4** brings the structure to state **P** (shown as the final step in Figure 4.23), which increases symmetry by cleaving the Zn2-N2 bond (reaching *ca.* 5.5 Å, as shown in Figure S6). Although theoretical description of the path bringing from **C4** to **P** at processing temperature involves many changes in bonds that one cannot activate using simple metadynamics, and thus one cannot calculate **P**'s contribution to the FES, its PES suggests that this final state is possible, although not probable at 0K because of the high-energy barriers imposed by **C4** (more than 15 kcal/mol). Consequently, the most important observation is that this final **P** state is possible at higher temperatures, and it can suffer cleavage of deprotonated-EA arms to give the cyclic species measured by EGA, as well as of acetate bridges to produce pure ZnO.

More detailed information is given in Tables S3 to S6, which show the optimized atomic coordinates and the ESP charges of the **C2**, **C3**, **C4** and **P** structures, to allow corroborating the chemical evolution for each step. Additionally, Table S7 summarizes the charge increments in every step from the initial dimer to the final state. As the main conclusion of this analysis, a decomposition path is proposed in Figure 4.24. It is coherent with all the descriptions made until here about the evolution of the ZAD plus EA precursor during decomposition. Moreover, the Zn1-Zn2 bond lengths for all the optimized geometries (marked in Figure 4.24), agree with those found in the literature. In particular, many crystal structures[268] having dimeric Zn(II) complexes with one or more acetates or with bridging acetate ligands have been reported to be closely related to **C1**[269], **C2**[270, 271], **C3**[272], **C4**[273] and **P**[274, 275]. Consequently, the previous literature supports the optimized geometries for all the structures in the proposed decomposition mechanism.

4.3. MOLECULAR-DYNAMICS STUDY OF ZNO FORMATION FROM A SOL-GEL INK CONTAINING ETHANOLAMINE

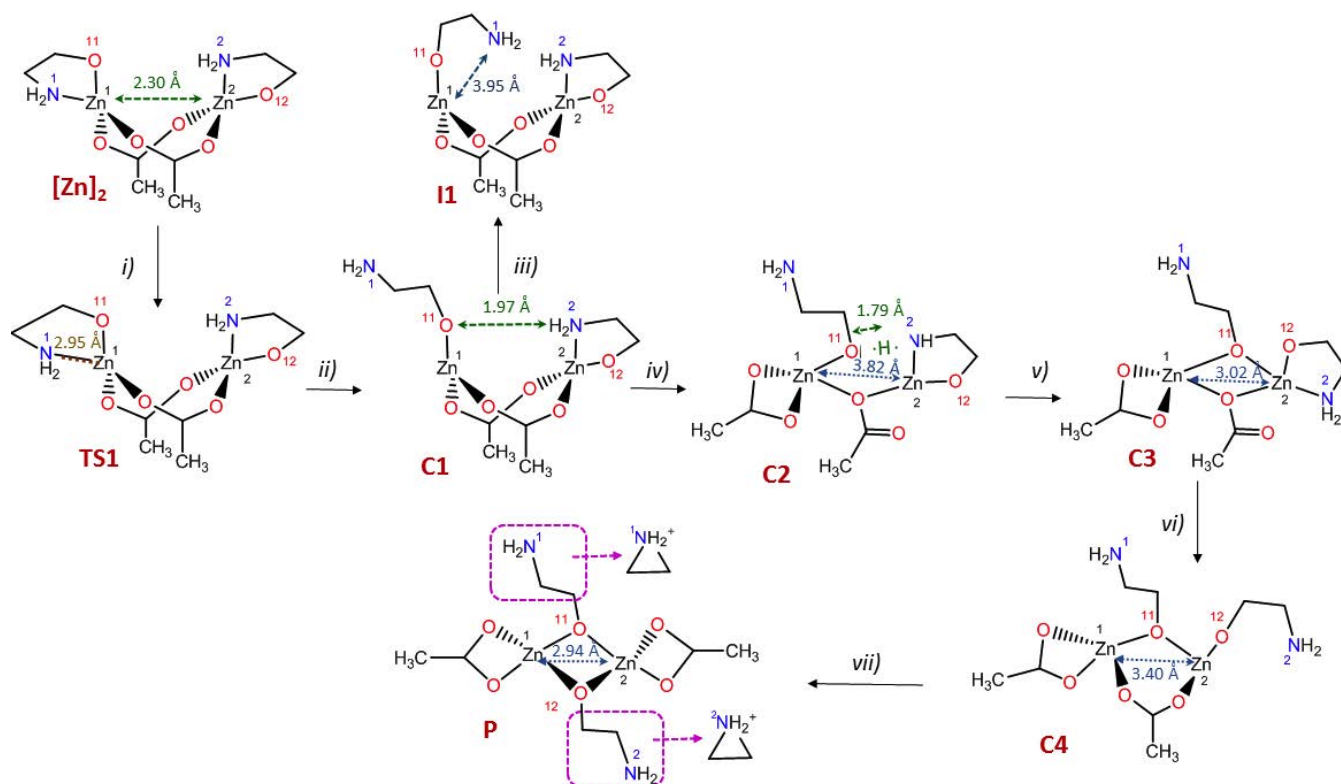


FIGURE 4.24. Scheme of the dimer modification to generate a triangular molecule, according to metadynamics.

The charge evolution (see Table S7) demonstrates important features that suggest which will be the first bond to cleave during the thermal decomposition. Keeping in mind that both Zn atoms show positive formal charge, they both will be attracted by O12 -whose formal charge is negative- while C22 is repelled because of its negative charge. Moreover, the charge variation of the pairs O11 / O12 and C21 / C22 (-0.197 / -0.380 and 0.208 / 0.506 e , respectively), as well as the elongation of these C-O bonds, suggest that they tend to cleave giving a cation $[C_2H_6N]^+$ in its triangular (most stable) form. The decomposition mechanism proposed in this paper allows the molecule to readjust itself to weaken one among the C-O bonds and form the triangular species, in good agreement with the experimental results presented previously to the calculations.

4.3.4 Conclusions

The studies summarized in this section provide conclusive evidences of the relevance of the ethanolamine used as stabilizer in the sol-gel formation of ZnO. Experimental studies point out that in the first steps of the thermal conversion of the precursor formed in the reaction of ZAD with EA in ME into the ZnO, cleavage of the Zn-N bond produces the opening of the five-membered chelate ring. This ring-opening process, causing the "-CH₂CH₂NH₂" unit as a pendant arm, may give rise to the cation " $C_2H_6N^+$ ". Its triangular form is proposed as origin of a

family of cyclic nitrogenated structures detected in EGA experiments. These results agree with those obtained from the CPMD simulation, that confirms that the Zn-N bond of the chelating ethanolamine is more prone to cleave than the Zn-O of the same ligand.

Moreover, the variations detected in the Zn-O(acetate) bond lengths in the dimer, as well as the distances between the two metal ions, suggest that during decomposition the "[Zn(-AcO)₂Zn]" central core undergoes significant structural changes. These include the change of the binding mode and hapticity of one of the AcO⁻ ligands to fulfil the coordination sphere of one of the Zn(II) centres after the opening of the five-membered chelate "Zn(O-CH₂CH₂NH₂)". Additional metadynamics simulations provide an overview of the dimer evolution by the cleavage of the Zn-N bond, the structural changes produced and their effects on the Zn(II)-centers environment. The obtained structures suggest that i) the hydrogen atoms attached to the amino group, and ii) the intermolecular N···H···O interactions in intermediate species, play a key role in the evolution of the initial dimer and the release of the "C₂H₆N⁺" cations (linear or triangular).

"So much the better, but study hard what interests you the most in the most undisciplined, irreverent and original manner possible"

- Richard P. Feynman in a letter to J.M.Szabados (1965)

SUBSTITUENT EFFECTS IN NITROGEN-BASED ZNO PRECURSORS

The previous chapter identified the molecular nature of the ZAD+EA precursor complex that constitutes the worldwide long-term used sol-gel ZnO precursor and also demonstrated the non-innocent role of ethanolamine in its decomposition process to the desired ZnO material. Since some particular volatiles were detected by EGA experiments on this precursor at various decomposition stages, in this context thermally induced-reaction mechanisms and their correct interpretation are strongly dependent on the characterization of the evolved species. When the nature of volatile products released by a substance under heating is online determined, *e.g.* by evolved gas analysis (EGA), the results allow describing the reactions taking place.

In the first section of this chapter, the processes involved in the stability at room conditions as well as the thermal decomposition of some precursors have been analysed by thermo-analytical and structural techniques, as well as with EGA. It has been argued that the molecule flexibility must have strong influence on bond torsion and breaking, and then onto the thermal decomposition process of the precursor film[154]. With this in mind, and with the aim of studying the role of the molecular architecture of the stabilizer in the final ZnO material, several aminoalcohols with different molecular rigidity have been analysed as stabilizer (Figure 5.1 where, in this section, only the five stabilizers formed by the aromatic amino-alcohols and the aliphatic ones with R'=H were chosen). The obtained results indicate that keeping tabs on the use of ethanolamine as stabilizer is worthwhile. The second section uses Gaussian and CPMD software to computationally elucidate the effects of using these EA-equivalent aminoalcohols as stabilizers in ZnO sol-gel precursors. Here also three additional aliphatic amino-alcohols were chosen (Figure 5.1, with R'=Me). These changes may affect the donor ability of the heteroatoms (N and O), the chelate size, its flexibility and, therefore, their stability. To compare and understand the experimental results, TD-DFT and MD tools were used. This information is crucial to enhance the design of

the ink, its thermal decomposition conditions and, ultimately, the ZnO properties. Finally, as some *posteriori* but non-published results reinforce even more the conclusions regarding these two sections, the reader will find these new results in the last two sections of this chapter.

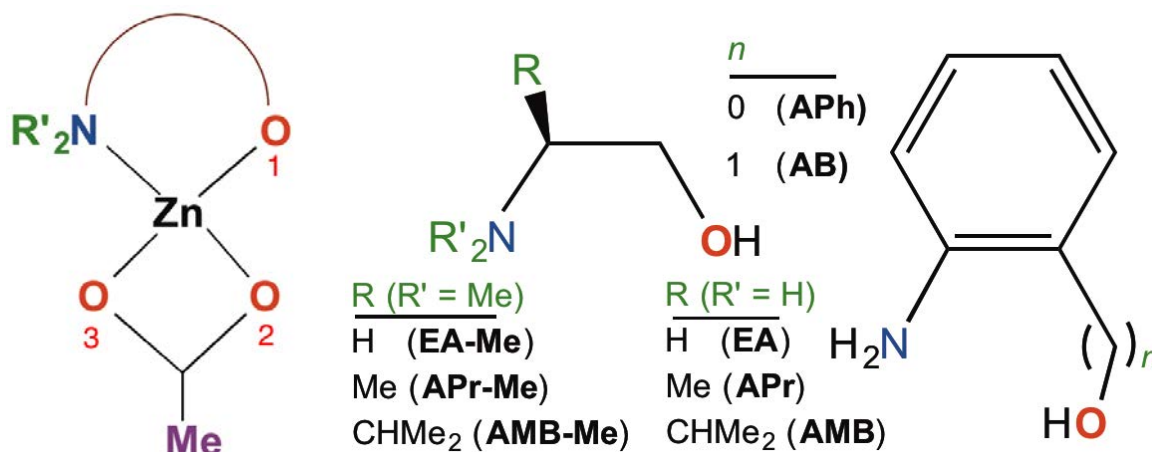


FIGURE 5.1. Chemical formula of the precursor (left) where the eight amino-alcohols used in this study form an aliphatic (center) or an aromatic (right) center. For the first section only five of those were used (the aromatics and the aliphatics with R'=H).

5.1 Comparison of the thermal decomposition processes

5.1.1 Experimental procedure

5.1.1.1 Samples preparation

Zinc acetate dihydrate (**ZAD**) was purchased from Panreac, 2-methoxyethanol (**2-ME**) from Aldrich, ethanolamine (**EA**) from Acrös Organics and the other amino-alcohols [(S)-(+)-2-amino-1-propanol (**APr**), (S)-(+)-2-amino-3-methyl-1-butanol (**AMB**), 2-amino-phenol (**APh**) and 2-amino-benzyl alcohol (**AB**)] from Aldrich. All the reagents were used as received. Figure 5.1 shows the molecular structure of **EA** and the other closely related amino-alcohols used in this study. The inks were prepared as follows: 0.5 g of **ZAD** (2.3 mmol) were treated with an equimolar amount of the corresponding stabilizer (**EA**, **APr**, **AMB**, **APh** or **AB**) and mixed in 5 mL of solvent (**2-ME**). All mixtures were kept at 60 °C under continuous stirring for 30 min. Except for the inks containing aromatic stabilizers (**APh** and **AB**), that became dark due to their strong photo-reactivity, the other ones remained transparent clear solutions for weeks. Thin films were deposited by drop coating on glass substrates.

5.1.1.2 Thermal analysis

To study the thermal evolution of the inks, thermogravimetric (TGA), and differential scanning calorimetry (DSC) analyses were done in dry air and pure oxygen atmospheres (flow

rate of 50 mL/min) at a heating rate of 10 °C/min up to 600 °C in uncovered alumina and aluminium pans, respectively. A drop of ink corresponding to a ZnO mass around 200 µg was poured inside the pans. The ink wetted the inner walls of the pan leaving behind a film of "nominal thickness" (*i.e.* the thickness of ZnO, if it were a dense homogeneous film) around 0.5 µm. We used the TGA-851e and DSC-822e apparatus of Mettler-Toledo. Complementary Evolved Gas Analysis (EGA) of the evolved species during ink decomposition was done in vacuum at 20 °C/min up to 600 °C, using a MKS quadrupole mass spectrometer (Microvision Plus).

5.1.1.3 Structural analyses

The films structure was analysed after heating them at 10 °C/min in air up to 300 and 600 °C. The first samples were kept for 5 min at 300 °C, whereas the second ones were cooled down without any delay after reaching 600 °C. X-ray diffraction (XRD) measurements were carried out with a PANalytical X'Pert PRO MPD Alpha1 powder diffractometer in Bragg-Brentano $\theta/2\theta$ geometry with Cu K $_{\alpha 1}$ radiation ($\lambda = 1.5406 \text{ \AA}$). Films were scratched from the substrate and the resulting powder was put inside KBr pellets for infrared (IR) spectroscopy with a Nicolet 400FTIR instrument. Carbon and nitrogen content was quantified by elemental organic analyses (EOA) with the Thermo EA Flash 2000 (Thermo Scientific, Milan, Italy) equipment working in standard conditions (helium flow: 140 mL/min; combustion furnace at 950 °C; chromatographic column oven at 65 °C). Finally, film morphology was observed by scanning electron microscopy (SEM) with a JEOL JSM-7100F and a JEOL J-6510 in planar and cross-section views.

5.1.2 Results and discussion

5.1.2.1 TGA/DSC experiments

After solvent evaporation, that finishes below 150 °C (**2-ME** boiling point, 124 °C), thermal decomposition of the inks is revealed by two mass-loss steps (Figure 5.2). According to previous observations on the EA ink (see section 4.1 or [246]), ZnO appears after the first decomposition step with maximum decomposition rate in the 230-270 °C range depending on the particular stabilizer. DSC experiments indicate that the first decomposition step is endothermic (in the case of **EA** and **APr**) or isenthalpic (for **APh** and **AB**) and, when exothermic in air (as in the case of **AMB**-Figure 5.2a), the decomposition temperature remains the same as in pure oxygen. This observation shows that a higher oxygen concentration does not advance the decomposition reaction; *i.e.* this step is not triggered by reaction with the oxygen molecules of the furnace atmosphere.

The second mass-loss step that corresponds to elimination of the organic residue is much more dependent on the particular stabilizer. It is centred on around 270 °C for the aliphatic stabilizers (**Fig. 2a**) whereas it appears at higher temperature for the **APh** (440 °C) and **AB** (480 °C) inks (Figure 5.2b). Furthermore, the inks with aromatic stabilizers lose much more mass during the second step (Figure 5.2b), as expected because of the large mass and high thermal stability of the

aromatic ring. Elimination of the organic residue proceeds through reaction with oxygen leading to prominent exothermic DSC peaks (Figure 5.2), the decomposition heat being higher for the aromatic stabilizers. It must be pointed out that the second mass-loss step is not related with evaporation of the stabilizer. Firstly, because its temperature is not correlated with the stabilizer boiling point (300 °C for **APh** and 160 °C for **AB**). Secondly, because during ink formation the stabilizer probably reacts with **ZAD** to form a complex precursor molecule, as shown for **EA**[246].

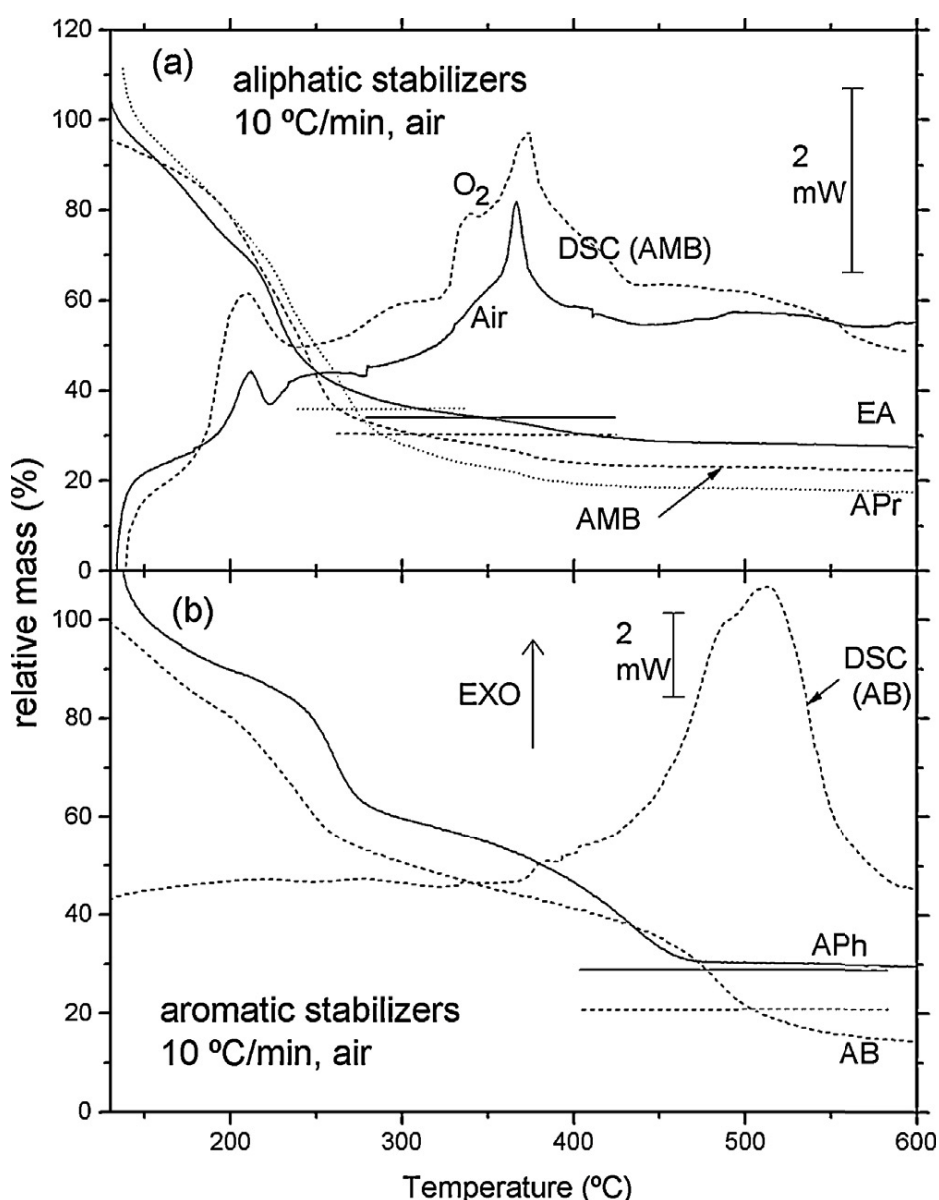


FIGURE 5.2. TG and DSC curves of ink decomposition for: a) aliphatic and b) aromatic stabilizers. TG curves are normalized to the mass after solvent evaporation. Horizontal lines are the expected final masses if the residue is 100 % ZnO.

Finally, it is worth noting that, except for the **APh** TG curve, the recorded mass at 600 °C is smaller than the expected mass for pure ZnO (horizontal lines in Figure 5.2). In other words, Zn atoms have been lost during the decomposition process (presumably during the first step). This phenomenon has already been reported for **ZAD**[132] and for CuO metal organic precursors[244]. The Zn loss has been accurately quantified for the **EA** ink by measuring the mass of the residue outside the TG furnace with an independent more stable microbalance, and comparing this mass with the one obtained after repeating the experiment with the ink spread on a glass substrate.

The TG curves normalized to the final mass are shown in Figure 5.3. The horizontal line marks the mass of **ZAD + EA** precursor if Zn were not lost. Although we cannot discard that some **2-ME** evaporation still occurs up to 150 °C, comparison of this level with the experimental TG curves suggests that more than 25 % of Zn is lost during decomposition. This experiment is also useful to assess that the TG experiments done with alumina pans (those of Figure 5.2) reproduce reasonably well what occurs in films. Anyway, since, as said above, oxygen does not trigger decomposition, the observed shift by 20 °C in the first decomposition step can be attributed to a surface effect, *i.e.* an easier transport of volatiles out of films than out of bulk material[244].

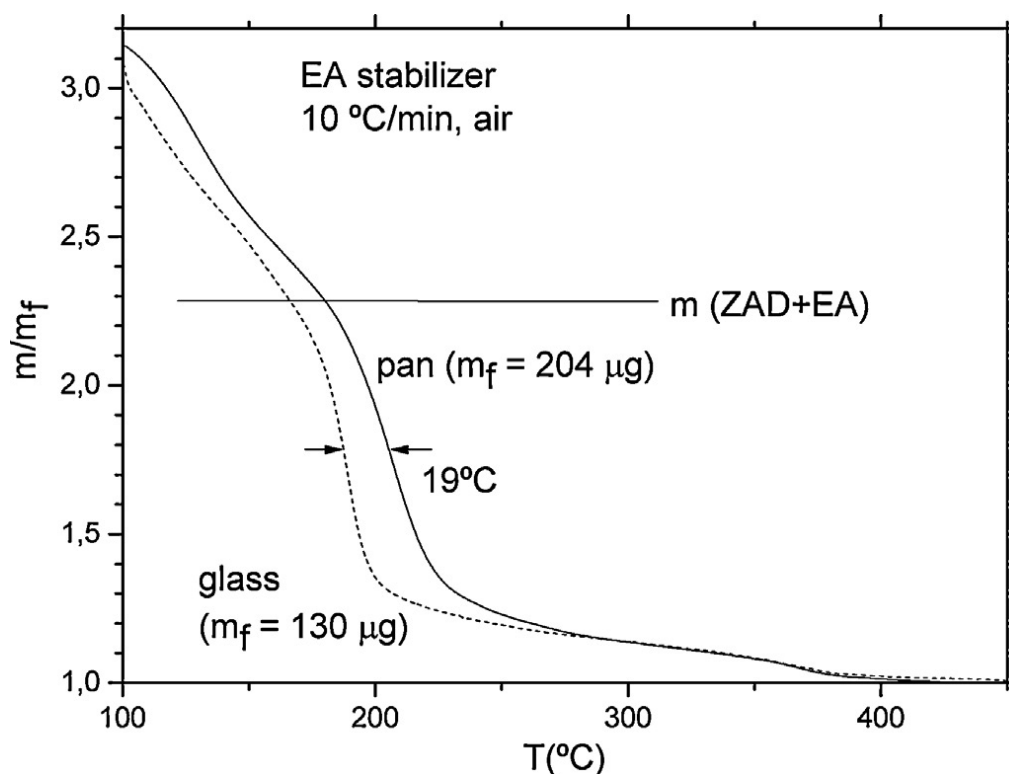


FIGURE 5.3. TG curves of the **EA** ink decomposed inside an alumina pan and on a glass substrate. Mass is normalized to the final mass measured externally to the TG apparatus. Horizontal line: mass of the **ZAD + EA** precursor if no Zn atoms were lost.

5.1.2.2 XRD, IR and EOA results

ZnO formation after the first mass-loss step has been assessed by XRD (Figure 5.4). Except for **A_{Ph}** that, after the second step, degraded becoming a powder and consequently will not be included in the studies for 600 °C presented in the following sections, after heating up to 300 °C all the inks exhibit the characteristic peaks of hexagonal ZnO sometimes with (002) preferential orientation (Figure 5.4a). In the **AB** curve, one additional peak of unknown origin (nor does it correspond to the ZnO cubic phase) is observed. All peaks are very broad. Application of Scherrer's formula delivers crystal size values ranging between 7 and 13 nm; these extreme values are for **EA** and for **AB** films, respectively. This poor crystalline quality is partially due to the large content of organic residue revealed by IR spectroscopy.

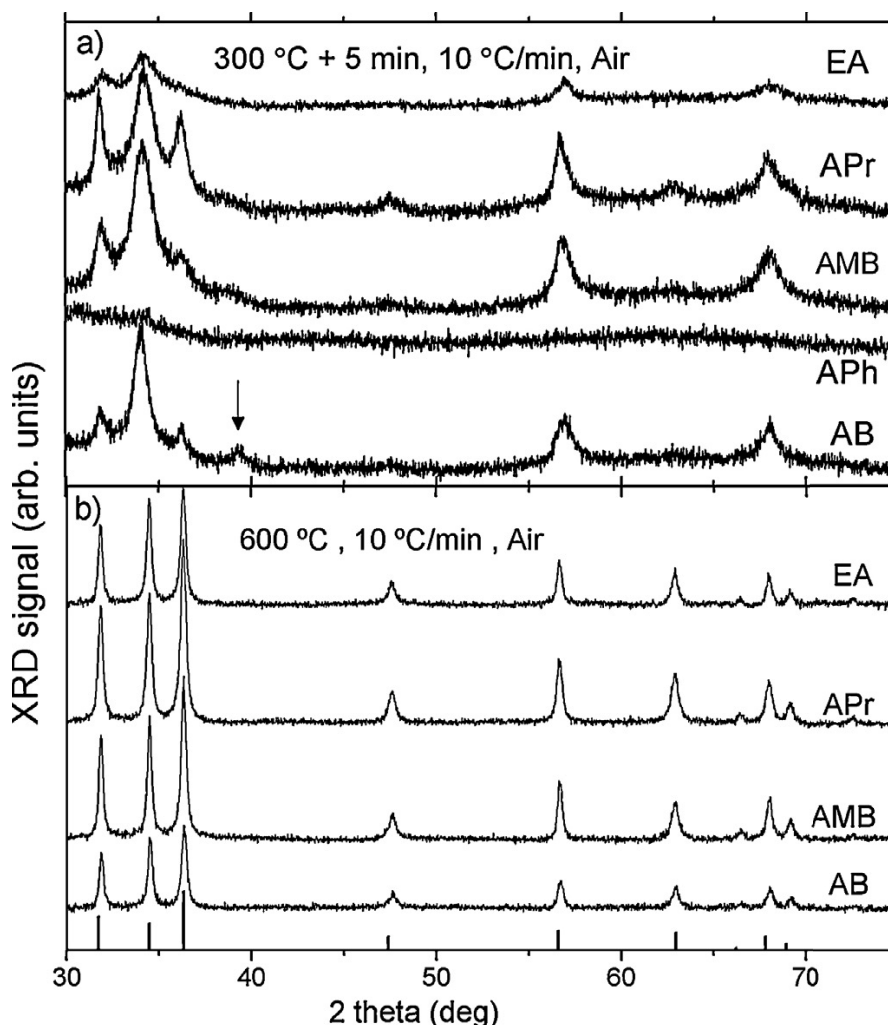


FIGURE 5.4. XRD spectra measured after heating the films up to 300 °C (a) and 600 °C (b) (the A_{Ph} film did not survive at this temperature). At the bottom of figure b, the bars are the pattern of pure ZnO (JCPDS 36-1451). The arrow in a) indicates the peak of an unknown phase.

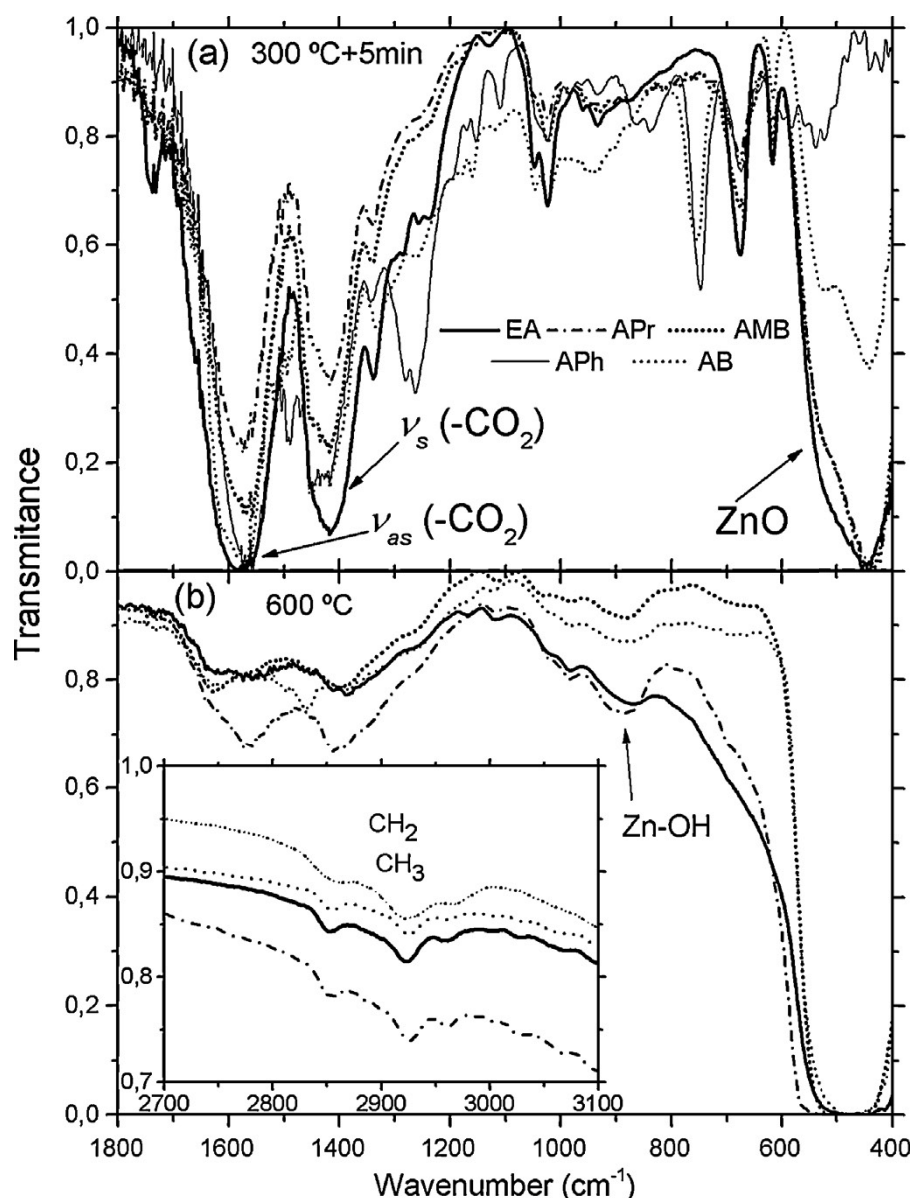


FIGURE 5.5. IR spectra measured after a heat treating of 300 °C (a) and 600 °C (b).
Inset: detail of the bands related to CH₃ and CH₂ groups.

IR spectra are consistent with XRD results in the sense that all films, except the **APh** film, have the characteristic vibrational band of ZnO at 400-600 cm⁻¹[276] already at 300 °C (Figure 5.5a). The absence of this band for the **APh** film means that ZnO has not been produced after the first decomposition step. In addition, all IR spectra contain very intense carboxylate bands centred at 1580 and 1410 cm⁻¹. Again, retardation of **APh** film decomposition is confirmed by the bands at 1500 (weak) and 1280 (intense) cm⁻¹ related to the precursor[277]. The organic residue contribution to the IR spectra is substantially reduced after the heat treatment at 600

¹K. Nakamoto, *Infrared and Raman Spectra of Inorganic and Coordination Compounds*, 5th ed., Wiley, New York, USA, 1997.

°C (Figure 5.5b). Now, the absorbance due to ZnO reaches saturation (zero transmittance) for all films. Unfortunately, the method used to make these measurements (film flakes inside KBr pellets) precludes any attempt of quantification. Consequently, although one can see varying intensities of the carboxylate and (aliphatic) C-H-stretching bonds (inset of Figure 5.5b) from film to film, from these slight differences one cannot infer higher or lower organic content. Instead, the elemental C and N contents have been quantified by EOA.

The determined percentage of N is below the technique sensitivity (0.2 %), but quantification of C has been possible (see Table 5.1). **EA** and **APr** films have the lowest carbon content (0.2-0.3 %) and the **AB** film, the highest (3.5 %). Removal of the organic residue as well as thermal activation of grain growth improves considerably the film crystalline quality at 600 °C. XRD peaks are much narrower and attributable to wurtzite ZnO (Figure 5.4b). The **AB** and **APr** films have the largest crystal sizes (27-28 nm) whereas the smallest ones are found in the **AMB** and **EA** films (21 nm) (Table 5.1). The lack of any significant preferential crystalline orientation can be due to the use of low-boiling temperature solvent[48]. However, use of adequate substrates (Pt(111) and amorphous SiN_x on c-Si) can promote preferential orientation along the c-axis even for **ZAD + EA** inks dissolved in **2-ME**[278].

Table 5.1: Average ZnO crystal size at 600 °C obtained from the XRD curves by applying Scherrer's formula to the (100), (002) and (101) diffraction peaks and carbon content measured by elemental analysis at the same temperature.

	EA	APr	AMB	AB
Crystal size (nm)	21.1	26.8	21.2	28.0
C content (%)	0.2-0.3		0.4	3.5

5.1.2.3 Analysis of the evolved gases

EGA experiments in vacuum have allowed detecting the volatile products of the inks decomposition. Many fragments have been detected up to $m/z = 150$ whose identification has been based on the computational and experimental work of Bouchoux's group on the reactivity of aliphatic amino-alcohols[243] (see also the previous chapter of this work). These authors found that their dissociation produces a number of nitrogenated cyclic fragments, the simplest ones being azidine ($m/z = 44$), azetidine(58), pyrrolidine (68) and piperidine (85). In Figure 5.6a is plotted the EGA curves of several intense signals that can be assigned to these cyclic fragments during decomposition of the **AMB** ink.

These curves can be compared with the mass-loss curve (dTGA curve) of 5.6b. Notice that, whereas some cycles ($m/z = 127$ and 85) evolve during the first decomposition step (the first dTGA intense peak) or up to the second decomposition step (the smallest peak at 380 °C), two cycles ($m/z = 44$ and 68) still evolve at the highest temperature of the experiment. Consequently, the EGA results constitute a proof that nitrogen still remains as an impurity after the usual maximum temperature (600 °C) of ZnO film synthesis from **ZAD** inks.

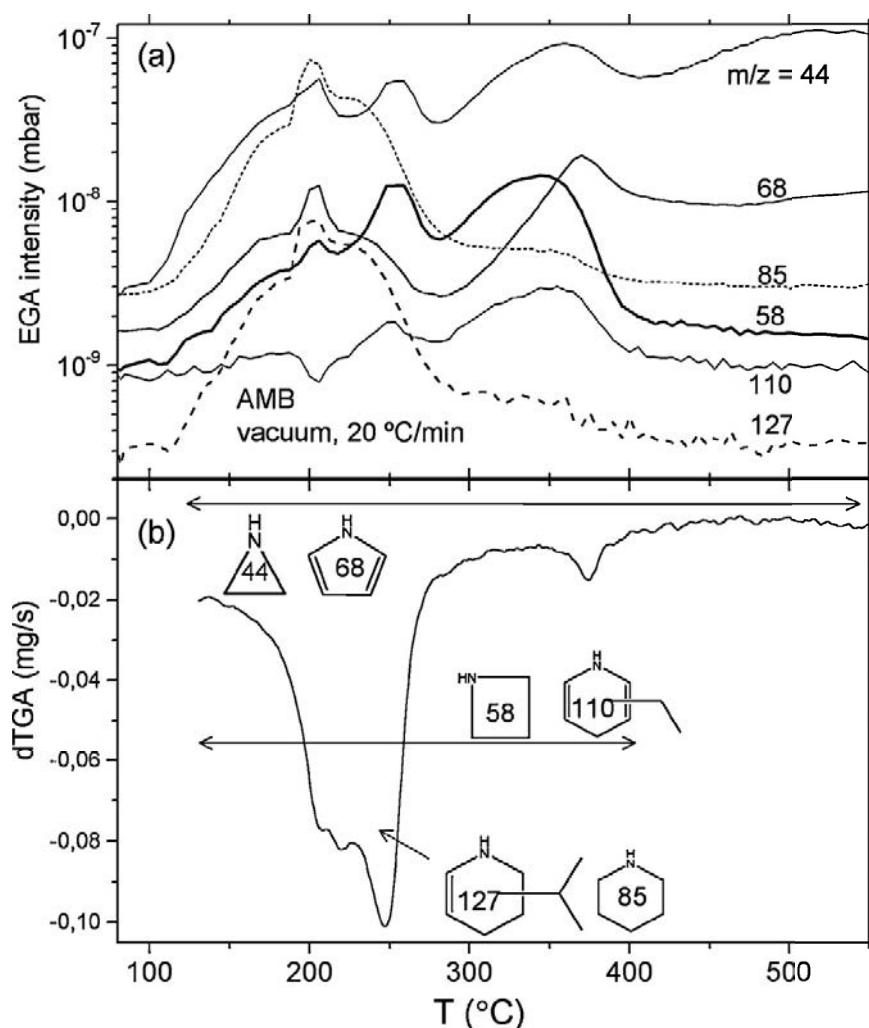


FIGURE 5.6. (a) EGA curves of intense volatile fragments detected during decomposition of the **AMB** ink in vacuum. (b) Mass-loss rate curve during decomposition of **AMB**, drawn to indicate the temperature range in which main volatiles are detected.

This conclusion can be extended to all the inks studied here. In 5.7 are summarized the nitrogenated cyclic fragments detected for the other inks and their evolution.

5.1.2.4 Film morphology

Finally, the films surface morphology has been observed in plane-view by SEM (Figure 5.8). With the exception of the **APh** one, all inks have led to continuous ZnO films without cracks. However, films are far from flat and exhibit pronounced ripples giving rise to characteristic patterns similar to those already reported for ZnO[279] and for other oxide films[280]. They probably arise during the first decomposition step. Since precursor decomposition results in a drastic reduction of its volume whereas the substrate hinders any in-plane contraction, stress arises in the film. Ripples are a mean to relieve this stress[280] but, with the typical cracks, are defects that make difficult to obtain high-quality thick films by chemical-solution routes. Among

our films, **AMB** leads to the flattest surface whereas, with **EA**, ripples are the most pronounced.

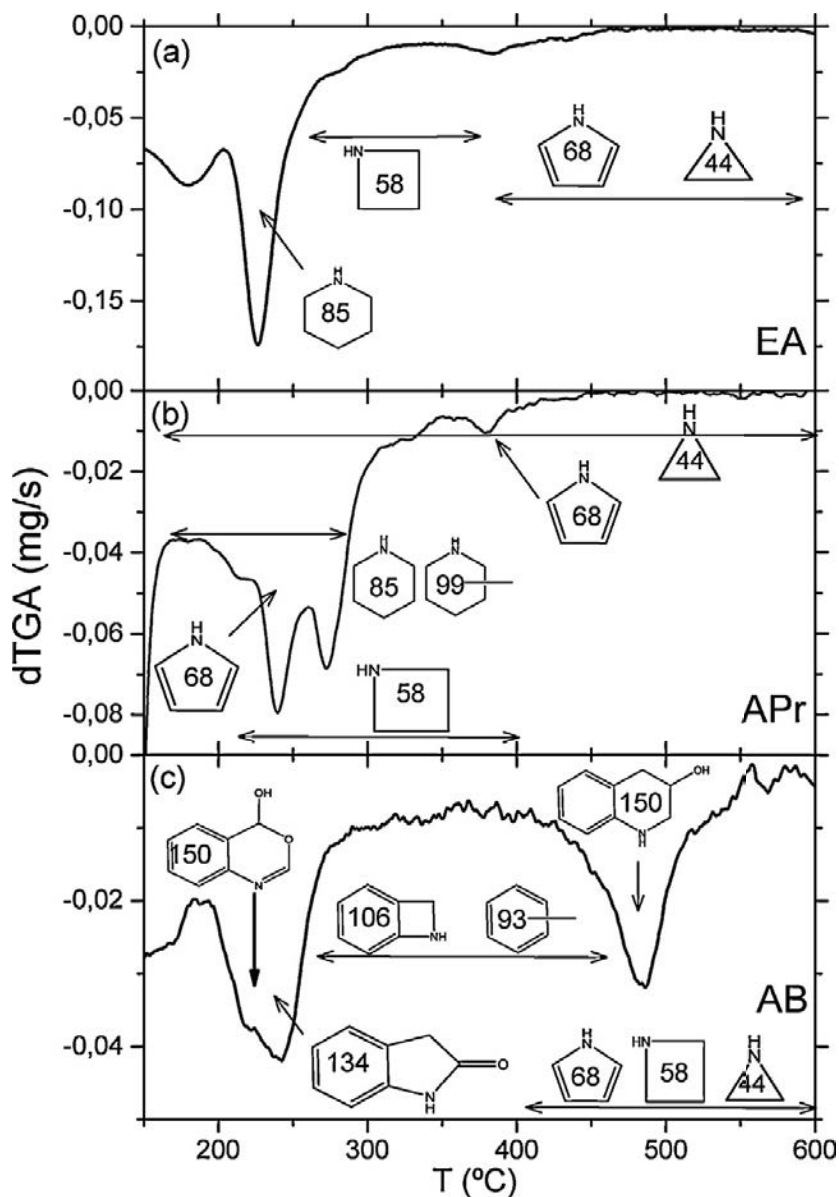


FIGURE 5.7. Approximated temperature range in which nitrogenated cyclic fragments are detected by EGA during decomposition of the **EA** (a), **APr** (b) and **AB** (c) inks.

5.1.3 Conclusions

ZnO films have been prepared from inks containing Zn acetate dihydrate and several amino-alcohols. Concerning thermal decomposition, the aliphatic stabilizers (**EA**, **APr** and **AMB**) behave similarly with a main decomposition step around 250 °C followed by a minor mass-loss step at 370 °C. This is in contrast with the aromatic stabilizers (**APh** and **AB**), that experience an important mass-loss step above 400 °C. Although crystalline ZnO can be found already at 300

°C, crystal quality is poor unless films are heated upto 600 °C to reduce the organic residue and promote crystal growth.

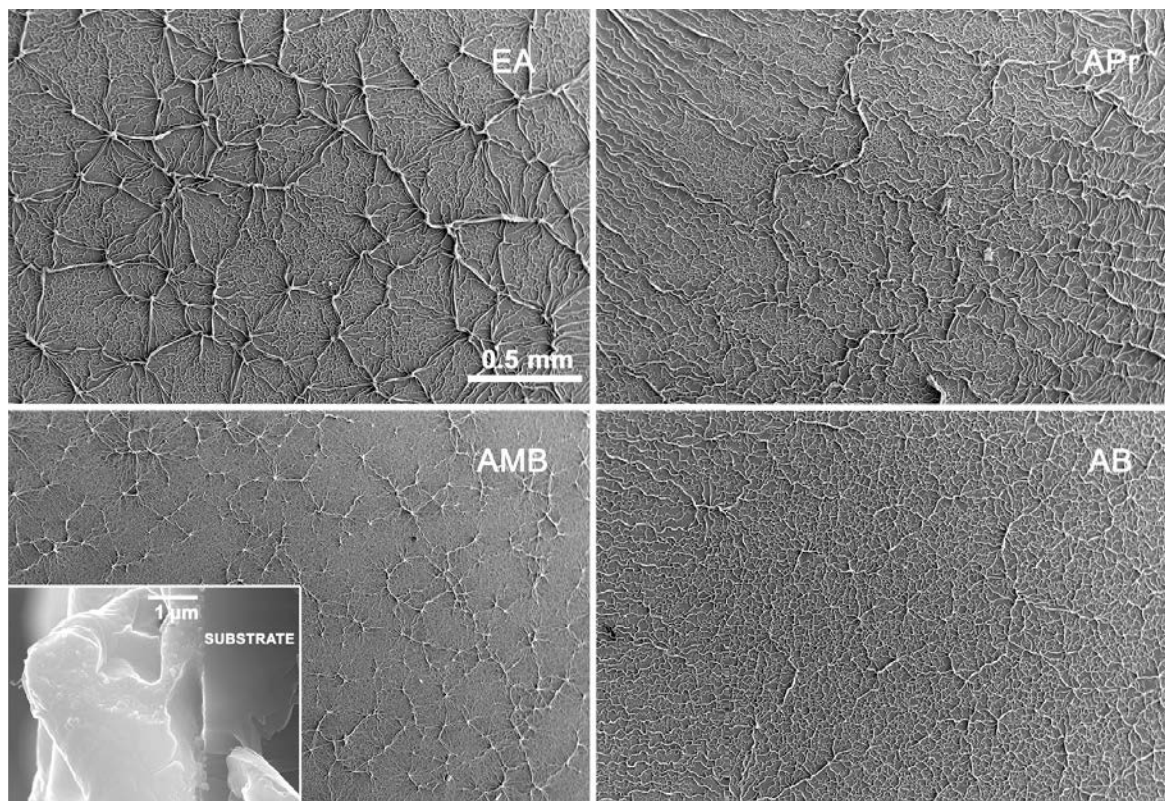


FIGURE 5.8. SEM micrographs of the films treated at 600 °C. Inset: cross section of the **AMB** film.

Compared with **EA**, ZnO crystallites are larger for the **AB** and **APr** inks and of similar size with **AMB**. In contrast, **APh** degrades to powder. Carbon contamination quantified by EOA reaches a minimum concentration with **EA** and **APr**, while for **AB** it is 10 times higher. Contamination by nitrogen could not be quantified. However, analysis of the evolved gases indicates that nitrogen atoms have not been completely removed at 600 °C. Films are not homogeneous; all of them have ripples that arise from internal stresses during decomposition. To sum up, the comparative studies undertaken for the 5 amino-alcohols proposed as stabilizers in ink manufacture and their evolution to ZnO films demonstrate the influence and effect of the linkers (spacers of the amino-alcohol on the global process). We have proved that: a) aromatic amino-alcohols behave worse than **EA** due to either their degradation and transformation to powdered material (**APh**) or the retention of higher contents of carbon after the thermal treatment; b) aliphatic amino-alcohols are clearly a better choice, giving ZnO films with less doping carbon but showing ripples whose height decreases as the substituent R (Figure 5.1) increases in size as follows **EA** > **APr** > **AMB**. These amino-alcohols $\text{H}_2\text{N-CH(R)CH}_2\text{OH}$ only

differ in the nature and bulk of the substituent R that could play a key role in determining the morphology and also the crystal sizes of the films.

5.2 Electronic and dynamic DFT studies

5.2.1 Methodology

Computational studies (optimization of the geometries, calculation of total energies and frequencies and molecular dynamics) of the eight precursors formed by treatment of ZAD and the amino-alcohols shown in Figure 5.1 were performed with the UB3LYP method implemented in the Gaussian 03[163] software, using the LANLD2Z basis set, whose good behavior with Zn compounds was demonstrated in previous works[246] (see previous chapter). In order to determine the temperature effect over our systems, full-QM molecular dynamics simulations (CPMD)[162] based on density functional theory (DFT)[225] were performed. For each molecule, the electronic density was calculated using a plane waves package of 70 Ry (maximum value of the electronic degrees of freedom of 10^{-7} a.u.) and Stumpf, Gonze, and Scheffler pseudopotential[158] adapted for the LDA functional theory ([281, 282]).

For a molecular dynamics (MD) where reactivity is not involved, the LDA functional gives quite acceptable results for organometallic systems[179]. For the Lagrangian electronic mass and the simulation time step 850 a.m.u. and 5.0 a.u. values were selected, respectively. Once selected, the parameters for the systems, their geometries were optimized using a threshold of 5×10^{-4} a.u. for the maximum component of the nuclear forces. Starting from the optimized structure, the adiabaticity of each system was tested in a 2500-step molecular dynamics. These simulations give an approach of the expected value of the electronic kinetic energy. To carry the productive molecular dynamics, the use of two Nosé-Hoover thermostats[283, 264] is very important, in order to control the electronic kinetic energy and the temperature of the systems, whose frequencies at 10000 and 3500 cm^{-1} , respectively, improve the independent movement of the nuclei and the electrons. Four molecular dynamics at different temperatures (300, 500, 600, and 700 K) were run during 20000 MD steps, 5000 steps per temperature.

5.2.2 Results and discussion

5.2.2.1 Electronic behaviour at 0 K

As a first step, computational studies based on DFT by means of the Gaussian software were used to optimize the geometries of the eight precursors without imposing any restrictions². The bond lengths and angles of the final geometries were consistent with those reported for the related Zn(II) complexes with "Zn(O,O')(N,O)" cores[240]. The calculated energies (E_T) and free energies (ΔG) for all the precursors are presented in Table 5.2.

²The final atomic coordinates for the obtained geometries are presented in Figure S1-S8 of the Supporting Information *Electronic and dynamic DFT studies on the substituent effects of amino-alcohol stabilizers in sol-gel ZnO precursor* in Appendix A

After this geometry optimization, molecular orbital calculations were carried out. Figure 5.9 shows the frontier orbitals for the eight systems under study. For the non-methylated derivatives, the HOMO is mainly centred on the de-protonated oxygen of the corresponding amino-alcohol. For the APh, which may be used as a redox agent[284], there is a tiny additional contribution of the π orbital of the phenyl ring. Similarly, the LUMO is mainly located on the acetate ligand in all cases except for the Zn-APh, for which there is also some participation of the π orbital of the phenyl ring. As shown in Figure 5.9, the frontier orbitals for precursors Zn-AE-Me, Zn-APr-Me, and Zn-AMB-Me are quite similar to those of their non-methylated analogs, except for subtle differences in (i) the contribution of the donor-atom orbitals and (ii) formal charges on the Zn(II), N, and O atoms.

The calculated values of the Mulliken charges of the Zn and N atoms (herein after are respectively) are: 0.968 and 0.728 (for Zn-EA); 0.941 and 0.310 (for Zn-EA-Me); 0.966 and 0.739 (for Zn-APr); 0.944 and 0.313 (for Zn-APr-Me); 0.961 and 0.761 (for Zn-AMB); 0.938 and 0.313 (for Zn-AMB-Me); 1.015 and 0.831 (for Zn-APh); 1.010 and 0.803 (for Zn-AB). Charges over Zn non-methylated: Ph > AB >> EA > APr > AMB. Charges over N non-methylated: Ph < AB < AMB < APr < EA. Charges over Zn methylated: APr > EA > AMB. Charges over N methylated: AMB < APr < EA. Thus, the net charge separation between Zn and N atoms varies depending on the amino-alcohol and, consequently, it causes significant variations in the N basicity and precursor reactivity (*i.e.*, with nucleophilic and/or electrophilic species).

Table 5.2: Fundamental energy (E_T) and free energy (ΔG) calculated from DFT-optimized structures for the eight studied precursors.

	non-N-methylated amino-alcohols				
	Zn-EA	Zn-APr	Zn-AMB	Zn-AB	Zn-APh
E_T (a.u.)	-503.9025	-543.2143	-621.8265	-695.6121	-656.3216
ΔG (a.u.)	0.1000	0.1264	0.1794	0.1483	0.1210
	N-methylated aminoalcohols				
	Zn-EA-Me	Zn-APr-Me	Zn-AMB-Me		
E_T (a.u.)	-582.5001	-621.8085	-700.4150		
ΔG (a.u.)	0.1533	0.1801	0.2338		

In a further step, and as a first approach to estimate the photo-behaviour of the precursors, the energy gap was also calculated after DFT. Data comparison reveals that, for compounds with R=H, the energy difference between HOMO and LUMO ($\Delta E = E_{LUMO} - E_{HOMO}$) - determined at 0K - increases as follows: Zn-APh << Zn-AB < Zn-EA < Zn-AMB < Zn-APr. This evolution shows that arrays containing aromatic rings produce a significant decrease of the ΔE . Moreover, among aliphatic precursors, those with methylated amino group have greater ΔE than their analogs with the NH₂ moiety. This can be attributed to the better donor ability of the NMe₂ unit in relation to that of the NH₂ one, which also affects the contribution of the Zn(II) atom in the frontier orbitals.

With the objective of elucidating the photo-behavior differences observed experimentally for

the precursors, a study based on the time-dependent (TD) DFT methodology was undertaken to describe the main electronic transitions and their associated energies. The excitation energies and the corresponding oscillator strengths were determined from the optimized geometries (Table 5.3). Although frontier orbitals were quite similar for the eight precursors, TD-DFT calculations indicate that the energy income required to promote the electronic transitions is strongly dependent on the amino-alcohol. In particular, for the non-methylated ones, the energy increment required for an identical electronic transition increases according to the sequence Zn-APh \ll Zn-AB \ll Zn-EA \approx Zn-AMB \approx Zn-APr. Indeed, some of the most probable transitions involve radiation very close to the visible range. Taking into account that ΔE decreases with increasing temperature, this effect may be potentiated at room conditions. This may explain the experimental results that demonstrated the different behaviours in terms of photo-reactivity for the NH₂-based ZnO precursors reported in previous experiments[254] (see previous section).

Table 5.3: Excitation wavelengths (λ), oscillation strengths, and percent probabilities for the most probable HOMO-LUMO transitions for the optimized geometries of the eight precursors, as calculated with TD-DFT.

	λ (nm)	assignment	oscill. strength	wt. (%)		λ (nm)	assignment	oscill. strength	wt. (%)		
Zn-EA	269.07	HOMO \rightarrow LUMO	-0.298	18	Zn-EA-Me	266.7	HOMO \rightarrow LUMO	-0.405	33		
		HOMO \rightarrow LUMO+1	0.617	76			HOMO \rightarrow LUMO+1	0.561	63		
		HOMO \rightarrow LUMO+2	0.106	2			HOMO \rightarrow LUMO+4	-0.112	3		
		HOMO \rightarrow LUMO+3	-0.116	3			249.6	HOMO \rightarrow LUMO	-0.466	44	
	252.63	HOMO \rightarrow LUMO	-0.380	29		HOMO \rightarrow LUMO+1	0.521	54			
		HOMO \rightarrow LUMO+1	0.587	69		244.7	HOMO-1 \rightarrow LUMO	-0.374	28		
	246.81	HOMO-1 \rightarrow LUMO	-0.326	21		HOMO-1 \rightarrow LUMO+1	0.581	68			
		HOMO-1 \rightarrow LUMO+1	0.602	73		HOMO-1 \rightarrow LUMO+4	-0.109	2			
		HOMO-1 \rightarrow LUMO+3	-0.107	2		Zn-APr-Me	267.5	HOMO \rightarrow LUMO	-0.433	38	
		Zn-APr	266.66	HOMO \rightarrow LUMO+1				-0.684	94	HOMO \rightarrow LUMO+1	0.541
	HOMO \rightarrow LUMO+2			-0.106				2	HOMO \rightarrow LUMO+4	-0.103	2
	HOMO \rightarrow LUMO+4			0.112				3	250.5	HOMO \rightarrow LUMO	0.511
249.87	HOMO \rightarrow LUMO+1		0.692	96	HOMO \rightarrow LUMO+1	-0.477	45				
244.97	HOMO-1 \rightarrow LUMO+1		-0.683	93	245.6	HOMO-1 \rightarrow LUMO	0.404	33			
Zn-AMB	266.82		HOMO \rightarrow LUMO	0.196	8	HOMO-1 \rightarrow LUMO+1	-0.562	63			
			HOMO \rightarrow LUMO+1	0.653	85	HOMO-1 \rightarrow LUMO+4	0.102	2			
			HOMO \rightarrow LUMO+2	0.112	3	Zn-AMB-Me	268.1	HOMO \rightarrow LUMO	-0.441	39	
			HOMO \rightarrow LUMO+4	-0.116	3			HOMO \rightarrow LUMO+1	0.534	57	
251.14	HOMO \rightarrow LUMO		0.292	17	251.4			HOMO \rightarrow LUMO	0.534	57	
	HOMO \rightarrow LUMO+1		0.633	80	HOMO \rightarrow LUMO+1			-0.449	40		
246.37	HOMO-1 \rightarrow LUMO		-0.228	10	246.7	HOMO-1 \rightarrow LUMO	0.415	34			
	HOMO-1 \rightarrow LUMO+1	-0.645	83	HOMO-1 \rightarrow LUMO+1	-0.554	61					
	HOMO-1 \rightarrow LUMO+2	-0.102	2	Zn-AB	336.3	HOMO-3 \rightarrow LUMO	0.243	12			
	HOMO-1 \rightarrow LUMO+4	0.107	2			HOMO-3 \rightarrow LUMO+1	-0.315	20			
Zn-APh	346.42	HOMO-1 \rightarrow LUMO+1	-0.269			14	HOMO-2 \rightarrow LUMO	0.392	31		
		HOMO \rightarrow LUMO+1	0.520			54	HOMO-2 \rightarrow LUMO+1	0.291	17		
		HOMO \rightarrow LUMO+3	-0.375	28	HOMO-2 \rightarrow LUMO+3	-0.115	3				
		330.37	HOMO-1 \rightarrow LUMO+1	0.253	13	HOMO-1 \rightarrow LUMO	0.244	12			
HOMO \rightarrow LUMO+1	0.471		44	HOMO \rightarrow LUMO	0.111	2					
292.53	HOMO \rightarrow LUMO+3	0.444	39	289.2	HOMO \rightarrow LUMO	0.655	86				
	HOMO \rightarrow LUMO	0.606	73	HOMO \rightarrow LUMO+3	0.175	6					
	HOMO \rightarrow LUMO+2	0.350	24	274.4	HOMO \rightarrow LUMO	0.695	97				

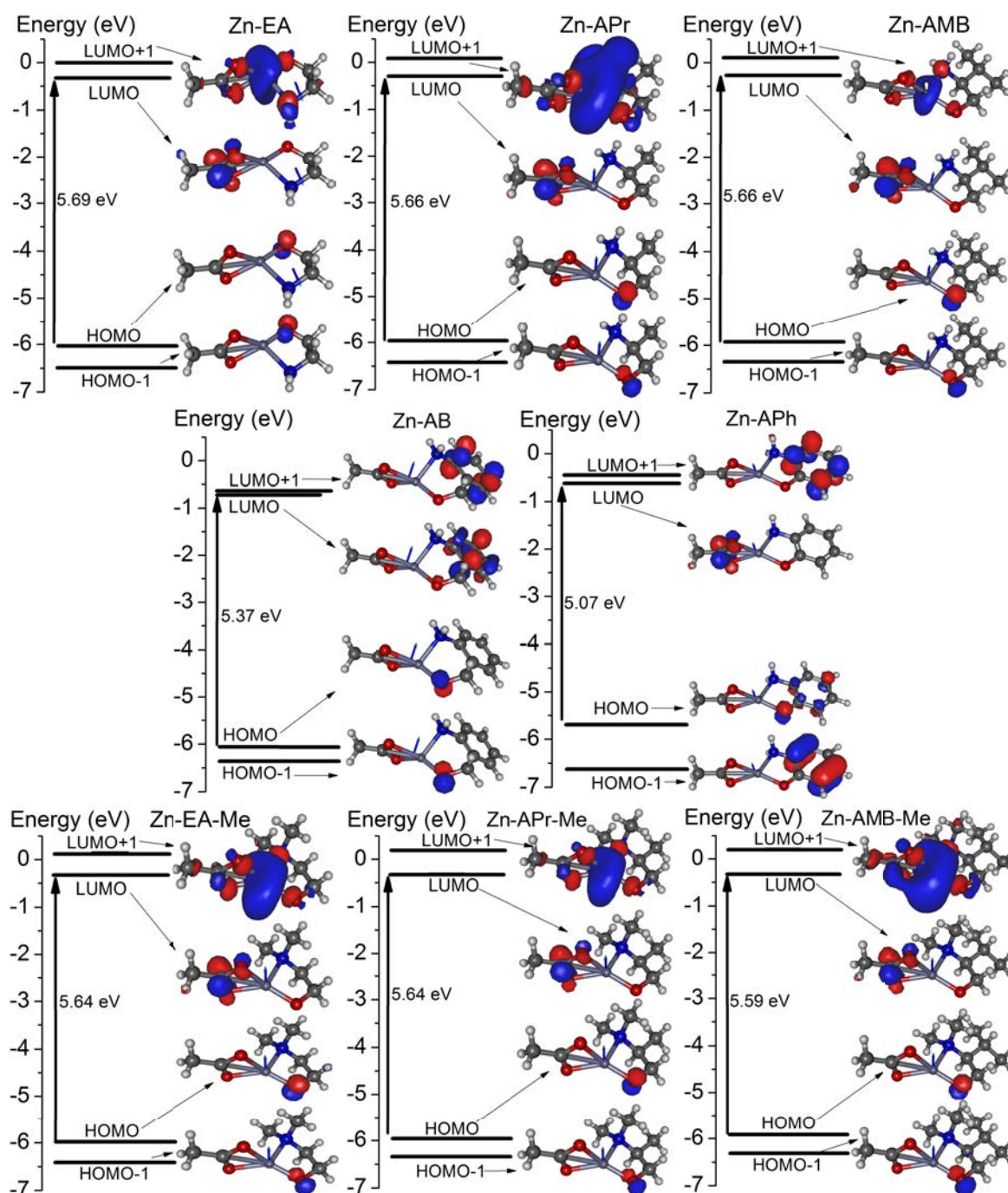


FIGURE 5.9. Frontier orbitals calculated with Gaussian03 for the eight precursors, with the excitation energies for the main transitions at 0K.

Moreover, it is well known that photoexcited states are more reactive, and consequently, upon the effect of light, the Zn-APh species are more prone to react with O_2 , CO_2 , or other air components giving dark brown products - as happens with the free amino-alcohol. It should be noted that methylation of the aliphatic amino-alcohols does not affect significantly the energy

required for a given electronic transition. The maximal difference between the calculated position of methylated precursor bands and their corresponding H₂N-derivative ones does not exceed 4 nm. Finally, Figure 5.9 shows that tertiary amines (R' = Me) present lower electron-excitation probability toward the LUMO concentrated in the Zn atom (and higher probability toward the acetate-based LUMO) than for the R' = H case. This effect, more evident in the case of Zn-APr and Zn-AMB may decrease the degradation effects, since the bond between the amine group and the Zn atom will not cleave so easily. Consequently, the purely aliphatic precursors are less prone to photodegradation than the aromatic ones. This is consistent with the experimental observations that showed that Zn-APh is more photosensible than Zn-AB and the later even more than the set Zn-EA, Zn-AMB and Zn-APr. All these results from TD-DFT calculations are consistent with those extracted after HOMO-LUMO difference comparison.

5.2.2.2 Molecular dynamics

As mentioned above, experimental studies of the thermal behaviour of the precursors Zn-EA, Zn-APr, Zn-AMB (that only differ in the substituent on the C atom attached to the amino group), and the pair Zn-AB and Zn-APh showed marked differences. In particular, conversion of the aromatic precursors into the final ZnO required higher temperatures than for the precursors built up with aliphatic amino-alcohols. On the other hand, in all cases the elemental analyses made by X-ray photoelectron spectroscopy revealed that the final ZnO isolated at high temperatures (600 K) contained small amounts of nitrogen. Since molecular dynamics (MD) has proved to be a powerful tool to understand the evolution of a variety of compounds during their thermal decomposition, the eight precursors were also studied via MD, in order to explain the presence of traces of N in the final ZnO material. First, and in order to test the stability and adiabaticity of the eight model precursors, the variations of their electronic kinetic energy $\langle \text{EKE} \rangle$ were analysed via a 2500-step MD test. The adiabaticity parameters obtained for these eight models are given in Table 5.4. They reach their maximum at 10^{-6} a.u./step assuming an increase of the electronic kinetic energy of 3 kcal/mol during a 5000-step MD, as a worst case scenario. This maximum suggests that the values for the Lagrangian electronic mass and the time step were correctly chosen.

Once the stability of our models was successfully tested and confirmed, the values of the electronic kinetic energy for the eight precursors were plotted versus temperature for comparison purposes (Figure 5.10). The calculated values for the total energy increase with temperature (Figure S2, Supporting information) as well as its fluctuation, so that the system is exploring a wider free energy surface region. Also, the $\langle \text{EKE} \rangle$ values predictably increase with temperature. The Nosé-Hoover thermostat has been modified to maintain the $\langle \text{EKE} \rangle$ around these expected values. As could be expected because of the increasing flexibility of the involved molecules, for a given T the $\langle \text{EKE} \rangle$ values of the precursors with aliphatic amino-alcohols increase according to the following trend: Zn-EA < Zn-APr < Zn-AMB, and in all cases these values are smaller than those of their N-methylated analogues. As to precursors with phenyl rings, the variation observed

in the $\langle \text{EKE} \rangle$ upon heating is larger for Zn-AB than for Zn-APh, which contains a more rigid five-membered chelate instead of the six-membered ring of Zn-AB.

As already mentioned, experimental results also showed that the final ZnO materials formed by thermal decomposition of these precursors retain small quantities of nitrogen. This is a problem, especially for the manufacture of high-purity ZnO. The knowledge of the origin of this issue may allow optimizing the sol-gel methods of ZnO formation by the proper design and selection of a stabilizer better than EA. Therefore, the expected values for the Zn-N bond length for the eight precursors at $T = 300, 500, 600,$ and 700 K were calculated (Table 5.5), as a first approach to the problem. The expected values for the Zn-N bond length ($\langle \text{Zn-N} \rangle$ in Table 5.5) result from the analysis of Figure S3 (Supporting information), and might be correlated to the easy N release from the product. Keeping in mind the thermal stability of the Zn-N bond (see previous chapter), the effect of the precursor over this distance has been analysed computationally.

Table 5.4: Values of the adiabaticity obtained after the 2500-step MD test for each simulated molecule at different temperatures.

$(\times 10^{-7} \text{ a.u./step})$	300 K	500 K	600 K	700 K
Zn-EA	0.789	6.324	2.295	7.819
Zn-EA-Me	0.202	5.101	12.550	19.970
Zn-APr	0.485	4.218	6.427	7.096
Zn-APr-Me	15.630	4.267	7.501	0.926
Zn-AMB	3.522	16.090	9.279	8.759
Zn-AMB-Me	3.433	1.709	6.545	3.829
Zn-AB	1.065	5.365	7.173	5.922
Zn-APh	0.379	6.391	10.310	7.571

Table 5.5: Expected value for the Zn-N bond length ($\langle \text{Zn-N} \rangle$, in Å) at 300, 500, 600, and 700K with its standard deviation in parentheses ($\times 10^{-3} \text{ Å}$) for the eight precursors using CPMD calculations.

$\langle \text{Zn-N} \rangle (\text{Å})$	300 K	500 K	600 K	700 K
Zn-EA	1.701 (20)	1.713 (31)	1.707 (31)	1.709 (27)
Zn-EA-Me	1.702 (25)	1.707 (34)	1.707 (35)	1.709 (45)
Zn-APr	1.705 (29)	1.713 (57)	1.713 (47)	1.706 (42)
Zn-APr-Me	1.707 (31)	1.705 (48)	1.708 (49)	1.708 (53)
Zn-AMB	1.703 (30)	1.705 (37)	1.703 (36)	1.702 (45)
Zn-AMB-Me	1.703 (38)	1.718 (59)	1.724 (65)	1.727 (84)
Zn-AB	1.706 (29)	1.708 (35)	1.71 (42)	1.715 (43)
Zn-APh	1.703 (24)	1.708 (39)	1.715 (40)	1.704 (34)

The results at different temperatures suggest a subtle decrease in stability for precursors with tertiary amines ($R'=\text{Me}$). In the case of Zn-AMB-Me, its Zn-N distance behaviour is the most revealing, since it increases from $1.703(38)\text{Å}$ (300 K) to $1.727(84)\text{Å}$ (700 K). Another interesting feature arises from the comparison between data obtained for Zn-AMB and Zn-APr-Me. These precursors arise from EA, having identical empirical formulae and only differ in the location

of the methyl groups, but the $\langle EKE \rangle$ and Zn-N distance values obtained for the N-methylated derivative Zn-APr-Me are slightly larger than those of the Zn-AMB. This could be attributed to the steric effects induced by the NMe₂ unit. The temperature has some influence on the mean Zn-N bond length but the influence is even stronger on its dispersion (the bond vibrates more strongly at higher temperatures).

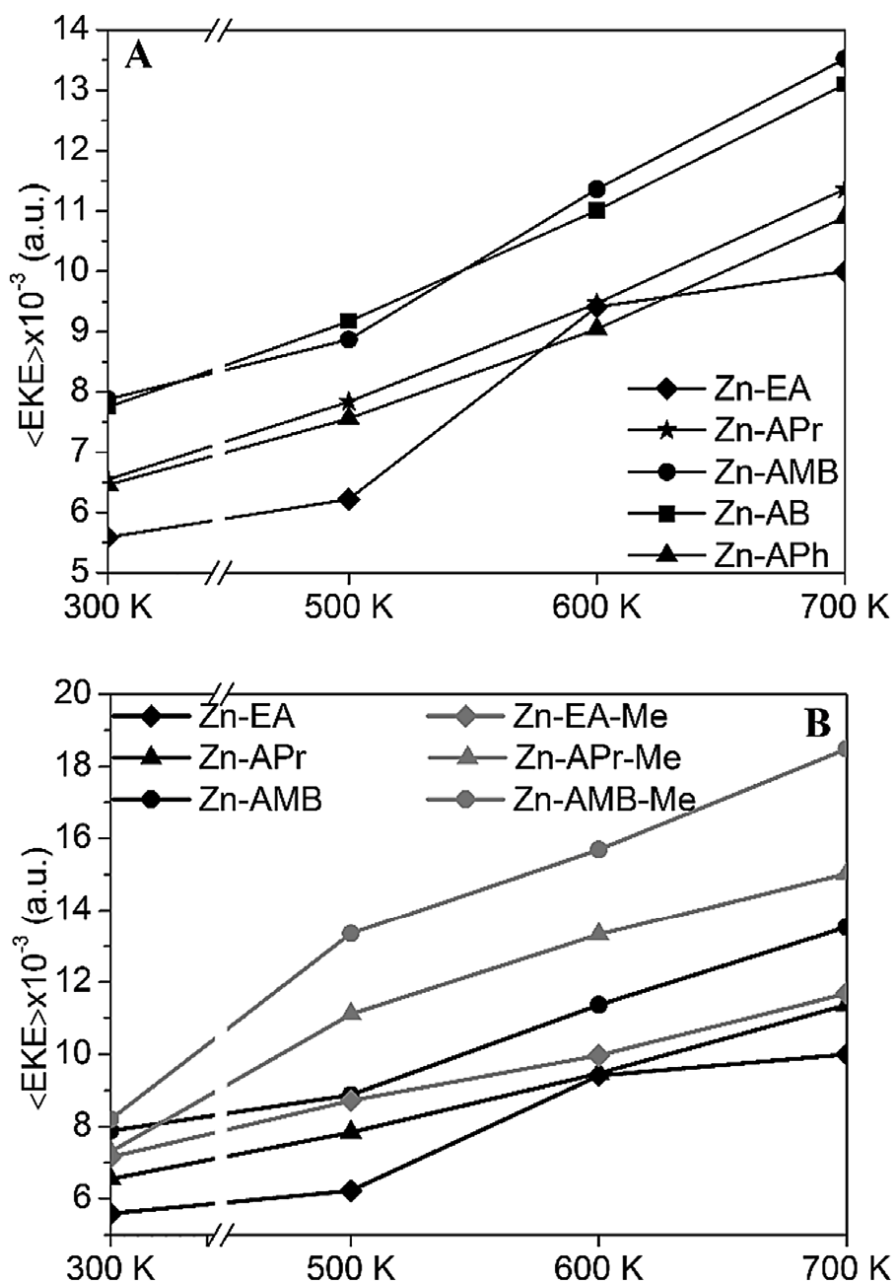


FIGURE 5.10. Expected value for the electronic kinetic energy $\langle EKE \rangle$ obtained after test simulations for precursors with R'=H (A) and for N-methylated and non-substituted aliphatic-based precursors (B), all at 300, 500, 600, and 700 K.

It should be also noted that despite the precursor formed by the reaction of ZAD with EA has been identified as a tetramer, MD studies for this product at 500 K reveal that it tends to undergo fragmentation to give dimeric species that later on lead to the monomeric units with an identical core to the one shown in Figure 5.1. In general, any relevant change in the stability of the precursor has not been noticed to improve the nitrogen elimination during the thermal process. On the other hand, the calculated Zn-N distances look quite short and uniform for all the studied cases. This observation might correspond to some limitation of the functional LDA describing the Zn atom. Further investigation were undertaken to improve this calculations and the results using the PBE functional instead of the LDA are presented in the last section of this chapter.

5.2.3 Conclusions

This work presents a comparative computational study on systems generated from ZAD and eight amino-alcohols and their transformation to ZnO. The results clarify the influence of incorporating substituents on the backbone of EA (the most typical stabilizer agent used in sol-gel ZnO processes) on the charge distribution in the precursors, their properties and their thermal stability. In general, for amino-alcohols holding aliphatic spacers between the N,O donor atoms, the HOMO is mainly located on the amine nitrogen and the energy gap increases when compared with those of precursors with more rigid cores derived from amino-alcohols with benzyl or phenyl separators. Moreover, methylation of the amino group increases the energy gap, thus reducing their proclivity to undergo photodegradation. Molecular dynamic calculations at different temperatures have also provided conclusive evidences of the "prevalence" of the amine nitrogen bond to the Zn(II) even at high temperatures. This may explain the N contamination detected in the ZnO formed even at high temperatures. These findings suggest that de-protonation of EA related amino-alcohols and their binding to the Zn(II) in the precursor affect its thermal behaviour, but in all cases the Zn-N bond is less prone to cleave than the Zn-O (acetate) one. Therefore these systems appear not to be the best candidate to achieve the optimal pure ZnO for printed electronics, because the nature of ink additives is not expected to affect the final material. Further investigation will be undertaken to improve these calculations.

5.3 The 300-600 °C range: New experimental results

5.3.1 Elemental Organic Analysis (EOA) and X-ray Diffraction (XRD)

The EOA results (Table 5.6) show very low values of N, C and H for the Zn-APr precursor above 500 °C. At 600 °C these quantities are similar to other precursors, except for the Zn-AB. Below 500 °C there is a considerable decrease in the C value for the aromatic precursors (specially the Zn-APr case), while for N and H values, the decrease is more humble. It has to be noticed the better performances of Zn-APr at low temperatures comparing to the typical Zn-EA precursor.

Table 5.6: Elemental Organic Analysis for the aliphatic-based (Top table) and aromatic-based (Bottom table) precursors (Abundance in % ($\pm 0,2$))

T (°C)	Zn-EA			Zn-APr			Zn-AMB		
	N	C	H	N	C	H	N	C	H
Initial	7.6	26.1	4.9	7.1	30.3	5.6	6.2	37.2	6.6
300	1.2	6.9	0.9	1.3	12.0	1.3	0.7	12.3	1.3
400	1.3	6.9	0.8	1.0	5.8	0.7	0.6	5.8	0.7
500		2.9	0.5		0.8			3.6	
600	≤ 0.2	≤ 0.2	≤ 0.2	≤ 0.2	≤ 0.2	≤ 0.2	≤ 0.2	0.4	≤ 0.2

T (°C)	Zn-AB			Zn-APh		
	N	C	H	N	C	H
Initial	5.7	43.9	4.5	6.0	41.4	3.9
300	2.2	32.2	3.5	5.2	42.2	3.2
400	4.3	29.3	2.0	4.5	33.3	2.4
500	0.6	7.1	0.9	3.0	20.7	1.9
600	0.4	3.5	≤ 0.2	≤ 0.2	0.7	≤ 0.2

Ex-situ XRD curves (Figures 5.11 and 5.12) show the characteristic ZnO peaks, with the larger crystallite size (Table 5.7) for the crystal ZnO arising from the Zn-APr (in this case, at all temperatures) and Zn-AB precursor decomposition (contribution from the substrate was also found and carefully removed), followed by Zn-EA and Zn-AMB. In addition, it has to be mentioned some crystal reorientations (the decrease in some crystal directions, e.g. the (101)). Care has to be taken with the Zn-APh, since the enormous combustion at high temperature produces no film but ZnO powder (explaining the motive why crystalline ZnO film is found and measured with XRD at 400 °C but lost at 500 °C) and so neither the XRD curve for Zn-APh at 600 °C nor the crystallite size calculations (on italic) can be compared with the others precursors. No crystalline ZnO was found either at 300 °C for in the decomposition process of the Zn-APh precursor.

Table 5.7: Crystallite size of the three ZnO principal reflections of the precursors (Zn-EA, Zn-APr, Zn-AMB, Zn-AB and Zn-APh) at different temperatures.

T (°C)\(hkl)	Zn-EA			Zn-APr			Zn-AMB		
	(100)	(002)	(101)	(100)	(002)	(101)	(100)	(002)	(101)
300	12.9	8.2	11.8	18.0	10.3	13.1	9.4	8.4	9.4
400	12.3	8.0	11.1	14.0	11.1	11.0	10.6	7.5	-
500	13.8	14.6	10.2	14.5	12.8	10.7	11.5	12.4	10.6
600	20.8	21.0	21.5	27.8	26.1	24.6	21.3	21.5	20.9

T (°C)\(hkl)	Zn-AB			Zn-APh		
	(100)	(002)	(101)	(100)	(002)	(101)
300	29.5	46.2	31.0	-	-	-
400	16.1	8.8	23.2	12.5	12.2	12.1
500	10.5	13.0	9.6	9.5	9.9	7.9
600	30.8	28.6	24.7	<i>35.9</i>	<i>36.2</i>	<i>33.4</i>

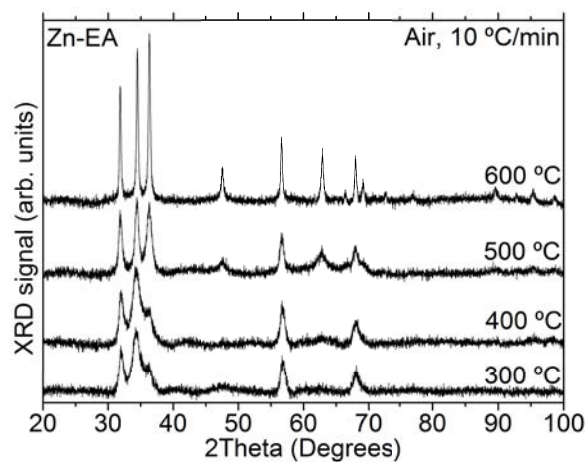


FIGURE 5.11. XRD spectra of Zn-EA at different temperatures.

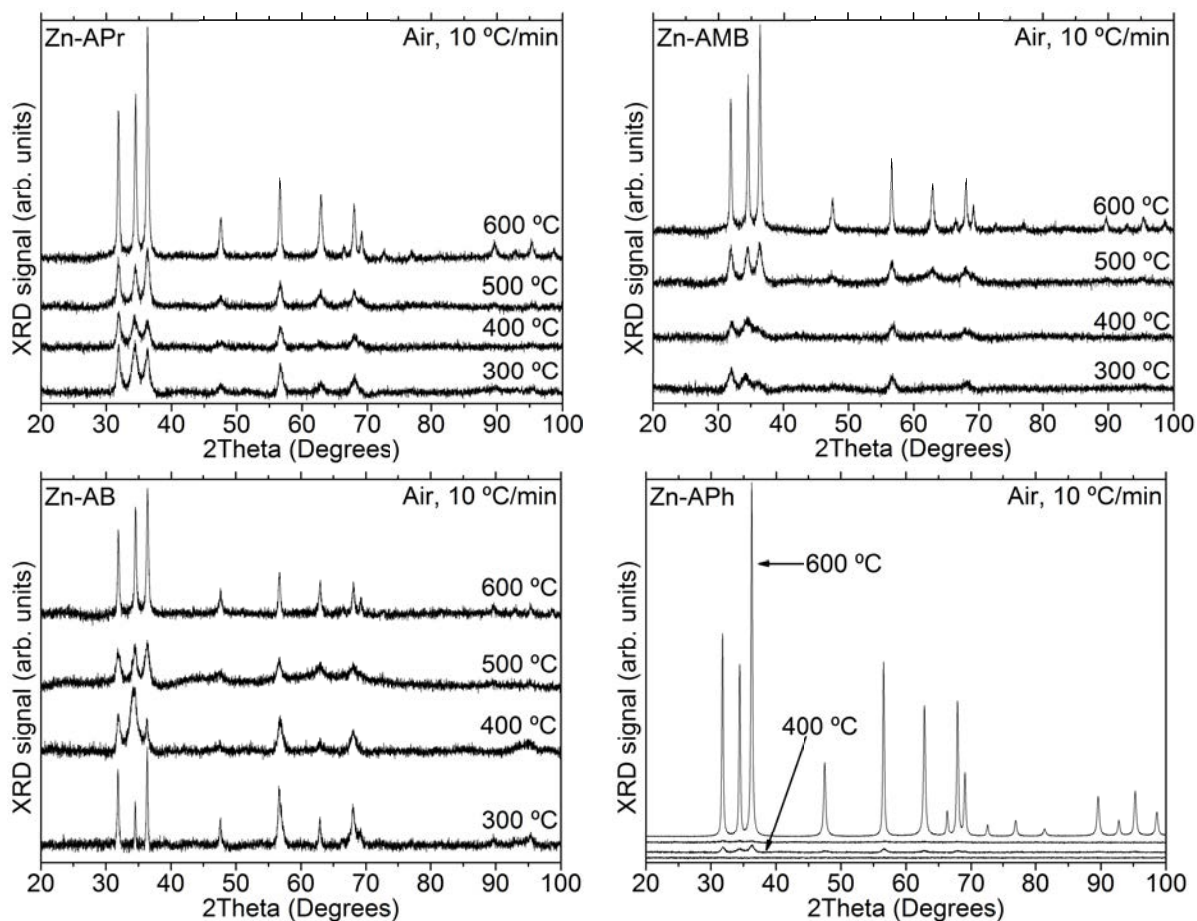


FIGURE 5.12. XRD spectra of the proposed precursors (Zn-APr, Zn-AMB, Zn-AB and Zn-APh) at different temperatures.

5.3.2 Scanning Electron Microscopy (SEM) and Infrared Spectroscopy (IR)

Since Zn-APh does not form a film for high temperatures, no SEM images (Figures from 5.13 to 5.16) are in that case. Although the nature of the observed wrinkles (or crumples) is still unknown in the literature, the textured metal-oxide films have better performance when used as photo-catalysts and as battery electrodes[285]. In addition, no uniformity is observed for the ZnO formed at various temperatures for all precursors. The thickness of the layers vary depending on these wrinkle-like structures but always remain ca. 1-3 μm .

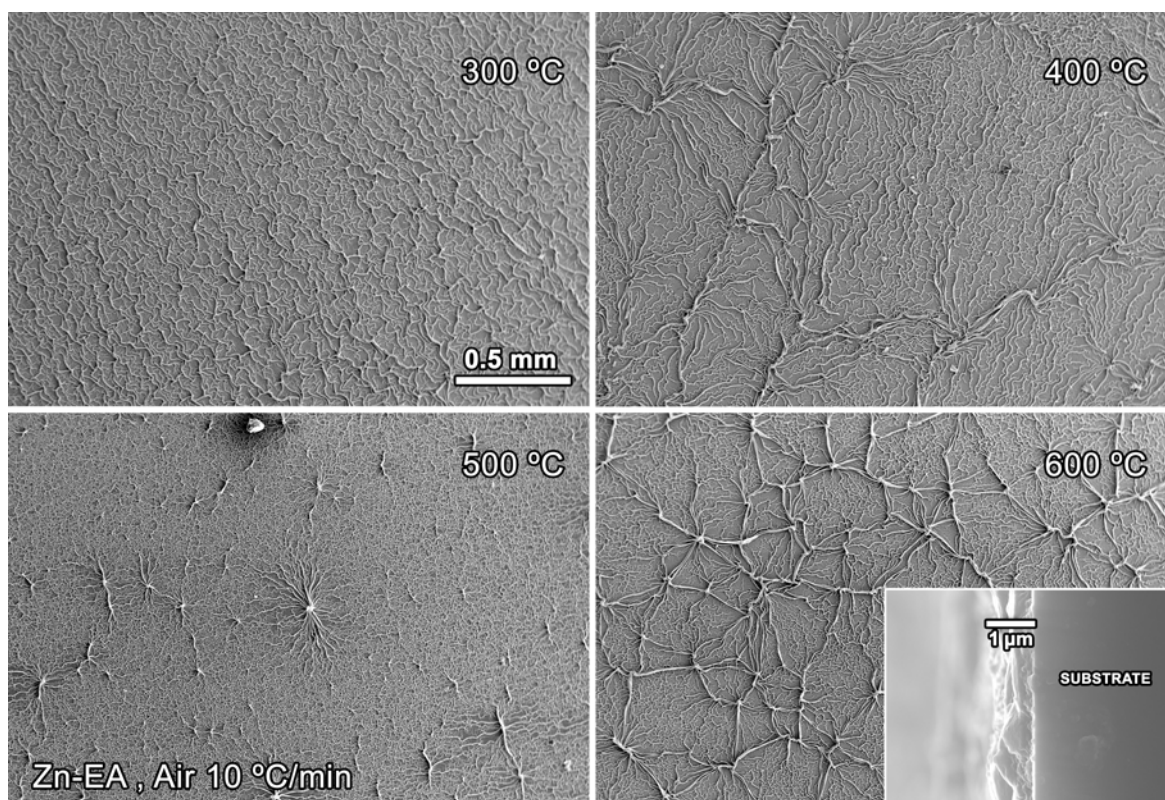


FIGURE 5.13. SEM images of Zn-EA at different temperatures, showing the morphology of the resultant ZnO films.

From the IR results (Figures 5.17 and 5.18), it can be noticed that the Zn-O absorption peak (ca. 470 cm^{-1}) is present for all temperatures in the Zn-APr case, although below 500 °C its ratio with respect to other (O-H or C=O) is approximately 1. Similar spectra can be found for Zn-EA and Zn-AMB case. Both Zn-AB and Zn-APh precursors have a similar IR spectra at 600 °C than the Zn-APr case, while below 500 °C (included) some considerable absorption bands arise due to C=C bonds from the aromatic rings.

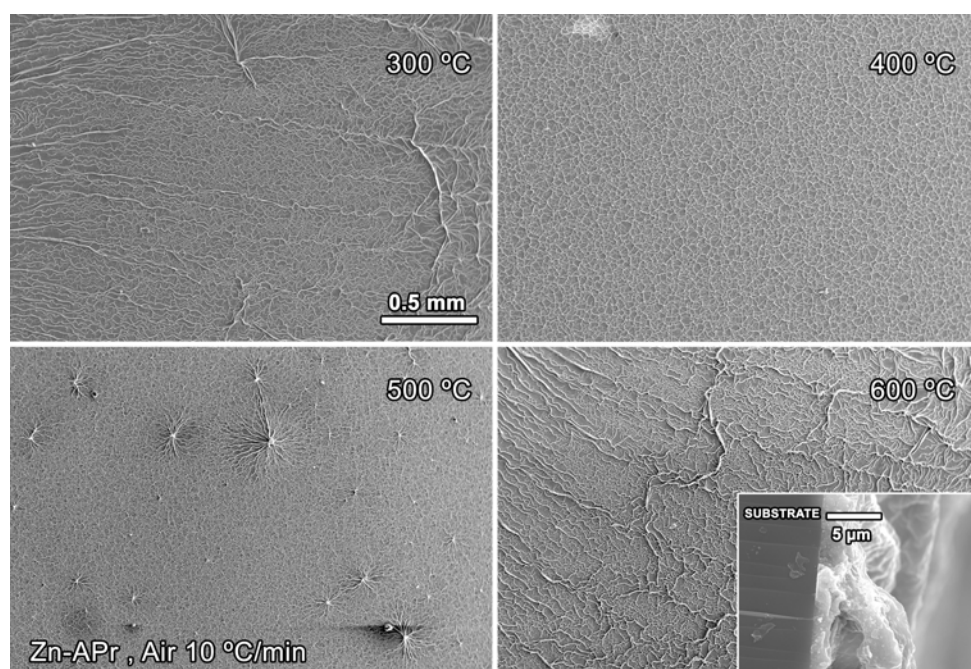


FIGURE 5.14. SEM images of Zn-APr at different temperatures, showing the morphology of the resultant ZnO films.

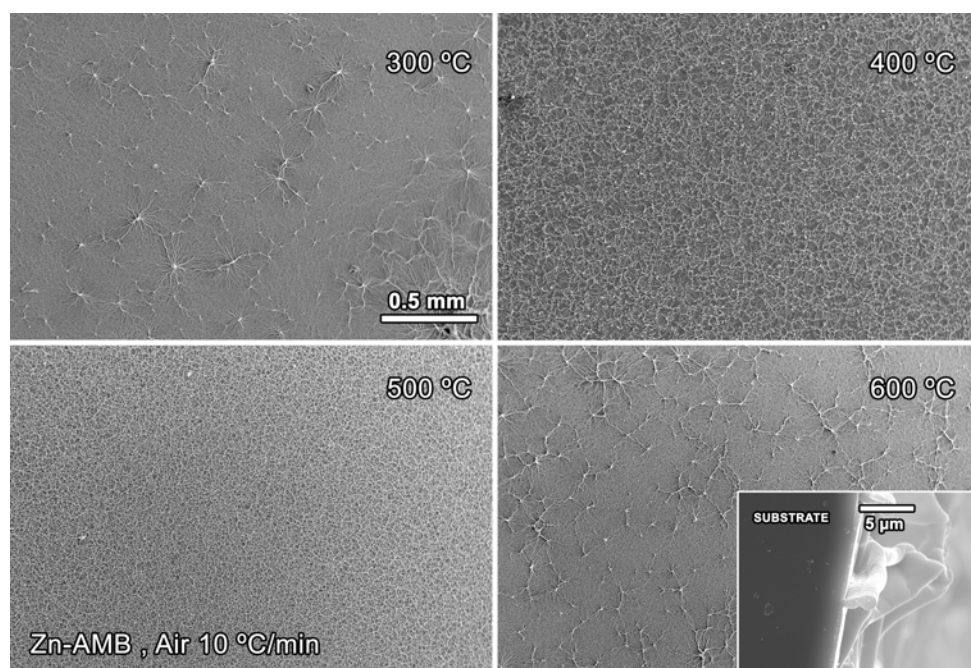


FIGURE 5.15. SEM images of Zn-AMB at different temperatures, showing the morphology of the resultant ZnO films.

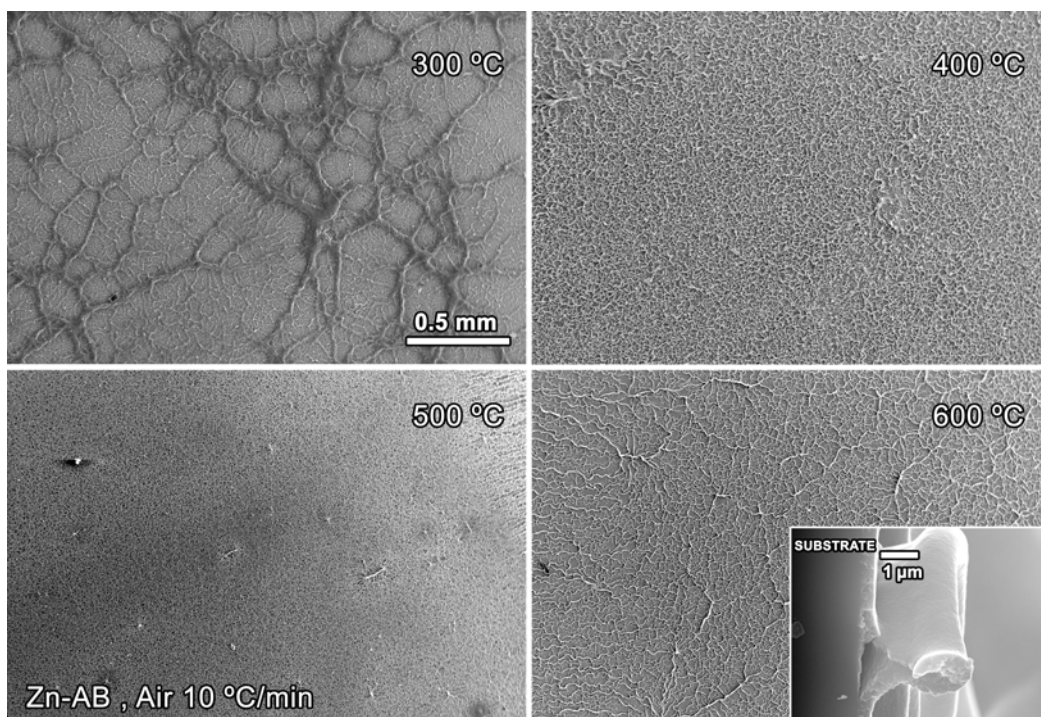


FIGURE 5.16. SEM images of Zn-AB at different temperatures, showing the morphology of the resultant ZnO films.

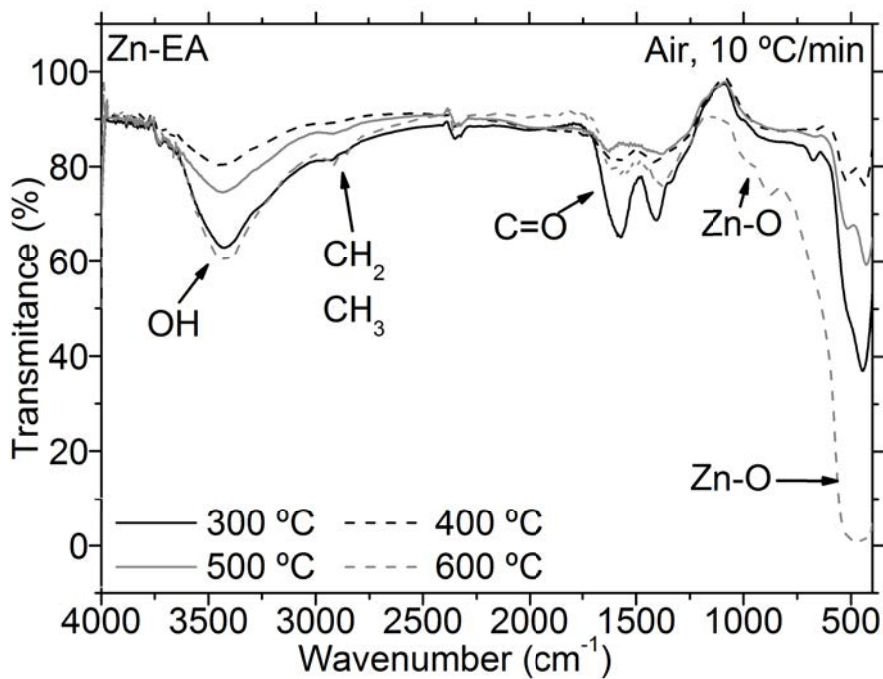


FIGURE 5.17. IR spectra of Zn-EA at different temperatures.

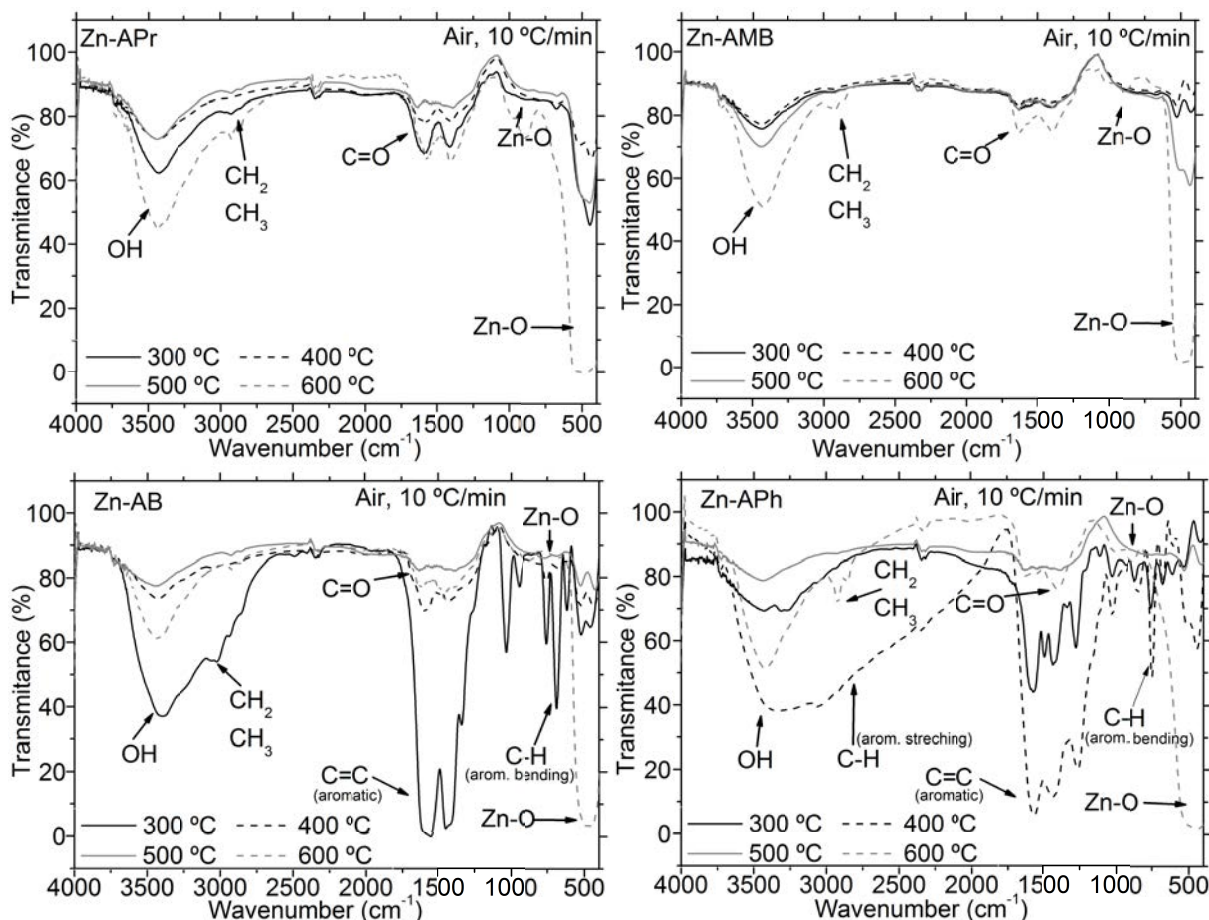


FIGURE 5.18. IR spectra of the proposed precursors (Zn-APr, Zn-AMB, Zn-AB and Zn-APh) at different temperatures.

5.4 Theoretical results using PBE

LDA and PBE functionals: A comparison. Although in the second section of this chapter the LDA functional for Zn (and so for the other atoms of the system as well) was used, by the time it was published, a much more advanced functional officially came out for the Zn atom, the PBE functional. LDA and PBE (section 3.3.1.2) are *de facto* controlled approximations to the average exchange-correlation hole. With LDA, the structural, elastic and vibrational properties are often well enough explained, with crystal bulk lattice constants accurate to within 3%, usually underestimated and with bulk *moduli* somewhat too large, up to 10% error (not uncommon for *d*-metals, e.g. the Zn atom). The binding energies are often too negative (over-binding), up to several eV and the activation energies in chemical reactions are unreliable, too small or absent.

Finally, the electronic structure can be usefully interpreted (density of states or band structures) except for band gaps, a thing more fundamental than LDA. With PBE there is an improvement in (i) the atomic and molecular total energies, (ii) in the cohesive energy in a solid, (iii) in the activation energy barriers in chemical reactions, although still too low, and (iv) in the description

of relative stability of bulk phases and the electrostatic hydrogen bonds. Zn behaviour is now better known thanks to the analysis of the electronic structure of complexed zinc molecules[159], the thermic fluctuations of $XZnO$ ($X = Al, Ga$ and In) materials around 3000-5000 K[160] and the speciation in $ZnCl_X$, ZnO and $ZnCO_3$ at different chloride concentrations[161].

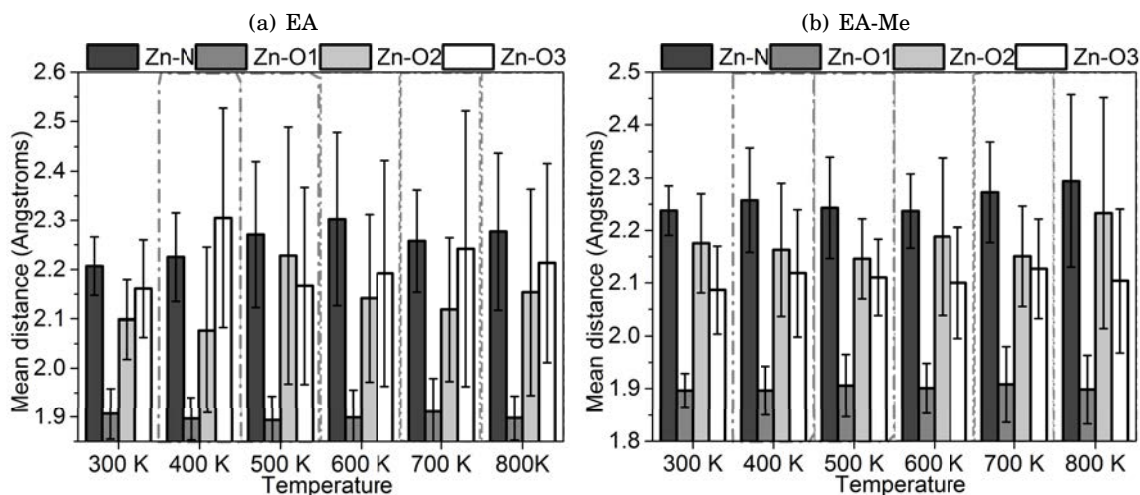


FIGURE 5.19. Expected value and standard deviations for Zn-EA and Zn-EA-Me precursor's mean bond lengths (in Å) using PBE functional.

New calculations. Consider the Zn atom located in the center of a distorted tetrahedron with the N and the de-protonated O of the amine group (Zn-N and Zn-O1) located in two vertices and the acetate group (Zn-O2 and Zn-O3) located in the remaining two (figure 5.1). Then, figures 5.19 and 5.20 show the results of the Molecular Dynamics carried out with the PBE functional. MD results provide even more evidence that for non-methylated aliphatic stabilizers (EA, APr, AMB) the nitrogen remains bonded to the Zn atom, explaining the N-contamination detected even at high temperatures in the first article. For aromatic precursors this contamination is highly present up to 750 K, precisely when the ring is oxidizing. The PBE analysis presents a significant increase of the Zn-N bond instability for Zn-APr-Me and Zn-AMB-Me comparing to that of the second article, using LDA. A consequence of this fact should be a lower N-contamination in the desired ZnO film, thus increasing its quality and its value. Steric effects in the Zn-AMB-Me case might explain the differences comparing to the aromatic precursors, although neither this effect nor collisions between molecules were taken into account for more accurate conclusions. In addition, these results prove that the PBE functional predicts a precise behaviour, allowing a more correlated discussions with respect to the experimental results in the first section of this chapter. In addition, the results reinforce the conclusion that Zn-N bond plays an important role in the ZnO film quality and that methylation of the amine group should be taken into account when using nitrogen-based ZnO precursors

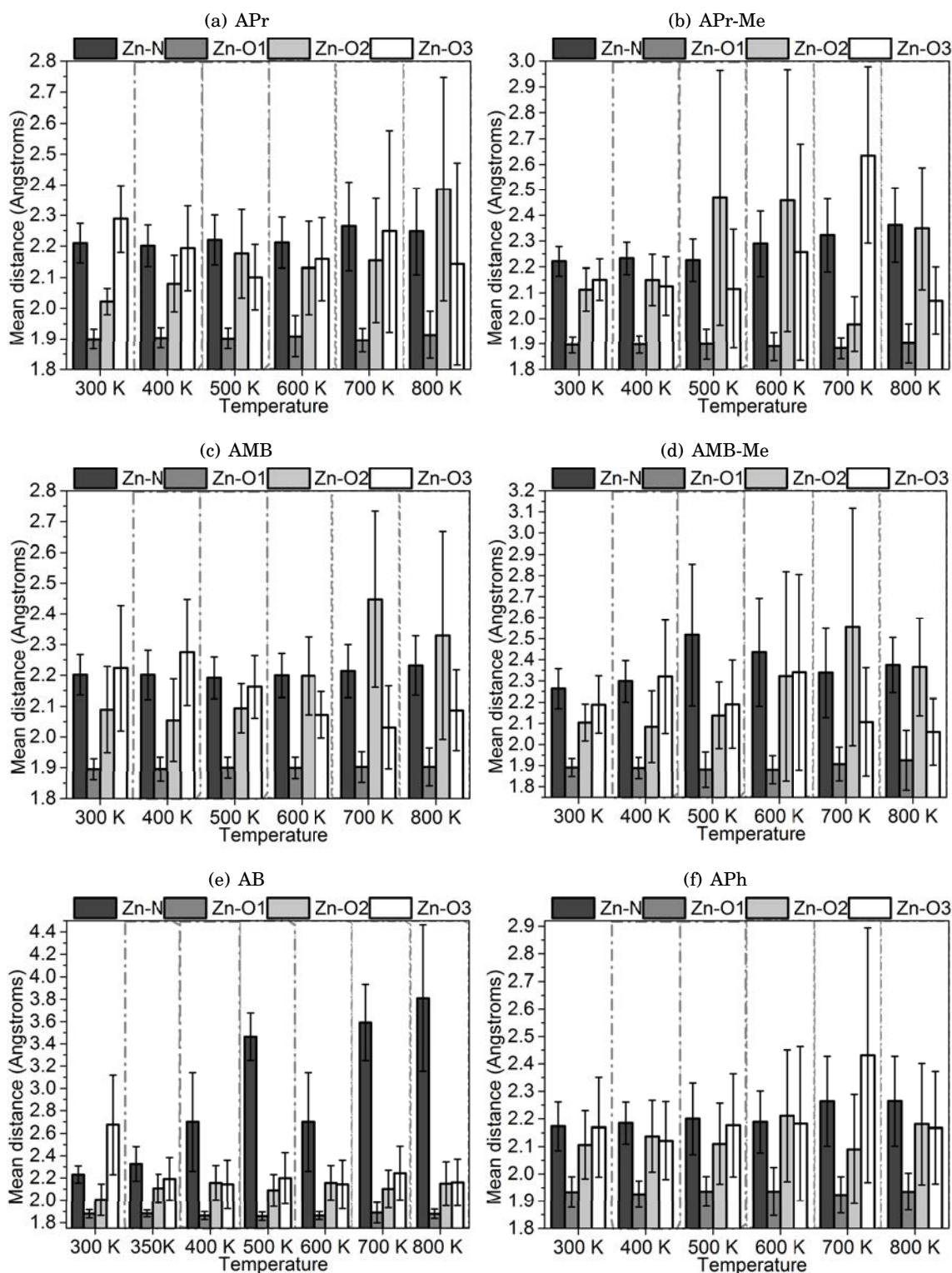


FIGURE 5.20. Expected value and standard deviations for the proposed precursor's mean bond lengths (in Å) using PBE functional.

*"I regret only one thing, which is that the days are so short
and that they pass so quickly. One never notices what has been done;
one can only see what remains to be done"*

- Maria Skłodowska-Curie in a letter to her brother (1894)

GREEN CHEMISTRY AS A NEW STRATEGY ROUTE TO ZnO

The trend in published articles is the use of aminoalcohols as additives in the sol-gel method to obtain ZnO. As it can be seen in previous chapters of this dissertation aminoalcohols stabilize Zn(II) when mixed with Zinc Acetate Dihydrate (ZAD) at room temperature but increase the reactivity of the resulted compounds with ambient light and carbon dioxide, leading to the destabilization, the importance of which depends on the aminoalcohol used, reported earlier. Furthermore, high temperatures are required to get rid of the nitrogen in their decomposition process, making the isolation of ZnO a challenge. The present chapter proposes a change in the *game plan* to achieve pure and nitrogen-free ZnO by the use of sol-gel method through a sustainable novel green synthetic strategy minimizing the use of toxic materials. For this purpose, several Coordination Polymers (CPs) will be tested in the present chapter, avoiding the use of additives and using only oxygen-containing ligands to stabilize the Zn(II) and to achieve mono-, di- and even poly-nuclear Zn(II)-complexes.

As mentioned before, CPs are valuable and efficient precursors for the production of nanoscale materials and metal oxides, with optimized morphologies and properties. The proper selection of the metal ion M^{m+} and the ligand allow the design and synthesis of CPs for a specific use or application. Those with $M^{m+} = d^{10}$ are particularly relevant due to their potential photophysical properties and their utility in photocatalysis. These findings together with characteristics of the Zn(II) ion, have triggered the development and design of novel multifunctional Zn(II)-CPs. Most of the examples known have polydentate organic ligands with N and O donor atoms, however those with natural occurring polycarboxylic acids as ligands are scarce. Here are presented the synthesis, structure, properties and thermal behavior of Zn(II) CPs based on ZAD and four multitopic acids: 2-hydroxypropanoic acid (*lactic acid*), 2-hydroxybenzoic acid (*salicylic acid*), butanedioic acid (*succinic acid*) and 2-hydroxypropane-1,2,3-tricarboxylic acid (*citric acid*). These

studies have allowed the isolation of new Zn(II)-CPs using an inexpensive, save and easily controllable process. X-ray crystal structures confirmed their mono- and polymeric nature. A comparative study of the influence of the organic multitopic ligands on their thermal stability and their conversion to pure ZnO is also reported.

On the other hand, Heteropolynuclear (HPN) organometallic compounds (OMC) are attracting great interest since long ago. In these products, the presence of several proximal metals with various oxidation numbers and spin states coexist in different crystalline environments[191]. The mutual interaction between these ions may modify their stability or catalytic and biological activity, and opens a bunch of applications with potential impact in Materials Sciences (as precursors for new materials) and new technologies (as single molecular magnets). Due to the increasing interest of the incorporation of Fe(II) or (III) in polymetallic arrays, the synthesis of new HPN derivatives with Zn(II) and Fe(II) or (III) has become a promising challenge. Here, as an extension of the previous studies, the synthesis and characterization of a new decametalllic (Fe_6Zn_4) OMC prepared at room temperature is presented.

6.1 Zn(II)-CPs as ZnO precursors

6.1.1 Procedure

6.1.1.1 Materials and Methods

Zinc acetate dihydrate [ZAD] and the organic acids (2- hydroxypropanoic acid [*lactic acid*, HL], 2-hydroxybenzoic acid [*salicylic acid*, HSa], butanedioic acid [*succinic acid*, H_2Su] and 2-hydroxypropane-1,2,3-tricarboxylic acid [*citric acid*, H_3Ci]) were obtained from commercial sources (ZAD and HL from Panreac and HSa, H_2Su and H_3Ci from Acrös Organics) and used as received. The methanol used for the preparation of the compounds was HPLC-grade. Elemental analyses were carried out using a Thermo EA Flash 2000 (Thermo Scientific, Milan, Italy) apparatus, working in standard conditions recommended by the supplier of the instrument (helium flow 140 mL/min, combustion furnace at 950 °C, chromatografic column oven at 65 °C). Infrared (IR) spectroscopy registered with a Nicolet 400FTIR instrument using KBr pellets. Thermogravimetric Analyses (TGA) and Differential Thermal Analyses (DTA) were carried out in an atmosphere of dry air with 50 mL/min flow rate and heating rate of 10 °C/min up to 600 °C, using a Mettler-Toledo TGA-851e thermobalance with uncovered aluminium crucibles (of 70 μL volume). Scanning electron microscope (SEM) was performed with a JSM-6510 (JEOL) apparatus, using a microanalysis system based on Inca 200 series (Oxford Instruments), a working distance of 15 mm and acceleration voltage of 20 kV.

6.1.1.2 Synthesis of the compounds

- Compound 1: 0.5 g of ZAD (2.3×10^{-3} mol) is dissolved in 2 mL of water. Then, double the amount in mols of HL (0.34 mL, 4.6×10^{-3} mol) dissolved in 2 mL of water is added dropwisely. The same compound is found when the molar ratio (acid:ZAD) is 1:1, thus decreasing the yield and wasting ZAD.

- **Compound 2:** 0.5 g of ZAD (2.3×10^{-3} mol) is dissolved in 4 mL of methanol. Then, an equimolar amount of HL (0.17 mL, 2.3×10^{-3} mol) dissolved in 2 mL of methanol is added dropwisely. A white precipitate is produced with a 2:1 (acid:ZAD) molar ratio.
- **Compound 3:** 0.5 g of ZAD (2.3×10^{-3} mol) is dissolved in 4 mL of methanol. Then, double the amount in mols of HSa (0.63 g, 4.6×10^{-3} mol) in 2 mL of methanol is added dropwisely. The same compound is found when the molar ratio (acid:ZAD) is 1:1, thus decreasing the yield and wasting ZAD.
- **Compound 4:** 0.5 g of ZAD (2.3×10^{-3} mol) is dissolved in 3 mL of water. Then, an equimolar amount of H₂Su (0.27 g, 2.3×10^{-3} mol) in 6 mL of water is added dropwisely. A white precipitate is produced when the molar ratio (acid:ZAD) is 1:1.
- **Compound 5:** 0.5 g of ZAD (2.3×10^{-3} mol) is dissolved in 2 mL of water. Then, double the amount in mols of H₃Ci (0.87 g, 4.6×10^{-3} mol) in 2 mL of water is added dropwisely. A white precipitate is produced when the molar ratio (acid:ZAD) is 1:1.

6.1.1.3 X-ray diffraction studies

Resolution and refinement of the crystal structures. A prismatic crystals of **1**, **2**, **3**, **4** and **5** were selected and mounted on a D8VENTURE System equipped with a multilayer monochromator and a Mo microfocus ($\lambda = 0.71073 \text{ \AA}$) at 100 K for **1**, **2**, **3** and **5** and 212 for **4**. The integration of the data using an orthorhombic (**1**, **2**) and a monoclinic (**3**, **4**, **5**) unit cells yielded a total of 5127 (**1**), 4987 (**2**), 7645 (**3**), 2565 (**4**) and 12963 (**5**) reflections to a maximum Θ angle of 27.27° (**1**), 30.54° (**2**), 30.60° (**3**), 29.07° (**4**) and 30.54° (**5**) of which 2070 (**1**), 3571 (**2**), 2217 (**3**), 720 (**4**) and 2527 (**5**) were non-equivalent by symmetry and 1859 (**1**), 3154 (**2**), 2155 (**3**), 717 (**4**) and 2408 (**5**) were greater than $2\sigma(F^2)$. The structure was solved using the Bruker SHELXTL Software Package¹ and refined with SHELXL, using the space group $P2_12_12_1$ (**1**, **2**), $C2$ (**3**, **4**) and $P2_1/c$ (**5**) with $Z = 4$ (**1**, **2**) and $Z = 2$ (**3**, **4**, **5**) for the formula unit $C_6H_{14}O_8Zn$ (**1**), $C_8H_{18}O_8Zn$ (**2**), $C_{14}H_{14}O_8Zn$ (**3**), $C_4H_4O_4Zn$ (**4**) and $C_{12}H_{14}O_{16}Zn_3$ (**5**). The final anisotropic full-matrix least-squares refinement on F^2 with 155 (**1**), 165 (**2**), 115 (**3**), 43 (**4**) and 151 (**5**) variables converged at $R_1 = 3.57\%$ (**1**), 3.37% (**2**), 2.29% (**3**), 1.47% (**4**) and 2.94% (**5**) for the observed data and $wR_2 = 8.90\%$ (**1**), 8.66% (**2**), 4.99% (**3**), 3.27% (**4**) and 8.80% (**5**) for all data.

The goodness-of-fit were 1.100 (**1**), 1.018 (**2**), 1.156 (**3**), 1.093 (**4**) and 1.133 (**5**). The largest peaks in the final difference electron density synthesis were $0.544 \text{ e}^-/\text{\AA}^3$ (**1**), $0.702 \text{ e}^-/\text{\AA}^3$ (**2**), $0.377 \text{ e}^-/\text{\AA}^3$ (**3**), $0.267 \text{ e}^-/\text{\AA}^3$ (**4**) and $0.607 \text{ e}^-/\text{\AA}^3$ (**5**) and the largest holes were $-0.764 \text{ e}^-/\text{\AA}^3$ (**1**), $-0.456 \text{ e}^-/\text{\AA}^3$ (**2**), $-0.413 \text{ e}^-/\text{\AA}^3$ (**3**), $-0.494 \text{ e}^-/\text{\AA}^3$ (**4**) and $-1.440 \text{ e}^-/\text{\AA}^3$ (**5**) with an RMSD of $0.137 \text{ e}^-/\text{\AA}^3$ (**1**), $0.102 \text{ e}^-/\text{\AA}^3$ (**2**), $0.082 \text{ e}^-/\text{\AA}^3$ (**3**), $0.066 \text{ e}^-/\text{\AA}^3$ (**4**) and $0.196 \text{ e}^-/\text{\AA}^3$ (**5**). On the basis of the final model, the calculated densities were 1.800 g/cm^3 (**1**), 1.591 g/cm^3 (**2**), 1.690 g/cm^3 (**3**), 2.257 g/cm^3 (**4**) and 2.438 g/cm^3 (**5**), and $F(000) 576 \text{ e}^-$ (**1**), 640 e^- (**2**), 384 e^- (**3**), 180 e^- (**4**) and 608 e^-

¹G.M. Sheldrick, *Acta Cryst. Section A*, A64, 112-122, 2008.

(5). Further details concerning the resolution and refinement of the crystal structures of the five products are given in Tables 6.1 and 6.2.

Table 6.1: Crystal data and details of refinement of the crystal structure for compounds **1-3**. The approximate crystal dimensions were (in mm×mm×mm) 0.058×0.075×0.504 (**1**), 0.168×0.212×0.574 (**2**) and 0.050×0.084×0.405 (**3**).

	Compound 1	Compound 2	Compound 3
Emp. formula	C ₆ H ₁₄ O ₈ Zn	C ₈ H ₁₈ O ₈ Zn	C ₁₄ H ₁₄ O ₈ Zn
FW	279.54	307.59	375.62
Crystal system	Orthorhombic	Orthorhombic	Monoclinic
Space group	P 2 ₁ 2 ₁ 2 ₁	P 2 ₁ 2 ₁ 2 ₁	C2
<i>a</i> / Å	6.0177(5)	7.8912(2)	15.437(10)
<i>b</i> / Å	11.9196(8)	8.9808(3)	5.3581(3)
<i>c</i> / Å	14.377(10)	18.1171(5)	8.9393(6)
$\alpha = \gamma$ / deg.	90	90	90
β / deg.	90	90	93.208(3)
T/ K	100(2)	100(2)	100(2)
λ / Å	0.71073	0.71073	0.71073
V/ Å ³	1031.28	1283.95(6)	738.28(8)
<i>Z</i>	4	4	2
<i>D</i> _{calc} / mg×m ⁻³	1.800	1.591	1.690
F(000)	576	640	384
μ / mm ⁻¹	2.404	1.939	1.704
Θ range col./deg.	2.219-27.273	2.531-30.540	2.282-30.598
# collec. refle.	5127	4987	7645
# variables	155	165	115
R ₁ / %	3.57	3.37	2.29
wR ₂ / %	8.90	8.66	4.99
Abs.Str.Param.	0.03(3)	0.01(2)	0.016(12)

Powder X-Ray Diffraction. XRD experiments were performed in a PANalytical X'Pert PRO MPD Alpha1 powder diffractometer in Bragg-Brentano $\theta/2\theta$ geometry of 240 millimetres of radius with a Cu $K\alpha_1$ radiation of 1.5406 Å, working power of 45 kV-40 mA, focalizing Ge(111) primary monochromator and with a sample spinning of 2 revolutions per second, a variable automatic divergence slit to get an illuminated length in the beam direction of 10 millimetres, a mask defining a length of the beam over the sample in the axial direction of 12 millimetres, a diffracted beam 0.04 radians Soller slits, a X'Celerator Detector with active length of 2.122°, applying a $\theta/2\theta$ scan from 4 to 100° with 2θ step size of 0.017° and measuring time of 50 seconds.

6.1.2 Results and Discussion

6.1.2.1 Characterization of the precursors

The IR spectra of compounds **1-5** are shown in Figure 6.1. Compounds **1** and **2** have almost exact IR spectrum, although **2** presents a wider carboxylate band at *ca.* 1600 cm⁻¹ due to the presence of bridging acetate. Moreover the absence of the -OH band at 3440 cm⁻¹ in compound **3**

may be due to the fact that Zn(II) is bonded to the Sa^- carboxylate. The comparison of the position of the bands observed in the range $1700\text{-}1400\text{ cm}^{-1}$ for compound **4** and the free succinic acid, suggest the deprotonation of the -OH unit of the -COOH group and the binding of the oxygens to Zn^{2+} ions. The difference of the position of both bands ($\nu_{as} - \nu_s$) suggests, according to the bibliography², that the two oxygen of each COO unit are bond to two different metal ions, thus bridging two Zn(II) atoms.

Table 6.2: Crystal data and details of refinement of the crystal structure for compounds **4** and **5**. The approximate crystal dimensions were (in $\text{mm}\times\text{mm}\times\text{mm}$) $0.237\times 0.0662\times 0.036$ (**4**) and $0.171\times 0.142\times 0.129$ (**5**).

	Compound 4	Compound 5
Emp. formula	$\text{C}_4\text{H}_4\text{O}_4\text{Zn}$	$\text{C}_{12}\text{H}_{14}\text{O}_{16}\text{Zn}_3$
FW	181.44	610.34
Crystal system	Monoclinic	Monoclinic
Space group	C2	P 2 ₁ /c
a/ Å	7.5830(11)	6.1139(8)
b/ Å	5.9493(9)	14.5428(19)
c/ Å	6.2408(10)	9.5756(12)
$\alpha = \gamma$ / deg.	90	90
β / deg.	108.506(6)	102.437(4)
T/ K	212(2)	100(2)
λ / Å	0.71073	0.71073
V/ Å ³	266.99(7)	831.42(19)
Z	2	2
D_{calc} / $\text{mg}\times\text{m}^{-3}$	2.257	2.438
F(000)	180	608
μ / mm^{-1}	4.523	4.389
Θ range col./deg.	3.443-29.075	2.590-30.539
$\#$ collec. refle.	2565	12963
$\#$ variables	43	151
R_1 / %	1.47	2.94
wR_2 / %	3.3	8.8
Abs.Str.Param.	0.278(19)	-

The IR spectrum of **5** did not show the typical bands due to the >CO groups of citric acid (at 1752 and 1704 cm^{-1}) but exhibited intense absorptions in the range expected for the asymmetric (ν_{as}) and symmetric (ν_s) stretching of carboxylate groups. These findings suggested, according to the bibliography the deprotonation of the three -COOH functional groups and their binding to the metal centre. Moreover, the existence of an absorption band due to the stretching of the -OH bond and its shift (*ca.* 40 cm^{-1}) to lower wavenumbers in relation to the free H_3Ci is indicative of the binding of the organic ligand's alcohol's oxygen to the Zn(II) atom. Although the importance of these findings, IR cannot discriminate between monomers and polymers

²K. Nakamoto, *Infrared and Raman Spectra of Inorganic and Coordination Compounds*, (5th Ed.), Wiley, New York, USA, 1997.

and so Mass Spectrometry (MS) was used to confirm the molecular m/z for compounds **1** and **3** (monomers) and the high m/z signals of compounds **2**, **4** and **5**, probably corresponding to fragments of polymers.

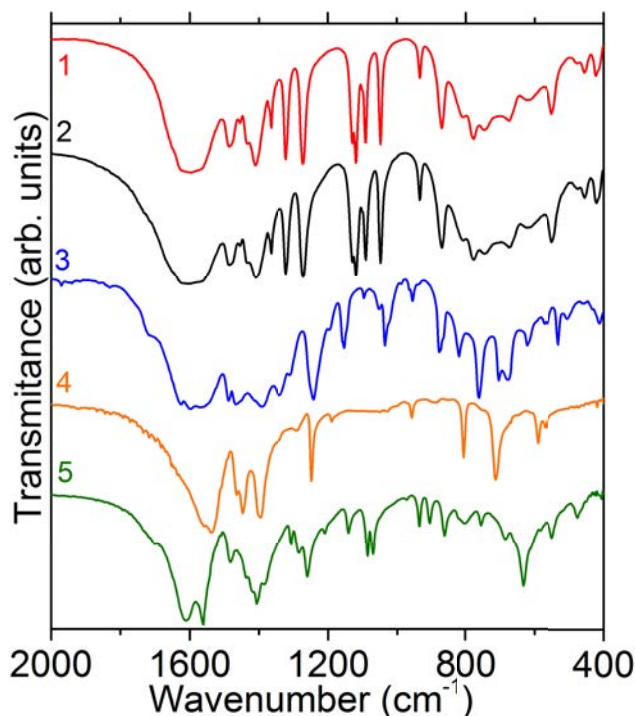


FIGURE 6.1. Infrared spectra ($2000 - 400 \text{ cm}^{-1}$) of the ZnO precursors (**1-5**) used on this study.

In addition, Figure 6.2 shows the synthesis of compounds **1**, **2**, **3**, **4** and **5**. In addition, Figures 6.3, 6.4, 6.5, 6.6 and 6.7 present, for the compounds **1**, **2**, **3**, **4** and **5** respectively, the coordination environment of Zn (II) atoms, the binding of the organic acids, the propagation of the resulting structural units and the selected bond lengths (in Å) and angles (in degrees). Crystals of compound **1**, appearing when synthesized the ZAD+HL mixture in water, show " $\text{Zn}(\text{L})_2(\text{H}_2\text{O})_2$ " (L^- = lactate ligand) monomers arising. The Zn(II) atom is six-coordinated, bond to the lactate ligand through the deprotonated OH units of the alcohol. The remaining coordination sites are occupied by two water molecules. The monomers are linked with their neighbors by the hydrogen-bonds O7-O1, O6-O2, O8-O2 and O3-O5, thus shaping a network (Figure 6.3). When the synthesis is performed in MeOH (Compound **2**), a Zn-CP is formed by " $\text{Zn}_3(\text{L})_6(\text{MeOH})_4$ " (L^- = lactate ligand) arrays. The Zn(II) is six-coordinated, five of which are with the deprotonated oxygen of both carboxylates (O1 and O4) and with the OH ligands (O3 and O6) and with a methanol molecule (O7). In addition the sixth Zn-coordination is produced through the other oxygen of the carboxylate (O2), which shapes the polymer acting as a link between other Zn moieties. The non-bonded-to-Zn methanol molecules (O8) stabilize the Zn-CP by H-bonding with the O4 and O6 atoms and the final Zn-CP forms pillars (Figure 6.4).

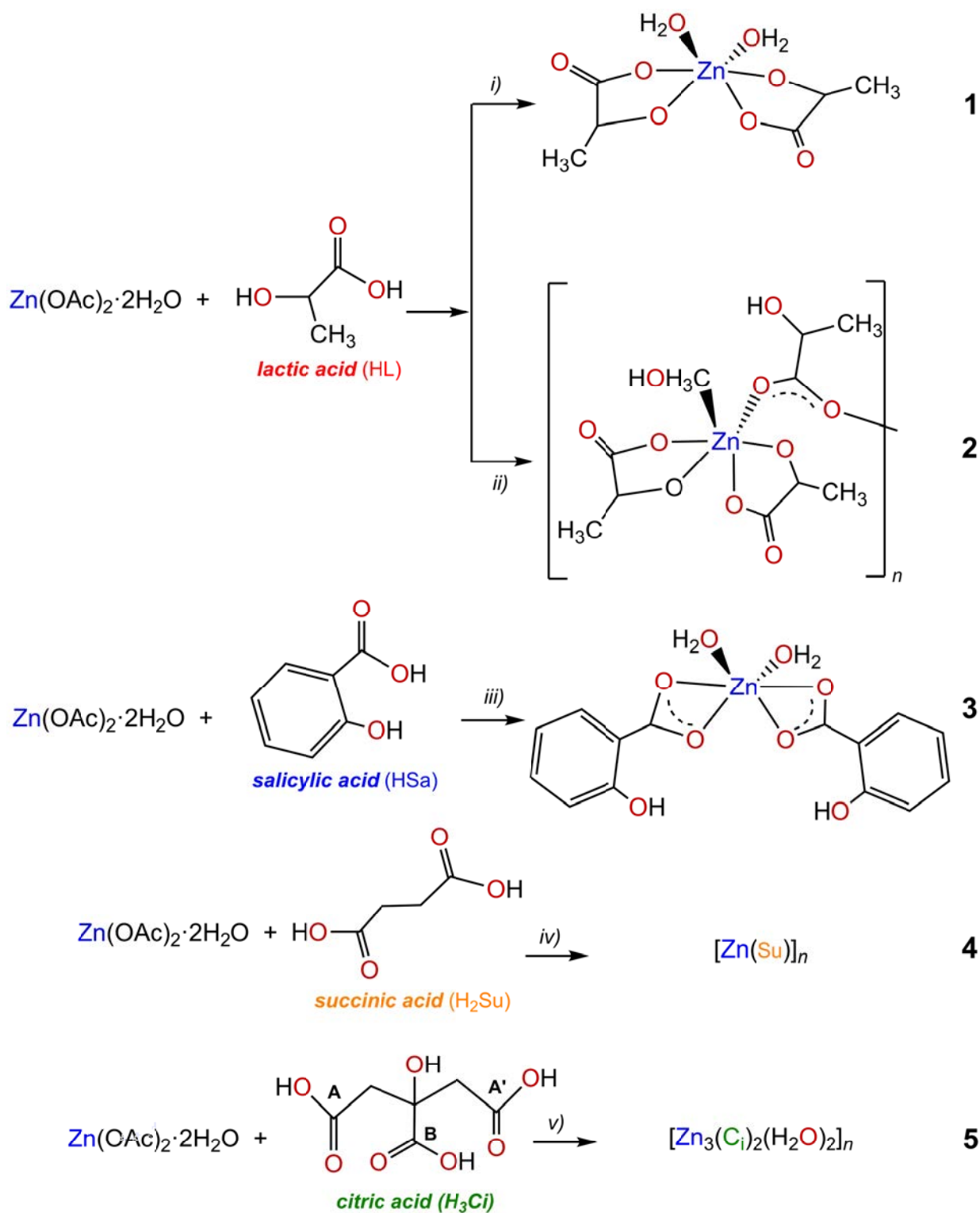


FIGURE 6.2. Synthesis of compounds **1**, **2**, **3**, **4** and **5**. (letters **A**, **A'** and **B** have been added in order to differentiate the terminal (**A** and **A'**) and central (**B**) -COOH units and to ease the reading of the description of the X-ray crystal structure of **4**).

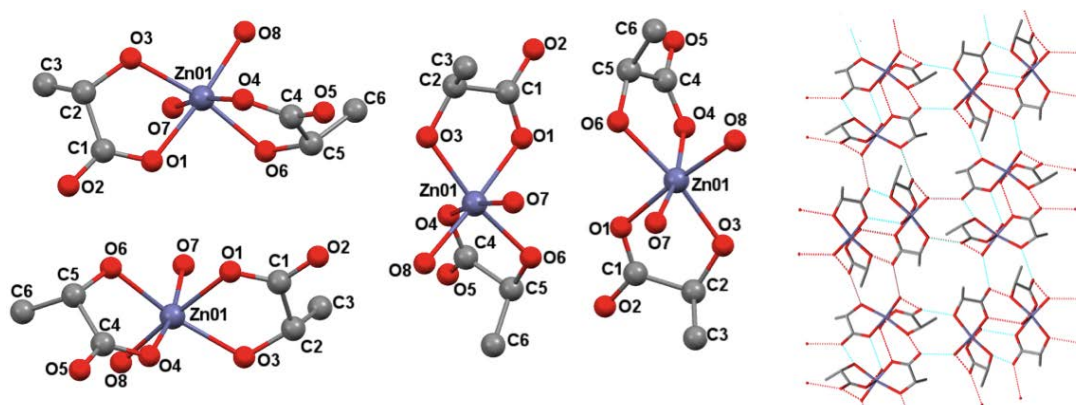


FIGURE 6.3. Compound 1: Left - View of the coordination environment of Zn(II) atom and the binding of the lactic acid. Right - Assembly of the resulting structural units. Selected bond lengths (in Å) and angles (in deg.): Zn1-O8, 2.046(4); Zn1-O1, 2.074(3); Zn1-O4, 2.082(5); Zn1-O7, 2.084(5); Zn1-O6, 2.084(3); Zn1-O3, 2.095(3); O8-Zn1-O1, 174.59(17); O8-Zn1-O4, 91.38(17); O1-Zn1-O4, 91.92(16); O8-Zn1-O7, 89.57(17); O1-Zn1-O7, 88.06(16); O4-Zn1-O7, 168.26(14); O8-Zn1-O6, 93.80(16); O1-Zn1-O6, 91.15(15); O4-Zn1-O6, 76.36(15); O7-Zn1-O6, 91.90(16); O8-Zn1-O3, 98.07(15); O1-Zn1-O3, 77.09(14); O4-Zn1-O3, 100.85(16); O7-Zn1-O3, 90.59(17); O6-Zn1-O3, 167.89(16).

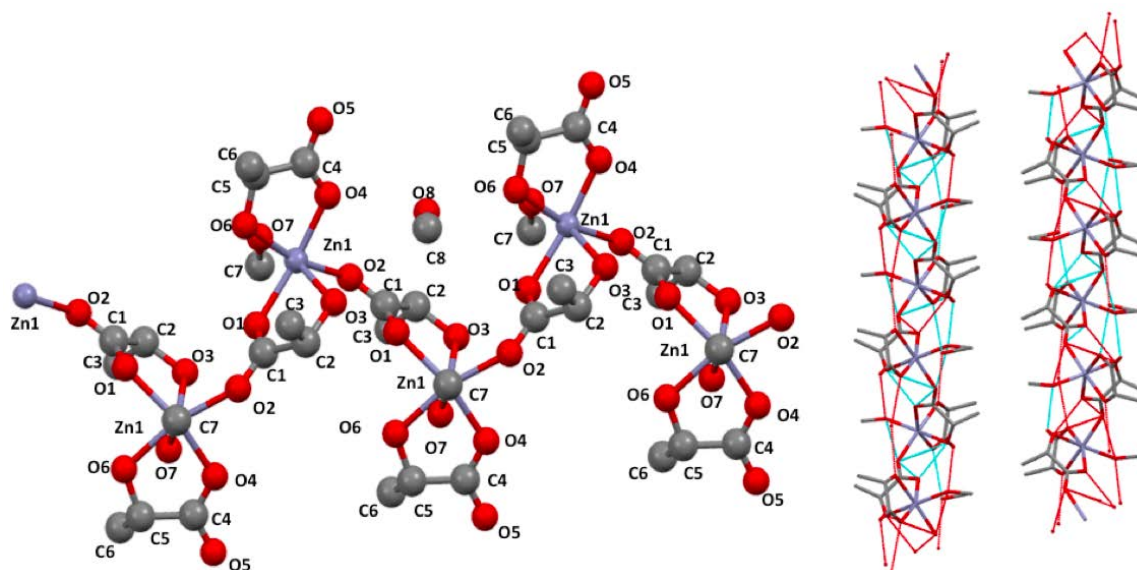


FIGURE 6.4. Compound 2: Left - View of the coordination environment of Zn(II) atom and the binding of the lactic acid and the MeOH. Right - Assembly of the resulting structural units. Selected bond lengths (in Å) and angles (in deg.): Zn1-O4, 2.025(3); Zn1-O7, 2.062(2); Zn1-O2#1, 2.064(2); Zn1-O1, 2.078(2); Zn1-O6, 2.149(3); Zn1-O3, 2.177(3); O4-Zn1-O7, 99.97(11); O4-Zn1-O2#1, 91.49(10); O7-Zn1-O2#1, 85.30(10); O4-Zn1-O1, 159.21(10); O7-Zn1-O1, 92.86(10); O2#1-Zn1-O1, 105.91(10); O4-Zn1-O6, 76.78(10); O7-Zn1-O6, 90.46(10); O2#1-Zn1-O6, 166.67(11); O1-Zn1-O6, 86.90(10); O4-Zn1-O3, 92.55(10); O7-Zn1-O3, 166.13(11); O2#1-Zn1-O3, 88.44(10); O1-Zn1-O3, 76.97(9); O6-Zn1-O3, 98.26(10); Symmetry transformations used to generate equivalent atoms: #1 ($x-1/2, -y+3/2, -z+1$) and #2 ($x+1/2, -y+3/2, -z+1$).

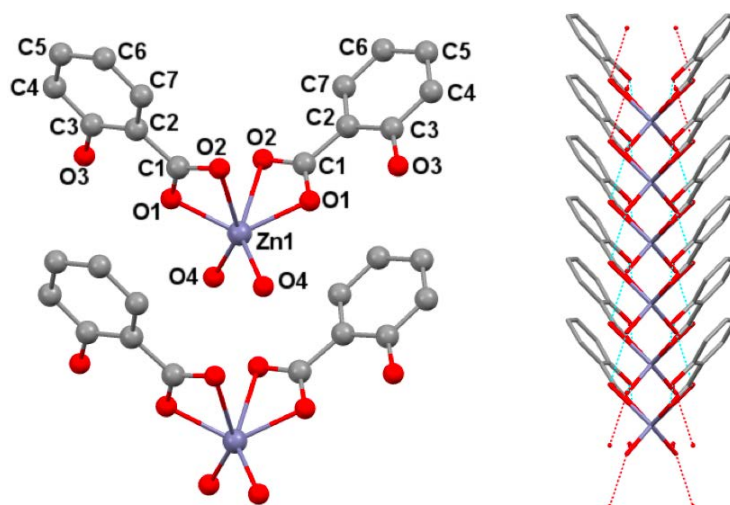


FIGURE 6.5. Compound **3**: Left - View of the coordination environment of Zn (II) atom and the binding of the salicylic acid. Right - Assembly of the resulting structural units. Selected bond lengths (in Å) and angles (in deg.): Zn1-O4, 1.9794(17); Zn1-O4#1, 1.9794(17); Zn1-O1, 1.9906(15); Zn1-O1#1, 1.9906(15); O4-Zn1-O4#1, 101.77(11); O4-Zn1-O1, 120.11(7); O4#1-Zn1-O1, 92.78(7); O4-Zn1-O1#1, 92.77(7); O4#1-Zn1-O1#1, 120.11(7); O1-Zn1-O1#1, 128.31(9); Symmetry transformations used to generate equivalent atoms: #1 (-x+1,y,-z+1).

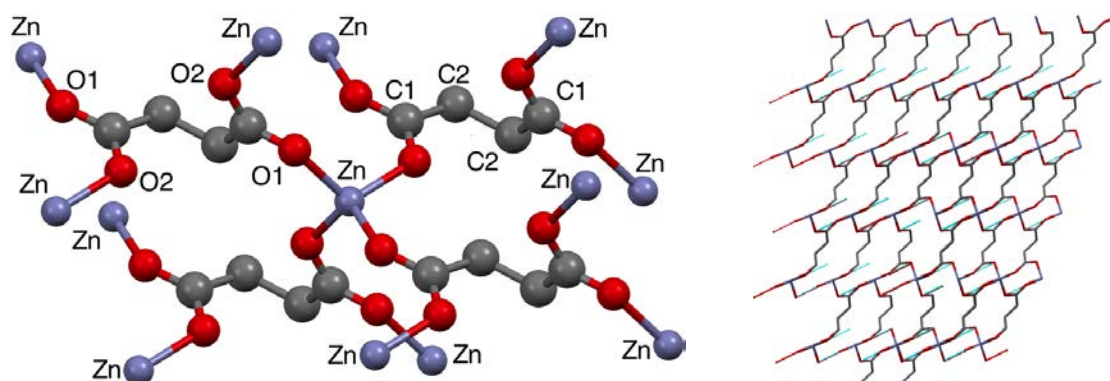


FIGURE 6.6. Compound **4**: Left - View of the coordination environment of Zn (II) atom and the binding of the succinic acid. Right - Propagation of the resulting structural units. Selected bond lengths (in Å) and angles (in deg.): Zn-O2#1, 1.9468(17); Zn-O2#2, 1.9468(17); Zn-O1#3, 1.9484(16); Zn-O1, 1.9484(16); O2-Zn#4, 1.9468(17); O2#1-Zn-O2#2, 106.71(11); O2#1-Zn-O1#3, 108.57(7); O2#2-Zn-O1#3, 115.01(7); O2#1-Zn-O1, 115.02(7); O2#2-Zn-O1, 108.57(7); O1#3-Zn-O1, 103.23(10); C(1)-O1-Zn, 130.20(16); C(1)-O2-Zn#4, 121.43(16); O2-C(1)-O1, 121.4(2); O2-C(1)-C(2), 117.9(2); O1-C(1)-C(2), 120.6(2); C(1)-C(2)-C(2)#5, 114.26(17).

The crystal structure of **3** (Figure 6.5), both in methanol and in water (with no dependence on the solvent observed) and the Zn-CP crystal structure of **4** (Figure 6.6) in water revealed that the compounds **3** and **4** are formed by the assembly of "Zn(Sa)₂(H₂O)₂" (Sa⁻ = salicylate ligand) monomers and of "ZnSu" (Su²⁻ = succinate ligand) arrays respectively, being the Zn(II) atoms six-coordinated (for **3**) with the carboxylate of each Sa⁻ and with the oxygen of two water molecules (similar to compound **1**) and four-coordinated (for **4**) with one carboxylate's oxygen of

four deprotonated Su^{2-} molecules. The OH group of the Sa^- ligand (O3) forms an hydrogen-bond with the oxygen of the carboxylate (O1) and the structure of **3** is propagated through space forming a Herringbone due the hydrogen-bonds between the water molecules (O4) with both the other oxygen of the carboxylate (O2) and the OH group of H Sa ligand (O3) and due to the π -stacking of the rings. In addition, the structure of **4** is assembled by the bridging of Zn(II) atoms through the deprotonated carboxylates of the Su^{2-} .

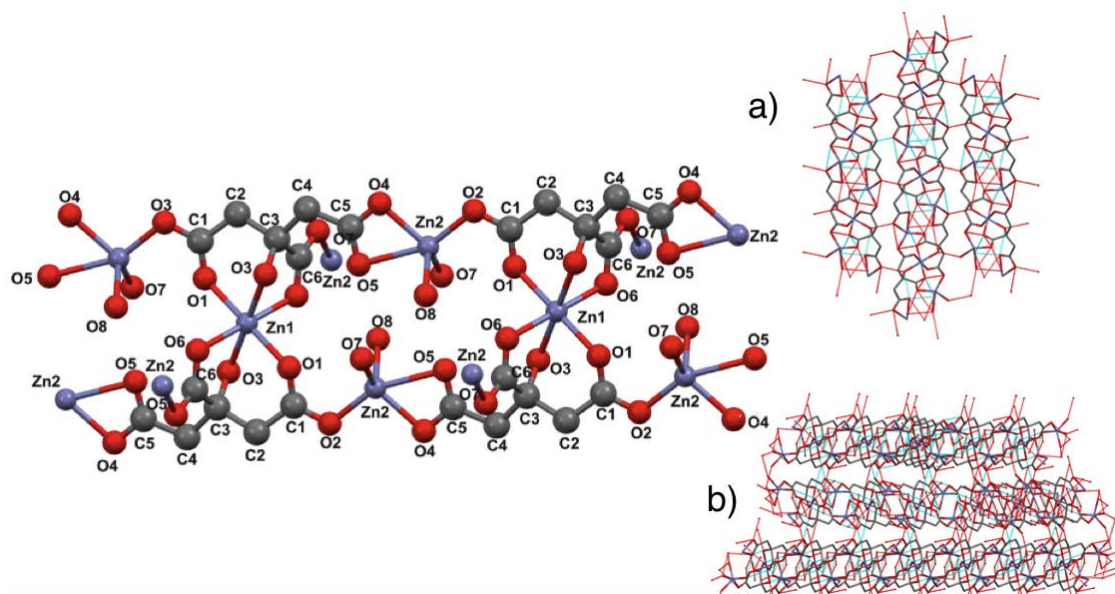


FIGURE 6.7. Compound **5**: Left - Views of the coordination environment of the two different types of Zn (II) atoms [Zn1 and Zn2], the binding of the citrate ligand (Ci_3^-) and the propagation of the resulting structural unit. In this plot the oxygen atoms O3 and O8 belong to the -OH unit of the organic ligand and water molecule, respectively. Hydrogen atoms have been omitted for clarity. Right - Schematic views of the assembly of pillars by strong hydrogen bonds along planes (100) (a) and (001) (b). Selected bond lengths (in Å) and angles (in deg.): Zn1-O1, 2.0861(16); Zn1-O3, 2.0861(16); Zn1-O6, 2.0411(16); Zn2-O2, 1.9797(16); Zn2-O4, 2.0648(17); Zn2-O5, 2.3317(18); Zn2-O4, 2.0648(17); Zn2-O5, 2.3317(18); Zn2-O7, 2.0179 (17); Zn2-O8, 2.0243(18); O1-Zn1-O3, 84.83(6); O1-Zn1-O6, 88.85(7); O3-Zn1-O6, 77.66(6); O2-Zn2-O7, 115.63(7); O2-Zn2-O4, 96.78(7); O4-Zn2-O7, 123.76(7); O4-Zn2-O8, 113.62(7); O5-Zn2-O8, 86.45(7); O5-Zn2-O8, 82.90(7) and O7-Zn2-O8, 102.87(7).

The crystal structure of compound **5**, synthesized in water, revealed that (Figure 6.7) it is a Zn-CP formed by assembly of " $\text{Zn}_3(\text{Ci})_2(\text{H}_2\text{O})_2$ " (Ci_3^- = citrate ligand) arrays, which contain two types of Zn(II) ions (here in after referred to as Zn1 and Zn2). One of them (Zn1) is six-coordinated with the oxygen atom (O3) of the alcohol group of the citrate occupying the axial positions of a slightly distorted octahedron. Two oxygen atoms (O1 and O6) belonging to the central (**B**) and the terminal (**A**) -COO- units of the ligand, respectively, are on two equatorial sites. Since the Zn1 atom is located on an inversion center, the coordination polyhedron is completed by symmetry. The " $\text{Zn}_3(\text{Ci})_2(\text{H}_2\text{O})_2$ " moiety also contains two Zn2-type atoms with a slightly distorted square-pyramidal geometry. The basal plane is defined by: a) the two oxygen atoms (O4 and O5) of the third -COO- unit (**A'**) forming a four-membered chelate ring, (η^2 - mode of binding); and b) the

O2 and O7 atoms of two different carboxylate arrays (**A** and **B**). The Zn2-O(carboxylate) bond lengths, as well as those around Zn1, fall in the ranges reported for other Zn-CPs containing polycarboxylates[240].

6.1.2.2 Thermal study of the precursors

In order to investigate the thermal stability of the compounds **1-5**, TGA experiments were carried out in air between room temperature and 600 °C. The TGA experiments (Figure 6.8) revealed that, for compounds **1** and **2**, their thermal evolution is equivalent, with a difference in terms of thermal stability of the MeOH and H₂O molecules in the first decomposition step (below 140 °C) that produces the temperature and mass discrepancies. For **3**, the first process with a weight loss of *ca.* 10 %, corresponds to its dehydration (theoretically 9.6 %) and the second (*ca.* 5 %) to an OH loss. Above 250 °C, degradation proceeds in two steps, which can be ascribed to the evolution of the two rings. At $T > 510$ °C, the overall weight lost is *ca.* 79 %, fairly consistent with that expected (78.3 %) for the conversion of **3** into zinc oxide.

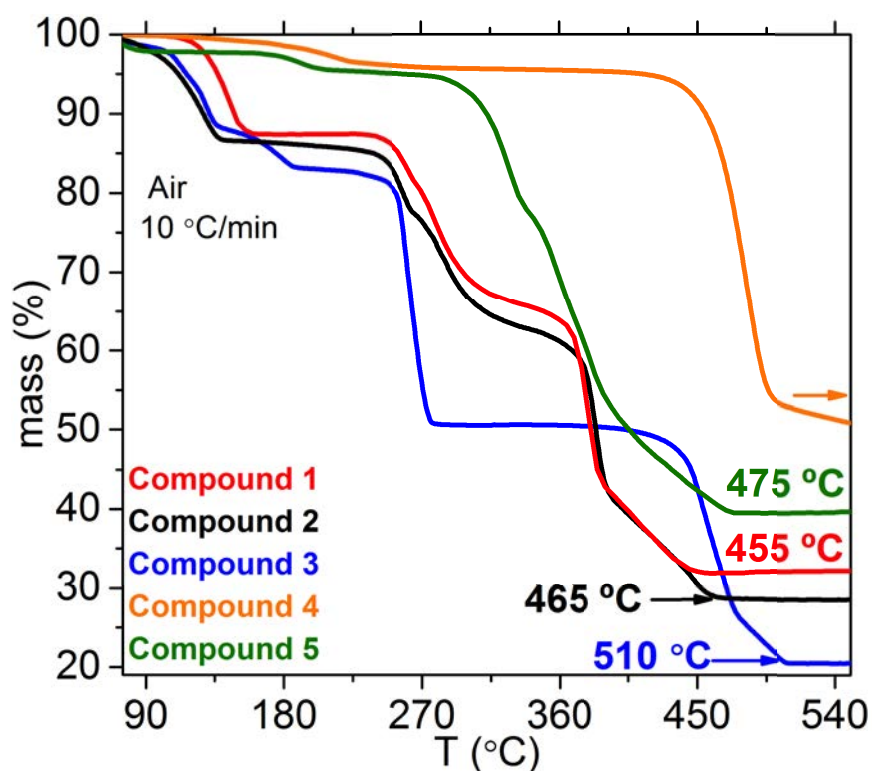


FIGURE 6.8. TGA curves for the compounds **1-5**. Temperatures where a flat TG is achieved is shown as an inset, as well as the final %mass and the corresponding ZnO %mass for each compound.

An important decomposition that lasts *ca.* 50 °C step arises for the compound **4** at *ca.* 450 °C with a *ca.* 40 % weight loss that can be ascribed to the succinate ligand decomposition and ZnO formation, since the final mass that corresponds to the ZnO % weight calculated. The TGA analyses of **5** revealed that the first process, with a weight loss of *ca.* 6.1 %, corresponds to its

dehydration (theoretically 5.9 %). Above 300 °C, degradation proceeds in several consecutive steps, which, according to the literature, can be ascribed to the formation and evolution of CO₂ and water commonly observed for other zinc carboxylates[286]. At T > 475 °C, the overall weight lost is *ca.* 59.8 %, fairly consistent with that expected (60.0 %) for the conversion of compound **5** into zinc oxide. The discrepancy between the final %mass and the calculated ZnO %mass corresponding to each precursor fits the 1-2 %mass error of the TG apparatus. The solids obtained after calcine the precursors at 550 °C were studied by XRD and elemental analysis. As shown in Figure 6.9, the XRD patterns match with the standard pattern of the typical wurtzite structure of ZnO (JCPDS No.36-1451). The sharp diffraction peaks suggested a good crystallinity of the ZnO particles, and peaks due to impurities were not observed. Furthermore, elemental analyses (C and H) of these calcined materials revealed extremely low contents of C and H, practically within the experimental error ranges, thus suggesting that **1-5** produce highly pure ZnO. Although precursor **3** presents a flat TGA curve at 510 °C, while lower temperatures are needed for **1**, **2** and **5** precursors, achieves the higher crystal size (28 nm) and almost three times lower concentration of carbon dopant at 550 °C.

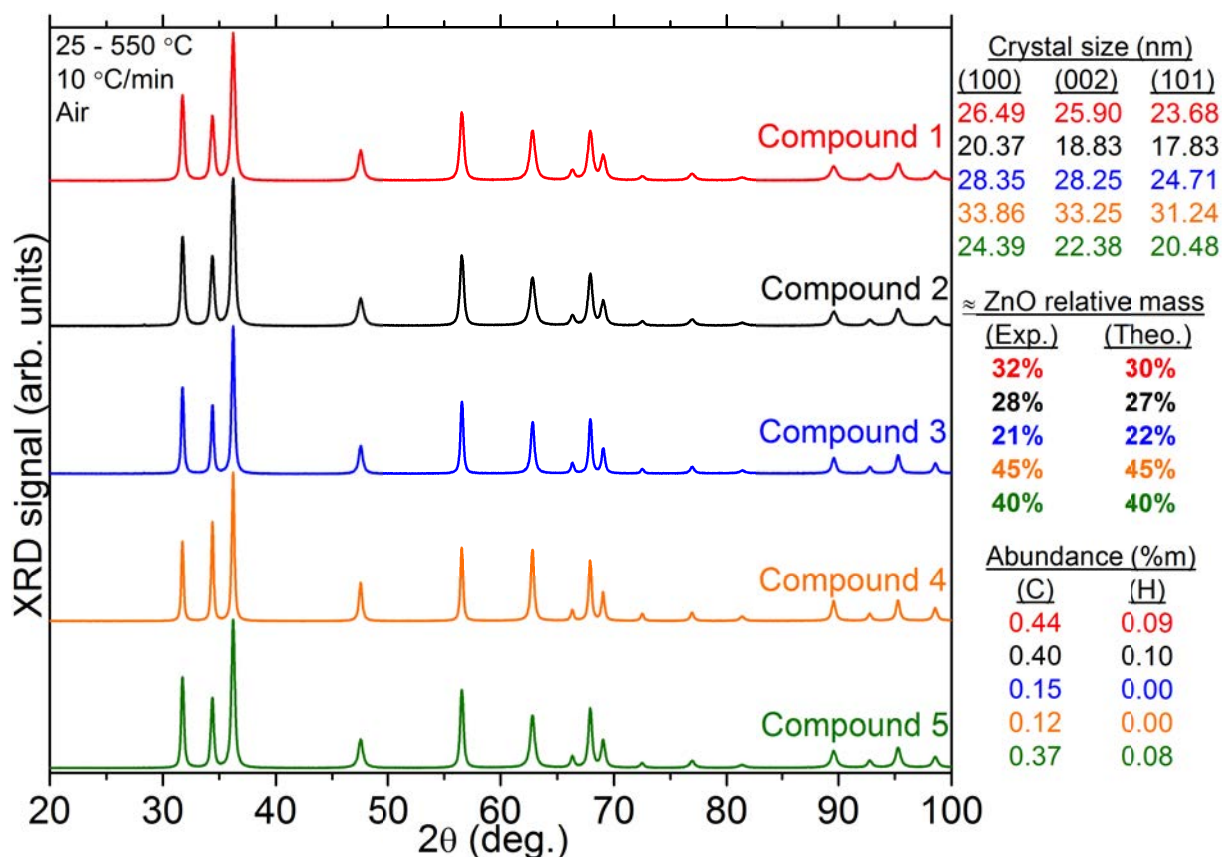


FIGURE 6.9. XRD curves for the ZnO precursors. The carbon and hydrogen atom concentrations are shown as an inset.

6.1.2.3 Thermal study of the inks

Once it has been demonstrated that these compounds have a non-toxic decomposition process leading to a flat TG curve and with a significant decrease in impurities of the resultant ZnO at temperatures up to 150 °C below the 600 °C, comparing to the nitrogen-based precursors (the three major problems of using those nitrogen-based ZnO precursors), it can be confirmed that the present compounds can be suitable for printing. Since it has to be a *green* synthesis (see section 2.4) the solubility is tested first in water and then in ethanol (if solubility in water is scarce). After testing in several solvents with no additives, compounds **2** and **3** were chosen (also due to the fact that single crystals of these compounds, and contrary to the other compounds, can be obtained abundantly in a few days) and inks were prepared in water (for compound **2**, with a solubility of 0.06 g/mL; **Ink-1**) and in ethanol (for compound **3**, with a solubility greater than 0.3 g/mL; **Ink-2**) obtaining transparent inks using no additives.

In order to decrease even more the ZnO temperature conversion and their availability for printed electronics applications as a substituent of nitrogen-based precursors, their thermal decomposition at various heating rates and dwelling times were deeply studied and several experiments were performed. Even though the idea is to print the prepared inks, the aim of this previous study is to analyze the ZnO formation after a thermal decomposition process. To do so, there is no need for printing more than for drop-coating them on a 2×2 cm² glass substrate, thus avoiding the use of unnecessary amounts of cartridges, preventing waste (energy and residues) and senseless expenses. The drop-coated films are then submitted to a thermal treatment in an oven applying a series of concrete Maximum Temperatures (MTs), Heating Rates (HR) and Dwell Time (DwT) at that MT.

The IR results of the **Ink-1** at various MT, HR and DwT are presented in Figure 6.10. On the one hand, a marked absorption band around 440-490 cm⁻¹ is easy to distinguish and it can be related to crystalline ZnO stretching[3]. On the other hand, the double peak at approximately 1600 cm⁻¹ and 1400 cm⁻¹ is due to the presence of the carboxylate group and is generated by the asymmetric and symmetric stretching as shown in the figure³. At 350 °C crystalline ZnO arise while the carboxylate doublet still appears very deep (although is shrinking). This tendency is also seen at higher temperatures and the carboxylate doublet almost disappears at 550 °C. Apart from the MT factor, it can be seen that the DwT and the HR also affect the formation of ZnO, being the longest DwT (+ 20 min) and the slowest HR (5 °C/min) more favourable. Additionally, a shift to higher frequency of the ZnO peak can be observed from 440 cm⁻¹ to 490 cm⁻¹. The same comparison between IR spectra is shown for **Ink-2** in Figure 6.11. In this case, the presence of crystalline ZnO cannot be confirmed at 350 °C. At this temperature absorption bands produced by the phenol group can be identified as an overlapping with the carboxylate doublet 1600 cm⁻¹-1400 cm⁻¹. Absorption peaks around 1200 cm⁻¹ can be related to C-O stretching of the phenol group.

³K. Nakamoto, *Infrared and Raman Spectra of Inorganic and Coordination Compounds*, (5th Ed.), Wiley, New York, USA, 1997

The characteristic ZnO band starts to appear at 450 °C, where it is relatively intense compared to the other absorption bands. Similarly as with **Ink-1**, both HR and DwT, contribute to the ZnO formation, being a long DwT the more characteristic aspect. At 550 °C ZnO absorption is almost the only contribution to the IR spectra. The Zn-O band also suffers a shift, although the range is shorter and the frequencies of the peak are lower than in the case of **Ink-1**. Therefore a loss of coordination is expected but probably the ZnO formed has Zn vacancies in comparison with the ZnO generate **Ink-1**. That fact will be confirmed latter with EDX/EDS analysis.

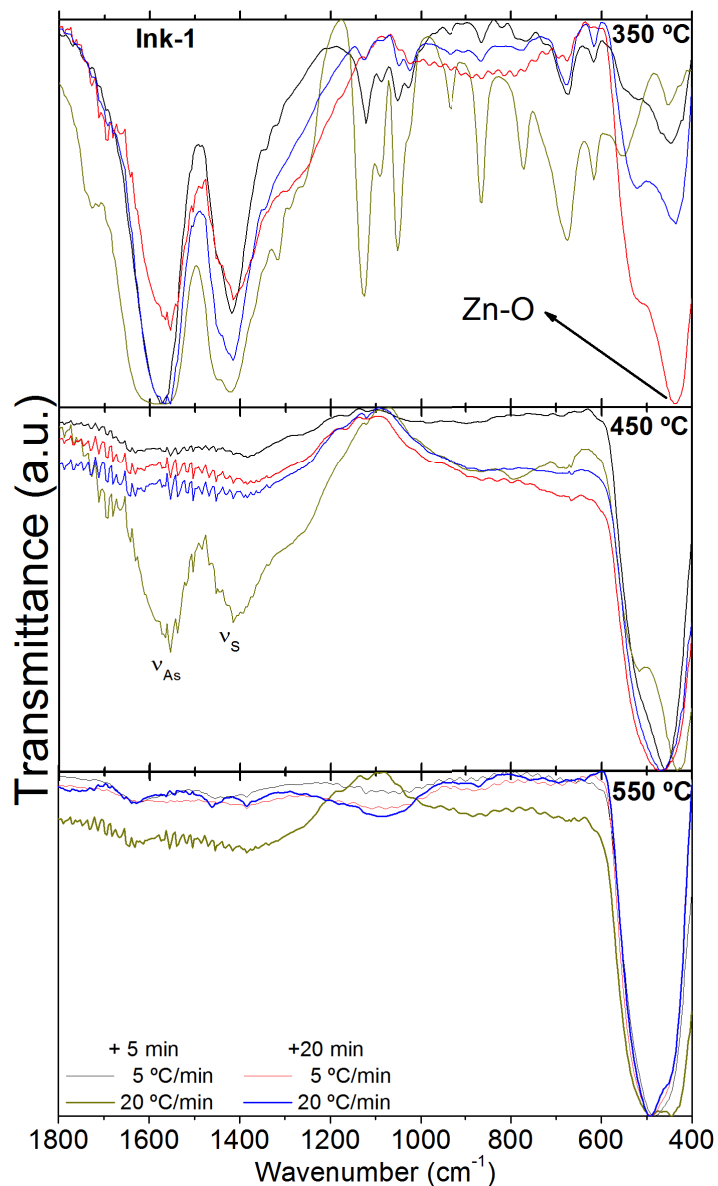


FIGURE 6.10. Infrared spectra of the **Ink-1** (Compound 2 in water) at various MT, HR and DwT.

To be able to quantify the organic residues, Elemental Organic Analysis EOA are required. Figures 6.12 and 6.14 show the C and H contents after each treatment. For **Ink-1**, high concen-

trations of organic residues are found at 350 °C (around 25 % of C and above 1.7 % of H), however an important decrease of C and H content is observed at 450 °C with a DwT of 20 min instead of 5 min or by slowing down the HR, reaching 0.34 % C and a percentage of H below the quantification limit (0.2 %) with HR = 5 °C/min and DwT = 20 min. At 550 °C H content is below 0.2 % for all treatments while for carbon content is also below 0.2 % for the two thermal treatments with DwT = 20 min and near 0.2 % for the remaining films with DwT = 5 min (0.3 % and 0.4 % for HR = 5 °C/min and 20 °C/min respectively). This results explain the shrinking of the carboxylate doublet at 450 °C (Figure 6.10) and its relation with the huge decrease of C and H content.

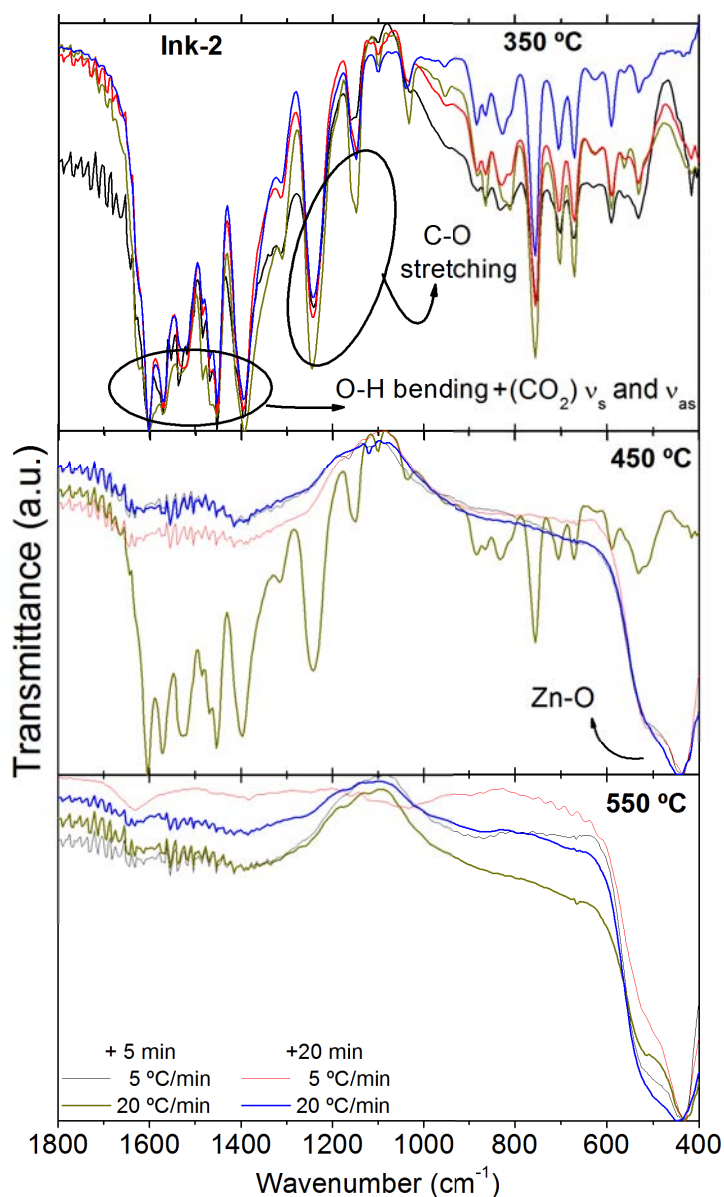


FIGURE 6.11. Infrared spectra of the **Ink-2** (Compound **3** in ethanol) at various MT, HR and DwT.

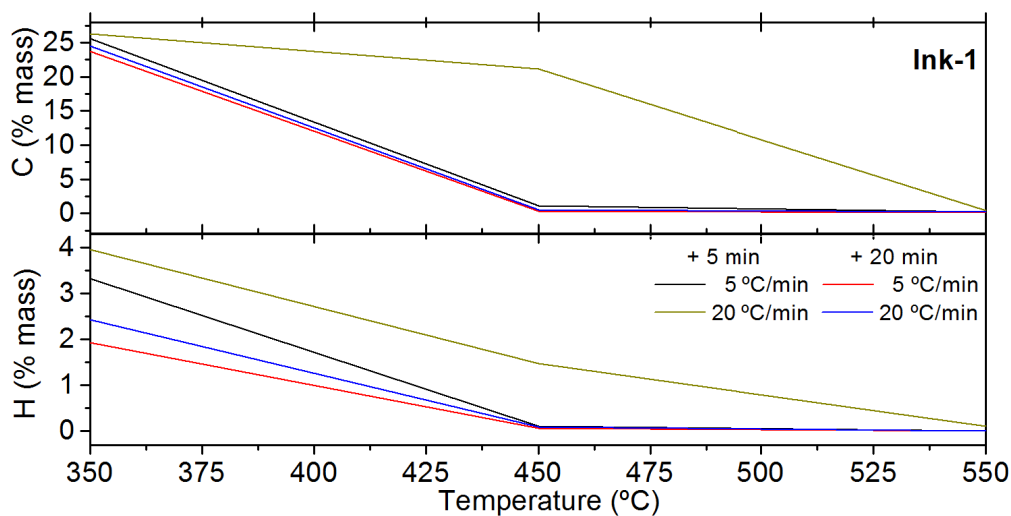


FIGURE 6.12. Elemental Analysis of **Ink-1** at various MT, HR and DwT.

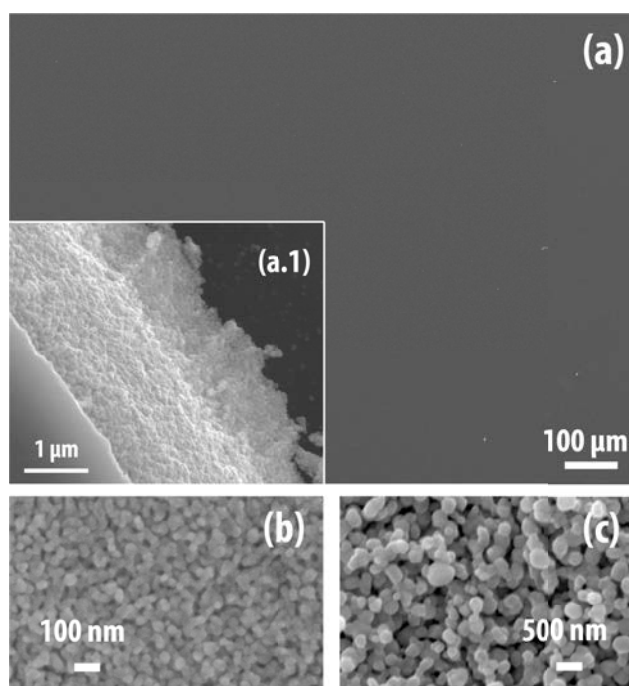


FIGURE 6.13. SEM micrographs for thermal treated **Ink-1** (HR = 5 °/min, DwT = 20 min) film at MT = 450 °C (a), where a.1 shows the crack in the edge of the film. The morphology inside de bubbles at (b) MT = 450 °C and (c) MT = 550 °C, are also shown.

As expected from the IR spectroscopy of **Ink-2**, the carbon and hydrogen content follow a similar behaviour as with **Ink-1**. The decreasing of C and H at 450 °C can be related to the decomposition of the precursor, when big organic groups evolve. A decrease in the HR and an increase in the DwT improves the ZnO purity at each MT. In general, organic content for each treatment is slightly higher than for **Ink-1**, although values < 0.2 % for C and H are also achieved

at 550 °C. Finally, film homogeneity and surface morphology have been studied by SEM (Figures 6.13 and 6.15).

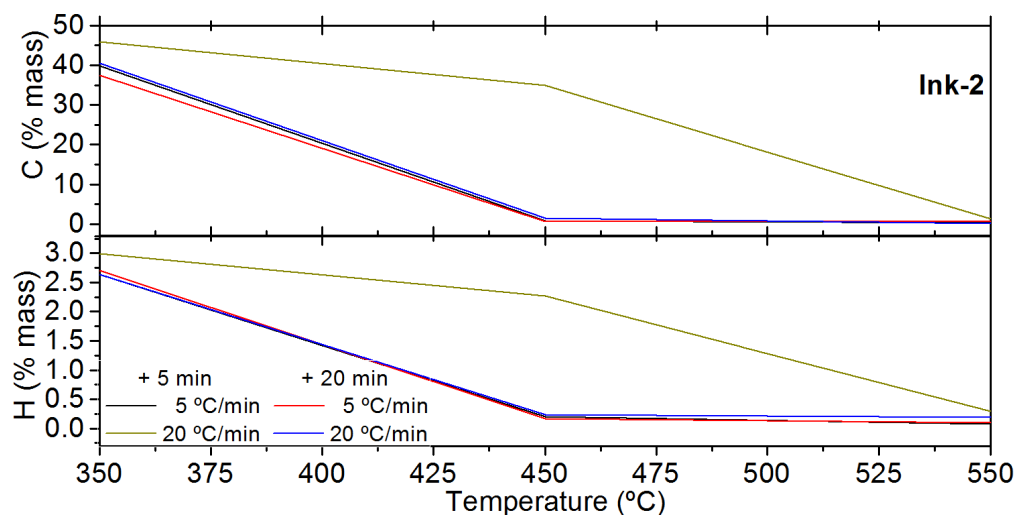


FIGURE 6.14. Elemental Analysis of **Ink-2** at various MT, HR and DwT.

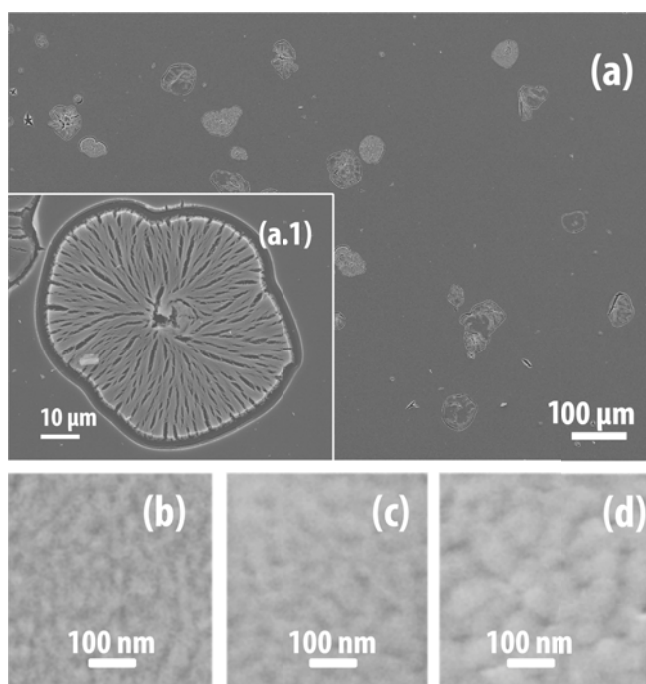




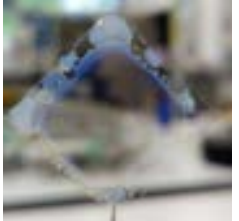






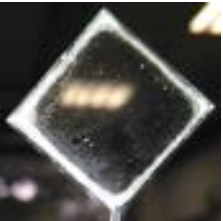

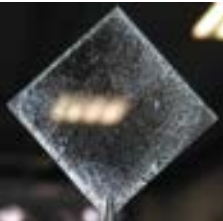
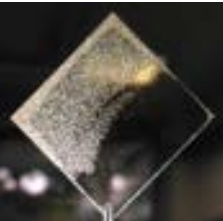
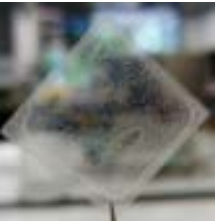
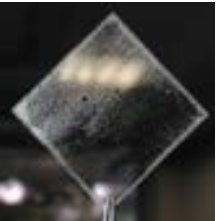
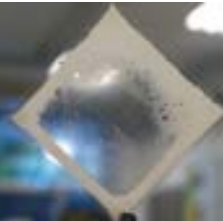
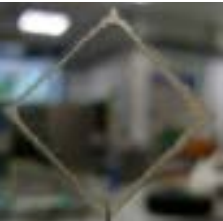
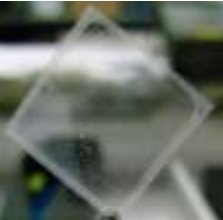

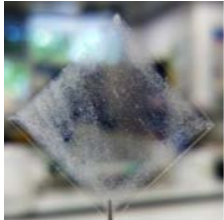


FIGURE 6.15. SEM micrographs for **Ink-2** films (a) annealed at MT= 450 °C with HR = 5 °C/min and DwT = 5min. It is show in detail also the circular-shaped cracks in (a.1). Finally, the morphology of the homogeneous part at (b) 450 °C | 5 °C/min | 5min, (c) 550 °C | 20 °C/min | 5min and (d) 550 °C | 5 °C/min | 5min is also presented.

Table 6.3: Layer images when different HR, DwT and MT are applied to **Ink-1** and **Ink-2** in a $2 \times 2 \text{ cm}^2$ glass substrate.

Ink-1	DwT=5min		DwT=20min	
	5 °C/min	20 °C/min	5 °C/min	20 °C/min
350 °C				
450 °C				
550 °C				
Ink-2	DwT=5min		DwT=20min	
	5 °C/min	20 °C/min	5 °C/min	20 °C/min
350 °C				
450 °C				
550 °C				

Ink-1 leads to a flat film surface (contrary to those ZnO films formed from nitrogen-based precursors) in which big bubbles arise on the edges (Figure 6.13). During the evaporation, a capillary flow towards the edge of the film is induced by the differential evaporation rates across the film, caused by the high surface tension of water, the so-called *coffee-ring* effect. The higher amount of material at the edges is the source of bigger bubbles. Those bubbles burst eventually leaving less material below. When increasing the temperature the in-homogeneity left behind by the small bubbles disappears, indicating a reorganization of the film particles and the reach of a highly homogeneous and flat film except for the edge, where the remaining material is not flat, revealing the bulk morphology. It can be seen that, in the case of **Ink-1**, the film is formed by a dense conglomerate of ZnO spherical crystallites of a diameter of around 30 nm (at 450 °C) that grow up to 100 nm at 550 °C. The homogeneous and flat part of the film appears to be transparent while the roughness of the edge leads to a transmittance loss observed on figures of Table 6.3. The effect of this surface morphology on the optical properties has already been described before[287]. **Ink-2** films only start to present a flat surface when MT is set at 450 °C at least and HR = 5 °C/min (regardless of the DwT) as shown on Figure 6.15. The film homogeneity is broken by circular-shaped cracks of around 50 μm (6.15 a.1). The increase of temperature does not diminish the quantity of circular-shaped cracks and the same happens with the layers not losing the translucency (figures in Table 6.3) when increasing the MT.

On the other side, similarly as with **Ink-1** films, these films are composed by a compact conglomerate of globular ZnO crystallites which grow from 50 nm to 100 nm when increasing temperature and decreasing the HR. The DwT does not affect the grain growth. In EDX/EDS analysis the detection of carbon content is completely misrepresented, because the films have been carbon-coated to increase the conductivity and thus not to distort the image. Hence, the only information able to get is the Zn/O ratio. For both **Ink-1** and **Ink-2** films, the proportion increases with the MT from *ca.* 0.3 to 0.9 (**Ink-1**) and from *ca.* 0.2 to 0.8 (**Ink-2**). This result shows oxygen vacancies that leads to a decrease of Zn(II)-coordination. Moreover, this oxygen deficiency of **Ink-2** compared to **Ink-1** matches with the previous IR deductions. Despite the fact that both inks are very promising, **Ink-1** provides a more interesting performance.

6.1.3 Conclusions

The studies presented in the previous sections of this chapter have shown that carboxylic acids are not only valuable agents to achieve highly pure ZnO through thermal processes, but also to produce Zn(II)-CPs, containing O-donor ligands, which are gaining relevance in view of their applications with specific properties (chemical or physical) in a variety of fields such as in photonics, separation processes, for gas storage, as magnetic materials, homogeneous catalysis, as multimodal biomedical imaging, drug delivery (as lozenges and also exhibiting potent antibacterial activity), as well as precursors of metal oxides and as chemotherapeutic agents[92, 93, 94, 95, 288]. One of the most promising strategies used at present to improve their efficiency is based on the preparation of new Zn(II) derivatives with higher content of Zn (II) than

those used for treatments and, in this context, the Zn-CPs are those with a better perspective.

Unfortunately, some polymeric compounds with high Zn(II) content presented in this chapter did not show the required solubility in water as to evaluate their antibacterial activity in the Institute for Molecular Bioscience (University of Queensland; UQ IMB) and the monomeric products, more soluble than the CPs, showed no activity at all⁴. In order to overcome the solubility problems of the Zn-CPs it is widely accepted that the incorporation of ferrocenyl moieties into the frameworks of potentially bioactive cores commonly modifies the lipophilicity and solubility of the products and in general widens up their biological activity, increasing their interest. The anchorage of ferrocenyl units or the use of ferrocene derivatives as ligands might lead to hetero di- tri or, in general, polymetallic compounds or polymers. In this aspect, Heteropolynuclear (HPN) compounds are attracting a growing interest ([190, 191, 192]) to produce new materials for even more utilizations. For this aspect, the novel ferrocene derivatives are one of the most exciting areas of organometallic Chemistry since they also can be used as active centers in a wide variety of applications (catalysis, biomedicine...) ([193, 194, 195, 196, 197, 198]). One can ask oneself whether is possible to add the individual properties of two metals, Zn and Fe in this case, in a single CP and also whether is there any mutual Zn-Fe cooperation[199]. This approach is called Molecular Hybridization and, in spite of its potential, few Zn-Fe CP are reported ([200, 201]). Thus, the study of the reaction between ZAD and the ferrocenecarboxylic to form an HPN Organometallic Compound (HPNOMC) was the next goal of this work.

The last question would be concerning the viability of the material arising after thermal decomposition of this HPNOMC. In this aspect, the spinel Franklinite [ZnFe_2O_4 or $(\text{Zn,Fe}^{2+})(\text{Fe}_2^{3+}\text{O}_4)$] is recently known to be a p-type semiconductor with a bandgap of 1.96 eV ([289]) and, depending on the Fe valence, to have magnetic properties as well[290]. It is used in energy engineering and environmental sciences[291] to produce H_2 gas upon visible-light irradiation in aqueous suspension or to degrade organic pollutants, thus absorbing up to *ca.* 40 % of the solar radiation. For this purpose, a novel HPNOMC based on Zn and Fe atoms was synthesised in order to be studied as a precursor of a material with magnetic[292, 293], sensing ([294, 295, 296, 297]) or energy engineering[298, 299] applications. Efforts the HPNOMC synthesis, characterization and Franklinite-ZnO production will be presented in the next section of this chapter.

6.2 Zn(II)-Fe(II or III) HPNOMC

6.2.1 Procedure

6.2.1.1 Materials and methods

Ferrocenecarboxylic acid was purchased from Aldrich and used as received. Sodium ferrocenecarboxylate (hereinafter referred to as NaFcCOO) was prepared as described previously⁵.

⁴The bacteria *E. coli*, *K. pneumoniae*, *A. baumannii*, *P. aeruginosa*, *S. aureus* (MRSA) and the fungus *C. neoformans* and *C. Albicans* were used for testing.

⁵*Gmelin Handbuch der Anorganische Chemie. Eisen Organische Verbindungen*, Springer-Verlag, Berlin, Germany, vol.A3, p.58, 1976.

Elemental analyses (C and H) were carried out using the Thermo EA Flash 2000 (Thermo Scientific, Milan, Italy) equipment working in standard conditions (helium flow: 140 mL/min; combustion furnace at 950 °C; chromatographic column oven at 65 °C). Mass spectra were obtained with a VG-Quattro Fission Instrument using 3-nitrobenzylalcohol (NBA) as matrix. Infrared spectra were recorded in the range 4000-400 cm^{-1} with a Nicolet Impact 400 instrument using KBr pellets. The morphology was observed by scanning electron microscopy (SEM) with a JEOL JSM-7100F. X-ray diffraction (XRD) measurements were carried out with a PANalytical X'Pert PRO MPD Alpha1 powder diffractometer in Bragg-Brentano $\theta/2\theta$ geometry with $\text{CuK}\alpha_1$ radiation ($\lambda = 1.5406 \text{ \AA}$).

^{57}Fe Mössbauer spectrum was acquired at room temperature using a conventional transmission Mössbauer spectrometer with a $^{57}\text{Co}/\text{Rh}$ source. The source was moved at constant velocity and the γ counts were collected in a 512 multichannel analyzer. Velocity calibration was done using a 25- μm thick metallic Fe foil. To study the thermal evolution of the inks, thermogravimetric (TGA), and differential scanning calorimetry (DSC) analyses were done in dry air and pure nitrogen atmospheres (flow rate of 50 mL/min) at a heating rate of 10 °C/min up to 700 °C in uncovered alumina and aluminium pans, respectively. We used the TGA-851e and DSC-822e apparatus of Mettler-Toledo. Complementary Evolved Gas Analysis (EGA) of the evolved species during ink decomposition was done in vacuum at 20 °C/min up to 700 °C, using a MKS quadrupole mass spectrometer (Microvision Plus).

6.2.1.2 Synthesis and crystal resolution

For the synthesis of the HPNOMC (hereinafter referred to as compound **6**), 0.5 g of ZAD (2.3×10^{-3} mol) were dissolved in 6 mL of methanol and mixed with an equimolar amount of NaFcCOO (0.58 g, 2.3×10^{-3} mol) in 12 mL of methanol. The dissolved NaFcCOO was added dropwise to the dissolved ZAD. An orange prism-like specimens of **6** appeared after 2 weeks with a slow evaporation of the solvent (Figure 6.16). One of these orange-prism-like specimens of **6** ($\text{C}_{66}\text{H}_{62}\text{Fe}_6\text{O}_{17}\text{Zn}_4$) of size $0.132 \times 0.088 \times 0.076 \text{ mm}^3$ was used for the X-ray crystallographic analysis. The X-ray intensity data were measured on a D8 Venture system equipped with a multilayer monochromator and a Mo microfocus ($\lambda = 0.71073 \text{ \AA}$). The frames were integrated with the Bruker SAINT software package using a narrow-frame algorithm. The integration of the data using a triclinic unit cell yielded a total of 18071 reflections to a maximum θ angle of 30.58° (0.70 \AA resolution), of which 18071 were independent (average redundancy 1.000, completeness = 99.7 %, $R_{\text{sig}} = 5.61$ %) and 12751 (70.56 %) were greater than $2\sigma(F^2)$. The final cell constants of $a = 11.2507(4) \text{ \AA}$, $b = 15.8537(7) \text{ \AA}$, $c = 17.7612(8) \text{ \AA}$, $\alpha = 81.417(2)^\circ$, $\beta = 72.822(2)^\circ$, $\gamma = 78.304(2)^\circ$, volume = $2950.3(2) \text{ \AA}^3$, are based upon the refinement of the XYZ-centroids of reflections above $20 \sigma(I)$. Data were corrected for absorption effects using the multi-scan method (SADABS). The calculated minimum and maximum transmission coefficients (based on crystal size) are 0.6416 and 0.7461. The structure was solved and refined using the Bruker SHELXTL Software Package, using the space group P -1, with $Z = 2$ for the formula unit, $\text{C}_{66}\text{H}_{62}\text{Fe}_6\text{O}_{17}\text{Zn}_4$. The final

anisotropic full-matrix least-squares refinement on F^2 with 839 variables converged at $R_1 = 3.14\%$, for the observed data and $wR_2 = 8.10\%$ for all data. The goodness-of-fit was 1.003. The largest peak in the final difference electron density synthesis was $2.281 \text{ e}^-/\text{\AA}^3$ and the largest hole was $-0.993 \text{ e}^-/\text{\AA}^3$ with an RMS deviation of $0.118 \text{ e}^-/\text{\AA}^3$. On the basis of the final model, the calculated density was 1.940 g/cm^3 and $F(000)$, 1740 e^- .

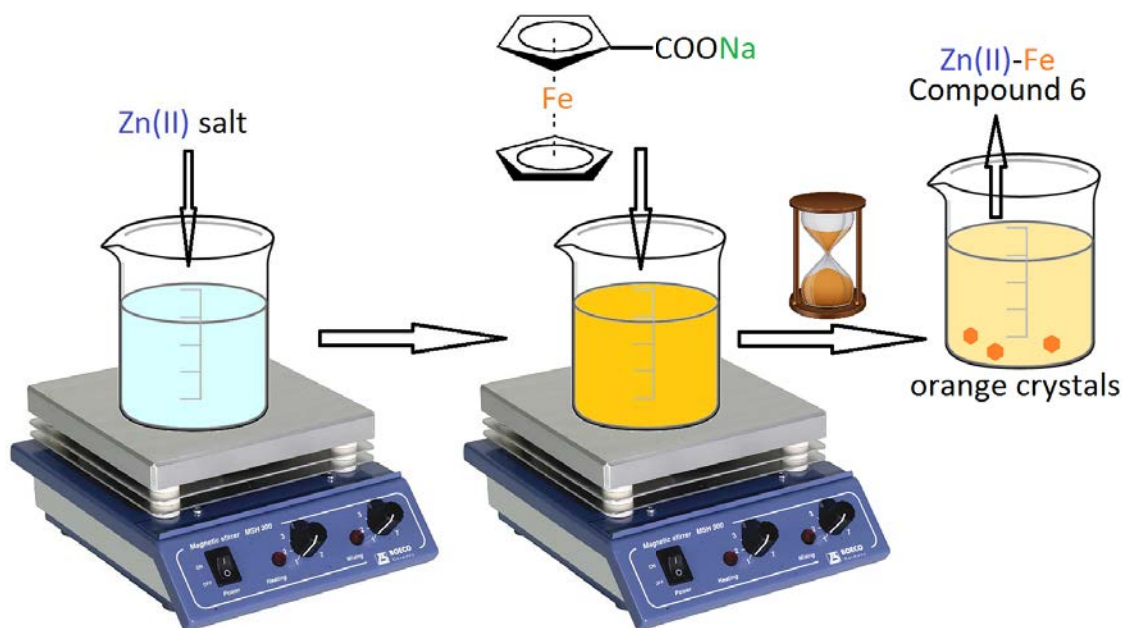


FIGURE 6.16. Scheme of the **HPNOMC** synthesis (compound **6**).

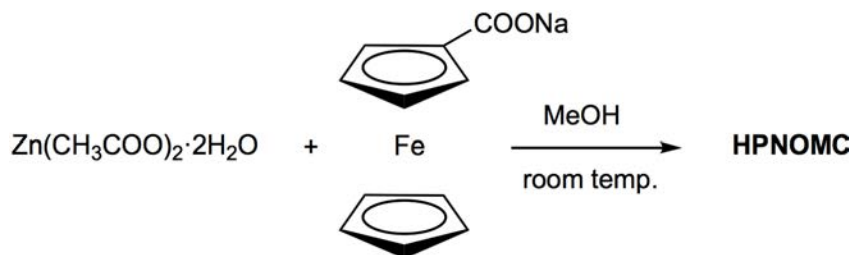


FIGURE 6.17. Reaction scheme of the compound **6** (**HPNOMC**).

6.2.2 Results and discussion

6.2.2.1 Characterization of the HPNOMC

The reaction between ZAD and sodium ferrocenecarboxylate in a 1:1 molar ratio in methanol at room temperature produced, after slow evaporation of the solvent bright orange crystals of compound **6** (Figure 6.17). The compound **6** was characterized by IR spectroscopy (figure 6.18), single-crystal X-ray diffraction, ^{57}Fe Mössbauer spectroscopy (figure 6.19), elemental analysis and mass spectrometry. IR spectra (6.18) of the sodium ferrocenecarboxylate and of compound **6** show some interesting bands in the range $1600\text{-}1400 \text{ cm}^{-1}$ attributed to the carboxylate ligands.

The widening of the bands of compound **6** with respect to the ferrocenecarboxylate salt may be due to the fact that now FcCOO units are bridging at least 2 Zn(II) atoms. Elemental analysis found for compound **6** shows a C content of 46.0 % and an H content of 3.6 % is consistent with the calculated from the formula $C_{66}H_{62}Fe_6O_{17}Zn_4$ (Molecular Weight = 1723.73 g/mol): C, 46.4 % and H, 3.4 %. Mass spectrometry confirmed the molecular weight (M) of *ca.* 1700 m/z and other peaks assigned to $M-(H_2O)_n$ and $M-(CO)_n$. It is well-known that the ^{57}Fe Mössbauer spectroscopic study of ferrocene derivatives is a very useful tool to elucidate the effects induced by the substituents upon the electronic environment of the iron(II) nuclei[300, 301, 302]. The spectrum is depicted in Figure 6.19 and hyperfine parameters for **6**, are presented in Table 6.4 together with those of ferrocene and its mono- or 1,1'-dicarboxylic acids.

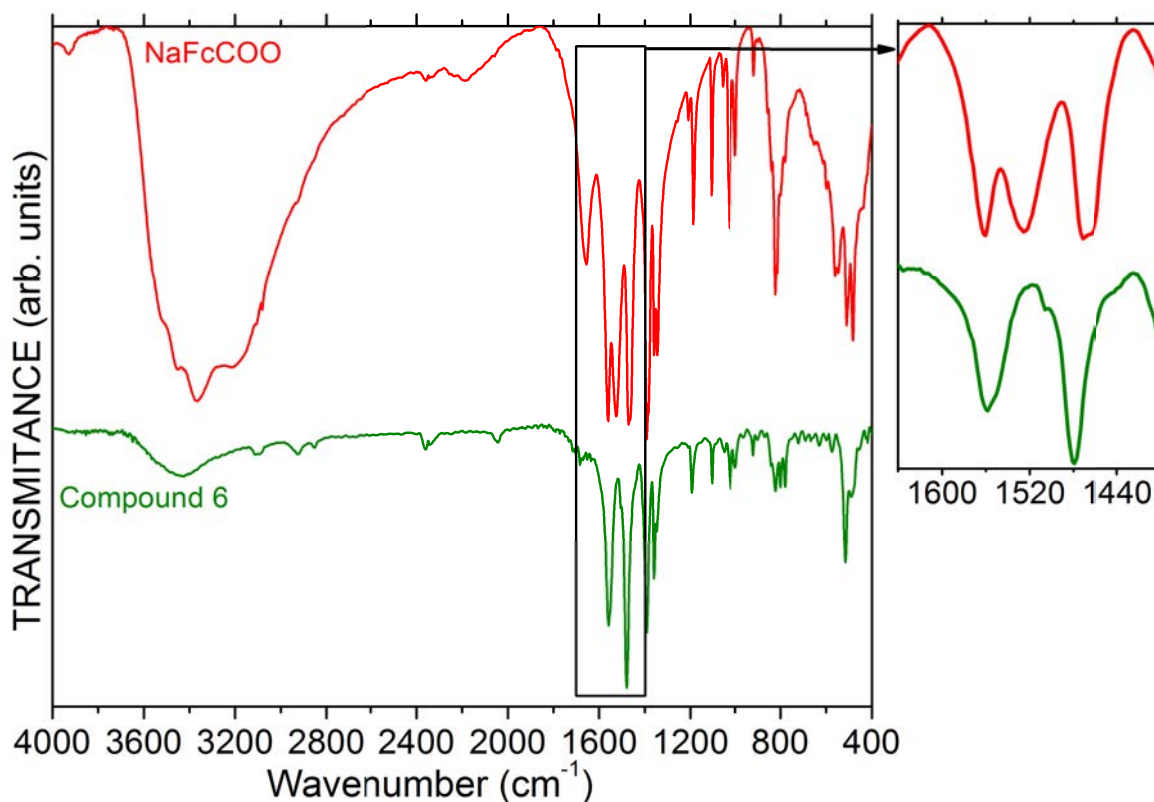


FIGURE 6.18. The IR spectra of the sodium ferrocenecarboxylate and of compound **6**.

The spectrum at 298 K consists of a single quadrupole doublet. The two components exhibited no asymmetry and their full width at half-height (Γ) is even smaller than the value reported for ferrocene. These findings indicate a unique iron site and that the tiny differences in the structural parameters, conformation and orientation of the pentagonal rings of the six organometallic arrays are not relevant enough as to produce any significant effect in the Mössbauer spectrum. The isomeric shift (*i.s.*) obtained for **6** falls in the typical range reported for ferrocene derivatives (Table 6.4). It is widely accepted that electron-donating substituents cause an increase in the

quadrupolar splitting parameter (ΔE_q) relative to ferrocene, whereas electron-withdrawing groups have the opposite effect[300, 301, 302]. For compound **6**, ΔE_q is smaller than that of the ferrocenecarboxylic acid, and quite similar to that of the imine: Fc-C(Me)=N-(C₆H₄-4Me), thus suggesting that the binding the Zn²⁺ produces a decrease of the electron withdrawing effect in relation to that of the COOH group of the ferrocenecarboxylic acid. In fact, according to the ΔE_q , the values are comparable to that of the -C(Me)=N-(C₆H₄-4Me).

Table 6.4: ⁵⁷Fe Mössbauer Hyperfine Parameters: isomer shift, *i.s.*, quadrupole splitting, ΔE_q , and full-width at half-height, Γ (in mm/s) for compound **6**. For comparison purposes data for ferrocene and some mono-substituted derivatives at 298 K and are also included (standard deviation parameters are given in parenthesis).

Compound	<i>i.s.</i>	ΔE_q	Γ	Reference
Compound 6	0.479(2)	2.264(2)	0.236(2)	This work
Fc	0.53(2)	2.41(2)	<i>Buscar en art.</i>	<i>a</i>
Fc-COOH	0.52	2.28	0.35	<i>b</i>
Fc-C(Me)=N-(C₆H₄-4Me)	0.44(1)	2.26 (1)	0.26(1)	<i>c</i>

a- B. Corain, B. Longato, G. Favero, D. Ajo, G. Pilloni, U. Russo, F. R. Kreissel, *Inorganica Chim. Acta*, 157, 259-266, 1989.

b- G. Davison, Spectroscopic Properties of Inorganic and Organometallic Compounds, *RSC publishers*, p340, 1995.

c- R. Bosque, M. Font-Bardía, C. López, J. Sales, J. Silver, X. Solans, *J. Chem. Soc. Dalton Trans.*, 747-752, 1994.

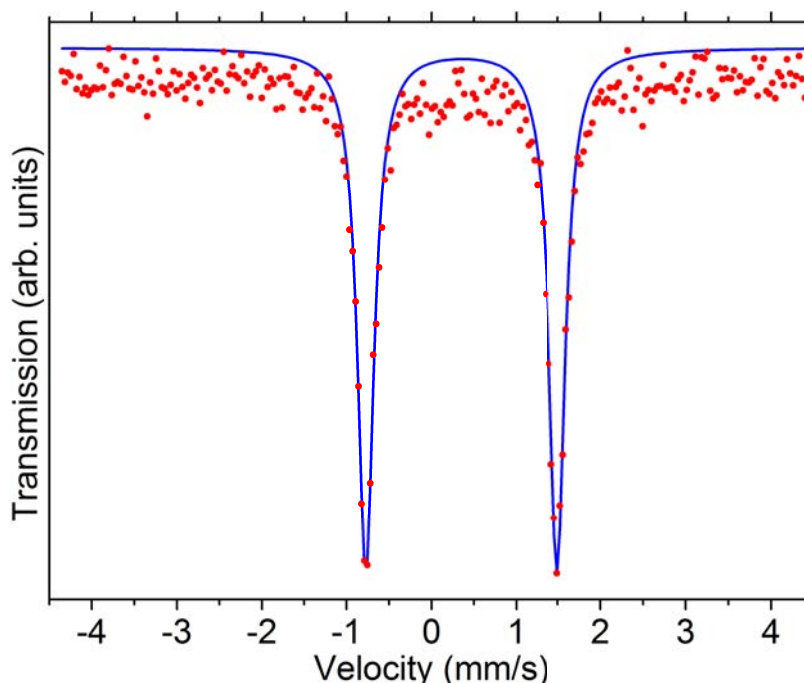


FIGURE 6.19. ⁵⁷Fe Mössbauer spectrum of compound **6** at room temperature.

Crystal structure resolution. Single-crystal X-ray diffraction experiments are useful in solving and describing new crystal structures. In this case crystal structure of compound **6** was also solved (Figure 6.20 - top) showing, in contrast with some CPs previously reported in this work, its non-polymeric nature. The core part of the molecule (Figure 6.20 - bottom left) is devised by a distorted cube formed by the four Zn(II) atoms, two oxygens (O16 and O17) and a water molecule (O14) at the apexes. In addition, another water molecule is confined in the centroid of the cube (O13). Thus, there are two types of Zn conformations depending on whether the Zn is bonded just to one of the water molecules (Zn3) or to both of them (Zn1, Zn2 and Zn4). These different conformations might cause the distortion of the cube. The four Zn(II) are also linked to each other in pairs by means of six Fc-COO units (Figure 6.20 - bottom right) so each pair of Zn atoms, the central water molecule (O13) and the protonated carboxylate ligand form six-membered chelate rings (Figure 6.21).

Moreover, each six-membered chelate ring form distorted boat-type conformations (Table 6.5 show the angle between every pair of these planes) and, although the pentagonal rings of each unit are planar and parallel, every Fc unit differs from another as shown in Table 6.6. Bond lengths and angles of the ferrocenyl units are similar to those reported for most monosubstituted ferrocene derivatives[240, 268]. Two of them, Fc-1 and Fc- 4, deviate by *ca.* 0.3 and 6.5° from the ideal eclipsed conformation (0°) while, in the remaining 4, the arrangement of the rings is intermediate between those expected for ideal eclipsed and the fully staggered conformations (36° - Table 6.6). The metal center separations (Fe···Fe and Zn···Zn) are greater than the sum of the Van der Waals radii[303], indicating that there are no direct interactions between them.

Table 6.5: Angles (in deg.) between every pair of six-membered chelate rings shown in figure 6.21

Plane angles (deg.)	Zn1-Zn2	Zn1-Zn3	Zn1-Zn4	Zn2-Zn3	Zn2-Zn4	Zn3-Zn4
Zn1-Zn2	0	67.8	56.71	58.64	62.91	73.22
Zn1-Zn3	67.8	0	58.51	54.55	77.92	61.69
Zn1-Zn4	56.71	58.51	0	75.61	62.24	62.97
Zn2-Zn3	58.64	54.55	75.61	0	65.76	64.68
Zn2-Zn4	62.91	77.92	62.24	65.76	0	57.65
Zn3-Zn4	73.22	61.69	62.97	64.68	57.65	0

Table 6.6: Tilt and Twist angles (in deg.) for each Fc unit.

Angles (deg.)	Fc-1	Fc-2	Fc-3	Fc-4	Fc-5	Fc-6
Tilt	2.33	1.77	2.94	2.43	0.66	0.44
Twist	0.31	-22.52	12.78	-6.52	14.51	-11.4

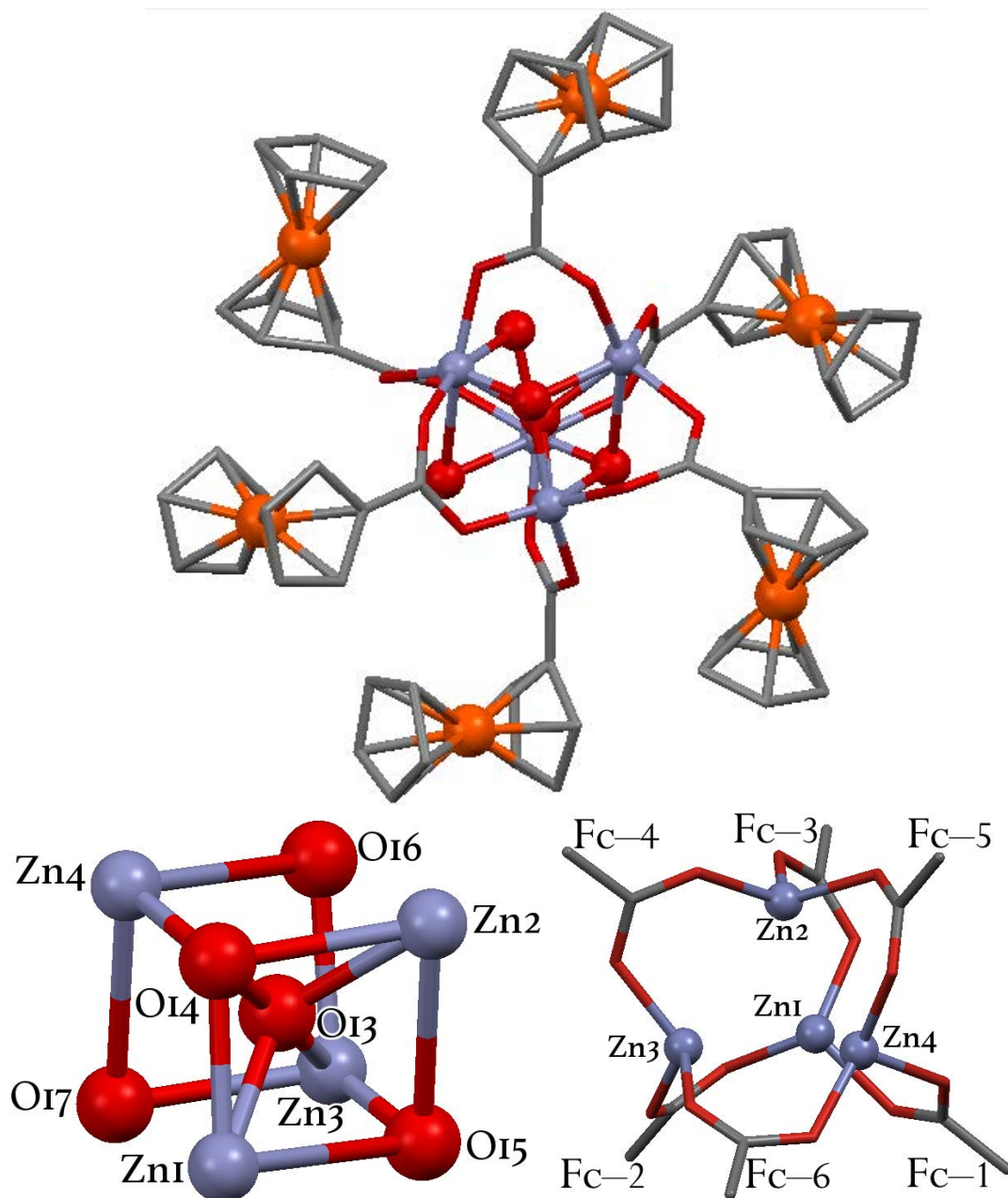


FIGURE 6.20. Crystal structure (top) and core part of compound **6** (bottom). Hydrogen atoms have been omitted for clarity. **Selected bond lengths (in Å) and angles (in deg.):** Zn1-O13, 1.9330(15); Zn1-O14, 2.0091(15); Zn1-Zn4, 3.1006(4); Zn1-Zn2, 3.1291(4); Zn2-O13, 1.9388(15); Zn2-O14, 2.1537(15); Zn2-Zn4, 3.1264(4); Zn2-Zn3, 3.1480(4); Zn3-O15, 1.6526(15); Zn3-O13, 1.9338(15); Zn3-O4, 1.9766(17); Zn3-O16, 2.0572(15); Zn3-O17, 2.1742(15); Zn4-O14, 1.6942(15); Zn4-O13, 1.9271(16); O(13)-Zn(1)-O(14), 43.33(6); O(13)-Zn(1)-Zn(4), 36.49(5); O(14)-Zn(1)-Zn(4), 30.09(4); O(13)-Zn(1)-Zn(2), 36.15(5); O(14)-Zn(1)-Zn(2), 43.04(4); Zn(4)-Zn(1)-Zn(2), 60.243(9); O(13)-Zn(2)-O(14), 41.30(6); O(13)-Zn(2)-Zn(4), 35.91(4); O(14)-Zn(2)-Zn(4), 31.01(4); O(13)-Zn(2)-Zn(1), 36.02(5); O(14)-Zn(2)-Zn(1), 39.55(4); O(13)-Zn(2)-Zn(3), 35.57(4); O(14)-Zn(2)-Zn(3), 76.70(4); Zn(4)-Zn(2)-Zn(3), 61.768(9); Zn(1)-Zn(2)-Zn(3), 61.490(8); O(15)-Zn(3)-O(13), 66.34(7); O(15)-Zn(3)-O(16), 113.52(7); O(13)-Zn(3)-O(16), 68.13(6); O(15)-Zn(3)-O(17), 108.68(6); O(13)-Zn(3)-O(17), 67.10(6); O(16)-Zn(3)-O(17), 94.72(6); O(15)-Zn(3)-Zn(2), 54.25(5); O(13)-Zn(3)-Zn(2), 35.68(5); O(16)-Zn(3)-Zn(2), 60.29(4); O(17)-Zn(3)-Zn(2), 102.63(4); O(14)-Zn(4)-O(13), 46.91(7); O(14)-Zn(4)-Zn(1), 36.48(5); O(13)-Zn(4)-Zn(1), 36.62(4); O(14)-Zn(4)-Zn(2), 40.91(5); O(13)-Zn(4)-Zn(2), 36.16(4); Zn(1)-Zn(4)-Zn(2), 60.330(9).

displace the oxygen, when decompose. On the other hand, experiments in nitrogen produced a more darker residue comparing to that experiment in air. Moreover no iron loss was detected, and thus the TG curve may be consider precise within 1 %. The reaction is slightly endothermic and after 500 °C, the mass indicates that Fe is progressively reducing.

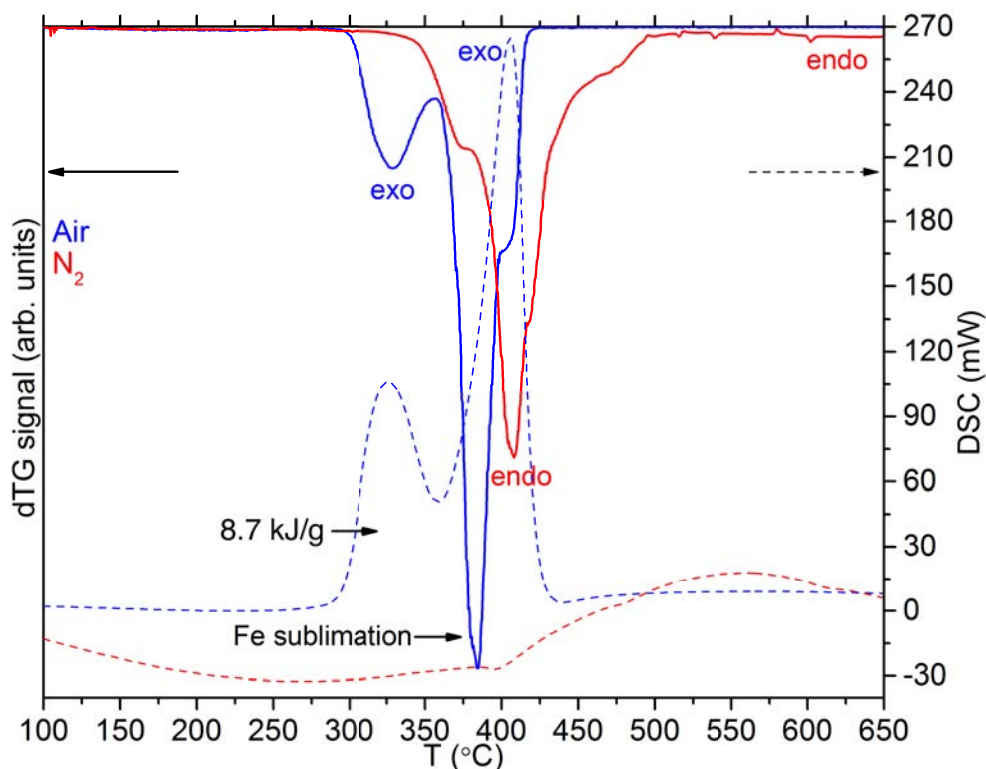


FIGURE 6.22. TGA and DSC curves of compound **6** with a 20 °/min heating rate up to 700 °C in N₂ and dry air.

In order to study the nature of the final materials in both N₂ and dry air, X-ray diffraction experiments were also performed with the residue left after thermally treating the compound **6**. The results are shown in figure 6.23. After carefully perform a phase identification it can be confirmed that traces of Hematite and metallic iron (below 2 %) are present when the compound **6** decomposes in dry air and N₂ respectively. This presence of Hematite (thus producing a Fe₂O₃/ZnFe₂O₄/ZnO nanocomposites) can also be interesting from the photochemical[304], magnetic[305, 306] (also the presence of Fe[307, 308]), energy engineering[309], sensing[310] or photocatalytic[311] point of view. Results also bolster the conclusion that the Franklinite/ZnO ratio after the thermal decomposition of the compound **6** can be controlled by regulating the ambient O₂/N₂ ratio, since the 75 % of the crystal phases are ZnFe₂O₄ and the other 25 % ZnO, while no Franklinite was detected when the calcination was performed in presence of pure N₂ and, in this context, XPS experiments would be useful to ascertain the dependence on the Franklinite's Fe³⁺/Fe²⁺ ratio as a function of the ambient O₂/N₂ ratio when decomposing. Also Electron paramagnetic resonance (EPR) would be useful for studying the magnetic properties of

the resultant material.

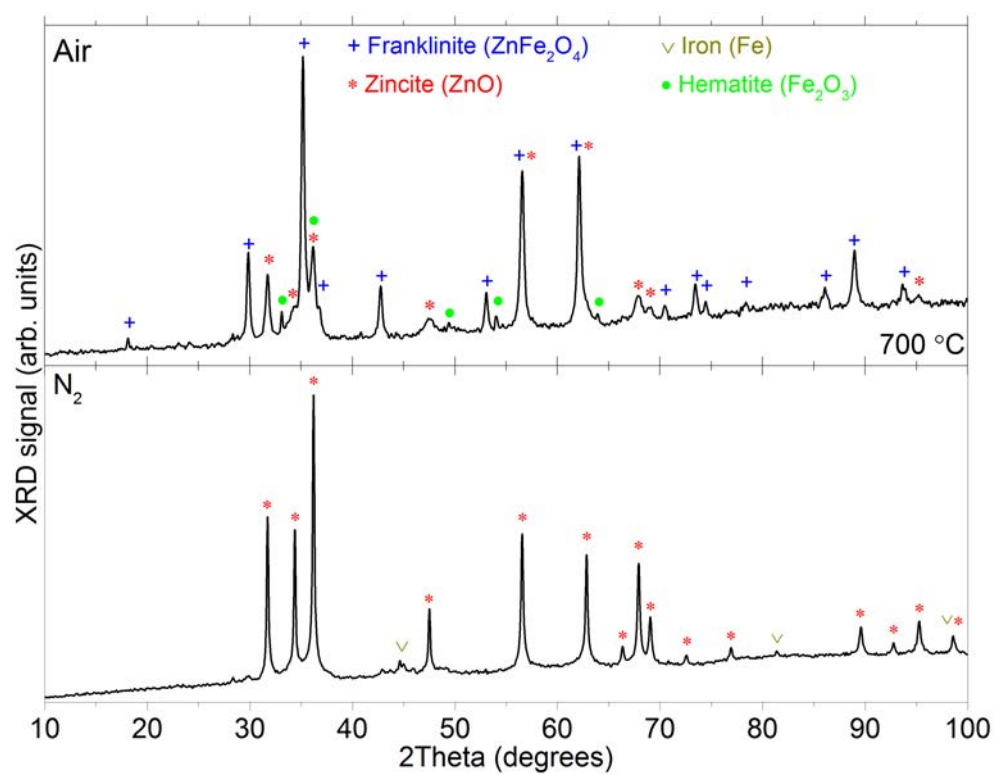


FIGURE 6.23. XRD curves after thermally treating the compound **6** with a 20 °/min heating rate up to 700 °C in N₂ and dry air.

*"The show must go on;
Inside my heart is breaking;
My make-up may be flaking;
But my smile still stays on..."*

- Brian May (Queen) for the song *The show must go on* (1991)

CONCLUSIONS AND HORIZONS

The first chapter of results (Chapter 4) studied in deep the bibliography's most used sol-gel precursor to thermally produce ZnO. The cause of this first study was the need of understanding and putting some order in the processes involved not only in the stability of this precursor but in its thermal decomposition to produce ZnO. After carefully characterize the precursor at room temperature, its thermal evolution was further analysed by looking at the atomic environment of the Zn, C, O and N atoms at different temperatures (up to 600 °C). Modified Auger parameter, calculated from the binding energy of Zn 2p_{3/2} photoelectron peak and the kinetic energy of Zn LM₄₅M₄₅ Auger peak was similar to the one (2010 eV) reported in the NIST database for ZnO, above 250 °C. In addition, the atomic ratio between Zn and N varied from 1 to 5, from room temperature to 180 °C, respectively. From 180 °C to 250 °C, the Zn/N ratio increased above 20 (step C in TGA curves) and some few N remained at the ink at T > 250 °C. Indeed, a weak N_{1s} signal still remained up to 600 °C, concluding that some N atoms were remaining after decomposition even at so high temperatures.

This chapter also shown that degradation is mainly driven by reaction of EA with atmospheric CO₂, and that EA reactivity increases when it is dissolved in ME and, even further, in the EA+ME+ZAD ink. This has been explained by TD-DFT calculations as due to the fact that N and O atoms of deprotonated EA become more nucleophilic in EA+ME and in EA+ME+ZAD, respectively. The diminution of EA concentration in the degraded ink has been seen by EGA and NMR experiments, which also delivered information about the degradation products. Experiments have also shown that reactivity with CO₂ is affected by illumination mainly when the sample contains Zn. In fact, the energy required for the first electronic transition decreases when EA+ZAD comes into contact with ME but CO₂ destabilizes the precursor, acting as assistant during photodegradation. Finally, calculations make clear that the dimmer is less stable under

photoexcitation than the monomer. This is relevant because, in solution, the monomers tend to combine into dimmers. The reaction path of this process has been elucidated. For the first time, degradation of a sol-gel ZnO precursor ink containing EA has been described, and the factors influencing its stability have been detailed.

Gaussian was thus useful in the study of the stability of this precursor and explaining the experimental results on its degradation in presence of light and CO₂: a) clarifying the effects of the binding mode of the AcO⁻ ligand (bidentate in [Zn]₁ and bridging in [Zn]₂) and of the compound nuclearity on the electronic density around the Zn(II) centers, and b) understanding the effect produced by 2-ME, CO₂ and both together on the reactivity and photo-sensibility of the two compounds at room conditions. In addition, experimental studies point out that in the first steps of the thermal conversion of the precursor formed in the reaction of ZAD with EA in ME into the ZnO, cleavage of the Zn-N bond produces the opening of the five-membered chelate ring. This ring-opening process, causing the "-CH₂CH₂NH₂" unit as a pendant arm, may give rise to the cation "C₂H₆N⁺". Its triangular form is proposed as origin of a family of cyclic nitrogenated structures detected in EGA experiments. These results agree with those obtained from the CPMD simulation, that confirms that the Zn-N bond of the chelating ethanolamine is more prone to cleave than the Zn-O of the same ligand.

Moreover, the variations detected in the Zn-O(acetate) bond lengths in the dimer, as well as the distances between the two metal ions, suggested that during decomposition the "[Zn(μ-AcO)₂Zn]" central core underwent significant structural changes. These included the change of the binding mode and hapticity of one of the AcO⁻ ligands to fulfil the coordination sphere of one of the Zn(II) centers after the opening of the five-membered chelate "Zn(O-CH₂CH₂NH₂)". Additional metadynamics simulations provided an overview of the dimmer evolution by the cleavage of the Zn-N bond, the structural changes produced and their effects on the Zn(II)-centers environment. The obtained structures suggest that i) the hydrogen atoms attached to the amino group, and ii) the intermolecular N...H...O interactions in intermediate species, play a key role in the evolution of the initial dimmer and the release of the "C₂H₆N⁺" cations (linear or triangular).

Although the moment of ZnO appearance, the thermal evolution of the crystal size and the purity were studied, among others, the presence of nitrogen at high temperatures as well as the toxic species that were evolving from the precursor when decomposing (NO_x and NH₃) were a serious matter to confront. The aim of the dissertation's next part (Chapter 5) was to investigate the substituent effects in this nitrogen-based ZnO precursor. To do so, up to seven aminoalcohols, with the same ethanolamine's skeleton but with different radical substitutions in concrete places of the aminoalcohol, were used in order to study the dependence of rigidity on the stability and the decomposition process of the precursor. Due to material accessibility, it was decided to experimentally study four of these seven aminoalcohols but to study them all computationally. In addition, three other aliphatic aminoalcohols, replacing the nitrogen protons with methyl groups (methylation), were used for computational purposes to characterize what dependence

these radicals used have on the intensity of the Zn-N bond for different scenarios (environmental and solvation).

Experiments confirmed that the use of any of the aliphatic aminoalcohols in the precursor produce high stability comparing to those using aromatic aminoalcohols, where the degradation occurs within minutes (2-amino-phenol) or hours (2-aminobenzyl alcohol). Moreover, the ZnO generation from the thermal decomposition of these aliphatic-based precursors did not produce any significant change, since a decomposition step was taking place at 250 °C followed by other at 370 °C, in contrast with the case when aromatic aminoalcohols had being used. In that case, an important exothermic decomposition process was showing up at 400 °C. In addition, when the most rigid aminoalcohol (2-amino-phenol) was used, the resultant ZnO did not produce a film, but nanoparticles, due to the reach of a tremendous combustion of the ring at this temperature. Comparing with the ethanolamine-based precursor, the ZnO appearance, from the crystal point of view, was similar to the (S)-(+)-2-amino-3-methyl-1-butanol-based one and the crystal size increased when (S)-(+)-2-amino-1-propanol or 2-aminobenzyl alcohol were used.

Nevertheless from the point of view of the purity, carbon and hydrogen traces fell into the detection capacity of the elemental analysis apparatus for the (S)-(+)-2-amino-1-propanol-based precursor, in contrast with the use of 2-aminobenzyl alcohol, where the carbon and hydrogen concentrations were up to 10 times greater, due to the need for the aromatic ring to be removed. This fact bolstered the conclusion that the aminoalcohol's rigidity was playing an important role, since the only difference between the 2-amino-phenol (no film formation) and 2-aminobenzyl alcohol was an extra elbow generated by a carbon atom between the aromatic ring and the oxygen, absent in the 2-amino-phenol, that was providing a greater flexibility when vibrations, twists and stresses were occurring while decomposing. Using electronic microscopy, it was discovered that the ZnO aspect of the layer was identical in all cases. Although no cracks were sighted, wrinkle-like structures appeared, due to internal tensions, twists and stresses during the decomposition processes. These wrinkles were decreasing in size when increasing the substituent's volume concluding that, indeed, the aminoalcohol's rigidity had a clear effect on the final material's quality. It was additionally confirmed that the use of flexible aromatic stabilizers (*e.g.* 2-aminobenzyl alcohol), could be counterproductive, regarding the poor stability and the ZnO purity, while the aliphatic-based aminoalcohols provide better performances.

Simulations were useful to comparatively study seven different aminoalcohols with the same skeleton of ethanolamine in terms of stability and molecular dynamics at different temperatures. These were, in addition to the five experimentally studied aminoalcohols, a methylated version (*i.e.* replacing the N protons by methyl groups) of the aliphatic aminoalcohols in order to clarify even more the influence of the substituents on the charge distribution, stability properties when bonded to the Zn atom and on the thermal decomposition of that specific aminoalcohol-based precursor. In general, for the six aliphatic-aminoalcohol-based precursors the HOMO was centred in the amino group and the HOMO-LUMO energy difference is much higher than for the uses of

aromatic-aminoalcohols, thus decreasing the probability of photoexcitation and demonstrating the reason of the several experimental behaviours explained before.

Dynamic simulations at different temperatures provided conclusive evidences on the nitrogen prevalence in the precursor even at high temperatures. This fact explained the reason why the final ZnO contained traces of nitrogen, suggesting that the Zn-N bond had effects on the thermal decomposition since, in all cases, this bond was the one with the least tendency to cleave, comparing with the Zn-O (acetate) bonds. Therefore, nitrogen was fulfilling his purpose - this is, intensively bonded to the metal atom to avoid agglomerations - too well, in absence of light and CO₂. For that reason, additives containing nitrogen might not be the best solution to stabilize the metal and to produce pure ZnO (or at least with control on the contamination) at the same time. An additive, as an stabilizer, should not influence the properties of the final material nor cause the release of toxic gases (NO_x and NH₃ in this case).

These conclusions were the *starting shot* for a change in the *game plan*, giving a step to the last part of results of this dissertation (Chapter 6). Since there was no control over the effects these nitrogen-based aminoalcohols, *a priori* innocuous, had on the final and desired material, one cannot settle for this nitrogen-based solution as long as one may desire to increase the number of Zn-O (weaker) interactions at the expense of eliminate the Zn-N bonds (stronger). Moreover, since new precursors had to be designed, it was the perfect opportunity to use the so-popular *Green Chemistry*. Up to five ZnO precursors were synthesised following these principles, solving their crystal structure and studying their thermal decomposition. The starting Zn-based salt used was the acetate and, in order to increase the stability of the transition metal in the precursor, it was decided to resort to natural occurring carboxylic acids such as salicylic, citric, succinic and lactic acids. In addition, two different lactic-based precursors were synthesised and thus two monomers (based on salicylate and lactate) and three polymers (based on succinate, lactate and citrate) were assembled.

Thermal analysis found decomposition processes lasting *ca.* 150 °C less than the required temperature for nitrogen-based precursors. Furthermore these decomposition processes consisted of cleaner steps and purer ZnO (not only the final ZnO did not contained nitrogen at all, but also the carbon and hydrogen contents were falling within the detection limit of the elemental organic apparatus, 0.2 %) with a lower temperature. In addition, the final mass corresponded to the theoretical ZnO mass, assuming that no Zn was sublimating. X-ray diffraction experiments showed crystal sizes of 20 - 35 nm. Two of the five precursors were chosen, taking into account their delay in synthesising and their solubility in common solvents (water and ethanol), to compare the behaviour of inks based on these precursors with the ones based on nitrogen compounds from the previous study. This work showed numerous improvements for the ZnO precursor-based printing technologies. Continuous and homogeneous films of highly pure ZnO were obtained at lower temperatures adjusting the dwell time at the maximum temperature as well as the heating rate with either one of the inks generated and, additionally, with less toxic

evolving gases (mainly CO₂).

At this point, there was only one proposal to make: the addition of new properties to those already existing in this ZnO. Although from an electronic point of view ZnO was highly valued, it was considered interesting to be able to add magnetic properties by including a second metal, iron, without losing sight of the principles of Green Chemistry. Thus, the objective of the last work was to synthesize an heteropolymetallic precursor that, through thermal decomposition, could generate the Franklinite / ZnO tandem with a variable iron content at will by controlling the atmosphere in which this precursor is decomposing. For the synthesis, the same procedure was followed as in the case of the other five "green" precursors. In this case, a carboxylic acid containing iron should be chosen and it had to be extensively used for biological, biochemical or biomedical purposes. The chosen acid was the Ferrocene carboxylic acid. Since it was likely that this acid could hardly interact with zinc acetate, thus entering into contradiction with the principle of green chemistry concerning to maximize the incorporation of all materials in the synthesis, thus preventing residues, a sodium salt was first designed by a technique commonly used by one of the collaborators in this work. Only then the synthesis of this heteropolymetallic compound synthesis could proceed. Doing so, the synthesis was redirected again towards the Green Chemistry.

The result was a success and the crystalline structure of this mixed compound of iron and zinc was solved. The next step, as always, was to study its thermal decomposition, this time depending on the atmosphere. Preliminary results - since these were the last experiments carried out - showed high Franklinite content in comparison to the ZnO was found when the decomposition took place in an oxidizing atmosphere while, on the contrary, a non-existent content of Franklinite was found when the thermal decomposition was performed in a reducing atmosphere. Traces of hematite and metallic iron were also found in the post-decomposition materials using an oxidizing and a reducing atmosphere, respectively. This fact shows that by controlling the atmosphere, the Zn:Fe ratio and, therefore, the potential magnetoelectronic properties could be controlled.

BIBLIOGRAPHY

- [1] S. Madgassi-(Editor), *The Chemistry of Inkjet Inks*.
World Scientific Publishing Co. Pte. Ltd., pp 345, 2010.
DOI: 10.1142/9789812818225_bmatter ; ISBN: 9812818219.
- [2] A. Janotti and C. G. van de Walle, "Fundamentals of zinc oxide as a semiconductor," *Reports on Progress in Physics*, vol. 72, p. 126501, 2009.
DOI: 10.1088/0034-4885/72/12/126501.
- [3] H. Morkoç and U. Özgür, *Zinc Oxide: Fundamentals, Materials and Device Technology*.
Wiley-VCH Verlag GmbH & Co. KGaA, pp 488, 2009.
DOI: 10.1002/9783527623945 ; ISBN: 9783527623945.
- [4] S. E. Harrison, "Conductivity and hall effect of ZnO at low temperatures," *Physical Review*,
vol. 93, pp. 52 – 62, 1954.
DOI: 10.1103/PhysRev.93.52.
- [5] A. R. Hutson, "Hall effect studies of doped zinc oxide single crystals," *Physical Review*,
vol. 108, pp. 222 – 230, 1957.
DOI: 10.1103/PhysRev.108.222.
- [6] A. Janotti and C. G. Van de Walle, "Native point defects in ZnO," *Physical Review B*, vol. 76,
p. 165202, 2007.
DOI: 10.1103/PhysRevB.76.165202.
- [7] A. Janotti and C. G. V. de Walle, "Oxygen vacancies in ZnO," *Applied Physics Letters*, vol. 87,
p. 122102, 2005.
DOI: 10.1063/1.2053360.
- [8] A. Janotti and C. G. V. de Walle, "New insights into the role of native point defects in ZnO,"
Journal of Crystal Growth, vol. 287, pp. 58 – 65, 2006.
DOI: 10.1016/j.jcrysgro.2005.10.043.
- [9] A. Janotti and C. G. Van de Walle, "Native point defects in ZnO," *Physical Review B*, vol. 76,
p. 165202, 2007.
DOI: 10.1103/PhysRevB.76.165202.

BIBLIOGRAPHY

- [10] A. Janotti and C. G. Van de Walle, “Hydrogen multicentre bonds,” *Nature Materials*, vol. 6, pp. 44 – 47, 2007.
DOI: 10.1038/nmat1795.
- [11] M. D. McCluskey, S. J. Jokela, K. K. Zhuravlev, P. J. Simpson, and K. G. Lynn, “Infrared spectroscopy of hydrogen in ZnO,” *Applied Physics Letters*, vol. 81, pp. 3807–3809, 2002.
DOI: 10.1063/1.1520703.
- [12] D. M. Hofmann, A. Hofstaetter, F. Leiter, H. Zhou, F. Henecker, B. K. Meyer, S. B. Orlinskii, J. Schmidt, and P. G. Baranov, “Hydrogen: A relevant shallow donor in zinc oxide,” *Phys. Rev. Lett.*, vol. 88, p. 045504, 2002.
DOI: 10.1103/PhysRevLett.88.045504.
- [13] M. G. Wardle, J. P. Goss, and P. R. Briddon, “First-principles study of the diffusion of hydrogen in ZnO,” *Physical Review Letters*, vol. 96, p. 205504, 2006.
DOI: 10.1103/PhysRevLett.96.205504.
- [14] S. J. Jokela and M. D. McCluskey, “Structure and stability of O-H donors in ZnO from high-pressure and infrared spectroscopy,” *Physical Review B*, vol. 72, p. 113201, 2005.
DOI: 10.1103/PhysRevB.72.113201.
- [15] G. A. Shi, M. Stavola, S. J. Pearton, M. Thieme, E. V. Lavrov, and J. Weber, “Hydrogen local modes and shallow donors in ZnO,” *Physical Review B*, vol. 72, p. 195211, 2005.
DOI: 10.1103/PhysRevB.72.195211.
- [16] C. Jagadish and S. Pearton, *Zinc Oxide Bulk, Thin Films and Nanostructures*. Elsevier Science Ltd, pp 590, 2006.
DOI: 10.1016/B978-008044722-3/50000-2 ; ISBN: 978-0-08-044722-3.
- [17] Y. Varshni, “Temperature dependence of the energy gap in semiconductors,” *Physica*, vol. 34, pp. 149 – 154, 1967.
DOI: 10.1016/0031-8914(67)90062-6.
- [18] D. Look, “Quantitative analysis of surface donors in ZnO,” *Surface Science*, vol. 601, pp. 5315 – 5319, 2007.
DOI: 10.1016/j.susc.2007.09.030.
- [19] M. Larciprete, D. Haertle, A. Belardini, M. Bertolotti, F. Sarto, and P. Günter, “Characterization of second and third order optical non-linearities of ZnO sputtered films,” *Applied Physics B*, vol. 82, pp. 431 – 437, 2006.
DOI: 10.1007/s00340-005-2022-z.

- [20] Ü. Özgür, X. Gu, S. Chevtchenko, J. Spradlin, S. J. Cho, H. Morkoç, F. H. Pollak, H. O. Everitt, B. Nemeth, and J. E. Nause, "Thermal conductivity of bulk ZnO after different thermal treatments," *Journal of Electronic Materials*, vol. 35, pp. 550 – 555, 2006.
DOI: 10.1007/s11664-006-0098-9.
- [21] F. Tuomisto, K. Saarinen, D. C. Look, and G. C. Farlow, "Introduction and recovery of point defects in electron-irradiated ZnO," *Physical Review B*, vol. 72, p. 085206, 2005.
DOI: 10.1103/PhysRevB.72.085206.
- [22] F. Oba, A. Togo, I. Tanaka, J. Paier, and G. Kresse, "Defect energetics in ZnO: A hybrid Hartree-Fock density functional study," *Physical Review B*, vol. 77, p. 245202, 2008.
DOI: 10.1103/PhysRevB.77.245202.
- [23] T. R. Paudel and W. R. L. Lambrecht, "First-principles calculation of the O vacancy in ZnO: A self-consistent gap-corrected approach," *Physical Review B*, vol. 77, p. 205202, 2008.
DOI: 10.1103/PhysRevB.77.205202.
- [24] M. G. Wardle, J. P. Goss, and P. R. Briddon, "Theory of li in ZnO: A limitation for li-based p-type doping," *Physical Review B*, vol. 71, p. 155205, 2005.
DOI: 10.1103/PhysRevB.71.1552056.
- [25] R. A. Laudise and A. A. Ballman, "Hydrothermal synthesis of zinc oxide and zinc sulfide," *The Journal of Physical Chemistry*, vol. 64, pp. 688–691, 1960.
DOI: 10.1021/j100834a511.
- [26] M. A. Verges, A. Mifsud, and C. J. Serna, "Formation of rod-like zinc oxide microcrystals in homogeneous solutions," *J. Chem. Soc., Faraday Trans.*, vol. 86, pp. 959 – 963, 1990.
DOI: 10.1039/FT9908600959.
- [27] L. Vayssieres, K. Keis, S.-E. Lindquist, and A. Hagfeldt, "Purpose-built anisotropic metal oxide material: 3d highly oriented microrod array of zno," *The Journal of Physical Chemistry B*, vol. 105, pp. 3350 – 3352, 2001.
DOI: 10.1021/jp010026s.
- [28] Z. W. Pan, Z. R. Dai, and Z. L. Wang, "Nanobelts of semiconducting oxides," *Science*, vol. 291, pp. 1947 – 1949, 2001.
DOI: 10.1126/science.1058120.
- [29] M. H. Huang, Y. Wu, H. Feick, N. Tran, E. Weber, and P. Yang, "Catalytic growth of zinc oxide nanowires by vapor transport," *Advanced Materials*, vol. 13, pp. 113 – 116, 2001.
DOI: 10.1002/1521-4095(200101)13:2<113::AID-ADMA113>3.0.CO;2-H.

BIBLIOGRAPHY

- [30] B. D. Yao, Y. F. Chan, and N. Wang, "Formation of ZnO nanostructures by a simple way of thermal evaporation," *Applied Physics Letters*, vol. 81, pp. 757–759, 2002.
DOI: 10.1063/1.1495878.
- [31] W. Park, G.-C. Yi, M. Kim, and S. Pennycook, "ZnO nanoneedles grown vertically on Si substrates by non-catalytic vapor-phase epitaxy," *Advanced Materials*, vol. 14, pp. 1841 – 1843, 2002.
DOI: 10.1002/adma.2002900158.
- [32] W. I. Park, D. H. Kim, S.-W. Jung, and G.-C. Yi, "Metalorganic vapor-phase epitaxial growth of vertically well-aligned ZnO nanorods," *Applied Physics Letters*, vol. 80, pp. 4232 – 4234, 2002.
DOI: 10.1063/1.1482800.
- [33] H. Yuan and Y. Zhang, "Preparation of well-aligned ZnO whiskers on glass substrate by atmospheric MOCVD," *Journal of Crystal Growth*, vol. 263, pp. 119 – 124, 2004.
DOI: 10.1016/j.jcrysgro.2003.11.084.
- [34] Y. W. Heo, V. Varadarajan, M. Kaufman, K. Kim, D. P. Norton, F. Ren, and P. H. Fleming, "Site-specific growth of ZnO nanorods using catalysis-driven molecular-beam epitaxy," *Applied Physics Letters*, vol. 81, pp. 3046–3048, 2002.
DOI: 10.1063/1.1512829.
- [35] Y. Sun, G. M. Fuge, and M. N. Ashfold, "Growth of aligned ZnO nanorod arrays by catalyst-free pulsed laser deposition methods," *Chemical Physics Letters*, vol. 396, pp. 21 – 26, 2004.
DOI: 10.1016/j.cplett.2004.07.110.
- [36] J.-I. Hong, J. Bae, Z. L. Wang, and R. L. Snyder, "Room-temperature, texture-controlled growth of ZnO thin films and their application for growing aligned ZnO nanowire arrays," *Nanotechnology*, vol. 20, p. 085609, 2009.
DOI: 10.1088/0957-4484/20/8/085609.
- [37] W.-T. Chiou, W.-Y. Wu, and J.-M. Ting, "Growth of single crystal ZnO nanowires using sputter deposition," *Diamond and Related Materials*, vol. 12, pp. 1841 – 1844, 2003.
DOI: 10.1016/S0925-9635(03)00274-7.
- [38] C. Xu, G. Xu, Y. Liu, and G. Wang, "A simple and novel route for the preparation of ZnO nanorods," *Solid State Communications*, vol. 122, pp. 175 – 179, 2002.
DOI: 10.1016/S0038-1098(02)00114-X.
- [39] D. Lin, W. Pan, and H. Wu, "Morphological control of centimeter long aluminum-doped zinc oxide nanofibers prepared by electrospinning," *Journal of the American Ceramic Society*, vol. 90, pp. 71 – 76, 2007.

DOI: 10.1111/j.1551-2916.2006.01366.x.

- [40] D. Lin, H. Wu, and W. Pan, "Photoswitches and memories assembled by electrospinning aluminum-doped zinc oxide single nanowires," *Advanced Materials*, vol. 19, pp. 3968 – 3972, 2007.
DOI: 10.1002/adma.200602802.
- [41] X. M. Sui, C. L. Shao, and Y. C. Liu, "White-light emission of polyvinyl alcohol ZnO hybrid nanofibers prepared by electrospinning," *Applied Physics Letters*, vol. 87, pp. 113 – 115, 2005.
DOI: 10.1063/1.2048808.
- [42] J.-J. Wu, H.-I. Wen, C.-H. Tseng, and S.-C. Liu, "Well-aligned zno nanorods via hydrogen treatment of ZnO films," *Advanced Functional Materials*, vol. 14, pp. 806 – 810, 2004.
DOI: 10.1002/adfm.200305092.
- [43] H. Zhang, D. Yang, X. Ma, N. Du, J. Wu, and D. Que, "Straight and thin ZnO nanorods: Hectogram-scale synthesis at low temperature and cathodoluminescence," *The Journal of Physical Chemistry B*, vol. 110, pp. 827–830, 2006.
DOI: 10.1021/jp055351k.
- [44] P. C. Chang and J. G. Lu, "Zno nanowire field-effect transistors," *IEEE Transactions on Electron Devices*, vol. 55, pp. 2977 – 2987, 2008.
DOI: 10.1109/TED.2008.2005181.
- [45] S. Xu, Y. Wei, M. Kirkham, J. Liu, W. Mai, D. Davidovic, R. L. Snyder, and Z. L. Wang, "Patterned growth of vertically aligned ZnO nanowire arrays on inorganic substrates at low temperature without catalyst," *Journal of the American Chemical Society*, pp. 14958–14959, 2008.
DOI: 10.1021/ja806952j.
- [46] K. Govender, D. S. Boyle, P. B. Kenway, and P. O'Brien, "Understanding the factors that govern the deposition and morphology of thin films of ZnO from aqueous solution," *J. Mater. Chem.*, vol. 14, pp. 2575 – 2591, 2004.
DOI: 10.1039/B404784B.
- [47] S. Xu, N. Adiga, S. Ba, T. Dasgupta, C. F. J. Wu, and Z. L. Wang, "Optimizing and improving the growth quality of zno nanowire arrays guided by statistical design of experiments," *ACS Nano*, vol. 3, pp. 1803–1812, 2009.
DOI: 10.1021/nn900523p.
- [48] L. Znaidi, "Sol-gel-deposited zno thin films: A review," *Materials Science and Engineering: B*, vol. 174, pp. 18 – 30, 2010.

BIBLIOGRAPHY

- DOI: 10.1016/j.mseb.2010.07.001.
- [49] M. Guglielmi and G. Carturan, "Precursors for sol-gel preparations," *Journal of Non-Crystalline Solids*, vol. 100, pp. 16 – 30, 1988.
DOI: 10.1016/0022-3093(88)90004-X.
- [50] M. Z.-C. Hu, E. Payzant, and C. H. Byers, "Sol-gel and ultra-fine particle formation via dielectric tuning of inorganic salt-alcohol-water solutions," *Journal of Colloid and Interface Science*, vol. 222, pp. 20 – 36, 2000.
DOI: 10.1006/jcis.1999.6610.
- [51] L. Armelao, D. Barreca, G. Bottaro, A. Gasparotto, D. Leonarduzzi, C. Maragno, E. Tondello, and C. Sada, "Tailored synthesis of zno:er(iii) nanosystems by a hybrid rf-sputtering/sol-gel route," *Journal of Vacuum Science & Technology A: Vacuum, Surfaces, and Films*, vol. 24, pp. 1941–1947, 2006.
DOI: 10.1116/1.2333573.
- [52] D. W. Bahnemann, C. Kormann, and M. R. Hoffmann, "Preparation and characterization of quantum size zinc oxide: a detailed spectroscopic study," *The Journal of Physical Chemistry*, vol. 91, pp. 3789–3798, 1987.
DOI: 10.1021/j100298a015.
- [53] E. Matijević, "Monodispersed metal (hydrrous) oxides - a fascinating field of colloid science," *Accounts of Chemical Research*, vol. 14, pp. 22–29, 1981.
DOI: 10.1021/ar00061a004.
- [54] L. Znaidi, G. S. Illia, R. L. Guennic, C. Sanchez, and A. Kanaev, "Elaboration of ZnO thin films with preferential orientation by a soft chemistry route," *Journal of Sol-Gel Science and Technology*, vol. 26, pp. 817 – 821, 2003.
DOI: 10.1023/A:1020795515478.
- [55] S. Chakrabarti, D. Ganguli, and S. Chaudhuri, "Substrate dependence of preferred orientation in sol-gel-derived zinc oxide films," *Materials Letters*, vol. 58, pp. 3952 – 3957, 2004.
DOI: 10.1016/j.matlet.2004.09.002.
- [56] M. Ohyama, H. Kozuka, T. Yoko, and S. Sakka, "Preparation of ZnO films with preferential orientation by sol-gel method," *Journal of the Ceramic Society of Japan*, vol. 104, pp. 296 – 300, 1996.
DOI: 10.2109/jcersj.104.296.
- [57] E. Hosono, S. Fujihara, T. Kimura, and H. Imai, "Non-basic solution routes to prepare zno nanoparticles," *Journal of Sol-Gel Science and Technology*, vol. 29, pp. 71 – 79, 2004.

DOI: 10.1023/B:JSST.0000023008.14883.1e.

- [58] D. Sun, M. Wong, L. Sun, Y. Li, N. Miyatake, and H.-J. Sue, "Purification and stabilization of colloidal ZnO nanoparticles in methanol," *Journal of Sol-Gel Science and Technology*, vol. 43, pp. 237 – 243, 2007.
DOI: 10.1007/s10971-007-1569-z.
- [59] Z. Hu, G. Oskam, and P. C. Searson, "Influence of solvent on the growth of ZnO nanoparticles," *Journal of Colloid and Interface Science*, vol. 263, pp. 454 – 460, 2003.
DOI: 10.1016/S0021-9797(03)00205-4.
- [60] E. A. Meulenkaamp, "Synthesis and growth of ZnO nanoparticles," *The Journal of Physical Chemistry B*, vol. 102, pp. 5566 – 5572, 1998.
DOI: 10.1021/jp980730h.
- [61] S. Fujihara, E. Hosono, and T. Kimura, "Fabrication of porous metal oxide semiconductor films by a self-template method using layered hydroxide metal acetates," *Journal of Sol-Gel Science and Technology*, vol. 31, pp. 165 – 168, 2004.
DOI: 10.1023/B:JSST.0000047980.69279.9b.
- [62] H. Wang, C. Xie, and D. Zeng, "Controlled growth of ZnO by adding H₂O," *Journal of Crystal Growth*, vol. 277, pp. 372 – 377, 2005.
DOI: 10.1016/j.jcrysgro.2005.01.068.
- [63] M. Tokumoto, V. Briois, C. Santilli, and S. Pulcinelli, "Preparation of ZnO nanoparticles: Structural study of the molecular precursor," *Journal of Sol-Gel Science and Technology*, vol. 26, pp. 547 – 551, 2003.
DOI: 10.1023/A:1020711702332.
- [64] Y.-S. Kim, W.-P. Tai, and S.-J. Shu, "Effect of preheating temperature on structural and optical properties of ZnO thin films by sol-gel process," *Thin Solid Films*, vol. 491, pp. 153 – 160, 2005.
DOI: 10.1016/j.tsf.2005.06.013.
- [65] C. Shaoqiang, Z. Jian, F. Xiao, W. Xiaohua, L. laiqiang, S. Yanling, X. Qingsong, W. Chang, Z. Jianzhong, and Z. Ziqiang, "Nanocrystalline zno thin films on porous silicon/silicon substrates obtained by sol-gel technique," *Applied Surface Science*, vol. 241, pp. 384 – 391, 2005.
DOI: 10.1016/j.apsusc.2004.07.040.
- [66] R. Ghosh, B. Mallik, S. Fujihara, and D. Basak, "Photoluminescence and photoconductance in annealed ZnO thin films," *Chemical Physics Letters*, vol. 403, pp. 415 – 419, 2005.
DOI: 10.1016/j.cplett.2005.01.043.

BIBLIOGRAPHY

- [67] Y. Ohya, H. Saiki, and Y. Takahashi, "Preparation of transparent, electrically conducting ZnO film from zinc acetate and alkoxide," *Journal of Materials Science*, vol. 29, pp. 4099–4103, 1994.
DOI: 10.1007/BF00355977.
- [68] D. Bao, H. Gu, and A. Kuang, "Sol-gel-derived c-axis oriented ZnO thin films," *Thin Solid Films*, vol. 312, pp. 37 – 39, 1998.
DOI: 10.1016/S0040-6090(97)00302-7.
- [69] Y. Natsume and H. Sakata, "Zinc oxide films prepared by sol-gel spin-coating," *Thin Solid Films*, vol. 372, pp. 30 – 36, 2000.
DOI: 10.1016/S0040-6090(00)01056-7.
- [70] X.-H. Wang, J. Shi, S. Dai, and Y. Yang, "A sol-gel method to prepare pure and gold colloid doped ZnO films," *Thin Solid Films*, vol. 429, pp. 102 – 107, 2003.
DOI: 10.1016/S0040-6090(03)00057-9.
- [71] Y. Kavanagh and D. Cameron, "Zinc sulfide thin films produced by sulfidation of sol-gel deposited zinc oxide," *Thin Solid Films*, vol. 398-399, pp. 24 – 28, 2001.
DOI: 10.1016/S0040-6090(01)01298-6.
- [72] L. Bahadur and T. N. Rao, "Photoelectrochemical investigations on particulate ZnO thin film electrodes in non-aqueous solvents," *Journal of Photochemistry and Photobiology A: Chemistry*, vol. 91, pp. 233 – 240, 1995.
DOI: 10.1016/1010-6030(95)04104-9.
- [73] R. Brenier and L. Ortéga, "Structural properties and stress in ZnO films obtained from a nanocolloidal sol," *Journal of Sol-Gel Science and Technology*, vol. 29, pp. 137–145, 2004.
DOI: 10.1023/B:JSST.0000023852.75244.49.
- [74] Z. Jiwei, Z. Liangying, and Y. Xi, "The dielectric properties and optical propagation loss of c-axis oriented ZnO thin films deposited by sol-gel process," *Ceramics International*, vol. 26, pp. 883 – 885, 2000.
DOI: 10.1016/S0272-8842(00)00031-6.
- [75] M. Aslan, A. Oral, E. Mensur, A. Gül, and E. Basaran, "Preparation of c-axis-oriented zinc-oxide thin films and the study of their microstructure and optical properties," *Solar Energy Materials and Solar Cells*, vol. 82, pp. 543 – 552, 2004.
DOI: 10.1016/j.solmat.2003.06.016.
- [76] H. Y. Bae and G. M. Choi, "Electrical and reducing gas sensing properties of ZnO and ZnO-CuO thin films fabricated by spin coating method," *Sensors and Actuators B: Chemical*, vol. 55, pp. 47 – 54, 1999.

DOI: 10.1016/S0925-4005(99)00038-6.

- [77] Y. Ohya, H. Koyama, T. Ban, and Y. Takahashi, "Electrical properties of p-n contact with oxide semiconductor thin films fabricated by liquid phase method," *Materials Science and Engineering: B*, vol. 54, pp. 55 – 59, 1998.
DOI: 10.1016/S0921-5107(98)00127-5.
- [78] Y. Takahashi, M. Kanamori, A. Kondoh, H. Minoura, and Y. Ohya, "Photoconductivity of ultrathin zinc oxide films," *Japanese Journal of Applied Physics*, vol. 33, p. 6611, 1994.
DOI: 10.1143/JJAP.33.6611.
- [79] R. Ghosh, D. Basak, and S. Fujihara, "Effect of substrate-induced strain on the structural, electrical, and optical properties of polycrystalline ZnO thin films," *Journal of Applied Physics*, vol. 96, pp. 2689–2692, 2004.
DOI: 10.1063/1.1769598.
- [80] D. Basak, G. Amin, B. Mallik, G. Paul, and S. Sen, "Photoconductive UV detectors on sol-gel-synthesized ZnO films," *Journal of Crystal Growth*, vol. 256, pp. 73 – 77, 2003.
DOI: 10.1016/S0022-0248(03)01304-6.
- [81] Y. Zhang, B. Lin, X. Sun, and Z. Fu, "Temperature-dependent photoluminescence of nanocrystalline ZnO thin films grown on si (100) substrates by the sol-gel process," *Applied Physics Letters*, vol. 86, p. 131910, 2005.
DOI: 10.1063/1.1891288.
- [82] H. Li, J. Wang, H. Liu, H. Zhang, and X. Li, "Zinc oxide films prepared by sol-gel method," *Journal of Crystal Growth*, vol. 275, pp. e943 – e946, 2005.
DOI: 10.1016/j.jcrysgro.2004.11.098.
- [83] H. Li, J. Wang, H. Liu, C. Yang, H. Xu, X. Li, and H. Cui, "Sol-gel preparation of transparent zinc oxide films with highly preferential crystal orientation," *Vacuum*, vol. 77, pp. 57 – 62, 2004.
DOI: 10.1016/j.vacuum.2004.08.003.
- [84] S. Fujihara, C. Sasaki, and T. Kimura, "Crystallization behavior and origin of c-axis orientation in sol-gel-derived ZnO:Li thin films on glass substrates," *Applied Surface Science*, vol. 180, pp. 341 – 350, 2001.
DOI: 10.1016/S0169-4332(01)00367-1.
- [85] T. Nagase, T. Ooie, and J. Sakakibara, "A novel approach to prepare zinc oxide films: excimer laser irradiation of sol-gel derived precursor films," *Thin Solid Films*, vol. 357, pp. 151 – 158, 1999.
DOI: 10.1016/S0040-6090(99)00645-8.

BIBLIOGRAPHY

- [86] Y. Kokubun, K. Miura, F. Endo, and S. Nakagomi, "Sol-gel prepared β -Ga₂O₃ thin films for ultraviolet photodetectors," *Applied Physics Letters*, vol. 90, p. 031912, 2007.
DOI: 10.1063/1.2432946.
- [87] J.-H. Lee, K.-H. Ko, and B.-O. Park, "Electrical and optical properties of ZnO transparent conducting films by the sol-gel method," *Journal of Crystal Growth*, vol. 247, pp. 119 – 125, 2003.
DOI: 10.1016/S0022-0248(02)01907-3.
- [88] R. Castanedo-Pérez, O. Jiménez-Sandoval, S. Jiménez-Sandoval, J. Márquez-Marín, A. Mendoza-Galván, G. Torres-Delgado, and A. Maldonado-Alvarez, "Influence of annealing temperature on the formation and characteristics of sol-gel prepared ZnO films," *Journal of Vacuum Science & Technology A: Vacuum, Surfaces, and Films*, vol. 17, pp. 1811–1816, 1999.
DOI: 10.1116/1.581895.
- [89] Y. Natsume and H. Sakata, "Electrical and optical properties of zinc oxide films post-annealed in H₂ after fabrication by sol-gel process," *Materials Chemistry and Physics*, vol. 78, pp. 170 – 176, 2003.
DOI: 10.1016/S0254-0584(02)00314-0.
- [90] N. Asakuma, H. Hirashima, H. Imai, T. Fukui, and M. Toki, "Crystallization and reduction of sol-gel-derived zinc oxide films by irradiation with ultraviolet lamp," *Journal of Sol-Gel Science and Technology*, vol. 26, pp. 181–184, 2003.
DOI: 10.1023/A:1020782511960.
- [91] M. Ohyama, H. Kouzuka, and T. Yoko, "Sol-gel preparation of ZnO films with extremely preferred orientation along (002) plane from zinc acetate solution," *Thin Solid Films*, vol. 306, pp. 78 – 85, 1997.
DOI: 10.1016/S0040-6090(97)00231-9.
- [92] P. Kumar, A. Deep, K.-H. Kim, and R. J. Brown, "Coordination polymers: Opportunities and challenges for monitoring volatile organic compounds," *Progress in Polymer Science*, vol. 45, pp. 102 – 118, 2015.
DOI: 10.1016/j.progpolymsci.2015.01.002.
- [93] F.-X. Coudert, "Responsive metal-organic frameworks and framework materials: Under pressure, taking the heat, in the spotlight, with friends," *Chemistry of Materials*, vol. 27, no. 6, pp. 1905–1916, 2015.
DOI: 10.1021/acs.chemmater.5b00046.

- [94] G. Abellán, C. Martí-Gastaldo, A. Ribera, and E. Coronado, "Hybrid materials based on magnetic layered double hydroxides: A molecular perspective," *Accounts of Chemical Research*, vol. 48, no. 6, pp. 1601–1611, 2015.
DOI: 10.1021/acs.accounts.5b00033.
- [95] Y. Hasegawa and T. Nakanishi, "Luminescent lanthanide coordination polymers for photonic applications," *RSC Advances*, vol. 5, pp. 338–353, 2015.
DOI: 10.1039/C4RA09255D.
- [96] J. McCleverty and T. Meyer, *Comprehensive Coordination Chemistry II: From Biology to Nanotechnology (2nd Ed.)*. Pergamon, pp 8400, 2004.
ISBN: 9780080437484.
- [97] C. Paraschiv, A. Cucos, S. Shova, A. M. Madalan, C. Maxim, D. Visinescu, B. Cojocaru, V. I. Parvulescu, and M. Andruh, "New Zn(II) coordination polymers constructed from aminoalcohols and aromatic dicarboxylic acids: Synthesis, structure, photocatalytic properties, and solid-state conversion to ZnO," *Crystal Growth & Design*, vol. 15, pp. 799–811, 2015.
DOI: 10.1021/cg501604c.
- [98] X. Li, Y. Su, X. Li, G. Ma, and Q. Ling, "Syntheses, structures, and characteristics of six coordination polymers based on 1,4-bis(imidazol-1-yl)benzene and isophthalates containing coordination-inert substituents," *European Journal of Inorganic Chemistry*, vol. 2015, pp. 3274 – 3284, 2015.
DOI: 10.1002/ejic.201500281.
- [99] A. Karmakar, G. M. D. M. Rubio, M. F. C. Guedes da Silva, A. P. C. Ribeiro, and A. J. L. Pombeiro, "ZnII and CdII MOFs based on an amidoisophthalic acid ligand: synthesis, structure and catalytic application in transesterification," *RSC Advances*, vol. 6, pp. 89007 – 89018, 2016.
DOI: 10.1039/C6RA17518J.
- [100] H. Guo, Y. Yan, N. Wang, X. Guo, G. Zheng, and Y. Qi, "A series of entangled coordination polymers assembled by a v-shaped bisimidazole ligand and various dicarboxylic acids: synthesis, characterization and luminescence properties," *CrystEngComm*, vol. 17, pp. 6512–6526, 2015.
DOI: 10.1039/C5CE00903K.
- [101] W.-Y. Yin, Z.-L. Huang, X.-Y. Tang, J. Wang, H.-J. Cheng, Y.-S. Ma, R.-X. Yuan, and D. Liu, "Structural diversification and photocatalytic properties of Zn(II) polymers modified

BIBLIOGRAPHY

- by auxiliary N-containing ligands,” *New Journal of Chemistry*, vol. 39, pp. 7130–7139, 2015.
DOI: 10.1039/C5NJ01005E.
- [102] H. Erer, O. Z. Yesilel, and M. Arici, “A series of Zinc(II) 3D-3D interpenetrated coordination polymers based on thiophene-2,5-dicarboxylate and bis(imidazole) derivative linkers,” *Crystal Growth & Design*, vol. 15, no. 7, pp. 3201–3211, 2015.
DOI: 10.1021/acs.cgd.5b00276.
- [103] K. Liu, B. Ma, X. Guo, D. Ma, L. Meng, G. Zeng, F. Yang, G. Li, Z. Shi, and S. Feng, “Syntheses, structures, luminescence and magnetic properties of eleven coordination polymers constructed by a N,N'-sulfuryldiimidazole ligand,” *CrystEngComm*, vol. 17, pp. 5054–5065, 2015.
DOI: 10.1039/C5CE00807G.
- [104] M. R. Bryant, A. D. Burrows, C. M. Fitchett, C. S. Hawes, S. O. Hunter, L. L. Keenan, D. J. Kelly, P. E. Kruger, M. F. Mahon, and C. Richardson, “The synthesis and characterisation of coordination and hydrogen-bonded networks based on 4-(3,5-dimethyl-1h-pyrazol-4-yl)benzoic acid,” *Dalton Transactions*, vol. 44, pp. 9269–9280, 2015.
DOI: 10.1039/C5DT00011D.
- [105] B. Bhattacharya, R. Haldar, D. K. Maity, T. K. Maji, and D. Ghoshal, “Pillared-bilayer porous coordination polymers of Zn(II): enhanced hydrophobicity of pore surface by changing the pillar functionality,” *CrystEngComm*, vol. 17, pp. 3478–3486, 2015.
DOI: 10.1039/C5CE00143A.
- [106] P. Tang, W.-W. Dong, W. Xia, and J. Zhao, “Two new Zn(II)/Cd(II) coordination polymers based on rigid squaric acid: Crystal structure, topology and fluorescent properties,” *Journal of Inorganic and Organometallic Polymers and Materials*, vol. 25, no. 3, pp. 569–575, 2015.
DOI: 10.1007/s10904-014-0118-9.
- [107] K. Xing, R. Fan, S. Gao, X. Wang, X. Du, P. Wang, R. Fang, and Y. Yang, “Controllable synthesis of Zn/Cd(II) coordination polymers: dual-emissive luminescent properties, and tailoring emission tendency under varying excitation energies,” *Dalton Transactions*, vol. 45, pp. 4863–4878, 2016.
DOI: 10.1039/C5DT04759E.
- [108] R. Qiao, S.-S. Chen, L.-Q. Sheng, S. Yang, and W.-D. Li, “Syntheses, crystal structures, and properties of four complexes based on polycarboxylate and imidazole ligands,” *Journal of Solid State Chemistry*, vol. 228, pp. 199 – 207, 2015.
DOI: 10.1016/j.jssc.2015.04.041.

- [109] W.-G. Zhu, Y.-Q. Zheng, L.-X. Zhou, and H.-L. Zhu, "Structural diversity for three Zn(II) coordination polymers from 4-nitrobenzene-1,2-dicarboxylate and bispyridyl ligand," *Journal of Coordination Chemistry*, vol. 69, pp. 270–285, 2016.
DOI: 10.1080/00958972.2015.1105365.
- [110] N. Hiroshi, "Coordination programming: A new concept for the creation of multifunctional molecular systems," *Chemistry Letters*, vol. 43, pp. 388–395, 2014.
DOI: 10.1246/cl.140010.
- [111] X. Chen, K. Guo, F. Li, L. Zhou, and H. Qiao, "Synthesis and properties of Zn²⁺/Cd²⁺-directed self-assembled metallo-supramolecular polymers based on 1,4-diketo-pyrrolo[3,4-c]pyrrole (DPP) derivatives," *RSC Advances*, vol. 4, pp. 58027–58035, 2014.
DOI: 10.1039/C4RA10685G.
- [112] S. Jung, W. Cho, H.-J. Lee, and M. Oh, "Self-template-directed formation of coordination-polymer hexagonal tubes and rings, and their calcination to ZnO rings," *Angewandte Chemie International Edition*, vol. 48, pp. 1459 – 1462, 2009.
DOI: 10.1002/anie.200804816.
- [113] X. Liu, "Zinc oxide nano- and microfabrication from coordination-polymer templates," *Angewandte Chemie International Edition*, vol. 48, pp. 3018–3021, 2009.
DOI: 10.1002/anie.200805972.
- [114] F. Molaei, F. Bigdeli, A. Morsali, S. W. Joo, G. Bruno, and H. A. Rudbari, "Synthesis and characterization of different zinc(ii) oxide nano-structures from two new zinc(ii)-quinoxaline coordination polymers," *Journal of Molecular Structure*, vol. 1095, pp. 8 – 14, 2015.
DOI: 10.1016/j.molstruc.2015.03.070.
- [115] Y. Lu, H. Cao, S. Zhang, and X. Zhang, "Shape controlled synthesis of superhydrophobic zinc coordination polymers particles and their calcination to superhydrophobic zno," *Journal of Materials Chemistry*, vol. 21, pp. 8633–8639, 2011.
DOI: 10.1039/C1JM10957J.
- [116] F.-L. Hu, W. Wu, P. Liang, Y.-Q. Gu, L.-G. Zhu, H. Wei, and J.-P. Lang, "Construction of entangled coordination polymers based on M²⁺ ions, 4,4'-[1,2-Phenylenebis(methylene)]bis(oxy)dibenzoate and different N-donor ligands," *Crystal Growth & Design*, vol. 13, pp. 5050–5061, 2013.
DOI: 10.1021/cg401212s.
- [117] F.-l. Hu, Y.-X. Shi, H.-H. Chen, and J.-P. Lang, "A Zn(II) coordination polymer and its photocycloaddition product: syntheses, structures, selective luminescence sensing of

- Fe(III) ions and selective absorption of dyes," *Dalton Transactions*, vol. 44, pp. 18795–18803, 2015.
DOI: 10.1039/C5DT03094C.
- [118] D. Liu and J.-P. Lang, "Regiospecific photodimerization reactions of an unsymmetrical alkene in two coordination compounds," *CrystEngComm*, vol. 16, pp. 76–81, 2014.
DOI: 10.1039/C3CE41609G.
- [119] C. Klingshirn, "ZnO: From basics towards applications," *Physica Status Solidi (B)*, vol. 244, pp. 3027 – 3073, 2007.
DOI: 10.1002/pssb.200743072.
- [120] C. Klingshirn, "ZnO: Material, physics and applications," *Chemical Physics Physical Chemistry*, vol. 8, pp. 782–803, 2007.
DOI: 10.1002/cphc.200700002.
- [121] I. Y. Yu Bu and S. Chen, "Fully-solution processed ZnO nanowires/cupric heterojunction for low-cost photovoltaic applications," *Optik - International Journal for Light and Electron Optics*, vol. 130, pp. 427 – 432, 2017.
DOI: 10.1016/j.ijleo.2016.10.079.
- [122] L. T. Jule, F. B. Dejene, K. T. Roro, Z. N. Urgessa, and J. R. Botha, "Rapid synthesis of blue emitting ZnO nanoparticles for fluorescent applications," *Physica B: Condensed Matter*, vol. 497, pp. 71 – 77, 2016.
DOI: 10.1016/j.physb.2016.06.008.
- [123] S. Vallejos, I. Gràcia, E. Figueras, N. Pizurova, J. Hubálek, and C. Cané, "ZnO-based gas microsensors sensitive to CO at room temperature by photoactivation," *Procedia Engineering. Proceedings of the 30th anniversary Eurosensors Conference - Eurosensors 2016, 4-7. September 2016, Budapest, Hungary*, vol. 168, pp. 415 – 418, 2016.
DOI: 10.1016/j.proeng.2016.11.198.
- [124] N. Lalioti, C. P. Raptopoulou, A. Terzis, A. E. Aliev, I. P. Gerotheranassis, E. Manessi-Zoupa, and S. P. Perlepes, "High nuclearity Zn(II)/MeCO₂⁻/(C₅NH₄)₂CO₂²⁻ clusters by "depolymerization": Conversion of a three-dimensional coordination polymer containing hexameric units into its constituent hexanuclear complex," *Angewandte Chemie International Edition*, vol. 40, pp. 3211 – 3214, 2001.
DOI: 10.1002/1521-3773(20010903)40:17<3211::AID-ANIE3211>3.0.CO;2-X.
- [125] M. Hamid, A. A. Tahir, M. Mazhar, F. Ahmad, K. C. Molloy, and G. Kociok-Kohn, "Deposition and characterization of ZnO thin films from a novel hexanuclear zinc precursor," *Inorganica Chimica Acta*, vol. 361, pp. 188 – 194, 2008.
DOI: 10.1016/j.ica.2007.07.013.

- [126] R. C. Hoffmann, S. Dilfer, A. Issanin, and J. J. Schneider, "Solution processed ZnO: Challenges in processing and performance on flexible substrates," *Physica Status Solidi (A)*, vol. 207, pp. 1590 – 1595, 2010.
DOI: 10.1002/pssa.200983749.
- [127] J. J. Schneider, R. C. Hoffmann, J. Engstler, O. Soffke, W. Jaegermann, A. Issanin, and A. Klyszcz, "A printed and flexible field-effect transistor device with nanoscale zinc oxide as active semiconductor material," *Advanced Materials*, vol. 20, pp. 3383 – 3387, 2008.
DOI: 10.1002/adma.200800819.
- [128] Y. S. Wang, P. J. Thomas, and P. O'Brien, "Nanocrystalline ZnO with ultraviolet luminescence," *The Journal of Physical Chemistry B*, vol. 110, pp. 4099 – 4104, 2006.
DOI: 10.1021/jp0566313.
- [129] J. J. Schneider, R. C. Hoffmann, J. Engstler, S. Dilfer, A. Klyszcz, E. Erdem, P. Jakes, and R. A. Eichel, "Zinc oxide derived from single source precursor chemistry under chimie douce conditions: formation pathway, defect chemistry and possible applications in thin film printing," *Journal of Material Chemistry*, vol. 19, pp. 1449 – 1457, 2009.
DOI: 10.1039/B816376F.
- [130] V. F. Rivera, F. Auras, P. Motto, S. Stassi, G. Canavese, E. Celasco, T. Bein, B. Onida, and V. Cauda, "Length-dependent charge generation from vertical arrays of high-aspect-ratio ZnO nanowires," *Chemistry - A European Journal*, vol. 19, pp. 14665 – 14674, 2013.
DOI: 10.1002/chem.201204429.
- [131] M. Laurenti, V. Cauda, R. Gazia, M. Fontana, V. F. Rivera, S. Bianco, and G. Canavese, "Wettability control on ZnO nanowires driven by seed layer properties," *European Journal of Inorganic Chemistry*, vol. 2013, pp. 2520 – 2527, 2013.
DOI: 10.1002/ejic.201201420.
- [132] T. Arii and A. Kishi, "The effect of humidity on thermal process of zinc acetate," *Thermochimica Acta*, vol. 400, pp. 175 – 185, 2003.
DOI: 10.1016/S0040-6031(02)00487-2.
- [133] U. Kumar, J. Thomas, R. Nagarajan, and N. Thirupathi, "3,5-Lutidine coordinated zinc(ii) aryl carboxylate complexes: Precursors for zinc(ii) oxide," *Inorganica Chimica Acta. Special Volume: Protagonists in Chemistry Dedicated to Professor S. S. Krishnamurthy*, vol. 372, pp. 191 – 199, 2011.
DOI: 10.1016/j.ica.2011.01.083.

BIBLIOGRAPHY

- [134] K. G. Kanade, B. B. Kale, R. C. Aiyer, and B. K. Das, "Effect of solvents on the synthesis of nano-size zinc oxide and its properties," *Materials Research Bulletin*, vol. 41, pp. 590 – 600, 2006.
DOI: 10.1016/j.materresbull.2005.09.002.
- [135] A. V. Ghule, B. Lo, S.-H. Tzing, K. Ghule, H. Chang, and Y. C. Ling, "Simultaneous thermogravimetric analysis and in situ thermo-raman spectroscopic investigation of thermal decomposition of zinc acetate dihydrate forming zinc oxide nanoparticles," *Chemical Physics Letters*, vol. 381, pp. 262 – 270, 2003.
DOI: 10.1016/j.cplett.2003.09.125.
- [136] T. Kozawa, A. Onda, K. Yanagisawa, A. Kishi, and Y. Masuda, "Effect of water vapor on the thermal decomposition process of zinc hydroxide chloride and crystal growth of zinc oxide," *Journal of Solid State Chemistry*, vol. 184, pp. 589 – 596, 2011.
DOI: 10.1016/j.jssc.2011.01.015.
- [137] A. V. Ghule, K. Ghule, C.-Y. Chen, W.-Y. Chen, S.-H. Tzing, H. Chang, and Y.-C. Ling, "In situ thermo-TOF-SIMS study of thermal decomposition of zinc acetate dihydrate," *Journal of Mass Spectrometry*, vol. 39, pp. 1202 – 1208, 2004.
DOI: 10.1002/jms.721.
- [138] T. Biswick, W. Jones, A. Pacuła, E. Serwicka, and J. Podobinski, "Evidence for the formation of anhydrous zinc acetate and acetic anhydride during the thermal degradation of zinc hydroxy acetate, $Zn_5(OH)_8(CH_3CO_2)_2 \cdot 4H_2O$ to ZnO," *Solid State Sciences*, vol. 11, pp. 330 – 335, 2009.
DOI: 10.1016/j.solidstatesciences.2008.06.018.
- [139] S. Labuayai, V. Promarak, and S. Maensiri, "Synthesis and optical properties of nanocrystalline ZnO powders prepared by a direct thermal decomposition route," *Applied Physics A*, vol. 94, pp. 755 – 761, 2009.
DOI: 10.1007/s00339-008-4984-2.
- [140] A. Moezzi, A. McDonagh, A. Dowd, and M. Cortie, "Zinc hydroxyacetate and its transformation to nanocrystalline zinc oxide," *Inorganic Chemistry*, vol. 52, pp. 95 – 102, 2013.
DOI: 10.1021/ic302328e.
- [141] C.-C. Lin and Y.-Y. Li, "Synthesis of ZnO nanowires by thermal decomposition of zinc acetate dihydrate," *Materials Chemistry and Physics*, vol. 113, pp. 334 – 337, 2009.
DOI: 10.1016/j.matchemphys.2008.07.070.

- [142] A. Tarat, R. Majithia, R. Brown, M. Penny, K. Meissner, and T.G.G.Maffeis, "Synthesis of nanocrystalline ZnO nanobelts via pyrolytic decomposition of zinc acetate nanobelts and their gas sensing behavior," *Surface Science*, vol. 606, pp. 715 – 721, 2012.
DOI: 10.1016/j.susc.2011.12.010.
- [143] X. Su, Z. Zhang, Y. Wang, and M. Zhu, "Synthesis and photoluminescence of aligned ZnO nanorods by thermal decomposition of zinc acetate at a substrate temperature of $\approx 250^\circ\text{C}$," *Journal of Physics D: Applied Physics*, vol. 38, p. 3934, 2005.
DOI: 10.1088/0022-3727/38/21/015.
- [144] Y. Yang, H. Chen, B. Zhao, and X. Bao, "Size control of ZnO nanoparticles via thermal decomposition of zinc acetate coated on organic additives," *Journal of Crystal Growth*, vol. 263, pp. 447 – 453, 2004.
DOI: 10.1016/j.jcrysgr.2003.12.010.
- [145] Y. Wang, Y. Li, Z. Zhou, X. Zu, and Y. Deng, "Evolution of the zinc compound nanostructures in zinc acetate single-source solution," *Journal of Nanoparticle Research*, vol. 13, p. 5193, 2011.
DOI: 10.1007/s11051-011-0504-y.
- [146] P. Morvillo, R. Diana, R. Ricciardi, E. Bobeico, and C. Minarini, "High efficiency inverted polymer solar cells with solution-processed ZnO buffer layer," *Journal of Sol-Gel Science and Technology*, vol. 73, pp. 550 – 556, 2015.
DOI: 10.1007/s10971-014-3514-2.
- [147] A. Singh, D. Kumar, P. K. Khanna, M. Kumar, and B. Prasad, "Post annealing effect on structural and optical properties of ZnO thin films derived by sol-gel route," *Journal of Materials Science: Materials in Electronics*, vol. 24, pp. 4607 – 4613, 2013.
DOI: 10.1007/s10854-013-1451-4.
- [148] K. Foo, M. Kashif, U. Hashim, and W.-W. Liu, "Effect of different solvents on the structural and optical properties of zinc oxide thin films for optoelectronic applications," *Ceramics International*, vol. 40, pp. 753 – 761, 2014.
DOI: 10.1016/j.ceramint.2013.06.065.
- [149] M. Caglar and S. Ruzgar, "Influence of the deposition temperature on the physical properties of high electron mobility ZnO films by sol-gel process," *Journal of Alloys and Compounds*, vol. 644, pp. 101 – 105, 2015.
DOI: 10.1016/j.jallcom.2015.04.167.
- [150] A. Diallo, M. Gaceur, S. B. Dkhil, Y. Didane, O. Margeat, J. Ackermann, and C. Videlot-Ackermann, "Impact of surfactants covering ZnO nanoparticles on solution-processed

- field-effect transistors: From dispersion state to solid state,” *Colloids and Surfaces A: Physicochemical and Engineering Aspects*, vol. 500, pp. 214 – 221, 2016.
DOI: 10.1016/j.colsurfa.2016.04.036.
- [151] K. Sivakumar, V. Senthil Kumar, N. Muthukumarasamy, M. Thambidurai, and T. S. Senthil, “Influence of pH on ZnO nanocrystalline thin films prepared by sol–gel dip coating method,” *Bulletin of Materials Science*, vol. 35, pp. 327 – 331, 2012.
DOI: 10.1007/s12034-012-0305-7.
- [152] F. Boudjouan, A. Chelouche, T. Touam, D. Djouadi, S. Khodja, M. Tazerout, Y. Ouerdane, and Z. Hadjoub, “Effects of stabilizer ratio on photoluminescence properties of sol-gel ZnO nano-structured thin films,” *Journal of Luminescence*, vol. 158, pp. 32 – 37, 2015.
DOI: 10.1016/j.jlumin.2014.09.026.
- [153] A. Zawadzka, P. Plóciennik, J. Strzelecki, and B. Sahraoui, “Transparent amorphous zinc oxide thin films for NLO applications,” *Optical Materials*, vol. 37, pp. 327 – 337, 2014.
DOI: 10.1016/j.optmat.2014.06.021.
- [154] P. H. Vajargah, H. Abdizadeh, R. Ebrahimifard, and M. Golobostanfard, “Sol-gel derived ZnO thin films: Effect of amino-additives,” *Applied Surface Science*, vol. 285, Part B, pp. 732 – 743, 2013.
DOI: 10.1016/j.apsusc.2013.08.118.
- [155] O. Azizova, A. Islomov, D. Roshchupkin, D. Predvoditelev, and A. Remizov, “Free radicals formed during uv-irradiation of biological membrane lipids,” *Biofizika*, vol. 24, pp. 396 – 402, 1979.
- [156] C. L. Mathis, B. M. Gist, C. K. Frederickson, K. M. Midkiff, and C. C. Marvin, “Visible light photooxidative cyclization of amino alcohols to 1,3-oxazines,” *Tetrahedron Letters*, vol. 54, pp. 2101 – 2104, 2013.
DOI: 10.1016/j.tetlet.2013.02.031.
- [157] F. Viñes and F. Illas, “Electronic structure of stoichiometric and reduced ZnO from periodic relativistic all electron hybrid density functional calculations using numeric atom-centered orbitals,” *Journal of Computational Chemistry*, vol. 38, pp. 523–529, 2017.
DOI: 10.1002/jcc.24705.
- [158] J. P. Perdew, K. Burke, and M. Ernzerhof, “Generalized gradient approximation made simple,” *Phys. Rev. Lett.*, vol. 77, pp. 3865 – 3868, Oct 1996.
DOI: 10.1103/PhysRevLett.77.3865.
- [159] I. Oyarzabal, J. Ruiz, E. Ruiz, D. Aravena, J. M. Seco, and E. Colacio, “Increasing the effective energy barrier promoted by the change of a counteranion in a Zn-Dy-Zn

- SMM: slow relaxation via the second excited state,” *Chemical Communications*, vol. 51, pp. 12353–12356, 2015.
DOI: 10.1039/C5CC04495B.
- [160] A. Pandey, H. Scherich, and D. Drabold, “Density functional theory model of amorphous zinc oxide (a-ZnO) and a- $X_{0.375}Z_{0.625}O$ (X= Al, Ga and In),” *Journal of Non-Crystalline Solids*, vol. 455, pp. 98 – 101, 2017.
DOI: 10.1016/j.jnoncrysol.2016.10.035.
- [161] Y. Mei, D. M. Sherman, W. Liu, B. Etschmann, D. Testemale, and J. Brugger, “Zinc complexation in chloride-rich hydrothermal fluids (25-600 °C): A thermodynamic model derived from ab initio molecular dynamics,” *Geochimica et Cosmochimica Acta*, vol. 150, pp. 265 – 284, 2015.
DOI: 10.1016/j.gca.2014.09.023.
- [162] R. Car and M. Parrinello, “Unified approach for molecular dynamics and density-functional theory,” *Physical Review Letters*, vol. 55, pp. 2471–2474, Nov 1985.
DOI: 10.1103/PhysRevLett.55.2471.
- [163] M. J. Frisch, G. W. Trucks, H. B. Schlegel, G. E. Scuseria, M. A. Robb, J. R. Cheeseman, J. A. Montgomery-Jr., T. Vreven, K. N. Kudin, J. C. Burant, J. M. Millam, S. S. Iyengar, J. Tomasi, V. Barone, B. Mennucci, M. Cossi, G. Scalmani, N. Rega, G. A. Petersson, H. Nakatsuji, M. Hada, M. Ehara, K. Toyota, R. Fukuda, J. Hasegawa, M. Ishida, T. Nakajima, Y. Honda, O. Kitao, H. Nakai, M. Klene, X. Li, J. E. Knox, H. P. Hratchian, J. B. Cross, V. Bakken, C. Adamo, J. Jaramillo, R. Gomperts, R. E. Stratmann, O. Yazyev, A. J. Austin, R. Cammi, C. Pomelli, J. W. Ochterski, P. Y. Ayala, K. Morokuma, G. Voth, P. Salvador, J. J. Dannenberg, V. G. Zakrzewski, S. Dapprich, A. D. Daniels, M. C. Strain, O. Farkas, D. K. Malick, A. D. Rabuck, K. Raghavachari, J. B. Foresman, J. V. Ortiz, Q. Cui, A. G. Baboul, S. Clifford, J. Cioslowski, B. Stefanov, G. Liu, A. Liashenko, P. Piskorz, I. Komaromi, R. L. Martin, D. J. Fox, T. Keith, M. A. Al-Laham, C. Y. Peng, A. Nanayakkara, M. Challacombe, P. M. W. Gill, B. Johnson, W. Chen, M. W. Wong, C. Gonzalez, and J. A. Pople *Gaussian 03, Revision C.02 (Gaussian, Inc, Wallingford CT)*, 2004.
- [164] A. Laio and M. Parrinello, “Reactive molecular dynamics simulation of the pyrolysis and combustion of benzene: ultrahigh temperature and oxygen-induced enhancement of initiation pathways and their effect on carbon black generation,” *RSC Advances*, vol. 99, pp. 12562–12566, 2002.
DOI: 10.1073/pnas.202427399.
- [165] P. H. Vajargah, H. Abdizadeh, R. Ebrahimifard, and M. Golobostanfard, “Sol-gel derived ZnO thin films: Effect of amino-additives,” *Applied Surface Science*, vol. 285, Part B, pp. 732 – 743, 2013.

DOI: 10.1016/j.apsusc.2013.08.118.

- [166] T. Shimoaka, C. Wakai, T. Sakabe, S. Yamazaki, and T. Hasegawa, "Hydration structure of strongly bound water on the sulfonic acid group in a nafion membrane studied by infrared spectroscopy and quantum chemical calculation," *Physical Chemistry Chemical Physics*, vol. 17, pp. 8843 – 8849, 2015.

DOI: 10.1039/C5CP00567A.

- [167] K. Xu, D.-Q. Wei, X.-R. Chen, and G.-F. Ji, "Thermal decomposition of solid phase nitromethane under various heating rates and target temperatures based on ab initio molecular dynamics simulations," *Journal of Molecular Modeling*, vol. 20, p. 2438, 2014.

DOI: 10.1007/s00894-014-2438-7.

- [168] J. Chang, P. Lian, D.-Q. Wei, X.-R. Chen, Q.-M. Zhang, and Z.-Z. Gong, "Publisher's note: Thermal decomposition of the solid phase of nitromethane: Ab initio molecular dynamics simulations [phys. rev. lett. 105, 188302 (2010)]," *Physical Review Letters*, vol. 105, p. 229902, 2010.

DOI: 10.1103/PhysRevLett.105.229902.

- [169] J. Li, S. M. Kathmann, H.-S. Hu, G. K. Schenter, T. Autrey, and M. Gutowski, "Theoretical investigations on the formation and dehydrogenation reaction pathways of $\text{H}(\text{NH}_2\text{BH}_2)_n\text{H}$ ($n = 1-4$) oligomers: Importance of dihydrogen interactions," *Inorganic Chemistry*, vol. 49, pp. 7710 – 7720, 2010.

DOI: 10.1021/ic100418a.

- [170] P. P. Kumar, A. G. Kalinichev, and R. J. Kirkpatrick, "Dissociation of carbonic acid: Gas phase energetics and mechanism from ab initio metadynamics simulations," *The Journal of Chemical Physics*, vol. 126, p. 204315, 2007.

DOI: 10.1063/1.2741552.

- [171] X. Liu, J.-H. Zhan, D. Lai, X. Liu, Z. Zhang, and G. Xu, "Initial pyrolysis mechanism of oil shale kerogen with reactive molecular dynamics simulation," *Energy & Fuels*, vol. 29, pp. 2987 – 2997, 2015.

DOI: 10.1021/acs.energyfuels.5b00084.

- [172] C. Domene, P. Portius, P. W. Fowler, and L. Bernasconi, "Simulating the pyrolysis of polyazides: a mechanistic case study of the $[\text{P}(\text{N}_3)_6]$ -anion," *Inorganic Chemistry*, vol. 52, pp. 1747 – 1754, 2013.

DOI: 10.1021/ic301178h.

- [173] X. Dong, X. Fan, Y. Fan, and Y. Wen, "Reactive molecular dynamics simulation of the pyrolysis and combustion of benzene: ultrahigh temperature and oxygen-induced en-

- hancement of initiation pathways and their effect on carbon black generation,” *RSC Advances*, vol. 5, pp. 43695 – 43704, 2015.
DOI: 10.1039/C5RA02247A.
- [174] M. Zheng, X. Li, J. Liu, Z. Wang, X. Gong, L. Guo, and W. Song, “Pyrolysis of liulin coal simulated by GPU-based reaxff md with cheminformatics analysis,” *Energy & Fuels*, vol. 28, pp. 522–534, 2014.
DOI: 10.1021/ef402140n.
- [175] J. qin Li, F. Wang, X. ming Cheng, and X. yuan Li, “Reactive molecular dynamics simulation on thermal decomposition of n-heptane,” *Chinese Journal of Chemical Physics*, vol. 26, pp. 211 – 219, 2013.
DOI: 10.1063/1674-0068/26/02/211-219.
- [176] Q. Wu, W. Zhu, and H. Xiao, “An ab initio molecular dynamics study of thermal decomposition of 3,6-di(azido)-1,2,4,5-tetrazine,” *Physical Chemistry Chemical Physics*, vol. 16, pp. 21620 – 21628, 2014.
DOI: 10.1039/C4CP02579B.
- [177] L. Ramin, M. H. N. Assadi, and V. Sahajwalla, “High-density polyethylene degradation into low molecular weight gases at 1823 k: An atomistic simulation,” *Journal of Analytical and Applied Pyrolysis*, vol. 110, pp. 318 – 321, 2014.
DOI: 10.1016/j.jaap.2014.09.022B.
- [178] C. Jee, Z. Guo, S. Stoliarov, and M. Nyden, “Experimental and molecular dynamics studies of the thermal decomposition of a polyisobutylene binder,” *Acta Materialia*, vol. 54, pp. 4803 – 4813, 2006.
DOI: 10.1016/j.actamat.2006.06.014.
- [179] N. J. Mosey and T. K. Woo, “Finite temperature structure and dynamics of zinc dialkyldithiophosphate wear inhibitors: A density functional theory and ab initio molecular dynamics study,” *The Journal of Physical Chemistry A*, vol. 107, pp. 5058–5070, 2003.
DOI: 10.1021/jp034085c.
- [180] S. Alonso-Gil, A. Males, P. Z. Fernandes, S. J. Williams, G. J. Davies, and C. Rovira, “Computational design of experiment unveils the conformational reaction coordinate of GH125 α -mannosidases,” *Journal of the American Chemical Society*, vol. 139, pp. 1085–1088, 2017.
DOI: 10.1021/jacs.6b11247.
- [181] T. Demes, C. Ternon, D. Riassetto, H. Roussel, L. Rapenne, I. Gélard, C. Jimenez, V. Stambouli, and M. Langlet, “New insights in the structural and morphological properties

- of sol-gel deposited ZnO multilayer films,” *Journal of Physics and Chemistry of Solids*, vol. 95, pp. 43 – 55, 2016.
DOI: 10.1016/j.jpcs.2016.03.017.
- [182] B. N. Joshi, H. Yoon, H. Y. Kim, J. H. Oh, T. Y. Seong, S. C. James, and S. S. Yoon, “Effect of zinc acetate concentration on structural, optical and electrical properties of ZnO thin films deposited by electrostatic spray on an ito substrate,” *Journal of The Electrochemical Society*, vol. 159, pp. H716 – H721, 2012.
DOI: 10.1149/2.077208jes.
- [183] D. G. Ayana, R. Ceccato, C. Collini, L. Lorenzelli, V. Prusakova, and S. Dirè, “Sol-gel derived oriented multilayer ZnO thin films with memristive response,” *Thin Solid Films*, vol. 615, pp. 427 – 436, 2016.
DOI: 10.1016/j.tsf.2016.07.025.
- [184] M. Z. Sahdan, N. Nafarizal, S. A. Kamaruddin, C. A. Norhidayah, and S. N. Mohd Tawil, “Effects of ageing time of ZnO sol on properties of ZnO films by sol gel spin coating,” *Advanced Materials Research*, vol. 925, pp. 329 – 333, 2014.
DOI: 10.4028/www.scientific.net/AMR.925.329.
- [185] I. Jeon, J. W. Ryan, T. Nakazaki, K. S. Yeo, Y. Negishi, and Y. Matsuo, “Air-processed inverted organic solar cells utilizing a 2-aminoethanol-stabilized ZnO nanoparticle electron transport layer that requires no thermal annealing,” *Journal of Materials Chemistry A*, vol. 2, pp. 18754 – 18760, 2014.
DOI: 10.1039/C4TA04595E.
- [186] S. Khodja, T. Touam, A. Chelouche, F. Boudjouan, D. Djouadi, Z. Hadjoub, A. Fischer, and A. Boudrioua, “Effects of stabilizer ratio on structural, morphological, optical and waveguide properties of ZnO nano-structured thin films by a sol-gel process,” *Superlattices and Microstructures*, vol. 75, pp. 485 – 495, 2014.
DOI: 10.1016/j.spmi.2014.08.010.
- [187] S. Aydemir and S. Karakaya, “Effects of withdrawal speed on the structural and optical properties of sol-gel derived ZnO thin films,” *Journal of Magnetism and Magnetic Materials*, vol. 373, pp. 33 – 39, 2015.
DOI: 10.1016/j.jmmm.2014.01.077.
- [188] Y. N. Liang, B. K. Lok, L. Wang, C. Feng, A. C. W. Lu, T. Mei, and X. Hu, “Effects of the morphology of inkjet printed zinc oxide (ZnO) on thin film transistor performance and seeded ZnO nanorod growth,” *Thin Solid Films*, vol. 544, pp. 509 – 514, 2013.
DOI: 10.1016/j.tsf.2013.01.032.

- [189] C. P. Tsangarides, H. Ma, and A. Nathan, "ZnO nanowire array growth on precisely controlled patterns of inkjet-printed zinc acetate at low-temperatures," *Nanoscale*, vol. 8, pp. 11760 – 11765, 2016.
DOI: 10.1039/C6NR02962K.
- [190] R. Costa, C. López, E. Molins, and E. Espinosa, "Synthesis, Structure, and Properties of a Tetrametallic Ferrocenecarboxylato-Bridged Copper(II) Complex," *Inorganic Chemistry*, vol. 37, pp. 5686–5689, 1998.
DOI: 10.1021/ic980409d.
- [191] R. Costa, C. Lopez, E. Molins, E. Espinosa, and J. Perez, "Heterodimetallic copper(ii) compounds containing ferrocenecarboxylato(-1) and triamines as ligands," *Journal of the Chemical Society, Dalton Transactions*, pp. 2833–2837, 2001.
DOI: 10.1039/B102030G.
- [192] C. Lopez, R. Costa, F. Illas, C. de Graaf, M. M. Turnbull, C. P. Landee, E. Espinosa, I. Mata, and E. Molins, "Magneto-structural correlations in binuclear copper(ii) compounds bridged by a ferrocenecarboxylato(-1) and an hydroxo- or methoxo-ligands," *Dalton Transactions*, pp. 2322–2330, 2005.
DOI: 10.1039/B502264A.
- [193] W. I. Pérez, Y. Soto, C. Ortíz, J. Matta, and E. Meléndez, "Ferrocenes as potential chemotherapeutic drugs: synthesis, cytotoxic activity, reactive oxygen species production and micronucleus assay," *Bioorganic & medicinal chemistry*, vol. 23, pp. 471 – 9, 2015.
DOI: 10.1016/j.bmc.2014.12.023.
- [194] A. Togni and T. Hayashi, *Ferrocenes: Homogeneous Catalysis, Organic Synthesis, Materials Science*.
Wiley-VCH Verlag GmbH, pp 540, 2007.
DOI: 10.1002/9783527615599 ; ISBN: 9783527615599.
- [195] P. (Editor)-Stepnicka, *Ferrocenes: Ligands, Materials and Biomolecules*.
Wiley-VCH Verlag GmbH, pp 670, 2008.
ISBN: 978-0-470-03585-6.
- [196] L.-X. Dai and X.-L. Hou, *Chiral Ferrocenes in Asymmetric Catalysis: Synthesis and Applications*.
Wiley-VCH Verlag GmbH, pp 431, 2009.
ISBN: 978-3-527-32280-0.
- [197] F. A. Larik, A. Saeed, T. A. Fattah, U. Muqadar, and P. A. Channar, "Recent advances in the synthesis, biological activities and various applications of ferrocene derivatives," *Applied Organometallic Chemistry*, 2016.

BIBLIOGRAPHY

- DOI: 10.1002/aoc.3664.
- [198] M. Denisov, A. Gorbunov, M. V. Dmitriev, P. Slepukhin, and V. Glushkov, "Synthesis and structure of ferrocenol esters," *International Journal of Organic Chemistry*, 2016.
DOI: 10.4236/ijoc.2016.62012.
- [199] R. A. Layfield, "Organometallic single-molecule magnets," *Organometallics*, vol. 33, pp. 1084 – 1099, 2014.
DOI: 10.1021/om401107f.
- [200] Z. H. Chohan, A. Scozzafava, and C. T. Supuran, "Synthesis of Biologically Active Co(II), Cu(II), Ni(II) and Zn(II) Complexes of Symmetrically 1,1'-Disubstituted Ferrocene-Derived Compounds," *Synthesis and Reactivity in Inorganic and Metal-Organic Chemistry*, vol. 33, pp. 241–257, 2003.
DOI: 10.1081/SIM-120017783.
- [201] S. Ali, G. Yasin, Z. Zuhra, Z. Wu, I. S. Butler, A. Badshah, , and I. ud Din, "Ferrocene-Based Bioactive Bimetallic Thiourea Complexes: Synthesis and Spectroscopic Studies," *Bioinorganic Chemistry and Applications*, vol. 15, p. 386587, 2015.
DOI: 10.1155/2015/386587.
- [202] B. Cullity and S.R.Stock, *Elements of X Ray Diffraction*.
Addison-Wesley Publishing Company, Inc., pp 514, 1956.
DOI: 10.1119/1.1934486 ; ISBN: 9781178511420.
- [203] C. M. Clark and B. L. Dutrow, "Single-crystal X-ray Diffraction." http://serc.carleton.edu/research_education/geochemsheets/techniques/SXD.html.
Accessed: 2017-02-06.
- [204] M. Martínez-Ripoll, "Crystallography-Cristalografia." <http://www.xtal.iqfr.csic.es/Cristalografia/index-en.html>.
Accessed: 2016-12-22.
- [205] R. Dinnebier and S. Billinge-(Editors), *Powder Diffraction: Theory and Practice*.
The Royal Society of Chemistry, pp 604, 2008.
DOI: 10.1039/9781847558237 ISBN: 978-0-85404-231-9.
- [206] P. de Wolff, "A simplified criterion for the reliability of a powder pattern indexing," *Journal of Applied Crystallography*, vol. 1, pp. 108 – 113, 1968.
DOI: 10.1107/S002188986800508X.
- [207] G. Smith and R. Synder, " F_N : A criterion for rating powder diffraction patterns and evaluating the reliability of powder-pattern indexing," *Journal of Applied Crystallography*, vol. 12, pp. 60 – 65, 1979.

- DOI: 10.1107/S002188987901178X.
- [208] A. le Bail, H. Duroy, and J. Fourquet, "Ab-initio structure determination of LiSbWO_6 by x-ray powder diffraction," *Materials Research Bulletin*, vol. 23, pp. 447 – 452, 1988.
DOI: 10.1016/0025-5408(88)90019-0.
- [209] A. Boultif and D. Louër, "Indexing of powder diffraction patterns for low-symmetry lattices by the successive dichotomy method," *Journal of Applied Crystallography*, vol. 24, pp. 987 – 993, 1991.
DOI: 10.1107/S0021889891006441.
- [210] D. Louër and M. Louër, "Méthode d'essais et erreurs pour l'indexation automatique des diagrammes de poudre," *Journal of Applied Crystallography*, vol. 5, pp. 271 – 275, 1972.
DOI: 10.1107/S0021889872009483.
- [211] A. Boultif and D. Louër, "Powder pattern indexing with the dichotomy method," *Journal of Applied Crystallography*, vol. 37, pp. 724 – 731, 2004.
DOI: 10.1107/S0021889804014876.
- [212] D. Louër and A. Boultif, "Powder pattern indexing and the dichotomy algorithm," *Zeitschrift für Kristallographie, Supplement*, vol. 1, no. 26, pp. 191 – 196, 2007.
DOI: 10.1524/zkri.2007.2007.suppl_26.191.
- [213] T. Hahn-(Editor), *International Tables for Crystallography, Volume A, Space-group symmetry*.
International union of crystallography, Springer, 5th edition, pp 910, 2005.
ISBN: 0-7923-6590-9.
- [214] H. M. Rietveld, "Line profiles of neutron powder-diffraction peaks for structure refinement," *Acta Crystallographica*, vol. 22, pp. 60 – 65, 1967.
DOI: 10.1107/S0365110X67000234.
- [215] H. M. Rietveld, "A profile refinement method for nuclear and magnetic structures," *Journal of Applied Crystallography*, vol. 2, pp. 65 – 71, 1969.
DOI: 10.1107/S0021889869006558.
- [216] V. Favre-Nicolin and R. Černý, "FOX, Free Objects for Crystallography: A modular approach to ab initio structure determination from powder diffraction," *Journal of Applied Crystallography*, vol. 35, pp. 734 – 743, 2002.
DOI: 10.1107/S0021889802015236.
- [217] O. H. Duparc, "Pierre Auger - Lise Meitner: Comparative contributions to the Auger effect," *International Journal of Materials Research*, vol. 100, pp. 1162 – 1166, 2009.
DOI: 10.3139/146.110163.

BIBLIOGRAPHY

- [218] R. Sietmann, “False attribution,” *Physics Bulletin*, vol. 39, p. 316, 1988.
DOI: 10.1088/0031-9112/39/8/017.
- [219] L. Meitner, “Über den zusammenhang zwischen β - und γ -strahlen,” *Zeitschrift für Physik*, vol. 9, pp. 145 – 152, 1922.
DOI: 10.1007/BF01326963.
- [220] L. Meitner, “Das β -strahlenspektrum von ^{137}I und seine deutung,” *Zeitschrift für Physik*, vol. 17, pp. 54 – 66, 1923.
DOI: 10.1007/BF01328663.
- [221] P. Auger, “Sur les rayons β secondaires produits dans un gaz par des rayons X,” *Comptes rendus de l’Académie des sciences*, vol. 177, pp. 169 – 171, 1923.
- [222] E. de Hoffmann and V. Stroobant, *Mass Spectrometry: Principles and Applications*.
John Wiley & Sons Ltd, 3d Edition, pp 502, 2007.
ISBN: 978-0-470-03310-4.
- [223] A. Szabo and N. S. Ostlund, *Modern Quantum Chemistry: Introduction to Advanced Electronic Structure Theory*.
Dover Publications, Inc., pp 480, 1982.
ISBN: 978-0486691862.
- [224] P. Hohenberg and W. Kohn, “Inhomogeneous electron gas,” *Physical Review*, vol. 136, p. B864, 1964.
DOI: 10.1103/PhysRev.136.B864.
- [225] W. Kohn and L.J.Sham, “Self-consistent equations including exchange and correlation effects,” *Physical Review*, vol. 140, p. A1133, 1965.
DOI: 10.1103/PhysRev.140.A1133.
- [226] P. Dirac, “Note on exchange phenomena in the thomas atom,” *Mathematical Proceedings of the Cambridge Philosophical Society*, vol. 26, pp. 376 – 385, 1930.
DOI: 10.1017/S0305004100016108.
- [227] J. P. Perdew and W. Yue, “Accurate and simple density functional for the electronic exchange energy: Generalized gradient approximation,” *Physical Review B*, vol. 33, pp. 8800 – 8802, Jun 1986.
DOI: 10.1103/PhysRevB.33.8800.
- [228] C. Lee, W. Yang, and R. G. Parr, “Development of the colle-salvetti correlation-energy formula into a functional of the electron density,” *Physical Review B*, vol. 37, pp. 785 – 789, Jan 1988.
DOI: 10.1103/PhysRevB.37.785.

- [229] E. Runge and E. K. U. Gross, "Density-functional theory for time-dependent systems," *Phys. Rev. Lett.*, vol. 52, pp. 997–1000, Mar 1984.
DOI: 10.1103/PhysRevLett.52.997.
- [230] E. K. U. Gross and W. Kohn, "Local density-functional theory of frequency-dependent linear response," *Phys. Rev. Lett.*, vol. 55, pp. 2850–2852, Dec 1985.
DOI: 10.1103/PhysRevLett.55.2850.
- [231] L. Verlet, "Computer "experiments" on classical fluids. i. thermodynamical properties of lennard-jones molecules," *Phys. Rev.*, vol. 159, pp. 98 – 103, Jul 1967.
DOI: 10.1103/PhysRev.159.98.
- [232] D. J. E. Callaway and A. Rahman, "Microcanonical ensemble formulation of lattice gauge theory," *Phys. Rev. Lett.*, vol. 49, pp. 613–616, Aug 1982.
DOI: 10.1103/PhysRevLett.49.613.
- [233] T. D. Kühne, M. Krack, F. R. Mohamed, and M. Parrinello, "Efficient and accurate Car-Parrinello-like approach to born-oppenheimer molecular dynamics," *Phys. Rev. Lett.*, vol. 98, p. 066401, Feb 2007.
DOI: 10.1103/PhysRevLett.98.066401.
- [234] A. Barducci, M. Bonomi, and M. Parrinello, "Metadynamics," *Wiley Interdisciplinary Reviews: Computational Molecular Science*, vol. 1, no. 5, pp. 826–843, 2011.
DOI: 10.1002/wcms.31.
- [235] A. Laio and F. L. Gervasio, "Metadynamics: a method to simulate rare events and reconstruct the free energy in biophysics, chemistry and material science," *Reports on Progress in Physics*, vol. 71, no. 12, p. 126601, 2008.
DOI: 10.1088/0034-4885/71/12/126601.
- [236] M. Iannuzzi, A. Laio, and M. Parrinello, "Efficient exploration of reactive potential energy surfaces using Car-Parrinello molecular dynamics," *Phys. Rev. Lett.*, vol. 90, p. 238302, Jun 2003.
DOI: 10.1103/PhysRevLett.90.238302.
- [237] C. Sudbrake and H. Vahrenkamp, "Neue ons-liganden und ihre zinkkomplexe mit bezug zum zinkenzym alkoholdehydrogenase," *Zeitschrift für anorganische und allgemeine Chemie*, vol. 627, no. 5, pp. 857–862, 2001.
DOI: 10.1002/1521-3749(200105)627:5<857::AID-ZAAC857>3.0.CO;2-7.
- [238] N. Hollingsworth, M. Kanna, G. Kociok-Kohn, K. C. Molloy, and S. Wongnawa, "Synthesis and characterisation of new titanium amino-alkoxides: precursors for the formation of TiO₂ materials," *Dalton Transactions*, pp. 631–641, 2008.

- DOI: 10.1039/B712375B.
- [239] B.-H. Ye, X.-Y. Li, I. D. Williams, and X.-M. Chen, "Synthesis and structural characterization of di- and tetranuclear zinc complexes with phenolate and carboxylate bridges. correlations between ^{13}C NMR chemical shifts and carboxylate binding modes," *Inorganic Chemistry*, vol. 41, pp. 6426–6431, 2002.
DOI: 10.1021/ic025806+.
- [240] F. H. Allen, "The Cambridge Structural Database: a quarter of a million crystal structures and rising," *Acta Crystallographica Section B*, vol. 58, pp. 380 – 388, 2002.
DOI: 10.1107/S0108768102003890.
- [241] J. Farjas, J. Camps, P. Roura, S. Ricart, T. Puig, and X. Obradors, "The thermal decomposition of barium trifluoroacetate," *Thermochimica Acta*, vol. 544, pp. 77 – 83, 2012.
DOI: 10.1016/j.tca.2012.06.020.
- [242] H. Eloussifi, J. Farjas, P. Roura, J. Camps, M. Dammak, S. Ricart, T. Puig, and X. Obradors, "Evolution of yttrium trifluoroacetate during thermal decomposition," *Journal of Thermal Analysis and Calorimetry*, vol. 108, pp. 589–596, 2012.
DOI: 10.1007/s10973-011-1899-5.
- [243] G. Bouchoux, N. Choret, F. Berruyer-Penaud, and R. Flammang, "Thermochemistry and unimolecular reactivity of protonated α,ω -aminoalcohols in the gas phase," *International Journal of Mass Spectrometry*, vol. 217, pp. 195 – 230, 2002.
DOI: 10.1016/S1387-3806(02)00577-8.
- [244] P. Roura, J. Farjas, H. Eloussifi, L. Carreras, S. Ricart, T. Puig, and X. Obradors, "Thermal analysis of metal organic precursors for functional oxide preparation: Thin films versus powders," *Thermochimica Acta*, vol. 601, pp. 1 – 8, 2015.
DOI: 10.1016/j.tca.2014.12.016.
- [245] L. Yang, Q. Zhao, M. Willander, X. Liu, M. Fahlman, and J. Yang, "Origin of the surface recombination centers in ZnO nanorods arrays by X-ray photoelectron spectroscopy," *Applied Surface Science*, vol. 256, pp. 3592 – 3597, 2010.
DOI: 10.1016/j.apsusc.2009.12.160.
- [246] A. Gómez-Núñez, C. López, S. Alonso-Gil, P. Roura, and A. Vilà, "Study of a sol-gel precursor and its evolution towards ZnO," *Materials Chemistry and Physics*, vol. 162, pp. 645 – 651, 2015.
DOI: 10.1016/j.matchemphys.2015.06.038.
- [247] A. D. Becke, "Density-functional thermochemistry. III. The role of exact exchange," *The Journal of Chemical Physics*, vol. 98, pp. 5648–5652, 1993.

DOI: 10.1063/1.464913.

- [248] C. Lee, W. Yang, and R. G. Parr, "Development of the colle-salvetti correlation-energy formula into a functional of the electron density," *Physical Review B*, vol. 37, pp. 785 – 789, 1988.

DOI: 10.1103/PhysRevB.37.785.

- [249] W. R. Wadt and P. J. Hay, "Ab initio effective core potentials for molecular calculations. Potentials for main group elements Na to Bi," *The Journal of Chemical Physics*, vol. 82, pp. 284–298, 1985.

DOI: 10.1063/1.448800.

- [250] P. J. Hay and W. R. Wadt, "Ab initio effective core potentials for molecular calculations. Potentials for the transition metal atoms Sc to Hg," *The Journal of Chemical Physics*, vol. 82, pp. 270–283, 1985.

DOI: 10.1063/1.448799.

- [251] J. Tomasi, B. Mennucci, and R. Cammi, "Quantum Mechanical Continuum Solvation Models," *Chemical Reviews*, vol. 105, pp. 2999–3094, 2005.

DOI: 10.1021/cr9904009.

- [252] F. Furche and R. Ahlrichs, "Erratum: "Time-dependent density functional methods for excited state properties" [J. Chem. Phys. 117, 7433 (2002)]," *The Journal of Chemical Physics*, vol. 121, pp. 12772–12773, 2004.

DOI: 10.1063/1.1824903.

- [253] G. Scalmani, M. J. Frisch, B. Mennucci, J. Tomasi, R. Cammi, and V. Barone, "Geometries and properties of excited states in the gas phase and in solution: Theory and application of a time-dependent density functional theory polarizable continuum model," *The Journal of Chemical Physics*, vol. 124, p. 094107, 2006.

DOI: 10.1063/1.2173258.

- [254] A. Gómez-Núñez, P. Roura, C. López, and A. Vilà, "Comparison of the thermal decomposition processes of several aminoalcohol-based ZnO inks with one containing ethanolamine," *Applied Surface Science*, vol. 381, pp. 48 – 53, 2016.

DOI: 10.1016/j.apsusc.2016.03.138.

- [255] A. Gómez-Núñez, S. Alonso-Gil, C. López, and A. Vilà, "Electronic and dynamic dft studies on the substituent effects of aminoalcohol stabilizers in sol-gel zno precursor," *physica status solidi (a)*, vol. 213, no. 9, pp. 2329–2335, 2016.

DOI: 10.1002/pssa.201532885.

BIBLIOGRAPHY

- [256] P. V. Kortunov, M. Siskin, L. S. Baugh, and D. C. Calabro, "In Situ Nuclear Magnetic Resonance Mechanistic Studies of Carbon Dioxide Reactions with Liquid Amines in Non-aqueous Systems: Evidence for the Formation of Carbamic Acids and Zwitterionic Species," *Energy & Fuels*, vol. 29, pp. 5940–5966, 2015.
DOI: 10.1021/acs.energyfuels.5b00985.
- [257] E. Quaranta and M. Aresta, *The Chemistry of N-CO₂ Bonds: Synthesis of Carbamic Acids and Their Derivatives, Isocyanates, and Ureas*, pp. 121 – 167.
Wiley-VCH Verlag GmbH & Co. KGaA, 2010.
DOI: 10.1002/9783527629916.ch6.
- [258] S. J. Vevelstad, M. T. Johansen, H. Knuutila, and H. F. Svendsen, "Extensive dataset for oxidative degradation of ethanolamine at 55-75 °C and oxygen concentrations from 6 to 98 %," *International Journal of Greenhouse Gas Control*, vol. 50, pp. 158 – 178, 2016.
DOI: 10.1016/j.ijggc.2016.04.013.
- [259] P. J. Taylor, *The "Basicity Method" for Estimating Tautomer Ratio: A Radical Re-Appraisal*, pp. 305 – 335.
Wiley-VCH Verlag GmbH & Co. KGaA, 2013.
DOI: 10.1002/9783527658824.ch12.
- [260] L. Lazar and F. Fülöp, "Recent Developments in the Ring-Chain Tautomerism of 1,3-Heterocycles," *European Journal of Organic Chemistry*, vol. 2003, pp. 3025 – 3042, 2003.
DOI: 10.1002/ejoc.200300142.
- [261] X. Ge, S. L. Shaw, and Q. Zhang, "Toward Understanding Amines and Their Degradation Products from Postcombustion CO₂ Capture Processes with Aerosol Mass Spectrometry," *Environmental Science & Technology*, vol. 48, pp. 5066 – 5075, 2014.
DOI: 10.1021/es4056966.
- [262] T. Zhang and Z. Zhang, "Computational Study of CO₂ Absorption in Aqueous and Non-aqueous Solutions Using MEA," *Energy Procedia*, vol. 63, pp. 1347 – 1353, 2014.
DOI: 10.1016/j.egypro.2014.11.144.
- [263] C. J. Kim, A. M. Palmer, and G. E. Milliman, "Absorption of carbon monoxide into aqueous solutions of potassium carbonate, methyl-diethanolamine, and diethylethanolamine," *Industrial & Engineering Chemistry Research*, vol. 27, pp. 324–328, 1988.
DOI: 10.1021/ie00074a019.
- [264] S. Nosé, "A unified formulation of the constant temperature molecular dynamics methods," *The Journal of Chemical Physics*, vol. 81, pp. 511–519, 1984.
DOI: 10.1063/1.447334.

- [265] R. Silverstein, F. Webster, and D. Kiemle, *Spectrometric Identification of Organic Compounds, 8th Edition*. CRC Press LLC, pp 464, 2014. ISBN: 978-0-470-61637-6.
- [266] K. Van Werde, D. Mondelaers, G. Vanhoyland, D. Nelis, M. K. Van Bael, J. Mullens, L. C. Van Poucke, B. Van Der Veken, and H. O. Desseyn, "Thermal decomposition of the ammonium zinc acetate citrate precursor for aqueous chemical solution deposition of ZnO," *Journal of Materials Science*, vol. 37, pp. 81–88, 2002. DOI: 10.1023/A:1013141723764.
- [267] S. Mihaiu, I. M. Szilágyi, I. Atkinson, O. C. Mocioiu, D. Hunyadi, J. Pandelescu, A. Toader, C. Munteanu, S. Boyadjiev, J. Madarász, G. Pokol, and M. Zaharescu, "Thermal study on the synthesis of the doped ZnO to be used in TCO films," *Journal of Thermal Analysis and Calorimetry*, vol. 124, pp. 71–80, 2016. DOI: 10.1007/s10973-015-5147-2.
- [268] C. R. Groom, I. J. Bruno, M. P. Lightfoot, and S. C. Ward, "The Cambridge Structural Database," *Acta Crystallographica Section B*, vol. 72, pp. 171 – 179, 2016. Accessed on March 2017. DOI: 10.1107/S2052520616003954.
- [269] A. K. Gupta, A. Dhir, and C. P. Pradeep, "Multifunctional Zn(II) Complexes: Photophysical Properties and Catalytic Transesterification toward Biodiesel Synthesis," *Inorganic Chemistry*, vol. 55, pp. 7492–7500, 2016. DOI: 10.1021/acs.inorgchem.6b00804.
- [270] R. Puglisi, F. P. Ballistreri, C. M. A. Gangemi, R. M. Toscano, G. A. Tomaselli, A. Pappalardo, and G. T. Sfrassetto, "Chiral Zn-salen complexes: a new class of fluorescent receptors for enantiodiscrimination of chiral amines," *New Journal of Chemistry*, vol. 41, pp. 911–915, 2017. DOI: 10.1039/C6NJ03592B.
- [271] V. V. Karambelkar, D. Krishnamurthy, C. L. Stern, L. N. Zakharov, A. L. Rheingold, and D. P. Goldberg, "A new bis(imidazolyl)(alkylthiolate) tripodal ligand and the spontaneous formation of a disulfide-linked, hydroxo-bridged dinuclear zinc complex," *Chemical Communications*, pp. 2772 – 2773, 2002. DOI: 10.1039/B207770A.
- [272] A. L. Johnson, N. Hollingsworth, G. Kociok-Köhn, and K. C. Molloy, "Organozinc Aminoalcohols: Synthesis, Structure, and Materials Chemistry," *Inorganic Chemistry*, vol. 47, pp. 12040–12048, 2008. DOI: 10.1021/ic801591d.

BIBLIOGRAPHY

- [273] M. Umayal and G. Mugesh, "Metallo- β -lactamase and phosphotriesterase activities of some zinc(II) complexes," *Inorganica Chimica Acta*, vol. 372, pp. 353 – 361, 2011.
DOI: 10.1016/j.ica.2011.03.064.
- [274] N. Hollingsworth, M. Kanna, G. Kociok-Kohn, K. C. Molloy, and S. Wongnawa, "Synthesis and characterisation of new titanium amino-alkoxides: precursors for the formation of TiO₂ materials," *Dalton Transactions*, pp. 631 – 641, 2008.
DOI: 10.1039/B712375B.
- [275] P.-U. Maheswari, S. Barends, S. Özalp Yaman, P. de Hoog, H. Casellas, S. J. Teat, C. Massera, M. Lutz, A. L. Spek, G. P. van Wezel, P. Gamez, and J. Reedijk, "Unique Ligand-Based Oxidative DNA Cleavage by Zinc(II) Complexes of Hpyramol and Hpyrimol," *Chemistry - A European Journal*, vol. 13, pp. 5213 – 5222, 2007.
DOI: 10.1002/chem.200601525.
- [276] H. He, F. Zhuge, Z. Ye, L. Zhu, B. Zhao, and J. Huang, "Defect-related vibrational and photoluminescence spectroscopy of a codoped ZnO:Al:N film," *Journal of Physics D: Applied Physics*, vol. 39, p. 2339, 2006.
DOI: 10.1088/0022-3727/39/11/004.
- [277] W. P. Griffith and T. Y. Koh, "Vibrational spectra of 1,2-benzenedithiol, 2-aminothiophenol and 2-aminophenol and their SER spectra," *Spectrochimica Acta Part A: Molecular and Biomolecular Spectroscopy*, vol. 51, pp. 253 – 267, 1995.
DOI: 10.1016/0584-8539(94)E0086-P.
- [278] S. H. Yoon, D. Liu, D. Shen, M. Park, and D.-J. Kim, "Effect of chelating agents on the preferred orientation of ZnO films by sol-gel process," *Journal of Materials Science*, vol. 43, pp. 6177 – 6181, 2008.
DOI: 10.1007/s10853-008-2929-y.
- [279] N. V. Kaneva, G. G. Yordanov, and C. D. Dushkin, "Manufacturing of patterned ZnO films with application for photoinitiated decolorization of malachite green in aqueous solutions," *Bulletin of Materials Science*, vol. 33, pp. 111 – 117, 2010.
DOI: 10.1007/s12034-010-0015-y.
- [280] K. Zalamova, N. Romà, A. Pomar, S. Morlens, T. Puig, J. Gázquez, A. E. Carrillo, F. Sandi-umenge, S. Ricart, N. Mestres, and X. Obradors, "Smooth stress relief of trifluoroacetate metal-organic solutions for YBa₂Cu₃O₇ film growth," *Chemistry of Materials*, vol. 18, pp. 5897–5906, 2006.
DOI: 10.1021/cm061556+.
- [281] J. C. Slater, *The Self-consistent Field for Molecules and Solids. Quantum Theory of Molecules and Solids; Volume 4. Pure & Applied Physics.*

- McGraw-Hill Inc.,US; 1st edition, pp 640, 1974.
DOI: 10.1063/1.3129035 ; ISBN: 978-0070580381.
- [282] S. H. Vosko, L. Wilk, and M. Nusair, “Accurate spin-dependent electron liquid correlation energies for local spin density calculations: a critical analysis,” *Canadian Journal of Physics*, vol. 58, pp. 1200–1211, 1980.
DOI: 10.1139/p80-159.
- [283] W. G. Hoover, “Canonical dynamics: Equilibrium phase-space distributions,” *Physical Review A*, vol. 31, pp. 1695 – 1697, 1985.
DOI: 10.1103/PhysRevA.31.1695.
- [284] C. Pulgarin and J. Kiwi, “Iron oxide-mediated degradation, photodegradation, and biodegradation of aminophenols,” *Langmuir*, vol. 11, pp. 519–526, 1995.
DOI: 10.1021/la00002a026.
- [285] P.-Y. Chen, M. Liu, T. M. Valentin, Z. Wang, R. Spitz Steinberg, J. Sodhi, I. Y. Wong, and R. H. Hurt, “Hierarchical metal oxide topographies replicated from highly textured graphene oxide by intercalation templating,” *ACS Nano*, vol. 10, pp. 10869–10879, 2016.
DOI: 10.1021/acsnano.6b05179.
- [286] N. Montoya Sánchez and A. de Klerk, “Oxidative ring-opening of aromatics: Decomposition of biphenyl carboxylic acids and zinc biphenyl carboxylates,” *Energy & Fuels*, vol. 29, pp. 7910–7922, 2015.
DOI: 10.1021/acs.energyfuels.5b02066.
- [287] C.-Y. Tsay, K.-S. Fan, S.-H. Chen, and C.-H. Tsai, “Preparation and characterization of ZnO transparent semiconductor thin films by sol-gel method,” *Journal of Alloys and Compounds*, vol. 495, pp. 126 – 130, 2010.
DOI: 10.1016/j.jallcom.2010.01.100.
- [288] H. Hemilä, E. J. Petrus, J. T. Fitzgerald, and A. Prasad, “Zinc acetate lozenges for treating the common cold: an individual patient data meta-analysis,” *British Journal of Clinical Pharmacology*, vol. 82, pp. 1393 – 1398, 2016.
DOI: 10.1111/bcp.13057.
- [289] J. Hu, Y. Xie, X. Zhou, and J. Yang, “Solid-state synthesis of ZnO and ZnFe₂O₄ to form p-n junction composite in the use of dye sensitized solar cells,” *Journal of Alloys and Compounds*, vol. 676, pp. 320 – 325, 2016.
DOI: 10.1016/j.jallcom.2016.03.082.
- [290] A. Mekap, P. R. Das, and R. N. P. Choudhary, “Dielectric, magnetic and electrical properties of ZnFe₂O₄ ceramics,” *Journal of Materials Science: Materials in Electronics*, vol. 24, pp. 4757 – 4763, 2013.

DOI: 10.1007/s10854-013-1470-1.

- [291] Y. Sun, W. Wang, L. Zhang, S. Sun, and E. Gao, "Magnetic ZnFe₂O₄ octahedra: Synthesis and visible light induced photocatalytic activities," *Materials Letters*, vol. 98, pp. 124 – 127, 2013.

DOI: 10.1016/j.matlet.2013.02.014.

- [292] J. Feng, Y. Wang, L. Zou, B. Li, X. He, Y. Ren, Y. Lv, and Z. Fan, "Synthesis of magnetic ZnO/ZnFe₂O₄ by a microwave combustion method, and its high rate of adsorption of methylene blue," *Journal of Colloid and Interface Science*, vol. 438, pp. 318 – 322, 2015.

DOI: 10.1016/j.jcis.2014.10.009.

- [293] M. Yasumoto, I. Sakamoto, H. Nakayama, R. Kinoshita, M. Koike, and S. Honda, "Transmission electron microscopy investigation of ZnFeO/ZnO multilayered dilute magnetic semiconductor," *Japanese Journal of Applied Physics*, vol. 53, 2014.

DOI: 10.7567/JJAP.53.05FB07.

- [294] J. Ma, Y. Cai, X. Li, S. Yao, Y. Liu, F. Liu, and G. Lu, "Synthesis of hierarchical ZnO/ZnFe₂O₄ nanoforests with enhanced gas-sensing performance toward ethanol," *CrystEngComm*, vol. 17, pp. 8683 – 8688, 2015.

DOI: 10.1039/C5CE01919B.

- [295] S. Wang, J. Zhang, J. Yang, X. Gao, H. Zhang, Y. Wang, and Z. Zhu, "Spinel ZnFe₂O₄ nanoparticle-decorated rod-like ZnO nanoheterostructures for enhanced gas sensing performances," *RSC Advances*, vol. 5, pp. 10048 – 10057, 2015.

DOI: 10.1039/C4RA14033H.

- [296] M. Zhuo, T. Yang, T. Fu, and Q. Li, "High-performance humidity sensors based on electrospinning ZnFe₂O₄ nanotubes," *RSC Advances*, vol. 5, pp. 68299 – 68304, 2015.

DOI: 10.1039/C5RA09903J.

- [297] S. Wang, X. Gao, J. Yang, Z. Zhu, H. Zhang, and Y. Wang, "Synthesis and gas sensor application of ZnFe₂O₄-ZnO composite hollow microspheres," *RSC Advances*, vol. 4, pp. 57967 – 57974, 2014.

DOI: 10.1039/C4RA10659H.

- [298] D.-D. Qin and C.-L. Tao, "A nanostructured ZnO-ZnFe₂O₄ heterojunction for the visible light photoelectrochemical oxidation of water," *RSC Advances*, vol. 4, p. 16968, 2014.

DOI: 10.1039/c4ra00204k.

- [299] Y. Bu, Z. Chen, and W. Li, "A ZnFe₂O₄-ZnO nanorod array p-n junction composite and its photoelectrochemical performance.," *Dalton transactions (Cambridge, England : 2003)*, vol. 42, pp. 16272 – 5, 2013.

DOI: 10.1039/c3dt52000e.

- [300] R. J. Corriu, W. E. Douglas, Z. xin Yang, Y. Karakus, G. H. Cross, and D. Bloor, "Preparation of diphenylsilylene polymers containing main-chain acetylene and (hetero)aromatic groups: $\chi^{(2)}$ non-linear optical and other properties," *Journal of Organometallic Chemistry*, vol. 455, no. 1, pp. 69 – 76, 1993.

DOI: 10.1016/0022-328X(93)80382-L.

- [301] A. Houlton, J. R. Miller, R. M. G. Roberts, and J. Silver, "Studies of the bonding in iron(ii) cyclopentadienyl and arene sandwich compounds. part 1. an interpretation of the iron-57 mossbauer data," *Journal of the Chemical Society, Dalton Transactions*, pp. 2181–2184, 1990.

DOI: 10.1039/DT9900002181.

- [302] A. Houlton, J. R. Miller, R. M. G. Roberts, and J. Silver, "Studies of the bonding in iron(ii) cyclopentadienyl and arene sandwich compounds. part 2. correlations and interpretations of carbon-13 and iron-57 nuclear magnetic resonance and iron-57 mossbauer data," *Journal of the Chemical Society, Dalton Transactions*, pp. 467–470, 1991.

DOI: 10.1039/DT9910000467.

- [303] A. Bondi, "Van der Waals Volumes and Radii," *Journal of Physical Chemistry*, vol. 68, pp. 441–451, 1964.

DOI: 10.1021/j100785a001.

- [304] Q. Liu, F. Cao, F. Wu, W. Tian, and L. Li, "Interface reacted ZnFe_2O_4 on $\alpha\text{-Fe}_2\text{O}_3$ nanoarrays for largely improved photoelectrochemical activity," *RSC Advances*, vol. 5, no. 97, pp. 79440 – 79446, 2015.

DOI: 10.1039/C5RA15596G.

- [305] R. Rameshbabu, R. Ramesh, S. Kanagesan, A. Karthigeyan, and S. Ponnusamy, "Synthesis and study of structural, morphological and magnetic properties of ZnFe_2O_4 nanoparticles," *Journal of Superconductivity and Novel Magnetism*, vol. 27, pp. 1499 – 1502, 2014.

DOI: 10.1007/s10948-013-2466-z.

- [306] A. A. Jahagirdar, N. Dhananjaya, D. L. Monika, C. R. Kesavulu, H. Nagabhushana, S. C. Sharma, B. M. Nagabhushana, C. Shivakumara, J. L. Rao, and R. P. S. Chakradhar, "Structural, EPR, optical and magnetic properties of $\alpha\text{-Fe}_2\text{O}_3$ nanoparticles," *Spectrochimica Acta - Part A: Molecular and Biomolecular Spectroscopy*, vol. 104, pp. 512 – 518, 2013.

DOI: 10.1016/j.saa.2012.09.069.

- [307] A. Baranowska-Korczyn, K. Fronc, J. B. Pełka, K. Sobczak, D. Klinger, P. Dłuzewski, and D. Elbaum, "Structural studies of magnetic Fe doped ZnO nanofibers," *Radiation Physics and Chemistry*, vol. 93, pp. 21 – 24, 2013.
DOI: 10.1016/j.radphyschem.2013.02.038.
- [308] J. J. Beltrán, J. A. Osorio, C. A. Barrero, C. B. Hanna, and A. Punnoose, "Magnetic properties of Fe doped, Co doped, and FeCo co-doped ZnO," *Journal of Applied Physics*, vol. 113, pp. 2011–2014, 2013.
DOI: 10.1063/1.4799778.
- [309] C. C. Wu, F. C. Chang, W. S. Chen, M. S. Tsai, and Y. N. Wang, "Reduction behavior of zinc ferrite in EAF-dust recycling with CO gas as a reducing agent," *Journal of Environmental Management*, vol. 143, pp. 208–213, 2014.
DOI: 10.1016/j.jenvman.2014.04.005.
- [310] S. S. Karpova, V. A. Moshnikov, S. V. Mjakin, and E. S. Kolovangina, "Surface functional composition and sensor properties of ZnO, Fe₂O₃, and ZnFe₂O₄," *Semiconductors*, vol. 47, pp. 392 – 395, 2013.
DOI: 10.1134/S1063782613030123.
- [311] J. P. Dhal, B. G. Mishra, and G. Hota, "Hydrothermal synthesis and enhanced photocatalytic activity of ternary Fe₂O₃/ZnFe₂O₄/ZnO nanocomposite through cascade electron transfer," *RSC Advances*, vol. 5, no. 71, pp. 58072 – 58083, 2015.
DOI: 10.1039/C5RA05894E.



SUPPORTING INFORMATIONS

The present chapter recollects the Supporting information of the several articles not only published during the present work (*i.e. Study of a sol-gel precursor and its evolution towards ZnO* and *Electronic and dynamic DFT studies on the substituent effects of aminoalcohol stabilizers in sol-gel ZnO precursor cases*), but submitted while this dissertation was being written (*i.e. Role of ethanolamine on the stability of a sol-gel ZnO ink* and *Molecular-dynamics study of ZnO formation from a sol-gel ink containing ethanolamine*). No emphasis has been placed on the style of what this chapter contains, since its sole purpose is to present some graphs and tables that contain a lesser relevance than those that appear in the body of the manuscript, although every table and figure presented here has been properly cited in the dissertation.

Study of a sol-gel precursor and its evolution towards ZnO

Alberto Gómez-Núñez¹, Concepción López², Santiago Alonso-Gil³, Pere Roura⁴, Anna Vilà^{1†}

¹University of Barcelona, Department of Electronics, Martí i Franquès 1, E08028-Barcelona, Spain.

²University of Barcelona, Department of Inorganic Chemistry, Martí i Franquès 1, E08028-Barcelona, Spain.

³University of Barcelona, Department of Organic Chemistry, Martí i Franquès 1, E08028-Barcelona, Spain.

⁴University of Girona, Department of Physics, Campus Montilivi, Edif. PII, E17071-Girona, Spain.

SUPPORTING INFORMATION

Contents:

1. Supplementary figures:

Figure S1. (ESI⁺) Mass spectrum of the precursor:

2. Supplementary Tables:

Table S1. Final atomic coordinates of the optimized geometry of the monomer.

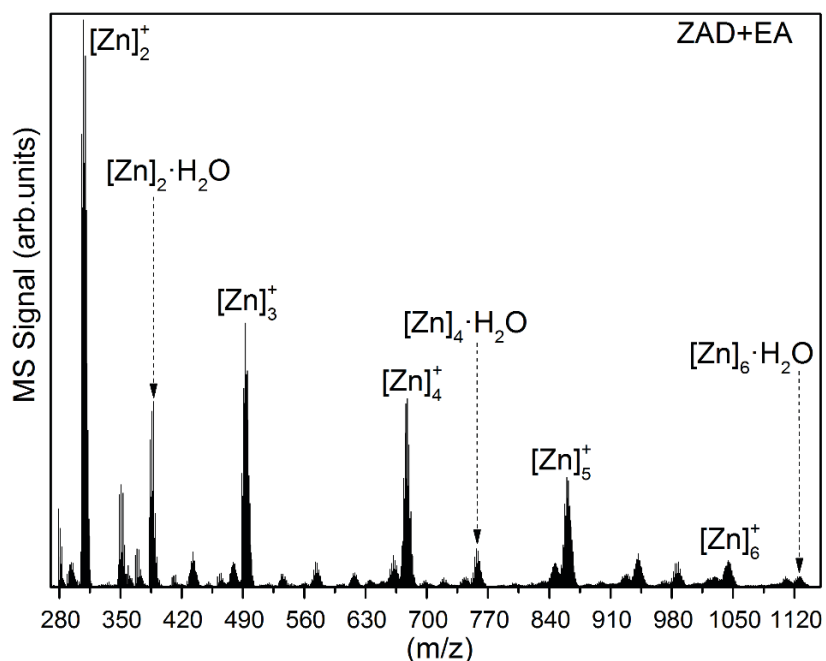
Table S2. Final atomic coordinates of the optimized geometry of the dimer.

Table S3. Final atomic coordinates of the optimized geometry of the tetramer.

Table S4. Ground-state Energy, zero-point correction and 1st frequency values of monomer, dimer and tetramer.

1. Supplementary figures:

Figure S1. (ESI⁺) Mass spectrum of the precursor:



2. Supplementary Tables

Table S1. Final atomic coordinates (x, y, z) of the optimized geometry of the Monomer.

	x	y	z
Zn	0.0000000000	0.0000000000	0.0000000000
O	0.0000000000	0.0000000000	2.1238910000
O	1.8906500000	0.0000000000	0.9310760000
O	-0.8888780000	0.8519280000	-1.4377680000
N	-0.6424750000	-1.8992800000	-0.8477020000
C	-0.9412890000	-1.4761500000	-2.2706370000
H	-1.5676280000	-2.2188200000	-2.7858550000
C	-1.6109420000	-0.0725100000	-2.2642480000
H	-1.6362330000	0.2884520000	-3.3048000000
H	-2.6610650000	-0.1763350000	-1.9259230000
H	0.0238910000	-1.4089010000	-2.7869080000
C	1.3084650000	0.0104720000	2.1061720000
C	2.1149640000	0.0634550000	3.3756000000
H	2.3902180000	1.1070000000	3.5776870000
H	3.0392610000	-0.5097540000	3.2612140000
H	1.5275970000	-0.3092240000	4.2178710000
H	-1.4890240000	-2.2117570000	-0.3626620000
H	0.0566830000	-2.6434010000	-0.8038220000

Table S2. Final atomic coordinates (x, y, z) of the optimized geometry of the Dimer

	x	y	z
Zn	1.7332630000	-0.7495790000	-1.0770980000
Zn	-1.4520590000	0.4192310000	0.1120260000
O	0.9903640000	0.9592310000	-1.8502540000
H	3.2811270000	0.6507700000	1.1452350000
H	0.4697590000	2.5322090000	-3.9540360000
H	5.1519720000	-0.6664660000	0.2963230000
O	3.6266800000	-1.0109900000	-1.0947920000
C	4.1534900000	-1.1317640000	0.2365330000
C	0.0539600000	1.8325740000	-1.9683280000
H	1.0868890000	3.5735470000	-2.6703500000
C	3.2389430000	-0.4362760000	1.2900260000
C	0.2329530000	2.9547080000	-2.9713860000
H	3.5755160000	-0.6628930000	2.3140050000
H	1.0921540000	-0.2733560000	1.5530820000
N	1.8116030000	-0.8530360000	1.0669080000
H	4.2712710000	-2.1976850000	0.5227210000
H	-0.6671370000	3.5693780000	-3.0292420000
O	-1.0386360000	1.8040970000	-1.2590070000
H	1.6752770000	-1.8307320000	1.3416570000
H	-1.7689360000	-0.2147820000	3.3693580000
O	-0.5071480000	0.4283010000	1.8121640000
C	-1.3745340000	0.7165920000	2.9165390000
O	-1.7803820000	-1.2966600000	-0.8355840000
H	-3.7581870000	0.1871020000	1.4385160000
H	-0.8349100000	1.2618060000	3.7078630000
H	-2.4416100000	-3.7594850000	-1.4777680000
C	-1.0313650000	-2.1320970000	-1.4974470000
O	0.2431850000	-2.0105540000	-1.6217130000
N	-3.1964550000	1.0157060000	1.2225050000
C	-2.5675580000	1.6029550000	2.4670000000
C	-1.7225040000	-3.3055540000	-2.1671650000
H	-2.2826050000	-2.9412580000	-3.0378490000
H	-3.3053660000	1.7164090000	3.2748070000
H	-3.7801060000	1.6953750000	0.7306060000
H	-2.1918090000	2.5950430000	2.1908700000
H	-0.9870990000	-4.0418760000	-2.4967440000

Table S3. Final atomic coordinates (x, y, z) of the optimized geometry of the Tetramer

	x	y	z
Zn	0.0000000000	0.0000000000	0.0000000000
Zn	0.0000000000	0.0000000000	3.8779000000
Zn	4.8182000000	0.0000000000	2.4921000000
Zn	3.8787000000	-0.2628000000	6.3071000000
H	4.2543000000	2.6859000000	-0.3388000000
H	3.7955000000	2.8363000000	1.3699000000
H	2.6739000000	3.4014000000	0.0761000000
H	-1.2644000000	-0.8336000000	-2.2002000000
H	-0.2266000000	0.3797000000	-2.6926000000
H	1.5861000000	-1.2162000000	8.1032000000
H	-0.0225000000	-2.0008000000	7.8399000000
H	1.5026000000	-2.9282000000	7.6705000000
H	2.5883000000	1.7076000000	5.1377000000
H	4.2292000000	1.9239000000	4.7804000000
H	2.4164000000	-0.9004000000	2.4535000000
H	2.8235000000	-1.2858000000	3.9963000000
H	6.6958000000	-3.7217000000	5.5121000000
H	7.8736000000	-2.4401000000	5.8056000000
H	7.7286000000	-3.1461000000	4.1641000000
H	6.4089000000	0.6862000000	0.3710000000
H	7.1183000000	-0.5707000000	1.2317000000
H	3.2768000000	2.2837000000	8.9018000000
H	1.9041000000	1.8346000000	7.8558000000
H	4.7551000000	2.5966000000	6.9949000000
H	-3.3605000000	1.6929000000	-0.2089000000
H	-3.3109000000	-0.0635000000	-0.4922000000
H	-1.5073000000	2.0921000000	-1.7412000000
H	0.5086000000	3.6646000000	4.3582000000
H	-0.5158000000	2.7304000000	5.4756000000
H	-0.5995000000	2.7581000000	2.4001000000
H	1.4079000000	-3.6489000000	2.5769000000
H	0.0205000000	-4.2813000000	1.6498000000
H	-0.2259000000	-3.4042000000	3.2001000000
H	-2.4764000000	1.0832000000	3.8952000000
H	-1.8784000000	0.9536000000	2.2931000000
H	6.8756000000	2.9929000000	3.4376000000
H	6.1183000000	3.0763000000	1.8328000000
H	7.7236000000	0.7438000000	3.0286000000
H	3.2473000000	3.4802000000	6.6471000000
H	-2.7186000000	1.0938000000	-2.5906000000
H	-1.8729000000	3.3258000000	3.5047000000
H	8.1948000000	1.7709000000	1.6457000000
C	-1.9884000000	1.1073000000	-1.7675000000
C	-2.6835000000	0.8454000000	-0.4067000000
C	2.7896000000	1.2572000000	0.3392000000
C	3.4088000000	2.6460000000	0.3610000000

C	-1.0768000000	2.5785000000	3.3700000000
C	-0.0108000000	2.7015000000	4.4900000000
C	0.2997000000	-2.1564000000	1.5321000000
C	0.3672000000	-3.4613000000	2.2811000000
C	7.3437000000	1.3087000000	2.1705000000
C	6.3504000000	2.3914000000	2.6753000000
C	6.1256000000	-1.8025000000	4.7269000000
C	7.1803000000	-2.8485000000	5.0605000000
C	3.6843000000	2.4773000000	6.7781000000
C	3.0028000000	1.7489000000	7.9767000000
C	1.1134000000	-1.5664000000	6.0599000000
C	1.0186000000	-1.9557000000	7.5153000000
O	1.5948000000	1.1392000000	-0.1727000000
O	3.4467000000	0.2626000000	0.8224000000
O	-1.7153000000	0.7039000000	0.6432000000
O	0.4810000000	-1.0117000000	2.1728000000
O	0.1009000000	-2.1034000000	0.2637000000
O	0.9303000000	1.6109000000	4.4274000000
O	6.0411000000	-1.3703000000	3.5162000000
O	5.3751000000	-1.4050000000	5.7051000000
O	5.1579000000	1.8062000000	3.2100000000
O	0.0376000000	-1.3638000000	5.3631000000
O	2.3000000000	-1.4124000000	5.5372000000
O	3.3979000000	0.3618000000	8.0690000000
O	3.1546000000	-1.0230000000	3.0869000000
N	-0.8929000000	0.0929000000	-1.9736000000
N	-1.6496000000	1.1804000000	3.3011000000
N	6.6194000000	0.3172000000	1.2997000000
N	3.5571000000	1.6538000000	5.5284000000

Table S4. Ground-state Energy, zero-point correction and 1st frequency values of monomer, dimer and tetramer.

	Monomer	Dimer	Tetramer
Ground-state Energy (Hartree)	-503.902579	-1007.8861	-2092.24773
Zero-point correction (Hartree/part)	0.139993	0.282842	0.594043
1st frequency (cm⁻¹)	26.0627	32.0211	19.4363

Role of ethanolamine on the stability of a sol-gel ZnO ink

A. Gómez-Núñez, S. Alonso-Gil, C. López, P. Roura and A. Vilà

Contents :

Table S1. Final atomic coordinates of the optimized EA.

Table S2. Final atomic coordinates of the optimized EA+ME

Table S3. Final atomic coordinates of the optimized [Zn]₁.

Table S4. Final atomic coordinates of the optimized [Zn]₁+ME.

Table S5. Final atomic coordinates of the optimized [Zn]₁+CO₂.

Table S6. Final atomic coordinates of the optimized [Zn]₁+ME+CO₂.

Table S7. Final atomic coordinates of the optimized [Zn]₂.

Table S8. Final atomic coordinates of the optimized [Zn]₂+ME.

Table S9. Final atomic coordinates of the optimized [Zn]₂+CO₂.

Table S10. Final atomic coordinates of the optimized [Zn]₂+ME+CO₂.

Fig. S1. Partial view of the ¹H-NMR spectrum (400MHz) in the range 6.7 < δ < 8.7 ppm of the sample containing EA+ME after 8 weeks exposed to light and air.

O	0.0305170000	0.0748430000	0.0216300000
N	0.0349490000	-0.0416000000	2.8116230000
C	1.3323420000	-0.0048700000	2.0991570000
H	2.1440200000	-0.5401660000	2.6222040000
C	1.1379840000	-0.5907340000	0.6859760000
H	2.0290510000	-0.4279560000	0.0705240000
H	0.9527120000	-1.6772700000	0.7521770000
H	1.6294880000	1.0469700000	2.0075440000
H	-0.2414220000	-0.9591520000	3.1535880000
H	-0.1028580000	0.6865030000	3.5058450000
H	-0.6444520000	0.2344940000	0.7252210000

Table S1. Final atomic coordinates of the optimized EA.

O	1.3566950000	-0.7090970000	-0.1552430000
N	-1.3376760000	-0.5558150000	0.1213550000
C	-0.6386140000	0.7029860000	-0.2416010000
H	-1.1056860000	1.6079240000	0.1770870000
C	0.8255400000	0.5960990000	0.2364550000
H	1.4488240000	1.3669070000	-0.2279430000
H	0.8769420000	0.7099100000	1.3309520000
H	-0.6582390000	0.7896700000	-1.3342910000
H	-1.6352460000	-0.5959930000	1.0953640000
H	-2.1004880000	-0.8033830000	-0.5045630000
H	0.5625090000	-1.3060620000	-0.1132790000

Table S2. Final atomic coordinates of the optimized EA+ME.

C	5.510948560810	4.230430816229	5.112007398233
C	4.896293723616	5.641963678690	5.151391109096
C	7.756197454255	5.732695548846	9.433710573137
C	8.536616791289	5.774222432280	10.724128228751
H	4.834111427559	3.514328376887	4.611525770599
H	4.766333486044	5.979912253554	4.102057690633
H	3.868923213076	5.561986171347	5.585895507211
H	6.462350899533	4.265922557223	4.556429961127
H	8.754673104150	6.827617325212	10.965492590293
H	9.495199563006	5.249936928928	10.613328954057
H	7.949582123988	5.349260503299	11.548773858021
H	4.990329109360	3.476134862775	6.990428939910
H	6.509566628423	3.036400131345	6.523513230069
O	6.474494843641	5.729174644932	9.460804830659
O	8.377217951871	5.724121694991	8.311722035561
O	5.690514423958	6.566593305444	5.853832901811
Zn	6.502643634282	5.726063017071	7.351478852678
N	5.834944173996	3.808230870638	6.507485633611

Table S3. Final atomic coordinates of the optimized [Zn]₁.

C	2.8459670000	0.7122610000	-0.3867440000
C	2.8527580000	-0.5956340000	0.4485470000
C	-2.4144260000	0.0674070000	0.0427130000
C	-3.9275110000	0.1047110000	0.0096250000
H	3.6955550000	1.3543770000	-0.1169360000
H	3.7396330000	-1.1766820000	0.1465280000
H	2.9783790000	-0.3337290000	1.5168410000
H	2.9195400000	0.4643920000	-1.4518290000
H	-4.3178460000	-0.8375860000	0.4162160000
H	-4.2844310000	0.1928550000	-1.0209460000
H	-4.3112290000	0.9300290000	0.6131170000
H	1.5204460000	1.9643160000	0.6831900000
H	1.3428030000	2.0835120000	-0.9617510000
O	-1.7097940000	0.6760910000	0.9737480000
O	-1.7479520000	-0.6251770000	-0.8709350000
O	1.6510330000	-1.3729960000	0.2421180000
Zn	0.1429480000	-0.1948940000	-0.0635850000
N	1.5345280000	1.4356470000	-0.1944550000

Table S4. Final atomic coordinates of the optimized $[\text{Zn}]_1+\text{ME}$.

Zn	-0.6263380000	-0.7430500000	-0.1488900000
O	1.4715790000	-0.1950690000	-0.2946010000
O	0.7651470000	-2.2011190000	0.3822800000
O	-2.1875810000	-0.5699220000	-1.2054890000
N	-1.4989340000	0.6529070000	1.2450270000
C	-2.9497410000	0.6340400000	0.8208440000
H	-3.4792900000	1.5346230000	1.1641940000
C	-3.0408280000	0.4824760000	-0.7252120000
H	-4.0896890000	0.2610800000	-0.9781350000
H	-2.7835830000	1.4506080000	-1.1973690000
H	-3.4055470000	-0.2448760000	1.2926160000
C	1.7688180000	-1.4004030000	0.1124160000
C	3.1910760000	-1.8715440000	0.2491140000
H	3.4202150000	-2.5560180000	-0.5776850000
H	3.3124730000	-2.4317640000	1.1815390000
H	3.8827660000	-1.0274330000	0.2129280000
H	-1.0374360000	1.5444150000	1.0347850000
H	-1.3871380000	0.4468190000	2.2391890000
C	1.8477490000	2.4933460000	-0.1154580000
O	0.7290340000	2.5460500000	0.3035370000
O	2.9652550000	2.5095870000	-0.5195750000

Table S5. Final atomic coordinates of the optimized $[\text{Zn}]_1+\text{CO}_2$.

Zn	-0.7050290000	-0.7483270000	-0.0887900000
O	1.4929450000	-0.2616560000	-0.3404770000
O	0.7258400000	-2.2269560000	0.4084070000
O	-2.3700400000	-0.6800390000	-1.0786760000
N	-1.4619840000	0.8628730000	1.1206180000
C	-2.9304850000	0.8578010000	0.7860700000
H	-3.3979600000	1.8245150000	1.0189970000
C	-3.1255310000	0.4956520000	-0.7093180000
H	-4.2019730000	0.3245750000	-0.8733450000
H	-2.8315660000	1.3657390000	-1.3273700000
H	-3.3970680000	0.0858600000	1.4090350000
C	1.7470820000	-1.4614220000	0.0932950000
C	3.1545510000	-1.9865220000	0.2239500000
H	3.3218430000	-2.7646870000	-0.5313540000
H	3.2929480000	-2.4484720000	1.2071560000
H	3.8841520000	-1.1871020000	0.0805290000
H	-0.9902750000	1.7168680000	0.8082910000
H	-1.3011170000	0.7504760000	2.1232690000
C	2.0498360000	2.4655010000	-0.1556960000
O	0.9011380000	2.6237570000	0.1232440000
O	3.2042480000	2.3593770000	-0.4282050000

Table S6. Final atomic coordinates of the optimized $[\text{Zn}]_1+\text{ME}+\text{CO}_2$.

O	0.9903640000	0.9592310000	-1.8502540000
H	3.2811270000	0.6507700000	1.1452350000
H	0.4697590000	2.5322090000	-3.9540360000
H	5.1519720000	-0.6664660000	0.2963230000
O	3.6266800000	-1.0109900000	-1.0947920000
C	4.1534900000	-1.1317640000	0.2365330000
C	0.0539600000	1.8325740000	-1.9683280000
H	1.0868890000	3.5735470000	-2.6703500000
C	3.2389430000	-0.4362760000	1.2900260000
C	0.2329530000	2.9547080000	-2.9713860000
Zn	1.7332630000	-0.7495790000	-1.0770980000
H	3.5755160000	-0.6628930000	2.3140050000
H	1.0921540000	-0.2733560000	1.5530820000
N	1.8116030000	-0.8530360000	1.0669080000
H	4.2712710000	-2.1976850000	0.5227210000
H	-0.6671370000	3.5693780000	-3.0292420000
O	-1.0386360000	1.8040970000	-1.2590070000
H	1.6752770000	-1.8307320000	1.3416570000
H	-1.7689360000	-0.2147820000	3.3693580000
O	-0.5071480000	0.4283010000	1.8121640000
Zn	-1.4520590000	0.4192310000	0.1120260000
C	-1.3745340000	0.7165920000	2.9165390000
O	-1.7803820000	-1.2966600000	-0.8355840000
H	-3.7581870000	0.1871020000	1.4385160000
H	-0.8349100000	1.2618060000	3.7078630000
H	-2.4416100000	-3.7594850000	-1.4777680000
C	-1.0313650000	-2.1320970000	-1.4974470000
O	0.2431850000	-2.0105540000	-1.6217130000
N	-3.1964550000	1.0157060000	1.2225050000
C	-2.5675580000	1.6029550000	2.4670000000
C	-1.7225040000	-3.3055540000	-2.1671650000
H	-2.2826050000	-2.9412580000	-3.0378490000
H	-3.3053660000	1.7164090000	3.2748070000
H	-3.7801060000	1.6953750000	0.7306060000
H	-2.1918090000	2.5950430000	2.1908700000
H	-0.9870990000	-4.0418760000	-2.4967440000

Table S7. Final atomic coordinates of the optimized $[\text{Zn}]_2$.

O	-1.0857360000	-0.9868340000	1.6895540000
H	-2.0319400000	2.7877350000	0.9406340000
H	-0.6882430000	-2.9572370000	3.4570000000
H	-4.4177590000	2.4978200000	0.5077370000
O	-3.6235350000	0.5562630000	0.3602180000
C	-3.7222340000	1.9156470000	-0.1214210000
C	0.0356550000	-1.3580730000	2.2165410000
H	-0.4099840000	-1.4379390000	4.3142190000
C	-2.3441110000	2.6355200000	-0.1009050000
C	-0.0092010000	-2.1013610000	3.5383610000
Zn	-1.8424390000	-0.1637560000	-0.0057500000
H	-2.4125600000	3.6207660000	-0.5863900000
H	-0.3170850000	2.0055690000	-0.4839470000
N	-1.3042510000	1.7674560000	-0.7493100000
H	-4.1174080000	1.9426840000	-1.1570930000
H	0.9871490000	-2.4404070000	3.8282410000
O	1.1949270000	-1.1201440000	1.6786660000
H	-1.3945470000	1.7827060000	-1.7690500000
H	2.6256290000	2.7371770000	-1.3798310000
O	1.3235400000	1.8350700000	0.0137150000
Zn	1.6351340000	-0.1086690000	-0.0137710000
C	2.5305400000	2.5660600000	-0.2907200000
O	1.0536560000	-1.3356830000	-1.4990070000
H	3.9722990000	0.2884090000	-1.2466690000
H	2.5213530000	3.5525630000	0.1996420000
H	0.6632880000	-2.5140940000	-3.8211660000
C	-0.0737100000	-1.8232230000	-1.9201840000
O	-1.2258170000	-1.4922300000	-1.4354780000
N	3.7172500000	0.3674700000	-0.2575980000
C	3.7796430000	1.8007380000	0.2104090000
C	-0.0188060000	-2.8522970000	-3.0342650000
H	0.3767350000	-3.7950810000	-2.6355600000
H	4.7034140000	2.2910720000	-0.1264600000
H	4.3442180000	-0.2311270000	0.2845680000
H	3.7748230000	1.7780550000	1.3062110000
H	-1.0141700000	-3.0300100000	-3.4463110000

Table S8. Final atomic coordinates of the optimized [Zn]₂+ME.

O	0.000000000	0.000000000	0.000000000
H	3.786064000	0.000000000	0.000000000
H	-1.467542000	2.078300000	0.000000000
H	4.403191000	0.336510000	-2.333719000
O	2.382751000	-0.202614000	-2.418660000
C	3.751005000	-0.525579000	-2.114992000
C	-0.844516000	0.244681000	0.930747000
H	-1.030381000	2.225698000	1.717211000
C	3.940051000	-0.897312000	-0.612952000
C	-1.534744000	1.591999000	0.975328000
Zn	1.193012000	-1.091803000	-1.217917000
H	4.957818000	-1.274417000	-0.426465000
H	2.742794000	-1.984922000	0.824489000
N	2.893498000	-1.895368000	-0.202132000
H	4.106992000	-1.372937000	-2.736232000
H	-2.576825000	1.481179000	1.285368000
O	-1.116373000	-0.626093000	1.874355000
H	3.100584000	-2.827816000	-0.571379000
H	2.494004000	-3.723885000	3.830330000
O	1.820760000	-2.456629000	2.297923000
Zn	-0.100483000	-2.370358000	1.930701000
C	2.112390000	-2.697197000	3.687224000
O	-0.729731000	-3.527690000	0.441125000
H	-0.250554000	-4.168874000	3.869878000
H	2.886397000	-2.003439000	4.052992000
H	-1.785299000	-5.366482000	-0.970853000
C	-0.752819000	-3.472666000	-0.861699000
O	-0.107843000	-2.602623000	-1.553815000
N	-0.339240000	-3.149539000	3.899182000
C	0.848782000	-2.511434000	4.574233000
C	-1.608554000	-4.488023000	-1.595791000
H	-2.576675000	-4.027802000	-1.833876000
H	1.017272000	-2.925747000	5.578723000
H	-1.224458000	-2.873330000	4.327660000
H	0.617956000	-1.443637000	4.674038000
H	-1.131371000	-4.768189000	-2.538748000
C	-3.338760000	-0.604726000	3.619526000
O	-2.840520000	-1.512606000	4.213699000
O	-3.883123000	0.297134000	3.067282000
C	1.749112000	-5.232913000	1.319488000
O	1.180974000	-5.538163000	2.324871000
O	2.323062000	-4.994326000	0.303087000

Table S9. Final atomic coordinates of the optimized $[\text{Zn}]_2+\text{CO}_2$.

O	0.2138410000	-2.4001350000	-0.3615390000
H	2.8412910000	-0.5584050000	-2.7366060000
H	-1.1953590000	-4.4434660000	-0.8050240000
H	4.8241210000	-1.8573250000	-2.1436810000
O	3.4546270000	-2.2626000000	-0.5993280000
C	4.3014510000	-1.3395020000	-1.3213920000
C	-1.0705910000	-2.3210520000	-0.4334790000
H	-2.4231470000	-3.4601950000	-1.6544050000
C	3.4835810000	-0.1702600000	-1.9355920000
C	-1.8621710000	-3.5835700000	-0.7202440000
Zn	1.8897180000	-1.3303860000	0.1131180000
H	4.1563880000	0.5844270000	-2.3703060000
H	1.7773350000	0.9692880000	-1.2573330000
N	2.5863730000	0.4175450000	-0.8900890000
H	5.0785730000	-0.9118690000	-0.6567650000
H	-2.5905950000	-3.7535410000	0.0796120000
O	-1.7328660000	-1.2088100000	-0.2821340000
H	3.1058280000	1.0085460000	-0.2358980000
H	-0.5210340000	3.6073910000	-1.7526400000
O	0.1874470000	1.6832120000	-1.2900350000
Zn	-1.0065080000	0.6784170000	-0.0705790000
C	-0.5450650000	2.5793020000	-2.1554410000
O	-0.3337560000	0.7399080000	1.8448600000
H	-2.7522960000	2.6977340000	-0.4112880000
H	-0.0960110000	2.6060180000	-3.1611800000
H	0.1749980000	1.2795360000	4.2947460000
C	0.5728540000	0.1051700000	2.5252750000
O	1.4302890000	-0.7076590000	2.0006010000
N	-2.5899750000	1.8379120000	-0.9425890000
C	-2.0228250000	2.1399250000	-2.3034530000
C	0.6098470000	0.3133060000	4.0284700000
H	0.0183690000	-0.4765690000	4.5103130000
H	-2.6056960000	2.9136020000	-2.8219960000
H	-3.4633740000	1.3087380000	-0.9903930000
H	-2.0782120000	1.2140240000	-2.8882080000
H	1.6358180000	0.2399310000	4.3987310000
C	-4.6640110000	-1.2760480000	0.2660580000
O	-4.7517230000	-0.2630330000	-0.3568050000
O	-4.6099530000	-2.2860830000	0.8944340000
C	1.0805760000	3.4259940000	0.8752140000
O	0.0349840000	3.9991920000	0.8511380000
O	2.1496170000	2.9014330000	0.9491060000

Table S10. Final atomic coordinates of the optimized [Zn]₂+ME+CO₂.

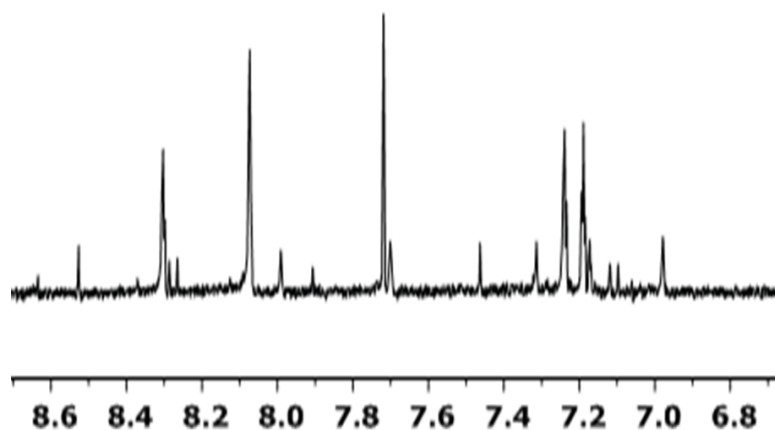


Fig. S1. Partial view of the ¹H-NMR spectrum (400MHz) in the range 6.7 < δ < 8.7 ppm of the sample containing EA+ME after 8 weeks exposed to light and air.

Molecular dynamics study of ZnO formation from a sol-gel ink containing ethanolamine

A. Gómez-Núñez, S. Alonso-Gil, C. López, P. Roura and A. Vilà

Contents:

Fig. S1. Normalized EGA signals with their required normalization factor in parenthesis classified into five groups (**A-E**) according to their mean m/z values.

Fig. S2. Evolution of the Zn-N and Zn-O distances in $[Zn]_1$ at 570, 670, 770 and 870 K, using CPMD.

Fig. S3. Evolution of the RMSD and the Zn-Zn, Zn-N and Zn-O distances in $[Zn]_2$ at 300, 570, 670, 770 and 870 K.

Fig. S4. Labelling scheme for charts S1-S7.

Fig. S5. Variation in interatomic distances, as given by the first metadynamic simulation, from $[Zn]_2$ to state C1.

Fig. S6. Free-energy surface of the collective variable Zn2-N2.

Fig. S7. Variation in interatomic distances, as given by the second metadynamic simulation, from state C1 to P.

Chart S1. Final atomic coordinates for the optimized geometry of the Dimmer and calculated charges.

Chart S2. Final atomic coordinates for the optimized geometry of the C1 state and calculated charges.

Chart S3. Final atomic coordinates for the optimized geometry of the intermediate C2 state and calculated charges.

Chart S4. Final atomic coordinates for the optimized geometry of the intermediate C3 state and calculated charges.

Chart S5. Final atomic coordinates for the optimized geometry of the intermediate C4 state and calculated charges.

Chart S6. Final atomic coordinates for the optimized geometry of the final P state and calculated charges.

Chart S7. ESP charge increments for every step shown in Figures 5 and 6.

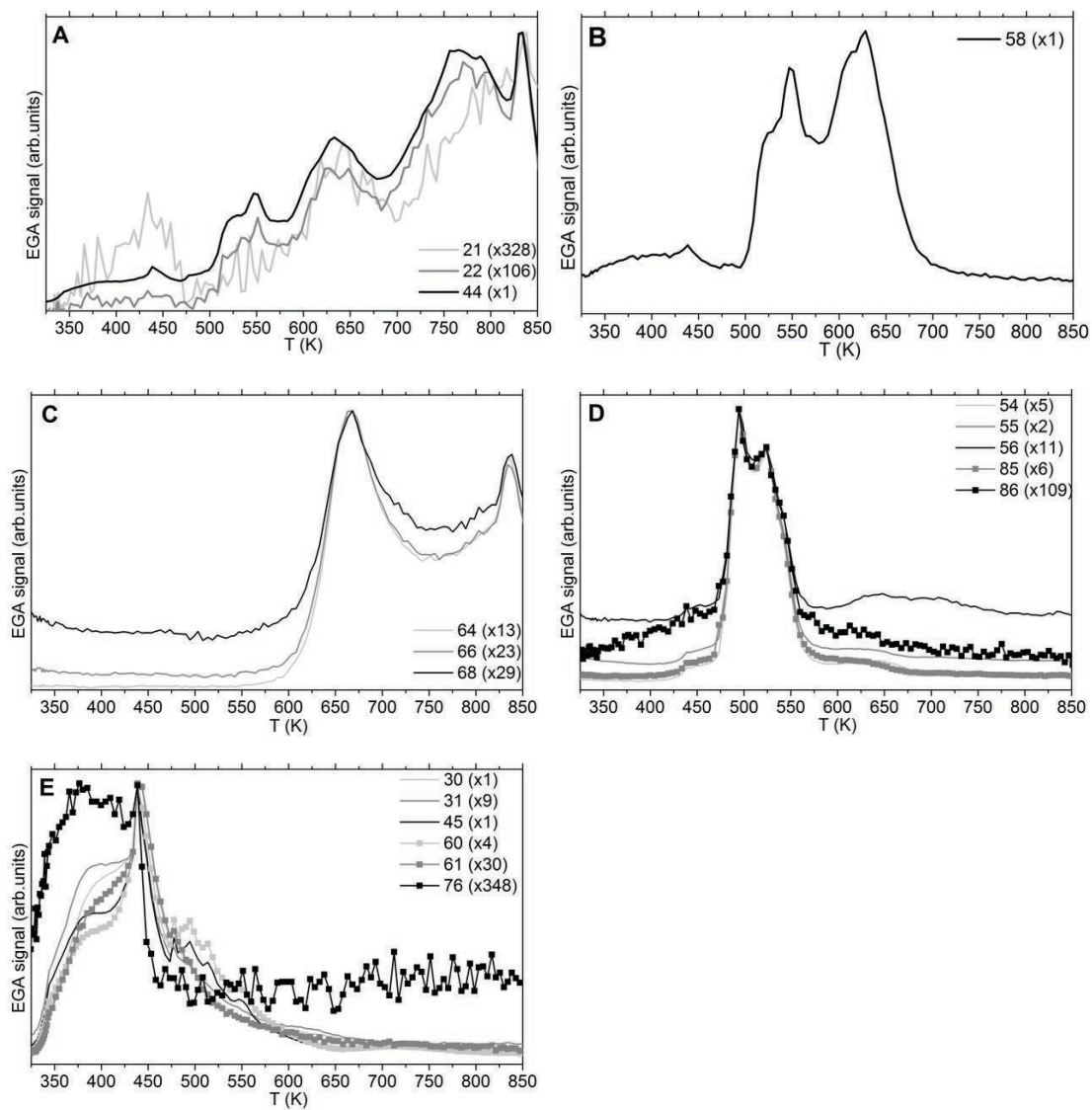


Fig. S1. Normalized EGA signals with their required normalization factor in parenthesis classified into 5 groups (A-E) according to their m/z values.

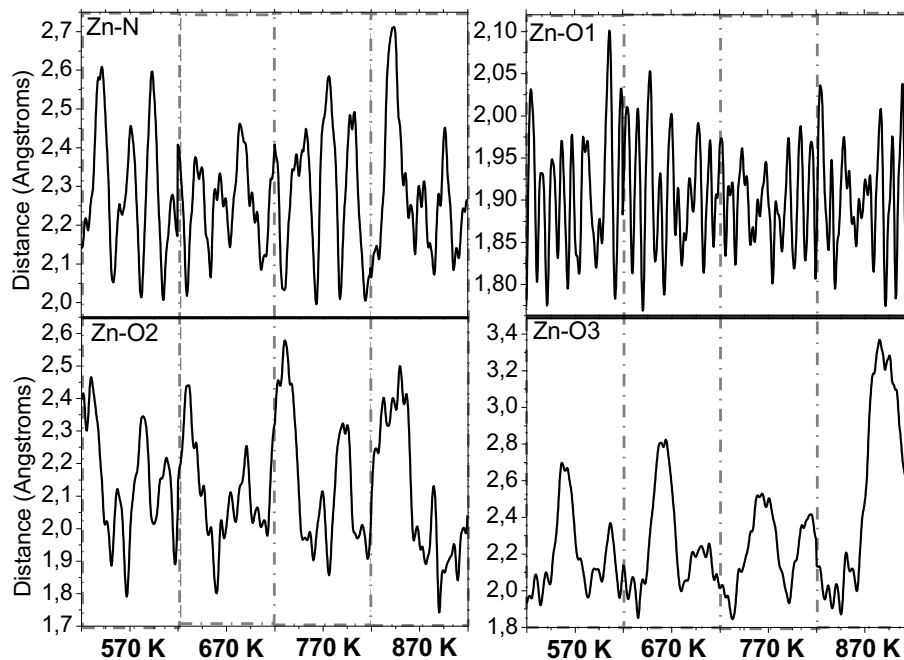
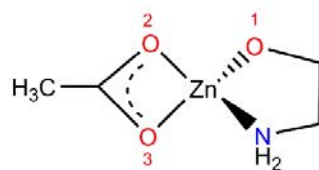


Fig. S2. Evolution of the Zn-N and Zn-O distances in $[Zn]_1$ at 570, 670, 770 and 870 K, using CPMD.

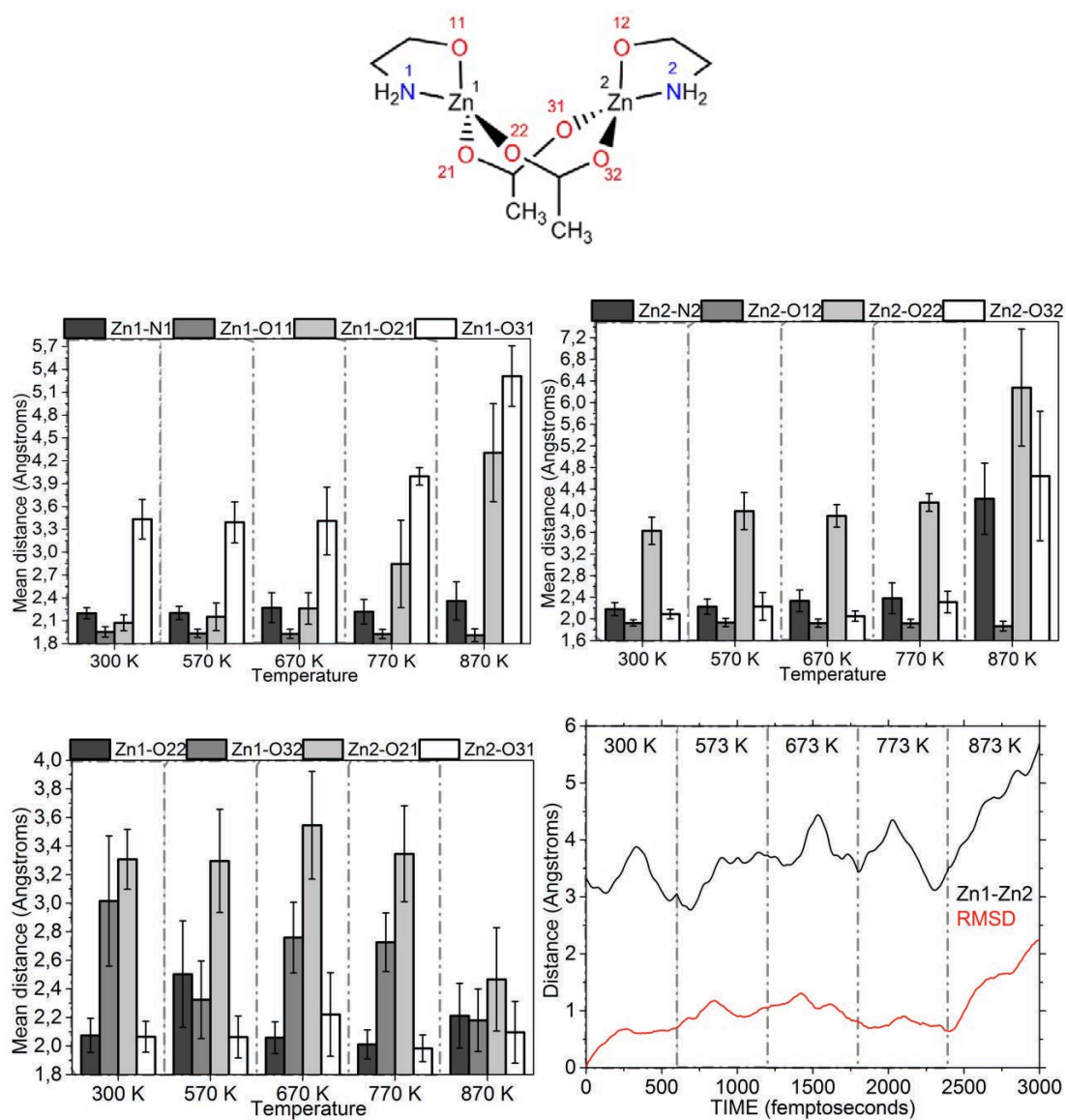


Fig. S3. Evolution of the RMSD and the Zn-Zn, Zn-N and Zn-O distances in $[Zn]_2$ at 300, 570, 670, 770 and 870 K.

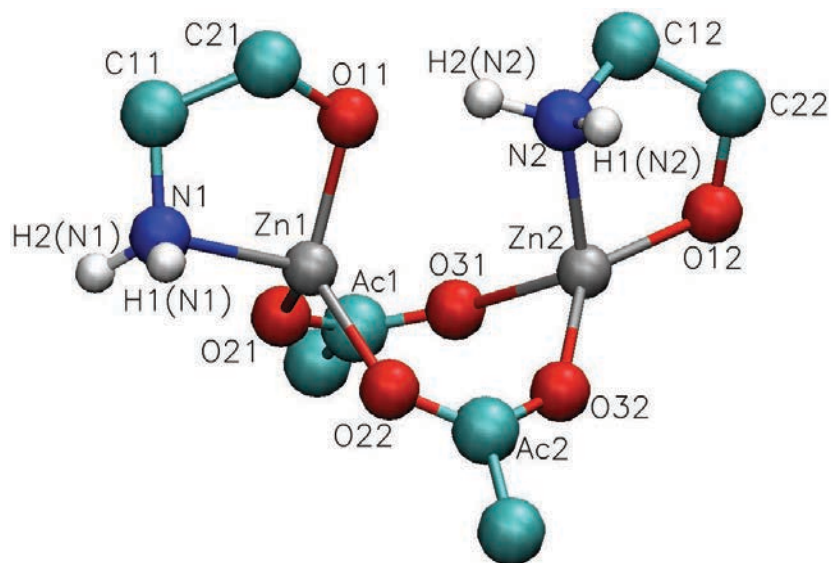


Fig. S4. Labelling scheme for charts S1-S7.

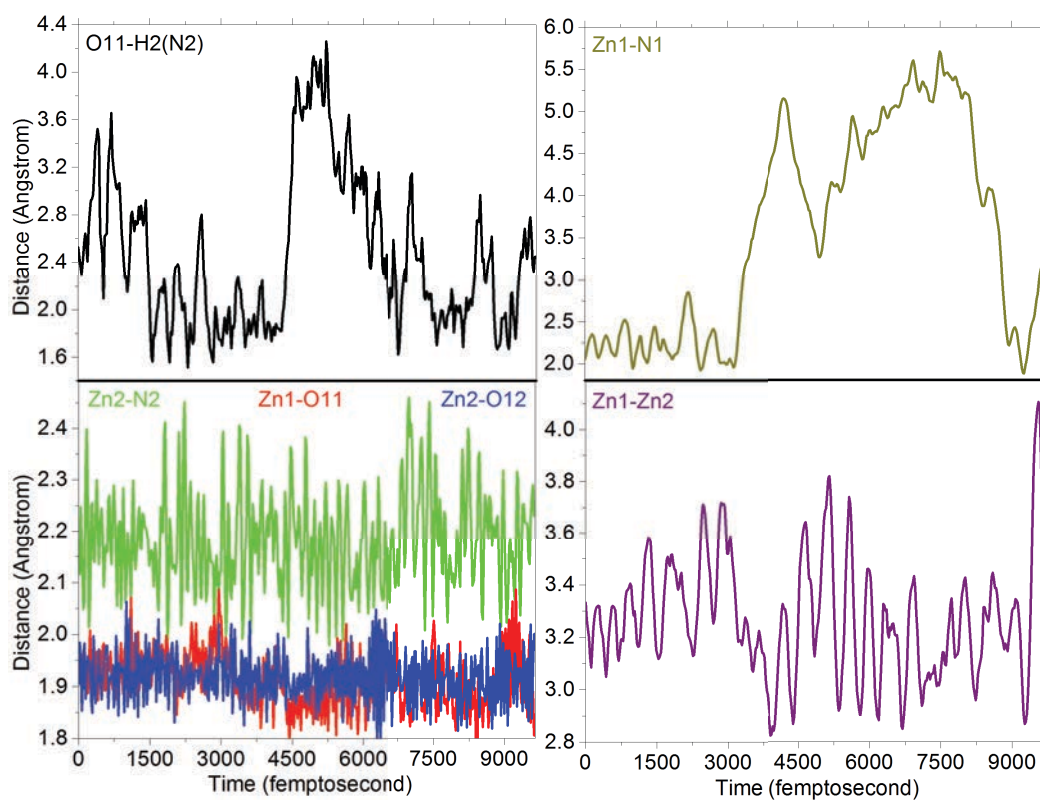


Fig. S5. Variation in interatomic distances, as given by the first metadynamic simulation, from $[Zn]_2$ to state C1.

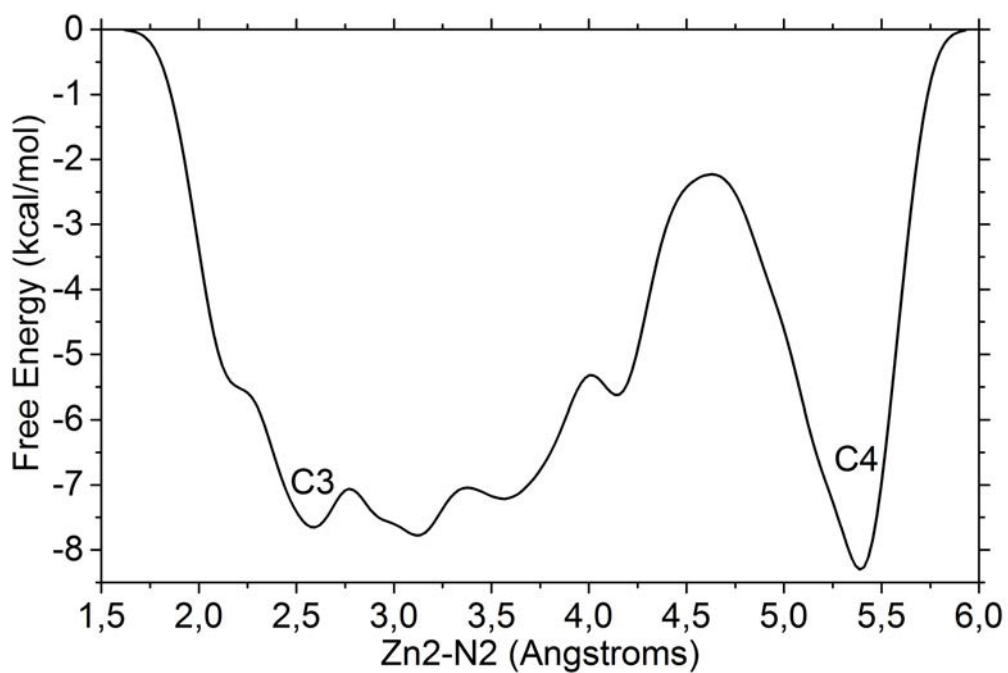


Fig. S6. Free-energy surface of the collective variable Zn2-N2.

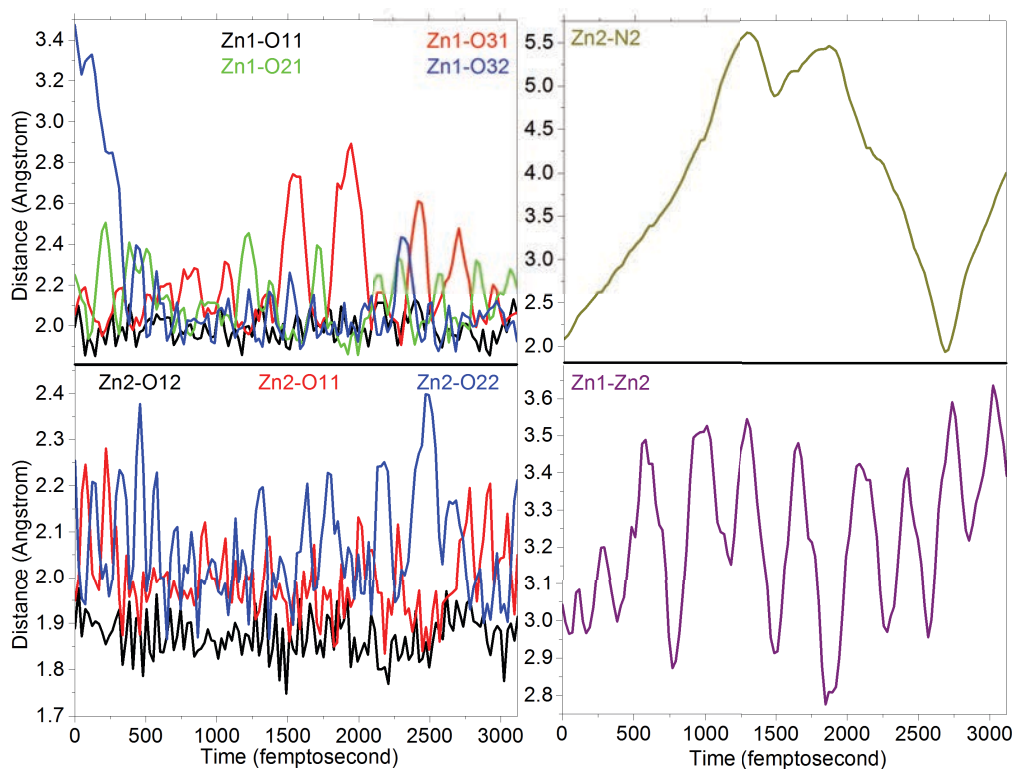


Fig. S7. Variation in interatomic distances, as given by the second metadynamic simulation, from state C1 to P.

LABELS	SPECIES	COORDINATES (a.u.)			CHARGES (e)	
		[Zn] ₂	X	Y	Z	INT
C22	C	22,5818	12,1549	15,1769	-0,025034	-0,094586
Ac1	C	15,0521	17,8446	11,0503	0,151537	1,041938
C12	C	21,0534	13,4083	17,3254	0,003501	-0,357987
Ac1	C	15,3126	19,9803	9,155	-0,082513	-0,868023
C21	C	12,2659	15,7117	20,1963	-0,017129	-0,01456
Ac2	C	13,0302	10,312	12,0931	0,153412	1,049594
C11	C	9,9806	17,285	19,3335	0,007668	-0,230169
Ac2	C	11,6845	8,1157	10,8304	-0,083654	-0,76633
H(EA2)	H	21,2054	15,4807	17,1634	0,033072	0,220395
Ac1	H	15,8529	19,2038	7,3036	0,036537	0,248736
H(EA2)	H	24,5612	12,8472	15,3185	-0,003041	0,126038
Ac1	H	16,8597	21,2326	9,7638	0,037998	0,275051
H(EA2)	H	21,778	12,8305	19,199	0,012856	0,20023
H2(N2)	H	17,0586	13,8943	17,9813	0,040346	0,355399
H(EA2)	H	22,656	10,0746	15,5732	-0,010422	0,109272
Ac1	H	13,5577	21,0725	8,9943	0,020874	0,244423
H1(N2)	H	18,0226	10,9176	17,5553	0,099239	0,311351
H(EA1)	H	11,5651	13,8227	20,8359	-0,000432	0,07861
H2(N1)	H	7,8978	14,6391	17,2635	0,109693	0,206512
H(EA1)	H	13,0809	16,6439	21,8901	0,008751	0,13104
Ac2	H	10,4405	7,1605	12,1945	0,028529	0,223186
Ac2	H	10,473	8,8595	9,3079	0,036713	0,245375
H(EA1)	H	8,5117	17,3585	20,8157	0,020228	0,114638
H1(N1)	H	7,8765	17,4821	15,9783	0,114944	0,208699
H(EA1)	H	10,6114	19,2262	18,9201	0,03702	0,18547
Ac2	H	13,0442	6,7752	10,0234	0,028179	0,218198
O31	O	16,9003	16,3406	11,2529	-0,097373	-0,713291
O12	O	21,6017	12,6676	12,7701	-0,27691	-0,543404
O21	O	12,982	17,7525	12,3134	-0,160085	-0,714753
O11	O	14,0928	15,4978	18,2802	-0,210673	-0,644981
O22	O	11,6408	11,7703	13,4379	-0,149739	-0,774225
O32	O	15,3863	10,5293	11,7058	-0,11663	-0,726064
Zn2	Zn	17,9944	13,0382	13,0145	0,234683	0,833794
Zn1	Zn	12,4416	15,1465	14,9822	0,224819	0,650438
N2	N	18,3411	12,7529	17,005	-0,109245	-0,603628
N1	N	8,9918	16,2066	16,9185	-0,096062	-0,226385

Chart S1. Final atomic coordinates for the optimized geometry of the dimer and calculated charges.

LABELS	SPECIES	COORDINATES (a.u.)			CHARGES (e)	
		C1	X	Y	Z	INT
C22	C	13,3372	10,661	9,7057	-0,020192	0,182267
Ac1	C	12,5744	14,3262	19,1467	0,148046	0,883735
C12	C	12,9275	13,54	9,8383	0,006057	-0,21994
Ac1	C	10,5789	13,7614	21,1165	-0,078577	-0,836316
C21	C	13,313	21,4724	14,386	-0,009055	-0,289865
Ac2	C	20,0764	13,4812	16,7542	0,163205	0,930138
C11	C	11,6963	22,0026	12,0362	-0,014671	0,188967
Ac2	C	22,7448	12,8825	17,5927	-0,078518	-0,914127
H(EA2)	H	11,1594	13,9433	10,8656	0,029144	0,155632
Ac1	H	10,1283	11,7389	21,154	0,034708	0,263519
H(EA2)	H	11,6546	9,8222	8,7732	0,004514	0,065912
Ac1	H	8,8534	14,8197	20,62	0,042273	0,237137
H(EA2)	H	12,7872	14,3663	7,9245	0,022308	0,099026
H2(N2)	H	14,6646	16,5863	11,809	0,043932	0,310292
H(EA2)	H	14,9723	10,3002	8,4143	0,001121	0,07506
Ac1	H	11,1947	14,4234	22,9867	0,031456	0,280612
H1(N2)	H	16,6548	14,7118	10,2578	0,11093	0,336588
H(EA1)	H	12,0334	21,0178	15,9887	0,010917	0,126114
H2(N1)	H	8,7411	23,845	13,8008	0,049539	0,331853
H(EA1)	H	14,3422	23,2273	14,9112	0,000632	0,173209
Ac2	H	23,0119	10,8375	17,7959	0,03259	0,288482
Ac2	H	24,0699	13,5959	16,153	0,04286	0,264603
H(EA1)	H	12,9623	22,3897	10,424	0,013936	0,133515
H1(N1)	H	10,8536	25,7723	12,5878	0,063722	0,3482
H(EA1)	H	10,623	20,2773	11,552	-0,001354	0,028345
Ac2	H	23,178	13,8653	19,37	0,035657	0,305963
O31	O	12,9583	12,7359	17,4023	-0,062994	-0,602358
O12	O	13,702	9,5404	12,0878	-0,278453	-0,680039
O21	O	13,7116	16,4692	19,3702	-0,171358	-0,655943
O11	O	15,0771	19,4811	13,8803	-0,250437	-0,599793
O22	O	19,4004	15,8031	16,9013	-0,143527	-0,651985
O32	O	18,7395	11,6643	15,9269	-0,121045	-0,636527
Zn2	Zn	15,3256	11,8857	14,2856	0,230497	0,776228
Zn1	Zn	15,976	17,265	16,518	0,29483	0,810072
N2	N	15,0236	14,7099	11,3171	-0,075163	-0,646845
N1	N	9,8997	24,1101	12,2627	-0,105347	-0,861732

Chart S2. Final atomic coordinates for the optimized geometry of the C1 state and calculated charges.

LABEL S	SPECIES	COORDINATES (a.u.)			CHARGES (e)	
		C2	X	Y	Z	INT
C22	C	15,9793	13,4981	7,0169	-0,022847	-0,094859
Ac1	C	11,5476	15,783	21,5152	0,075151	0,904142
C12	C	14,2082	15,5839	8,0069	0,007367	-0,150819
Ac1	C	11,2799	16,0013	24,3442	-0,078502	-1,187966
C21	C	8,4273	18,3922	13,8585	-0,006752	-0,474787
Ac2	C	16,823	12,4629	16,7366	0,135583	0,854651
C11	C	8,6363	20,7393	12,182	-0,011552	0,130614
Ac2	C	17,2915	12,2911	19,5255	-0,063993	-0,989109
H(EA2)	H	12,2693	14,8244	8,1184	0,033778	0,131754
Ac1	H	9,7678	17,3731	24,7592	0,043223	0,353386
H(EA2)	H	15,2268	12,8378	5,1751	0,008544	0,07892
Ac1	H	13,0333	16,7206	25,1898	0,029561	0,340046
H(EA2)	H	14,2021	17,2366	6,7288	0,022673	0,108896
H2(N2)	H	13,3655	16,8664	11,7026	0,04381	0,303374
H(EA2)	H	17,8733	14,3458	6,6256	0,002509	0,142037
Ac1	H	10,7391	14,1796	25,1756	0,030256	0,305517
H1(N2)	H	16,2178	17,7844	10,6149	0,108159	0,35213
H(EA1)	H	6,8282	17,2089	13,1849	0,004527	0,173978
H2(N1)	H	10,5286	19,1245	9,2098	0,032762	0,327903
H(EA1)	H	7,9435	19,0227	15,7992	0,020208	0,179491
Ac2	H	19,1048	11,3587	19,896	0,036453	0,344065
Ac2	H	17,3317	14,2189	20,3209	0,044927	0,311439
H(EA1)	H	6,8996	21,8748	12,4229	0,017214	0,122891
H1(N1)	H	7,4788	19,3375	8,7501	0,051501	0,347131
H(EA1)	H	10,2215	21,9138	12,8678	0,010136	0,119907
Ac2	H	15,7339	11,2746	20,4543	0,046882	0,266604
O31	O	10,2334	14,1279	20,3158	-0,146755	-0,472072
O12	O	16,1615	11,4339	8,7058	-0,275042	-0,447731
O21	O	13,0344	17,2563	20,3174	-0,126537	-0,57776
O11	O	10,7219	16,9315	13,8235	-0,236301	-0,271421
O22	O	14,5646	12,916	15,8856	-0,098334	-0,407958
O32	O	18,5929	12,1536	15,1473	-0,111203	-0,536208
Zn2	Zn	16,3022	12,8121	12,0133	0,352127	0,549697
Zn1	Zn	11,6868	15,4048	16,9161	0,252287	0,353894
N2	N	14,9452	16,3204	10,6311	-0,118893	-0,628574
N1	N	9,0078	20,301	9,4632	-0,110907	-0,863203

Chart S3. Final atomic coordinates for the optimized geometry of the intermediate C2 state and calculated charges.

LABELS	SPECIES	COORDINATES (a.u.)			CHARGES (e)	
		C3	X	Y	Z	INT
C22	C	16,3293	11,6471	7,8066	-0,020783	-0,026533
Ac1	C	12,3517	15,0128	21,3433	0,077967	0,847738
C12	C	17,488	14,1974	6,9847	0,005174	-0,38596
Ac1	C	11,1399	14,7692	23,9083	-0,073264	-1,039269
C21	C	11,5617	16,9177	12,5568	0,016414	-0,197338
Ac2	C	20,1326	14,5758	16,3323	0,135066	1,022253
C11	C	9,742	18,6875	13,9308	0,001935	0,114213
Ac2	C	20,9852	14,8536	19,0505	-0,071567	-1,00535
H(EA2)	H	15,9605	15,5736	6,6352	0,030255	0,188901
Ac1	H	10,4594	16,63	24,5411	0,036129	0,328237
H(EA2)	H	14,9815	11,0655	6,3049	0,00285	0,089582
Ac1	H	12,5735	14,1409	25,2821	0,038851	0,29358
H(EA2)	H	18,6157	13,9921	5,2381	0,018117	0,154871
H2(N2)	H	19,5405	17,059	8,8617	0,114118	0,332461
H(EA2)	H	17,8777	10,2035	7,801	-0,002396	0,131141
Ac1	H	9,5823	13,4007	23,8652	0,030807	0,305728
H1(N2)	H	20,6455	14,1906	9,3964	0,097855	0,36397
H(EA1)	H	11,8668	17,6132	10,6045	0,015886	0,137307
H2(N1)	H	12,2365	21,5414	14,7432	0,055967	0,364147
H(EA1)	H	10,7338	15,0028	12,4094	0,033904	0,127009
Ac2	H	22,8531	15,7556	19,1181	0,026522	0,319767
Ac2	H	19,6109	15,9338	20,1798	0,043259	0,275838
H(EA1)	H	7,8594	18,523	13,036	0,022123	0,077012
H1(N1)	H	10,5278	22,0827	12,2212	0,052073	0,350869
H(EA1)	H	9,5058	18,0153	15,9009	0,023848	0,097593
Ac2	H	21,1272	12,9588	19,9053	0,043764	0,285864
O31	O	11,8244	13,4533	19,5756	-0,12122	-0,530196
O12	O	15,0979	11,7585	10,1583	-0,271067	-0,496604
O21	O	13,9392	16,8216	20,9424	-0,147329	-0,609403
O11	O	14,0039	16,8266	13,7777	-0,213974	-0,52484
O22	O	17,6729	14,0815	16,002	-0,156263	-0,603738
O32	O	21,5838	14,72	14,5134	-0,108517	-0,676446
Zn2	Zn	16,6768	14,2782	12,2469	0,235631	0,546413
Zn1	Zn	14,2914	15,598	17,252	0,245312	0,670907
N2	N	19,0126	15,2135	9,126	-0,107955	-0,499827
N1	N	10,4414	21,3743	14,0264	-0,10684	-0,829898

Chart S4. Final atomic coordinates for the optimized geometry of the intermediate C3 state and calculated charges.

LABELS	SPECIES	COORDINATES (a.u.)			CHARGES (e)	
		C4	X	Y	Z	INT
C22	C	14,1155	19,6107	7,9841	-0,004851	0,153323
Ac1	C	14,5761	9,4614	19,8558	0,073955	1,029617
C12	C	15,979	18,5872	6,0089	-0,010961	-0,048117
Ac1	C	13,3968	7,234	21,1949	-0,074092	-0,972091
C21	C	11,3128	13,4936	14,0259	0,027897	-0,266914
Ac2	C	18,8882	17,7988	16,8711	0,168178	0,861021
C11	C	9,4515	12,5555	15,9989	0,002255	-0,038922
Ac2	C	21,1652	19,1444	17,956	-0,079941	-0,947983
H(EA2)	H	15,1889	16,8115	5,2459	0,013634	0,126586
Ac1	H	14,2368	7,0183	23,083	0,036987	0,329257
H(EA2)	H	14,8867	21,3847	8,7947	0,009639	0,099755
Ac1	H	13,6122	5,486	20,1015	0,025629	0,230026
H(EA2)	H	17,7941	18,0953	6,954	-0,000682	0,094443
H2(N2)	H	17,2453	19,5848	2,4517	0,055941	0,359666
H(EA2)	H	12,3464	20,1291	6,9866	-0,000827	0,111335
Ac1	H	11,3652	7,6102	21,4726	0,043617	0,275764
H1(N2)	H	17,292	21,9406	4,4556	0,056784	0,391844
H(EA1)	H	10,3423	14,7411	12,6644	0,02452	0,216131
H2(N1)	H	6,9575	14,0489	18,5903	0,057444	0,342125
H(EA1)	H	12,1133	11,8742	12,9759	0,035643	0,122221
Ac2	H	21,4205	18,5844	19,9425	0,037234	0,282904
Ac2	H	22,8605	18,4976	16,9256	0,049354	0,303256
H(EA1)	H	7,9911	11,416	15,0343	0,027972	0,167333
H1(N1)	H	9,5595	15,7078	18,2532	0,055227	0,344984
H(EA1)	H	10,4638	11,2459	17,2952	-0,002528	0,055694
Ac2	H	21,0067	21,2039	17,7788	0,027408	0,29361
O31	O	15,4243	9,2106	17,5986	-0,136102	-0,61275
O12	O	13,5297	17,7571	9,8618	-0,277134	-0,630546
O21	O	14,6362	11,6288	20,9395	-0,137096	-0,709
O11	O	13,3429	14,9355	15,2048	-0,25679	-0,113351
O22	O	17,3898	19,0869	15,4713	-0,140446	-0,52298
O32	O	18,6993	15,4615	17,438	-0,138365	-0,543127
Zn2	Zn	14,6781	17,83	13,1756	0,378841	0,36258
Zn1	Zn	15,7345	13,1688	17,458	0,268392	0,624466
N2	N	16,2411	20,4046	3,8959	-0,103603	-0,94827
N1	N	8,2208	14,6979	17,2697	-0,101852	-0,82389

Chart S5. Final atomic coordinates for the optimized geometry of the intermediate C4 state and calculated charges.

LABELS	SPECIES	COORDINATES (a.u.)			CHARGES (e)	
		P	X	Y	Z	INT
C22	C	15.632	12.744	19.3326	0.025274	-0.35321
Ac1	C	14.1601	16.329	10.5869	0.074363	0.908849
C12	C	14.5308	10.7185	17.597	0.004121	0.11843
Ac1	C	13.0369	16.6675	7.9897	-0.075033	-1.029009
C21	C	18.4513	21.5111	15.0767	0.027384	-0.47506
Ac2	C	21.4637	18.7737	22.8518	0.076092	0.911862
C11	C	16.4527	23.4946	14.4912	-0.004455	0.014977
Ac2	C	23.1445	19.4962	25.0348	-0.074077	-1.088458
H(EA2)	H	16.0948	9.6386	16.7414	0.026366	0.136833
Ac1	H	11.4241	15.3803	7.7375	0.035706	0.294111
H(EA2)	H	14.0739	13.6964	20.3628	0.025544	0.208554
Ac1	H	14.4546	16.3525	6.5108	0.028337	0.284778
H(EA2)	H	13.5111	11.6778	16.0231	0.01408	0.047656
H2(N2)	H	12.4959	7.4158	18.0132	0.062878	0.333416
H(EA2)	H	16.8661	11.8447	20.7554	0.023635	0.227212
Ac1	H	12.2978	18.6088	7.8338	0.039741	0.303767
H1(N2)	H	11.2799	9.8166	19.5579	0.06008	0.374363
H(EA1)	H	19.9287	22.3629	16.2815	0.024123	0.251524
H2(N1)	H	14.1564	25.9814	16.4304	0.056427	0.349542
H(EA1)	H	19.3394	20.8618	13.2991	0.028759	0.159004
Ac2	H	22.3285	21.1076	26.0609	0.035366	0.324758
Ac2	H	23.2442	17.8949	26.3636	0.041152	0.310765
H(EA1)	H	17.3488	24.9939	13.3462	0.019699	0.164834
H1(N1)	H	14.5909	23.273	17.8801	0.059901	0.326728
H(EA1)	H	14.9648	22.6103	13.2975	0.008889	0.034901
Ac2	H	25.0584	19.9429	24.3739	0.029299	0.33189
O31	O	16.5522	16.0469	10.8585	-0.132849	-0.538525
O12	O	17.0978	14.5469	17.9199	-0.23077	-0.250231
O21	O	12.7141	16.3872	12.5338	-0.137761	-0.577279
O11	O	17.3474	19.386	16.395	-0.239958	0.083809
O22	O	22.4225	18.2273	20.6994	-0.130202	-0.539953
O32	O	19.0534	18.6844	23.1679	-0.143211	-0.570195
Zn2	Zn	18.7071	17.6365	19.4024	0.289605	0.295774
Zn1	Zn	15.9949	16.2358	14.7763	0.259712	0.354195
N2	N	12.9571	8.9685	19.0755	-0.100734	-0.889601
N1	N	15.4948	24.6388	16.8381	-0.10517	-0.841011

Chart S6. Final atomic coordinates for the optimized geometry of the final P state and calculated charges.

LABELS	Increment of charges (e)				
	<u>C1-Zn2</u>	<u>C2-C1</u>	<u>C3-C2</u>	<u>C4-C3</u>	<u>P-C4</u>
C22	0.276853	-0.277126	0.068326	0.179856	-0.506533
Ac1	-0.158203	0.020407	-0.056404	0.181879	-0.120768
C12	0.138047	0.069121	-0.235141	0.337843	0.166547
Ac1	0.031707	-0.351650	0.148697	0.067178	-0.056918
C21	-0.275305	-0.184922	0.277449	-0.069576	-0.208146
Ac2	-0.119456	-0.075487	0.167602	-0.161232	0.050841
C11	0.419136	-0.058353	-0.016401	-0.153135	0.053899
Ac2	-0.147797	-0.074982	-0.016241	0.057367	-0.140475
H(EA2)	-0.064763	-0.023878	0.057147	-0.062315	0.010247
Ac1	0.014783	0.089867	-0.025149	0.001020	-0.035146
H(EA2)	-0.060126	0.013008	0.010662	0.010173	0.108799
Ac1	-0.037914	0.102909	-0.046466	-0.063554	0.054752
H(EA2)	-0.101204	0.009870	0.045975	-0.060428	-0.046787
H2(N2)	-0.045107	-0.006918	0.029087	0.027205	-0.02625
H(EA2)	-0.034212	0.066977	-0.010896	-0.019806	0.115877
Ac1	0.036189	0.024905	0.000211	-0.029964	0.028003
H1(N2)	0.025237	0.015542	0.011840	0.027874	-0.017481
H(EA1)	0.047504	0.047864	-0.036671	0.078824	0.035393
H2(N1)	0.125341	-0.003950	0.036244	-0.022022	0.007417
H(EA1)	0.042169	0.006282	-0.052482	-0.004788	0.036783
Ac2	0.065296	0.055583	-0.024298	-0.036863	0.041854
Ac2	0.019228	0.046836	-0.035601	0.027418	0.007509
H(EA1)	0.018877	-0.010624	-0.045879	0.090321	-0.002499
H1(N1)	0.139501	-0.001069	0.003738	-0.005885	-0.018256
H(EA1)	-0.157125	0.091562	-0.022314	-0.041899	-0.020793
Ac2	0.087765	-0.039359	0.019260	0.007746	0.03828
O31	0.110933	0.130286	-0.058124	-0.082554	0.074225
O12	-0.136635	0.232308	-0.048873	-0.133942	0.380315
O21	0.058810	0.078183	-0.031643	-0.099597	0.131721
O11	0.045188	0.328372	-0.253419	0.411489	0.19716
O22	0.122240	0.244027	-0.195780	0.080758	-0.016973
O32	0.089537	0.100319	-0.140238	0.133319	-0.027068
Zn2	-0.057566	-0.226531	-0.003284	-0.183833	-0.066806
Zn1	0.159634	-0.456178	0.317013	-0.046441	-0.270271
N2	-0.043217	0.018271	0.128747	-0.448443	0.058669
N1	-0.635347	-0.001471	0.033305	0.006008	-0.017121

Chart S7. ESP charge increments or every step shown in Figures 5 and 6.

Supporting Information for

Electronic and dynamic DFT studies on the substituent effects of aminoalcohol stabilizers in sol-gel ZnO precursor

Alberto Gómez-Núñez¹, Santiago Alonso-Gil^{2,3}, Concepción López⁴, and Anna Vilà^{*,1}

¹University of Barcelona, Department of Electronics, Martí i Franquès 1, 08028 Barcelona, Spain

²University of Barcelona, Department of Organic Chemistry, Martí i Franquès 1, 08028 Barcelona, Spain

³Institute of Theoretical and Computational Chemistry, University of Barcelona, Martí i Franquès 1, 08028 Barcelona, Spain

⁴University of Barcelona, Department of Inorganic Chemistry, Martí i Franquès 1, 08028 Barcelona, Spain

Received 30 October 2015, revised 10 March 2016, accepted 14 March 2016 Published online April 2016

Keywords oxides, Car-Parrinello molecular dynamics, Gaussian software, ab-initio calculations, ZnO

*Corresponding author: e-mail anna.vila@ub.edu

Supplementary Figures:

Figure S1. Density of states (arb. units) and molecular orbitals for all 8 precursors at 0 K.

Figure S2. Evolution of the Nuclear energy (Temperature - K) and the Total energy (Hartree).

Figure S3. Evolution of $\langle \text{Zn-N} \rangle$ (Mean Zn-N distance - Angstroms) and Root Mean Square Distance (RMSD - Angstroms).

Supplementary Tables:

Table S1. Final atomic coordinates for Zn-EA at 0 K.

Table S2. Final atomic coordinates for Zn-EA-Me at 0 K.

Table S3. Final atomic coordinates for Zn-APr at 0 K.

Table S4. Final atomic coordinates for Zn-APr-Me at 0 K.

Table S5. Final atomic coordinates for Zn-AMB at 0 K.

Table S6. Final atomic coordinates for Zn-AMB-Me at 0 K.

Table S7. Final atomic coordinates for Zn-AB at 0 K.

Table S8. Final atomic coordinates for Zn-APh at 0 K.

Figure 1. Density of states and molecular orbitals for all 8 precursors at 0 K.

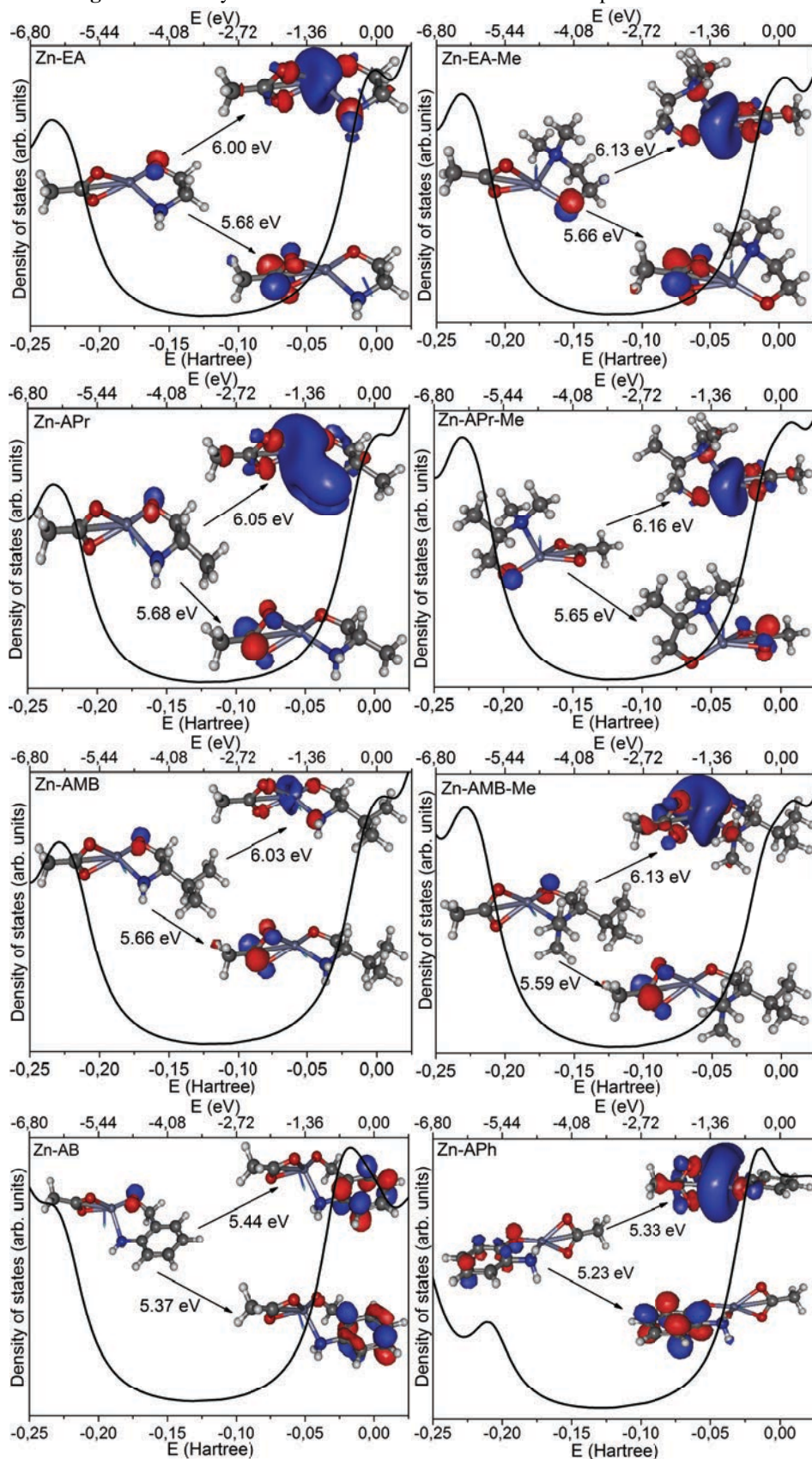


Figure S2. Evolution of the Nuclear energy (Temperature - K) and the Total energy (Hartree).

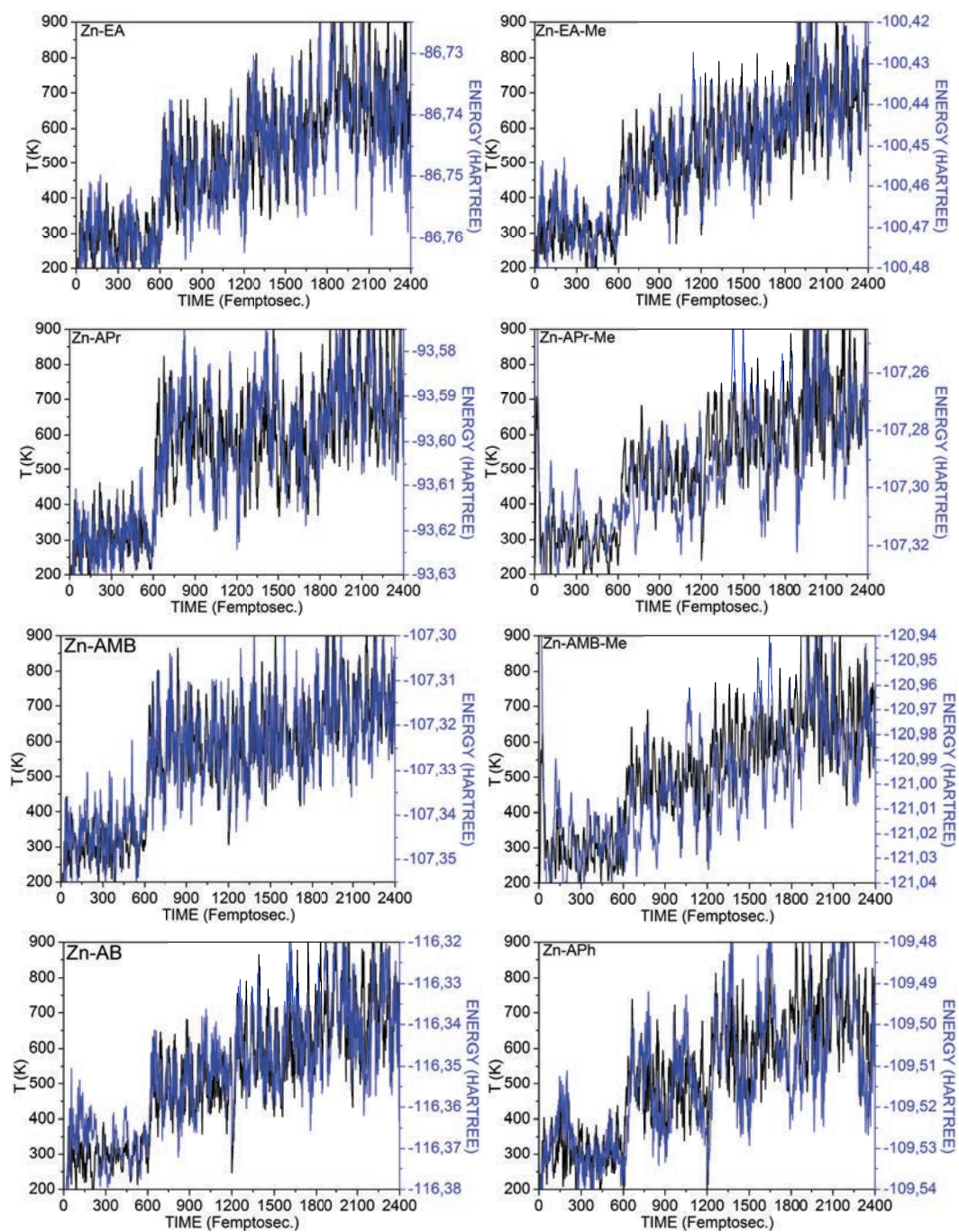


Figure S3. Evolution of $\langle \text{Zn-N} \rangle$ (Mean Zn-N distance - Angstroms) and Root Mean Square Distance (RMSD - Angstroms).

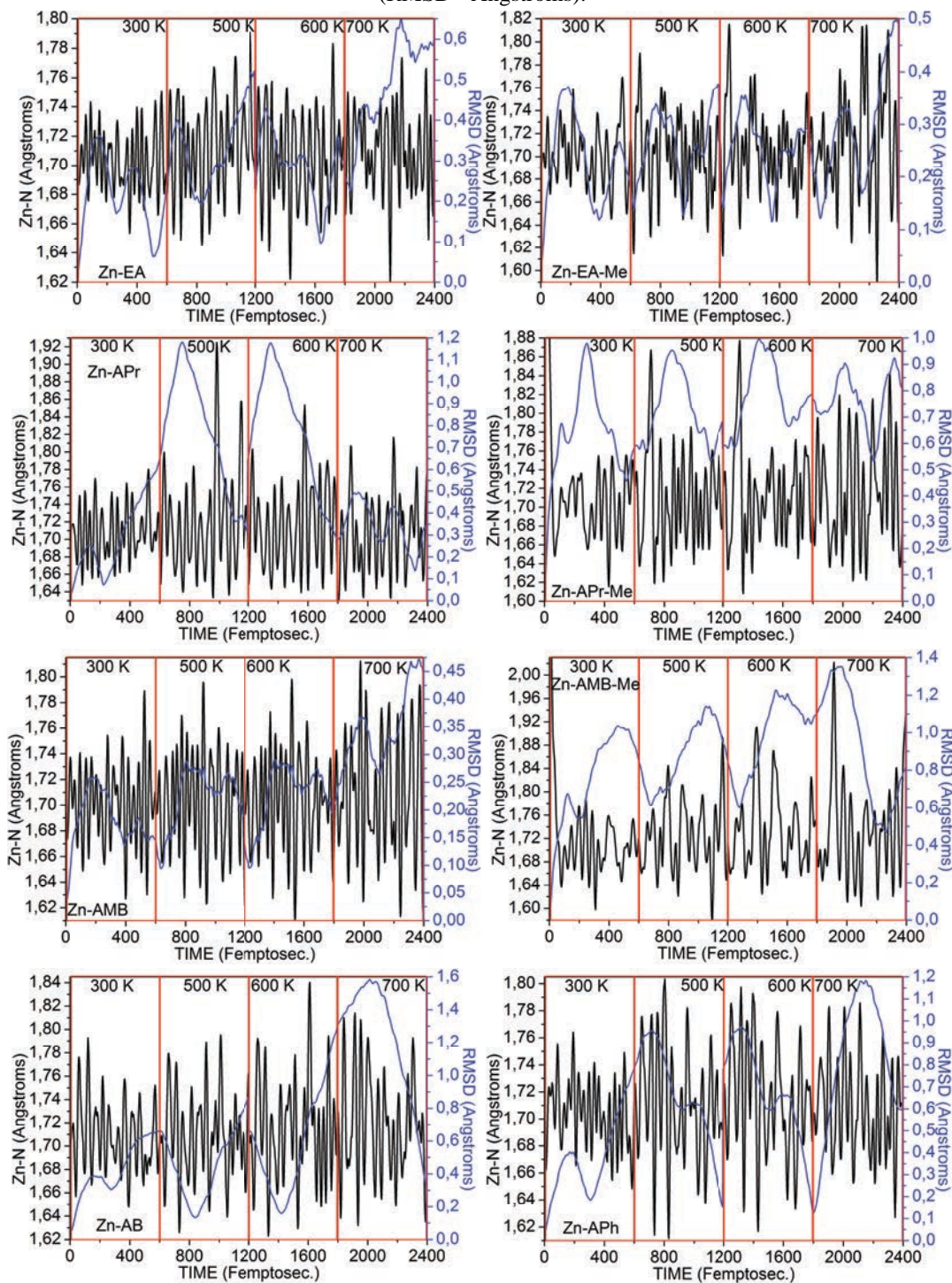


Table S1. Final atomic coordinates for Zn-EA at 0 K

	X	Y	Z
Zn	0.0000000000	0.0000000000	0.0000000000
O	0.0000000000	0.0000000000	2.1238910000
O	1.8906500000	0.0000000000	0.9310760000
O	-0.8888780000	0.8519280000	-1.4377680000
N	-0.6424750000	-1.8992800000	-0.8477020000
C	-0.9412890000	-1.4761500000	-2.2706370000
H	-1.5676280000	-2.2188200000	-2.7858550000
C	-1.6109420000	-0.0725100000	-2.2642480000
H	-1.6362330000	0.2884520000	-3.3048000000
H	-2.6610650000	-0.1763350000	-1.9259230000
H	0.0238910000	-1.4089010000	-2.7869080000
C	1.3084650000	0.0104720000	2.1061720000
C	2.1149640000	0.0634550000	3.3756000000
H	2.3902180000	1.1070000000	3.5776870000
H	3.0392610000	-0.5097540000	3.2612140000
H	1.5275970000	-0.3092240000	4.2178710000
H	-1.4890240000	-2.2117570000	-0.3626620000
H	0.0566830000	-2.6434010000	-0.8038220000

Table S2. Final atomic coordinates for Zn-EA-Me at 0 K

	X	Y	Z
Zn	0.0124120000	0.0214010000	-0.0383800000
O	-0.0008950000	-0.0827410000	2.0965610000
O	1.8892870000	0.0765740000	0.9126250000
O	-0.8887680000	0.8694500000	-1.4731870000
N	-0.6396350000	-1.8941500000	-0.8381130000
C	-0.9463410000	-1.4775140000	-2.2581630000
H	-1.5799200000	-2.2334950000	-2.7527500000
C	-1.6033240000	-0.0670850000	-2.2972420000
H	-1.5926530000	0.2702350000	-3.3461430000
H	-2.6634180000	-0.1385150000	-1.9900260000
H	0.0145200000	-1.4282560000	-2.7857370000
C	1.3048960000	-0.0025760000	2.0840500000
C	2.1048530000	0.0311690000	3.3585990000
H	2.2004060000	1.0740070000	3.6889070000
H	3.1088630000	-0.3658740000	3.1891500000
H	1.5920480000	-0.5278240000	4.1456840000
C	0.3873690000	-2.9766430000	-0.7849890000
H	0.6168290000	-3.2124580000	0.2599520000
H	0.0331230000	-3.8934080000	-1.2836850000
H	1.3070330000	-2.6408410000	-1.2744550000
C	-1.8756490000	-2.3070620000	-0.1012580000
H	-2.3083300000	-3.2230830000	-0.5347040000
H	-1.6320170000	-2.4862550000	0.9507790000
H	-2.6223100000	-1.5091600000	-0.1505260000

Table S3. Final atomic coordinates for Zn-APr at 0 K

	X	Y	Z
Zn	-0.0106000000	0.0041000000	0.0145000000
O	0.0141000000	0.0620000000	2.1348000000
O	1.8931000000	-0.0499000000	0.9287000000
O	-0.8796000000	0.8566000000	-1.4356000000
N	-0.6818000000	-1.8814000000	-0.8199000000
C	-0.9554000000	-1.4865000000	-2.2622000000
C	-1.5967000000	-0.0651000000	-2.2674000000
H	-1.5975000000	0.2929000000	-3.3096000000
H	-2.6554000000	-0.1560000000	-1.9491000000
H	0.0350000000	-1.4020000000	-2.7307000000
C	1.3225000000	0.0150000000	2.1065000000
C	2.1370000000	0.0651000000	3.3711000000
H	2.2952000000	1.1154000000	3.6495000000
H	3.1134000000	-0.3997000000	3.2147000000
H	1.5994000000	-0.4227000000	4.1887000000
H	-1.5463000000	-2.1757000000	-0.3525000000
H	-0.0024000000	-2.6435000000	-0.7564000000
C	-1.8049000000	-2.5305000000	-3.0050000000
H	-1.9887000000	-2.2037000000	-4.0365000000
H	-1.3089000000	-3.5093000000	-3.0455000000
H	-2.7826000000	-2.6585000000	-2.5188000000

Table S4. Final atomic coordinates for Zn-APr-Me at 0 K

	X	Y	Z
Zn	0.0096110000	0.0109990000	-0.0572450000
O	-0.0063630000	-0.1721120000	2.0749510000
O	1.8758350000	0.1370960000	0.9081010000
O	-0.9219980000	0.8599800000	-1.4685530000
N	-0.5883640000	-1.9030540000	-0.8929840000
C	-0.8780830000	-1.4796870000	-2.3300570000
C	-1.5729030000	-0.0813580000	-2.3348550000
H	-1.5448030000	0.2873970000	-3.3733200000
H	-2.6396040000	-0.2021670000	-2.0630540000
H	0.1175280000	-1.3393100000	-2.7766030000
C	1.2924450000	-0.0152990000	2.0727580000
C	2.0840580000	0.0228710000	3.3524000000
H	2.1210590000	1.0588250000	3.7146470000
H	3.1090730000	-0.3132360000	3.1769170000
H	1.5993690000	-0.5871570000	4.1191120000
C	-1.6582980000	-2.5189480000	-3.1574190000
H	-1.7385240000	-2.1670940000	-4.1937750000
H	-1.1600660000	-3.4963170000	-3.1793350000
H	-2.6784370000	-2.6587440000	-2.7796470000
C	0.4742080000	-2.9487400000	-0.8054680000
H	0.7246900000	-3.1244070000	0.2467590000
H	0.1511210000	-3.9033610000	-1.2488050000
H	1.3760560000	-2.6056720000	-1.3228590000
C	-1.8062000000	-2.3302150000	-0.1316010000
H	-2.1957510000	-3.2940940000	-0.4896230000
H	-1.5488550000	-2.4239070000	0.9287580000
H	-2.5908420000	-1.5739460000	-0.2287930000

Table S5. Final atomic coordinates for Zn-AMB at 0 K

	X	Y	Z
Zn	-0.0034000000	0.0193000000	0.0333000000
O	-0.0029000000	0.0338000000	2.1579000000
O	1.8894000000	-0.0045000000	0.9681000000
O	-0.8795000000	0.8754000000	-1.4069000000
N	-0.6494000000	-1.8531000000	-0.8301000000
C	-0.9361000000	-1.4631000000	-2.2723000000
C	-1.5778000000	-0.0370000000	-2.2651000000
H	-1.5573000000	0.3499000000	-3.2939000000
H	-2.6425000000	-0.1321000000	-1.9668000000
H	0.0512000000	-1.3802000000	-2.7516000000
C	1.3060000000	0.0213000000	2.1414000000
C	2.1080000000	0.0668000000	3.4143000000
H	2.2492000000	1.1156000000	3.7070000000
H	3.0926000000	-0.3818000000	3.2611000000
H	1.5702000000	-0.4391000000	4.2207000000
H	-1.5076000000	-2.1610000000	-0.3597000000
H	0.0412000000	-2.6040000000	-0.7691000000
C	-1.7792000000	-2.5348000000	-3.0146000000
H	-2.7368000000	-2.6350000000	-2.4730000000
C	-2.0998000000	-2.0931000000	-4.4635000000
H	-2.6333000000	-2.8918000000	-4.9946000000
H	-2.7280000000	-1.1964000000	-4.4918000000
H	-1.1773000000	-1.8787000000	-5.0216000000
C	-1.0823000000	-3.9173000000	-3.0267000000
H	-0.9165000000	-4.3167000000	-2.0171000000
H	-1.6947000000	-4.6501000000	-3.5671000000
H	-0.1090000000	-3.8591000000	-3.5353000000

Table S6. Final atomic coordinates for Zn-AMB-Me at 0 K

	X	Y	Z
Zn	0.0312080000	0.0070950000	-0.0673890000
O	-0.0307750000	-0.1532530000	2.0666340000
O	1.8777830000	0.1391930000	0.9399560000
O	-0.8347060000	0.8291980000	-1.5229160000
N	-0.5712310000	-1.9219000000	-0.8851440000
C	-0.9070170000	-1.5570500000	-2.3322420000
C	-1.5242080000	-0.1097930000	-2.3583910000
H	-1.4775230000	0.2481000000	-3.3955500000
H	-2.5955520000	-0.1745680000	-2.0804810000
H	0.0697830000	-1.5017360000	-2.8375320000
C	1.2678250000	0.0056630000	2.0928210000
C	2.0293350000	0.0659910000	3.3896890000
H	2.0777190000	1.1111020000	3.7231480000
H	3.0521840000	-0.2923230000	3.2478220000
H	1.5164830000	-0.5138690000	4.1612930000
C	-1.8085070000	-2.5704490000	-3.1062860000
H	-2.7809070000	-2.6217420000	-2.5916860000
C	-2.0788430000	-2.0625660000	-4.5482020000
H	-2.6320170000	-2.8228300000	-5.1147170000

H	-2.6723130000	-1.1430010000	-4.5635070000
H	-1.1375710000	-1.8677850000	-5.0819380000
C	-1.2307900000	-4.0056840000	-3.1824330000
H	-1.2020210000	-4.5038110000	-2.2073290000
H	-1.8527990000	-4.6238440000	-3.8427930000
H	-0.2120260000	-4.0016860000	-3.5946970000
C	0.5885380000	-2.8522790000	-0.7091640000
H	0.3516920000	-3.8879610000	-0.9803990000
H	1.4289620000	-2.5108860000	-1.3221450000
H	0.9025920000	-2.8369050000	0.3417290000
C	-1.7483830000	-2.3638260000	-0.0734720000
H	-2.1011440000	-3.3637440000	-0.3635100000
H	-1.4679460000	-2.3824930000	0.9854210000
H	-2.5704170000	-1.6517870000	-0.1966790000

Table S7. Final atomic coordinates for Zn-AB at 0 K

	X	Y	Z
Zn	-0.2545000000	0.3654000000	-0.3382000000
O	0.0332000000	0.0014000000	1.7481000000
O	1.6691000000	-0.2283000000	0.2422000000
O	-1.0909000000	1.6674000000	-1.4009000000
N	-1.5211000000	-1.2673000000	-1.0465000000
C	1.2837000000	-0.2852000000	1.4957000000
C	2.2534000000	-0.6365000000	2.5915000000
H	2.8009000000	0.2692000000	2.8837000000
H	2.9832000000	-1.3673000000	2.2321000000
H	1.7208000000	-1.0158000000	3.4667000000
H	-2.4337000000	-1.0247000000	-0.6475000000
H	-1.2402000000	-2.1903000000	-0.7100000000
C	-1.5207000000	-1.1921000000	-2.5130000000
C	-1.8158000000	0.0435000000	-3.1444000000
C	-1.1824000000	-2.3334000000	-3.2602000000
C	-1.1399000000	-2.2690000000	-4.6650000000
C	-1.4450000000	-1.0593000000	-5.3142000000
C	-1.7751000000	0.0783000000	-4.5532000000
H	-0.8744000000	-3.1522000000	-5.2400000000
H	-0.9534000000	-3.2689000000	-2.7514000000
H	-1.9883000000	1.0185000000	-5.0571000000
H	-1.4159000000	-0.9989000000	-6.3990000000
C	-2.1249000000	1.3096000000	-2.3390000000
H	-3.0969000000	1.1837000000	-1.8178000000
H	-2.2565000000	2.1413000000	-3.0464000000

Table S8. Final atomic coordinates for Zn-APh at 0 K

	X	Y	Z
Zn	0.0561000000	-0.1257000000	-0.2179000000
O	-0.1169000000	-0.1111000000	1.8771000000
O	1.8590000000	0.0551000000	0.8490000000
O	-0.7892000000	0.7225000000	-1.7143000000
N	-0.3111000000	-1.9937000000	-1.2232000000
C	1.1845000000	0.0179000000	1.9726000000
C	1.8664000000	0.1475000000	3.3061000000
H	1.8822000000	1.2068000000	3.5947000000
H	2.8987000000	-0.2049000000	3.2421000000
H	1.3127000000	-0.4029000000	4.0710000000
H	-0.8981000000	-2.6060000000	-0.6483000000
H	0.5706000000	-2.4780000000	-1.4186000000
C	-1.0011000000	-1.5764000000	-2.4694000000
C	-1.2084000000	-0.1745000000	-2.6472000000
C	-1.4302000000	-2.5107000000	-3.4271000000
C	-2.0808000000	-2.0726000000	-4.5936000000
C	-2.2935000000	-0.6881000000	-4.7844000000
C	-1.8667000000	0.2474000000	-3.8313000000
H	-2.4148000000	-2.7905000000	-5.3374000000
H	-1.2573000000	-3.5739000000	-3.2630000000
H	-2.0264000000	1.3125000000	-3.9701000000
H	-2.7964000000	-0.3403000000	-5.6842000000

APPENDIX



RELATED ARTICLES PRIOR TO THIS WORK



Influence of In and Ga additives onto SnO₂ inkjet-printed semiconductor



A. Vilà^{a,*}, A. Gomez^a, L. Portilla^a, J.R. Morante^{a,b}

^a Electronics Department–M2E–IN2UB, Universitat de Barcelona, Martí i Franqués 1, E-08028 Barcelona, Spain

^b Institut per a la Recerca en Energia de Catalunya, Jardins de les Dones de Negre 1, E-08930 Sant Adrià de Besòs, Spain

ARTICLE INFO

Available online 28 December 2013

Keywords:

Inkjet
SnO₂
Additives
In
Ga
TFT
Thin-film transistor

ABSTRACT

Tin oxide is a multifunctional semiconductor that offers excellent capabilities in a variety of applications such as solar cells, catalysis and chemical sensors. In this work, tin-based semiconductors have been obtained by means of solution synthesis and inkjet, and compared to similar materials with In and Ga as additives. The effect of different thermal treatments after deposition is also studied. n-Type behavior with saturation mobility > 2 cm²/Vs has been observed, and suitability as a semiconductor for thin-film transistors (TFTs) demonstrated with on/off ratios of more than 8 decades. Both In and In–Ga additives are shown to provide superior environmental stability, as well as significant change from depletion to enhancement operation modes in TFTs.

© 2013 Elsevier B.V. All rights reserved.

1. Introduction

Thin-film transistors (TFTs) based on a class of materials known as transparent amorphous oxide semiconductors have recently received much attention [1]. A combination of several technologically important features (high electron mobility, high transparency and low temperature process availability) has made these materials attractive for the active layer of TFTs for various applications such as flat-panel displays and e-papers [2]. However, the results point to its critical drawback: bias stability [3]. Under various stability tests (positive gate bias stress and negative illumination bias stress), a wide shift in threshold voltage has been reported, which is detrimental for commercial applications. To address this issue, as well as to optimize electrical performances, several compositions have been explored, but definitive results have not been demonstrated.

Most transparent metal oxide semiconductors are n-type conducting, but enabling different operation modes for the TFTs would open the possibilities for a complete transparent logic [4]. Among those, SnO₂ exhibits a direct band gap of 3.6 eV, high exciton binding energy (130 meV) and high carrier mobility (around 250 cm²/Vs) [5], which makes it a promising host material for next-generation optoelectronic devices and extensively used for transparent electrodes [6]. Even solution synthesized transparent p-type conducting thin films have been previously reported by doping SnO₂ with In or In–Ga [7–9].

To process these solution-synthesized semiconductors into TFTs, jet printing is a very promising technology because it requires no physical mask, reduces manufacturing costs and time, and enables roll-to-roll processing. Moreover, digital control of ejection and good layer-to-layer registration are provided by photoquality developments. These

characteristics are of particular interest in the large area electronics industry when the deposition of a material is required only at specific positions [10].

This work presents a simple and low-cost process to fabricate SnO₂-based TFTs via inkjet-printing. By adapting the fabrication of the reported thin films to the inkjet-printing technique and depositing the films on Si/SiO₂ substrates, n-type TFTs with different operation modes have been obtained.

2. Experimental

Three basic ink solutions were obtained by dissolving metallic chlorides in 2-methoxyethanol. When necessary, some acetic acid was added as a stabilizer to avoid precipitation. By mixing appropriate quantities on these basic inks, final solutions at concentrations of 0.35 M (slightly yellowish color), 0.35/0.07 M (clear yellowish) and 0.35/0.047/0.041 M (dark yellowish) for SnO₂ (TO), In:SnO₂ (TIO) and In–Ga:SnO₂ (TIGO) respectively were obtained. A Sn:In₂O₃ (ITO) ink with the standard ratio 90:10 wt.% for In₂O₃:SnO₂ was also synthesized by the same procedure for comparison. Further stirring at 50 °C for 24 h and aging at room temperature at least for 24 h allowed to rule out any sort of precipitation. Finally the solutions were inserted into respective inkjet cartridges by filtering them through a 0.2 μm polytetrafluoroethylene membrane filter.

Conventional microscope glass slides and heavily boron doped p+ silicon wafers with a 100.0 nm layer of silicon oxide and 50 nm aluminum or gold contacts spaced by 50 μm were used for optical, structural and electrical examinations, respectively. Prior to deposition, the substrates were ultrasonically cleaned in acetone for 30 min, rinsed with de-ionized water, dried with N₂ blowing and finally heated up to 500 °C in air for 30 min to further remove organic residue. A Dimatix 2800 inkjet material printer with piezoelectric cartridges that have a

* Corresponding author.

E-mail address: avila@el.ub.edu (A. Vilà).

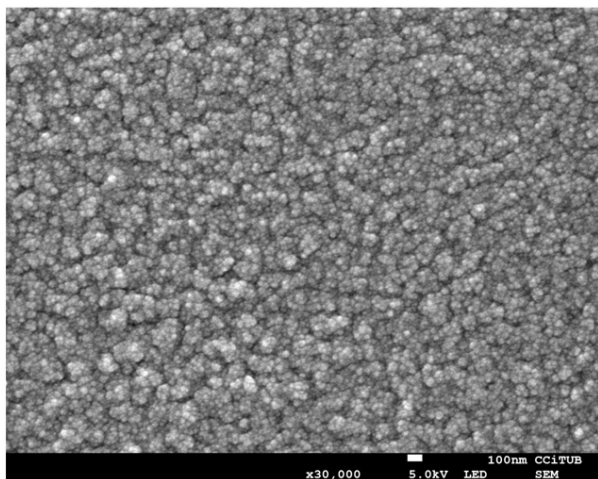


Fig. 1. FE-SEM image of a film obtained after depositing TIGO solution onto a Si wafer and annealing at 500 °C.

1 pL nominal drop volume was used to deposit films and fabricate TFTs. After deposition the films were annealed in air on a hot plate at temperatures up to 500 °C for 2 h.

UV–visible spectroscopy of the deposited films was measured using a Specord 205 from Analytik Jena, scanning electron microscopy (SEM) images were recorded with a FE-SEM Jeol JSM-840 microscope, and X-ray diffraction (XRD) patterns were obtained by means of a PANalytical X'PertPRO MPD Alpha1 powder diffractometer in Bragg–Brentano $\theta/2\theta$ geometry using the Cu $K\alpha_1$ radiation. Electrical characterization was performed using an HP4140b semiconductor parameter analyzer, in a Faraday cage under dark conditions at room temperature.

3. Results and discussion

For a preliminary characterization of the materials, the ink was deposited onto different substrates and annealed at different temperatures between 300 and 500 °C. The morphology of the obtained films was observed by SEM, showing good uniformity with granular appearance up to 30 nm in diameter (Fig. 1). On the other hand, structural characterization by XRD demonstrated the dominance of the SnO₂ cassiterite phase even in the samples with In and Ga (Fig. 2, where Al and Si peaks from the substrate appear at positions of around 38 and 69° and must not be taken into account for the layer characterization). As a first approximation to the grain dimension, direct application of the Scherrer formula to the most significant peaks indicated the presence of grains around 2.3 nm large. This small crystal dimension, together with

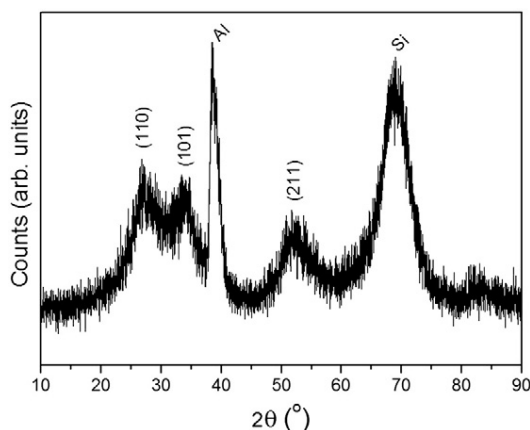


Fig. 2. XRD spectrum of the TIGO layer annealed at 500 °C, showing the main peaks of the cassiterite structure (PDF #21-1250) together with Al and Si peaks due to the substrate.

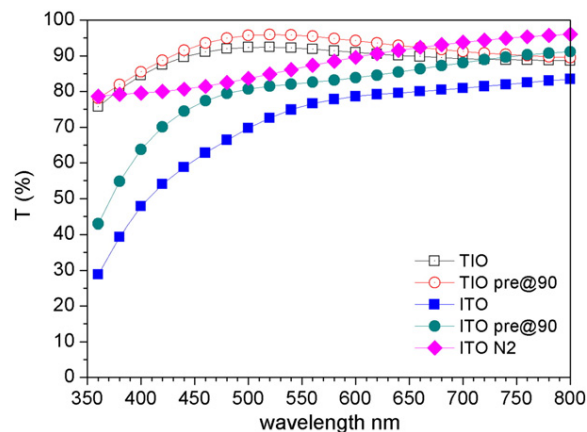


Fig. 3. Optical transmittance of the TIO and ITO layers of 250 nm thick, inkjet-printed on glass substrates with a drop spacing of 50 μm and annealed at 500 °C, without or with pre-annealing at 90 °C (marked with pre@90 °C), and an ITO film annealed at 500 °C in inert N₂ atmosphere.

the good morphological uniformity, provides quite flat layers suitable for subsequent deposits on them for more complex structures.

As an important performance of SnO₂-based semiconductors, transparency of the films deposited by inkjet was measured. UV–visible spectrometry showed a transmittance in the visible range over 85% for all films ~250 nm thick and annealed at 500 °C (Fig. 3). A slightly darker ITO layer annealed under N₂ ambient demonstrates some influence of the annealing atmosphere, as originating less stoichiometric oxides. This result agrees with a different resistivity measured using the Van der Pauw method, that gives a 2 orders of magnitude difference (from 0.008 to 0.3 $\Omega \cdot \text{cm}$ respectively) when annealed under N₂ or air atmospheres.

Top-gate staggered TFTs have been obtained by inkjet-printing the semiconductor over gold electrodes onto Si wafers (Fig. 4), and electrically characterized. As a major issue in these solution-synthesized devices, the repeatability of the electrical characteristics between TFTs is evaluated by characterizing an array of ten of such devices for each annealing temperature. The threshold voltage (V_T) and saturation mobility (μ_{sat}) were derived from a linear fitting of the plot of the square root of I_D versus V_G . Measurements were conducted one day after

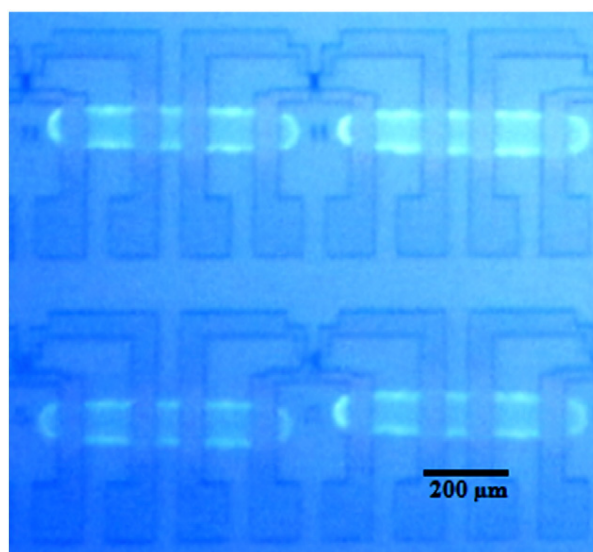


Fig. 4. Optical microscopy image of the inkjet-printed TFTs onto Si/SiO₂ substrate with gold electrodes.

Table 1Basic statistics of SnO₂ TFTs annealed at 300 °C, 400 °C and 500 °C with $V_{DS} = 1$ V.

Properties	300 °C			400 °C			500 °C		
	Mean	Median	Std. dev.	Mean	Median	Std. dev.	Mean	Median	Std. dev.
Threshold voltage (V)	-30.28	-30.25	2.50	-20.95	-18.98	10.23	-23.50	-25.41	6.57
On-off current ratio (decades)	6.76	6.76	0.50	6.74	6.57	0.58	5.73	5.85	0.63
Subthreshold slope (V/decade)	4.10	3.95	0.78	4.25	4.28	1.19	4.39	4.30	1.10
Mobility (cm ² /Vs)	0.0469	0.0476	0.0033	0.0562	0.0628	0.0137	0.0280	0.0323	0.0122

annealing at $V_{DS} = 1$ V. The array annealed at 300 °C gives the most consistent device parameters, with a V_T standard deviation of 2.50 V. A reduction in consistency is observed in the array annealed at 400 °C, showing a V_T standard deviation of 10.23 V. However, this large deviation is mainly due to one specific sample, and discarding this sample as defective gives a standard deviation of 5.21 V. All arrays show a slow subthreshold slope with a median of ~4 V/decade and standard deviation of ~1 V/decade. Consistent on-off current ratios of $>10^6$ are present in arrays annealed at 300 °C and 400 °C. Table 1 summarizes the obtained statistical parameters from the characterized TO TFT arrays.

To appreciate the full potential of the devices, output and transfer characteristics were measured in saturation mode with $V_{DS} = 20$ V. TO devices annealed at 300 °C and 400 °C (Fig. 5) showed promising properties such as mobilities >1 cm²/Vs and on-off current ratios $>10^8$ which are comparable to those of amorphous silicon TFTs [11]. Annealing at 500 °C resulted prejudicial in the device performance by reducing the mobilities to ~0.5 cm²/Vs as well as the on-off current ratio to $>10^7$. However, TFTs showed poor stability over time when stored in a transparent container enclosed in air at room temperature. In Fig. 6, a >30 V shift in the threshold voltage of the devices can be

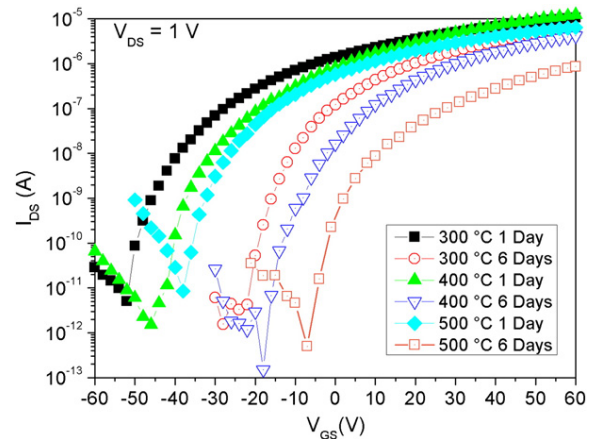


Fig. 6. Stability over time of the SnO₂ TFTs. Clear shifts in the threshold voltages can be observed just 6 days after fabrication.

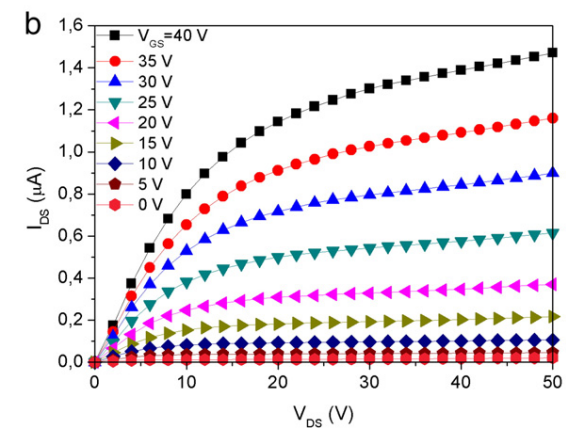
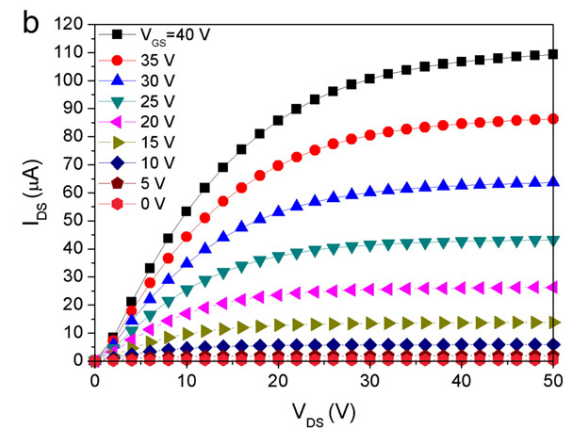
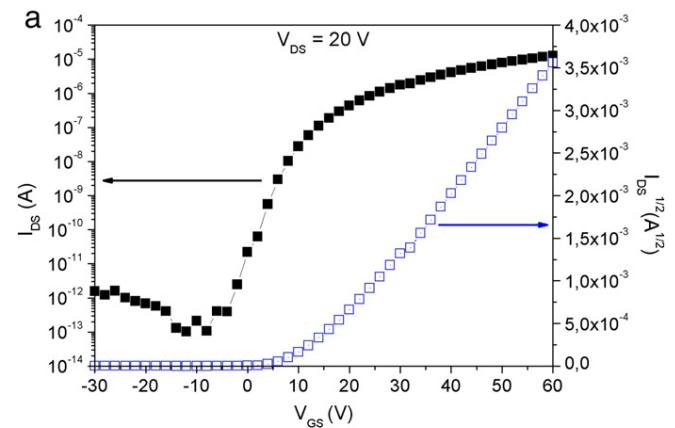
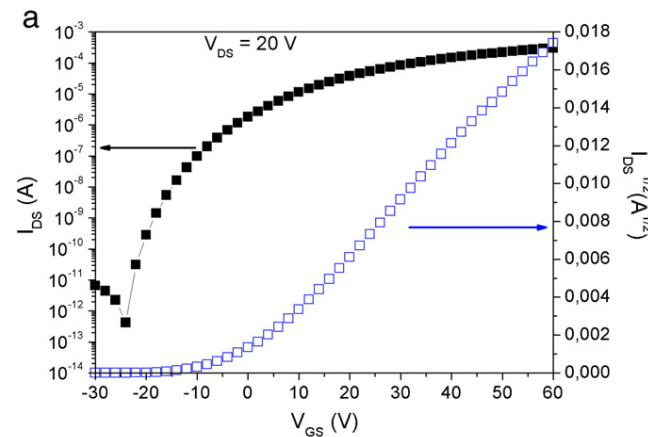


Fig. 5. Transfer and output characteristics of SnO₂ TFTs annealed at 400 °C.

Fig. 7. Transfer and output characteristics of In:SnO₂ TFTs annealed at 400 °C.

Table 2Basic statistics of In:SnO₂ TFTs annealed at 400 °C and 500 °C, measured one day after processing at V_{DS} = 20 V.

Properties	400 °C			500 °C		
	Mean	Median	Std. dev.	Mean	Median	Std. dev.
Threshold voltage (V)	18.84	15.47	7.80	−2.17	−2.28	4.73
On–off current ratio (decades)	7.76	7.90	0.27	7.09	6.97	0.47
Subthreshold slope (V/decade)	3.97	3.76	1.30	4.02	4.02	0.40
Mobility (cm ² /Vs)	0.20	0.18	0.05	0.16	0.17	0.05

observed after six days. Moreover the TFTs annealed at 500 °C change from working in depletion to enhancement mode. This instability in the V_T represents a major difficulty for the implementation of the technique in practical applications, as well as for the electrical characterization of the devices, independently of the consistency of other parameters. It is known that SnO₂ interacts with humidity [12], while the positive shift on the V_T could be attributed to oxygen adsorption [13].

Similarly, an array of ten TiO TFTs was fabricated, annealed at different temperatures and characterized (Fig. 7). The arrays annealed up to 300 °C showed no measurable electrical functionality, and the statistical characteristics of the devices annealed at 400 and 500 °C are shown in Table 2. Reaching a median mobility of only ~0.18 cm²/Vs, it is shown that indium doping reduced the saturation mobility of the TFTs. Likewise in SnO₂, annealing the films at 500 °C was prejudicial to the performance of TFTs. However, it yielded devices operating in enhancement mode with V_T ranging from −2 to +18 V as well as maintaining an on–off current ratio of ~10⁷. The stability study was performed 32 days after processing (Fig. 8), and shows that the V_T of TFTs annealed at 400 °C remained stable while a shift of ~30 V towards the TFTs annealed at 400 °C is present in the TFTs annealed at 500 °C. This could be due to the film being in an unstable state when annealed at 500 °C and overtime reaching a stable state, like the films annealed at 400 °C.

The In–Ga:SnO₂ arrays were similarly conducted with V_{DS} = 20 V. As in the previous case, the array showed no conduction after 300 °C annealing, and deviations of the devices annealed at 400 °C and 500 °C are summarized in Table 3. These devices operated in enhancement

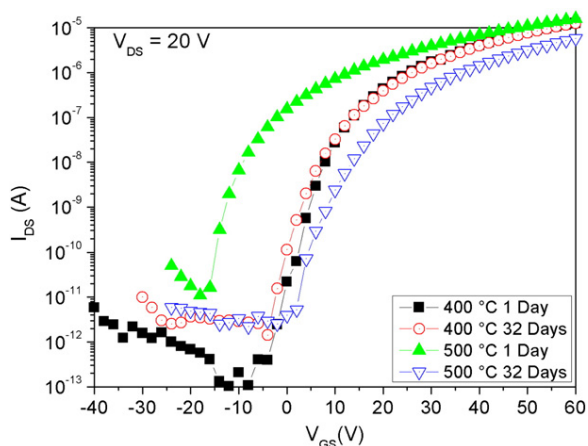


Fig. 8. Stability over time of In:SnO₂ TFTs. A clear shift in the threshold voltage can be observed on the TFT annealed at 500 °C.

Table 3Basic statistics of In–Ga:SnO₂ TFTs annealed at 400 °C and 500 °C, measured one day after processing at V_{DS} = 20 V.

Properties	400 °C			500 °C		
	Mean	Median	Std. dev.	Mean	Median	Std. dev.
Threshold voltage (V)	12.73	13.93	2.83	19.36	20.43	3.87
On–off current ratio (decades)	8.64	8.64	0.88	8.38	8.19	0.32
Subthreshold slope (V/decade)	4.19	4.43	1.43	4.01	4.14	0.40
Mobility (cm ² /Vs)	0.95	1.01	0.14	0.85	0.51	0.26

mode, reaching a median mobility of 1 cm²/Vs, with a median on–off current ratio of 10⁸. After observation, annealing at 500 °C is prejudicial just as in the previous cases. Fig. 9 shows the transfer and output graphs of specific devices. As referred to stability over time, less variation is observed in Fig. 10 on the V_T of the TiGO devices when compared to the previous channel materials. This stability over forty days can prove valuable for the fabrication of environmentally stable TFTs.

According to these results, inkjet-printing of tin oxide with indium seems to produce an instable phase that is difficult to make into devices with controlled characteristics. Although In is thought to allow for high mobility that is driven by the overlap of its large and spherical 5s orbitals that enhance the cation band conduction, instability could be related to high-density oxygen vacancies, which generate high carrier density. Thus, the improvement obtained after incorporating gallium ions can be due to the less carrier generation via oxygen vacancy formation, because Ga ions form stronger chemical bonds with O than In and Sn. This observation supports the multicomponent concept, in an effort to engineer the desired properties by mainly tailoring the cationic species incorporated in the final structures. Therefore, tin oxide with both In and Ga constitutes a promising candidate for having active layers useful to contribute to the so-called post-silicon electronic era, by playing an important role in transparent electronics.

4. Conclusions

Demonstration of the inkjet technique for the fabrication of SnO₂-based TFTs was evaluated. Transistors with similar performances to those of amorphous silicon TFTs were fabricated and characterized.

SnO₂ depletion mode n-type TFTs, with >1 cm²/Vs saturation mobilities and 10⁸ on–off current ratios, were fabricated by annealing the deposited films at 300 °C. The properties of the TFTs were further improved to saturation mobilities >2 cm²/Vs by annealing at 400 °C. However, annealing the films at 500 °C was prejudicial to the TFT performance.

By doping SnO₂ with In or In–Ga, n-type enhancement mode TFTs were fabricated. Indium-doped TFTs showed saturation mobilities of ~0.20 cm²/Vs, while In–Ga-doped TFTs had mobilities of ~1 cm²/Vs. In both cases, annealing the films at 500 °C deteriorated the TFT performance. TFTs annealed at 300 °C showed no measurable electrical properties.

In–Ga co-doping of SnO₂ was observed to have desirable properties such as >1 cm²/Vs saturation mobilities, operation in enhancement mode as well as superior environmental stability compared to that of undoped SnO₂. In all cases it is observed that a 400 °C anneal is the optimal temperature.

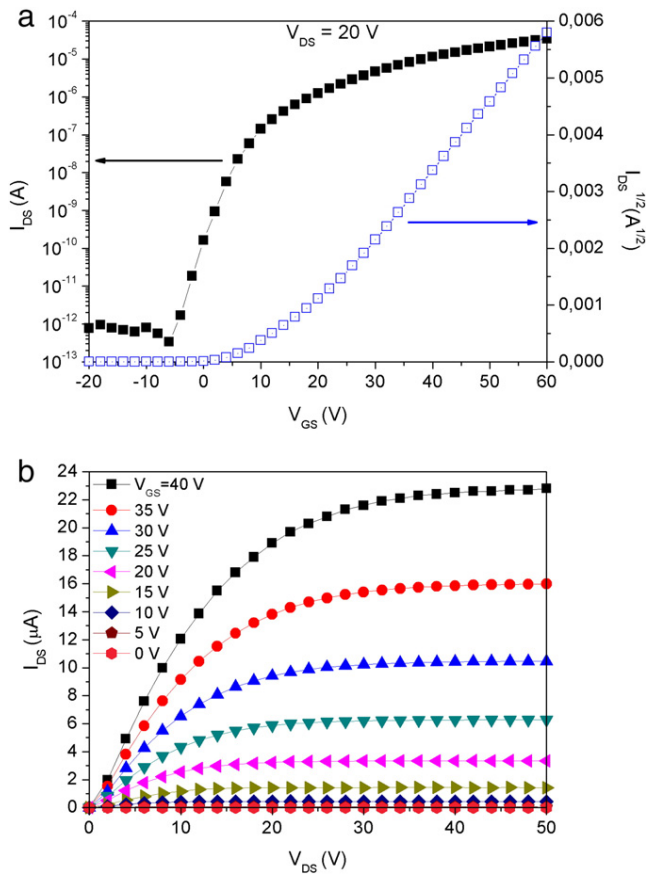


Fig. 9. Transfer and output characteristics of In-Ga:SnO₂ TFTs annealed at 400 °C.

Therefore, tin oxide with both In and Ga constitutes a promising candidate for having active layers useful to contribute to the transparent electronics era.

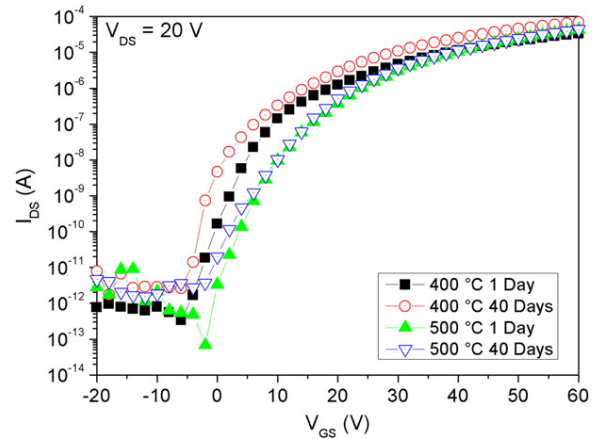


Fig. 10. Stability over time of In-Ga:SnO₂ TFTs. In this case the V_T is visibly more stable.

References

- [1] H. Hosono, J. Non-Cryst. Solids 352 (2006) 851.
- [2] T. Kamiya, H. Hosono, NPG Asia Mater. 2 (2010) 15.
- [3] M. Fakhri, P. Görrn, T. Weimann, P. Hinze, T. Riedl, Appl. Phys. Lett. 99 (2011) 123503.
- [4] H. Kawazoe, M. Yasukawa, H. Hyodo, M. Kurita, H. Yanagi, H. Hosono, Nature 389 (1997) 939.
- [5] M. Batzill, U. Diebold, Prog. Surf. Sci. 79 (2005) 47.
- [6] A.K. Singh, A. Janotti, M. Scheffer, C.G. van de Walle, Phys. Rev. Lett. 101 (2008) 055502.
- [7] Z. Ji, Z. He, Y. Song, K. Liu, Z. Ye, J. Cryst. Growth 259 (2003) 282.
- [8] Q. Mao, Z. Ji, L. Zhao, Phys. Status Solidi B 247 (2010) 299.
- [9] D. Juan, J. Zhen-Guo, Acta Phys. Sin. 56 (2007) 2388.
- [10] R.A. Street, W.S. Wong, S.E. Ready, M.L. Chabiny, A.C. Arias, S. Limb, A. Salleo, R. Lujan, Mater. Today 9 (4) (2006) 32.
- [11] S. Seo, C.G. Choi, Y.H. Hwang, B. Bae, J. Phys. D: Appl. Phys. 42 (2009) 5.
- [12] F. Hernandez-Ramirez, S. Barth, A. Tarancon, O. Casals, E. Pellicer, J. Rodriguez, A. Romano-Rodriguez, J.R. Morante, S. Mathur, Nanotechnology 18 (2007) 424016.
- [13] P.K. Nayak, J.V. Pinto, G. Gonçalves, R. Martins, E. Fortunato, J. Disp. Technol. 7 (2011) 640.

Metal Oxides as Functional Semiconductors. An Inkjet Approach

Journal:	<i>2013 MRS Spring Meeting</i>
Manuscript ID:	MRSS13-1552-S04-28.R1
Manuscript Type:	Symposium S
Date Submitted by the Author:	n/a
Complete List of Authors:	Vila, Anna Gomez, Alberto; University of Barcelona, Electronics Department Portilla, Luis; University of Barcelona, Electronics Department Cirici, Marti; University of Barcelona, Electronics Department Morante, J.; University of Barcelona, Electronics Department; Institute for Research on Energy of Catalonia, IREC, Advanced Materials for Energy
Keywords:	solution deposition, ink-jet printing, electronic material

Metal oxides as functional semiconductors. An inkjet approach

Anna Vilà¹, Alberto Gomez¹, Luis Portilla¹, Marti Cirici¹ and Juan Ramon Morante^{1,2}

¹M2E-IN2UB, Electronics Department, Marti i Franques 1, 08028-Barcelona, Spain.

²Institute for Research on Energy of Catalonia, Jardins de les Dones de Negre 1, 08930-Sant Adria de Besos, Spain.

ABSTRACT

Inkjet printing provides an interesting technology for electronic devices, as it is a versatile minimum-waste cost-effective technique for direct writing on almost every surface without need of masks or sacrificial layers. Among the fields in which it has been tested, transparent and flexible electronics offer a variety of applications ranging from large-area roll-to-roll (such as OLEDs for lighting or solar cells) to small low-consumption biocompatible devices such as biosensors.

This work aims to present some advances in the field of semiconductors synthesized by sol-gel and patterned by inkjet printing. Chemical routes are used to obtain suitable inks, based on salts of Ga, In, Zn, Cu and Sn and solvents as methoxyethanol. Inkjet printing provides thin layers 20-300nm thick, with morphology strongly depending on the materials. Different thermal treatments are tested, and some chemical and optical characterization of the obtained layers allows optimizing the technology for each material.

The effectiveness of the inks and the technique is demonstrated by the electronic behavior of thin-film transistors fabricated by the proposed technology. The different devices are compared, suggesting the properties of the different materials analyzed, as a step ahead in the development of a complete logic for such promising applications of the flexible electronics.

INTRODUCTION

Inkjet-printing is an interesting technique for fabrication of electronic devices mainly due to the fact that it is a direct-write method. Patterning and deposition can be accomplished in the same step without the need of a mask and a lift-off step used in most conventional techniques such as photolithography, vapor deposition and sputtering [1]. Therefore, the needed material and resources can be reduced drastically, and the process complexity is diminished, leading to a more flexible process, lesser waste generation and lower overall costs. These characteristics are of particular interest in the large-area electronics industry when deposition of material is required only at specific positions [2].

In recent years there has been a rapid development in the area of inorganic transparent electronics using metal oxides as the channel material [3]. In particular, important advances have been reported in ZnO-based semiconductors, which with additives such as In or Ga are proposed to provide better electrical properties and chemical stability respectively [4]. However, most metal oxide semiconductors are n-type conducting, and only little success has been reported for transparent p-type conducting films [5]. For instance, previous studies have shown that undoped SnO₂ exhibits high n-type conductivity and a direct band gap of 3.6 eV, what makes it mostly used for transparent electrodes [6]; however solution synthesized transparent p-type conducting thin films have been also reported by doping SnO₂ with In or In-Ga followed by a 500 °C annealing [7].

On the other hand, copper oxides have been reported to show p-type conductivity and have attracted interest as promising semiconductor materials for optoelectronic applications, although their non-transparency. The two common forms of copper oxides are copper (I) oxide, or cuprous oxide, Cu_2O , and copper (II) oxide or cupric oxide, CuO . Both are reported to act as p-type semiconductors with a band gap of 1.9–2.1 eV and 2.1–2.6 eV respectively. Cu_2O crystallizes in a cubic structure, while CuO in a monoclinic one [8]. Cu_2O has better mobility, and it has been regarded as a promising material for optoelectronics and solar cells applications due to its high-absorption coefficient in the visible region, non-toxicity, abundant availability, and low-cost production [9]. The p-type character of Cu_2O is attributed to the negatively charged copper vacancies (VCu), which introduce an acceptor level at about 0.3 eV above the valence band and a deep donor level at 0.9 eV from it [10].

This work aims to analyze the suitability of inkjet printing for synthesizing and patterning inorganic transparent conductor and semiconductor oxides (TCOs and TSOs respectively), as well as to provide a comparison between inks based on most current metal oxides, such as Ga, In, Zn, Cu and Sn. Repeatability and electronic properties have been assessed for so-fabricated Thin-Film Transistors (TFTs). Technology has been optimized for ZnO -, SnO_2 -based inks, and results on pure CuO are presented. The properties of the obtained electronic devices show a variety of behaviours ranging from n-type, both enhancement and depletion modes, to p-type, opening the possibility of a complete transparent metal-oxide complementary logic.

EXPERIMENT

2-Methoxyethanol (2ME) and isopropyl alcohol (IPA) were selected as solvents for ink fabrication, due to the ease to meet the fluid specifications of viscosity, surface tension, boiling point, etc. of the inkjet cartridges. However, IPA was rejected because it did not show enough stability, leading to a low printing quality due to an inappropriate jet or to unjettable inks. Several ink solutions were prepared by dissolving metallic precursors in 2ME according to the procedure described in figure 1.

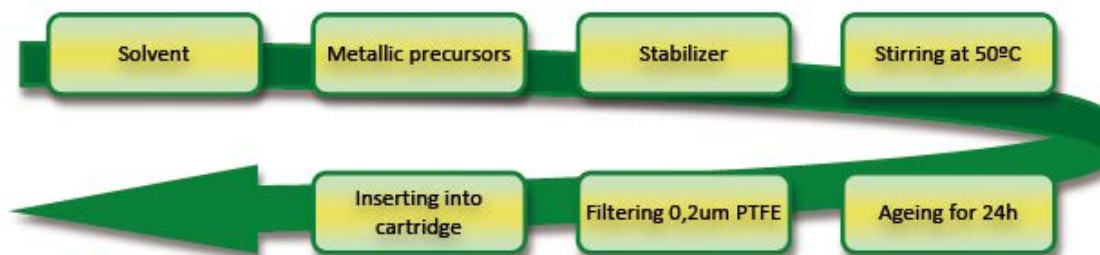
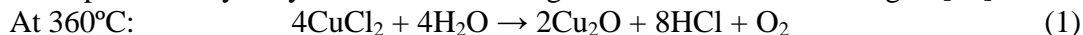


Figure 1. Flowchart for the preparation of the inks.

For the SnO_2 (TO) ink, a 0.35M solution with a slightly yellowish color was obtained after dissolving $\text{SnCl}_2 \cdot 2\text{H}_2\text{O}$ and glacial acetic acid in 2ME. Attempting to improve conductivity, an In: SnO_2 (TIO) ink was also synthesized by dissolving the same quantity of $\text{SnCl}_2 \cdot 2\text{H}_2\text{O}$ and $\text{InCl}_3 \cdot x\text{H}_2\text{O}$ in 2ME and glacial acetic acid, producing a clear 0.35M/0.07M solution with a yellowish color. But to still improve stability, some Ga was added to the previous solution, and an In-Ga: SnO_2 (TIGO) ink was produced by dissolving $\text{SnCl}_2 \cdot 2\text{H}_2\text{O}$, $\text{InCl}_3 \cdot x\text{H}_2\text{O}$ and GaCl_3 in

2ME and glacial acetic acid. A clear 0.35M/0.047M/0.041M solution with a dark yellowish color was produced.

Finally, copper-based inks were prepared by dissolving $\text{CuCl}_2 \cdot 2\text{H}_2\text{O}$ in 2ME. The cupric chloride is expected to hydrolyze and react forming a thin solid film according to [11]:



where HCl and O_2 are released at high temperature, theoretically leaving thin films of Cu_2O and CuO depending on the annealing temperature.

Films were deposited using a Dimatix 2800 materials inkjet printer with piezoelectric printheads that have a 1 pl nominal drop volume. Deposition of the films was performed on conventional microscope glass slides for optical measurements. For the characterization of the electrical properties, they were deposited on heavily boron doped p^+ silicon wafers with a 100 nm layer of silicon oxide and 50 nm gold contacts with 50 μm spacing between contacts (Figure 2). After deposition the films were annealed in air on a hot plate at temperatures up to 500 $^\circ\text{C}$ for 20 minutes. Transparent devices were obtained after deposition of both semiconductor and conductor onto ATO/ITO/glass.

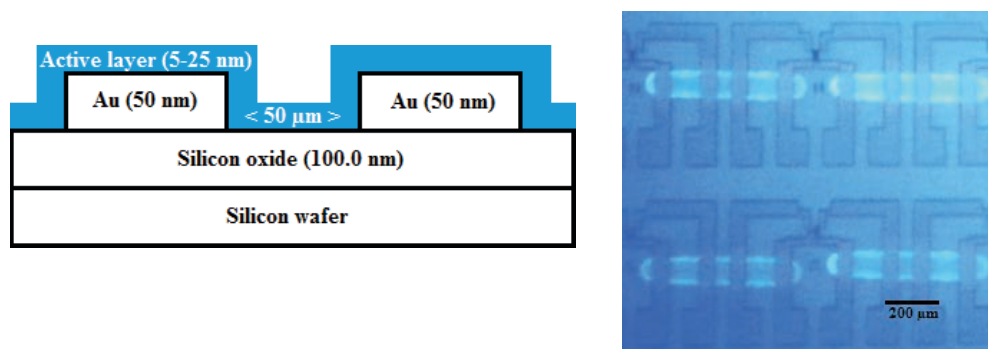


Figure 2. Schematic illustration of deposited film on Au contacts (left) and micrograph of some inkjet-printed TFTs on a Si/SiO₂ substrate with Au contacts (right).

DISCUSSION

Optical absorption, x-ray diffraction, scanning electron microscopy and energy-loss x-ray spectrometry were used to characterize the obtained films. Electrical characterization was provided by the I-V curves of the fabricated TFTs. Ga-In-Zn-oxides (GIZO) films characterization was published elsewhere [12]. Transparent n-type TFTs were demonstrated with good properties. TO films were slightly more transparent than TIO and TIGO ones (figure 3), but in all cases the printed films exhibited high transparency in the visible range, while CuO deposited films are dark. On the other hand, X-ray diffraction indicated that all these materials are essentially amorphous, with a small quantity of CuO tenorite monoclinic structure in the case of copper-based inks. In the case in which no stabilizer was used, these copper inks gave rise to large precipitations in star shape that avoided their use in TFTs.

Once good solutions are obtained, TFTs were fabricated and analyzed using an HP4140b semiconductor parameter analyzer (Figure 4). Measurements were conducted in a Faraday cage under dark conditions at room temperature. The threshold voltage (V_T) and saturation mobility (μ_{sat}) were derived from a linear fitting of the plot of the square root of intensity I_D vs. gate voltage, V_G .

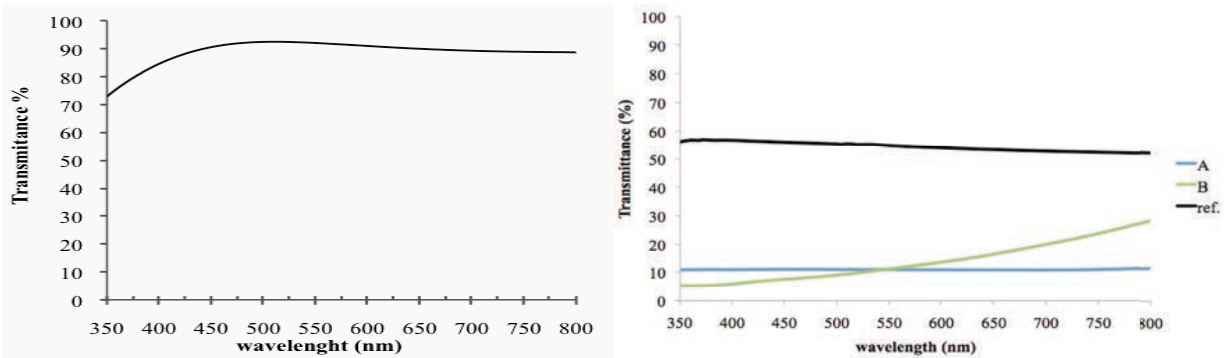


Figure 3. Optical transmittance spectra of In:SnO₂ (left) and CuO annealed at 400°C, sample A, and at 320°C, sample B, (right) inkjet-printed thin films on a conventional glass slide.

SnO₂ (TO) devices annealed at 300 and 400°C show promising properties such as >1 cm²/Vs mobilities and >10⁸ on-off current ratios which are comparable to those of amorphous silicon TFTs [13] (Figure 4). Annealing at 500 °C resulted prejudicial in the device performance by reducing both parameters. However, a >30 V shift in the V_T of the devices can be observed after some weeks stored in air at room temperature. This instability represents a major difficulty for the implementation of the technique in practical applications as well as for the electrical characterization of the devices, independently of the consistency of other parameters.

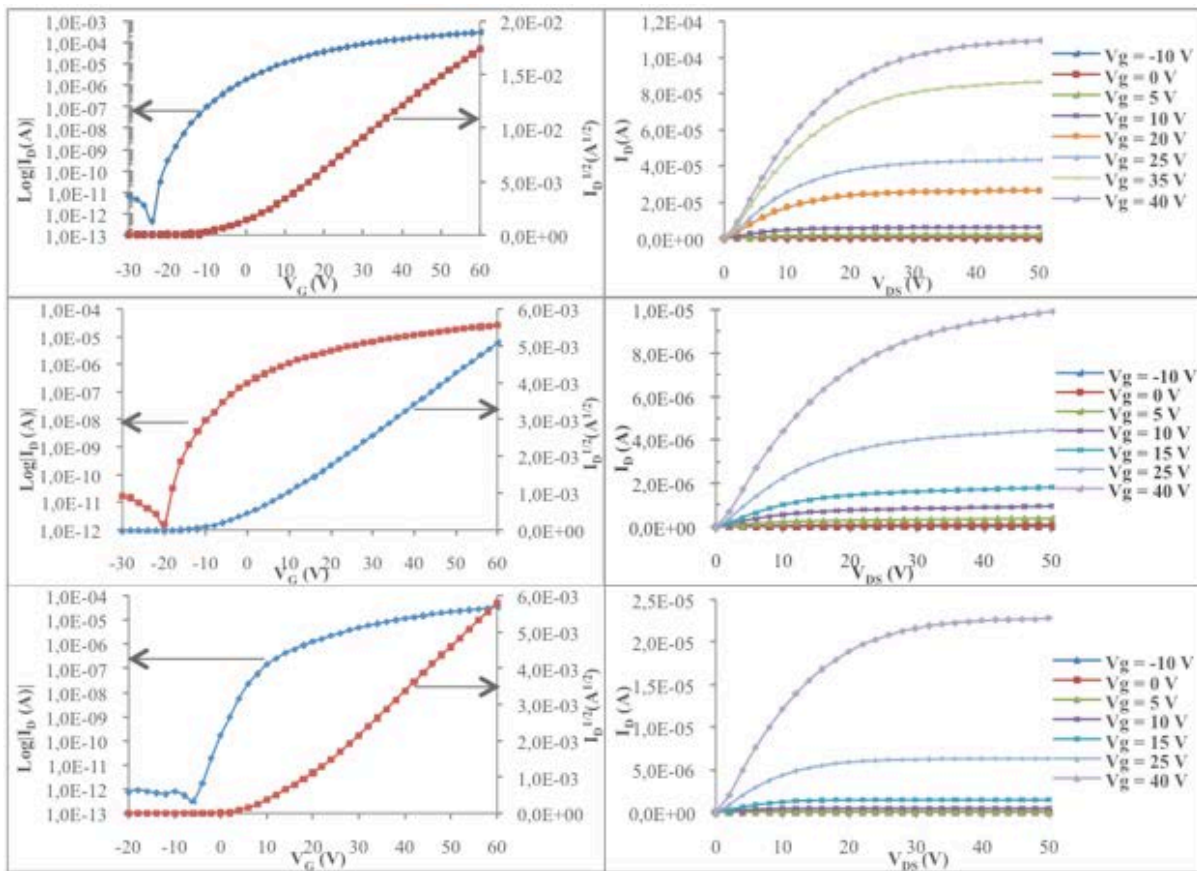


Figure 4. Transfer and output characteristics of SnO₂ (top), In:SnO₂ (middle) and In-Ga:SnO₂ (bottom) TFTs annealed at 400 °C.

In doping is expected to improve conductivity. But, reaching a median mobility of only $\sim 0.18 \text{ cm}^2/\text{Vs}$, it resulted prejudicial for the saturation mobility of the TFTs (Figure 4, middle). However, it yielded devices operating in enhancement mode with V_T ranging from -2 to $+18\text{V}$, while maintaining an on-off current ratio of $\sim 10^7$. In this case, the V_T of TFTs annealed at 400°C remained stable over time, while a V_T shift of $\sim 30\text{V}$ towards the TFTs annealed at 400°C is present in the TFTs annealed at 500°C . This could be due to the film being in an unstable state when annealed at 500°C and overtime reaching a stable state.

In-Ga:SnO₂ (TIGO) devices operated in enhancement mode, reaching a median mobility of $1 \text{ cm}^2/\text{Vs}$, with median on-off current ratio of 10^8 (Figure 4, bottom). It is observed that annealing at 500°C is prejudicial just as in the previous cases. A much smaller variation is observed on the V_T of the In-Ga devices when compared to the previous TFTs, agreeing with the expectations from the literature. This stability can prove valuable for the fabrication of environmentally stable TFTs.

Referring to CuO inkjet TFTs, their transfer and output characteristics show clearly the p-type character (Figure 5). On/off ratios were higher than 2 orders of magnitude but could not be precisely determined because of the fact that gate voltages needed to saturate were too high and destroyed the samples. Low mobilities are coherent with other experimental data obtained from bottom gate structured TFTs fabricated using CuO layers operated in a p-type enhancement mode [14], and are associated to a high estimated density of microstructural defects created during oxidation. Further research is being done to improve these mobilities.

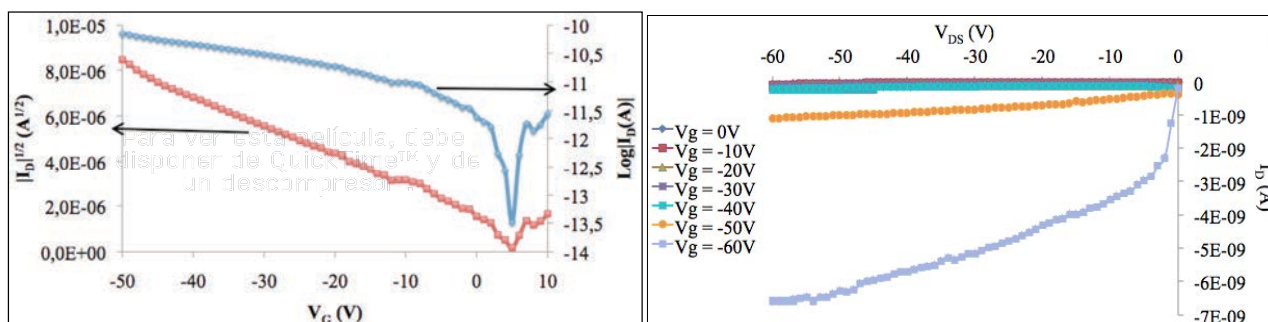


Figure 5. Transfer and output characteristics of CuO TFTs annealed at 450°C .

Table I summarizes the electrical parameters obtained for TO, TIO, TIGO and CuO TFTs obtained at different temperatures, taken one day after their fabrication. GIZO [12] and amorphous Si [13] are also included for comparison.

	TO 400°C	TIO 400°C	TIGO 400°C	GIZO 2:2:2	GIZO 2:4:2	GIZO 2:4:1	CuO 400°C	CuO 450°C	a-Si
V_T (V)	-3,8	+19	-13	-0,5	-1,5	-2,5	-48	-6,8	<3
μ_{FE} (cm^2/Vs)	2,6	0,2	0,95	0,2	0,5	3,0	$4 \cdot 10^{-8}$	$8 \cdot 10^{-4}$	<1
On/Off	$7 \cdot 10^8$	$6 \cdot 10^7$	$4 \cdot 10^8$	$9 \cdot 10^4$	$8 \cdot 10^5$	$7 \cdot 10^6$	-	-	$>10^6$
Slope (V/dec)	3,2	4,0	4,2	1,2	0,6	0,6	-	-	<0.5
Character	n-type	n-type	n-type	n-type	n-type	n-type	p-type	p-type	both
Working mode	Depl.	Enh.	Enh.	Depl.	Depl.	Depl.	Enh.	Enh.	both

Table I. Properties of the different channel materials for the analyzed TFTs and those from references [12] and [13].

CONCLUSIONS

SnO₂-based TFTs with similar performances to that of amorphous silicon TFTs were fabricated by inkjet printing and characterized. SnO₂ depletion mode n-type TFTs, with >2 cm²/Vs saturation mobilities and 10⁸ on-off current ratios were fabricated by annealing the deposited films at 400 °C. By doping SnO₂ with In or In-Ga, n-type enhancement mode TFTs were fabricated. In-doped TFTs showed saturation mobilities of ~0.20 cm²/Vs, while In-Ga ones had mobilities of ~1 cm²/Vs. Moreover, In-Ga co-doping of SnO₂ was observed to have desirable properties such as superior environmental stability. In all cases it is observed that a 400 °C anneal is the optimal temperature. Inkjet printing has also been demonstrated to be a suitable technique for fabrication of bottom-gate p-type enhancement mode CuO TFTs. Ink process has been proposed and implemented, and the measurements showed electrical properties similar to the ones obtained from other deposition techniques. Optimal temperature has been found to be 450°C, and Cu₂O has not been detected up to this temperature.

REFERENCES

- [1] T. Kawase, S. Moriya, C. J. Newsome and T. Shimoda, "Inkjet Printing of Polymeric Field-Effect Transistors and Its Applications", *J. Appl. Phys.* 44, 3649-3658 (2005).
- [2] R. Parashkov, E. Becker, T. Riedl, H-H. Johannes and W. Kowalsky. "Large Area Electronics Using Printing Methods", *Proceedings of the IEEE* 93 (7), 1321 (2005).
- [3] R.L. Hoffman, B.J. Norris and J.F. Wager, "ZnO-based transparent thin-film transistors", *Appl. Phys. Lett.* 82 (5), 733 (2003).
- [4] P. Barquinha, A.M. Vilà, G. Gonçalves, L. Pereira, R. Martins, J.R. Morante, and E. Fortunato, "Gallium–indium–zinc-oxide-based thin-film transistors: Influence of the source/drain material," *IEEE Trans. Electron Devices* 55 (4), 954–960 (2008).
- [5] H. Kawazoe, M. Yasukawa, H. Hyodo, M. Kurita, H. Yanagi, and H. Hosono, "P-type Electrical Conduction in Transparent Thin Films of CuAlO₂", *Nature* 389 [6654], 939-42 (1997).
- [6] A.K. Singh, A. Janotti, M. Scheffler and C.G. Van der Walle, "Sources of Electrical Conductivity in SnO₂", *Phys. Rev. Lett.* 101, 055502 (2008).
- [7] Z. Ji, Z. He, Y. Song, K. Liu and Z. Ye, "Fabrication and Characterization of Indium-doped p-type SnO₂ Thin Films", *J. Cryst. Growth* 259, 282-85 (2005).
- [8] M.A. Rafea and N. Roushdy, "Determination of the optical band gap for amorphous and nanocrystalline copper oxide thin films prepared by SILAR technique", *J. Phys. D-Appl. Phys* 42, 6 (2009).
- [9] P. Luzeau, X.Z. Xu, M.Lagues, N. Hess, J.P. Contour, M. Nanot, F. Queyroux, M. Touzeau and D. Pagnon, "Copper oxide thin-film growth using an oxygen plasma source", *J. Vac. Sci. Technol. A* 8 (6), 3938 (1990).
- [10] H. Raebiger, S. Lany and A. Zunger, "Origins of the p-type nature and cation deficiency in Cu₂O and related materials", *Physical Review B* 76, 045209 (2007).
- [11] S.C. Ray, "Preparation of copper oxide thin film by the sol-gel-like dip technique and study of their structural and optical properties", *Solar Energy Materials & Solar Cells* 68, 307-312 (2001).
- [12] A. Olziersky, A. Vilà, J.R. Morante, "Multicomponent oxide thin-film transistors fabricated by a double-layer inkjet printing process", *Thin Solid Films* 520, 1334-1340 (2011).
- [13] Y. Kuo. "Thin Film Transistor Technology—Past, Present, and Future". *The Electrochemical Society Interface - Spring* 2013, 55-61 (2013).
- [14] S. Y. Sung , S. Y. Kim , K. M. Jo , J. H. Lee , J. J. Kim , S. G. Kim , K. H. Chai , S. J. Pearton , D. P. Norton , Y. W. Heo , "Fabrication of p-channel thin-film transistors using CuO active layers deposited at low temperature", *Appl. Phys. Lett.* 97, 222109 (2010).

